LAWRENCE
LIVERMORE
NATIONAL
LABORATORY

UCRL-TR-230900

Gemini Planet Imager: Preliminary Design Report

B. Macintosh

May 11, 2007

Gemini Planet Imager

Preliminary Design Document
Volume 2 – Instrument Design

Lawrence Livermore National Laboratory
National Research Council, Herzberg Institute of Astrophysics
National Science Foundation Center for Adaptive Optics
University of California, Los Angeles
Jet Propulsion Laboratory
University of California, Santa Cruz
American Museum of Natural History
Université de Montréal
University of California, Berkeley

Preliminary Design Documents
Volume 1 – Scientific Motivation
Volume 2 – Instrument Design
Volume 3 – Software Documents
Volume 4 – Management Description

UCLR-TR-230900

GPI-PROJ_SYS-017

This work was performed under the auspices of the U.S. Department of Energy by University of California, Lawrence Livermore National Laboratory under Contract W-7405-Eng-48.

Table of Contents

1 Overview

For the first time in history, direct and indirect detection techniques have enabled the exploration of the environments of nearby stars on scales comparable to the size of our solar system. Precision Doppler measurements have led to the discovery of the first extrasolar planets, while high-contrast imaging has revealed new classes of objects including dusty circumstellar debris disks and brown dwarfs. The ability to recover spectrophotometry for a handful of transiting exoplanets through secondary-eclipse measurements has allowed us to begin to study exoplanets as individual entities rather than points on a mass/semi-major-axis diagram and led to new models of planetary atmospheres and interiors, even though such measurements are only available at low SNR and for a handful of planets that are automatically those most modified by their parent star. These discoveries have galvanized public interest in science and technology and have led to profound new insights into the formation and evolution of planetary systems, and they have set the stage for the next steps—direct detection and characterization of extrasolar Jovian planets with instruments such as the Gemini Planet Imager (GPI).

As discussed in Volume 1, the ability to directly detect Jovian planets opens up new regions of extrasolar planet phase space that in turn will inform our understanding of the processes through which these systems form, while near-IR spectra will advance our understanding of planetary physics. Studies of circumstellar debris disks using GPI's polarimetric mode will trace the presence of otherwise-invisible low-mass planets and measure the build-up and destruction of planetesimals.

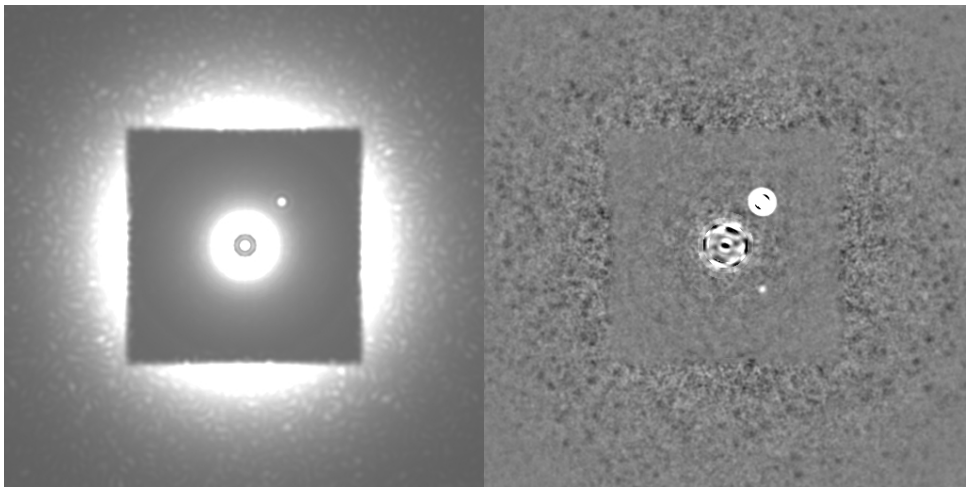

Figure 1-1: Simulated 2hr GPI exposure of a K7V star 10 pc, age=100 Myr, with 5 M_J (ΔH=12) and 1 M_J (ΔH=17.5) companions at 4 AU separation. Left: direct narrowband 1.59 μm image with no post-processing. Right: image after spectral differencing. Simulation includes both dynamic atmospheric errors (extrapolated from a 10 second exposure) and quasi-static GPI errors including wave-optics PSF and coronagraph chromaticity. See Appendix 2.25 for more discussion.

To accomplish the science mission of GPI will require a dedicated instrument capable of achieving contrast[1] of 10^{-7} or more. This is vastly better than that delivered by existing astronomical AO systems. Currently achievable contrast, about 10^{-5} at separations of 1 arc second or larger, is completely limited by quasi-static wave front errors, so that contrast does not improve with integration times longer than about 1 minute. Using the rotation of the Earth to distinguish companions from artifacts or multi-wavelength imaging improves this somewhat, but GPI will still need to surpass the performance of existing systems by one to two orders of magnitude—an improvement comparable to the transition from photographic plates to CCDs. This may sound daunting, but other areas of optical science have achieved similar breakthroughs, for example, the transition to nanometer-quality optics for extreme ultraviolet lithography, the development of MEMS wave front control devices, and the ultra-high contrast demonstrated by JPL's High Contrast Imaging Test-bed. In astronomy, the Sloan Digital Sky Survey, long baseline radio interferometry, and multi-object spectrographs have led to improvements of similar or greater order of magnitude. GPI will be the first project to apply these revolutionary techniques to ground-based astronomy, with a systems engineering approach that studies the impact of every design decision on the key metric—final detectable planet contrast.

1.1 Document roadmap

As of this writing, the Gemini Planet Imager is completing its preliminary design phase, leading to a Preliminary Design Review (PDR) on May 23-24 2007. A preliminary design must focus on verifying the practicality of the instrument design, identifying and resolving major technical risks, and (for a complex assembly such as GPI) defining the interactions and interfaces between major subsystems and verifying that the instrument as a whole will function together to meet its goals. To that end, we have produced a detailed optical and software design for each subsystem and the instrument as a whole. We have verified the performance of key algorithms and components, and made preliminary selections for most key components such as the deformable mirrors. We have completed design elements and trades not addressed in the GPI/ExAOC conceptual design such as an atmospheric dispersion corrector. The system error budget and performance modelling has been advanced to integrate the AO system, optics, coronagraph, and post-processing by the data pipeline. Finally, the mechanical design has been moved to a detailed level to verify that the instrument as a whole will meet Gemini volume, mass, and CG constraints and to define the envelope and interfaces for subsystems.

This document (Volume 2 of the PDR report) and its appendices will present the results of that study. Each major subsystem (such as the Integral Field Spectrograph) or area (such as Systems Engineering) is addressed in a chapter providing results of design trade studies and simulations, showing the design decisions that have been made, and discussing risks and work in subsequent phases. Each chapter is supported by an individual set of appendices (attached as separate files) containing more details on design studies, instrument design documents, supporting papers, etc.

Chapter 1: Introduction
Chapter 2: Systems engineering
Chapter 3: Adaptive Optics
Chapter 4: Coronagraph

[1] Defined as the ratio of detectable a companion planet's brightness to that of its parent star

Chapter 5: Integral Field Spectrograph
Chapter 6: Wavefront Calibration System
Chapter 7: Opto-mechanical Superstructure
Chapter 8: Electronics (top-level and OMSS)
Chapter 9: Top-level computer (TLC) Software
Chapter 10: Data Pipeline
Chapter 11: Integration & Test

Separately, Volume 1 reviews and motivates the GPI science program and the influence it has had on the current design. Volume 3 collates the detailed software design documents. Volume 4 updates the schedule, budget, and management plan for the project. The Operational Concept Definition Document (OCDD) and Functional and Performance Requirements Document (FPRD) document the operation and requirements of the instrument.

1.2 Instrument Overview

To achieve its contrast goal, GPI consists of six integrated subsystems. Figure 1-3 shows these subsystems in schematic form.

1. The adaptive optics (AO) system, responsible for fast measurement of the instantaneous wave front, and for providing wave front control via deformable mirrors (Chapter 3). The optical components and mechanisms for the AO system are provided by the OMSS. The AO system is the responsibility of LLNL.

2. The calibration unit (CAL) is a high-accuracy infrared wave front sensor tightly integrated with the coronagraph. It provides precise and accurate measurements of the time-averaged wave front at the science wavelength and coronagraph focal plane, so that persistent speckles caused by quasi-static wave front errors not dominate the final image (Chapter 6.) It also provides pointing, focus, and low-order aberration sensing to keep the target star centered on the coronagraph. The CAL system is the responsibility of JPL.

3. The coronagraph uses a combination of apodized masks and focal-plane stops to control diffraction and pinned speckles (Chapter 4.) The coronagraph masks are the responsibility of the AMNH team; the optical and mechanical components such as pupil wheels or collimating optics will be provided by the other subsystems.

4. The science instrument—an integral field spectrograph (IFS)—produces the final scientific image or data cube, including simultaneous multiple wavelength channels to suppress residual speckle noise (Chapter 5) and polarimetric capability. It also provides a diagnostic pupil-viewing mode and contains the final Lyot stop for the coronagraph. The IFS is being designed and constructed by UCLA in collaboration with University of Montreal.

5. The upper-level software running on the Top-Level Computer (TLC) coordinates sequencing and communication between subsystems and between GPI and the observatory software. It also provides motion control for all the subsystems (Chapter 9 and Volume 3.) In the

previous conceptual design, this was referred to as the Supervisory and Control Computer (SCC). The TLC is being produced by HIA.

6. The opto-mechanical superstructure (OMSS) mounts and connects all the subsystems and mates to the Gemini ISS. The AO optics and elements mount directly to the OMSS' optics bench, while a flexure-sensitive frame holds other major subsystems. This is in turn surrounded by an environmental enclosure with attached electronics racks. The OMSS is also the responsibility of HIA, described in Chapter 7.

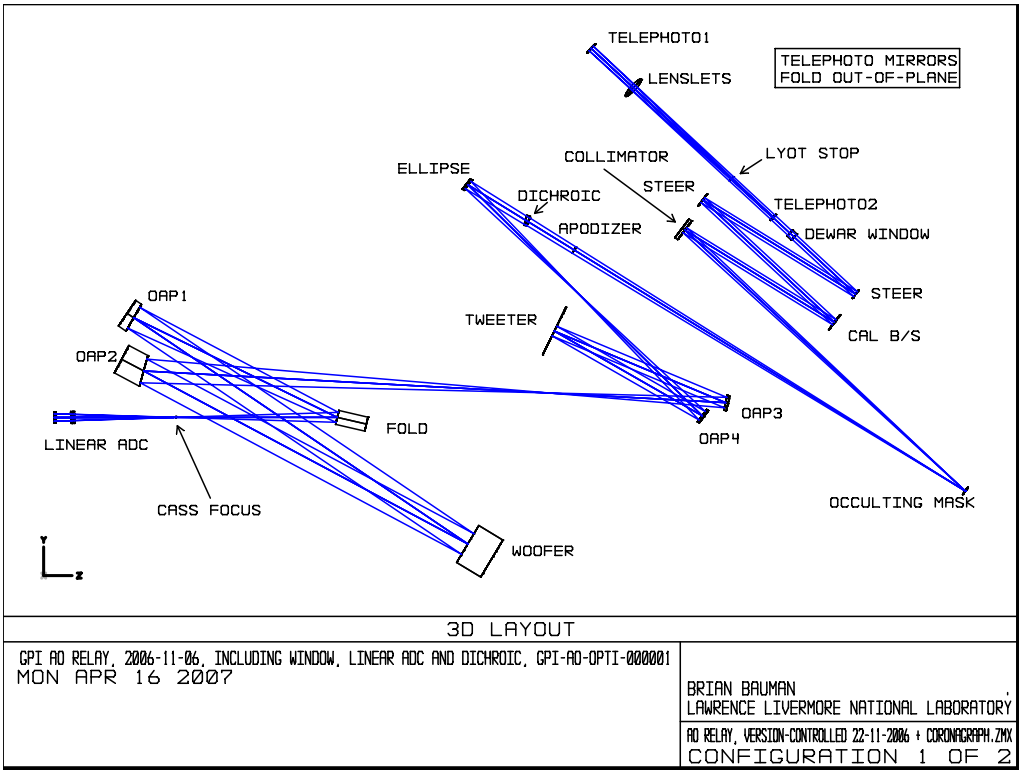

Figure 1-2: Optical layout of the science-path light up the IFS lenslet plane.

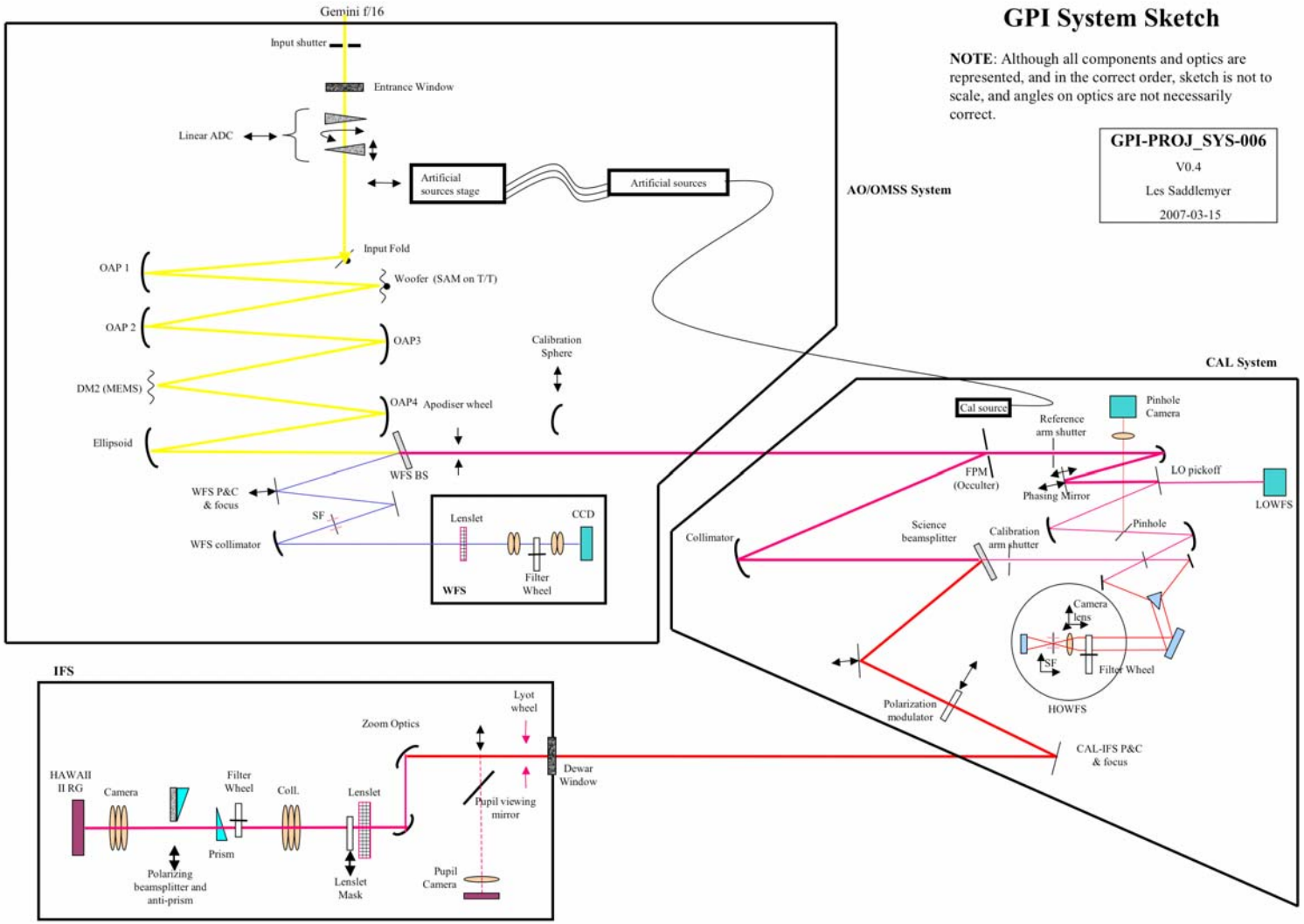

Figure 1-3: Schematic diagram of the Gemini Planet Imager showing the light path and major subsystems.

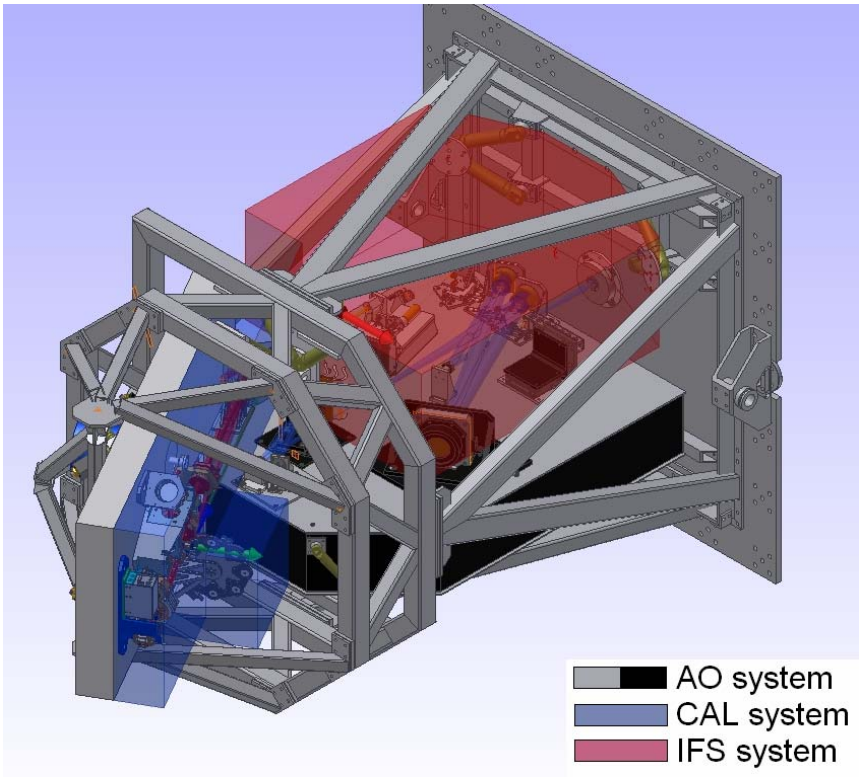

Figure 1-4: OMSS flexure-sensitive structure showing the AO, CAL, and coronagraph units. The plate on the right mounts to the Gemini ISS.

1.3 Subsystem descriptions

1.3.1 Adaptive Optics (AO) subsystem (Chapter 3)

The adaptive optics (AO) subsystem is responsible for making fast, visible-light measurements of the wavefront external to GPI (primarily atmospheric phase errors) and correcting that wavefront using its deformable mirrors. It is tightly integrated with other subsystems. All AO optics are the responsibility of HIA's OMSS, which provides mounting and motion control. (The AO optical design is therefore discussed in Chapter 7.) The AO system responds to wavefront and pointing feedback from the CAL subsystem. CAL measurements of the time-averaged IR wavefront passing through the coronagraph are used to update the reference wavefront control point (reference Shack-Hartmann centroids) for the AO system as small systematic errors build up. Similarly, pointing changes sensed by the CAL low-order wavefront sensor (LOWFS) are used to steer the pointing of the AO spatially-filtered wavefront sensor (SFWFS).

The AO system is approximately an order of magnitude more complex than previous astronomical systems, with ~1600 controlled actuators. The primary deformable mirror is a silicon micro-electro-mechanical-system (MEMS) 64 × 64-actuator continuous face sheet mirror manufactured by Boston Micromachines (section 3.5.1), with a 45-actuator-diameter region illuminated by the Gemini pupil. A

second low-order 9x9 piezostack "woofer" deformable mirror removes high-stroke low-spatial-frequency wavefront errors.

A spatially filtered Shack-Hartmann wavefront sensor (SFWFS), equipped with a fast (~ 2 kHz) CCD, measures the wavefront. The baseline detector is a Lincoln Laboratories CCID-18 device. A bandpass or short-cutoff filter limits the wavelength range seen by the SFWFS (nominally to 0.7-0.9 μm), since its performance improves with increasing Strehl at the sensing wavelength, and since the spatial filter size can only be precisely matched to spatial frequency cutoff at a single wavelength.

The baseline AO control algorithm is the Optimized-gain Fourier Controller (OFC) algorithm developed by Poyneer and Veran. This is an adaptive modal gain algorithm using Fourier modes as its basis set, allowing both efficient reconstruction and a direct match to sensor geometry and the PSF. The real-time AO computer (AOC) controls the AO system. The baseline AOC is a four-processor commercial computer such as the HP ProLiant DL580 G4, possibly supplemented by a math accelerator with a goal of 2 kHz overall operation with < 750 μs of delay. LLNL will develop the real-time AO software and computer. Optical components and mechanisms for the AO portion of the light path are part of the overall OMSS, to be constructed at HIA.

The MEMS deformable mirror is the AO subsystem component that requires most development . During PDR a consortium funded a preliminary design study by Boston Micromachines on design and packaging of a high-stroke (3–4 μm) 64 × 64 MEMS deformable mirror. Based on the results of this study, we have proceeded with a Phase 2/3 contract to complete the design and manufacture a "science-grade" device. MEMS yield and stroke goals have been met during the current study phases; the remaining concern is high-frequency "scalloping" structure on the MEMS surface (see Section 3.5.1.3).

1.3.2 Coronagraph subsystem

GPI's coronagraph is intended to block the coherent portion of the incoming wavefront that produces the familiar Airy diffraction pattern. Even with a perfectly flat wavefront, such a diffraction pattern would completely swamp the presence of any planetary signal.

The baseline coronagraph for GPI is the Apodized Pupil Lyot Coronagraph (APLC). Figure 1-5 center image shows a schematic of such a coronagraph. The light from the AO system is passes through a pupil plane A containing a transmissive apodizer mask (left-hand image) that tapers the intensity of light across the pupil. The light is brought to a focus at a focal plane mask (FPM) where the central core of the PSF is removed. The off-axis light continues to the re-imaged pupil (D). The combination of the initial apodizer and the focal plane mask channels the coherent portion of the off-axis light outside the re-imaged pupil, where it is blocked by a Lyot stop. In the final focal plane, at the design wavelength, diffraction is almost perfectly suppressed.

In the GPI architecture, the FPM is a super polished mirror with a central hole, allowing the on-axis light to pass into the CAL system. The final Lyot stop is located inside the IFS dewar.

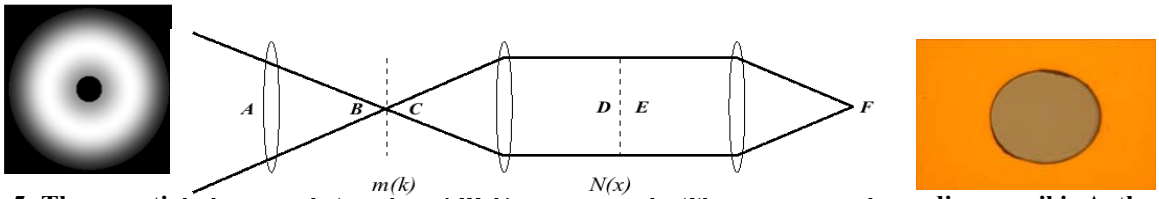

Figure 1-5: The essential planes and stops in a APLC coronagraph. The coronagraph apodizer pupil is A, the direct image at B falls on a focal plane mask (FPM) whose transmission function is m(k). The re-imaged pupil plane D, after being modified by passage through a Lyot stop E with a transmission function N(x), is sent to the coronagraphic image at F. A, D, and E are pupil planes, and B, C, and F are image planes In the GPI APLC design, Plane A is apodized with a transmission function T(x). At left: apodizer transmission profile. At right: Lyot Project reflective FPM with gold-coated mirror with occulting hole.

As with the AO system, HIA's OMSS provides the optics and mechanisms for the coronagraph. The coronagraph group at AMNH is responsible for designing, manufacturing, and characterizing these masks, including an end-to-end test bed that will be ready during the CDR phase. The apodizer masks are the most difficult item to manufacture—they must match a calculated transmission profile to ~ 1% without inducing significant wavefront errors (particularly chromatic phase errors.) Three technologies are being studied for these masks: electron-beam-sensitized (HEBS) glass, thin Inconel films, and binary microdot patterns, with a final selection based on test data coming in CDR. The APLC design does have inherent chromaticity from the scaling of the FPM size with wavelength; individual apodizers and FPMs will be matched to particular wavelength bands.

1.3.3 Calibration (CAL) subsystem

Unsensed and uncorrected non-common path wave front errors will set the limit for achievable contrast for a ground-based AO system. These errors are particularly vexing due to their temporal evolution. If they were perfectly static, they could be measured once and then subsequently removed in post processing. If they were perfectly random, they would average out to a smooth floor over long integrations. Non-common path errors that limit contrast tend to evolve over times scales of a few minutes to 10's of minutes and therefore must be sensed and corrected during a science observation. The main goal of the calibration system for GPI is to sense these wave front errors at the science wavelength and coronagraph FPM location and provide this measurement to the AO system so that they may be corrected.

The CAL system has two main sensors: a high-order wavefront sensor (HOWFS) and a low-order LOWFS. The basic principal of the HOWFS is illustrated in Figure 1-6. In essence, it is a white-light interferometer integrated with the coronagraph. At the coronagraph focal plane mask, the on-axis light and off-axis light are split. The on-axis light becomes the reference signal—it is phase-shifted and spatially filtered (not shown) to create a flat wavefront. A portion of the off-axis science light is taken to be interfered with this reference wavefront. Conventional phase-stepping techniques reconstruct the wavefront. The coronagraph itself acts to convert pure phase errors into (primarily) amplitude errors, which makes the HOWFS extremely robust against non-common-path errors in its internal optics. Measurements from the HOWFS are passed to the AO system to update its reference wavefront centroids.

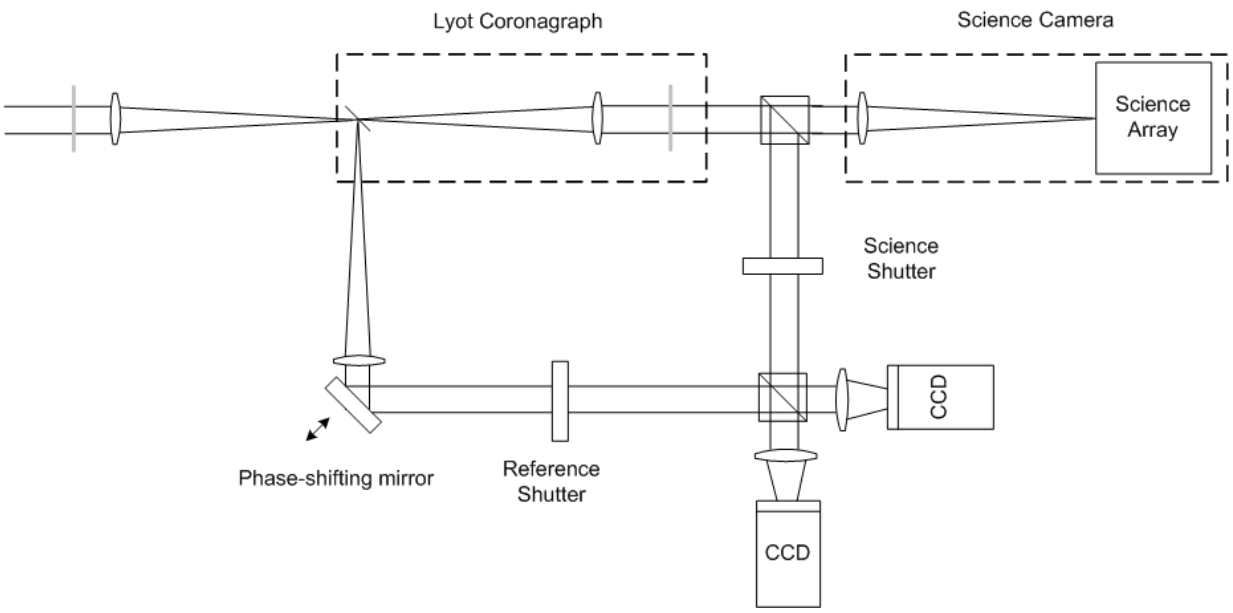

Figure 1-6: Conceptual sketch of the calibration wavefront sensor. In the actual GPI design, the interferogram images are combined onto a single IR detector rather than individual CCDs. This sketch shows a conventional Lyot coronagraph with the off-axis light transmitted past a FPM mirror.

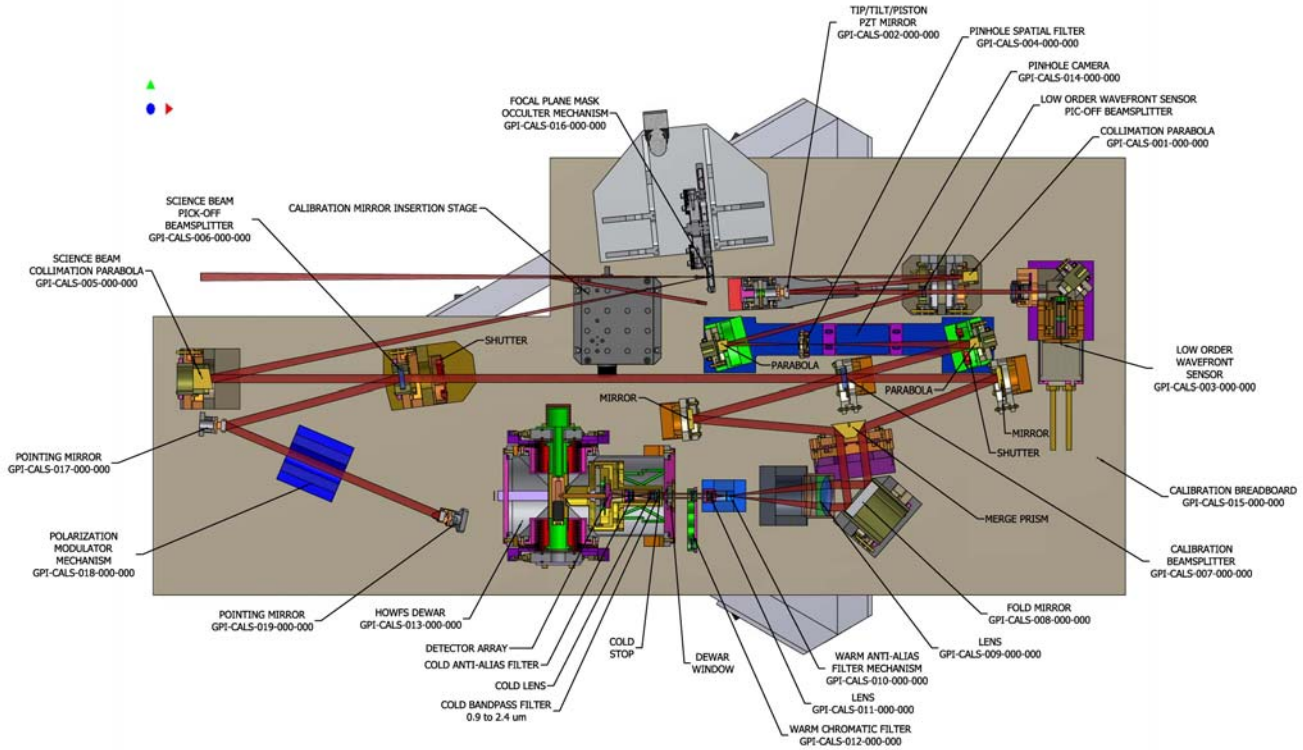

Figure 1-7: Functional layout of the calibration system.

The calibration system LOWFS channel uses a portion of the on-axis light to feed a low-order Shack-Hartmann sensor that measures wavefront components such as tip and tilt and focus. The tip and tilt and

focus information is fed back to the TLC to adjust the AO WFS position to keep the starlight centered precisely on the focal-plane occultor, while the other modes it measures are folded into the wavefront updates sent to the AOC. Figure 1-7 show the layout of the calibration system.

1.3.4 Science Integral Field Spectrograph (IFS) subsystem

The primary purpose of the GPI science instrument is to record broadband images and near-infrared spectra of planetary companions and detect circumstellar disks in linear polarization in the presence of speckle noise. A key requirement of the GPI science instrument is therefore to be able to use the wavelength-dependent properties of the PSF to distinguish true companions from noise, and similarly to use polarization to reveal circumstellar dust. To achieve this, the science instrument is a lenslet-based Integral Field Spectrograph (IFS) that records a low-resolution ($\lambda/\delta\lambda \sim 45$) spectrum of every spatial element in its 2.8 × 2.8 arc second field of view

The IFS operates over a ~ 18% bandwidth in one of the *Y, J, H* or *K'* bands at a time, selected by an internal filter wheel. A reflective zoom relay using super polished spherical mirrors produces a 0.014 arc second/lenslet plate scale. The lenslet grid slices the focal plane up into discrete subimages. After the lenslets, the light passes through a refractive camera/collimator and a prism disperser producing a grid of individual spectra corresponding to each position in the field of view. The IFS is based on the successful OSIRIS instrument, adapted to planet detection with lower spectral resolution, higher spatial resolution, and more widely spaced spectra to reduce scattered light. Figure 1-8 shows the IFS layout.

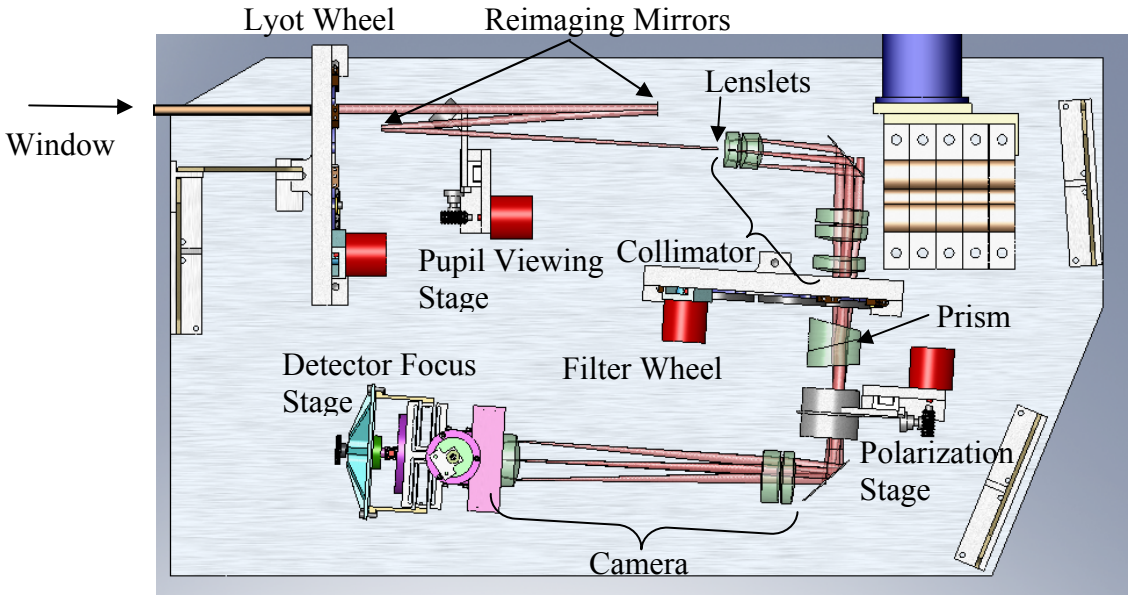

Figure 1-8: Rendering of the IFS optical layout within the vacuum chamber and cold shield.

In addition to spectroscopic capability, the IFS can carry out simultaneous dual-channel polarimetric imaging. A Wollaston prism enters the beam after the lenslets, displacing the two polarization states by half the separation between spectra. A co-mounted prism partially cancels the spectral dispersion,

producing two very-low-resolution spectra corresponding to the two orthogonal polarization states. A rotating wave plate modulator located in the OMSS provides access to the complete set of Stokes parameters.

A data pipeline, to be produced by University of Montreal, will assemble the raw IFS images into data cubes and process those to extract planetary or debris-disk signals. .

1.3.5 Opto-Electric-Mechanic Superstructure (OMSS)

The Opto-Mechanical Superstructure (OMSS) comprises two independent sub-systems: the External Frame Structure (EFS) and the Flexure Sensitive Structure (FSS). The external frame structure supports the electronics cabinets, provides proper routing of wiring and services, provides external lifting and handling features, and incorporates light tight panels to enclose the optics. The flexure sensitive structure contains the major optical sub-systems: the AO module, coronagraph, Calibration module (CAL), Integral Field Spectrograph (IFS), as well as a mechanical framework that locates and supports each optical system (Figure 1-4). The support framework is attached to the shared mounting plate in a similar fashion to the EFS. This framework, in turn, supports each optical sub-system through the use of semi-kinematic bipod flexures. The primary role of the framework is to provide a lightweight and stiff structure to locate each of the optical sub-systems. These sub-systems house the optical elements, mounts and mechanisms needed to achieve the optical requirements of the system.

A key feature of the GPI design is the use of super polished optics throughout the light path, to minimize non-common-path and phase-induced amplitude errors. A typical GPI optic requires ~ 1 nm RMS wavefront error at mid spatial frequencies, well within the state of the art for modern small optics manufacturing. We have quotes on the aspheric optics from Tinsley and have identified possible other vendors. Several optics are spherical; super polished spheres are available at moderate cost. Transmissive optics, particularly the atmospheric dispersion corrector (which is located close to a focus) remain an area of possible concern.

1.3.6 Top Level Computer (TLC) and instrument software

The components of GPI interact with each other and the observatory via the Top Level Computer (TLC) and its attendant software. Each major subsystem (AO, CAL, IFS) has its own stand-alone computer responsible for managing its “fast” functionality—detector readout, real-time AO control, etc.—while the TLC manages sequencing, communication, and “slow” motion (e.g., filter wheels and steering mirrors.)

GPI will be the first instrument to use the new Gemini Instrument API (GIAPI). We are in close contact with the Gemini software staff developing this API, but the delivery schedule for the API remains a possible risk area.

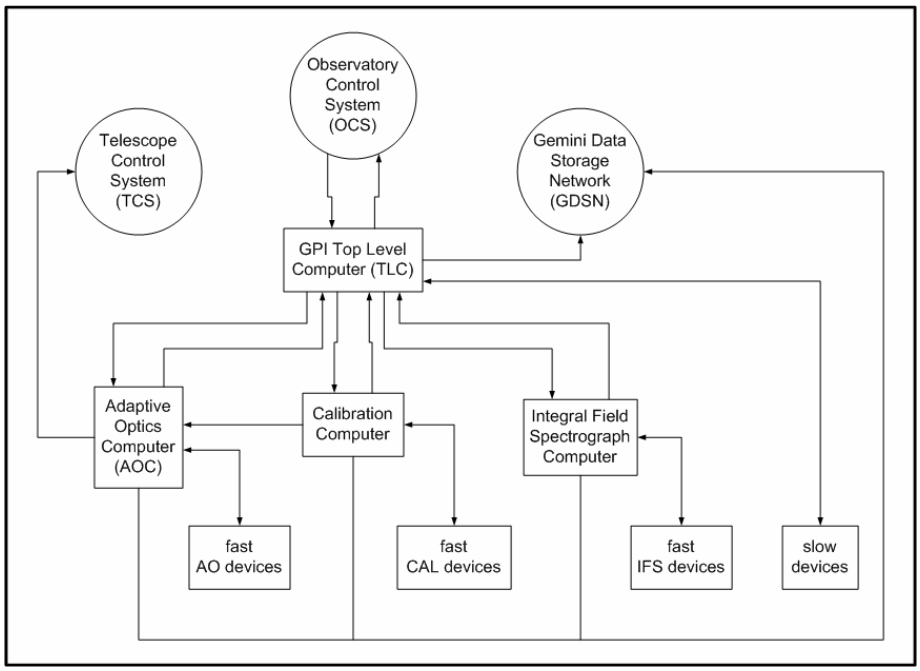

Figure 1-9: Block diagram of the GPI computer architecture.

1.3.7 Simulations and expected performance

To verify the performance of GPI we have carried out an extensive series of simulations. An integrated end-to-end simulation of GPI would be challenging: many effects, e.g., small CAL system residuals, only become apparent in integration times of tens of minutes; a prohibitively long time to simulate at sub-millisecond time resolution. We have therefore used four families of simulations to evaluate the capabilities of each subsystem and combined their results through analytic performance modelling:

- Adaptive optics (AO) simulations (see Section 3.7). These are highly detailed simulations of the AO control loop, including multi-layer atmospheres, woofer/tweeter correction, and the full GPI AOC algorithm set. The resulting phase screens are fed through the APLC to produce far-field images. These simulations have been run for timescales of up to 30 seconds to e.g. evaluate the effects of residual atmospheric speckles on final image contrast.

- Static wave-optics simulations (see Appendix 2.25). These simulations use a Talbot formalism to propagate phase and intensity from arbitrary surfaces within the system, to evaluate the chromaticity and structure of the quasi-static components of the final GPI PSF. These include a full APLC simulation and speckle-suppression post-processing.

- APLC high-res simulations: Using a new numerical approach, we can carry out simulations of the APLC with a resolution in the focal plane of up to 0.01 lambda/D, allowing us to study small misalignments, deviations in the shape of the FPM, etc. These simulations have also been used for coronagraph tolerancing (e.g. sensitivity to focus errors.)

- CAL system simulations: these simulate the end-to-end operation of the CAL interferometer. Input wavefronts are provided by a simple statistical simulation of the AO system and used to determine the ability of the CAL system to measure small static wavefront offset, evaluate the photometric signal to noise, etc.

The results of these simulations (primarily the first two) have been combined analytically to produce final-contrast predictions such as Figure 1-10.

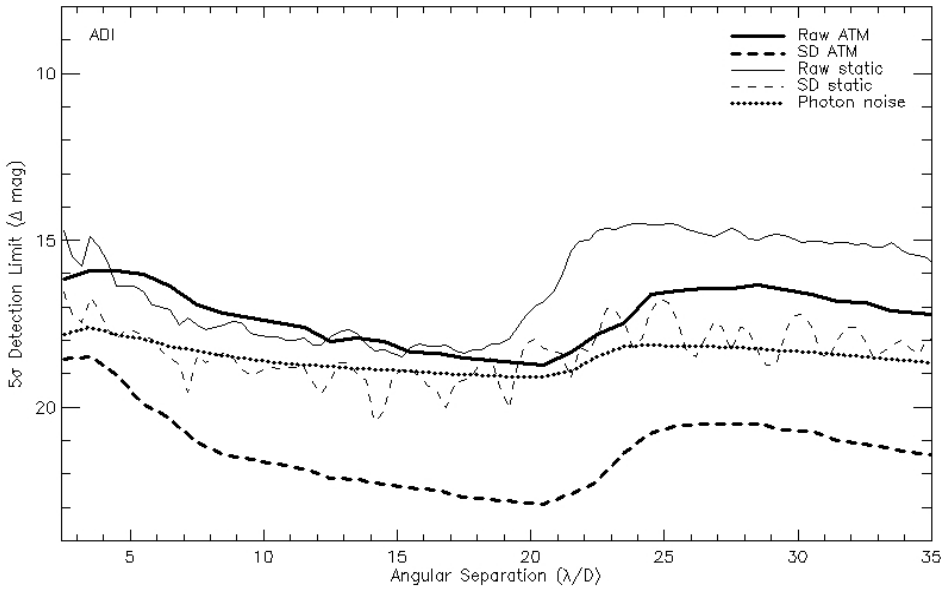

Figure 1-10: Contrast prediction for 2-hour exposure on a *H* = 5, *I* = 6 mag. target star, evaluated in a 4% bandpass at 1.59 µm. The thick solid line shows the 5-sigma speckle contrast in the raw image. The two solid lines show the raw contrast for residual atmospheric speckle noise (thick) and for static speckles (thin). The two dashed lines show the contrast after spectral differencing for atmospheric specklse (thick) and for static speckles (thin). The dotted line represents the estimated photon noise.

1.3.8 Risk areas

The PDR phase has paid particular attention to technical risk areas. As discussed in the Systems Engineering section (Chapter 2) and in individual chapters, most technical risks have been adequately addressed; for example, instrument flexure is well within our ability to tolerate (Chapter 7), SNR on the CAL system is easily adequate with available detector technology (Chapter 6), etc.

Two areas of significant technical risk remain. The first is the development of the MEMS deformable mirror. Boston Micromachines has succeeded in designing a 4096-actuator MEMS mirror that meets our stroke, yield, and RMS wavefront error requirements. However, sub-actuator "scalloping" of the mirror surface remains a concern; although the RMS figure of the mirror is good (< 10 nm RMS), the scalloping can reach 50 nm or more peak-to-valley over portions of the mirror near its edge. Fraunhofer optical modelling indicates this level is still tolerable, but full Fresnel optics modelling is necessary to verify this conclusion and set final requirements on the MEMS peak-to-valley surface. Boston

Micromachines is also working on improving this surface quality (see Appendix 3.13.) Finally, once the APLC is implemented on the UCSC MEMS testbed, we will be able to verify the effects of the scalloping on high-contrast far-field images. See Section 3.5.1.3 for a discussion of this effect.

Second, the apodizer component of the APLC remains a technical risk. Material samples of IR-doped HEBS glass, the original baseline apodizer, show significant wavefront errors (see Chapter 4 and appendices), which are larger than previous visible-light-optimized samples. We are working with the manufacturer to explore the source of these aberrations, and also exploring alternative apodizer technologies as discussed in Chapter 4. Samples of these are now in-hand and will be characterized in the laboratory at AMNH and on the UCSC test bed. AMNH is constructing a highly capable IR coronagraph test bed that will be operational in the latter half of CDR, allowing a final technology selection and validation before the critical design review.

2 Systems Engineering

This section covers topics apply to the instrument as a whole such as interfaces, system-level error budgets and performance models, as well as risk analysis. In many cases related topics are treated in greater detail in individual chapters which will be referenced here.

2.1 GPI contrast design philosophy

Classical AO systems – and indeed most optical instruments – are ultimately designed based on an image quality error budget. The ultimate metric of success is the sharpness of the final image delivered to the focal plane, whether that sharpness is measured by spot size quantities such as FWHM or wave front quantities such as RMS wave front error or Strehl ratio.

Extreme AO systems must be governed by a different philosophy. The ultimate metric of success is the detectability of a faint companion near a bright star, which in turn flows not just from the Strehl ratio of the companion but from the detailed behavior of the halo of scattered light surrounding the star. The overall intensity of that halo at an angle θ is determined, to second order, by the wave front error spatial power spectrum evaluated at spatial frequency $\theta/(\lambda/d)$ in cycles per aperture. High spatial frequency errors, scattering light far beyond the region of interest, and low spatial frequency errors, moving light around behind the coronagraph mask, are therefore much less critical than mid spatial frequency errors from 3-22 cycles/pupil.

Equally critical is the temporal behavior of errors. Detectability depends not just on the local intensity of scattered light but on the smoothness of the scattered light halo. Unbiased error sources, such as atmospheric errors, will ultimately (albeit slowly) average out to produce a smooth halo; any bias to this process will produce a pattern of fixed speckles that could swamp the signal of a planet.

The key optical principals underlying the GPI design are:

(1) Uncorrected static wave front errors must be ~1-2 nm over the mid-spatial frequency range.

(2) The point at which the wave front must be most correct is the coronagraph focal plane. Errors up to that point can scatter light from the PSF core into speckles in the wings, reducing contrast. After that point, the total available intensity has been reduced, and errors are less able to scatter light

(3) Optical errors after the lenslet plane are even less significant; speeding the sub-divided beam up with lenslets sharply reduces the opportunity for light to scatter between adjacent spatial elements

(4) For multiwavelength speckle suppression to work effectively, the static optical errors before the lenslet array must be identical (at the nm level) between different wavelength channels.

(5) The effects of internal wave front errors will never be perfectly corrected in both phase and intensity. Using the highest quality optics practical will minimize static wave front effects.

(6) Optical errors on surfaces close to focus will have the longest propagation distance to reach a pupil plane and hence see the most phase to amplitude mixing. As a result, optics near focus should be minimized and of the highest quality. (See Appendix 2.25)

It is worth distinguishing between several different optical paths; static optical errors in each will be correctable to the AO system to different levels, and the residual uncorrected errors will have different impacts on final contrast.

Pure common path: optics before the dichroic. These are sensed by the fast WFS (modulo chromaticity issues) and should be corrected. If WFS operates correctly (and the spatial filter should insure that it does), the only constraint on these optics is the extent to which they cause residual intensity errors after propagation to the pupil plane and the extent to which they cause different aberrations across an IR band.

IR common path: after the dichroic but before the coronagraph focal plane. These are sensed by the calibration WFS, which will cause these errors to also be corrected. The main effect will be (a) intensity errors as above, and (b) changes in this path that occur too quickly for the calibration system to correct.

Post-coronagraph IR common path: after the coronagraph focal plane but before the beam-splitter for the cal system. These will be partially sensed by the calibration WFS but (as with all post-coronagraph errors) cannot be corrected by the AO system, but have less effect on contrast.

Post coronagraph non-common path: after the coronagraph focal plane and after the calibration beam-splitter. These errors are unsensed (except through daytime calibration procedures using the science camera such as phase retrieval), but again have little effect on contrast.

Errors after the coronagraph focal spot are not as bad as those before the coronagraph since there is less light left for them to scatter, but are effectively uncorrectable and can still have two detrimental effects two reasons: (a) they reduce the off-axis (planet) strehl ratio, and (b) they may scatter light coming from the uncorrected PSF halo into quasi-static patterns. To first order the scattered light intensity is proportional to $(1\text{-}S)\sigma_{pc}^2$ where S is the Strehl ratio and σ_{pc}^2 is the WFE of the post-coronagraph optics. This results in comparable requirements on the post-coronagraph optics. (Because these errors are after the focal plane stop they should not be corrected - if the AO system control point is adjusted to fix them the WF hitting the focal plane stop will get worse, resulting in degraded images.) Since the calibration system primarily measures an intensity signal (the coronagraph acts to convert phase errors into intensity), wave front errors on the post-coronagraph surfaces are mostly not corrected by the calibration system – which is the appropriate response.

Post-lenslet errors: After the science beam has been dissected by the lenslet array, it becomes extremely difficult to scatter light from one spatial location to another. The lenslet demagnifies each input pixel into a grid of well-separated pupil images. To first order this decreases residual speckle noise by a factor $(f_{in}/f_{lenslet})^2$. Combined with the fact that the lenslets are after the coronagraph, this makes post-lenslet errors negligible.

Phase-induced amplitude errors: One of the most significant terms in the performance modeling for GPI are phase-induced amplitude errors – the instrumental equivalent of scintillation. Consider a phase error

on an arbitrary optical surface not conjugate to the deformable mirror. As light propagates towards the deformable mirror, the resulting aberration will change from a pure phase error to a mixed phase/amplitude error – the Talbot effect. In the limit of an infinite aperture and a single sine wave aberration, the aberration will switch between a pure phase and pure amplitude error and back over a propagation length equal to the Talbot length $\tau_L = 2\Lambda^2/\lambda$ where Λ is the aberration spatial period and λ the wavelength of the light.

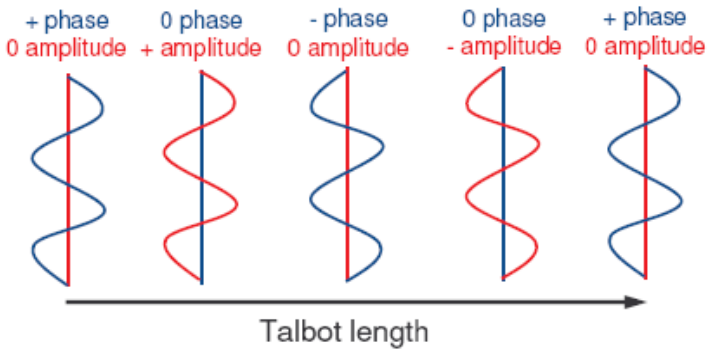

Figure 2-1: The Talbot effect. A pure phase aberration is oscillating between a pure phase to a pure amplitude aberration over a propagation length equal to a Talbot length.

More formally, this effect can be modeled with numerical wave-optics propagation codes, but the Talbot formalism provides a good approximation that leads to physical insights; for example, we can see that phase/amplitude mixing is more rapid for high spatial frequency errors. These effects are particularly troublesome in that they produce that does not have a simple magnification/demagnification with wavelength, particularly for optics near focus, and hence does not perfectly subtract with multi-wavelength imaging techniques [3] .

During the conceptual design a analytic error budget spreadsheet was used for contrast predictions, with individual terms normalized to simulation results and simple scaling laws. This was used to set preliminary requirements on individual optical surfaces and to identify the most significant sources limiting final contrast – the fundamental AO error terms (servo lag and WFS measurement noise) and the phase-induced amplitude effects from GPI's internal optics and (if used) the Gemini science fold M3. Figure 2-2 shows a representative result (for a *I*=5 mag. star with no speckle suppression post-processing.) During the CoDR phase, we have moved beyond this tool to full numerical modeling of the system contrast, described in Section 2.3 and Appendix 2.25.) We have also developed a more sophisticated analytic tool that evaluates the fundamental AO and atmospheric error terms, including scintillation and chromaticity, and is used for rapidly exploring AO parameter space (discussed in Chapter 3.)

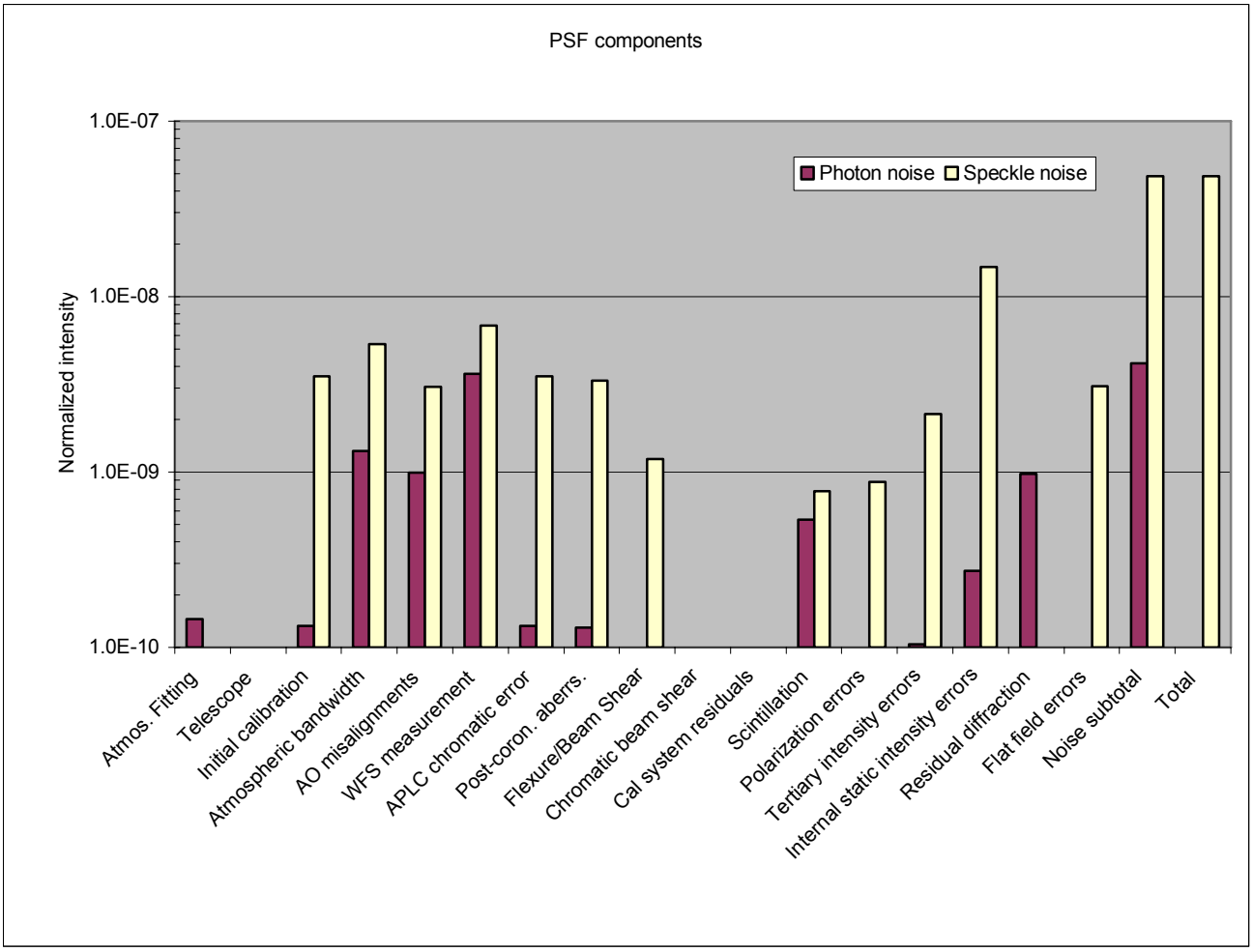

Figure 2-2: Representative analytic error budget using an enhanced version of the CoDR tool.

Contrast can in principal be enhanced through a variety of post-processing techniques – subtraction of reference PSFs, Angular Differential Imaging [2] , and multiwavelength imaging [4] . GPI's contrast goal is (1) to achieve contrasts on the order of 10-7 on bright stars without any post-processing; (2) to be roughly equally limited by dynamic (atmosphere+AO) effects and quasi-static (internal aberration) effects in a 1-hour exposure; and (c) to achieve photon-noise limited performance on moderate targets (I=6 mag., H= 5 mag.) after multi-wavelength post-processing.

2.2 Assumed Wave-Front Disturbances

GPI will have to correct for atmospheric turbulence and windshake induced tip-tilt errors. This section details our assumptions on these disturbances.

2.2.1 Atmospheric Turbulence

Our simulations (see Chapter 3) are based on a median turbulence profile at Cerro Pachon, provided by Gemini during the CoDR phase and derived from models used for the GLAO study. The total r0 is 14.5 cm.

Altitude (m)	r0 (m)	Wind speed (m/s)	Direction (deg)
0	0.4	6.9	284
25	0.78	7.5	267
50	1.07	7.8	244
100	1.12	8.3	267
200	0.84	9.6	237
400	0.68	9.9	232
800	0.66	9.6	286
1600	0.91	10.1	293
3400	0.4	7.2	270
6000	0.5	16.5	269
7600	0.85	23.2	259
13300	1.09	32.7	259
16000	1.08	5.7	320

Table 2-1: Full Cerro Pachon median turbulence profile provided by Gemini

The full profile is used primarily semi-analytical simulations, to calculate effects that depends on the altitude of the different layers, such as scintillation.

The full profile can be condensed into a two-layer profile, given in Table 2-2.

Altitude (m)	r0 (m)	Wind speed (m/s)	Direction (deg)
0	0.203124	8.03482	-96.5282
0	0.239365	16.4996	-94.5801

Table 2-2: 2-layer Cerro Pachon median turbulence profile

Note that the altitude of the two layers is assumed to be zero, since we are considering on-axis performance only and neglect scintillation. This profile is used for most numerical AO simulations.

Since that model has winds going in nearly the same direction (producing a strong 'butterfly') we also use a random-wind model, which distributes the turbulence much more evenly among five different directions. See Table 2-3.

Altitude (m)	r0 (m)	Wind speed (m/s)	Direction (deg)
0	0.352853	22.703	246.403
0	0.404815	3.2867	70.68
0	0.411772	16.5541	293.683
0	0.35148	5.89229	150.481
0	0.395264	19.8384	14.0042

Table 2-3: 5-layer Cerro Pachon median turbulence profile distributed among random wind layers

2.2.2 Windshake

In addition to the atmospheric turbulence described above, we assume that the telescope faces windshake that creates image motion (T/T). There is still much debate within the astronomical community as to what is the typical windshake at a give site, and, at the time of writing (April 2006) the GPI team is still awaiting real WFS data from Gemini to establish a workable windshake PSD for Gemini South. In the meantime, the have chosen to start from the original windshake profile that Gemini originally gave the Altair team (see Altair CDR book, appendix 30). This profile has 42 mas rms of tilt, and a flat PSD followed by a power 8 roll-off, with a cut-off frequency of 6.4 Hz. In order to be conservative in our study, we have increased the cut-off frequency to 10 Hz. We are also considering different cases, corresponding to different rms values: 25, 50, 100 and 200 mas rms. Note that for Gemini 1 mas rms of tilt error corresponds to roughly 10 nm rms of wave-front error. Note that for the TMT NFIRAOS Conceptual Design study, the TMT Telescope group recommended to use the 25 mas rms of windshake. The comparison between the TMT profile and the 25 mas rms profile we adopted in our study is shown in Chapter 3. Our PSD has a faster roll-off but a higher cut-off frequency and is overall more pessimistic. Correct information on the windshake at the telescope site is critical to specify the bandwidth of our T/T platform (see Chapter 3, section 3.5.2.1 and Appendix 3.5) and the algorithm that splits the T/T correction between the T/T platform and the woofer surface (see Chapter 3, section 3.3.1.6.3).

2.2.3 Optical surfaces

In general, optical surfaces have been modeled with a power-law surface wave front error with an index of -2.5 and a roll-off at one cycle per aperture. Most results are relatively insensitive to the exact power-law. Reflectivity variations are modeled with a similar power law, though when data is available we intend to model the measured Gemini M1 reflectivity profile. For the purposes of the simulations discussed below and in Appendix 2.25, individual optics have been grouped into several key conjugate planes.

Surface	Grouped conj. altitude (Km)	True conj. altitude (Km)	0-4λ/D^{-1} RMS WFE (nm) RMS)	4-22λ/D^{-1} RMS WFE (nm)	Ampl. error (% RMS)	Total 0-4λ/D (nm RMS)	Total RMS WFE 4-22λ/D (nm RMS)	Total Ampl. error (% RMS)
ADC01*	250	250	7	1.4	0.14	7	1.4	0.14
ADC02*	110	110	7	1.4	0.14	7	1.4	0.14
Window*	73.2	55.7	2.5	0.5	0.1	9.4	1.9	0.22
Ellipse		73.2	5	1	0.1			
OAP3		63.3	5	1	0.1			
OAP4		58.7	5	1	0.1			
Folding flat		67.7	2.5	0.5	0.1			
Beam-Splitter*	40	40	7	1.4	0.14	7	1.4	0.14
OAP1	27	27	5	1	0.1	7	1.4	0.14
OAP2		27.4	5	1	0.1			
M3	0	17.6	5	14	0.3	8.7	52	0.52
Woofer + tweeter		0	-	-	-			
M1		0.1	5	50	0.3			
M2		0	5		0.3			

Table 2-4: Optical surfaces used in numerical performance modelling. To simplify calculations, GPI optics have been grouped into five conjugate planes.

2.3 Performance simulations and contrast predictions

As discussed in Chapter 1, we have used two primary simulation tools to predict the final long-exposure image contrast.

2.3.1 Static aberration modeling

The first is a Talbot wave-optics model that predicts the speckle noise due to static and quasi-static error sources. These are evaluated based on the conservative assumption that they evolve too slowly to produce any noise reduction through time-averaging (except for that occurring due to the parallactic rotation of the field with respect to GPI), but are also too unstable for reference PSF subtraction. The full chromatic behavior of the aberrations and other system components (such as the coronagraph) is modeled to quantify the gains obtained through post-processing.

Appendix 2.25 discusses these models in considerable detail. These models have been used primarily to set requirements on individual GPI optics, given in Table 2-4. Figure 2-3 shows the resulting static contrast in direct imaging (i.e. no post-processing.) and Figure 2-4 shows the contrast after post-processing.

One key insight gained through these simulations is that the chromaticity of the APLC coronagraph plays a significant role in final contrast – as a result, the APLC will be tuned carefully for scientific return, e.g. at *H* with a mask set optimized at 1.59 microns (where the planet is bright) and another optimized for broad *H* band performance.

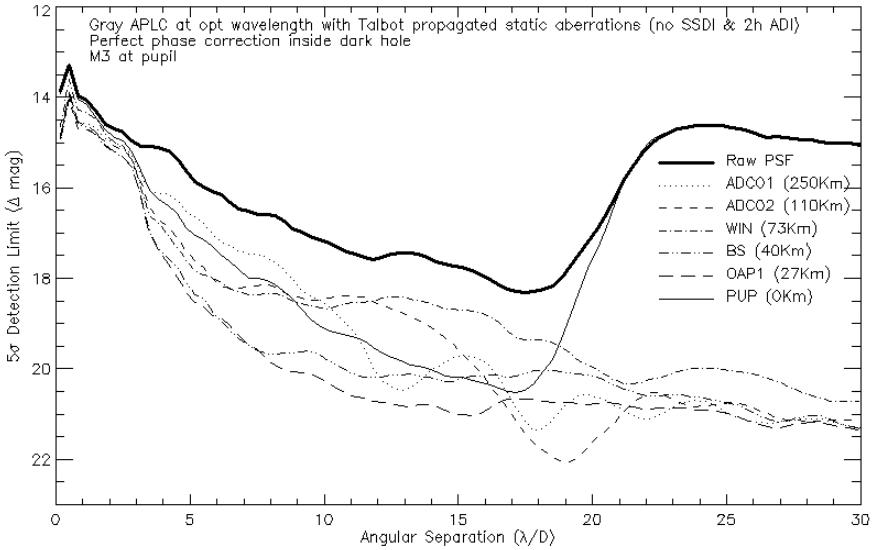

Figure 2-3: GPI static optical error PSF 5 sigma contrast detection limit at 1.625 microns. A 2h rotational-averaging speckle attenuation gain is assumed, no other post-processing Solid thick line is the raw PSF 5 sigma contrast curve while other curves are the contrast limitation from each individual conjugated plane.

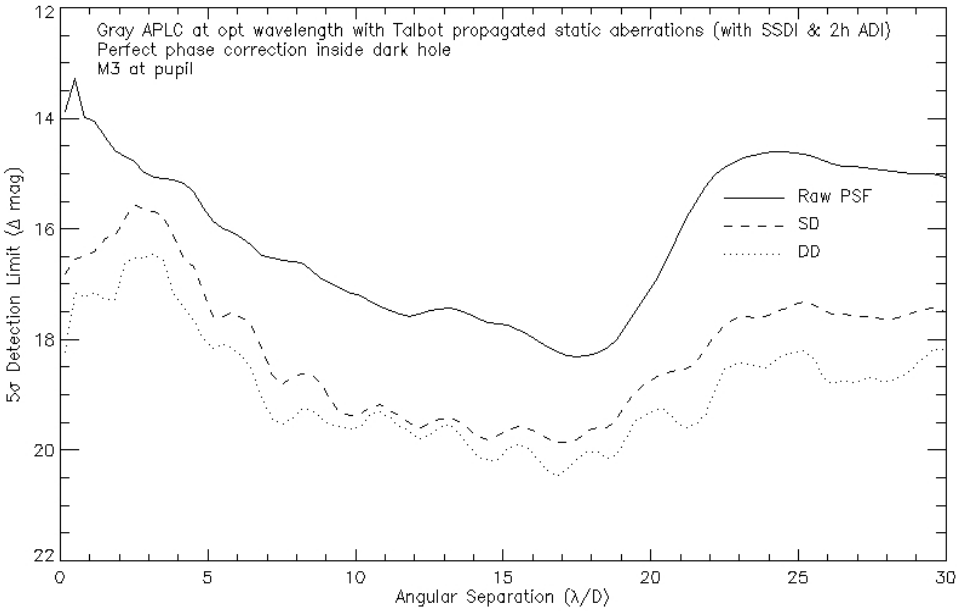

Figure 2-4: Static contrast after combining ADI, speckle symmetry and SSDI speckle attenuation techniques. Solid line shows GPI raw contrast at 1.625 microns, while the dashed and dotted lines show respectively the SD and DD obtain after combining images at 1.515, 1.57 and 1.625 microns.

2.3.2 Dynamic AO simulations

The AO simulator code used is discussed at length in Section 3.7. This code can be run for the equivalent of tens of seconds to predict speckle and photon noise from atmospheric and AO controller sources. The resulting contrasts are then scaled by exposure time and added to the quasi-static contrast predictions above. Figure 2-5 shows the resuls; GPI achieves its goal of being roughly equally limited by dynamic and static contrast effects on typical targets, and should reach the photon noise limit with post-processing.

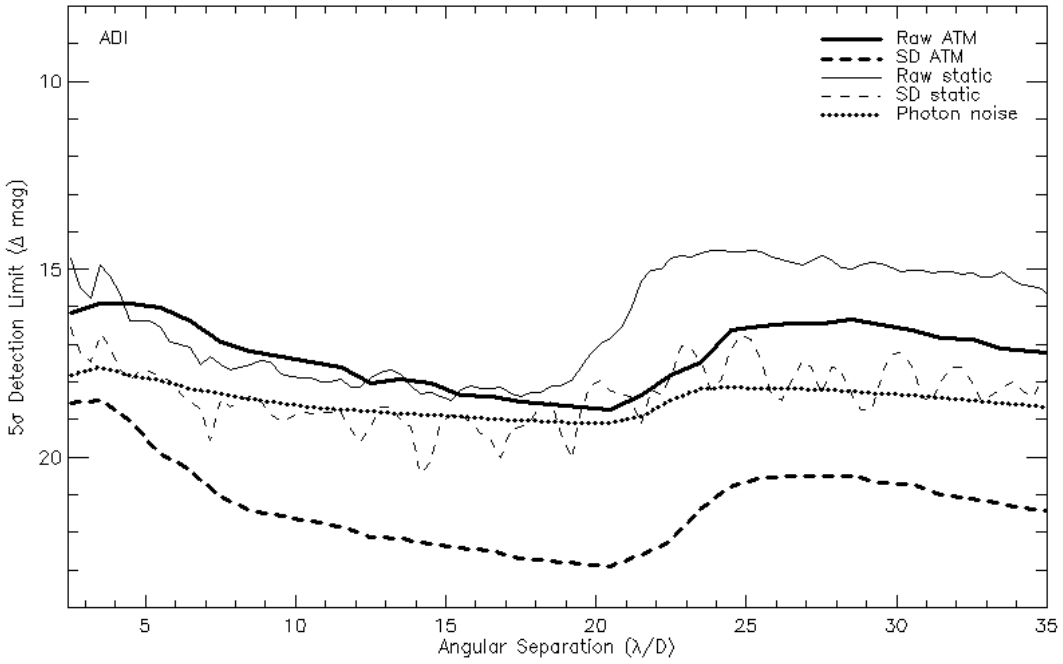

Figure 2-5: Contrast prediction for 2-hour exposure on a *H* = 5, *I* = 6 mag. target star, evaluated in a 4% bandpass at 1.59 µm. The thick solid line shows the 5-sigma speckle contrast in the raw image. The two solid lines show the raw contrast for residual atmospheric speckle noise (thick) and for static speckles (thin). The two dashed lines show the contrast after spectral differencing for atmospheric specklse (thick) and for static speckles (thin). The dotted line represents the estimated photon noise.

2.4 Requirements: AO correction

The GPI AO system must provide an extremely high level of correction. The main AO components are: the spatially filtered AO Wave-Front Sensor (AOWFS) and the wave-front correcting devices: the woofer DM, mounted on a tip-tilt platform (TTP), and the tweeter DM. They are controlled in real-time by the real-time AO computer (AOC). In addition, the AO system includes a number of optical elements, some of which are actively controlled to maintain alignment. These are discussed in section 2.7.1.

Because of the very high level of correction required, all the AO components carry a significant level of challenge, and therefore risk. This originate mostly from three major performance requirements:

- A very high DM actuator density (45x45 actuators)
- A very high frame rate (up to 2.0 kHz) and a very low servo-lag (latency 2 frames, with a goal of 1 frame)
- A very high DM actuator stroke to minimize the probability of saturation (5-sigma saturation margin for any actuator in median seeing conditions).

The high frame rate makes the choice of a AOWFS detector challenging. Since 45x45 actuators are required, we need at least 88x88 pixels. For such large detectors, high frame rates usually come with a significant read-noise penalty, leading to reduced sky coverage. At PDR, we have identified one proven detector that would almost meet our requirements: the 128x128 MIT/Lincoln Lab CCID-18. We are also pursuing several alternative devices, with less proven, but potentially better, performance, and are planning a final AOWFS detector down-select by mid-CDR. For a more thorough discussion of the AOWFS detector options, see Chapter 3, section 3.6.

The space constraints in GPI make it impossible to accommodate a traditional 5-7mm pitch piezo-stack DM with the required actuator density. We have therefore initiated the development of a novel 64x64 MEMs DM. Initial results have been encouraging, with the main problem being poor surface quality. Even if successfully developed, the MEMs will not have the very high stroke required. For more details on the MEMs DM, see Chapter 3, section 3.5.1. The MEMs (tweeter DM) will work in conjunction with a conventional low-order (9x9) high stroke DM (woofer DM), which will be mounted on a tip-tilt platform (TTP). See Chapter 3, section 3.5.2. Such a woofer-tweeter wave-front control scheme has never been tried on the sky, although it has been demonstrated in the lab and does not pose any conceptual problem. We are carrying a DM stroke budget that demonstrates that our choice of woofer-tweeter pair meets our requirements. See Chapter 3, section 3.5.3.

Finally, the high frame rate low latency requirements make the AOC challenging. Our plan is to use Commercial off-the-shelf hardware, and C-language software running under the Linux Operating System. Our hardware and software design (summarized in Chapter 3, section 3.4, and detailed in Volume 3) is based on a detailed computational budget, presented in Appendix 2.21. In this budget, we carry two AO controller options: the baseline is the Optimized-gain Fourier Control; the alternative is the Predictive Fourier Control, which is more computationally intensive, but could achieve better performance, especially in low SNR conditions (see Chapter 3, section 3.3.2.2 for a more detailed discussion of these options). Benchmark results show that are design is likely going to meet the requirements, with currently, or very near-term, available hardware.

2.5 Data/control flows

The top level GPI data flow diagram is given in Figure 2-6.

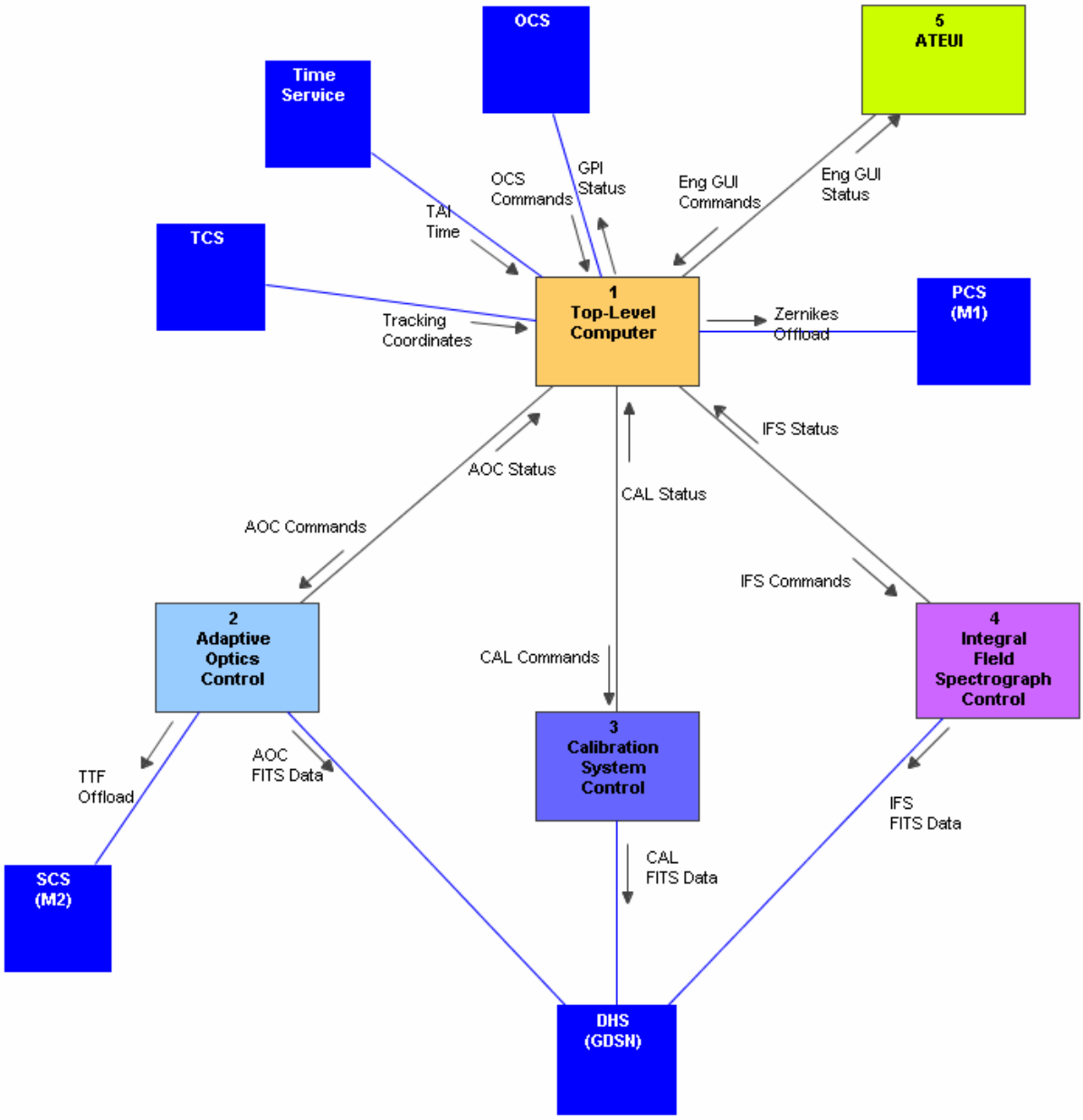

Figure 2-6: GPI top-level data flow diagram

A dedicated computer controls each major sub-system (AO, CAL, IFS). A Top-Level Computer (TLC) controls the sub-system computers by sending commands and receiving status in return. The TLC, AO, CAL and IFS computers can communicate with each other via a shared memory called Global Memory Block (GMB). In general, sub-system computers only communicate with the TLC, with the exception of the CAL computer, which sends its measurements directly to the AO computer. Common software will run the mechanisms of each sub-system. The TLC will control all mechanisms by sending commands to the relevant sub-system computer.

The TLC is also the main interface to the rest of the Gemini observatory:

- The Observatory Control System (OCS), which executes the observing sequences, sends commands to the TLC accordingly, and receives GPI status in return;
- The Telescope Control System (TCS), which sends tracking coordinates that the TLC for active GPI mechanisms that operate in track mode.
- The Primary Control System (PCS), which receives slow off-loading information from the AOC, via the TLC
- Other services, such as the Gemini Timebus and the Gemini Interlock System (GIS)

All communications between the TLC and Gemini is done through the standard Gemini Instrument API (GIAPI), provided by Gemini.

In order to fully exercise GPI when GPI is not yet at Gemini, the TLC will include an Acceptance Testing and Engineering User Interface (ATEUI), which will simulate all communications that normally originate from Gemini.

In addition to the communications via the TLC, each of the AO, CAL, IFS will send data directly to the Gemini Data Handling System (DHS) for archiving purposes. The AOC will also send fast off-loading data directly to the Secondary Control System (SCC).

All communications between GPI and Gemini, and between the GPI computers are specified in ICDs, included in Volume 3 of this document.

The data/control flow in each sub-system is described in the chapter dedicated to that sub-system: Chapter 3 (section 3.3) for the AOC, Chapter 5 (section XX) for the IFS, and Chapter 6 (section XX) for the Calibration System.

2.6 Throughput budget

The top level throughput budget is shown in Appendix 2.8 and summarized in Table 2-5. The throughput is driven by 2 main sources: the relatively high optic count (e.g. mirror and AR coatings) and the attenuation due to the coronagraph. Our throughput requirement for detected photons at the science detector (excluding the telescope and atmosphere) is 13% in J. We are on track to meeting this. However we'll likely not meet the original requirement of a 70% throughput to the AOWFS (excluding detector QE). We've relaxed this to a requirement of 60% with a goal of 70%.

	Throughput [%]	Requirement [%]	Comment
Science Path (in H)	15	13	From GPI input to detected photons (FPRD REQ-FPR-0350)
AOWFS (700 – 900 nm)	63	60	From GPI input up to but not including WFS QE (FPRD REQ-FPR-0400)
CAL Module	~8 (HOWFS) ~9 (LOWFS)	N/A	No FPRD requirement on throughput, only final SNR. Stated from pre-APLC to detector.

Table 2-5 GPI Primary top-level optical throughputs

Protected gold has been selected as the baseline mirror coating due to its high performance over the overall working wavelengths of 0.7 to 2.4 microns and resistance to degradation. Even at the lower WFS limit (0.7 microns), gold is superior to enhanced silver. The baseline coating is the Epner Technology hard gold. However we're also investigating coatings from Denton Vacuum and Newport. During CDR we plan to have sample flat mirrors coated from at least three vendors to test reflection and uniformity performance. Appendix 2.8 includes a table of advertised reflectivities for these three coatings

The wide operating wavelength range provides a challenge for an efficient AR coating. Although total throughput is currently more vital in the AOWFS band, ghosting is a major concern in the science band and will likely drive the specifications. During CDR we will procure and test a sample from at least 2 vendors. A pair of sample design AR coatings are shown in Figure 2-7.

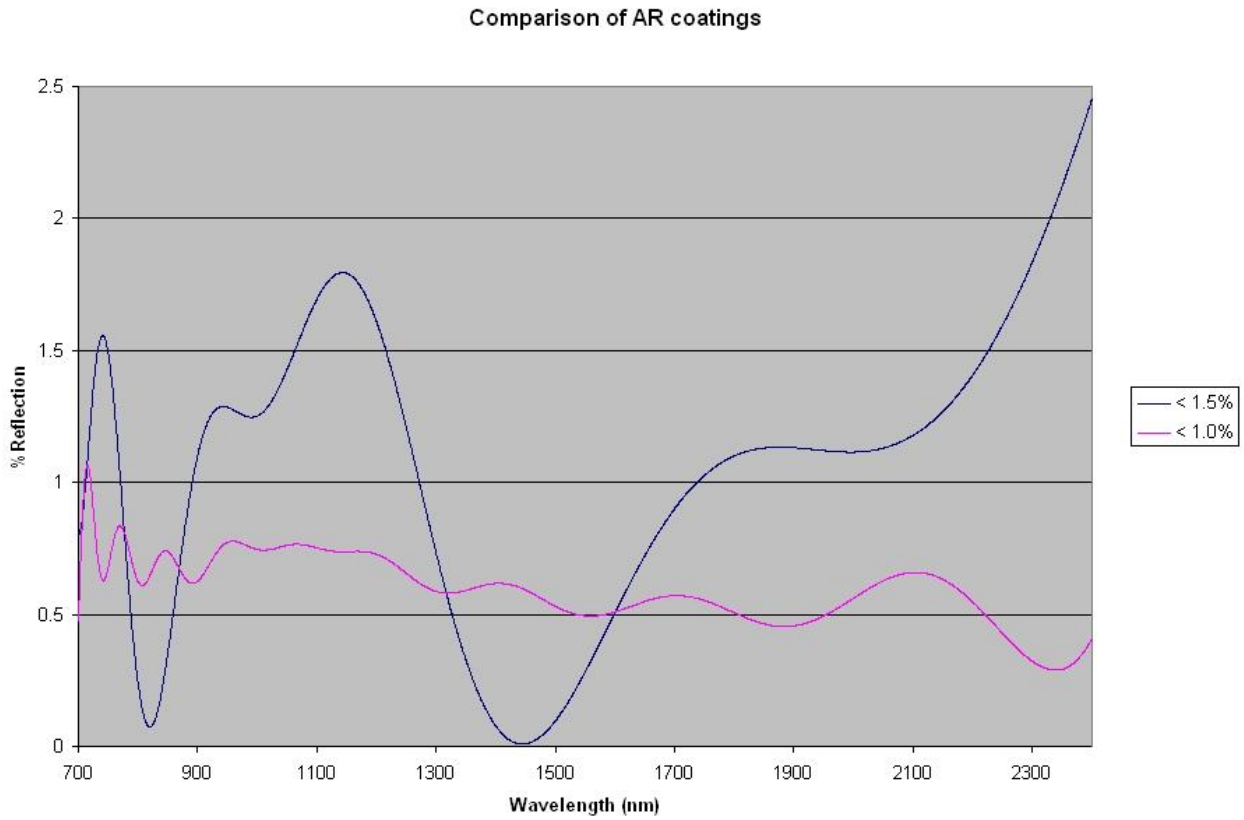

Figure 2-7 Two sample AR coating designs. The blue curve is a routine coating while the purple is considered probably achievable.

2.7 Flexure & alignment budget

A preliminary alignment budget has been created for the overall OMSS, treating the CAL module and IFS as independent rigid-body structures. This arrangement has facilitated the independent design, development and analysis of the three main opto-mechanical structures. A set of common gravitational and temperature cases has been created allowing the behavior of the structures to be directly compared

and integrated. These are discuss in Chapter 6 for the CAL module, Chapter 5 for the IFS and Chapter 7 for the OMSS. Combining the results into an overall GPI level budget is an early CDR phase task.

2.7.1 Alignment Budget

See Appendix 2.2 for the GPI alignment budget. This spread-sheet is being used to track the top-level alignment performance of GPI, currently treating the CAL and IFS as independent rigid-body structures.

From the perspective of GPI as a whole, we have a number of critical optical locations. These are summarized in Table 2-6.

Item	Alignment requirement [microns]	Alignment condition	Alignment control
M2 pupil	180	Illumination on tweeter	Closed-loop based on AOWFS pupil edge detection
Woofer (pupil)	500	w.r.t. tweeter 10% of 5mm woofer act. spacing	None
Tweeter (pupil)	0	System fiducial	Closed loop with AOWFS pupil edge detection
Apodizer plane (PPM) (pupil)	120	w.r.t. tweeter 1% of 12mm PPM pupil	None
Lyot pupil	100	w.r.t. PPM 1% of 10mm Lyot pupil	Open-loop with CAL-IFS P&C pair
AOWFS lenslet – tweeter registration	40	10% of 400 micron lenslet pitch	Open-loop with AOWFS P&C pair (two closed-loop algorithms in reserve)
Target location on Focal plane mask	2.5	1 mas	Feedback from CAL LOWFS
IFS focus	2.5	1 mas wrt FPM	Open-loop
AOWFS focus			Closed loop mechanism for CAL feedback to FPM

Table 2-6 GPI Critical optical locations

The tweeter pupil is defined as the GPI fiducial pupil. There are no degrees of control available between the tweeter, the woofer and the apodizer pupil planes; structural rigidity and physical proximity are relied on to maintain alignment between these planes.

The FPM is defined as the GPI fiducial focal plane, where coronagraphic performance relies upon good centering. Persistent pointing errors are detected by the CAL module and fed directly to the AOWFS P&C pair where there is sufficient precision and resolution to permit the AO system to operate T/T and focus in null mode (i.e. not use any electronic offsets).

The registration of the WFS lenslets to the tweeter will be maintained using the AOWFS P&C mirrors. The baseline approach is to rely on a flexure lookup table to maintain registration. Two contingency algorithms are being considered should the lookup table prove to be insufficient. These each use a test pattern applied to the tweeter; either a large amplitude momentary pattern during the IFS science detector readout, or continuously with a very low-amplitude dithering signal.

With the AOWFS well registered to the tweeter actuators, alignment of the telescope pupil onto the tweeter (M2) will be monitored by analyzing the illumination pattern of the pupil on the AOWFS, and hence on the tweeter. Error signals will be fed back to the input fold mirror to maintain pupil centering.

Alignment of the Lyot plane in the IFS will be adjusted using the P&C mirrors located between the CAL module and the IFS. A flexure lookup table will be determined initially from the FEA analysis, and refined during I&T based on the flexure tests.

For pupil alignment, we have allocated a 1% downsize of the pupil at a mask on the PPM (120 microns at the PPM) with respect to the tweeter, and a further 1% downsize at the Lyot stop (100 microns at the Lyot) with respect to the PPM for a total downsize of 2% of the Gemini telescope pupil.

2.7.2 Opto-mechanical Flexure and Thermal Effects

A preliminary FEA analysis has been performed, with data for individual optical motions of the AO relay optics, critical points, and the CAL and IFS as independent structures. There were a standard set of cases, at various gravity vectors and at three different temperatures agreed upon by entire GPI team. As well, a higher temperature fidelity run was performed at a single gravity vector. GPI mounted on a side ISS port, with the telescope at zenith and 20º C is the baseline case (i.e. I&T conditions) to which all the other cases are compared. The output of these cases was the displacements and tilts of all the optical elements, and critical optical locations with respect to the baseline case. See Chapter 7 for a more complete description of the FEA analysis.

Simply looking at the relative mechanical motions of the optical components and critical locations is an indication of the flexure effects, but a more reliable result is to ray-trace the system with the perturbed optics. This will capture the effects of tilted and displaced intermediate optics that only comparing the relative positions of, say the tweeter and PPM, would miss.

We have currently performed a ray-tracing of a single, representative case, one that, based on bulk physical motions, appeared to be a particularly extreme case; where GPI moves from the baseline orientation (20ºC, side-port, telescope at zenith) to a zenith distance of 60 degrees and almost ‘pointing down’. This case happened to be 0ºC so also represents almost the extreme temperature range. For this ray-tracing, the AOWFS path was not analyzed. However, the mechanical flexures of the AOWFS path

behave similarly to the other optics mounted on the AO relay optical bench, so we fully expect a similar performance.

A comprehensive analysis will be performed early in the CDR phase for all test cases in order to fully understand all operating orientations and temperatures. At this time the behavior will be combined with the CAL and IFS results for an end-to-end analysis.

A point to keep in mind is that in these flexure and ray tracing tables, X,Y and Z are measured in the GPI global coordinate system. This coordinate system is orthogonal to the ISS face with Z coming out of the ISS face. For the most part, the optical chief is close to the Z coordinate, as the optical path folds back and forth away from and towards the ISS. This is most incorrect at the FPM where there is about a 30 degree angle between the coordinate system Z and the chief ray. Hence these initial numbers for displacements, orthogonal to the focus direction, are an approximation.

There are two categories of flexure management. First is uncompensated, relying on the stiff mechanical structure to control relative motions. Secondly is the incorporation of compensation elements, for GPI, in all cases pointing and centering (P&C) pairs.

2.7.2.1 Uncompensated Management

The entire AO relay, OAPs, ellipsoid, woofer, tweeter, AOWFS beam splitter, AOWFS assembly and PPM assemblies are all in close proximity to each other on the main, very stiff, AO relay optical bench. The design strategy was to have all these assemblies mounted without computer controlled actuators, relying on the mechanical structure to control relative motions. This assembly flexes mainly as a unit, with relative motions in the few 10s of microns. Ray tracing on the sample case indicates that once the pupil is re-centered on the tweeter, the pupil illumination on the PPM and woofer is shifted by about 60-70 microns due to flexure, well under the 120 micron requirement for the PPM, allowing generous initial alignment and pupil illumination monitoring tolerances.

2.7.2.2 Compensated Management

Flexures within the individual optical tables (e.g. AO relay, CAL module and IFS dewar) are of acceptable amplitudes. However, these make relatively large motions with respect to each other. To provide flexure compensation, we've incorporated P&C mirror pairs between the major sub-systems.

Some of the motions are sensed and will be controlled in a closed-loop fashion. Others are not sensed, and open-loop models will be built, and calibrated during I&T and commissioning. Experience with previous instruments such as ALTAIR and GMOS support our approach by permitting > 75% of flexure being compensated for with an open-loop model in a well behaved mechanical structure.

These include:

1. AOWFS lenslet to tweeter actuator registration maintained by the AOWFS P&C pair. Not yet analyzed with ray-tracing, the relative motions are small (less than 100 microns) between the tweeter and the lenslet array. With a requirement of about 40 microns (10% of a lenslet pitch), we fully expect an open-loop model to be sufficient.

2. Tweeter (and by extension woofer and PPM) pupil alignment with the input fold mirror, of which M2 forms the second half of the input P&C pair. The test case indicates a shift of the pupil position on the tweeter, before any compensation, of less than 70 microns due to flexure within GPI. A nominal requirement would be 40 microns, or 10% of an actuator pitch, easily within the range of an open-loop compensation model. However, edge detection of the pupil position on the AOWFS images is straight forward to implement. This will be used to drive the pupil illumination very close to centre and allow a larger allocation to the relative flexure to the PPM. As well, active sensing and correcting of the actual pupil illumination within GPI will relax the interface to the telescope.

3. IFS pointing and centering maintained, with an open-loop lookup table, with a P&C pair between the output of the CAL module and the input of the IFS.

    - The Lyot pupil plane, in the test case, moves by about 300 microns, where our requirement is 1% of the 10mm pupil, or 100 microns, easily within the range of an open-loop model.

    - The pointing at the IFS focal plane (lenslets) shows a total motion for the test case of about 300 microns during 60 degrees of motion. The requirements are that motion is to be controlled to less than 4 mas/10 minutes (28 microns/10 minutes) of tracking. At the most extreme case, the telescope moves by 15 degrees/hour of tracking. Allocating the entire 300 microns of flexure in the test case to a one hour exposure, we'd see about 50 microns of flexure/10 minutes. Correcting this to within the 28 micron requirement is again well within the capabilities of an open-loop model.

2.7.2.3 Range and Resolution of Compensation

Of the fold mirrors (input, AOWFS P&C and CAL-IFS P&C), the mirrors that require the largest range of motion are the AOWFS P&C pair. These require the ability to compensate for at least 1 arcsec of motion of the guide star in order to compensate for the 0.8 arcsec of flexure induced motion at the FPM. This equates to a 2 mrad mechanical tilt at both mirrors.

Of the fold mirrors, the highest resolution required is the AOWFS pair. In order to be a negligible contributor to the FPM centering, we require that these stages have a resolution of motion less than ¼ the 1 mas pointing requirement on the FPM. This equates to 0.5 μrad.

The Mad City Labs PZT stages base lined for the OMSS stages [1] , exhibit a 5 mrad range and a resolution of 10 nrad, which comfortably exceeds our requirements for all stages.

2.7.2.4 Rate of Compensation

We need to ensure that flexures are compensated for with enough fidelity to not introduce significant additional errors due to lag in the control loops. We consider the flexure presented in the ray-traced flexure discussed in 2.7.2. For the purposes of this discussion, we make the conservative assumption that this 60 degree motion occurs in a single 1-hour exposure and at a linear rate.

The two classes of cases are:

1. For the closed-loop compensations, we assume that we can update the pointing frequently enough to keep the residual errors within our error budget. Of the closed-loop compensations, the largest motion occurs at the AOWFS P&C pair, the pointing following the CAL module updates for pointing. For our assumption case, we move an average of 0.8 arcsec/hour, or 0.2 mas/s. Keeping under the 1 mas requirement at all times is easily within a loop running at 1 Hz or slower. The CAL system will be providing updates at 1 Hz or faster to a precision of < 1 mas.

2. For open-loop compensation, we need to ensure that the sensing bandwidth, to the required precision, is fast enough to provide timely feedback in order to minimize overall errors. The CAL-IFS P&C pair is a good example, required to track the IFS focal plane and Lyot plane. The 300 microns of correction, assumed over 1 hour, would lead to an update rate of < 0.1 microns/s, well within specifications.

2.8 Preliminary alignment plan

The CAL, IFS and OMSS comprise the 3 main assemblies for GPI, with AMNH providing the actual coronagraphic elements. The GPI Optical Alignment Plan, Appendix 2.9, currently in draft form, is the repository for the optical alignment of each main sub-system, and the integration and alignment of the system as a whole.

The alignment plan includes additional sections dealing with maintenance (such as replacing an individual element) and aligning the DMs with the AOWFS.

Defined for each sub-system will be an absolute reference, likely a set of three tooling balls or sockets. For the sub-systems, their optical alignment will be made to these references, with the acceptance test confirming compliance. These will be used to initially position the CAL, then the IFS within the OMSS. The accuracy of the Coordinate Measuring Machine (CMM) to be utilized is on the order of 50 microns/reading. This is expected to provide near-final positioning, with the on-board detectors (e.g. LOWFS in the CAL) used for final optical alignment.

The order of integration will be:

- Installation and mechanical alignment (using CMM) of the CAL into the OMSS structure.
- Final alignment of the CAL orientation, input at the focal plane mask using the LOWFS and output to a test camera at the nominal IFS input location. Alignment accomplished using initially bulk shims on the mounting structure, then fine adjustment on the mount legs.
- Installation and mechanical alignment (using CMM) of the IFS into the OMSS structure.
- Final alignment of the IFS orientation. Input at the Lyot stop (using pupil viewing camera) and focal plane (using science detector). Alignment accomplished using bulk shims at the mounting points and final adjustments with the CAL-IFS fold mirror mounts.

2.9 Mass and Balance Budget

See Appendix 2.19 for the GPI mass and balance budget. The Gemini specification is a mass of 2000kg, on the optical axis 1000mm from the ISS face (see "ICD 1.9/2.7 Instrument Support Structure to Science Instruments ICD", Appendix 2.23), ;with the tolerance specified as a moment about the telescope elevation axis. Trimming GPI to the specified mass requires about 180 kg of ballast mass positioned in order to balance the instrument. This is a smaller contingency than we'd like to carry at this point. However, a number of things act in our favour.

1. The instrument layout quite naturally positions the CoG very near the Gemini requirement (a major consideration during the design phase).
2. There has not yet been any optimization to reduce mass of the main EFS, FSS and bulkhead structures where a substantial mass savings could be made.
3. The electronics in the enclosures and the IFS masses are calculated using the maximum allowable limits agreed to in the sub-system ICDs.

A summary of the current mass and budget are shown in Table 2-7.

		Component Mass (kg)
FSS		
	Bulkhead plate	192
	Main truss structure	146.2
	Interface ring	90.8
	CAL upper truss structure	9.5
	CAL lower truss structure	10
	CAL pyramid	16.4
	Optical bench	110
	Opto-Mech components	38
	IFS	300
	Cal-Unit	120
	Wiring / services	20
EFS		
	Truss structure + panels	350
	Electronics cabinet 1	90
	Electronics components 1	95
	Electronics cabinet 2	90
	Electronics components 1	90
	Wiring / services	50
	Ballast	182
	Mass total:	**2000**
	Ballast %	8.3%

Table 2-7 Current GPI balance summary

2.10 Thermal budget

We have two main thermal budgets to be concerned with, within the electronics enclosures (EE) and within the optics enclosure (OE). The GPI power budget is shown in Appendix 2.20. This is divided into estimates within the thermally insulated electronics enclosures (EE's) and the optics enclosure (OE).

2.10.1 Electronics Enclosures Power

We assume that the heat is dissipated in the electronics enclosures (EE) is worst case; equivalent to the entire power draw of the GPI electronics. This allows us to also equate the EE thermal budget with the GPI power budget. The power allocation from Gemini is a total of 4.0kW (see "ICD 1.9/3.6 Instrument to System Services ICD", Appendix 2.16). Of this we currently estimate a draw (and dissipation within the EEs) of 3.2 kW.

2.10.2 Optics enclosure

Within the OE we need to carefully manage heat in order to minimize detrimental turbulence. The thermal control within the OE is still in the preliminary stages of design and analysis. In general we're striving to utilize mechanisms and control strategies to minimize the total heat dissipated. The use of PZT stages for the P&C mirrors and balanced, servo-motor driven stages (e.g. PPM assembly) result in no significant power being dissipated while mechanisms are at rest. The major mechanisms also have very small duty cycles.

For the larger heat sources, such as the AOWFS camera, IFS closed-cycle cooler head and CAL module HOWFS camera, we anticipate circulating glycol to control heat. One attractive alternative is to circulate instead ambient temperature facility dry air through the heat exchangers eliminating the risk of damage due to a glycol leak.

To be analyzed during the CDR phase is the effect of the IFS dewar. Other than the closed cycle refrigerant (CCR) heat rejection site, the dewar as a whole will be a next thermal sink, absorbing about 20W. Nominally just as detrimental as a heat source, this is distributed evenly over the entire surface of the dewar, so isn't expected to be a significant heat source.

One potential solution we're investigating for equalization of the smaller heat sources, and the OE environment as a whole, is a very slow forced air circulation. Driven at an appropriate rate to not prove detrimental to the AO correction, this has the advantage of being very simple, and could prove particularly beneficial to the cooler IFS dewar. This will be evaluated during the CDR phase.

2.11 Upward ISS Only Advantages

GPI may benefit significantly from observations on the up-looking ISS port. Besides the minor throughput advantage of one fewer reflection feeding GPI, there are a set of additional advantages to restricting the use of GPI to the upward port on the ISS, most significantly through the elimination of a moderately low-quality optic. We describe some of the major advantages here. Note that, if implemented, none of these would preclude the operation of GPI on a side port, only that performance would not be guaranteed, nor would all lookup tables be developed and tested.

- The Science Fold (M3) mirror is at a poor conjugation for correction by the GPI DMs, and of lower surface quality than the internal GPI optics. Hence phase-induced amplitude errors from M3 are one of the "tall poles" in the error budget. See Appendix 2.25 for analysis; the raw

contrast is degraded by ~1 magnitude compared with observing on the upward looking port. This would reduce the reliance on speckle attenuation techniques, reducing overall risk.
- The FEA analysis and mechanical design would be simplified and possibly permit optimizations to improve the flexure performance in the reduced gravity orientation cases.
- Risk reduction to schedule. By reducing the number of gravity test and verification cases, and the associated flexure compensation loops, will provide some relaxing of the schedule.

2.12 Gemini Spares Philosophy

Along with the Gemini Observatory, we recommend sparing any hard to acquire items or those with very long lead times. Of course this has to be balance with the cost of such a spares list. Within the project, the teams have taken reasonable effort to utilize identical items where this will not drive cost or sacrifice performance. A complete list of recommended spares will be provided at CDR. A sample list is:

- Spare computers. With the current rapid rate of computer evolution, even 6 months can see a popular computer model change radically. Although typically faster and more capable, some interfaces might not be supported on newer hardware. We currently recommend spares for all the GPI computers. The IFS and TLC will use an identical model, and the CAL and AO computers another, nominally identical model from a different vendor.
- Spare Camera. Between the CAL module and the IFS, three copies of an identical commercial IR camera will be utilized.
- Galil motion control boards and amplifier modules. All opto-mechanical systems are utilizing the identical Galil motion control module. Two or at most 3 models of amplifiers (stepper and servo) are used. Sparing both of these would be prudent.
- Power supplies. Sparing the motor power supplies is a common recommendation.
- Common servo-motor/encoder assemblies. There will be a small set of different motor/encoder/gearbox assemblies.
- Tweeter DM. During the MEMS development plan we will receive an engineering-grade DM. MEMS DM manufacture in some ways resembles CCD manufacture, with large-scale foundry runs; it may be possible to arrange with Boston Micromachines to receive an additional science-grade spare, possibly un-bonded, for a reduced cost.

2.13 Key issues

2.13.1 Risk analysis and mitigation

For the current major risk and mitigation plan see Appendix 2.27. This table tracks the major risk items for the project, and are nominally reviewed monthly at a team lead meeting. The overall risk rating is a combination of the probability and severity of the risk. Items are retired once they have been resolved.

Risk Description	Overall Risk Rating	Current State
4k MEMs procurement	H	Phase 1 study complete with good results. Surface quality remains a concern.
AO processing power	M	High due to repercussions, this will likely be retired soon.
CAL system limited by GPI vibration environment	M	To be investigated during CDR. Mitigation very difficult. Design considerations driven to avoid critical frequencies.
IFS CCR vibration	H	Affecting the CAL and potentially AO systems. Vibration isolation and choice of frequency being selected to be relatively non-invasive. Expect to retire soon.
OMSS Mass budget margin too small	M	To be continued to monitored until final mass and balance values from all sub-systems. Currently within specifications. with some margin.
OMSS flexure/optical alignment	M	Have implemented fold mirrors for compensation, initial FEA with ray tracing indicates meet all requirements. Expect to retire early in CDR.
TLC delayed by GIAPI	M	GIAPI developing in collaboration, still relies on Gemini schedule and timetable.
Manufacture of apodizer	H	HEBS samples show strong wavefront errors. Evaluating other technologies beyond the HEBS and prototypes will be tested in early CDR.
SYS, relatively late systems level performance evaluation	H	Nominally have to wait for system integration to perform end-to-end performance tests. Inherent to project; simulations and possible bench-tests being investigated to alleviate.

Table 2-8

2.13.2 Technology Risk Areas

The two main technology risk areas identified above are the 64x64 actuator MEMS deformable mirror and the pupil apodizer for the coronagraph.

The state of the MEMS development is discussed in Chapter 3. In summary, design and packaging of a high-stroke 4096-actuator MEMS is proceeding on plan. An engineering-grade MEMS will be delivered in January 2008, and a science-grade MEMS in Octobre 2008, allowing significant schedule margin before final I&T. Actuator stroke and yield meet our requirements. Surface quality is a concern, particularly "scalloping" on some actuators of the mirror. Preliminary optical modeling indicates that we can accept surface quality equal to the current test actuators (~5-10 nm RMS and ~50 nm PV), but these models may not capture all relevant wave-optics effects. We will carry out additional modeling and tests in summer 2007, and Boston Micromachines is working to improve the surface quality.

The pupil apodizer development is discussed in Chapter 4. The baseline technology – electron-beam-sensitized HEBS glass – has shown significant wave front errors. We are working with the manufacturer to reduce these and exploring two alternative technologies involving metal deposited on glass substrate.

2.14 Trade studies summary

During the preliminary design phase, a number of explicit high-level trade studies were undertaken. These are summarized in Table

Title	Appendix	Result	Comments
WFS ADC	2.24	Not required	Would only provide a marginal improvement due to the relative narrow bandwidth (0.5 – 07 micron) of the AOWFS
Science ADC	2.7	Front-end deployable linear broad-band ADC.	Marginal improvement for AOWFS, required for coronagraphic performance, and major advantage to CAL system
Woofer down-select	3.5	Stacked actuator mirror on T/T platform	• Bimorph option (CoDR) needed too large a pupil to meet required stroke. • Higher order (9x9) to meet inter-actuator stroke budget. Relaxes tweeter global stroke to 2 microns.
Three V. Five AO relay design	2.1	The five mirror design (off-axis parabola) was selected	• Five mirror option offers greater modularity/flexibility and easier-to-manufacture optics, even if required surface quality is slightly higher.
IFS FOV V. Spectral resolution	OCDD Chapter 13	FOV = 2.85 arcsec R = 45	• Minimum spectral resolution to recover planet temperature.

Table 2-9 GPI Major trade study summary

2.15 ICDs

The design of GPI is driven and managed by a set of ICDs that define the instrument within the Gemini environment (external, Gemini, ICDs) and between the various sub-systems (internal ICDs). As well as a set of fundamental, overall set of ICDs (e.g. ICD G0014, "Gemini Observatory Optomechanical Coordinate System"), Gemini incorporates their sub-system ICDs in an N^2 format, with sub-systems being assigned a hierarchical numbering scheme. For example ICD 1.9/3.1 is the "Science Instrument to Observatory Control System" definition. GPI is assigned the designation 1.9.x. The sub-systems within GPI are assigned the following designations

AO Module	1.9.x.1
Coronagraph Module	1.9.x.2
IFS	1.9.x.3
CAL module	1.9.x.4
OMSS	1.9.x.5
TLC	1.9.x.6

Table 2-10 GPI internal designations

2.15.1 External (Gemini) ICDs

There are two, new, GPI specific Gemini ICDs that are necessary. The first has been written, the second will be completed in the CDR phase once the GIAPI is defined.

Number	Title	Description
3.1/1.9.x	Observatory Control System (OCS) to GPI Top-Level Computer (TLC)	Defines commands and status that GPI will adhere to.
3.2/1.9.x	Data Handling System to GPI Top-Level Computer (TLC)	This document is to be written, as the GIAPI progresses, in collaboration with Gemini, during the next phase

Table 2-11 Gemini GPI external ICDs

2.15.2 Internal ICDs (SW 9)

This section outlines and introduces the documentation that will define the interfaces between the main GPI modules (AO, COR, IFS, CAL Module). These are summarised in Table 2-12. The interfaces that are relatively simple are assembled into a single document "Supplemental GPI Sub-system ICDs" for simplicities sake. The specific software ICDs (TLC, AOC, IFS and CAL) are presented in the PDR Software Volume: 3. The remaining ICDs are presented in the Chapter 2 Appendices.

The internal ICDs are living documents and are not yet complete. In particular, the mechanical sub-system interfacing needs to be detailed. This will be accomplished early in the CDR phase.

Number	In supplemental	Description
1.9.x		This document
1.9.x.1/1.9.x.2	Y	AO to COR
1.9.x.1/1.9.x.3	Y	AO to IFS
1.9.x.1/1.9.x.4	Y	AO to CAL
1.9.x.1/1.9.x.5		AO to OMSS
1.9.x.2/1.9.x.3	Y	COR to IFS
1.9.x.2/1.9.x.4	Y	COR to Calibration
1.9.x.2/1.9.x.5		Coronagraph to OMSS
1.9.x.3/1.9.x.4	Y	CAL to IFS
1.9.x.3/1.9.x.5		IFS to OMSS
1.9.x.4/1.9.x.5		Calibration Module to OMSS
1.9.x.6/1.9.x.1		TLC to AOC
1.9.x.6/1.9.x.3		TLC to IFS
1.9.x.6/1.9.x.4		TLC to Calibration Module
1.9.x.6.GMB		Internal GPI Global Memory Block

Table 2-12 GPI Internal ICDs

2.16 Reliability, Availability and Maintainability (SE 12)

Various aspects of the instrument's reliability and maintainability are covered in the following chapters. From a project perspective, a number of common themes are aimed at gaining a highly reliable instrument. These include:

- Use of common, commercially available products whenever possible. As well as reducing costs, this keeps open a solution for easier replacements. Computers, power supplies, motor controllers and temperature monitors/regulators fall into this category.
- Cables produced by commercial outside vendors wherever possible. Specialized vendors have the experience, tools and verification equipment necessary to minimize cabling errors.
- High quality components. In the overall budget of GPI, the difference between basic and high-quality components is a small increment, and can have expensive consequences, both in cost and schedule. For example, only high quality servo-motors, gearboxes, stages and power supplies will be utilized.
- Due to the large, fast storage capacity requirements of, in particular, the AOC computer, local disk storage is a must. In order to improve reliability, we will be investigating reliable drives. Possibilities include: solid stage drives, redundant RAID and off-instrument storage (e.g. networked disks).
- A recommended list of spares for Gemini to acquire in order to minimize down-time.
- A regular maintenance regime. These will be developed during the CDR phase as the final design progresses, but will include preventative maintenance (such as the CCR heads for the IFS and CAL).

2.17 Safety

There are a number of potential safety issues within GPI. This is in the early stages as the design of GPI proceeds. Some potential issues are summarized in Table 2-13. As the critical design progresses, these, and any further identified issues, will be presented with the safety strategies.

Description	Safety Concern	Mitigation
High voltages for the DMs	Electrical shock risk	Approved connectors and cables. Appropriate warning labels at potential operator spots. Maximum current of DM drivers is very low.
Laser light sources	Personnel eye damage	Not an issue for the visible artificial source unit (class II), but the IR laser source is potentially dangerous. Will be evaluated during CDR to determine what power is required and the safety issues involved.
Stability during handling	Personnel injury	Handling of, in particular, partially assembled GPI. Ensuring that all handling rigs and carts can't tip when GPI partially assembled. Strict handling procedures outlined for all cases. Permanent labeling for handling rigs.
Installation pinch points	Personnel injury	Handling procedures outlined and labels
IFS vacuum dewar	Personnel and equipment injury	Appropriate handling procedures outlined. Safety blow-offs on dewars

Table 2-13 GPI Safety issues summary

2.18 Chapter 2 References

[1] Mad City Labs Nano-MTA Series 2-axis piezoelectric mirror tip/tilt actuators, http://www.madcitylabs.com/nano-mta.shtml

[2] Marois et al. 2006, ApJ, 641, 556

[3] Marois et al. 2006, proc. SPIE, 6269, 114

[4] Racine et al. 1999, PASP, 111, 587

3 AO Subsystem

3.1 Overview and requirements

The adaptive optics (AO) subsystem is the heart of GPI. It is responsible for making fast visible-light measurements of the wave front external to GPI (primarily atmospheric phase errors) and correcting that wave front using its deformable mirrors. It is tightly integrated with other subsystems. All AO optics are the responsibility of HIA's OMSS, which provides mounting and motion control. (The AO optical design is therefore discussed in Chapter 7.) The AO system responds to wave front and pointing feedback from the CAL subsystem. CAL measurements of the time-averaged IR wave front passing through the coronagraph are used to update the reference wave front control point (reference Shack-Hartmann centroids) for the AO system as small systematic errors build up. Similarly, pointing changes sensed by the CAL low-order wave front sensor (LOWFS) are used to steer the pointing of the AO spatially-filtered wave front sensor (SFWFS).

AO system key requirements:

- Provide real-time correction of atmospheric and telescope wave front errors up to spatial a frequency of 22 cycles per pupil (18 cm subapertures)
- Provide good wave front correction on targets with magnitude $I < 8$ mag. (goal $I < 9$ mag.)
- Operate fast enough to have residual servo-lag error < 25 nm in typical atmosphere conditions
- Provide diagnostic and telemetry data to the observatory (e.g. telescope offloading) and DHS (e.g. performance characterization data)
- Provide field steering capabilities over ~3 arc seconds through optical steering of the wave front sensor

AO system key interfaces:

- Accepts the Gemini *F*/16 beam
- All components mount to the optics bench of the OMSS
- Accept wave front calibration updates and pointing updates from the calibation system
- Accept commands and return status to the SCC
- Produce a converging *F*/16 beam with a finite pupil for input to the coronagraph optics

AO system design summary

- Two-stage wave front correction with piezo woofer and MEMS tweeter deformable mirrors
- Visible-light (0.7-0.9 μm) spatially-filtered Shack-Hartmann wave front sensor

3.2 AO system summary

The AO subsystem optical path begins at the entrance window. A steering mirror is available to align GPI's pupils with the Gemini entrance pupil. The beam is then collimated and relayed to the first deformable mirror. This high-stroke low-actuator count piezo DM (referred to as the "woofer") reduces the residual wave front error to a level controllable by the finer "tweeter" mirror. This DM will also serve as the tip/tilt mirror, mounted on a commercial FSM mount. A pair of optics relays the beam to the

"tweeter" DM. This is a 4096-actuator MEMS device (with a 45-actuator-diameter region illuminated). Two more conic optics produce a converging *F*/64 beam with a finite pupil for input into the coronagraph path. A 0.95-micron dichroic splits the visible light into the fast spatially-filtered wave front sensor (SFWFS). The visible light passes through a variable-size spatial filter, used to remove uncontrollable spatial frequency components that would be aliased into incorrect wave front measurements. Relay optics then reform the pupil on a lenslet array, and the resulting dot pattern is in turn relayed to a high-speed CCD. The final CCD downselect has not been made (in part because of the developmental status of several attractive CCD options, see section 3.6), but it will operate at 1-2 kHz with each subaperture corresponding to a 2x2 quad-cell. A bandpass or short-cutoff filter limits the wavelength range seen by the SFWFS (nominally to 0.7-0.9 microns), since spatial filter performance improves with increasing Strehl at the sensing wavelength, and since the spatial filter size can only be precisely matched to spatial frequency cutoff at a single wavelength.

The baseline AO control algorithm is the Optimized-gain Fourier Controller (OFC) algorithm developed by Poyneer and Veran. This is an adaptive modal gain algorithm using the Fourier modes as its basis set, allowing both efficient reconstruction and a direct match to sensor geometry and the PSF. We have also explored a predictive controller algorithm (Appendix 3.1). Although this is not yet the baseline, it has the potential to improve performance by a factor of 2 on dim stars, and/or allow performance at 1 kHz comparable to OFC performance at 2 kHz. We are specifying the AO control computer (AOC) with sufficient capability to support this predictive algorithm should we decide to implement it.

3.3 Adaptive optics wave front control algorithms

Figure 3-1 show the GPI control block diagram. The remainder of section 3.3 is a description of the algorithms associated with the different blocks, and the data flows between the blocks. Section 3.3.1 describes the real-time tasks; section 3.3.2 describes the non-real-time tasks.

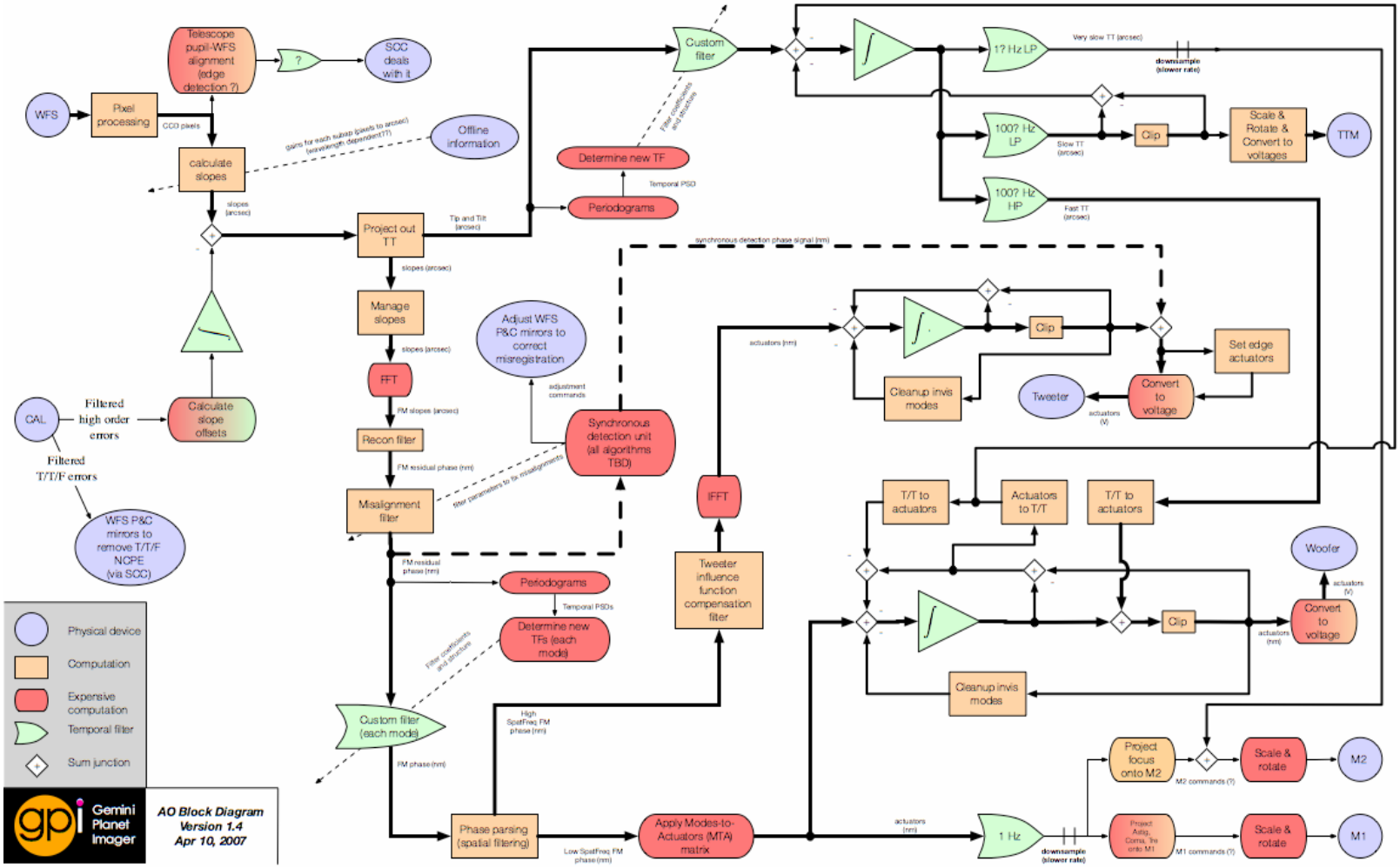

Figure 3-1 GPI control block diagram. Thick lines represent real-time data flows, thin lines represent non-real-time.

3.3.1 Real-time tasks

These are tasks that need to be executed at each frame. They need to be executed very quickly because they count towards the servo-lag, which we want to minimize.

3.3.1.1 Wave front slopes calculation and centroding

3.3.1.1.1 Pixel processing

Raw WFS pixels are processed with standard CCD analysis methods. First a dark frame (corresponding to the current WFS CCD exposure time) is subtracted, then the result is divided by the flat field image.

3.3.1.1.2 Slope calculations

For the quadcell WFS the slopes are calculated using the centroid algorithm.This baseline algorithm takes the four pixel values in each subaperture. For both slopes, the sum of all four pixel values is necessary. Then for the x-slope, the difference between the right pixels and the left is divided by the total. Likewise for the y-slope and the top and bottom pixels. The slopes are next multiplied by a known scaling factor to convert from pixels to arcsec (this scaling factor does not change with seeing because of the spatial filter).

3.3.1.1.3 Slope de-referencing

The AO system will operate off-null, which requires reference slopes to ensure that the AO system drives to an average-flat wave front in the science leg. The reference slope value captures the location of the WFS spot when the science wave front is flat. The operation of slope de-referencing is very simple and involves simply subtracting the reference value from the calculated slope value. For more on reference slope determination, see 3.3.2.3. These reference slopes will be continuously (~1 Hz) updated by corrections fed from the CAL system.

3.3.1.2 High order wave front reconstruction

Wave front reconstruction is accomplished with the Fourier Transform Reconstruction (FTR) algorithm. This method is a filtering method which inverts the WFS measurement process in the frequency domain. FTR is also a modal control method, where each Fourier mode of the residual wave front error is reconstructed. FTR is computationally efficient due to the use of a fast Discrete Fourier transform (e.g. FFTW) to convert from the spatial domain to the modal/frequency domain.

FTR has four distinct steps, three of which occur here. First, the slopes outside the aperture must be managed to ensure proper reconstruction. In the general case, if the slopes outside the illuminated aperture are left as all zeroes, the reconstructed phase will be incorrect. For GPI this slope management is accomplished with the Edge correction technique. This method manages the slopes just outside the aperture such that the reconstructed phase is as flat and close to zero as possible outside of the aperture.

This ensures accurate Fourier modal coefficient estimation, which enables optimization of the temporal control law.

Second, the two slope signals are each converted to the Fourier domain with fast DFTs. Third, the residual phase is reconstructed through application of the FTR inverse filter. After this third step the complex-valued Fourier coefficients are buffered for use by the optimizations (described in 3.3.2.2).

3.3.1.3 High order wave front control

Each Fourier mode is controlled independently. This is done in the Fourier modal space, where an integral-removed control law is applied. Each Fourier mode can have a unique controller. For the baseline optimized-gain integral controller (see 3.3.2.2), this means that each mode is multiplied by a gain. For the predictive controller (see 3.3.2.2), the predictive Kalman filter is applied here, but with the integration step factored out. After this stage the modal splitting occurs, as described in 3.3.1.4. The final integration will be performed in actuator space (see 3.3.1.5.1.) for each of the mirrors.

For the high-order wave front that is compensated on the tweeter, DM influence function compensation then occurs. This is accomplished by a scaling of each mode by a gain factor, which is based on the influence function of the tweeter. Then the final stage of FTR occurs and the phase signal is converted back to the spatial domain with an inverse DFT. This produces the desired residual phase on the tweeter.

3.3.1.4 Woofer-Tweeter wave front parsing

The filtered reconstructed wave front is represented by a 48x48 element vector of Fourier modal coefficients. The n_{low} first elements of this vector represent the Low Order Fourier Mode (LOFM) component; the 48x48-n_{low} remaining elements represent the High Order Fourier Mode (HOFM) component. The LOFMs are directed to the woofer and the HOFMs are directed to the tweeter. Our analysis presented in appendix 3.2 shows that, for a 9x9 piezostack woofer, the optimal value of n_{low} is 44. The LOFMs thus includes Fourier modes with 1 to 3 cycles across the pupil, which are well reproduced by the woofer. Conversion from the 44 LOFM coefficients to the 69 woofer actuators coefficients is achieved by multiplying by a 69x44 matrix Modes-To-Actuators (MTA) matrix. This method of parsing the wave front in the Fourier domain (Fourier partial parsing) is a major improvement in terms of computational burden to the method we presented at CoDR, where the parsing was done from the filtered reconstructed wave front in tweeter actuator space, and thus involved one ~69x1600 and one ~1600x69 VMMs (full parsing).

In appendix 3.2, we show that Fourier wave front parsing has no significant adverse effect on overall correction quality. The woofer, however, is not optimally utilized because the range of wave front it can actually produce is somewhat larger than, and does not fully include, the range of wave front spanned by the 44 first Fourier modes. The Fourier partial parsing method requires an additional ~0.5 micron of stroke from the tweeter, which has been accounted for in our DM actuator stroke budget (see section 3.5.3). In the Critical Design phase, we will investigate whether there is any advantage to adding temporal parsing, that is sending the high temporal frequencies of the LOFMs to the tweeter, and only the low temporal frequencies of the LOFMs to the woofer. The advantage of this approach would be to

be less sensitive to woofer (piezo)-specific effects such as hysteresis. The drawback is a more complex control system and a larger demand on tweeter stroke.

3.3.1.5 High order wave front correction

3.3.1.5.1 Integration

For both the woofer and tweeter, the wave front errors in actuator space are added to the previous commands using an integrator. This integrator has a very slow leak, so that slow drifts due e.g. to round-off errors can be leaked off. There are three different integrators, each operating on a vector: one for T/T, one for the woofer actuators and one for the tweeter actuators. Note that each mode is affected to only one integrator, i.e. T/T for example, which is corrected by both the woofer and by the TTP (see section 3.3.1.6.3), is only integrated by the T/T integrator, and is excluded from the woofer integrator. Similarly, the woofer modes are all excluded from the tweeter integrator. This is critical to prevent integrators fighting each others.

3.3.1.5.2 Clipping

At this point, we have the commands we would like to apply to the DMs in nm of actuator displacement. We check the desired commands against a stroke map, listing the positive and negative saturation limits of each actuator. Any value exceeding the limit is clipped. The stroke map in nm is derived from the actuator voltage limits using the inverse of the nm to volt conversion law (see section 3.3.1.5.3). Note that in the CD phase, we need to address the management of exceeding the inter-actuator stroke.

3.3.1.5.3 Convert wave front to voltages

Our baseline is to convert from actuator displacement in nm to actuator command in volts with a second-order polynomial law, where the three polynomial coefficients are calibrated off-line for each actuator (a simple order 1 fit will be sufficient for the woofer). During the CD phase, we will evaluate the need for a more sophisticated conversion law for the tweeter, able to compensate for the non-superposition of the MEMs influence function, a now well known undesirable feature of the MEMs that, in our closed-loop system, will slightly reduce the rejection bandwidth. Our hope is that this will not be necessary.

3.3.1.6 Tip-tilt control

3.3.1.6.1 Tip-tilt extraction from WFS slopes

The T/T component is extracted from the WFS slopes by computing the dot product with two prototype vectors: one for tip (horizontal vectors of unit length, except for the sup-apertures that are only partially illuminated where the length is less) and one for tilt (vertical vectors of unit length, same remark applies). The T/T component is fed to the T/T controller (section 3.3.1.6.2). The T/T removed slope vector is fed to the high order wave front reconstructor (section 3.3.1.2)

3.3.1.6.2 T/T controller

The temporal controller for tip and tilt will be optimized. Tip and tilt are very important for image stability and at the same time are highly influenced by not just the atmosphere but by wind-shake and instrument/telescope vibrations. Because tip and tilt are only two modes, optimization of a complex temporal filter is a relatively small portion of the computational budget but can yield important gains. Work by Petit (ref 0) has demonstrated the use of Kalman filtering to remove vibrations. Building on our own work at real-time optimization of Kalman filters based on data (see 3.3.2.2), the tip/tilt controller will at a minimum adjust the optimal gain and correct for narrow-band vibrations.

Further work in the CD phase will be conducted, based on experimental information about the expected tip/tilt at Gemini South.

3.3.1.6.3 Temporal splitting for tip-tilt

The T/T correction will be split between the woofer DM surface (that will receive the low amplitude, high temporal frequency T/T) and the tip-tilt platform (that will receive the high amplitude, low temporal frequency T/T) by a pair of low pass and high pass filters, which sum to one across the frequency domain of interest. In addition, persistent T/T will be offloaded to M2 (see section 3.3.2.1.1). T/T sent to the woofer DM surface is converted into actuator commands by a 2x69 matrix multiply.

3.3.1.7 Non time critical miscellaneous tasks

These tasks need to be performed at each frame but after all the actuators have been set. Thus they don't count towards servo-lag.

3.3.1.7.1 Clipping follow-up

To prevent wind-up, we must make sure that the output of the integrators reflects the actual shape of the DMs, even when clipping occurs. This is made easy in our current implementation, because the integrators just precede the clipping blocks. So in case of clipping, the difference between the clipped and unclipped actuator commands is simply fed as an error signal to the input of the integrator. Correction will occur during the next frame.

Clipping is somewhat more complex with T/T, because T/T is corrected by both the woofer and the TTP. If the woofer clips, the T/T component is extracted and fed back as an error signal to the input of the T/T integrator. So only the T/T free component of the clipped woofer command is fed back to the woofer integrator. This works well because the high pass and the low pass temporal filters sending T/T signals to the woofer and to the TTP respectively sum to 1 across the whole frequency band.

For more details on clipping, see appendix 3.3.

3.3.1.7.2 Invisible modes clean-up

Invisible modes are undesirable modes that appear on the tweeter and woofer surfaces and that would not be sensed as errors by the WFS. They result from round-off errors and (mostly) clipping. Invisible modes include:

- For the tweeter:
    - Modes that are poorly seen by the WFS, such as piston and waffle.
    - Modes that are supposed to be corrected by the woofer (44 Fourier modes + T/T)
- For the woofer:
    - Modes that are supposed to be corrected by the tweeter (23 modes =69 (number of actuators) – 44 (Fourier modes corrected by the woofer) – 2 (T/T))

Invisible modes clean-up involves:

1. Projecting from the actuator commands to the invisible modes
2. Projecting from the invisible modes back to actuator commands
3. Applying a clean-up gain and feeding the result as an error signal to the input of integrator, which will be taken into account at the next frame.

The complexity of the clean-up process can be reduced by noting that:

- Invisible mode clean-up is only required when clipping occurs. However, if we only clean when we clip, the clean-up gain has to be one.
- Step 1 and 2 could be implemented as a single matrix multiply. However, since there are many more actuators than invisible modes, a two steps implementation is usually more efficient.
- However, since only at most few actuators will clip at a given instant, a sparse VMM could be used, in which case the one step implementation might be more efficient. This is implemented by comparing the clipped actuator command to the unclipped actuator commands and only projecting the difference (which will be a very sparse vector) onto invisible modes (we know that the unclipped actuator commands do not contain invisible modes)

3.3.1.7.3 Edge actuator setting

At this time, we envision a simple slaving algorithm to drive the MEMs actuators outside the control pupil. During CD, we will investigate the need for a more sophisticated algorithm.

3.3.2 Non real-time tasks

These (often computationally intensive) tasks take place outside the main AO control loop at 10-0.1 Hz rates.

3.3.2.1 Off-loading to the Gemini Telescope

3.3.2.1.1 Off-loading to M2

Slow T/T/F is offloaded to M2. The M2 control system then offloads persistent T/T to the telescope drives to correct for tracking drift. Communication between GPI and Secondary Control System (SCS)

is through the Gemini Synchro Bus, which can accept data at up to 200 Hz frame rate. While M2 might be able to achieve a bandwidth of up to 20 Hz, we are not planning to drive it that fast, since our T/T platform will be even faster and will have plenty of stroke. Rather, we will send only data with frequency content up to 5 Hz. This can be done efficiently by writing a 50 Hz data stream to the Synchro Bus.

3.3.2.1.2 Off-loading to M1

Persistent low order Zernikes are offloaded to M1. The communication between GPI and the Primary Control System (PCS) is also through the Gemini Synchro Bus. Coma is actually applied by translating M2, but the command is issued by the PCS nevertheless. We are planning to send a 1 Hz stream to M1. The woofer commands are averaged for 1 second, then converted to Zernikes, scaled and rotated to the M1 frame of reference, and then written to the Synchro Bus.

3.3.2.2 Wave front controller optimization

The GPI controller will monitor observation conditions and adjust the temporal control as necessary. The baseline controller is Optimized-gain Fourier Control (OFC) (ref 0). In OFC each Fourier mode is controlled independently with an integral controller. Closed-loop telemetry of the Fourier modal coefficients are buffered. These are simply the coefficients directly available after reconstruction filter application. After a suitable-length interval (anywhere from 128 to 2048 samples - exact amount will be determined at a later date) the telemetry is used to estimate the joint closed-loop temporal power spectral density (PSD). This is done by first windowing the complex time-series with a suitable windowing function (e.g. Blackman or Hanning) then calculating the one-dimensional DFT. The magnitude-squared of this is then taken and accumulated over several iterations. This produces an unbaised estimate of the PSD. This joint closed-loop PSD is inverted to a joint open-loop PSD through multiplication with the known system transfer function. The gain on the integral controller is then optimized given the open-loop PSD estimate. This is accomplished in a fast root-finding on the derivative of the closed-loop response as a function of the gain. The new modal gains are instantiated into the modal gain filter.

OFC is the baseline algorithm for GPI for three major reasons. First, the fundamental principles of OFC (use of closed-loop telemetry to determine optimal gains) have already been demonstrated in Altair. This lowers the risk of the approach. Second, analysis and results from the Monte Carlo AO simulator show that modal gain optimization is necessary due to the variation of atmospheric power and WFS noise with spatial frequency. In the case of a dominant wind direction, optimal modal gain will use a range of 0.4 gain units (which is most of the range for a stable integral controller). Even in cases with no dominant wind direction, 0.15 gain units are necessary. Because of the wide range of optimal gains, use of OFC can improve reduce PSF intensity by up to 80% from the unoptimized value. The final reason OFC is a baseline for GPI is that the additional overhead for doing it is low. The amortized costs of temporal PSD estimation and gain optimization are only half of the total cost of FTR. As such, OFC fits reasonably into the GPI computational budget.

During PDR we have done further research into more-advanced control laws. Building on the Kalman filter framework of Le Roux et al (ref 0), and exploiting the independence and special characteristics of the Fourier modes under frozen flow atmosphere, we have developed Predictive Fourier Control (PFC)

(ref 0, appendix 3.1). As in OFC, it uses temporal PSDs as the basis for optimization. In the case of frozen flow atmosphere, the translation of each Fourier mode produces a concentrated spike of power in the temporal PSD of that modal coefficient. This spike is easily identifiable from closed-loop telemetry (even while the predictor is in operation). The specific power levels and temporal frequencies are used in a Kalman filter model to find the best predictive controller. The predictive controller is applied in Fourier space (see 3.3.1.3). Each Fourier modal goes through parallel integrators, one for each layer, and a final stabilizing highpass filter.

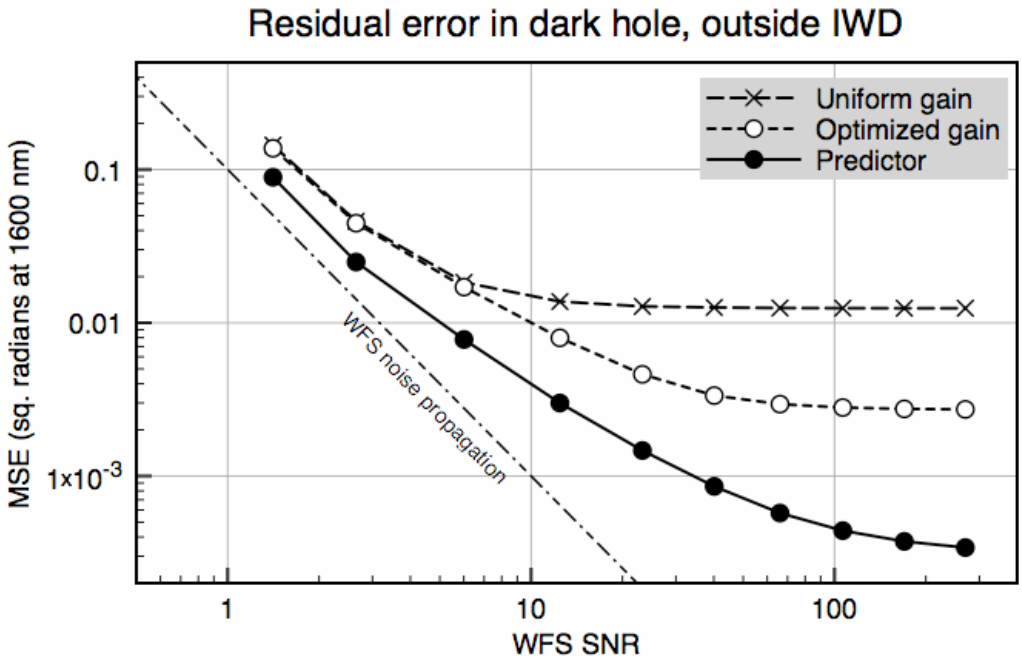

Figure 3-2: Wave front variance at controllable spatial frequencies vs WFS SNR for a plain controller, the baseline OFC controller, and the predictive controller. Dots correspond to *I*=0 to *I*=9 mag.

Unlike Zernike modes (or most other modal basis sets) the Fourier modes are both spatially and temporally uncorrelated under frozen flow. This allows the high-order matrix formulation to be broken into individual low-order controllers, allowin relative computational efficiency. At each time step the primary cost of PFC is due to application of the temporal filter. For many layers, this cost exceeds that of FTR itself. The secondary cost is the solving for the exact filter coefficients, but this process is amortized over many timesteps. (For further details, see Appendix 3.1 paper preprint) PFC will merit more study as GPI development proceeds. Unlike OFC, PFC assumes a specific model for the atmosphere. A survey of atmospheric conditions at Gemini will directly feed into PFC research and the development of the best atmospheric models to use.

3.3.2.3 Update of the reference slopes

The reference slopes control the wave front that the AO system drives to in closed loop. Though initially set through calibration, the values of these references will change during the course of on-sky operation. The changes could be due to relative motion of optical elements in the AO system caused by gravity or

temperature-induced flexures. The references will also compensate for small non-linearities, such as those caused by high-spatial-frequency errors on the edges of M2 which are passed through the spatial filter. In any case, the reference slopes will need to be updated during on-sky operation to ensure the flattest average residual wave front in the science instrument.

The process of updating the reference slopes has two key steps. First, the residual wave front error which must be removed with the references is measured by the Calibration system (see Volume 6), and the resulting phase map is passed on to the AOC .

Second, this phase map is converted into slope signals. The phase map will be on the same sampling as the WFS lenslet array. The phase is converted to slopes through the application of a filter that describes the process of Shack-Hartmann measurement. This is accomplished in the frequency domain in what is essentially a reverse of FTR. The phase signal is converted to Fourier modes with a DFT. If necessary, any x- and y-translational misalignments between the phase and lenslet grids are corrected with a shift filter. Then the x- and y-slope coefficients are generated by the multiplication with a forward filter which describes the WFS process. Two inverse DFTs go to the spatial domain signals for x- and y-slopes. These new slopes are offsets from the present values. They are then added onto the present reference values. This will be done with a temporal filter to ensure stability.

3.3.2.4 Registration and pupil tracking

Because FTR assumes exact alignment between the lenslet array and the actuator grid (especially on the tweeter), this alignment must be monitored. Misregistration, in particularly a translation along either the x- or y-axis of the tweeter actuator grid, will reduce bandwidth and introduce extra temporal error. GPI simulations indicate that up to a 15% of a subaperture translation can be tolerated until residual MSE in the controllable band is increased by 2%. The combined result of misregistration with device non-linearities has not been explored and as such there is a contingency plan for monitoring and correcting misregistrations. In our experimental work at the LAO (ref 0) we have developed an algorithm to measure misalignments through the injection of high-spatial-frequency patterns on the tweeter. To use this in closed loop, we would use the method of synchronous detection (ref 0), most likely while the science camera is shuttered but while the loop is still closed. Once the misalignment is measured, it would be fixed either through a linear-phase shift filter in the reconstruction process of through movement of WFS P&C mirrors. Detailed study of this algorithm (and whether or not it is necessary) remains for the CD phase.

Drifts in the position of the telescope pupil due to flexures will be sensed by analyzing the light distribution on the WFS. Any error will be reported to the SCC, which will adjust the position of the first fold mirror to correct for this error. We expect this loop to work at a frame rate of ~0.1 Hz. The algorithm for sensing the pupil location on the WFS will be developed during the CD phase and will likely involve edge detection, which appears to be more robust than the more straightforward center of mass techniques.

3.3.2.5 Diagnostics

For more details on diagnostics, see appendix 3.4.

3.3.2.5.1 Turbulence estimation

We will jointly estimate r_0 and L_0 from the variance of the first ~15 Zernikes (T/T and piston excluded) of the turbulence, based on an algorithm already developed for Altair. These variances will be obtained by multiplying the variance of the open-loop Fourier modes (which is a by-product of the controller optimization, see section 3.3.2.2) by a Fourier-to-Zernike projection matrix (this operation will be required only once per estimation). We are planning to perform this estimation every time we update our AO controller (every 10s or so).

3.3.2.5.2 Delivered PSF estimation

The telemetry data can also be used to estimate the long exposure PSF, based on work presented in reference 0. This is the PSF that would be obtained after an infinitely long exposure, with no non-common path errors and no residual atmospheric speckles. Such a PSF estimate is extremely useful for studies of diffuse structures such as circumstellar debris disks, allowing subtraction of the diffuse starlight to estimate the precise photometry of the unpolarized component of the disk light. The following statistical values need to be accumulated, starting at the beginning of the science exposure and finishing at the end:

- Mean and standard deviation of r0
- Mean PSD of each measured Fourier mode (this is a by-product of the controller optimization)
- Mean and standard deviation of the flux level in each sub-aperture (goal)

It might be possible to extract information on the residual non-common path aberrations from the CAL Unit telemetry, which could be included to give a more realistic PSF. It might also be possible to extract information on the atmospheric speckle lifetime from the AO telemetry, which could give an estimate of the difference between the real finite exposure PSF and the reconstructed long exposure PSF. Both possibilities will be researched during the CD phase and beyond.

3.3.3 CDR tasks

During the GPI Critical Design phase, we are planning to focus on the following tasks:

- Developing a full temporal model of GPI (possibly in Simulink) to analyse the interactions between all the loops.
- Study the effect of imperfections of the DMs, such non-linearities and mis-calibrations, especially their interaction with the clipping, invisible mode clean-up, and woofer-tweeter parsing.
- Finalize clipping and clean-up strategy
- Define our T/T control strategy, based on T/T telemetry data provided by Gemini
- Analyse the need and define auxiliary supervisory algorithms, such as telescope pupil tracking, mis-registration tracking, optimization of the Calibration System frame rate and exposure time.
- Statistical analysis of the Altair circular buffers, now acquired on a regular basis at Gemini, to refine our understanding of the observing conditions at Gemini and assess the benefits of Predictive Fourier Control.
- Validate PSF reconstruction method,

3.4 Adaptive Optics Computer (AOC) and real-time software

The AO Computer (AOC) is responsible for the realtime measurement, reconstruction, and control of the wave front as sampled by the SFWFS and corrected with the deformable mirrors. Due to severe timing, computational, and input/output (I/O) requirements, the AOC will be a high performance computer, possibly with a math accelerator, and with specialized electronics to permit fast communication with the hardware that it must interface with. The AOC and its peripheral boards will be commercial-off-the-shelf (COTS). None of the specialized electronics that the AOC will interface with will be developed specifically for GPI. However, the list of customers and suppliers for some of the electronics is short.

The preliminary design for the AOC is detailed in the "GPI Adaptive Optics Computer (AOC) SDD" section of the GPI PDR Documents, Volume 3. A brief summary is given in the following.

3.4.1 Timing

The AOC has 2 overarching timing requirements, that are the most challenging aspects of this computer deign:

	Requirement
aoc-req-p1	provide sufficient processing power to support a 2000 frames-per-second update rate
aoc-req-p2	complete all I/O and computations for a given camera frame within the following two frames; GOAL: complete all I/O and computations for a given camera frame within the following one frame

Table AOC2 shows the timing required to achieve these requirements with existing, or nearly existing, hardware and to meet the goal of completing all I/O and computations for a given WFS camera frame within the following frame. Of course, the main obstacle to achieving this is the CCD itself (3.6), but even if the CCD readout takes a substantial fraction of the frame time it is desirable that the total delay be less than 1.5 frames.

Operations, per frame	**Duration, Now (microseconds)**	**Duration, Goal (microseconds)**
Camera Stare	500	500
Read WFS and Centroid	412	250
Reconstruction computations	275	200
Write DMs	50	50
Totals, I/O and computations	737	500

Table 3-1: AOC times-per-frame, with existing, or nearly existing, hardware (Now) and to meet the goal of performing all I/O and computations in a single frame.

3.4.2 AOC Hardware

In order to meet the performance requirements for the GPI AO subsystem, a powerful computer will be required. Although the choice of this computer will be finalized in Critical Design, the current choice is the HP ProLiant DL580 G4 Server. Table 3-2 and Figure 3-3 show the AOC computer along with the peripherals required to meet its requirements.

Quant.	Hardware	Notes
1	HP ProLiant DL580 G4 Server	see specifications in table AOC15
1	Synchrobus interface board	
1	GE-Fanuc PCI-5565	local reflective memory board
1	EDT interface board [CD NOTE: model TBD]	interface to SciMeasure WFS camera electronics
1	VMETRO DPIO2 module	interface to tweeter DM drive electronics
1	ClearSpeed math accelerator	this is not certain yet
1	SciMeasure WFS camera electronics	
1	Cambridge Innovations tweeter DM drive electronics	see specifications in appendix A
1	tip/tilt / woofer DM drive electronics	the interface to this will be USB 2.0

Table 3-2: AOC hardware summary

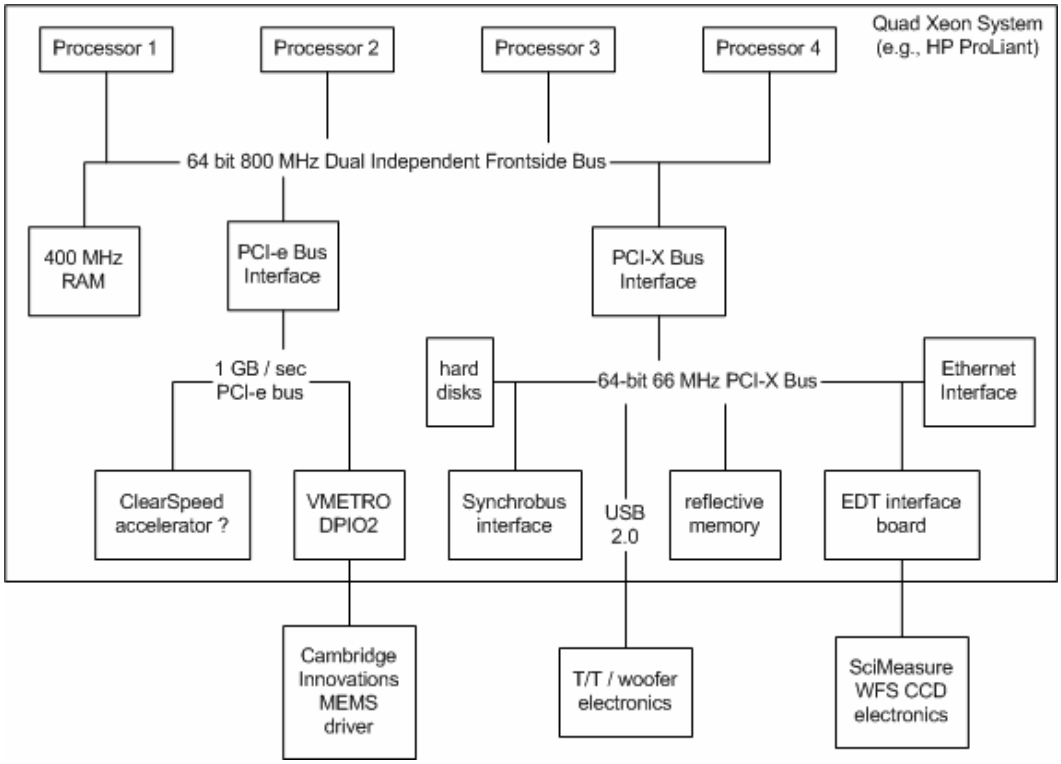

Figure 3-3: AOC with peripherals.

3.4.3 AOC Software

In order to make computations feasible in the time allotted above, the computationally efficient Fourier Transform Reconstructor (FTR) will be used. To enhance low-noise performance, the reconstructed wave fronts will be applied with modal or predictive gains as discussed in 3.3.1.3. These real-time processing tasks and others are as follows:

- read WFS data;
- perform centroiding;
- convert between device and physical units (in several cases, not just here);
- perform wave front reconstruction using FTR;
- apply optimized modal gains or predictive temporal filter;
- periodically use closed-loop telemetry to estimate modal gains or predictive filter coefficients
- parse wave front error between the tweeter, woofer, TT stage, M1, and M2;
- command tweeter, woofer, and TT stage accordingly;
- determine pupil location periodically and send to TLC
- collect and send display data to the TLC periodically, when commanded to do so
- collect real-time diagnostic data to disk, as commanded by the TLC
- calculate and report on-the-fly performance statistics (e.g., r0, Strehl, PSF, wave front error RMS)

In addition to these real-time tasks, the AOC must perform the following tasks (see the "GPI Top Level Computer (TLC) and Adaptive Optics Computer (AOC) ICD" for additional details):

- perform internal calibration steps as commanded by the TLC (WFS background and flat-fielding, reference centroids, etc.)
- receive operating parameters from the TLC (frame rate, camera gain, loop gain etc.) and set accordingly
- determine optimal operating parameters automatically as commanded by the TLC
- close and open AO loops as commanded by TLC

The block diagram in Figure 3-4 shows an overview of how the software will be structured to perform these tasks. Interactions between various parts of the software and between the software and the outside world are also shown.

The AOC software will be written in the C programming language. It will be built on Linux, with a real-time variant to assure efficient I/O interrupt handling (e.g., RTLinux (although RTLinux was recently bought by Wind River)). Other commercially available software packages will be used. Most notably, these packages include: software drivers provided with peripheral interface hardware, the fftw library or the Intel MKL library to perform Discrete Fourier Transforms (DFTs), and the cfitsio library to read and write fits files.

The AOC software will be multi-threaded to permit multiple tasks to occur at once (e.g., wave front reconstructing and saving diagnostic data to disk). The threads will be categorized as hard real-time (HRT) or soft real-time (SRT). The code in HRT threads will have to execute deterministically down to nearly the microsecond level, will run under a Linux RTOS variant, and will be assigned to three of the four AOC processors. Code in SRT threads will be able to get behind a bit (when storing buffered data to disk, for example), will run under Linux proper, and will be assigned to the fourth processor. The HRT code is the code that measures and corrects the wave front in closed-loop.

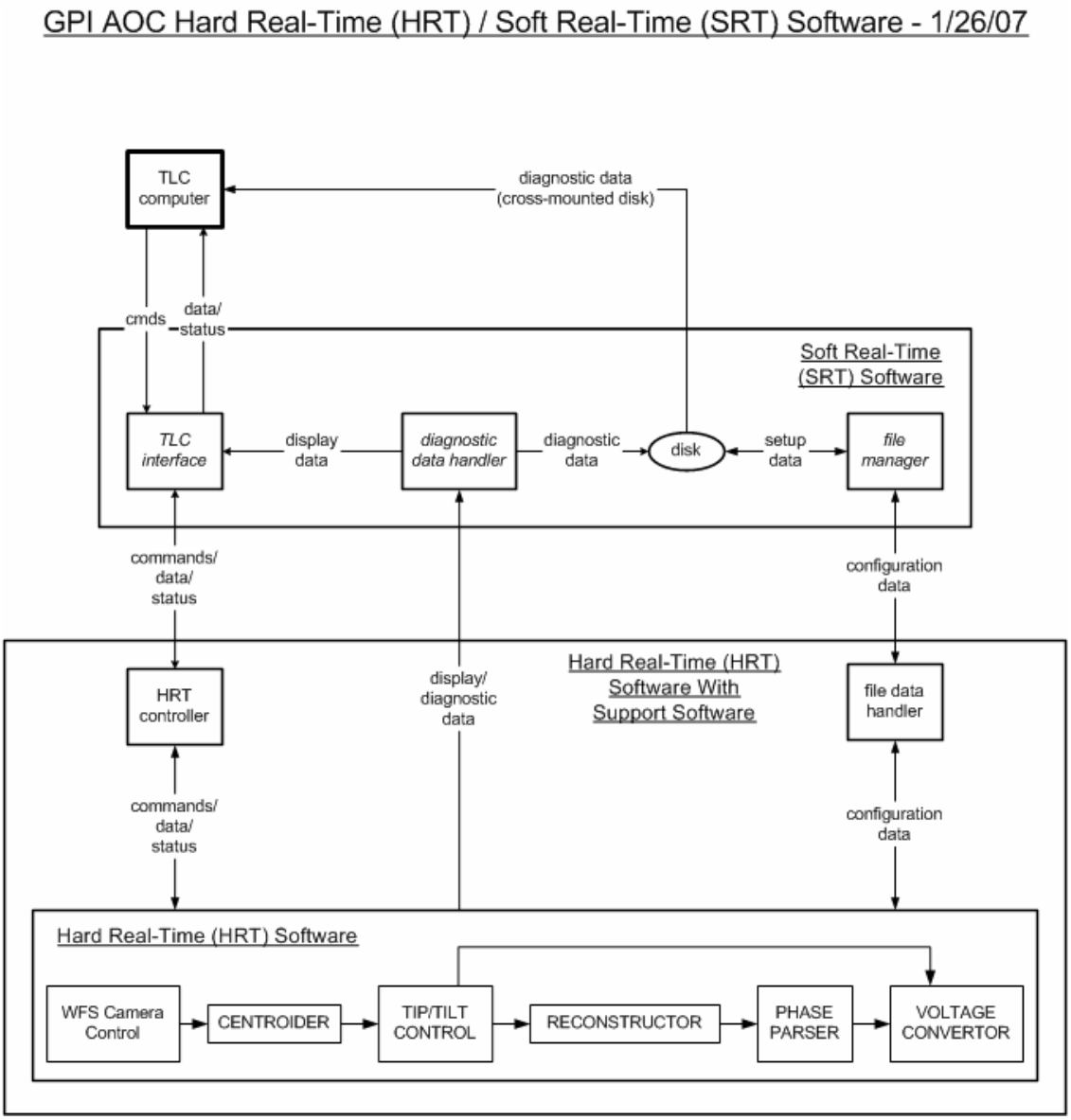

Figure 3-4: AOC software block diagram showing hard and soft realtime components

3.5 DMs and T/T mirrors

3.5.1 MEMs deformable mirror

The 4096-actuator MEMS deformable mirror is a key developmental component of the GPI AO system. Early in the PDR phase, it was clear it would be essentially impossible to package an instrument using conventional (5-8 mm pitch) piezo deformable mirror technology within the Gemini envelope. Higher-density "photonics" module DMs with 1-2.5 mm pitch have been developed by Xinetics, but have low stroke (0.5 microns inter-actuator and 1.4 microns total for a 1.8 mm pitch device); without a prohibitively complex woofer, these would limit GPI to operation in better-than-median seeing. (Use of

these remains one contingency option if MEMS development is slowed.) Overall, in spite of the development risk, we have selected the Boston Micromachines MEMS mirror as the enabling technology for GPI.

GPI requires at least a 48-actuator clear aperture MEMS; to provide some robustness against actuator failures and to enable cost-share partnerships, we have decided to develop a 64x64 device; if actuator failure rates are <0.3%, this gives a good probability of finding a suitable aperture in a foundry run. Currently Boston Micromachines markets 32x32 actuator MEMS mirrors with 1-2 microns (surface) stroke and 12x12 actuator MEMS with 3-4 micron stroke but poor surface quality. To reach the GPI goals, the following issues have to be overcome

- Development of a 64x64 architecture with buried wire layers
- Packaging of that architecture with suitable connectors
- Design of a 3-4 micron-stroke actuator with adequate surface quality (10 nm RMS, 30 nm peak-to-valley)
- Maintenance of actuator yields >99.7% to ensure delivery of a device with a 48-actuator-diameter functional aperture

At the beginning of the PDR phase we placed a development contract with Boston Micromachines for an actuator and layout design study. The results are attached as in the appendices to this chapter. Three promising actuator architectures were identified. Appendix 3.12 gives more details on the results of the study.

Actuator design	Stroke (overall)	Stroke (inter-actuator)	Surface finish (rms) nm	Surface finish (peak-to-valley) nm
2a	4.5 μm @ 265 V	1.5 μm @ 240 V	5	40
3a	4.5 μm @ 265 V	1.8 μm @ 230 V	5	41
3c	4.5 μm @ 240 V	1.2 μm @ 210 V	7	70
Requirement	4.0 μm @ 300 V	1.0 μm @ 300 V	10 (goal 5)	30

Table 3-3: Properties of actuator designs selected for GPI Phase 2 MEMS study.

These actuator designs exceed our requirements in every respect save peak-to-valley surface quality (see section 3.5.1.4.) We have now placed the Phase 2 and 3 contract with Boston Micromachines for continued development of these devices, discussed in Volume 4.

3.5.1.1 Packaging and cabling

Boston Micromachines in collaboration with HIA has developed a plan for packaging the 4096-actuator MEMS device. 528-pin MEGARRAY connectors will be integrated directly onto the back of the ceramic chip carrier, removing the need for a socket or separate carrier board. MEMS mounting is discussed further in Section 3.3.2.7.7.

To control humidity, the entire MEMS will be hermetically sealed. We are working with BM to define the properties of the window and its coating to control ghost reflections and ensure it meets GPI throughput requirements.

3.5.1.2 MEMS DM Electronics

MEMS driver electronics are being developed by Cambridge Innovations under contract to Boston Micromachines. Table 3-4 lists the specifications of these electronics.

Requirement	Value	Note
DIO Interface	32-bit LVDS (200 MB/s)	PMC / PCI card
Interface HV	16x 300pin Megarray (4096 channel)	Based on 256 Channels per driver board
Form factor	3U Chassis (5.25” x19” x14”)	
Frame Rate	>10 KHz (24 KHz goal) (4096 channel)	DIO-limited
Latency	45 us. (4096 channel)	1st word sent to last actuator (DAC) written.
Cross-talk	< 1% peak amplitude	
Power draw	40W	Mitigated by several factors
Current limitation output	0.7 mA max.	
Maximum Output voltage	295V	Amplifier spec.
Resolution	14-bit	
Power supply	HV & LV supplies should be compact	
Power supply type/location, HV&LV	compact and reside inside driver chassis	
Mirror protection	Default to 0V when driver is not being controlled	DACs reset to 0V upon power-up
Board size	3U x 160 mm (P.S., controller, driver); 3U x 80 mm (Output bd.)	
# channels per board	256	
HV line capacitance	~300 pF (TBD)	

Table 3-4: Cambridge Innovations MEMS driver specifications

3.5.1.3 MEMS development timetable

Major milestones in the MEMS development plan:

July 15, 2007 Technical report including design options for packaging

January 16, 2008 Delivery of engineering-grade mirror to UCSC LAO

Final design of packaging, cable interface, and cables

	Phase 2 report
May 8, 2008	Phase 3 interim report
October 16, 2008	Delivery of science-grade MEMS

Note that this schedule provides considerable time for iteration on science-grade MEMS development before the beginning of GPI I&T in early 2010.

3.5.1.4 MEMS development risk: surface scalloping

As seen in Table 3-3, while BM has met the overall surface RMS requirements for the MEMS, the peak-to-valley surface error exceeds our initial specifications. This is due to high-frequency structure on the MEMS surface (beyond the ability of the MEMS to flatten itself.) There are two morphologies for this structure: very sharp actuator print-through features and coarser "scalloping" of individual actuators, especially near the edge of the MEMS. Figure 3-5 shows a representative high-stroke MEMS (with a different actuator than any of the GPI downselected designs). The print-through is present on every actuator. The scalloping, which is caused by stresses in the MEMS membrane, varies across the surface and is generally worse near the edge. There is a risk that the scalloping will become more significant with a larger 64x64 device.

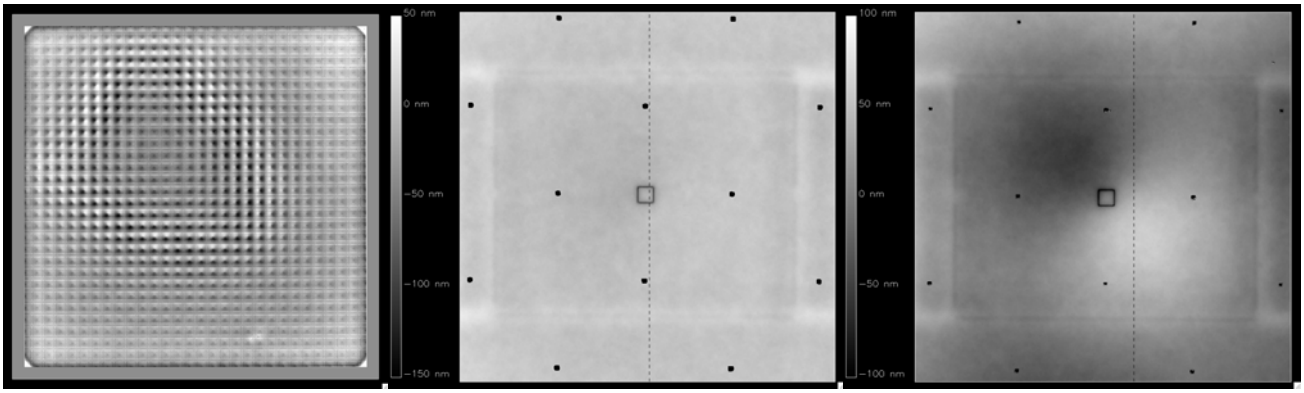

Figure 3-5: Zygo interferograms of the surface of a high-stroke 32x32 MEMS. Left: overall MEMS. Center: close-up of an actuator near device center dominated by print-through. Right: Close-up of an actuator near device edge dominated by scalloping.

We carried out preliminary simulations to assess the effects of these structures. We isolated a 22x22 actuator piece of the above MEMS (half the size of GPI) and used spatial-frequency filtering to decompose it into print-through and scallop components. Flattening of the DM was simulated by zeroing the wave front error within the controlled spatial frequency range. The two phase maps, normalized to 50, 100 and 200 nm peak-to-valley (phase) and fed through a scaled Fraunhofer-optics APLC simulation. As expected, the sharp print-through structures are relatively benign; they scatter power into an extremely broad diffraction pattern spaced by λ/dact, with almost no power near the dark hole region. The scallops create a broader pattern of diffuse light, with some scattering into the dark hole through fourth-order "folding" effects 0.

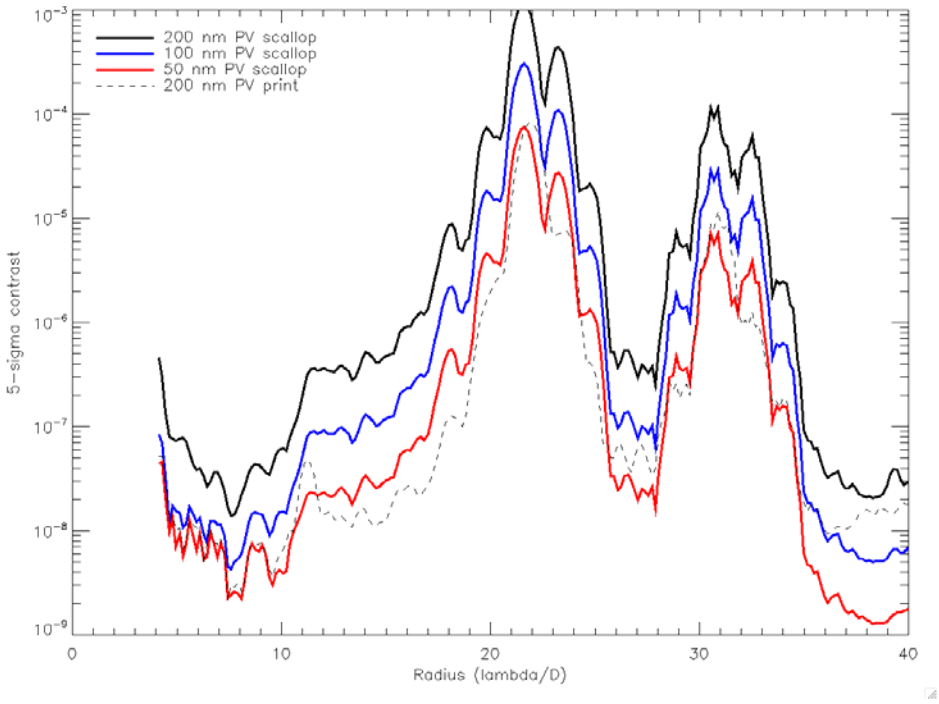

Figure 3-6: 5-sigma contrast vs radius for a simulated 22-actuator MEMS feeding an APLC. The MEMS surface has been simulated with 50, 100 and 200 nm peak-to-valley (phase) of scalloping structure and sperately with 200 nm of print-through. For this half-scale system, the "dark hole" extends out to 11 λ/D. Contrast within the dark hole would improve by ~4 with the full GPI 44x44 geometry.

From these, it can be seen that 50 nm PV phase scalloping will have negligible effects on contrast, 100 nm slightly effects, and 200 nm significant effects. The BM 2a and 3a actuator designs (40 nm PV surface) meet these requirements. The simulations will be extended to the full GPI aperture in early CDR.

However, an important disclaimer exists for these simulation results. These were carried out using the Fraunhofer approximation, where the electric field in the focal plane is just the Fourier transform of the electric field in the pupil plane (plus a quadratic phase factor that has no impact on measured intensity.) This approximation is formally correct for the GPI geometry with one crucial exception: it assumes infinite optics, ie no loss of light in intermediate planes.

Observations taken at the UCSC LAO (and similar JPL) testbed show the limitations of this Fraunhofer propagation. Measurements taken with a CCD conjugate to a uniformly illuminated MEMS show intensity variations tracking the pattern of the surface print-through and scallops (Figure 3-7). One possible cause for this is Talbot-propagation (analogous to the effect that is exploited in curvature-sensing. These effects would cause a slightly out-of-focus image of the MEMS will show phase-induced amplitude errors. Although this can result in 10% apparent variations in intensity across the MEMS, such an effect would not directly impact final contrast; in the Fraunhofer approximation, the far-field image can be created using the electric field at the MEMS itself, where the intensity is still uniform.

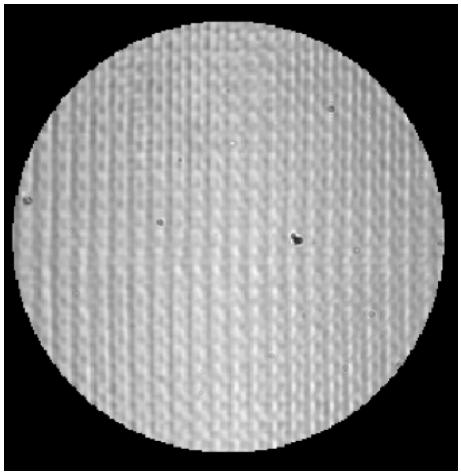

Figure 3-7: CCD image of the MEMS plane at the UCSC testbed. Intensity variations are approximately 10%.

If these effects were the only cause of amplitude variations, it should be possible (though difficult) to focus the CCD directly to the MEMS and see uniform illumination. Though we can minimize the variations we have so far been unable to make them go away completely. This could indicate that some intensity variations are due to finite optics sizes – light from the print-through pattern scattering outside of the beam area collected by the testbed optics. This latter effect could potentially impact final contrast. We cannot directly evaluate these effects on the far-field contrast with the current UCSC testbed due to its low-performance coronagraph; however, we will be upgrading to a APLC in June, allowing direct comparison of models to contrast. Evaluating the severity of the finite-optics effect requires more advanced wave-optics modelling of the testbed and GPI system. This modelling will be carried out in June-July 2007. To mitigate the risk we are oversizing GPI optics between the MEMS and the occulting mask. Finally, we are working with Boston Micromachines to minimize scallops in the delivered final MEMS. The GPI MEMS delivery schedule includes time for multiple foundry runs to iterate on MEMS process and select the final device with the best wavefront quality.

A related concern is that part of the intensity variations seen above are due to intrinsic non-uniformity of the MEMS gold coating. We have carried out electron-microscope measurements of the MEMS to look for variations in coating thickness; these show that any such variations are <1% RMS (of a ~90 nm thick coating.)

3.5.2 Woofer Deformable mirror

For the woofer, we chose a 9x9 piezo-stack DM, with 5mm inter-actuator spacing (pupil size = 40mm), mounted on a tip-tilt platform (TTP). This choice was driven by the current state of the art in DM technology and space constraints from the opto-mechanical packaging. See Appendix 3.5 for a complete trade-off analysis and Appendix 3.11 for a complete woofer requirements document.

Size of the woofer deformable mirror and the f/16 relay feeding it is one of the major drivers in packaging the GPI system. The opto-mechanical design calls for a maximum pupil size at the woofer of 40 mm. For piezo-stack deformable mirrors, the smallest actuator spacing actually demonstrated is 5mm, therefore the maximum actuator density for the GPI woofer is 9x9 (8 actuator spacing across the

40mm pupil). CILAS has recently delivered a 9x9 5mm pitch DM as a prototype for TMT. Xinetics have a similar product on their catalogue.

Table 3-5 show the stroke requirements for different woofer actuator densities, based on Monte-Carlo simulations using realistic influence functions to model the woofer. The stroke is computed to allow for a 5σ margin (i.e. saturation occurs at ±5σ). Our baseline wave-front parsing algorithm is the partial offload in Fourier space (offloading of the first 44 Fourier modes), for computational reasons (see section 3.3.1.4). The current state of the art for piezo-DM is 10 microns of global stroke and ~4 microns of inter-actuator stroke (as measured on the TMT prototype). Our specification for the MEMs woofer is 3 microns of global stroke and 1 micron of inter-actuator stroke (early results from Boston Micromachine suggest that the mirror may exceed these specifications, see section 3.5.1). The results from Table 3-5 show that the most constraining parameter is the inter-actuator stroke. This can appear surprising, especially for the woofer, because classical AO systems are usually not limited by the inter-actuator stroke. However, one should remember that a classical AO system would generally have a lower saturation margin (typically ±2-3σ) and ~ 15 actuators across the pupil to correct our nominal r0=14.4cm turbulence. Reducing the number of actuators does not change the global stroke, but does increase the inter-actuator stroke. We also note that for the MEMs tweeter, the inter-actuator stroke seems also more critical than the global stroke. The full stroke budget is presented in section 3.5.3.

			5x5 woofer	**7x7 woofer**	**9x9 woofer**	**11x11 woofer**	**13x13 woofer**
Full offload (actuator space)	Global stroke	woofer	5.19	5.14	5.09	4.86	4.62
		tweeter	1.99	1.51	1.20	1.01	0.90
	Inter-act stroke	woofer	6.52	5.13	4.20	3.57	3.15
		tweeter	0.81	0.82	0.80	0.76	0.79
Partial offload (Fourier space)	Global stroke	woofer			4.38		
		tweeter			1.61		
	Inter-act stroke	woofer			3.50		
		tweeter			0.98		

Table 3-5 Stroke requirements (global stroke and inter-actuator stroke) to correct a r0=14.4cm Kolmogorov turbulence (T/T excluded) with a 5σ saturation margin, as a function of the actuator density on the woofer. In the "Full offload" case, the wave-front is parsed in actuator space and the tweeter stroke is minimized. In the "Partial offload case (baseline), the wave-front is parsed in Fourier space, which is more computationally efficient. We have only explored this approach for a 9x9 woofer, which is our baseline.

We have also investigated whether we could use a bimorph DM instead of a piezostack DM. We found that in order to meet our maximum pupil size requirement of 40mm, we would have to specify a minimum radius of curvature somewhat beyond the current state of the art. That, and the fact that piezo-stack DMs are more widely used and better understood, led us to rank the bimorph solution as inferior. Also, even though bimorph DM can, in principle, achieve much greater T/T stroke than piezostack DMs, we found that we could not avoid the use of a separate platform (see section 3.5.2.1) without significantly increasing the overall DM assembly size, which is undesirable.

The 52-actuator (8x8) magnetic (voice-coil) DM recently developed at Laboratoire d'Astophysique de Grenoble, in France, appeared to be an appealing option, as it features a huge stroke on only a 17.4mm

pupil ! However, this option was rejected over concerns on reliability, especially in the cold (this DM has never been tested at a telescope) and power dissipation (the actuator are driven by current).

3.5.2.1 Tip-tilt platform

The woofer will be mounted on a tip-tilt platform (TTP), which would provide the bulk of the T/T correction. Because the TTP has to hold the ~ 1 kg mirror head, its bandwidth will be limited. Therefore the highest temporal frequencies of T/T will be corrected on the woofer surface. The TTP bandwidth is set by its first resonance frequency: the higher it is, the lower the T/T amplitude to be corrected on the woofer surface, minimizing the demand in additional actuator stroke. We have studied how much residual T/T we need to correct on the woofer surface as a function of the first resonance frequency of the T/T platform, for different observing condition. The results are found in Table 3-6.

Windshake	T/T platform resonance frequency								
	0 Hz	12.5 Hz	25 Hz	50 Hz	100 Hz	200 Hz	400 Hz	800 Hz	1.6 kHz
25 mas rms	1.015	0.273	0.151	0.087	0.046	0.023	0.013	0.011	0.01
50 mas rms	1.103	0.479	0.27	0.16	0.086	0.043	0.025	0.02	0.018
100 mas rms	1.402	0.921	0.523	0.313	0.168	0.085	0.049	0.038	0.035
200 mas rms	2.229	1.823	1.036	0.623	0.334	0.169	0.098	0.076	0.07

Table 3-6 PV one-axis tilt (arcsec on the sky) left for the woofer surface to correct, after correction from a T/T platform with a given resonance frequency, for different windshake scenarios. T/T residual includes atmospheric T/T for r0=14.4cm.

In our stroke budget, we have conservatively used the 100 mas rms windshake scenario and chose a 50 Hz TTP. The PV T/T to be corrected on the woofer surface is then 0.313 arcsec. It turns out that in fact a higher resonance frequency (up to 250 Hz) could be achieved, for example by the P-518 piezo platform from PI (Physik Instrumente), which is our baseline (for the specifications of the P-518 piezo-platform, see Appendix 7.42).

3.5.3 DM actuators stroke budget

Table 3-7 summarizes our current stroke budget.

	woofer stroke (nm)		tweeter stroke (nm)	
	Global	Inter-actu	Global	Inter-actu.
STATIC ERRORS				
woofer flattening	500	185	100	35
MEMs flattening	242	106	0	0
GPI optics				
M1				
M2	23	16	112	83
M3				
TOTAL STATIC	*765*	*307*	*212*	*118*

DYNAMIC ERRORS				
High order atmospheric turbulence	4376	3497	1614	983
High order Dome seeing				
T/T (windshake + seeing + vibrations)	6260	1517	0	0
TOTAL DYNAMIC	*7638*	*3812*	*1614*	*983*
GRAND TOTAL	**8403**	**4119**	**1825**	**1100**

Table 3-7 Stroke budget (global and inter-actuator stroke) for the woofer and the tweeter. A 5-sigma saturation margin is assumed.

The budget is split into static errors and dynamic errors. Dynamic errors are random and uncorrelated, and thus sum in quadrature. Static error contributions sum linearly, and their total sum linearly with the dynamic errors to give the grand total.

The static errors include:

- woofer flattening: woofer contribution is 500 nm PV, 122 nm rms (based on TMT prototype test report). We assume this is mostly defocus to find the inter-actuator stroke; the tweeter contribution is 100 nm PV (based on TMT prototype test report). We assume this is mostly a 5-cycle sine mode to find the inter-actuator stroke.
- MEMs flattening: woofer contribution corresponds to our spec of 70 nm rms residual after self flattening; tweeter contribution is set to zero, as self-flattening is included in the specified stroke.
- GPI optics (all the imagery path) is assumed to be small and is not yet accounted for in the budget.
- M2 figure correction numbers comes from the analysis of M2 interferograms, provided by Gemini: the stroke required is mostly at the edge of the pupil (turned-down edge).
- M1 and M3 figure correction is assumed to be small and is not accounted yet in the budget.

Dynamic errors include:

- High order atmospheric turbulence: these numbers come from Table 3-5, assuming a 9x9 woofer.
- High order dome seeing, which is TBD and not accounted for yet.
- Tip-tilt: these numbers come from Table 3-6, assuming a 100 mas rms windshake and a 50 Hz T/T platform. As discussed in section 3.5.2.1, the TTP is likely to achieve a higher bandwidth, and thus these numbers could be lowered. The MEMs is not involved in T/T correction.

Considering the current specifications / state of the art for the woofer and MEMs, we find that the inter-actuator stroke is more critical than the global stroke, especially for the woofer. As discussed in section 3.5.2, this led to the choice of a 9x9 woofer.

3.6 AOWFS detector

A key downselect (not yet complete) is the choice of the CCD for the SFWFS. It must meet several challenging requirements in the baseline design, most importantly:

- frame rates >2000 Hz (ideally with readout time even faster, ~0.250 ms)
- high QE in the red

- readout noise <7 electrons for dim-star performance

The final selection has been delayed in part due to rapid progress in fast CCD development. In addition, modelling to determine the optimum scientific trade between frame rate (setting the bright-star performance) and readout noise (setting dim-star performance) is still in progress. For example, a predictive controller could relax the need for high frame rates, while simultaneously letting us operate in low SNR regimes where readnoise is more significant than Poisson noise.

For this reason, the CCD downselect has been deferred until early CDR. We have implemented an optical design (7.2.1.5) that supports a variety of potential CCDs – even the large PN sensor pixels can be accommodated by swapping two relay elements. As a result, this trade is not significantly affecting the mechanical design of the instrument. In summer of 2007 we will complete a set of modelling trade studies and evaluate the procurement / manufacture risks of each CCD to produce a selection of two devices, with a final decision in mid-late CDR.

Requirements	**Minimum (Goal)**	**EEV CCD-50**	**MIT/LL CCID-18**	**MIT/LL CCID-56**	**PNSensors**
Number of pixels	128x128 (176x176)	128x128	128x128	160x160	264x264
Pixel size (microns)		24	21	18 to 21	50 microns
Number of outputs (amplifiers)		16	16	20	264 amplifiers multiplexed in ASICS down to 2 ADCs; 8 ADC upgrade possible
Average QE for Optical Light Normal Incidence 700-900 nm	60% (80%)		~65%	~80%	90%
Maximum full-frame rates (frames/sec) at given pixel rate		2018 Hz (at 2.5 MHz) 1245 Hz (1.5 MHz)	~2425 (at 4 MHz)	~700 at 1 MHz; ~3500 at 5 MHz	1100 (2 ADCs) 4000 (8 ADCs)
Estimated max. frame rate, illuminated rows only (μs)	2500	~2900 Hz (2.5 MHz) ~1810 Hz (1.5 MHz)	3527	~1300 at 1 MHz ~6300 at 5 MHz	3300
Minimum read-out time, illuminated rows only (μs)	500 (250)	345 (2.5 MHz) 550 (2.5 MHz)	~412	~786 at 1 MHz; ~158 at 5 MHz	303
Read noise (rms) (e-/macropixel)	8 (5-)	9.8 (2.5 MHz) 7.0 (1.5 MHz)	*9 to 12*	<2 at 1 MHz	2.3

Requirements	Minimum (Goal)	EEV CCD-50	MIT/LL CCID-18	MIT/LL CCID-56	PNSensors
Status / Availability		2.5 MHz electronics under testing at SciMeasure	proven device, available now.	1 MHz AODP version in test; 5 MHz being considered by LL	Unclear. HIA/GPI may order test device.

Table 3-8: CCD options under primary consideration

Frame time and readout noise values are based primary on information from testing by Charlie Bleau of Scimeasure. Frame rates are given both full-frame and assuming that only the 88 illuminated rows are read out.

Some comments on individual devices:

The Lincoln Laboratory CCID-18 device is the most proven for high-speed applications, in use e.g. in USAF AO systems. Against that, its noise performance is somewhat below our goals. Still, it remains the lowest-risk baseline. Expected noise performance at lower frame rates: ~5-7 e- rms (~695 fps – 1 Mhz), 7-9 e-rms (~1325 fps – 2 Mhz)9-12 e- rms (~2425 fps – 4 Mhz). Dark current <13,8000 e/pixel/second at –5C, so a second TE cooler stage for operation below –20 C would be required.

The EEV CCD-50 is normally operated at MHz pixel rates with 6-7 electron noise, but SciMeasure is currently experimenting with faster readout giving the performance described above. This makes it roughly comparable to the CCID-18, with preference to be given to whichever device is easier to obtain and integrate.

The NSF AODP-funded CCID-56 device is currently in testing. It is optimized for low noise at moderate frame rates, but Lincoln Labs is studying a faster version with 5-10 MHz output amplifiers on ~1 year timescales. Existing amplifiers may support 2 MHz operation. The existing version meets all requirements except frame rate, and this device could be selected if science modelling determines that dim-star performance is more valuable than bright-star performance. Dark current sufficiently low for operation at –5C with a single TE cooler.

The PNSensors thick CCD, developed for X-ray applications, has excellent reported characteristics (particularly QE at long wavelengths). However, WFS use is a new application for PN Sensors, a relatively small company, and attempts within the AO community to procure test samples have been frustrating. HIA had been negotiating an purchase of a prototype using internal funding, but the most recent price quote (30,000 Euros) exceeded HIA's available internal funding. We are considering ordering a CCD or complete camera system using GPI project funding; HIA would then provide manpower for a CCD test.

In addition, we will monitor the development of the EEV CCD60 L3 CCD. This device uses a avalanche-like output register to achieve near-zero readout noise, but at the cost of excess Poisson noise (effectively halving the QE). Concerns about this excess Poisson noise, stability of the register gain, and development timetable currently have moved this off our highest-probability list, particularly since the

GPI design emphasizes performance in the *I*=6-8 mag. range, and for our frame rates and geometries we would still require quad-cell operation.

We are carrying out preliminary simulations of different CCDs using the analytic code described in 3.7.1,which supports arbitrary system delays that are not a multiple of the CCD stare time. We compared the CCID-18 at rates of 500-2500 Hz with a CCID-56 at 500-1300 Hz, using the 13-layer Gemini atmosphere and the OFC. In each case, the simulation determined the optimum frame rate for a given target magnitude and evaluated the radially averaged intensity at 6, 12 and 24 λ/D. Figure 3-1 shows the results. In early CDR we will feed these models into our Monte Carlo planet detection simulations to evaluate the science capabilities of the two devices, and verify the analytic models with numerical AO simulations.

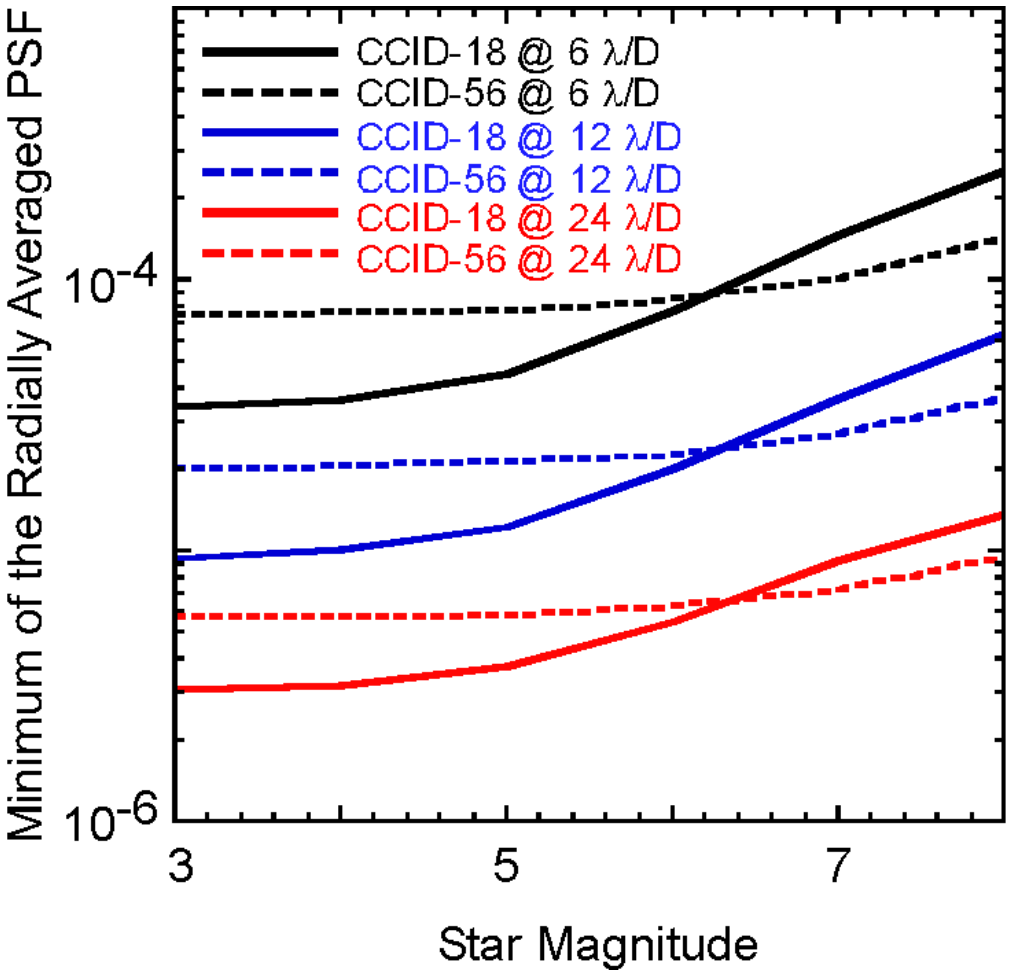

Figure 3-8: Performance comparison between a CCID-56 and CCID-18.

3.7 AO simulations

Simulations of the AO system have been used throughout the PDR design process. Some use analytic predictions of the WFE power spectrum, but wherever possible (e.g. the tolerancing of WFS alignment

discussed in Appendix 3.10, or the final contrast predictions for the GPI system in Appendix 2.25) we use a full Monte Carlo Fraunhofer AO simulation. This is also the primary simulation used in GPI AO algorithm development and performance analysis. An end-to-end simulation, it simulates both the wave fronts and the performance of the control system.

The atmospheric phase aberrations are based on multi-layer models under the assumption of frozen flow. For a given atmospheric profile, each layer's r0 and wind velocity vector are specified (see Section 2.4 for a table of the standard atmosphere model. This is a r0=14cm CP model provided by Gemini.) At the beginning of a simulation, specific turbulence realizations are created using the spectral factor white-noise filtering method to match the Kolmogorov spatial power spectrum, with adequate grid size. At any instant in time during the simulation, each layer is shifted with smoothed sub-pixel accuracy and the phases from each layer are summed. As such, the end-to-end simulation ignores scintillation. (The effects of scintillation on final contrast have been included in both the contrast tolerancing simulations in Appendix 2.# and the analytic PSF predictions discussed below.) At present the tip-tilt input in to the AO controller is just what is generated from the frozen flow of the layers - no further atmospheric modeling or telescope vibration are included.

The full atmospheric phase in conjugated with a Woofer-Tweeter-TT mirror arrangement. Both the woofer and tweeter are assumed to follow linear superposition, using the measured influence function of the ALtair DM. A main task for CD is to incorporate non-linear DM models to study the impact on performance.

After phase conjugation the residual wave front is sent to both the science unit and the WFS leg. In the science unit the full APLC has been implemented with Fourier Optics. The APLC can be run narrow-band or broadband. Due to the cost of the APLC, the more-efficient Blackman amplitude apodization can also be used to suppress diffraction.

The WFS leg uses multiple wavelengths in the WFS band and Fourier Optics. This enables study of spatial filter performance in broad-band situations (where the spatial filter is mis-sized for most of the light) as well as chromatic phenomena such as differential atmospheric refraction. The NGS guide star is specified by its black-body temperature (e.g. the sun would be 5560K), Cousins *I*-band magnitude and bandwidth on the WFS. Then with 25 nm spacing in the band, each wavelength of light is processed through the spatial filter. This can capture the effects of having the spatial filter incorrectly sized or having the star misaligned.

Other misalignments in the AO system can also be included. For the MEMS actuator grid to the WFS lenslet array, the pupils can be misaligned by translations in x or y, magnifications (i.e. off-optical-axis tilts) in x or y and rotations. Likewise, the WFS CCD grid of spots can be translated, magnified or rotated. This has allowed the study of the impact of misalignments and helped place tolerances on the allowable flexure in the AO relay.

Most of the PDR wave front controller design in actually implemented in the simulation. This includes: WFS centroid calculation and de-referencing, tip-tilt removal and control with an optimized controller, reconstruction of the phase with FTR and either optimized-gain or predictive control. The Fourier-splitting matrix technique for woofer-tweeter control is fully implemented. The primary aspect of the controller which is not in the simulation is that gain optimization and prediction are not supervisory

processes. This is instead done on saved telemetry with a helper procedure, then new gains or controllers are used in the next run.

3.7.1 Analytic PSF-prediction and evaluation of chromatic and scintillation effects

During PD we have developed a semi-analytic code to predict long-exposure PSF levels from fundamental system properties. This code serves several important functions: confirming results out of end-to-end monte carlo simulation, bridging the gap between monte carlo sims and the purely scaling-law error budget, and allowing fast parameter studies, such as of WFS CCD noise levels.

This code is based on an analytic examination of fundamental AO error terms. As such it builds upon the work of Guyon 0 (particularly for chromatic and amplitude-related error terms) and the power-spectrum approaches of Jolissant et al 0 and Ellerbroek 0. The code takes as input atmospheric profiles (assuming frozen flow) and NGS and AO system parameters.

Using a 2D grid for spatial frequencies/PSF locations, the code determines the following fundamental error terms, expressed as the PSD halo term of the PSF, normalized to the chosen coronagraph:

1) Fitting error
2) WFS noise propagation in closed-loop
3) Temporal lag correcting the atmosphere (shown below combined with (2) as "AO residual")
4) Scintillation (uncorrected amplitude errors)
5) Chromatic errors from the fact that the WFS band is different from the science wavelength:
    -chromatic fresnel propagation
    -chromatic shear of pupils due to differential atmospheric refraction
    -change in amount of phase aberration due to chromatic changes in the index of refraction.

The code ignores the classical AO error terms of anisoplanatism and aliasing, since they are not significant for GPI. The code can deal directly with a broad-band in the WFS leg and a non-uniform spectrum in that band, though it does still ignore the slight aliasing leak at the edges of the dark hole.

We have also developed a semi-analytic (because the analytic solution did not have a closed form) treatment of Optimized-gain Fourier control and used this to verify our previous work with OFC in the end-to-end simulation.

This simulation predicts the average intensity in the long-exposure PSF; it cannot directly predict residual speckle noise, though that can be estimated from speckle lifetime scaling laws. Figure 3-9 shows this results of such a calculation for the 13-layer CP atmosphere. From this, it can be seen that the only significant additional error term beyond the fundamental AO limits is scintillation, which may become marginally significant at the edge of the dark hole.

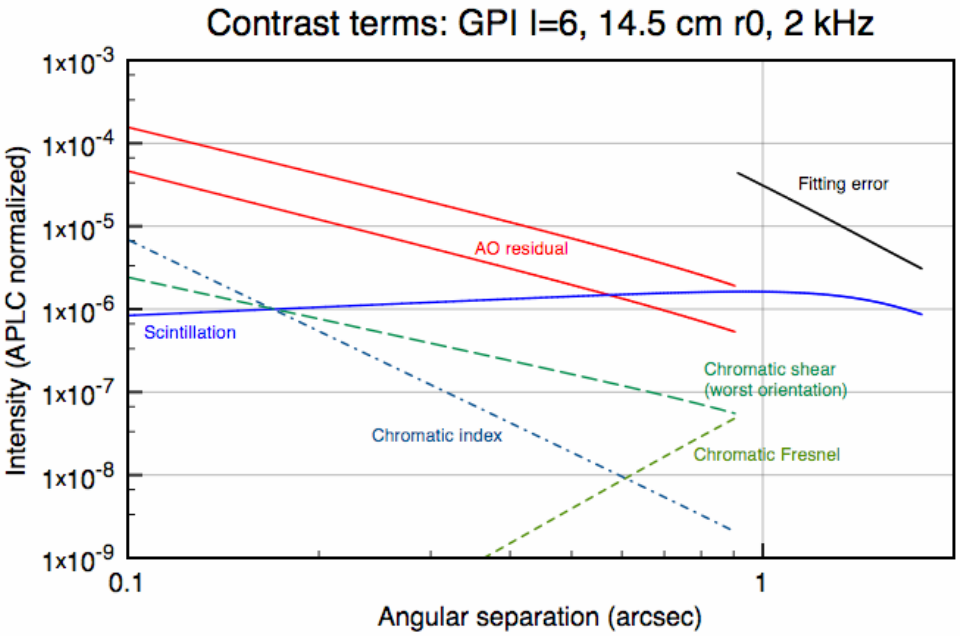

Figure 3-9: PSF intensity vs radius from analytic calculations of wave front phase and amplitude errors. "AO residual" shows the combined WFS measurement noise and temporal in the best and worst directions in the PSF. "Fitting error" is the classic atmospheric fitting term. "Scintillation" is normal intensity-fluctuation scintillation. "Chromatic shear" represents the different light paths between the visible WFS and IR science instrument at 30 degree Zenith angle. "Chromatic index" represents the path-length change due to dispersion of air.

3.8 Reliability, availability and maintainability

The single most expensive component in GPI is, of course, its MEMS deformable mirror. Our contract with BM requires that the MEMS operate for 33,000 hours under powered conditions. The CoDR design specified that GPI would humidity-control the entire instrument using overpressurized Gemini dry air, but we have been unable to predict what humidity level we could achieve with this approach, and recent BM tests show evidence of actuator damage after 20 hours of high-voltage operation even at moderately low humidity (~40%) , which raises the concern that lifetimes may not meet GPI requirements even at 20-30% humidity. To protect the MEMS from humidity and dust it will therefore be hermetically sealed. With such sealing, the MEMS should remain robust. To date, out of ~10 32x32 actuator MEMS operated at UCSC, we have seen only one actuator failure (which coincided with the device being removed and reinserted into its socket and hence is likely to be static damage.) We will work with BM to define handling procedures for the GPI MEMS and establish clear anti-static procedures for connecting and disconnecting the device. Overall, it is expected to be no more static sensitive than an infrared detector array.

3.9 AO References

J.-P. Véran, F. Rigaut, H. Maître, and D. Rouan, "Estimation of the adaptive optics long exposure point spread function using control loop data", J. Opt. Soc. Am. A, Vol. 14, pp. 3057-3069, 1997.

C. Petit, J.-M. Conan, C. Kulcsar, H.-F. Raynaud, T. Fusco, J. Montri, and D. Rabaud, "First laboratory demonstration of closed-loop Kalman based optimal control for vibration filtering and simplified MCAO," in Advances in Adaptive Optics II, B. L. Ellerbroek and D. B. Calia, eds., Proc. SPIE 6272, p. 62721T (2006).

B. Le Roux, J.-M. Conan, C. Kulcsar, H.-F. Raynaud, L. M. Mugnier, and T. Fusco, "Optimal control law for classical and multiconjugate adaptive optics," J. Opt. Soc. Am. A 21, 1261–1276 (2004).

L. A. Poyneer, J.-P. Véran, D. Dillon, S. Severson, and B. A. Macintosh, "Wave front control for the Gemini Planet Imager," in Advances in Adaptive Optics II, Proc. SPIE 6272, p. 62721N (2006).

S. Esposito, R. Tubbs, A. Puglisi, S. Oberti, A. Tozzi, M. Xompero, and D. Zanotti, "High SNR measurement of interaction matrix on-sky and in lab," in Advances in Adaptive Optics II, B. L. Ellerbroek and D. B. Calia, eds., Proc. SPIE 6272, p. 62721C (2006).

L. A. Poyneer and J.-P. Véran, "Optimal modal Fourier transform wave-front control," J. Opt. Soc. Am. A 22, 1515–1526 (2005).

L. A. Poyneer, B. A. Macintosh, and J.-P. Véran, "Fourier transform wave front control with adaptive prediction of the atmosphere," J. Opt. Soc. Am. A (submitted 2006).

Give'on, A., et al, "On representing and correcting wave front errors in high-contrast imaging systems", J. Opt. Soc. Am. A 23, 1063 (2006)

Guyon, O., "Limits of adaptive optics for High-Contrast Imaging", Ap.J., 629, 592 (2005)

L. Jolissaint, J.-P. Véran, and R. Conan, "Analytical modeling of adaptive optics: foundations of the phase spatial power spectrum approach," J. Opt. Soc. Am. A 23, 382–394 (2006).

B. L. Ellerbroek, "Linear systems modeling of adaptive optics in the spatial-frequency domain," J. Opt. Soc. Am. A 22, 310–322 (2005).

4 Coronagraph (AMNH)

4.1 Overview

The coronagraph subsystem effects the removal of as much of the diffracted portion of central star's light from the field of view as possible using only optical techniques, such as diffraction or interference along with careful use of optical stops or masks. The class of such techniques is generally referred to herein as coronagraphy.

Coronagraph system key requirements:

- Suppress diffraction to a residual intensity contrast of $6x10^{-8}$ averaged from 5-6 λ/D and $2x10^{-8}$at 10-12 λ/D, in the absence of wavefront and tilt errors, at optimal wavelength.
- Goal: achieve comparable performance over a 10% bandpass.
- Allow detection of companions at separations > 4 λ/D
- Any wavelength-dependent (chromatic) aberrations induced by the occultor must be <0.5 nm RMS in the mid-frequency (4-22 cycles/pupil) range across the J, H and K bands
- Provide a variety of occultor combinations to support different wavelengths and science goals
- Operate with acceptable tolerances on flexure and pointing accuracy
- Allow measurement of target star position accurate enough to enable astrometry at the science requirement levels (1.8 mas/axis at the 3σ significance level)

Coronagraph key interfaces:

- Accepts a converging *f*/64 beam with a finite pupil from the AO system
- Provide on-axis PSF core light to the calibration system reference arm
- Provide a fraction of the off-axis science light to the calibration system measurement arm
- Produce a collimated beam with a 1 cm pupil for the science instrument

Coronagraph design summary

- Apodized-pupil lyot coronagraph (APLC) combining mild pupil-plane apodization with an occultor and Lyot mask
- Selectable apodizers in a rotating wheel mechanism
- Selectable reflecting focal-pane occultors
- Final Lyot masks located inside science instrument
- $\lambda/100$ internal optics

For GPI during the CoDR phase we designed a flexible optical layout, studied multiple coronagraphic techniques, identified the best option including consideration of numerous sources of performance degradation, and designed a detailed plan for implementation, testing and integration with the rest of the optical system. The design selected was the Apodized Pupil Lyot Coronagraph (APLC), which combines a classic Lyot architecture with a mild initial pupil apodization that is optimally matched to the focal plane occultor to channel residual light outside of the pupil. This results in a Lyot coronagraph with very high performance (particularly at its design-optimal wavelength) without requiring any stopping down of the telescope pupil. See 4.1.1 for more discussion.

The powered optics of the coronagraph are part of the overall GPI optical design, which produces a converging f/64 beam at the coronagraph's input pupil, and the calibration system, which collimates the beam after the focal plane masks. The mechanisms (mask selection wheels) are also provided by the HIA OMSS. These are discussed further in Chapter 7. This chapter focuses primarily on simulations and tolerancing of the coronagraph performance, and on technology studies for the manufacture of the coronagraph masks, particularly the input apodizer, as well as a description of the testbed facility that will be built to demonstrate and validate the performance of delivered optics for GPI. The testbed will be built during the CDR phase of the GPI project and a CDR-level description of the testbed itself is in Appendix 4.7.

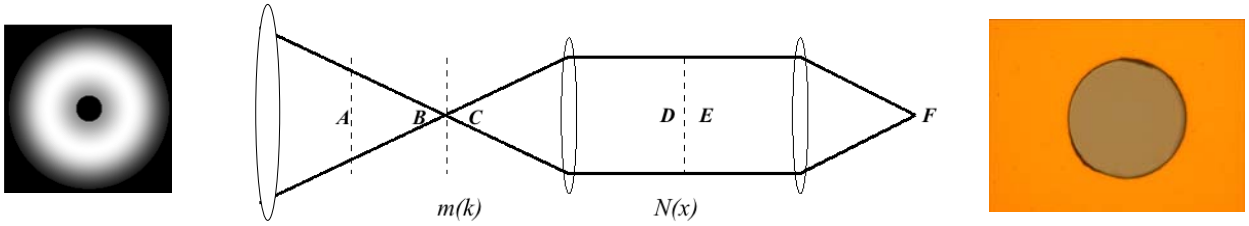

Figure 4-1: The essential planes and stops in a Lyot coronagraph. The entrance pupil in a converging beam is at A, the direct image at B falls on a focal plane mask (FPM) whose transmission function is m(k). The re-imaged pupil plane D, after being modified by passage through a Lyot stop E with a transmission function N(x), is sent to the coronagraphic image at F. A, D, and E are pupil planes, and B, C, and F are image planes. Plane A is apodized with a transmission function T(x) in the APLC design. An occulter *s* resolution elements wide in the FPM induces variations on scales of the order of D/*s* in the Lyot plane. At left: apodizer transmission profile. At right: Lyot Project reflective FPM with gold-coated mirror with occulting hole.

The most challenging component of the coronagraph is the apodizer. Our initial plan, adopted at CoDR, was to order the baseline apodizer and to characterize it in March 2007. Our plan was based on incomplete quotes and technical data from the manufacturer, Canyon Materials Inc. (CMI). The process of calibrating the apodizer writing process for our baseline choice of material, High Energy Beam Sensitive (HEBS) glass, was far more expensive and involved a process than CMI's initial quotes led us to believe. It turns out that writing near-IR apodizers on HEBS glass is still at an experimental stage. The test HEBS sample we characterized for CoDR possessed small enough WFE that we felt confident that a HEBS apodizer for the H band would be usable. This turned not to be the case. Thus our first milestone was converted into a materials characterization study rather than an apodizer characterization, and we started to characterize alternate apodizer fabrication methods (see 4.6.1). We continued to investigate HEBS glass for the apodizer because its chromatic optical density mitigates APLC design chromaticity (see 4.6.1.1).

Our current approach is to work with HEBS as the baseline but procede with microdot and metal (inconel alloy) deposit apodizers in addition to HEBS glass. Our timeline for testing prototype apodizers is in 4.6.1.5 (also see section 4.10, Recent Tests on Apodizers).

We will model the the GPI coronagraph design, but also build the AMNH testbed to test designs in the near IR bandpasses. There are limits to modeling optical trains. Out-of-pupil-plane effects, scratches, pits, and dust on focal plane masks, complex polarization effects are sometimes hard to model credibly. The testbed wavefront quality will not be as high as GPI's, but it will be good enough to test the modeling approaches used in GPI and to validate the performance in the presence of residual atmospheric wavefront errors. Our early modeling calculates tolerances for optomechanical alignments, which testbed experiments will confirm or refute. Coronagraphic alignment procedures will be worked out in-lab, and the apodizer and focal plane masks will be tested optically at their operating wavelengths at AMNH. They will also be characterized with AMNH's Fourier Transform Infrared Spectrometer (FTIRS) and its scanning electron microscope. In-house OPD measurements of the masks with a Zygo interferometer in the visible, and IR measurements at Zygo Corporation itself, at 1.55 microns, will feed testbed modeling. These models will be compared to lab data to develop and refine our understanding of the behavior of the APLC coronagraph in high Strehl ratio regimes.

4.1.1 APLC overview

The APLC (most recently, Soummer 2005) is an improvement over the ideas expounded by the originator of coronagraphy, B. Lyot (1939). The Lyot Coronagraph (LC) involves a focal plane stop or mask that blocks most of the light of the central star (or the Sun, as in the case for the original instrument), followed by a reimaged pupil plane. Diffraction by the focal plane stop serves to place the remaining light from the blocked star into a ring around the edge of the pupil. The eponymous Lyot stop is inserted into this pupil plane to downsize the pupil and block this diffracted starlight. In the presence of a secondary obscuration and spider vanes, the diffracted light also traces a bright ring around the secondary and bright spikes along the pupil positions of the spider vanes. Thus, the Lyot stop must also block these elements of the pupil image. Sivaramakrishnan et al. (2001) laid out the rules for matching and optimizing the size of both the focal plane stop (also called "focal plane mask", and hereafter denoted FPM) and the Lyot stop features. Please note that for LCs and APLCs the FPM and Lyot stops are hard edged optically. The FPM is easily understood as a hole in the center of a mirror, for example. The hole size is determined through optimization, and the Lyot stop size is determined by the FPM size.

However, researchers in high contrast imaging noted that if the pupil plane preceding the Lyot coronagraph's FPM were to be apodized, the suppression of the PSF in the final focal plane could be greatly improved.

To understand the APLC and why apodization improves performance, consider what a coronagraph does to the wave front amplitude of an on-axis point source in the final Lyot stop plane. A mathematical formalism can be derived that treats the field amplitude in this final pupil plane as the difference between the first pupil's amplitude distribution and the distribution caused by diffraction due to the FPM. Thus, to optimize the performance of a Lyot-style coronagraph, these two amplitude distributions must be as closely matched as possible. In Figure 4-2, we show these two functions for both an unapodized and an apodized first pupil plane.

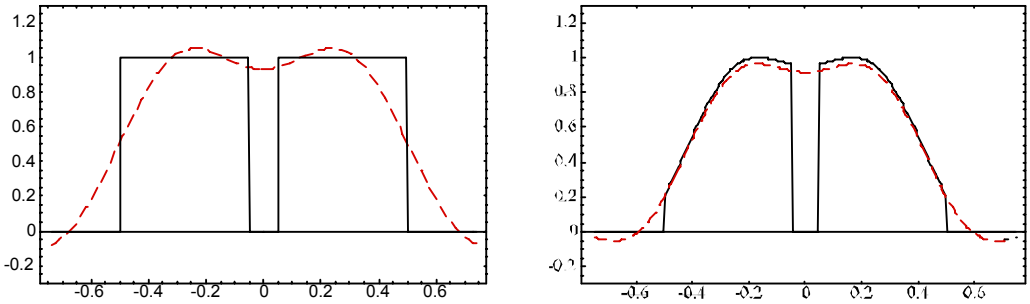

Figure 4-2 One dimensional plots of the normalized amplitude of the wave fronts that are differenced optically by the coronagraph. On the left is a clear aperture with a 10% central obscuration and on the right is an apodized system. The solid curves are the wave front amplitudes in the coronagraph's first pupil plane and the dashed curves represent the portion of the amplitude in the pupil plane after the FPM that has been diffracted by the FPM. In the final pupil plane, where the Lyot mask normally is placed, the resultant actual amplitude is the solid curve minus the dashed curve. This is the primary motivation for making an APLC.

The formal problem involves finding the combinations of FPM dimensions and apodizers that maximize total throughput while making these two wave amplitude distribution components as closely matched as possible. Doing so optimizes the cancellation in the second pupil plane, negating the need for a downsized Lyot stop and thus improving system throughput. In this case, the Lyot stop can simply serve as a baffle, mimicking the full primary aperture as imaged at this pupil plane. This not only improves throughput in comparison to traditional LCs, but also improves the angular resolution of the final PSF. With a traditional LC, the angular resolution is often limited by the Lyot stop. With a centrally obscured telescope, it is common to lose almost half of the angular resolution due to the Lyot stop dimensions, which downsize the primary and increase the size of the central obscuration (Sivaramakrishnan et al 2001). APLCs lose some angular resolution because of the entrance aperture apodization, but the effect is far smaller (about a 10% increase in FWHM of the PSF) than for traditional LCs. This is a particularly important benefit since this resoultion degradation translates directly into a reduction in detectable planet contrast, since it spreads the planet light out over a larger region of the PSF halo.

The recently discovered set of optimised APLC apodization functions (Soummer 2005) are general enough to allow APLCs to be optimized for arbitrary apertures, including structures such as central obscurations and support structures (e.g., "spider" vanes). For a given FPM size, a unique apodization function exists. Therefore, the throughput and performance of the APLC varies with the chosen mask size. The apodizer throughput and static PSF intensity at a radius of 5 λ/D from the center of an on-axis PSF is given in Figure 4-3. Figure 4-4 shows an example of an *H*-band apodization function optimized for Gemini.

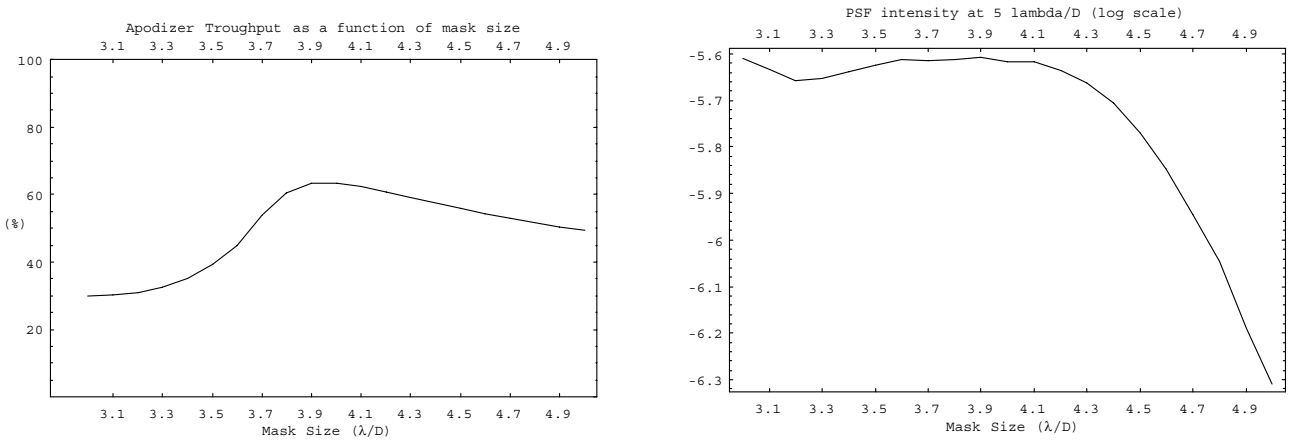

Figure 4-3 Illustration of APLC performance for the Gemini geometry. Left: throughput of the optimal apodizer as a function of the mask size. This number is the overall coronagraph throughput since there is no Lyot stop reduction. Right: PSF intensity, normalized to unity. Masks sizes over 4.7 λ/*D* a high throughput and therefore relatively higher angular resolution as well.

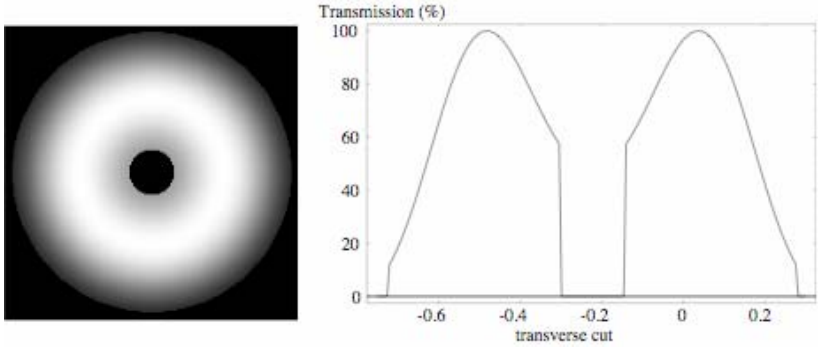

Figure 4-4 Example of apodizer transmission for the Gemini Telescope geometry. The minimum intensity transmission is 12% at the edges, and throughput is high: 63%. A classical Lyot coronagraph with an undersized Lyot stop has a typical throughput of 40% in contrast. The corresponding FPM has a diameter of 4.7 λ/D.

Suppression of the PSF by an APLC operating over a spectral band pass is necessarily worse than in the monochromatic case, since the apodizer and FPM must be chosen for a single wavelength (usually the effective wavelength of what ever band pass is being used). Thus, the FPM will appear too small on the red end of the band pass and too large on the blue end. However, the chromatic leakage is not uniform over the band pass, so this problem can be slightly mitigated using a numerical optimization of this leakage over the band pass. The result suggests the optimal polychromatic mask size is slightly larger than the initial monochromatic value. If the apodizer could be manufactured to affect the beam with a slightly different apodization as a function of wavelength, we could greatly improve the efficiency of the APLC in practice. It would approach the monochromatic performance, which is ten to one hundred times better.

4.1.2 APLC risk overview

The most technically challenging parts of the APLC design are the initial pupil-plane apodizer masks. Apodizer technology is relatively mature at monochromatic visible wavelengths because of their use in correcting illumination dropoff in Gaussian beams produced by lasers. This is not the case in the near-IR. Apodizer fabrication methods are still in an experimental stage. Our desire for an OPD that does not change form across a 10-20% bandpass adds to the difficulty of finding suitable apodizers. Furthermore, GPI requirements on the magnitude of the allowable OPD place stringent requirements apodizers. Chromatic OPD variation across the bandpass complicates post-processing, and larger OPDs diffract light through the coronagraphic optics. We have been actively looking for mitigation strategies. The chromaticity of apodizing material could assist coronagraphic design, but grey apodizers (which are cheaper and easier to make, and may well display smaller WFE) narrow the wavelength range over which the APLC performs well. We are therefore looking at 3 apodizer technologies in parallel, with a fourth, fallback option at this stage of the project (also see section 4.10, Recent Tests on Apodizers).

The pupil apodizer is central to coronagraphic suppression. Speckle suppression by post-detection processing of IFU (hyperspectral) data relies , to first order, on wavefront errors being proportional to the wavelength. Thus the apodizer WFE must be well-behaved across the bandpass. This creates a requirement on the apodizer material and fabrication.

Our baseline apodizer choice is still HEBS glass. HEBS glass blanks are doped in a chemical bath to prepare them for being written on by an electron beam. The e-beam writing causes optical density to build up in the doped surface layer. The chemistry of the doping baths are highly repeatable, although different recipes are used for different doping depths and properties. HEBS glasses are used commercially to generate photolithographic masks, using visible light. The process of calibrating and controlling this process for infrared apodizers is still experimental for the patent holder, CMI. In the IR, the doping layer must be deeper than for the visible. IR-customized bath can etch the glass, which results in poor wavefront quality.

This risk is being mitigated by studying the properties of different apodization methods using an optical wavelength Zygo interferometer and an FT infrared spectrometer (FTIRS), and close contact with manufacturers (Canyon Materials, Inc (CMI), MEMS Optical, and Reynard Corp.). In addition to work at AMNH, this kind of coronagraph will be tested on-sky in the Lyot Project coronagraph behind Palomar's AO system, with an IFU, before GPI integration.

Tolerancing the coronagraph design to aberrations and misalignment is also under way to assist the optomechanical and speckle-suppressing data reduction subsystems of GPI, with coronagraphic simulations feeding into IFU spectral resolution selection, and optical design of an atmospheric dispersion corrector (ADC).

4.2 Coronagraph project plan

The work on these techniques and the complete evaluation, testing, development and implementation of the coronagraphic masks will be conducted by the AMNH sub-group. Our plan is designed to provide not only the best combination of coronagraphic optics, but also the complete evaluation and understanding of the effects of these optics in the context of the end-to-end performance of the GPI instrument. To accomplish this, we will construct a precision coronagraphic, tabletop, test-bed at AMNH which will mimic the actual GPI optical layout but which needs far less stringent mechanical performance requirements. This test-bed permits the complete in-lab performance evaluation of all coronagraphic mask combinations to be supplied with the GPI without interrupting or impeding construction and testing of the coronagraph subsystem that will be delivered in the instrument. We will also address the issue of astrometry with coronagraphs. The test-bed will allow us to identify and implement the best scheme for retrieving the highly accurate astrometry demanded by the science goals of this instrument. Using the state-of-the art microscopy facilities at AMNH, we are mapping the complete structure of each optical mask for quality control, tolerance requirements, and, most importantly, specific understanding of the effects of each optic on the starlight. This is critical to ensure that the PSF produced by these optics has no features that would compromise science. In tandem with the laboratory work, a comprehensive suite of simulations, including the full propagative modeling of the light as well as all measured effects due to the masks, will provide the needed insight to ensure the unprecedented performance requirements of this component of the GPI project. The masks, after final acceptance and complete evaluation, will be delivered to the primary integration location.

The primary tasks for the Coronagraph subsystem are:

- Apodizer downselect. This includes wavefront mitigation, in particular HEBS WFE, performance of Inconel and microdot apodizers, interaction of coronagraph design with Science drivers and IFU design (trade-off between HEBS-glass achromatized APLC and grey apodizer with narrower bands). IR interferometric OPD measurements will be required. NICMOS 3 Veronica camera on loan to AMNH will also provide pre-testbed measurements in J and H bands soon after PDR. Section 4.6.1 discusses the apodizer material choices.

- Testbed construction. Immediately after PDR the AMNH testbed construction will be a top priority.

- Simulations: (a) some existing optomechanically-motivated tolerancing will be refined, and, (b) simulations modelling the AMNH testbed in order to understand its results in the context of predicted (lower) GPI WFE.

- Methods for astrometry and photometry will be developed using the AMNH testbed.

- Testbed results will be document for use in Subsystem Acceptance Test Plan (SATP) development.

The two major tasks between PDR and CDR are testbed construction, and selection, manufacture, and characterization of the apodizers.

An APLC has been designed for the LAO testbed and parts have been ordered (delivery date early June 07). These coronagraphic masks will be shipped to LAO for integration, and the AMNH team will assist in integration at LAO.

The AMNH team will refine and document observing scenarios, especially for astrometric and photometric calibration, test them on Palomar and with simulations.

4.3 Testbed Summary

This section outlines the final design of this test facility, specifying the optics that need to be produced and the set of tests that will be conducted with the testbed. The section summarizes Appendix 4.7, which is a full testbed design description.

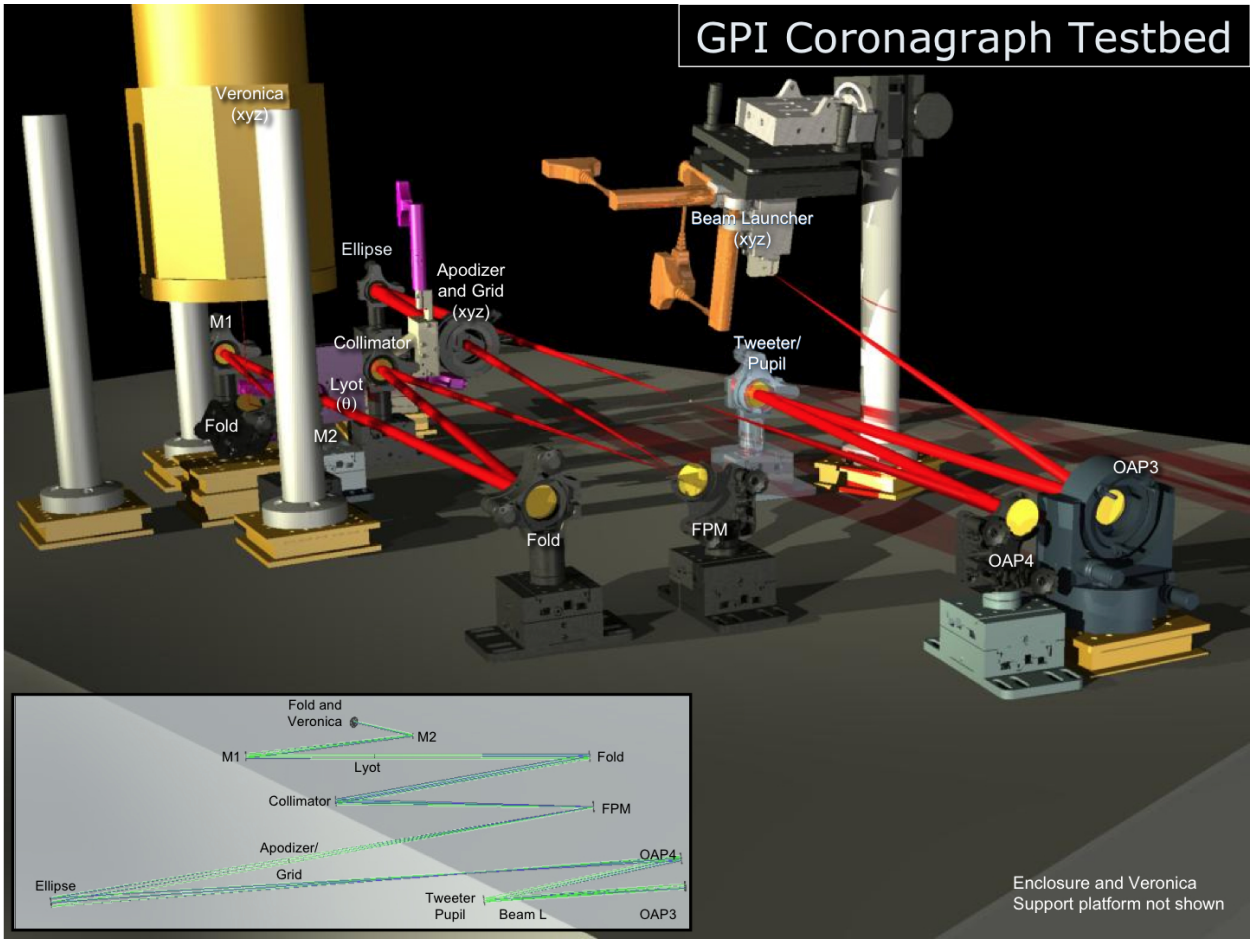

Figure 4-5 Rendering of AMNH testbed

The AMNH contract for the Gemini Planet Imager has the ultimate purpose of production of the coronagraphic (starlight suppressing) optics for GPI. These optics include an entrance aperture pupil apodization (PPM), a focal plane occulting mask (FPM) and a Lyot stop, as well as a solution to astrometric and photometric measurements with the instrument. For astrometry and photometry we

invented a technique using a reticulate grid of wires. The Reticular Grid may be an additional deliverable under the AMNH contract.

Several of these optics push the boundaries of optical fabrication techniques and come with certain risks. In particular the PPMs represent a wholly new type of optic, due to our requirements on optical quality and precision of the apodization of the telescope's pupil. The FPMs also pose some risk as they require sub-micron precision features to be carved into the optical surface. As such, the contract was structured to include the development of a testing facility in the AMNH Astrophysics Lab with two purposes: (1) to test the various techniques for making these masks, by procuring them from various vendors and placing them in a mock of the central part of the GPI optical train in order to evaluate their performance; and (2) to qualify and demonstrate the in-lab performance of the final optics to be delivered for integration into the full GPI instrument.

4.3.1 White light source and monochromator

We decided a Photon Etc. tunable source and monochromator for the IR light source. Its advantage over the other model we studied (produced by Oriel) is its flexibility and reduced set-up/calibration time. The choice of light source is of project-wide interest, as these items can be expensive, and require some thought to avoid unwanted imaging artefacts from appearing in data. Appendix 4-4 demonstrates the limits on non-uniform pupil illumination allowed in the GPI coronagraph. We plan to stay within these limits on the testbed.

Appendix 4.6 contains calculations for exposure times, and a description of the white light source to be purchased for the AMNH testbed. Exposure times of the order of a minute with 15nm bandwidth nIR light are our target on the testbed.

4.4 Coronagraph elements

- Incoming pupil
- Pupil plane mask
- Astrometric element
- Focal plane
- Focal plane mask
- (reimaging mirror to Lyot owned by CAL subsystem)
- Lyot plane in IFU
- (Lyot stop 1 in IFU owned by IFU?)
- (Lyot stop 2 in IFU owned by IFU?)
- Pupil plane mask wheel (owned by OMSS)
- Focal plane mask wheel (owned by OMSS)
- Lyot plane wheel 1 (owned by IFU)
- Lyot plane wheel 2 (owned by IFU)
- Polarization element –between FPM and Lyot plane.

4.4.1 Pupil Plane Masks

Pupil plane masks have hard-edged pupil-defining masks specified in the COR-to-OMSS ICD. These are opaque, with hard-edged outer & inner edges. These masks define the pupil for the GPI system. They will be slightly (1%) undersized with respect to the telescope pupil. The composite masks will be mounted in HIA-provided fixtures prior to integration.

4.4.1.1 Mask combinations

The FPRD states that AMNH will supply the following 6 pupil plane masks (PPM) (REQ-FPR-0510) :

PPM designation	Central Wavelength [microns]	Description
CLEAR	N.A.	Open, larger than GPI pupil
CLEARGP	N.A.	GPI pupil
APOD_Y	1.035 (16%)	Apodizer
APOD_J	1.225 (15%)	Apodizer
APOD_H	1.69 (18%)	Apodizer
APOD_K	2.10 (19%)	Apodizer

4.4.2 Focal Plane Masks

Concerns are hole quality and shape, WFE, and effects of surface pits. The Lyot Project has already prototyped the basic approach to FPM manufacture. The approach of gold on a silicon substrate will be tested as it promises better hole quality than Lyot Project FPMs. These will be tested on the AMNH testbed.

The FPRD states that AMNH will supply the following 7 focal plane masks (FPM) (REQ-FPR-0512) :

FPM designation	Target Wavelength [microns] ([bandpass])	Description Hole Diameter [micron/mas]
BLANK	N.A.	[No hole]
FPM_Y	1.035 (16%)	[331/135 TBD]
FPM_J	1.225 (15%)	[397/162 TBD]
FPM_H1	1.59 (10%)	[492/201 nominal TBD] H discovery mask
FPM_H2	1.70 (18%)	[526/215 nominal TBD] H broadband mask
FPM_K1	2.09 (10%)	[647/264 nominal TBD] Ks
FPM K2	2.20 (18%)	[704/287 nominal TBD] K
SPARE SPARE		Small pinhole for CAL tests? Future upgrades

4.4.3 Lyot Mask

Lyot plane masks are cryogenic (unlike the pupil and focal plane masks). The Lyot plane pupil wheel is part of the IFU design. The APLC design does not fundamentally require any undersizing of the Lyot masks – all diffracted light is located outside the nominal aperture of the telescope. However, these masks will be slightly (2%) undersized to allow for flexure and misalignment between the apodizer (itself undersized 1%) and the Lyot wheel. The Lyot masks are dimensioned in the 1.9.xn_supplemental_ICD. The FPRD states that AMNH will supply the following 8 Lyot masks, to be used in the following nominal configurations (REQ-FPR-0514)

Lyot Designation	ID/OD [mm +/- TBD]	Description
APLC_0	9.80/TBD	Optimized for baseline APLC, 2% undersize, spiders at 0 degrees
APLC_60	9.80/TBD	Optimized for baseline APLC, 2% undersize, spiders at 60 degrees
APLC_120	9.80/TBD	Optimized for baseline APLC, 2% undersize, spiders at 120 degrees
APLC_ALT_0	TBD/TBD	Alternate APLC, spiders at 0 degrees
APLC_ALT_60	TBD/TBD	Alternate APLC, spiders at 60 degrees
APLC_ALT_120	TBD/TBD	Alternate APLC, spiders at 120 degrees
CLASSIC	TBD/TBD	Classic Lyot stop, undersized by TBD, spiders at 0 degrees
BLANK	TBD	Open, no spider
SPARE		Not deliverable
SPARE		Not deliverable

Expected configurations for science (taken from the FPRD) are:

Coronagraph Configuration Designation	Central Wavelength [microns]	Description	PPM	FPM
COR_Y	1.035	Full Y band	APOD_Y	FPM_Y
COR_J	1.225	Full J band	APOD_J	FPM_J
COR_H1	1.59 TBD	Optimized for H1	APOD_H	FPM_H1
COR_H2	1.70 TBD	Optimized for H2	APOD_H	FPM_H2
COR_K1	2.09 TBD	Optimized for K1	APOD_K	FPM_K1
COR_K2	2.20 TBD	Optimized for K2	APOD_K	FPM_K2

4.5 Coronagraph Simulations Summary

Coronagraphic simulations are performed either monochromatically or polychromatically. Wide FOV coverage in the focal plane requires coarser pixel sampling, whereas fine-scale studies in the focal plane (mask shape and hole roughness) require very fine pixel sampling. These two types of Fourier-based simulations were developed and run for tolerancing coronagraph performance. Tolerancing studies performed monochromatically investigate the behavior of the optimized coronagraph to various misalignments or errors. Design chromaticity of the APLC makes wide spectral band tolerancing studies produce very loose tolerances. Since the science drivers require good coronagraphic performance at certain wavelengths (e.g. near the methane feature in H), monochromatic tolerancing of aberrations and misalignments is more stringent, and therefore more relevant for GPI. However, in order to investigate coronagraphic sensitivity to atmospheric differential refraction, polychromatic simulations are needed.

In addition to simpler Fraunhofer approximation code, Fresnel simulations were developed to tolerance out-of-pupil-plane effects.

Numerical optimization of apodizers (given the apodizer material's chromaticity) were also developed in preparation for AMNH measurements of chromaticity of HEBS and other apodizer materials. Details of this calculation are presented in Appendix 4.2, where coronagraph design optimization using a 4-parameter OD-chromaticity dependence are described. Simulations are summarized in the table below, and in more detail, in Appendix 4.1, Appendix 4.2, Appendix 4.3, and Appendix 4.4. Simulation work continues as questions develop across the project.

4.5.1 Simulations for optomechanical and aberration tolerancing

During the PD phase our focus was on providing tolerancing for use in the GPI optomechanical design. For example, the plots in Figure 4-4 place limits on tip-tilt, astigmatism, and defocus. Early GPI simulations were re-examined and redone in light of the fact that contrast requirements are stated most easily and clearly at the optimized wavelength (e.g. Figure 4-4) below).

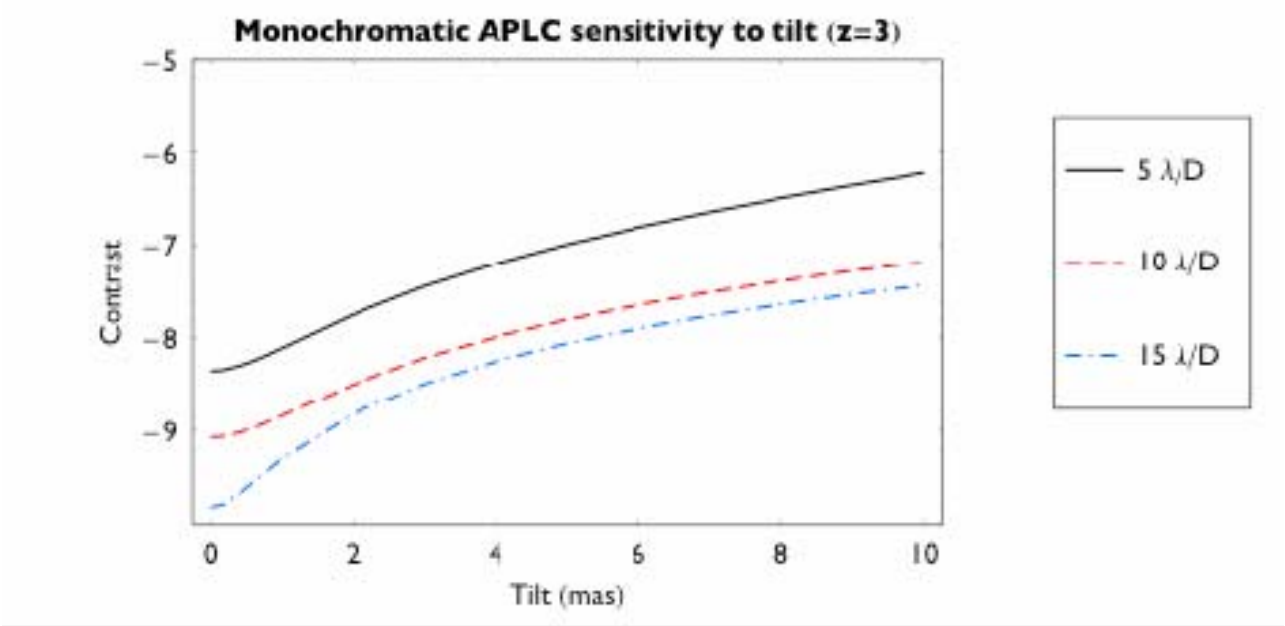
Monochromatic APLC sensitivity to tilt (z=3)
Contrast
−5
−6
−7
−8
−9
0
2
4
6
8
10
Tilt (mas)
5 λ/D
10 λ/D
15 λ/D

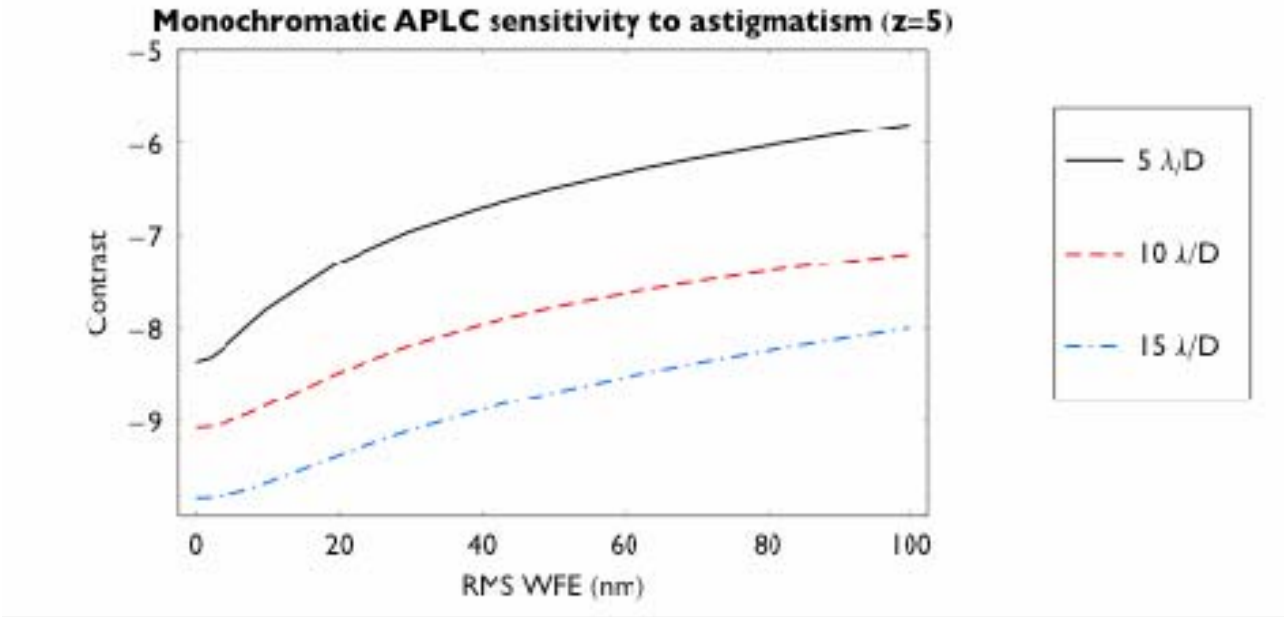
Monochromatic APLC sensitivity to astigmatism (z=5)
Contrast
−5
−6
−7
−8
−9
0
20
40
60
80
100
RMS WFE (nm)
5 λ/D
10 λ/D
15 λ/D

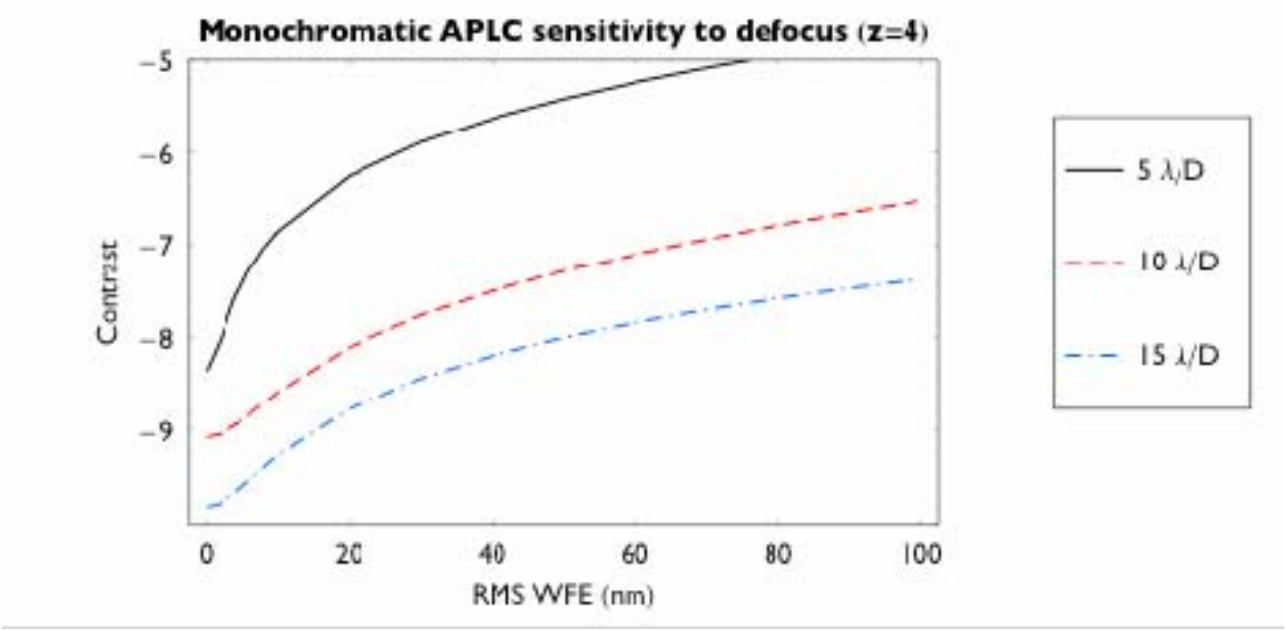

Figure 4-6 Aberration sensitivity of the APLC coronagraph design to tilt, astigmatism, and defocus in pupil. The focal plane mask occulter is 5.2 λ/D in diameter.

The following table lists the simulations and modeling that were done to understand coronagraphic sensitivities and estimate tolerances, especially to inform early optomechanical decisions. Tolerancing based on the performance at the optimal wavelength of the coronagraph design is typically done. This is because there is a high likelihood that the pupil apodizer optical density will be a function of wavelength in a way that decreases the APLC design chromaticity, in addition to the science driver of requiring high suppression at certain key wavelengths rather than average performance over a wide bandpass.

Tolerancing study	Method	Comments
Tip-tilt	Monochromatic, FT	At 5 λ/D < ~4mas for Contrast < 10^{-7} At 10λ/D < ~4mas for Contrast < 10^{-8} At 15λ/D < ~6mas for Contrast < 10^{-8} (Appendix 4.1)
ADR	Polychromatic, FT	Comments (Appendix 4.1, 4.2)
Higher order aberration	Monochromatic, FT	First several Zernikes. Sensitivity increases with radial order (Appendix 4.1)
FPM tilt	Monochromatic, FT	<5 degrees to beam (Appendix 4.1)
FPM curvature	Monochromatic, FT	Ruled out a possible CAL system design (Appendix 4.1)
Apodizer: # grey levels	Monochromatic, FT	Equal width rings, 100 grey levels (Appendix 4.1)
Apodizer: transmission error	Monochromatic, FT	As function of spatial frequency (Appendix 4.1)
HEBS chromaticity	Polychromatic, FT,	Consequences for speckle suppression

	four-parameter chromaticity model	(Appendix 4.2, 4.3)
Prelim. astrometric grid	Polychromatic, FT	Ghosts bright enough for single exposure alignment (Appendix 4.2)
Lyot Spider misalignment	Monochromatic, FT	No latitude –Lyot spiders must be safely oversized. Lyot stop would be to have spiders 2% of the pupil diameter (to allow +-1% alignment tolerances just from geometry), or +-120 microns (Appendix 4.2)
Spider contrast loss	Monochromatic, FT	Tolerable up to 2cm width spider (cabling can add 1cm to existing 1cm spider width) as long as Lyot stop obscures the spiders completely (Appendix 4.2)
APLC transfer function for phase aberrations	Monochromatic, FT	Consequences for CAL system (Appendix 4.2)
Amplitude errors in entrance pupil	Monochromatic, FT	Parameter exploration (Appendix 4.2)
FPM edge roughness	Monochromatic, FT	<0.5% of FPM diameter preferred, <1% possible (further study of 1% tolerance) (Appendix 4.2)
FPM longitudinal placement	Monochromatic, FT	+/-1mm or less (CAL system focus capture range may be more stringent) (Appendix 4.4)
Apodizer longitudinal placement	Monochromatic, Fresnel	Early estimate +/1mm, to be refined (Appendix 4.4)
Apodizer tilt	Monochromatic, Fresnel theory	<1 degree, could be loosened after more study (Appendix 4.4)
Testbed light source illumination non-uniformity	Monochromatic, FT	<2% center-to-edge Gaussian intensity profile (Appendix 4.4)
New Gemini North M2 OPD corrected by spatially-filtered WFS AO system	AO: End-to-end, no atmosphere (LLNL, Poyneer) OPD, Monochromatic FT coronagraph	M2 figure acceptable: atmospherics dominate loss of contrast (Appendix 4.4)

4.5.1.1 Apodizer tolerancing not covered above

Tilt of apodizer: simulations of tilted apodizers were carried out, but need to be cross-checked. Apodizer tilts up to a degree with respect to the beam propagation direction appear to be acceptable, but this figure needs to be confirmed. Fresnel simulations of the tilted apodizer need to be performed to check the effects of the elliptical projection of the secondary obstruction more carefully. Fresnel code for this has already been developed.

Clipping of any part of the apodizer by the edge of the telescope pupil by the apodizer is unacceptable.

4.5.1.2 Focal plane mask tolerancing not covered above

Dust, scratches, pits, and FPM flatness tolerancing still needs to be performed. Trauger and Traub (2007) developed a methodology to examine dust on the FPM, which is being extended at AMNH to cover the APLC case to estimate loss of contrast effects analytically from assumed dust properties. Our arbitrarily-fine FPM sampling code will also be used to study this numerically.

4.5.1.3 Atmospheric differential refraction tolerancing

Contrast loss from ADR (post-processing speckle suppression losses) studied by Marois are covered elsewhere (Science and CAL system chapters). Work by Soummer et al. (2007) on speckle statistics with coronagraphs (Appendix 4.5) is also relevant in this area, but is not directly in the AMNH coronagraphic testbed and mask development plan at this stage.

4.5.2 Coronagraphic transfer function

Aberration tolerancing also resulted in a quantitative understanding of the 'transfer function' of the coronagraph design. This impacts the way the AO, CAL and COR subsystems interact. We determined that (as expected) the coronagraphic stop set the scale of spatial frequencies that pass through the coronagraph substantially unaltered, and are thus calibratable by the high spatial frequency part of the CAL subsystem. Spatial frequencies corresponding to speckle placement within a resolution element of the edge of the occulter are strongly modified by the coronagraph. Low spatial frequencies pass through the occultiong FPM hole to the low spatial frequency part of the CAL subsystem. We show the Bode diagram for high spatial frequency phase aberrations below (with details in Appendix 4.2).

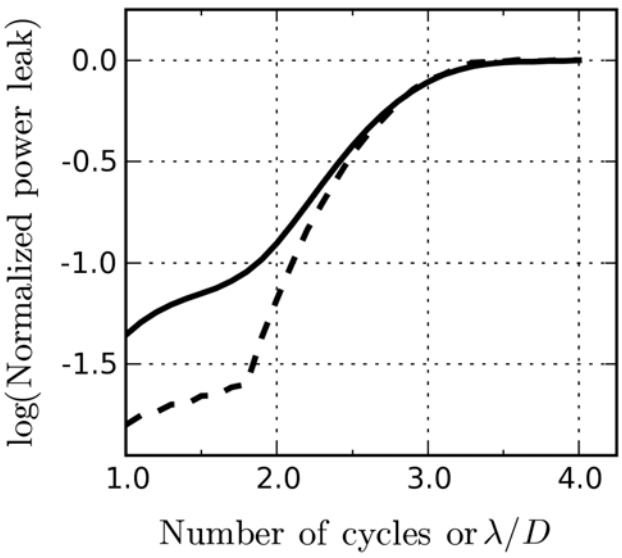

Figure 4-7 Transfer function of a phase ripple through an APLC with a 5.155 λ/D FPM. Power in the coronagraphic PSF (solid line), and the peak intensity of the first order speckles in the image at Nλ/D (dashed line) due to a small-amplitude phase ripple of N cycles across the aperture of the APLC are shown on a relative scale, as a function of the spatial frequency of the aberration. The variance of the phase ripple is fixed at 0.05 radians^2. At low spatial frequencies the speckles are essentially blocked out by the FPM. As the speckles approach within a resolution element of the edge of the 2.6 λ/D radius FPM their strength increases, asymptoting when they are λ/D past the edge of the FPM. Total leaked power is a smoother function of the aberration's spatial frequency than the peak speckle brightness. The behavior of speckles near the FPM edge mimics that found in the study of tilt error in classical Lyot coronagraphs (Lloyd and Sivaramakrishnan 2005).

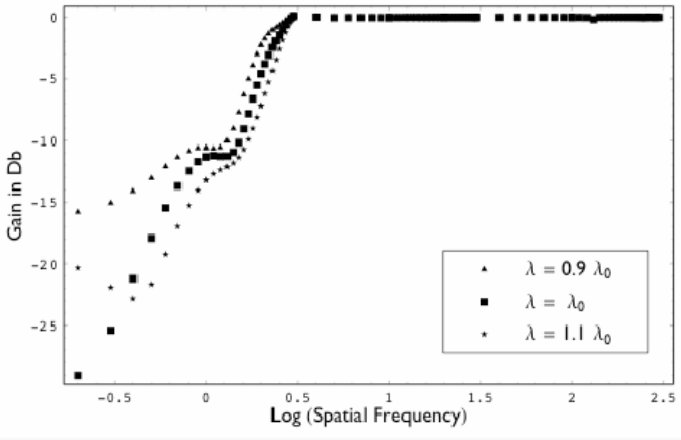

Figure 4-8 Bode diagram of a grey apodizer APLC across a 20% bandpass. Amplitude of a harmonic phase aberration in the Lyot plane relative to the amplitude of the same aberration win the entrance pupil is plotted. This shows that the coronagraph acts a high pass filter. A pupil with a 15% central obstruction and a monochromatically optimized apodization for a 4.5 lambda/D focal plane mask diameter was used. For spatial frequencies above 4.5 cycles across the aperture the amplitude response is flat, and equal to unity. We studied the influence of chromaticity on this amplitude response. Note that optimal rejection of low spatial frequencies aberrations is only obtained for the optimal wavelength of the coronagraph design.

The Bode diagram shows the attenuation (in Db) of an input aberration of acertain spatial frequency (in cycles across the pupil). There is no attenuation of this aberration above about 3 cycles per aperture diameter (log(3) ~ 0.5). A speckle caused by such an aberration would fall about one resolution element outside the FPM occulter. At spatial frequencies lower than about 2 cycles per aperture diameter the coronagraph passes less of the aberration though to the Lyot plane, so these frequencies need to be sensed with light that goes through the FPM's occulting hole. For frequencies whose speckles fall within a resolution element of the occulter's edge there is no simple interpretation of their passage through the coronagraph.

4.6 Evaluation and Testing Optics and Masks

4.6.1 Apodizer material characterization

Apodizer properties and manufacture are clearly risks for the GPI coronagraph. Current options for the apodizers are: HEBS, Inconel deposit on glass, microdots, and finally a lens-like clear/darkened doublet. The status of our investigations into HEBS properties detailed in Appendix 4.2 and 4. 3 (but also see section 4.10, Recent Tests on Apodizers). Note that any particular doping chemical process is highly repeatable. The path to downselecting, manufacturing, and testing GPI apodizers is as follows:

4.6.1.1 HEBS glass

HEBS glass WFE is a primary concern. HEBS is our baseline apodizer technology. Appendix 4.2 and 4.3 present results on HEBS OPD in the visible. HEBS chromaticity is also discussed in this introduction, and in more detail in Appendix 4.2 and 4.3. Lead times on HEBS doping, polishing, and writing are set by the vendor, and can vary.

CMI (the HEBS manufacturer) will deliver the re-polished H-band-specific doped glass 5-inch square sample with a re-written set of calibration patches (to calibrate the glass' electron dosage-OD curve) in mid-May (this vendor does not commit to specific delivery dates on our one-off requests, but has often been responsive to our need for rapid turnaround in the past). As soon as this glass is received, it will be tested for WFE, OD and chromaticity of the OD. This re-polishing will reduce the thickness of the doped layer by some amount, which has been specified to the vendor. The main risk is that the OD will not be sufficient enough for our design.

If the **WFE is satisfactory** (at least as good as the undoped glass sample we measured in the pre-PDR phase), and the OD is sufficient for our H-band design, we ask the vendor to write our first H-band apodizer on the re-polished glass immediately. If, even with the acceptable WFE, the doping (depth) is insufficient for GPI, we request a deeper doping, subsequent polishing, and writing of calibration patches, followed by WFE, OD, and OD chromaticity tests at AMNH. At this stage we can also consider **double-sided writing**, where the OD is developed by writing with the electron beam on BOTH sides of the glass, since the doping is identical on both sides. If the **WFE is unsatisfactory** we will consider a **sandwich** of doped and written-on HEBS glass with undoped HEBS glass using index-matched IR cement. This sandwich should have satisfactory WFE. Chris Shelton (JPL) has experience with these cements, and has suggested vendors.

If we decide to go forward with writing the first apodizer on the glass we expect to receive mid-May, our first H-band apodizer will arrive in July or August (depending on vendor turnaround), which enables testing at AMNH with direct imaging using the nIR NICMOS 3 VERONICA camera on loan to AMNH, and, after the testbed is assembled, on the AMNH testbed with coronagraphic optics.

The double-sided writing makes it possible to consider using HEBS in the **K-band**. The H-band-specific doping will not produce sufficient OD for a K-band apodizer to meet the GPI science-driven goal of a 3.5λ/D IWD.

Since the path to final HEBS apodizers depend on intermediate test results (as described in the introduction to this chapter), we present HEBS costs for particular stages of the process. Any particular apodizer is hard to cost without knowing the results of the intermediate tests.

- HEBS substrate + one doping run: $10k
- Polishing: $0.5k
- Writing calibration patches: $3k
- Writing an apodizer: $9k/11k (100/200 gray levels)

Note: Several apodizers can fit on one substrate.

FTIRS data on HEBS glass doped for the near IR indicate that the approach could work for YJH bands, but for K band the required optical density (OD) needed for a 5λ/D focal plane occulting mask (FPM) may be insufficient (Appendix 4-3). This risk was already identified in CoDR which included plans for a custom HEBS glass for the K band. As a contingency, alternative apodizer manufacturing techniques are being pursued. During CoDR, HEBS doped for visible wavelengths was studied. Although, the wavefront quality for this visible sample was acceptable, we discovered that HEBS glass doped for the deeper layers required by H-band apodization possessed very poor OPD (Appendix 4.3). We are currently mitigating this problem by polishing the doped HEBS glass. We will evaluate the result by the analysis of new calibration patches and wavefront measurements. Another possible mitigation can be obtained by sandwiching glass doped for the H-band between undoped HEBS glass sheets using index-matching IR cement. A positive aspect of using HEBS is that the design chromaticity of the APLC can be mitigated by the slope of the OD vs. wavelength property of HEBS (Figures 4-9). Such behaviour enables more effective suppression of diffracted light over a wider spectral range around the wavelength that produces optimum suppression.

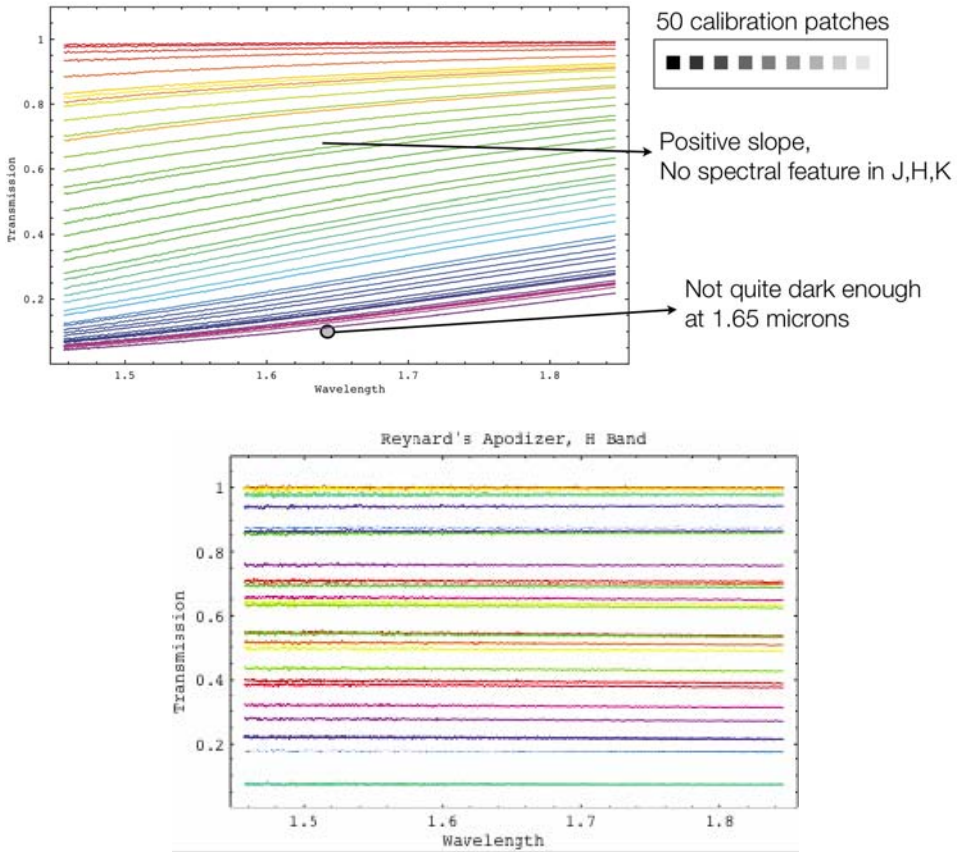

Figure 4-9 Top: OD vs. wavelength data measured at AMNH from calibration patches written on HEBS glass doped for the H band. This study confirms the positive slope necessary to mitigate coronagraph chromaticity. Darker patches might be needed for this glass and are being written. Bottom: ESO SPHERE Inconel apodizer measured at AMNH (apodizer on loan from U. Nice).

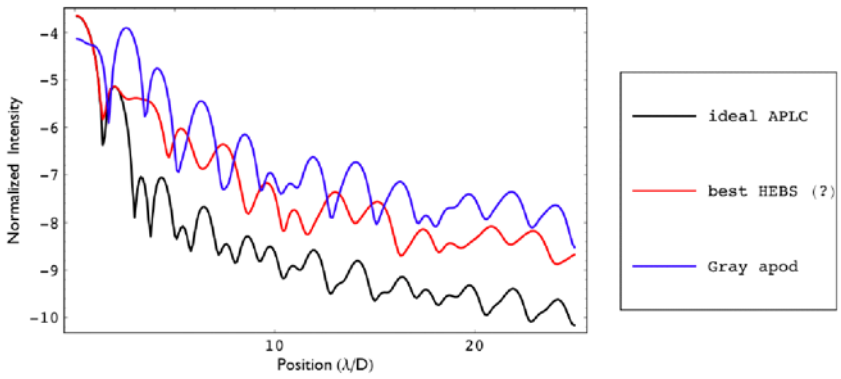

Figure 4-10 Comparison between the theoretical limit given by the achromatic H band APLC (black), a gray apodizer (blue) and an APLC with a glass using a theoretical model for the chromaticity of OD.

4.6.1.2 Inconel deposit

These apodizers have been studied in the optical for ESO/SPHERE at U. Nice, and in the IR at AMNH. Their OD is essentially grey (Figure 4-9). It seems the precision of the transmission profile has been an issue in the first sample purchased by U. Nice. We have ordered a sample with a much tighter tolerance and will evaluate if the company is able to produce the required transmission. We will evaluate the impact of the inconel deposit on the wavefront error (see section 4.10, Recent Tests on Apodizers). In the future, we can provide and test the substrate plate before inconel deposit. A possible issue with inconel is the amount of light reflected back by the apodizer.

Reynard Corporation agreed to deliver an inconel apodizer begining of May. In the month of May we will test this device for chromaticity, wavefront quality, microscopy, and IR transmission profile. It will also be tested on sky at the Lyot project run at AEOS in June 2007, with the goal of evaluating the effect of the apodizer on the unocculted image, and its phase shift in the infrared. A comparison with the Lyot Project's classical Lyot coronagraph (if relevant) will also be done. Testing in the lab in July/August with VERONICA is also planned.

Inconel's grey transmission has been confirmed with FTIRS data, on a sample apodizer on loan from the University of Nice (France). Its wavefront quality / phase shift has been measured in the visible with our Zygo. The wavefront quality of this sample seems to be dominated by the substrate. The precision of its transmission profile will be measured in the scanning mode of the FTIRS, or with VERONICA.

Reynard quotes $4k for one apodizer (substrate + AR coating).

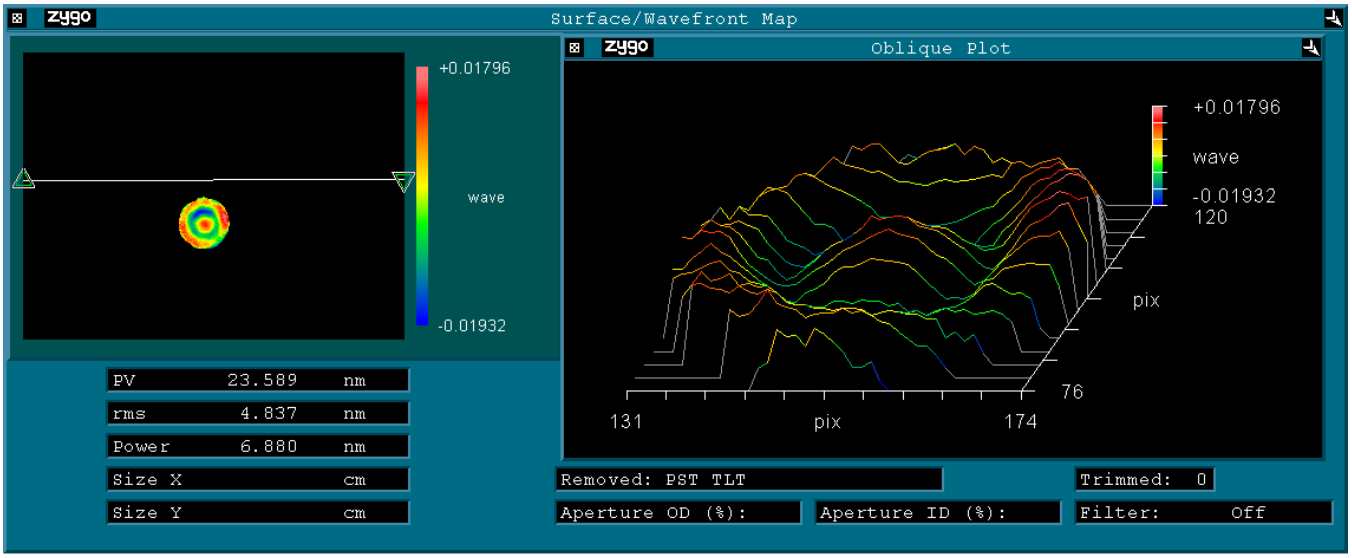

Figure 4-11 Early results from 1.5cm dia apodizer from Reynard (on loan from U. Nice) suggest usable WFE.

Figure 4-12 New Inconel Reynard apodizer at AMNH for AEOS pupil geometry. This will be used in an observing run immediately after GPI PDR to demonstrate on-sky performance of the APLC.

4.6.1.3 Microdots

One micron chromium squares are written at prescribed locations to create the apodizer. Thus the near-field WFE is set by diffraction due to individual squares (up to a few Fresnel lengths – as set by the dot size – from the apodizer (see section 4.10, Recent Tests on Apodizers). Wide angle scatter results in the far field, and needs to be baffled. These apodizers are expected to be possess grey OPDs (to be measured before PDR)

The Lyot project microdot apodizer was delivered early in May (Fig. 4-12). Its chromaticy, wavefront quality, and transmission profile will be measured with the FTIR spectrograph, VERONICA, and AMNH's microscopes. It will be tested on sky in June at the Lyot Project run at AEOS. A second apodizer with an astrometric grid written on it was also received, and will also be characterized.

We expect these apodizers to possess grey transmission, the FTIR may confirm this property if it functions correctly in a scanning mode with the microdot structure in these apodizers. We will also be measure the chromaticity of the OD using VERONICA. OPD and WFE of these apodizers will be measured in the visible with the Zygo, and possibly at 1.55 microns (we are investigating ways to test the wavefront quality in the infrared).

Two apodizers and FPM for the LAO testbed will be delivered in June to AMNH: this apodizer will be tested in the visible at the UCSC/LAO ExAO testbed. This test at LAO will use a GPI-like aperture as well as an unobstructed aperture to obtain measurements of the coronagraphic behavior of the APLC. The LAO testbed provides sub-nanometer wavefront correction through a MEMS deformable mirror and precision interferometer, and so will allow testing of apodizers under GPI-like wavefront quality.

MEMS Optical quotes $13k (substrate λ/20 + AR coating) for 2 identical sets of 4 apodizers (total of 8 apodizers).

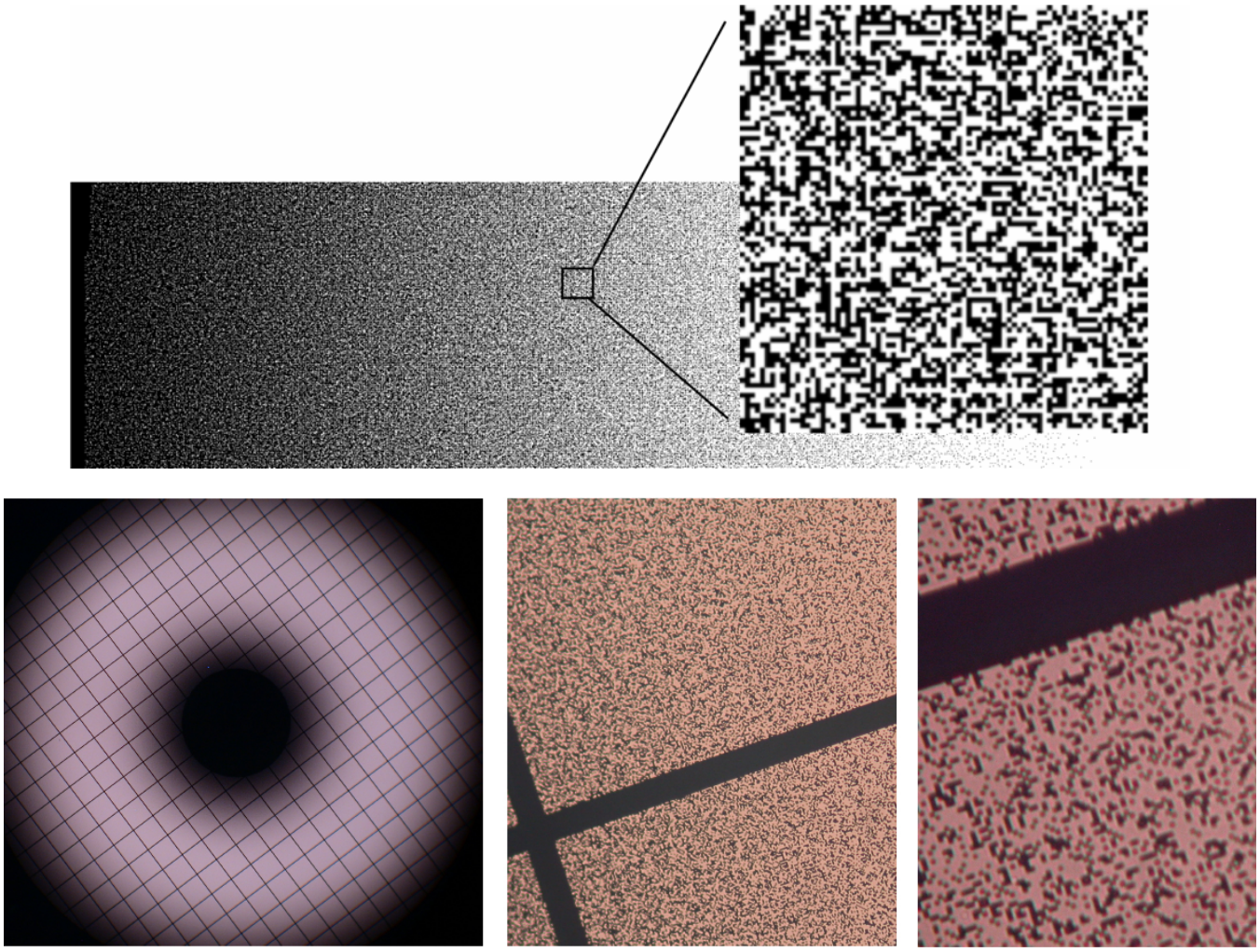

Figure 4-13 Microdot mask file provided to MEMS optical/Jenoptik (top), and a microdot apodizer with an astrometric grid at different magnifications (bottom).

4.6.1.4 Lens-like

This existing technology uses ND glass and clear glass in a doublet. For example, an unpowered doublet can be made by cementing together a positive lens with dyed glass, and a negative lens with clear glass in order to flatten a Gaussian intensity profile of a beam. For GPI, concerns with this approach are WFE, manufacturability given the required glass profiles, and chromaticity. This apodizer concept is still to be developed. We will consider this over the summer after PDR as a fallback solution, which is potentially interesting because it can theoretically correct the chromaticity of the APLC design when non-gray absorbing glass is used. This option was discussed in some detail in the CoDR.

In conclusion by June 2006 we should have all the basic lab results on chromaticity and transmission, as well as initial data from the Lyot Project. LAO testbed results in the visible will be available in July/August 2007, as will tests at AMNH with VERONICA.

4.6.1.5 Calendar for apodizer downselect

Dates for apodizer deliveries and downselect

1. Delivery dates
   Early May: Delivery microdots (MEMS optical) and Inconel (Reynard)
   June: HEBS glass plate, re-polished with new calibration patches

2. Calendar for the tests for the apodizers

2.1. Before PDR
   FTIR spectra on inconel and radial mapping of the transmission
   Test of FTIR feasibility on microdots, spectra and radial mapping if possible
   Microscopy of components surfaces on inconel and microdots (optical, SEM, confocal if possible)
   Visible zygo measurements on microdots and inconel

2.2 End July
   Infrared mapping of inconel and microdots with Veronica
      End-to-end testing of microdot apodizer on UCSC LAO testbed.
  Wavefront analysis of HEBS substrate
   Calibration of HEBS patches with FTIR
   Decision to order HEBS apodizer or give up on this technique
   Final apodizer method downselect, end of July

After it is constructed, the AMNH testbed will be used to test available apodizers coronagraphically under more carefully controlled conditions in the nIR.

4.6.2 Focal plane masks

See table of focal plane masks for dimensions. The reflective coating will be gold. Tolerances are presented in the table in (4.5.1).

4.6.3 Lyot plane masks

Tolerances are presented in the table in (4.5.1).

4.7 Astrometry with Coronagraphs

A solution to the problem of relative astrometry and photometry between the occulted star and a faint apparent companion was proposed independently by Sivaramakrishnan and Oppenheimer (2006) and Marois et al. (2006). This is described in Appendix 4.2, and the two references above. Ghosts images on GPI about 12 magnitudes fainter than the occulted star will be induced with a fine grid of opaque lines written on the apodizer. Tests with the Lyot Project coronagraph on AEOS are planned. Further tests with the Lyot Project coronagraph placed behind the P1640 IFU using the Palomar Hale adaptive optics system will be conducted before GPI goes on sky to develop coronagraphic astrometric and photometric techniques and data reduction methods. We have ordered apodizers with the astrometric grid written on the substrate, and we will evaluate this manufacturing solution at the Lyot project coronagraph and in the lab.

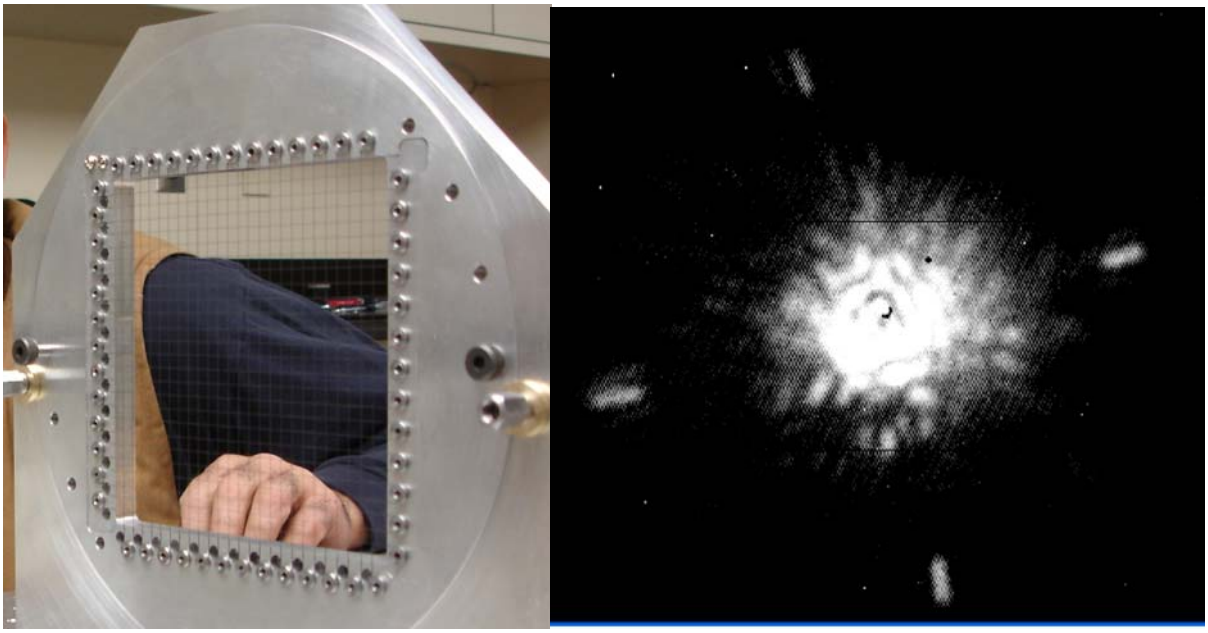

Figure 4-14 Astrometric grid prototype used on the Lyot Project with its 10cm dia pupil (left) and the coronagraphic image with fiducial spots at 20 resolution elements from the occulted star (right). The target star is behind a 4 resolution element wide FPM. On GPI the grid will be written on the 12mm pupil plane apodizer of the coronagraph.

Controlled ghosts in the first focal plane can be induced by periodic structures (in phase or amplitude) in a preceding pupil plane. Two approaches are possible – a DM can be used to put a low-amplitude ripple on the wavefront, or a grid of fine black wires can be placed over a pupil. Angular Differential Imaging post-processing requires alignment of different frames, so the fiducial ghosts must be visible above raw speckle noise in each frame. For GPI this is estimated to be about 12 magnitudes fainter than the AO target star behind the oculter. Data from the Lyot Project (Hinkley et al., 2007) suggest a 9 magnitude difference on AEOS. The latter contrast ratio was attempted with a grid of wires over a 10.4cm pupil in the Coude room at AEOS. While the resulting Lyot Project images have not been fully reduced yet, the resulting ghost images do not show unexpected photometry or morphology. Distortions visible in the fiducial ghost 'stripes' can be calibrated as long as they are stable. The radial elongation of the fiducial spots is induced by the 20% bandwidth of the H band in this test data. Distortion of these fiducials seen

in Lyot Project data are likely due to tilted focal planes due to a divergence in the beams after they are split into two polarizations by a Wollaston prism.

Marois (2007 private communication) estimates speckle noise will be the dominant source of astrometric error in estimating the positions of the fiducial spots. A relative brightness of 12 magnitudes between the on-axis occulted star an the fiducial is his recommendation. In order to place the fiducials at the corners of the AO control square we assume 24 wires across a re-imaged pupil. We give the counts in each image plane pixel in a slice of the reduced IFU data assuming a 30 second exposure in Sivaramakrishnan and Oppenheimer (2006), and Appendix, 4.2.

For a coronagraph pupil 12mm across, placing ghosts at 24λ/D 12 magnitudes fainter involves **2 micron** thick lines in the grid, at a spacing of **500 microns**. A microdot apodizer including the grid is being fabricated for tests on the AMNH testbed, it will place fiducials at 10λ/D from the testbed point source, 8 magnitudes or so fainter, in order for the fiducials to be clearly visible.

The alternative approach of using the tweeter DM to place a phase ripple on the wavefront is a fallback approach. Obviously this is a more flexible approach, since the ripple parameters and pattern are programmable. However, using the DM to create these ripples restricts the fiducials to lie only within the AO control square. One suggestion for placement of the fiducials is that they be placed closer than the corners of the control square, but further than half the side of the control square (Macintosh, private communication): with this choice, different grid orientations could place these spots either *inside* or *outside* the dark square of the AO system. Such an arrangement would not be possible if the tweeter was used to imprint a phase ripple on the wavefront for astrometric and photometric purposes. Residual speckle noise can impact astrometric and photometric accuracy (Sivaramakrishnan and Oppenheimer 2006).

The grid placement is completely tolerant to in-plane positioning errors in the pupil, and to tilt of the grid with respect to the wavefront, as long as this tilt remains repeatable. A tilt of 12 degrees to the beam results in a separation change of 2% in the fiducial spots. Sivaramakrishnan and Oppenheimer (2006) detail these sensitivities, as well as the photometry of the fiducials in relation to that of the occulted star.

Calibrating the astrometry and photometry of the fiducials will need to be performed on-sky initially, and checked for stability over the life of the instrument. Astrometric calibration binary stars are likely to be the calibration targets for both purposes. Astrometric and photometric calibration targets will be identified before CDR.

4.8 Risk and Long Lead Time Items

Apodizers: There are significant risks with the apodizer optics which are the most un-tested component of this coronagraph. These risks (detailed in the PDR document) include HEBS wave front performance, chromaticity of the apodization function (which can be exploited to improve performance), achromaticity of alternate techniques. All of these issues are being addressed with a variety of other testing facilities available at AMNH, including FTIR spectroscopy and SEM and Confocal microscopy.

FPM etching coating and polishing order may have an impact on quality of the final optic. Procurement will proceed with both possible orderings to ensure best results. These optics will also be investigated with SEM and confocal microscopy to ensure the quality of the holes and hole edges.

Phase Corrector mirror and Gemini Pupil Definer (tweeter Surrogate): The testbed may require a corrective phase plate, because there is no adaptive correction of the wave front. The guiding principle behind the testbed design has been to use superpolished optics (0.5 nm WFE rms) so that the performance is as close to the budgeted performance of GPI on-sky as possible. However, the different apodizer techniques may introduce wave front error that must be corrected to estimate actual performance of the system on sky. MEMS optical is capable of making a mirror with an arbitrary surface (etched through a grey-scale etching technology). They will produce this optic as necessary and it will be placed at the tweeter Surrogate location (which also defines the pupil geometry). This could induce a $20-30K additional cost in testbed development (but see also section 4.10, Recent Tests on Apodizers).

4.9 Integration

HIA fixtures will receive AMNH masks. However, the AMNH testbed schedule is decoupled from HIA's schedule because the testbed will use commercial holders for the masks (Appendix 4.7). All masks will be made with fiducials for mask alignment.

Pre-ship and post-integration tests will be developed and documented. AMNH has the responsibility for mounting the masks in the HIA fixtures prior to instrument integration.

4.10 Recent tests on apodizers (added May 9 2007)

Tests completed as this document was frozen show that the doped HEBS H band sample that showed very poor WFE during the Preliminary Design phase appears to be anomalous. CMI has just provided us with samples that we tested recently. These samples showed far better OPDs than the first H-band sample. In addition, other very recent test results suggest that microdot and Inconel apodizers' WFE is in the 5nm range (judging by Zygo data that has not had the reference flat WFE subtracted from the measurements yet). **Thus apodizer WFE risks for GPI are now appear to be significantly lower than the second HEBS characterization results suggested**.

This results will be documented and circulated as soon as tests of recently received apodizers and HEBS samples are completed, most likely before the May 23 review.

4.11 Coronagraph Reference

Hinkley, S., Oppenheimer, B. R., Soummer, R., Sivaramakrishnan, A., Roberts, L. C., Jr., Kuhn, J., R., Makidon, R. B., Perrin, M. D., Lloyd, J. P., Kratter, K., Brenner, D. 2007, ApJ 654, 633

Lloyd, J. P. and Sivaramakrishnan, A. 2005, ApJ. 621 1153

Lyot, B. 1939, MNRAS, 99, 538

Marois, C., Lafreniere, D., Macintosh, B. A., and Doyon, R. 2006, ApJ, 647, 612

Sivaramakrishnan, A. and Oppenheimer, B. R. 2006, ApJ. 647, 620

Sivaramakrishnan, A., Koresko, C. D., Makidon, R. B., Berkefeld, T., and Kuchner, M. J. 2001, ApJ 552, 397

Soummer, R. 2005, ApJ, 618, L161

Trauger, J. T. and Traub, W. A. 2007, Nature 446, 771

5 Integral Field Spectrograph

The science instrument for GPI is an integral field spectrograph based on a lenslet array. The integral field nature of the instrument allows for a full mapping of the focal plane at coarse spectral resolution. With such a data cube, artifacts within the PSF such as residual speckles can be suppressed (see Appendix 2.25 for detailed simulations.). Additionally, the initial detection of any candidate planet will include spectral information that can be used to distinguish it from a background object, and candidates can be followed up with detailed spectroscopic observations. A lenslet design is chosen because it is intrinsically low in wavefront error (especially chromatic wavefront error) and can be scaled to the required 40,000 field points.

Overall responsibility for the IFS development is with UCLA (PI Larkin), where a related integral field spectrograph (OSIRIS) was constructed and delivered to Keck in early 2005 and where several other facility class instruments have been built since 1989. The spectrograph optics after the lenslet array are being managed as a subcontract to the University Laval (ULaval/ImmerVision) and University of Montreal (UdeM) under the leads of Thibault and Doyon. They will also be using heritage from previous near infrared systems including WIRCAM for CfHT and GSAOI.

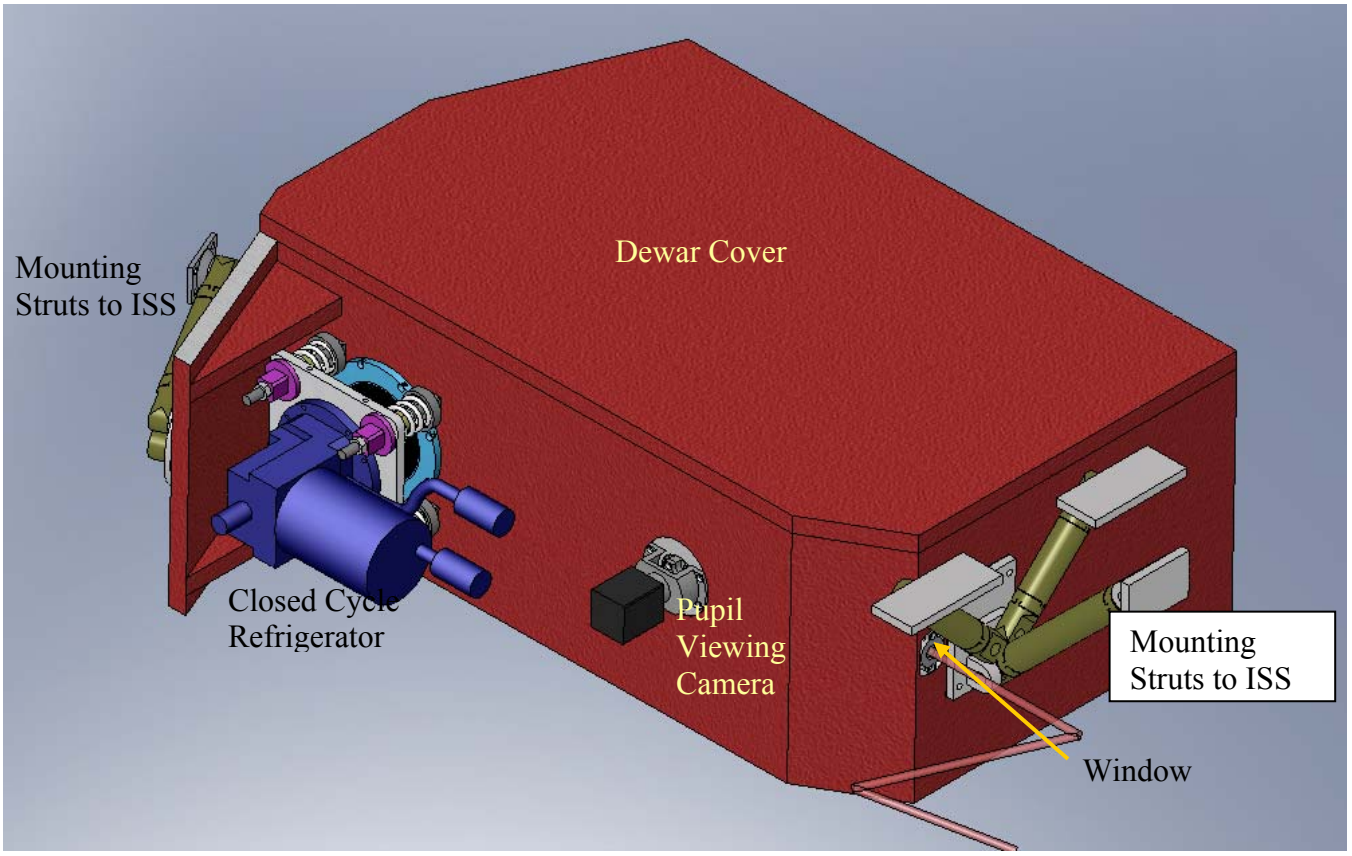

Figure 5-1 Rendering of the vacuum enclosure with some of the external components labelled.

5.1 Overview

The IFS is constructed as a cryogenic vessel that mounts to the ISS and resides above the AO bench. Figure 5.1 shows a rendering of the vacuum chamber with some of the external components identified. The AO bench is below the dewar from this point of view and the telescope beam is to the upper left. The thin red cylinders leading to the window are the beam coming from the calibration system into the IFS. The bends in these beams are the locations of the steering mirrors on the calibration system. Cables and connectors enter through a bulkhead on the opposite side of the dewar as the pupil viewing camera.

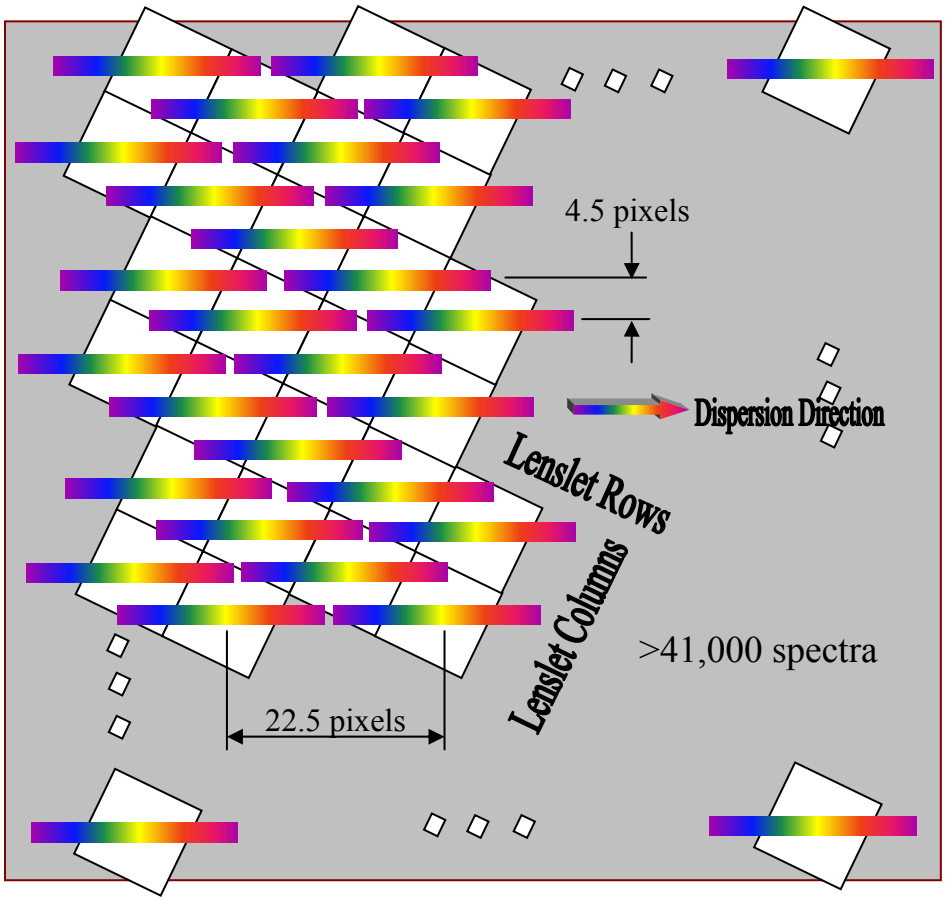

Figure 5.2a Schematic of the layout of spectra on the detector. The lenslet array is rotated 18.33 degrees relative to the dispersion axis so the spectra are interleaved between each other. Each spectrum is separated from neighboring lenslets by 22.5 pixels along the dispersion direction and 4.5 pixels perpendicular to the dispersion. The filter bandpasses and the dispersion of the prism are set so that spectra don't overlap.

The primary data product of the IFS is a data cube consisting of slightly more than 200x200 spatial locations, each with typically 18 spectral channels. This data is produced simultaneously for all spatial locations by using a lenslet array to interleave the spectra. Figure 5.2a shows a cartoon of the spectral layout on the detector. Each of the white boxes is the footprint of a single lenslet element on the sky. Each lens forms an image of the pupil behind it which serves as the input to a traditional spectrograph.

By rotating the lenslet by 18.33 degrees with respect to the dispersion axis, neighboring elements are displaced by 4.5 pixels vertically on the detector (shown as the overall gray box). If the spectra were allowed to run over more than 22.5 pixels, then they would run into the ends of spectra from other rows. This is controlled by limiting the filter bandpasses to approximately 20% of the filter central wavelength which limits the spectral length to about 20 pixels. The final field of view is 2.8 arcseconds on a side, with 14 mas sampling. A spectral resolution of 45 is achieved in the two primary bands of H and K.

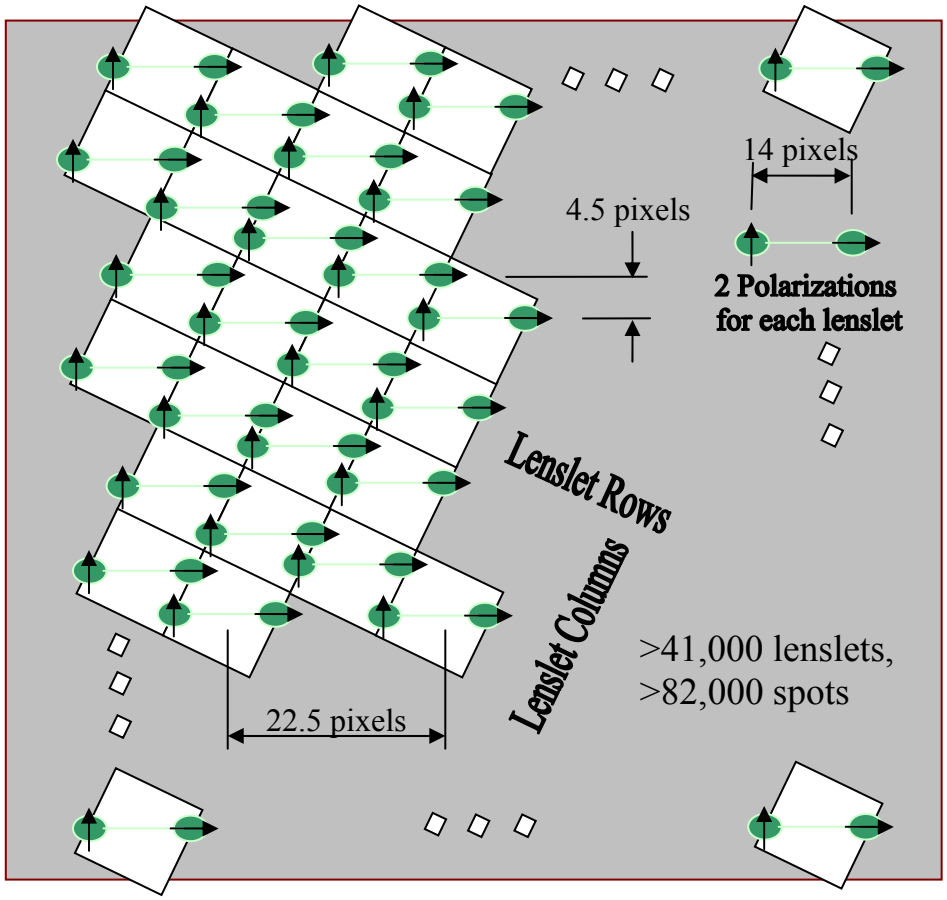

Figure 5.2b Schematic of the layout of polarization states on the detector. The lenslet array is the same as in figure 5.2a. An un-prism has removed the spectral dispersion, and a Wollaston prism separates the two polarization states by 14 pixels on the detector.

To make polarization measurements, a second prism is inserted into the collimated space to "un-disperse" the light back to a white light beam. On the same stage, a Wollaston prism is also inserted into the beam to separate out the two polarization states. The prism has a few low angle so the two states are only separated by 14 pixels in the same orientation as the spectrum had originally been spread. So again, the light from each lenslet are kept apart on the detector. In conjunction with the Wollaston prism, a wave plate is used in the calibration unit's path so polarizations can be selected for a particular observation. So the full field is maintained in polarimetry mode, but no significant spectral dispersion remains.

5.2 Optical Design

5.2.1 Overview

The IFS optical system can be broken into several functional pieces (see Figure 5.3) and we'll discuss each in the sub-sections below. Initially, a collimated beam enters through an infrared transmissive window that serves as a vacuum seal. A wheel of cold Lyot stops are in the pupil plane. Next, a pair of spherical mirrors provide a telephoto system for reimaging the focal plane at F/200 onto the lenslet array. The lenslet array samples the focal plane and produces a grid of "spots" which are each an image of the telescope pupil. This pupil plane is the input conjugate plane for a fairly standard prism spectrograph. The spectrograph is an all refractive design with a collimator and camera system based on Petzval lens systems. The filter and prism lie in between the collimator and camera. The detector finally sits at the conjugate plane to the pupil plane from the lenslet array. In this section, we'll detail each of these subcomponents. For the polarization mode, there is also an un-prism to remove the spectral dispersion and a Wollaston prism to separate 2 polarization states.

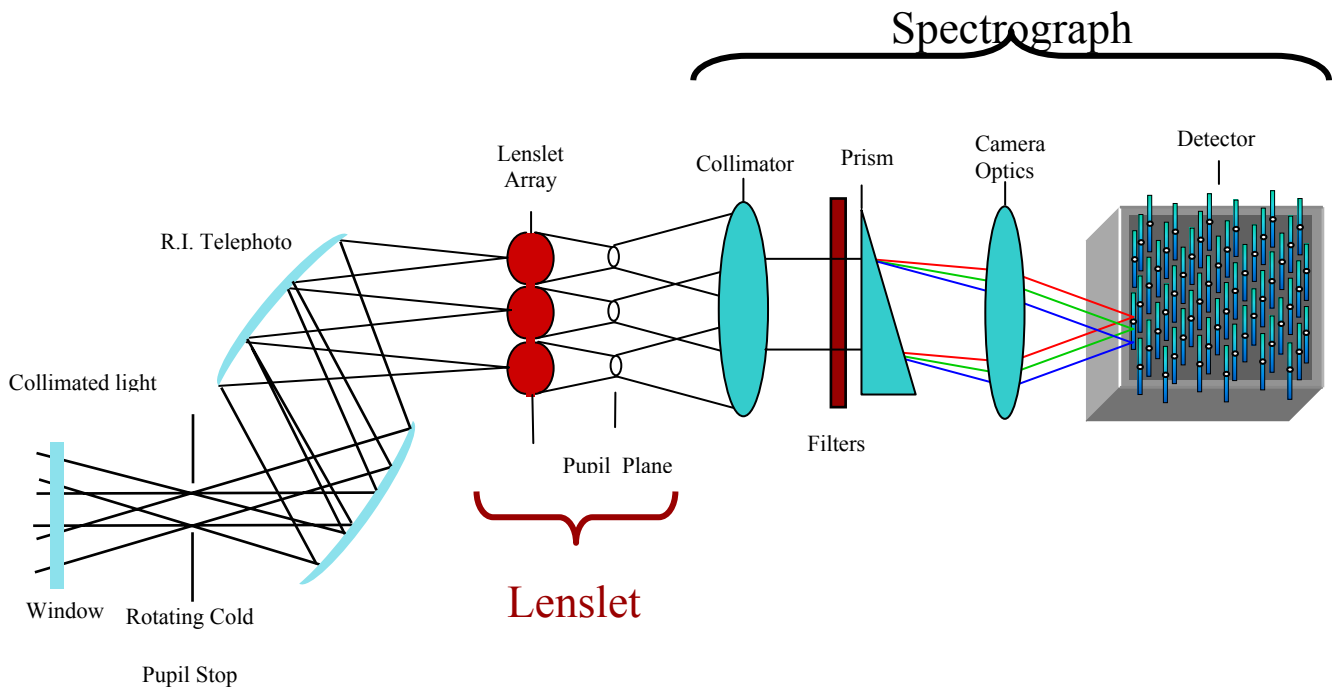

Figure 5.3 Schematic of Functional Sections of the Optical Design

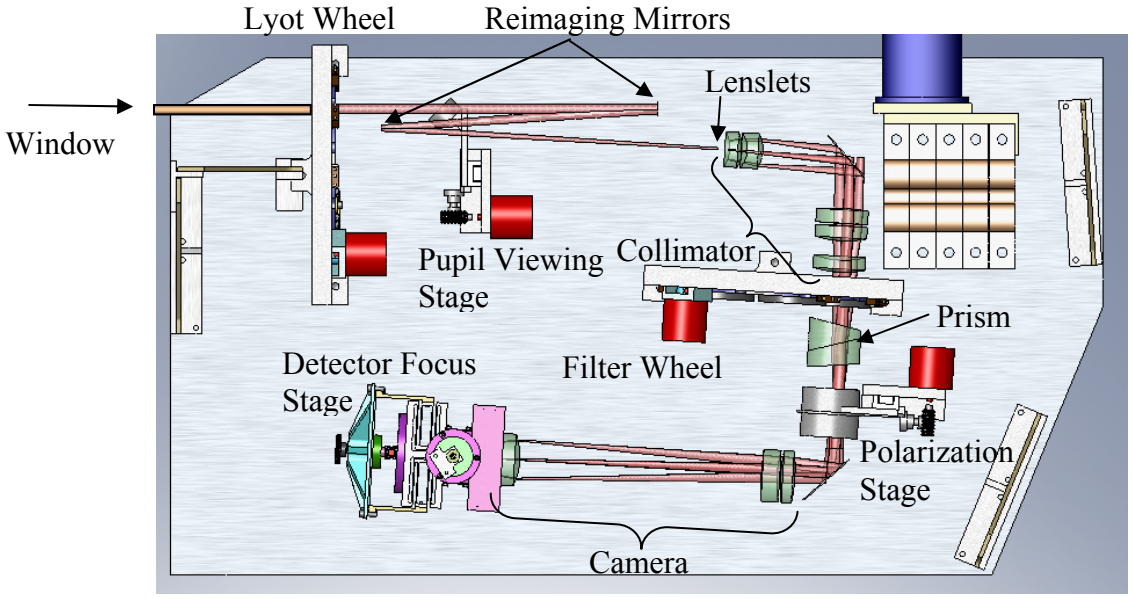

Figure 5.4 Rendering of the optical layout within the vacuum chamber and cold shield.

Figure 5.4 Rendering of the optical path within the vacuum chamber. The functional sections mentioned above are all labeled.

5.2.2 Window

The window is a refractive non-common path element. As such it must have excellent wavefront quality, transmission and low chromatic dispersion. It is also a primary vacuum seal. We've selected to use a fused quartz window with low OH content (Infrasil 302). This is a standard infrared window material and can be highly polished (~λ/20 @HeNe) and excellent AR coatings are possible (see Section 5.5.1).

5.2.3 Reimaging System

After the Lyot stop, a reimaging system is used to focus the input collimated beam into an image on the lenslet array. With an input pupil diameter of 1 cm and the requirement of an F/200 beam at the lenslet with the desired scale of 0.014" per lenslet, the effective focal length of this system is 200 cm. In order to fit this into the allowed volume, the reimaging system is a pair of spherical mirrors used as a telephoto system. As non-common path components that must operate at cryogenic temperatures, we've selected to use highly polished ULE glass for the substrates. Superpolished spherical mirrors with <1 nm RMS WFE are currently available for relatively low cost.

5.2.4 Lenslet Array

The lenslet array is the heart of the optical system and serves as the location where the field of view is sampled. Each lenslet then concentrates the light from its patch of the sky into a tiny pupil image. These concentrated images are well separated from each other and their spectra can be interleaved on the detector. The vendor selected is MEMs optical which also fabricated the OSIRIS lenslet arrays. They are made with a grayscale lithographic technique which provides the benefit of no internal surfaces. One of the goals of the lenslet design was to minimize the amount of light lost at the gaps between adjacent lenslets. For custom products, MEMS optical can keep these gaps to 2 microns in size. To further reduce their impact, our lenslet design has a very large radius of curvature on the front surface and most of the lens power on the rear surface. This has an additional benefit that the focus of a lenslet element occurs behind the substrate. Given the need for an effective focal length of 578 microns, this is essential to allow the substrate to be thick enough to support itself. We've selected a 1 mm substrate fabricated out of Infrasil 302. Figure 5.5 shows a raytrace of three adjacent lens elements within the array. The fill factor of the lenslet array should be greater than 95%. Since the lens material is standard Infrasil the throughput of an AR coating is expected to be excellent (>99% per surface).

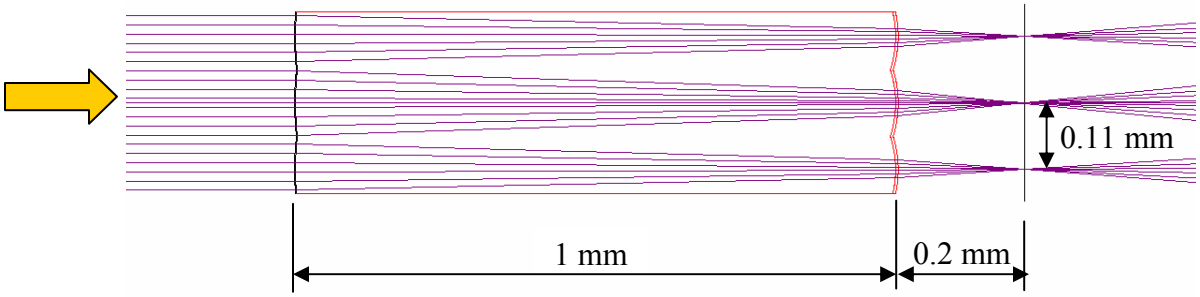

Figure 5.5 Ray trace of 3 adjacent lenslets. The light enters from the left side of the figure and the image plane forms on the left suface of the lenslet array. The lenslets' job is to concentrate the light down into well separated pupil images just after the array. Notice the large change in focal ratio occurring within the array. F/200 light impinges on the lenslet to form the image, and the outgoing beam is F/3.52 including the corners of the square lens elements.

Given the diffraction limited sampling of the lenslets, the size of the pupils is dominated by diffraction effects and geometric aberrations are negligible for the very slow input beam. An early task within the project was to model the effects of this "pupil diffraction". This is discussed in some detail in Appendix 5.11.

5.2.5 Spectrograph

The grid of pupil images formed just behind the lenslet array serves as the input location for the spectrograph optics. Since the lenslet works by producing an optical fast beam (F/3.52) to separate the field points, the spectrograph must accept this beam and have a field angle that encompasses the complete lenslet array (~22 mm on a side). It must also relay the these pupil images onto the detector which is 36 mm on a side. This dictates that the focal ratios of the spectrograph collimator and camera must be F/3.52 and F/5.89, respectively. For the optical design, the beam between the collimator and camera should obviously be as small as possible, but we will need space to insert a filter, the main

prism, an un-dispersing prism, and a wollaston prism. So making the collimated beam fairly long is beneficial. The overall footprint allowed for the spectrograph (from lenslet to detector) is roughly 400mm by 600mm. At the start of the PDR phase we investigated both a reflective and a refractive design and quickly came to the conclusion that an all reflective design would require much larger, more expensive optics so we have selected and focused on a refractive design.

In order to avoid any problem with glass transmission, the preferred form uses Barium Floride, Cleartran and F-STM16, which has recently been identified as a very good glass choice for such NIR system (Brown, Epps & Fabricant, 2004, PASP, 116:833-841). The similar system using Barium Floride, Cleartran and SF6 explored at the CoDR level has been discarded due to larger absorption from the SF6 at 2.3 um. As described during the conceptual design, a Petzval design (flat field lens) is the best choice for both the collimator and the camera optics.

Lens	Material	Spacing / Center thickness (mm)	R1 (mm)	R2 (mm)
Spacing		10.00		
Collimator 1	Cleartran	12.00	-33.05	-36.67
Spacing		5		
Collimator 2	BaF2	15.00	-27.18	-34.61
Spacing		90.00		
Mirror		40.00	∞	-
Collimator 3	BaF2	14.65	218.11	-782.38
Spacing		2.00		
Collimator 4	BaF2	14,65	682.70	-102.46
Spacing		18.75		
Collimator 5	Cleartran	11.50	-81.20	-103.93
Spacing		125.00		
STOP		5.00		
Prism (airspace-1mm)	BaF2/ SRTIO3	15 15	∞	∞
Spacing		37.50		
Mirror		37.50	∞	-
Camera 1	BaF2	14.00	147.43	-140.69
Spacing		3.40		
Camera 2	S-FTM16	15.00	-117.69	-313.18
Spacing		233.08		
Camera 3	Cleartran	21.00	64.80	54.81
Spacing		15.00		

Table 5.1 Optical description of each element specifying material, spacings and radii of curvatures.

Table 5.2 summarizes the spot qualities achieved at selected wavelengths across the field for just the spectrograph optics. In all cases the image quality is diffraction limited (see figure 5.6) and is dominated by pupil diffraction and is discussed in the overall performance section 5.2.6.

Wavelength (μm)	*Airy diameter (μm)*	*Spot size RMS radis(μm) / Coordinates(X,Y) on the image plane (mm)*		
		Field 1 /Coord. (0,0)	*Field 2 /Coord. (0,10.4)*	*Field 3 /Coord. (10.4,10.4)*
1.20	17.14	7.133 / (0,-0.666)	7.033 / (0,-18.069)	5.475 / (-18.350,-18.145)
1.65	23.76	5.900 / (0,-0.005)	5.069 / (0,-17.374)	5.420 / (-18.295,-17.453)
2.20	30.28	4.641 / (0,0.593)	7.063 / (0,-16.703)	10.169 / (-18.200,-16.784)

Table 5.2 Geometric spot radii for three wavelengths and three field points for the spectrograph optics.

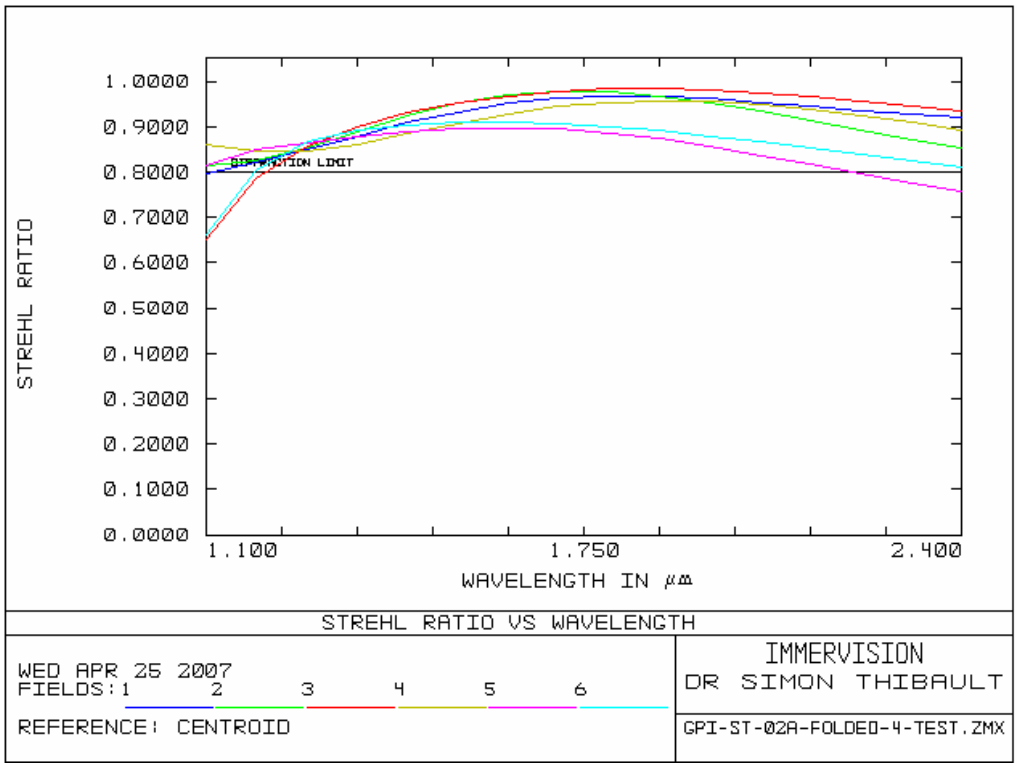

Figure 5.6 Spectrograph Strehl ratio as a function of wavelength at five representative field points. Note that the image quality does not actually fall off at short wavelengths, only in comparison to the diffraction limit which has become much smaller than a pixel.

5.2.5.1 Direct vision prism

Since we may require both a dispersed and undispersed mode, it is important for the prism to have zero net deviation for the central wavelength. This requires the development of a direct vision prism. In the conception of a direct vision prism, it can be important to minimise the prism angles in order to reduce the distortion introduced by the different glass thicknesses in the optical path. To maximise their efficiency, one glass will disperse the light while the other one will be used to reflect the beam to obtain a direct vision prism. So, one prism will have a low V-number (flint glass) while the other one will have

an important one (crown glass). By definition, a direct vision prism must have a zero deviation at a central wavelength λ:

$$\alpha_1(n_1 - 1) + \alpha_2(n_2 - n_1) = 0,$$

where α_1 and α_2 are the prism angle defined in Figure 5.7 and the glasses index are taken at the central wavelength. At a wavelength $\lambda+\delta\lambda$, glasses have refraction index $n_1+\delta n_1$ $n_2+\delta n_2$ and the dispersion Δ compared to the central wavelength is then:

$$\Delta = \alpha_1 \delta n_1 - \alpha_2 \delta n_2 .$$

Putting those two equations together, the deviation is given by:

$$\Delta = \alpha_2 (n_2 - 1)\left(\frac{1}{V_2} - \frac{1}{V_1}\right),$$

where V_1 and V_2 are the Abbe-number of the glasses. Assuming a dispersion law following $\lambda_{\max} = \lambda_{\min}(1+1/R)^{d_s/2}$, the required dispersion between wavelength associated with the last spectrum pixel (λ_{max}) and the one associated with the first one (λ_{min}) can be obtained from the following equation:

$$\Delta = \frac{2q}{F_{cam} D} \frac{\log(\lambda_{\max}/\lambda_{\min})}{\log\left(1+\frac{1}{R}\right)}.$$

Using the above equation, the prisms angles can be determined for one waveband. We can also find the condition to be satisfied to have a constant spectral resolution through multiple wavebands. Grouping the fix parameters in those equations, the right-hand side of the following equation has to be constant in all wavebands to conserve the same spectral resolution:

$$C = \frac{2q}{\alpha_2 F_{cam} D \log\left(1+\frac{1}{R}\right)} = \frac{(n_2 - 1)}{\log(\lambda_{\max}/\lambda_{\min})}\left(\frac{1}{V_2} - \frac{1}{V_1}\right).$$

For example, GPI requires the IFS to operate in the *J*, H and K bands. The factor C ratio of the *H* and *K* bands over the *J* band value are shown in table 5.3 for different flint glasses and crown glasses combinations. The best combinations found are prisms made of BaF2 – IrG2, BaF2 – SrTiO3, KBr – SrTiO3 and CsBr – SrTiO3. The use of SrTiO3 is particularly desirable for its high dispersion in all three bands as it can be seen in Figure 5.8. It will then minimise the prism angles.

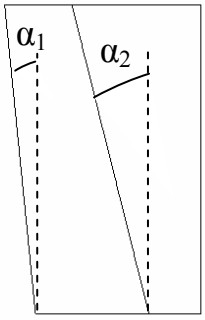

Figure 5.7 Prism angles definition

Glass 1	Glass 2	J-band	H-band	K-band
BaF2	Fused Silica	1.000	1.746	2.449
BaF2	IrG2	1.000	0.949	0.933
BaF2	SrTiO3	1.000	0.852	0.768
KBr	Fused Silica	1.000	2.865	4.496
KBr	IrG2	1.000	1.710	2.996
KBr	SrTiO3	1.000	1.033	1.087
CsBr	Fused Silica	1.000	2.722	4.230
CsBr	IrG2	1.000	1.642	2.162
CsBr	SrTiO3	1.000	1.032	1.086

Table 5.3: Computation of the C factor ratio for the three wavebands investigated.

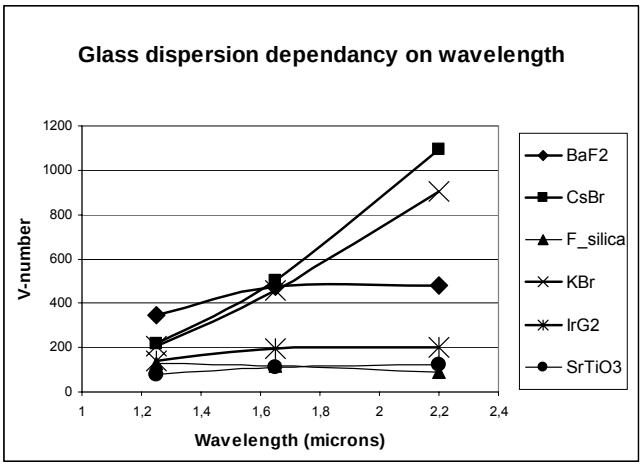

Figure 5.8: V-number computed for the different glasses investigated in the *J*, *H* and *K* band.

Here BaF2/SrTiO3 is the optimum combination. SrTiO3 shows some absorption at 2.9µm that does not influence the IFU performance.

Band:	H	J	K
V1 (Abbe)	471.91781	344.683592	480.238606
n1 (index)	1.4657115	1.46719041	1.46396694
V2 (Abbe)	112.669626	75.5122756	121.014118
n2 (index)	2.2801435	2.29795033	2.2608246
dispersion:			
delta x (mm)	0.34	0.5276523	0.30635599
Angle (rad)	0.0010989	0.0017054	0.00099016
Resolution:	**47.225**	**53.735**	**58.1516667**

Table 5.4 BaF2/SrTIO3 pair (baseline option)

At the time of writing, several vendors have been contacted for the procurement of the prism pair. BaF2 is clearly not a problem, it is used and will be used in many cryogenic optical systems of various sizes. However, the SrTiO3 is not as common as BaF2. SrTiO3 is a ferroelectrics material of high refraction index and high dispersion currently used for laser component and thin film (sputtering target). It is rarely used as a large size component. Recently, a prism pair using SrTiO3 has been used with success in a cryogenic camera (CONICA - VLT).

We have contacted Mr Rainer Leisen from Max-Planck-Institut für Astronomie who has designed the prism for CONICA. He cooled it down to 80K without any problem (the prisms were not cemented). He recommended that we contact MTI Corporation (www.mticrystal.com), who were the manufacturer of the SrTiO3 crystal. They produce blank sizes up to 50 mm in diameter.

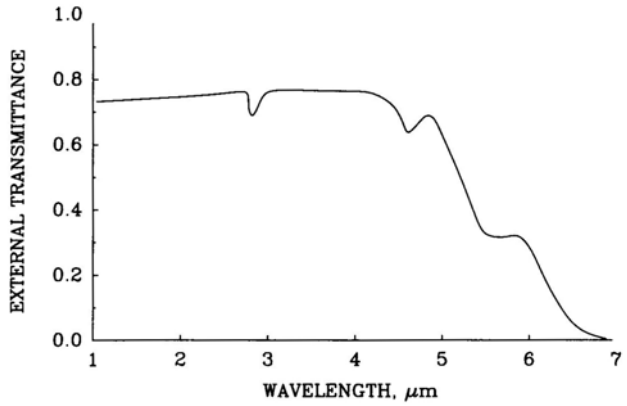

Figure 5.9 – Transmission of the SrTIO3

5.2.5.2 Filters

The GPI instrument is a low dispersion instrument working from the ground. The filter selection is dominated by the available atmospheric windows in the 1-2.5 micron range and the desire to cover as many wavelengths as possible. Figure 5.10 below shows the ATRAN (Lord, S.D. 1992) model for the atmospheric transmission for Mauna Kea at an airmass of 1.0 and a water vapor column of 1.6 mm. This comes from the Gemini website (www.gemini.edu). I've labeled the windows with their traditional names of Y, J, H and K. Overlaid are rectangles showing the wavelength ranges of the filters selected by the science team. The bandpasses, expected spectral resolutions and number of spectral channels for each filter are given in Table 5.5.

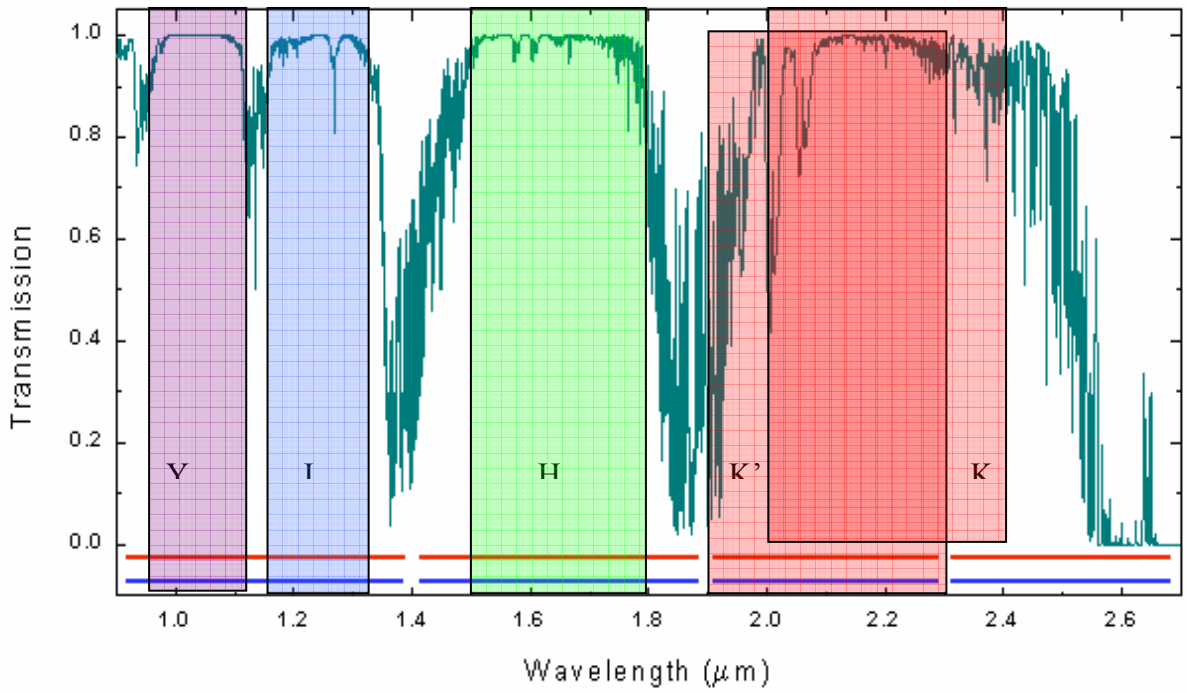

Figure 5.10 Atmosphere transmission with approximately 1.6 mm of precipitable water vapour overlayed with the GPI IFS filter complement.

Filter Name	½ power wavelengths	%bandpass	Spectral Resolution	# spectral channels
Y	0.95-1.12 μm	16%	60	19
J	1.15-1.33	15%	50	15
H	1.50-1.80	18%	45	16
K'	1.9-2.3	19%	45	17
K	2.0-2.4	18%	45	16

Table 5.5 Filter half power points, required spectral resolutions and number of spectral channels in the cubes.

In order to estimate the efficiency of each filter, we plot in Figure 5.11 a set of very similar filters delivered with the OSIRIS spectrograph to Keck. These were manufactured on a white crown glass that was previously polished to AO quality (~λ/20). These filters were manufactured by Barr Associates which is a likely vendor for the GPI filters. The measured transmissions are between 75 and 95% with the H filter have a mean transmission of 90%. For OSIRIS, very steep spectral cut-offs were required. Relaxing this requirement for the much lower dispersion GPI IFS should result in a slight increase in throughput.

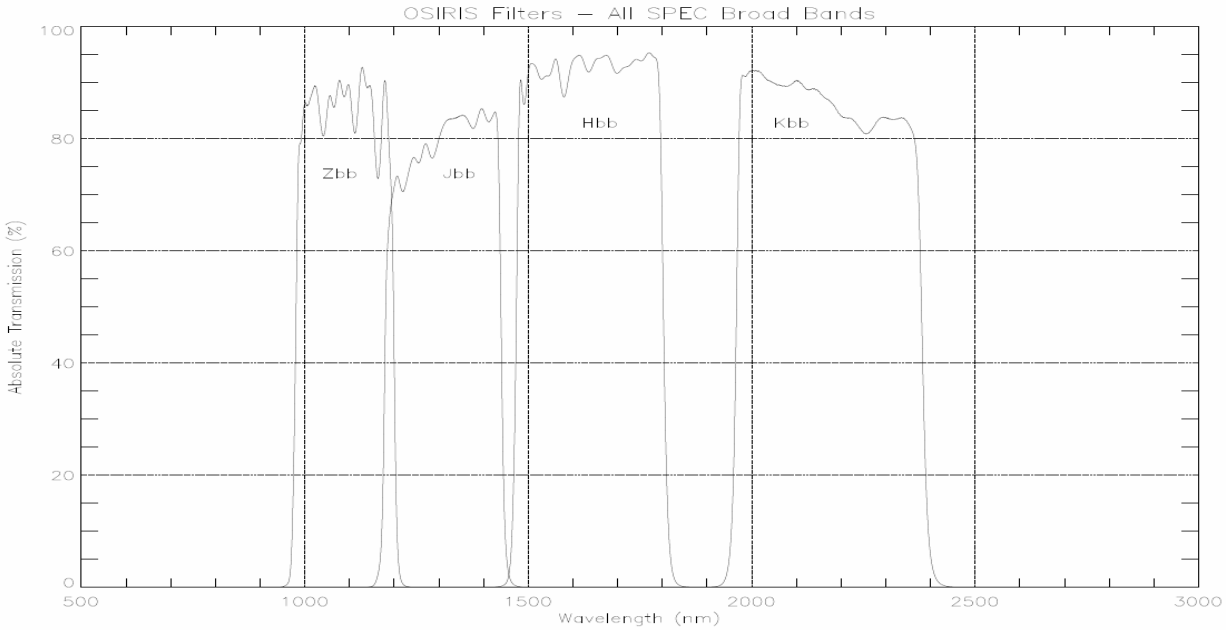

Figure 5.11 Measured transmission of the infrared filters in OSIRIS.

5.2.5.3 Component Mounts and Mounting Tolerancing

All lenses are mounted in the same manner (Figures 5.12 and 5.13). The lens is first placed in a cell with a conical surface tangent to its surface at periphery. The lens is then maintained axially via a ring loaded with 18 beryllium-copper springs. The force applied on the lens is about 5 times its weight. The lens-mounting scheme is the following: The cell is centered on a rotary table using sapphire ball mechanical gauge. The lens is then optically centered on the rotation axis of the rotary table by adjusting its position within the cell by means of a laser and a position-sensing device. Once this step is completed, the lens is fixed axially by loading the beryllium-copper springs, and the exact length required for the teflon/nylon pads is measured with a depth gauge to a precision of about 10 μm. The lens is then fixed in place with the pads. Once the lens is fixed in place, the residual centering error between the lens and its cell is measured by first centering the optical axis of the lens with the rotary table using the laser and position-sensing device, and then by measuring mechanically the decenter of the cell with the sapphire ball sensor. The phase of the decentering and its amplitude is noted for future use in assembling the optical train. The observed residual decenterings on CPAPIR and WIRCAM were between 5 μm and 35 μm.

Most cells will have six or eight mounting screws, allowing for a partial registering of the residual decenterings. All decentering axes are aligned as much as possible during the final mounting of the optical bench. A simple Monte-Carlo simulation shows that this reduces the RMS decentering in the optical bench by a factor of two compared to a random positioning of the decentering phases.

Figure 5.12 – Schematic view of the athermal lens mounting (left). The lens is held in place by an axial ring loaded by beryllium copper springs. One of the three accesses to the lens periphery, used for athermal centering, is shown in this schematic view. The view at right shows a cross-section of the mount. Nylon pads center the lens.

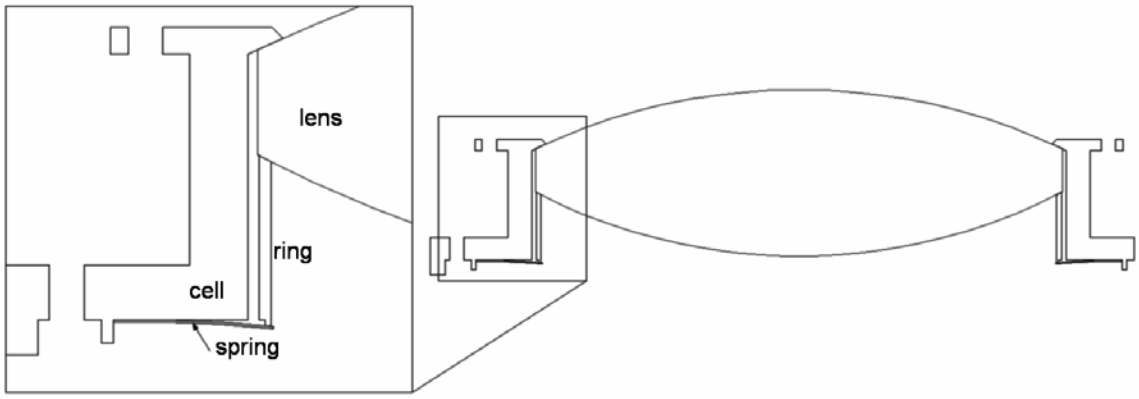

Figure 5.13 – Same as Figure 5.12 left panel, but in a section view.

Table 5.6 shows a list of the alignment tolerances determined from the Zemax raytraces. The safety margin for the centering is very large. This safety factor will ensure the lens positions meet the requirements for the IFS performance in operation.

Component	Tilt[1] (±)	Decenter (±mm)	Distance (±mm)
Collimator 1	See note 1	0.050	0.10

Collimator 2	See note 1	0.050	0.10
Collimator 3	See note 1	0.050	0.10
Collimator 4	See note 1	0.050	0.10
Collimator 5	See note 1		
Filter #1 (not shown)	-	-	0.10
Prism (disperson)	-	0.10	0.2
UnPrism	-	0.10	0.2
Wollaston	-	0.10	0.2
Camera #1	See note 1	0.025	0.1
Camera #2	See note 1	0.025	0.1
Camera #3	See note 1	0.050	0.1
Group 1 (coll. 1 &2)	0.1	0.05	0.1
Group 2 (coll. 3-5)	0.1	0.05	0.1
Group 3 (camera 1-3)	0.1	0.05	0.1
Mirror tilt (two mirrors)			

[1] 0.025 mm / lens diameter

Table 5.6 Alignment tolerances for optical components

5.2.5.4 Ghosts

For the spectrograph optics, the ghost image must be studied carefully. In large part, this due to the near-telecentric camera image plane; reflections from the detector tend to fall into the detector after a reflection off an optical surface. GPI images after the coronagraph will have dynamic range of ~500:1with the brightest pointlike source (the spot of Arago) having a intensity equal to about 10^{-4} of the unocculted starlight, so ghost at the 0.1% level can create spurious planet signals. Significant ghost images are discussed as follows.

Ghost images are formed by an even number of spurious reflections from optical surfaces. The surface reflectivity is small (less than 2% and 1.0%), and so those ghosts produced by double reflections tend to dominate. The most important ghosts tend to involve a first reflection from the detector because it has high reflectivity (20% to be conservative).

The complex structure of the IFS also produces strong ghosts due to multiple reflections from the prism and filter surfaces. Proper study of these ghosts within the IFS wiill be done using non-sequential ray tracing and/or ASAP software during the critical design phase. A few examples are shown in figures 5.14 through 5.16.

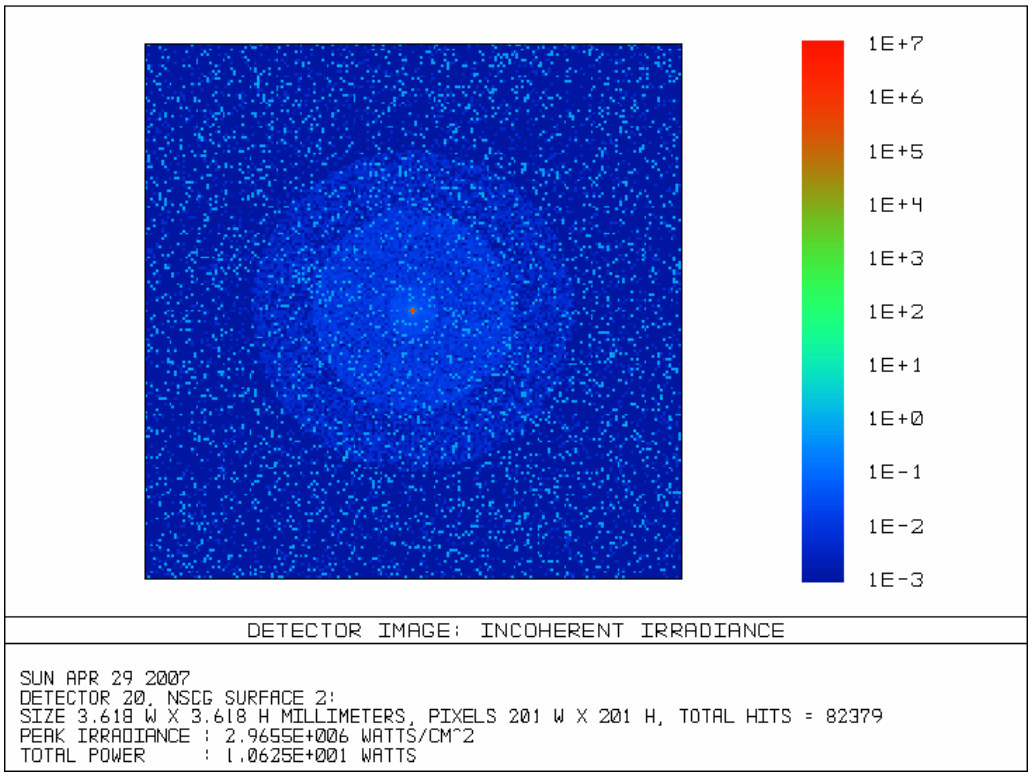

Figure 5.14 – Ghost - central light source.

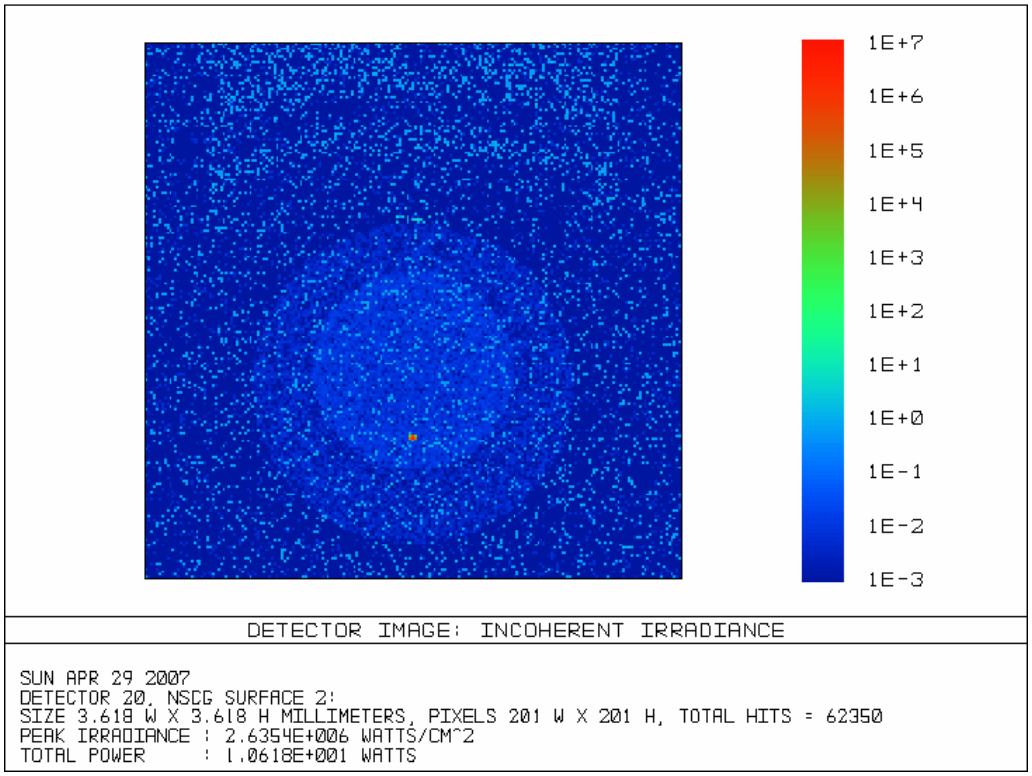

Figure 5.15 – Ghost - Off axis light source.

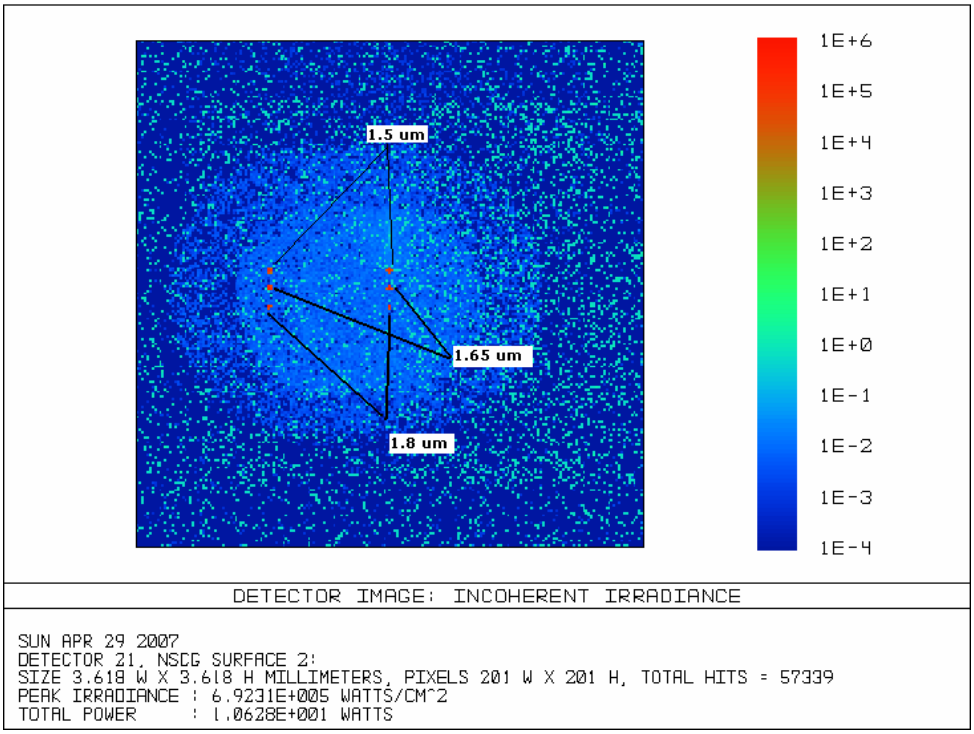

Figure 5.16 – Ghost - On-axis and off-axis source (including dispersion).

5.2.5.4.1 Filter Ghosts

Filters are placed near the prism, where the beam is roughly collimated. Internal reflection within the filter produces a ghost image of the field. The filter is a plane parallel element, and so the ghost image is harmlessly coincident with signal. Any wedge error within the filter will cause the ghost field to be displaced laterally from the signal.

Assuming that the reflectivity of each surface of the filter is 2%, the ghost intensity ratio will be 0.0004. According to filter supplier Barr Associates, a realistic wedge tolerance for the proposed filters is 10-30 arcsec. The maximum displacement between the ghost field and the parent field is then 0.1 pixels. A three degrees tilt of the filter is sufficient to throw this ghost off the detector.

5.2.5.4.2 Detector Substrate Ghost

The ghost image caused by reflection in the detector substrate will not be a problem because the incident beam is telecentric (or close) for the optical design. A ghost image is produced but it is then coincident with the signal. As long as defocus is not significant then the ghost is not offensive. We recall here that the intensity ratio of this ghost image is independent of the optical design but it is due to the detector only. The IFS detector will be a Rockwell HAWAII-2RG device. These detectors use a 0.82 mm thick CdZnTe substrate in front of the HgCdTe detector material. The refractive index of this substrate material is uncertain, but is estimated to be ~3.29 at a wavelength of 1 μm and a temperature of 80 K.

The ghost intensity cannot be estimated accurately, so a conservative estimate is made based on past experience. The GSAOI Conceptual Design Review estimates a 0.008 ghost intensity ratio (10% from the detector layer, 10% back from the window and 80% photon efficiency).

5.2.6 Combined performance in normal operation

Figure 5.17 shows representative spectra after passing through all optical elements including the lenslet array. Sixteen configurations are presented horizontally which correspond to four separate lenslets: centered (configurations 1-4), displaced to one edge (conf. 5-8), perpendicular edge (9-12), other perpendicular direction (13-16). For each lenslet a Y, J, H and K spectrum is presented in each of the four configurations for that lenslet. For each spectrum, the wavelengths run vertically and the bottom and top spots correspond to the lower half-power point and the upper half-power point for that filter. The central wavelength is shown with a circle of the diameter of the Airy radius at that wavelength. As can be seen, in all cases these geometric spots are well inside the Airy pattern and true spots will be diffraction limited at every wavelength. Each row of the figure shows light from a different area of the lenslet array. Zemax seems limited in its ability to overlay these in this multi-configuration plot. In all cases, all light from a given lenslet forms together inside the Airy pattern again indicating diffraction limited performance.

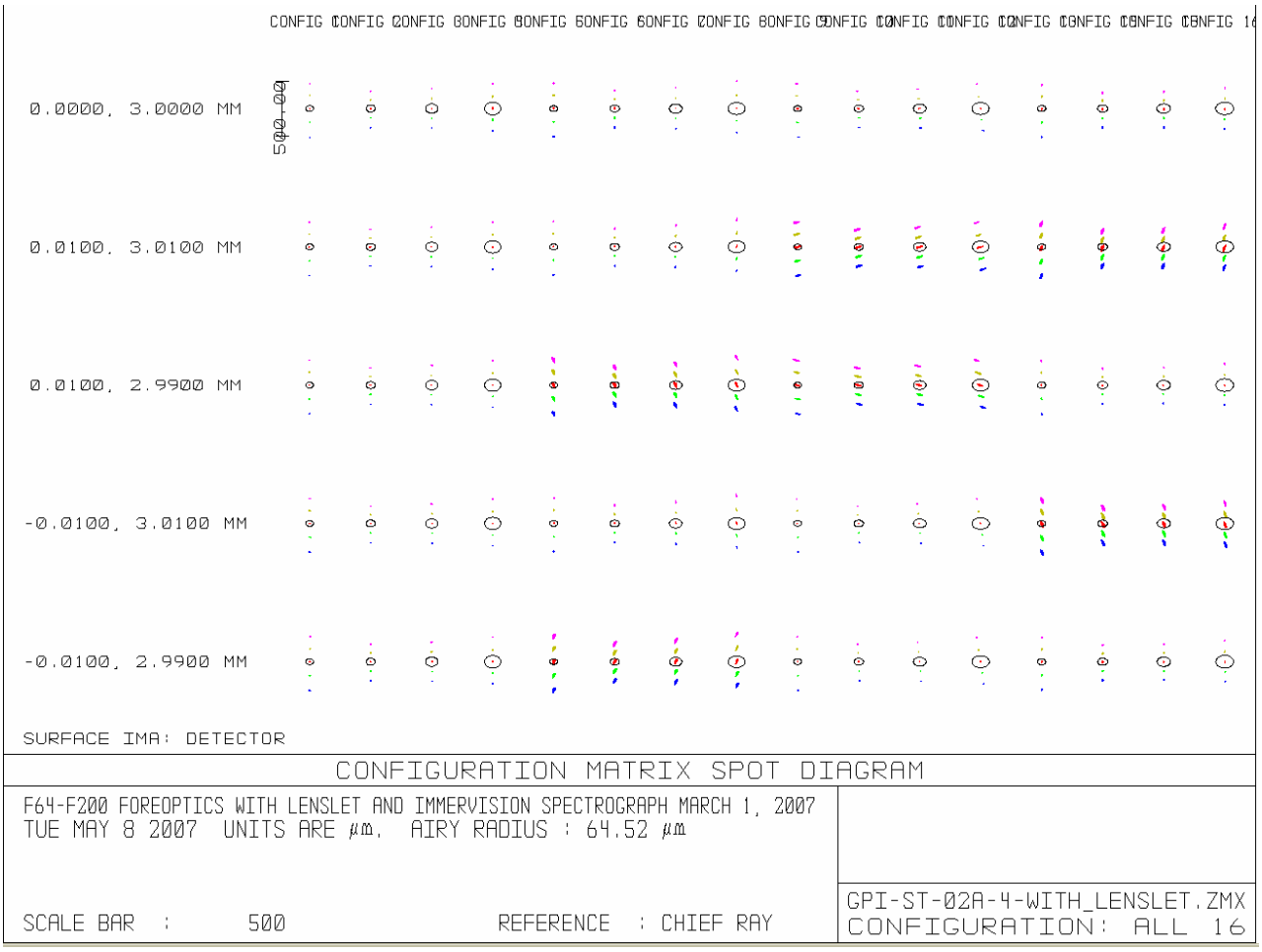

Figure 5.17 Example spot diagrams when the entire optical system including reimaging optics and lenslet array are combined with the AO bench. Four separate lenslets are presented which are: centered (configurations 1-4), displaced to one edge (conf. 5-8), perpendicular edge (9-12), other perpendicular direction (13-16). See text for details.

5.2.7 Polarimetry mode

We seek to have the two polarizations separated on the detector by 10 pixels (i.e. each polarization displaced by 5 pixels from the central position they would both share if nondispersed.) This provides maximum separation between polarizations without approaching adjacent lenslets, since there are 22.5 pixels between the centers of each lenslet image.

The physical pixel scale is 18 μm/pixel, hence 10 pixels is 0.18 mm. The camera focal length is 235.6 mm. Hence obtaining a displacement of 10 pixels requires a beam split of 0.18/235 = 0.044 degrees. That is the full split angle; each polarization should be displaced by half of that, or 0.022 degrees.

The single-beam displacement, $\Delta\theta$, of a Wollaston prism with birefringence Δn and prism angle α is given by

$$\Delta\theta = \Delta n \tan(\alpha)$$

Re-arranging to solve for α gives

$$\alpha = \tan^{-1}(\Delta\theta/\Delta n)$$

We can thus compute the necessary properties of the prism for a variety of materials.

	MgF2	Quartz	Sapphire	YLF
Δn	0.011	0.009	0.008	0.022
Prism angle α, deg.	1.83°	2.44°	2.75°	1.00°
Min. thickness, mm	1.3	1.7	1.9	0.7

Table 5.7 Wollaston Properties

All materials shown here result in prism angles of 1-3 degrees. Because we're in a small angle regime, the required fractional precision for the angle is the same as that of the displacement (i.e. if the goal is 10 pixels displacement ± 10%, then the above angles are allowed ±10% error).

The thicknesses listed are the *minimum* thicknesses due to the prism angle itself; the prism can certainly be manufactured thicker if desired for handling reasons.

Because of the post-lenslet array location, we are not vulnerable to image smearing due to "lateral chromatism" a.k.a. chromatic birefringence. For a 10 pixel split using one of these materials, lateral chromatism will blur each spot by no more than ~0.1 pixels.

5.2.7.1 Choice of Wollaston Material

Choosing between these various materials should be done based on fabrication cost and risks. One area of concern is bonding the two prism faces together, and the thermal stresses that will arise when cooling to 75 K due to differential contraction of the crystal axes.

Previous discussions of optical materials for Wollaston prisms (e.g. Oliva et al. 1997) use different criteria than are applicable to GPI, so their recommended materials are not necessarily the best for our purposes. In particular, Oliva et al. focus on the chromatic birefringence of the various glasses (also called lateral chromatism), seeking to identify materials with very achromatic birefringence. This is important for maintaining image quality in direct imaging polarimeters—but for GPI, the lenslet array pixellates the image plan prior to polarization splitting, and so we do *not* need to worry about chromatic birefringence. Oliva et al. also seek to identify materials with large birefringence, capable of producing large image separations and hence large fields of view. Given our small field of view and the fact that we need to displace each beam only a very small amount, we do not require a large birefringence. Hence we are free to choose from a wide range of glasses with acceptable properties, and almost certainly will not need to use any exotic materials like YLF.

Calcite is not considered because it turns opaque to one polarization beyond 2 microns. YLF is expensive and hard to get in large sizes, and we don't need its very low chromatism, so it is unlikely to be the best choice.

5.2.7.2 Fabrication Costs

We have currently requested quotes from a variety of optics manufacturers for the Wollaston prism and waveplates.

In the mean time, a rough boundary on the cost may be estimated as follows:

1) Off-the-shelf Wollastons and waveplates are relatively inexpensive optics, $500-$1000 depending on properties.
2) The custom YLF Wollaston for IRCAL cost $7k. A larger, 13 mm YLF Wollaston was priced for the Lyot Project coronagraph, with a resulting quote of $13k. These costs were both high due to the difficulty of obtaining YLF, and the precision required for the optical contacting used to make the prism.

GPI will require custom polarizing optics, but out of materials less exotic than used in IRCAL (although also several times larger in size for the Wollaston). Hence the cost for the GPI Wollaston will most likely be within the above two extremes.

5.2.8 Pupil Viewing Camera

GPI requires a pupil-viewing mode after the Lyot stop for alignment and diagnostic purposes. For the pupil viewing camera we've selected the same InGaAs camera that JPL will use within the calibration system. We've modeled a single BaF2 lens as the reimaging lens for the pupil camera. See section 5.4.2

for a discussion of the camera. The camera wavelength range will be controlled by a single filter (broad H or narrow 1.59 microns to be selected based on CDR modelling.)

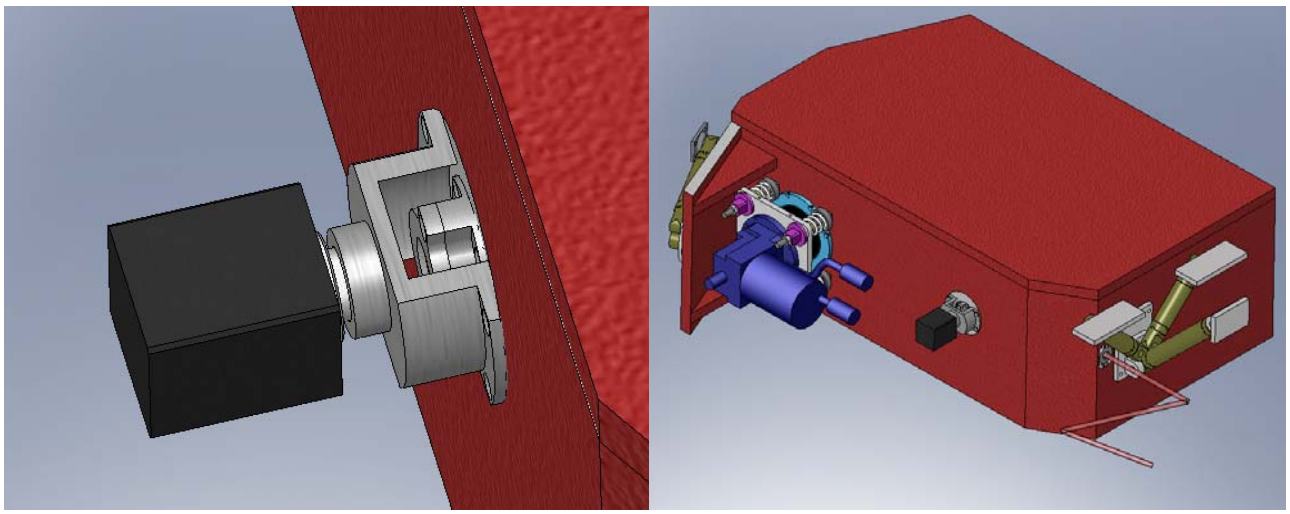

Figure 5.17– Pupil viewing camera with its window mount. A single BaF2 lens is located just inside the dewar and cold shield.

5.3 Mechanical Design

5.3.1 Overview

The GPI IFS mechanical design relies heavily on heritage developed from previous instruments. It contains five cryogenic mechanisms based on OSIRIS and MOSFIRE mechanisms which in turn are based on previous generations of mechanisms for the NIRSPEC and GEMINI instruments. Like OSIRIS and NIRC2, it is entirely cooled with a mechanical closed cycle refrigerator (CCR). Similarly the CCR has a vibration isolation system based on the ones used for the NIRC2 and OSIRIS instruments at Keck.

5.3.2 Vacuum Chamber

The vacuum chamber is an aluminum box with one inch thick wall thicknesses (see figure 5.18). There is a flat bottom plate which is parallel to the AO optical bench. The 7 “walls” of the chamber are rigidly welded to each other and to the bottom plate. The mounting struts to the ISS mate to three ports on these side plates. On the inside of the walls at the locations of the mounting struts, we will weld mounting flanges where we mount the fiberglass (G10) internal struts that support the optical bench and all internal structures. The top of the vacuum chamber is a single flat plate, one inch thick. It has an o-ring groove cut into its surface and a bolt pattern for sealing it to the walls of the chamber. The walls have a pattern of tapped holes around the top exposed surface just outside the o-ring seal. Since it is an inch thick, no mating flange is necessary. The OSIRIS spectrograph was fabricated in an identical manner with a welded 5 sided box and a cover plate with bolt holes directly placed into the walls of the chamber. All penetrations for cabling, light paths, and the closed cycle refrigerator are made through the walls of the chamber.

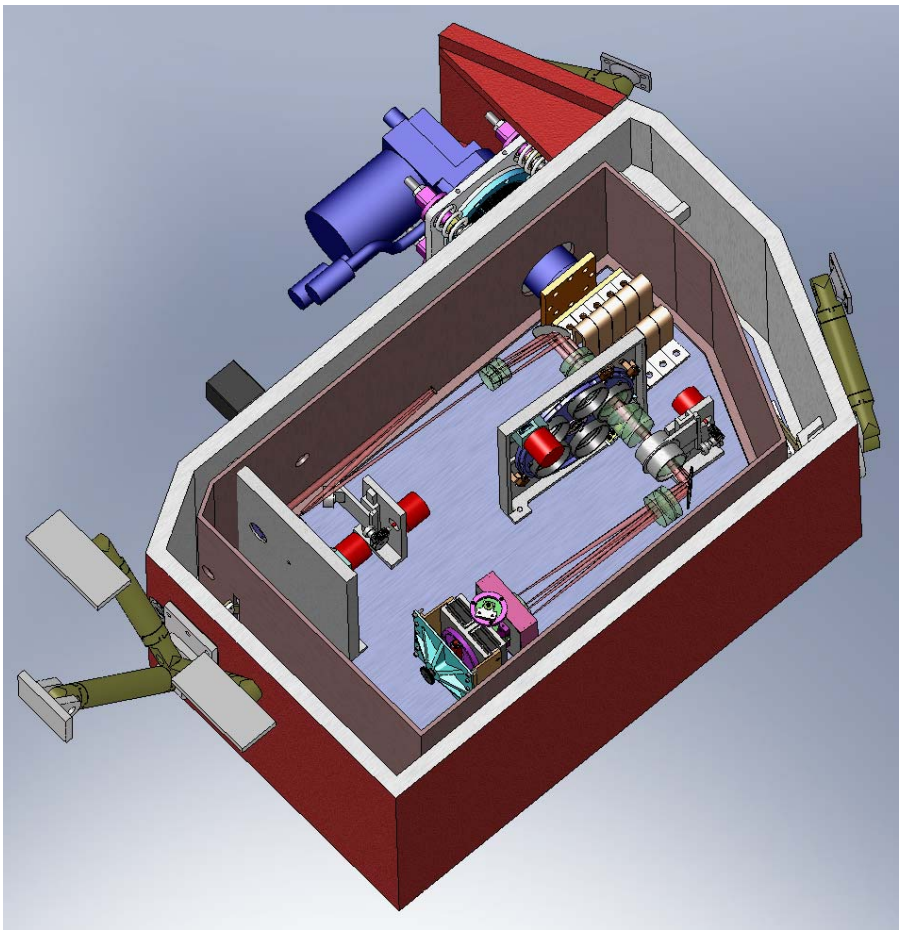

Figure 5.18– Rendering of the entire dewar with external struts and internal components revealed.

The optical bench and cold shield use a similar pattern where the walls are welded to the optical plate for excellent thermal contact and shield rigidity. Penetrations through the vacuum chamber are carried through the cold shield. To access internal components, the upper vacuum plate is removed, then a simple cover for the cold shield is removed.

5.3.3 Mechanisms

Five unique mechanisms are planned for the IFS and all have an extended heritage at UCLA in instruments such as OSIRIS, MOSFIRE, NIRSPEC and GEMINI. All mechanisms use cryogenically prepared stepper motors directly mounted to the mechanisms. Similar motors have demonstrated lives over a decade within existing instruments built at UCLA.

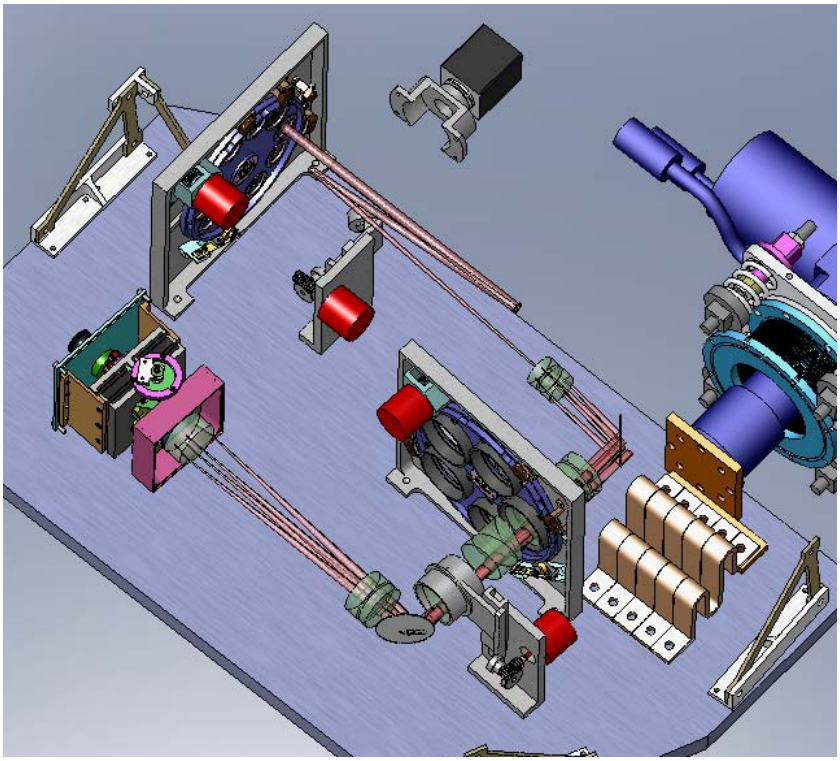

Figure 5.19 Layout of the internal components including the five mechanisms.

Lyot Wheel – A basic wheel in the pupil plane with 10 positions containing Lyot masks of different aperture diameters to allow selection of how much of the pupil to remove from the outer edge. Each mask sits in a substrate with an outer diameter of 25 mm and a possible thickness of 6mm. The masks themselves are fabricated under the supervision of the AMNH and are described in the coronagraph portion of this report.

Pupil Viewing Stage – A two position stage to insert and remove a pick-off mirror to direct light into the pupil viewing camera. This stage is after the Lyot wheel and before the lenslet array. It will be out of the beam for normal operation. Like the other slide, a magnetic catch will hold the stage in either position when motor power is removed.

Filter Wheel – A wheel mechanism containing 5 filter positions is located between the spectrograph collimator and camera. The final size of the filters is expected to be 50 mm in diameter and the wheel can handle 60 mm filters.

Undisperser-Polarization Stage – A two position stage between the spectrograph collimator and camera to insert an additional prism that "undisperses" the light and a Wollaston prism to separate two polarization states. It will be out of the beam for normal operation.

Detector Focus – A single axis linear stage to move the detector along the beam axis. This is anticipated to be necessary only during assembly and alignment. The motor will either be removed or prevented from normal activation once the IFS is delivered. An identical stage has been fabricated for the MOSFIRE instrument and is undergoing extensive cryogenic testing at UCLA. Figure 5.20 below shows

some of the details of the mechanism. The key component is a titanium flexure block that is wire EDM'ed to leave behind thin flexures.

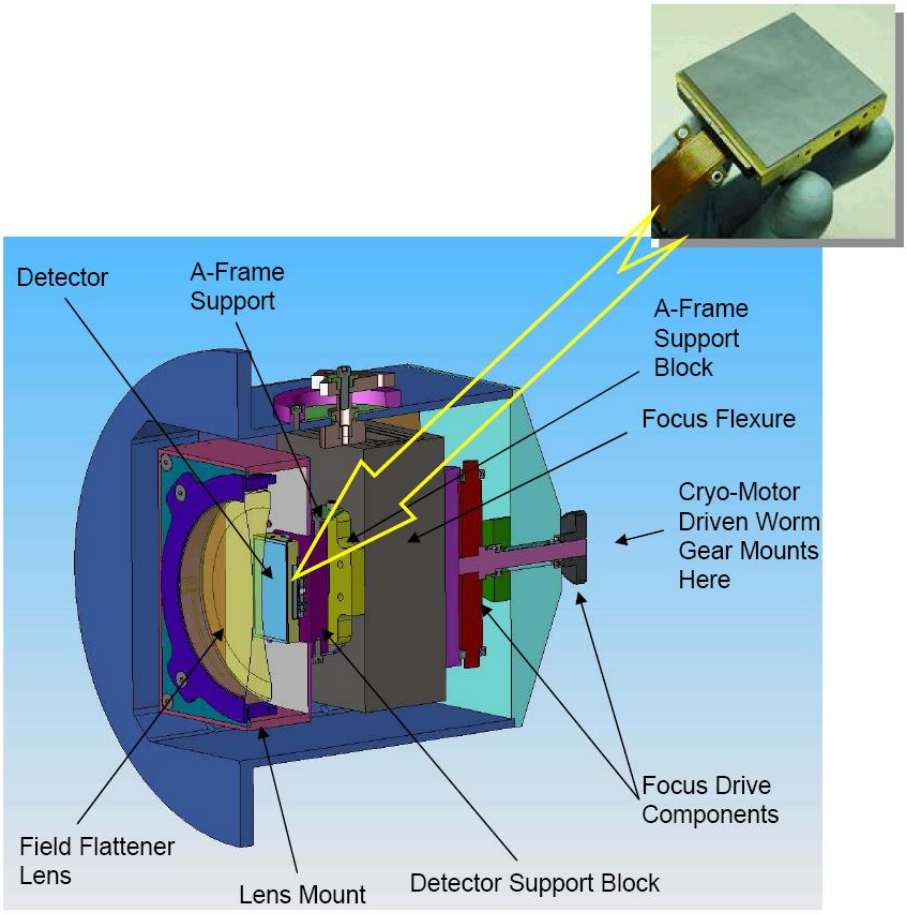

Figure 5.20 Detail of the detector focus mechanism including the titanium focus flexure and final field lens mounted to the structure.

5.3.4 Flexure Analysis

The GPI IFS must maintain stable performance in a wide range of gravity vectors. But because the internal components must be thermally isolated from the outside world, we are limited to relatively flexible materials such as G10, a type of low conduction fiberglass. In order to estimate the amount of flexing that we're likely to see in operation, Evan Kress at UCLA used the ALGOR finite element analysis program to model the effects under a few of the most extreme orientations. Figure 5.21 shows the worst case deflection of the optical bench relative to the fixed constraints which mount to the dewar wall and which directly connect to the outside support struts to the ISS. In this example, the optical bench is oriented along the gravity vector which is 90° from the zero deflection case (optical bench horizontal). As the figure shows, the dominant motion is due to flexing of the G10 A-frames which support the bench. Masses for optics and other components are simulated by adding extra mass uniformly to the optical bench. During the critical design phase, we will complete a more detailed FEA

including the cold shield and bench components. We anticipate that the cold shield will help to stiffen the bench and mounting structure, so the present analysis is conservative.

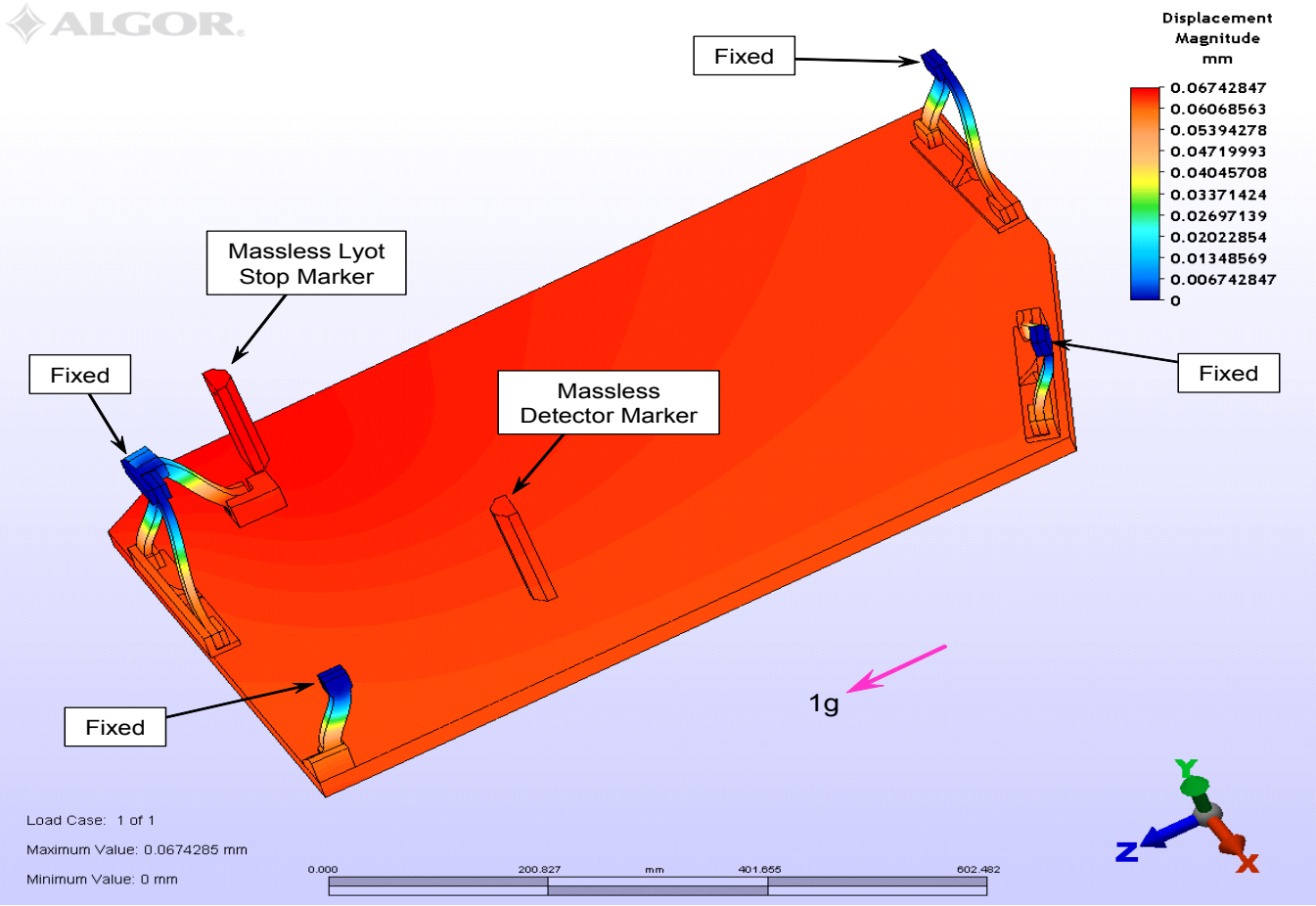

Figure 5.21 Example flexure of the optical bench mounted on thermally isolating G10 struts. This is the most extreme case when the gravity vector (shown as a purple arrow) is along the long axis of the optical plate. This is the position when the telescope is at the Zenith and GPI is mounted to the up-looking port. For reference, zero deflection is defined as the position of the bench when it is horizontal (i.e. gravity along the –y axis in the figure).

Load Case	Total Lyot Stop Deflection				Lyot Difference From Nominal			
	X (μm)	Y (μm)	Z (μm)	Mag (μm)	X (μm)	Y (μm)	Z (μm)	Mag (μm)
1g +Z	-7.18	-20.68	63.55	67.21	0.00	0.00	0.00	0.00
1g +Z +X	21.88	-17.57	58.58	64.95	29.06	3.11	-4.97	29.64
1g +Z –X	-36.23	-23.78	68.52	81.08	-29.05	-3.10	4.97	29.64
1g +Z +Y	-5.19	-10.58	55.21	56.45	1.99	10.10	-8.34	13.25
1g +Z –Y	-9.17	-30.78	71.89	78.74	-1.99	-10.10	8.34	13.25

Load Case	Total Detector Deflection				Detector Difference From Nominal			
	X (μm)	Y (μm)	Z (μm)	Mag (μm)	X (μm)	Y (μm)	Z (μm)	Mag (μm)
1g +Z	-13.60	-6.88	62.53	64.36	0.00	0.00	0.00	0.00
1g +Z +X	13.37	-4.50	52.08	53.96	26.96	2.38	-10.44	29.01
1g +Z –X	-40.56	-9.26	72.97	84.00	-26.96	-2.38	10.44	29.01
1g +Z +Y	-7.89	-0.18	54.46	55.03	5.70	6.70	-8.07	11.94
1g +Z –Y	-18.85	-15.32	70.73	74.78	-5.25	-8.44	8.20	12.89

Table 5.8 Absolute and relative motions of the Lyot plane and detector plane under 5 extreme orientations.

Table 5.8 gives five example motions of the optical bench relative to the external mounting points. The 1g +Z is the vertical case shown in Figure 5.21. The others represent the telescope moved to 45 degrees elevation in four different azimuths around the circle. The four columns called "Deflection" are in absolute microns from the bench position if it were horizontal. The four "Difference" columns on the right are relative to the vertical case to indicate the amount of relative motion that occurs during large motions of the telescope. For the Lyot stop, the only number of any concern is the 29 microns of "x" motion that occurs when the bench is on its side. This motion is not only the largest, but also is a side-to-side motion of the Lyot stop relative to the incoming beam. Thankfully, this is only a 0.3% shift of the pupil with respect to the mask and can be compensated with the beam steering mirrors on the calibration system. (The requirement for the total shift of the Lyot pupil with respect to the GPI apodizer pupil is 1% of the pupil diameter.) For the detector, there is a similar 27 micron shift sideways that would be 1.5 pixels. But since the Lyot stop moves almost the same amount, the vast majority of this shift is a common motion of the optical bench and will not induce motion of the light on the detector. And as can be seen from the total magnitudes of the displacements (29.6 and 29.0 microns), the bulk of the difference is still a global motion of the bench which includes a rotation. The relative motion of the Lyot plane to the detector on the optical bench is essentially the 0.6 microns of differential magnitude. This is about 0.03 pixels and is essentially undetectable.

5.3.5 Thermal Analysis

This instrument will be cooled by a single stage closed-cycle helium refrigeration system (CCR). Depending on the desired cooling time and power constraints, we plan to use either the Helix Cryodyne Model M-350 or M-1050 CCR. In this document we estimate the GPI IFS thermal flows for both of these CCRs, using the baseline performance estimates as provided by the vendor. The GPI IFS CCR cold head will be connected directly to the optical bench with high-conductivity copper straps. The cooling rate can be moderately adjusted by changing the A/L of the copper straps. In addition, the cooling rate of the detector can be set by heating resistors imbedded in the detector mounting block.

The GPI IFS instrument is intended to have an operating temperature slightly below liquid nitrogen (77K). In order to maintain the thermal separation from the outside world, the internal optics and the detector must have a thermal isolation from the outer vacuum walls of the instrument. We create a thermal separation by using low-conductivity G-10 A-frames to stand the optical bench off the dewar walls. The design also includes one highly reflective cold shield to reduce radiative heating from the dewar walls. We plan to wrap the cold shield with layers of gold kapton which will act as a multi-layer insulation (MLI).

For past instruments including OSIRIS, we've developed a thermal analysis program in the IDL language. We've used this program to estimate the cooling and warming of the cryostat and to estimate steady state loads and temperatures. Details of the modelling process are given in the IFS mechanical design note 03.00 (Appendix 5.10). It includes knowing the heat capacities and conductivities of all of the materials as a function of temperature and the variable heat conduction of air as a function of pressure.

The results from the thermal analysis model can be most easily viewed in Figures 5.22 and 5.23. The two figures can be used to compare the expected thermal course of the assembled IFS with the M-350 or the M-1050 CCRs. Although the mechanical design of the instrument will remain the same with either configuration, the GPI team will decide during the critical design phase which CCR will be included in the final instrument design.

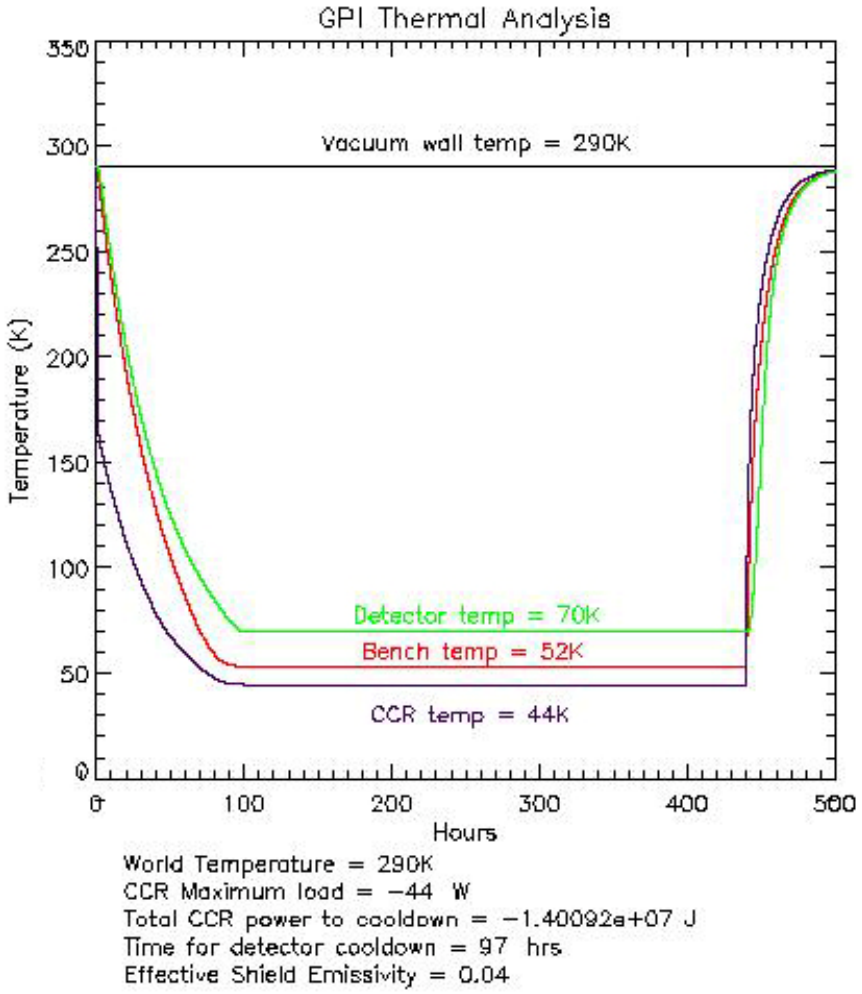

Figure 5.22 The GPI IFS thermal course as predicted by a thermal model written in IDL. This figure assumes the Helix Technology M-350 CCR cools the system by attaching directly to the optical bench. The estimated cooling time is 97 hours or approximately 4 days.

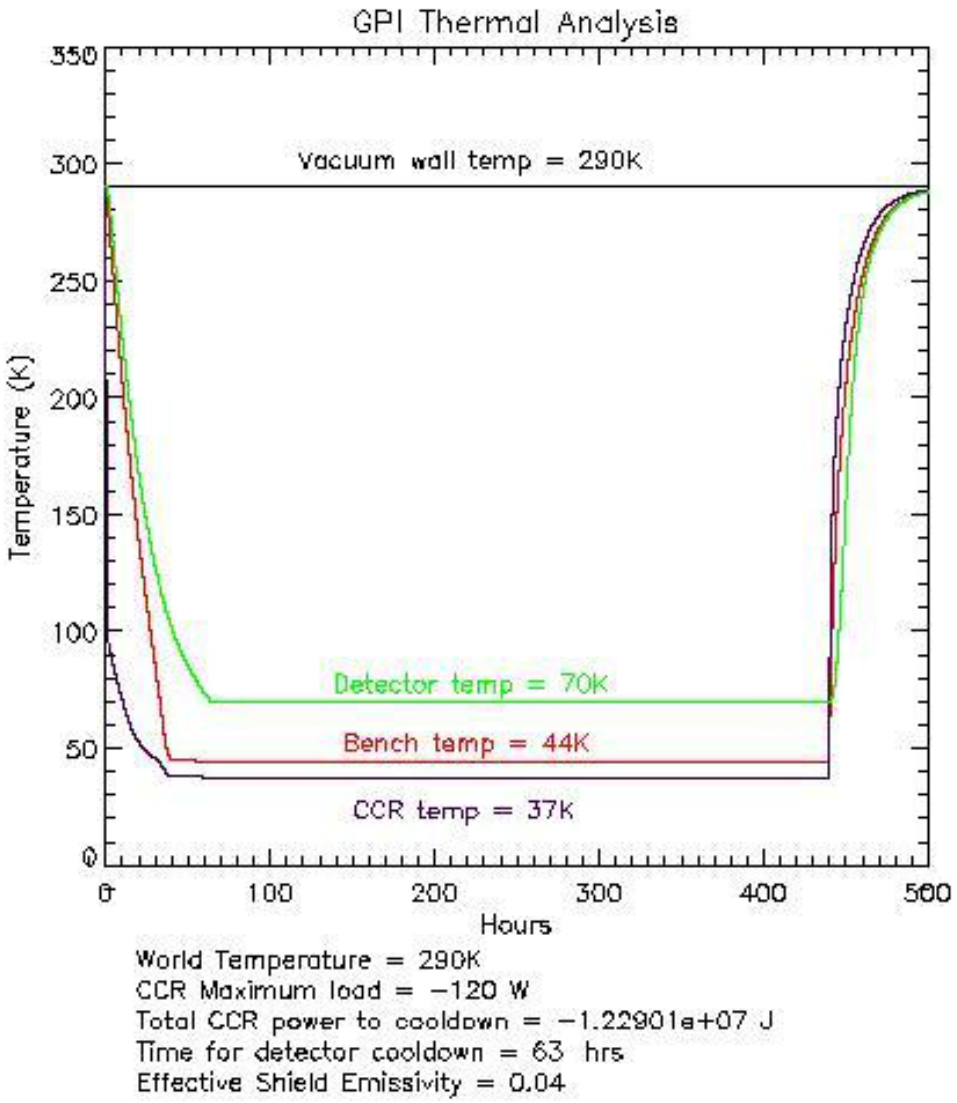

Figure 5.23. The GPI IFS thermal course as predicted by a thermal model. This figure assumes the same mechanical design as Figure 5.22, but these cooling curves assume the Helix Technology M-1050 CCR is attached to the optical bench. The estimated cooling time is 63 hours or approximately 2.6 days.

5.4 Electronics

All of the GPI electronics must be mounted within two 19 inch racks mounted at the sides of the instrument on the telescope. The IFS is allocated a total of 7U within one of the racks. The Dell 2950 will occupy 2U, leaving 5U for custom packaging the other components. Individual rack elements are limited to a depth of 500 mm. Racks must also be able to slide forward for servicing without disconnecting, so all internal cables require 400 mm of extra cable length.

5.4.1 Spectrograph Detector

We have selected the HAWAII-2 RG 2K x 2K HgCdTe array from Teledyne Imaging Sensors (formerly Rockwell Scientific) for the IFS. This detector, which has 18 μm pixels and a 2.5 μm cut-off wavelength, is the same device architecture selected for JWST and many ground-based instruments, including MOSFIRE, also a UCLA project. Consequently, we stand to benefit from the considerable development work undertaken to solve many difficult detector issues such as charge persistence, QE, noise, dark current and delamination. Recent proprietary data presented to us by Teledyne suggests that excellent progress has been made in all these factors and that our performance goals will be achieved. Dark currents of <0.005 e^-/s have been measured in devices operated at 35 K; our goal is < 0.01 e^-/s at 77 K. We will negotiate the contract with Teledyne to obtain H-2RG arrays with the lowest read noise possible. Currently, Teledyne is measuring between 17 and 22 e- CDS over the temperature range of 35 K to 80 K for SWIR arrays. R&D efforts are underway to improve read noise, and any improvements available to support the deliverable focal plane arrays will be incorporated in our devices. Multiple sampling (16 Fowler reads or Up-the-Ramp samples) can achieve ~5-6 electrons rms according to tests of devices for JWST and other groups. The IFS device will be substrate-removed and AR-coated to yield QE > 80% across our spectral range.

Teledyne is now offering H-2RG devices with an ASIC (Application Specific Integrated Circuit) that implements all of the detector readout functions. The ASIC, proprietary name "SIDECAR", provides clocks and bias voltages to the detector and digitizes the detector outputs. The SIDECAR ASIC is packaged separately on a small board that is located inside the dewar next to the detector head. Just outside the dewar wall is another board, the Jade2, which provides the interface between the ASIC and USB 2.0. The UCLA team on the MOSFIRE project, in order to become familiar with the operation of these devices, obtained a prototype ASIC mounted on a development (non-cryogenic) board, plus a Jade2 interface card and software (as shown on the left side of Figure 5.24). We have been operating this device since February 2006, and have been working closely with Teledyne staff to develop software to control the ASIC.

We are expecting to receive the cryogenic ASIC carrier board (shown in the center of Figure 5.24) and an engineering grade H2-RG detector very soon. A prototype of the MOSFIRE detector head has already been built and has been installed with the ASIC and carrier board in a LN_2 cooled dewar to gain experience using the ASIC to control and readout the detector array. The GPI IFS project will benefit from this experience with the detector system.

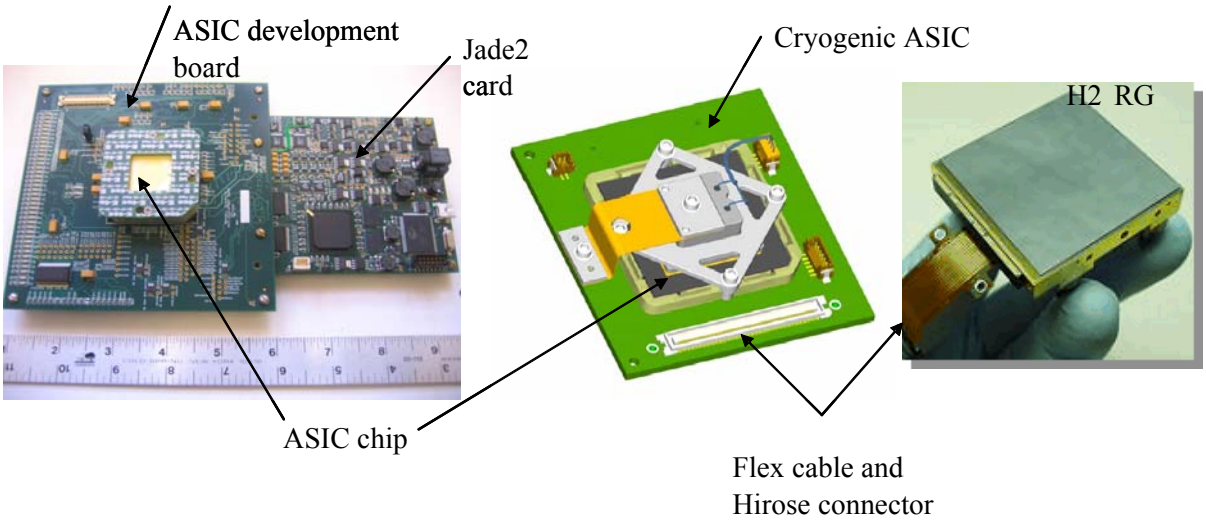

Figure 5.24 The ASIC Development Board and Cryogenic ASIC Carrier Board

Overall Architecture

Figure 5.25 is a block diagram of the hardware and software components of the IFS detector system. This system consists of the detector, SIDECAR ASIC, Jade2 card, two computer systems (the IFS host and the detector target) and the software modules required to control and read out the science detector.

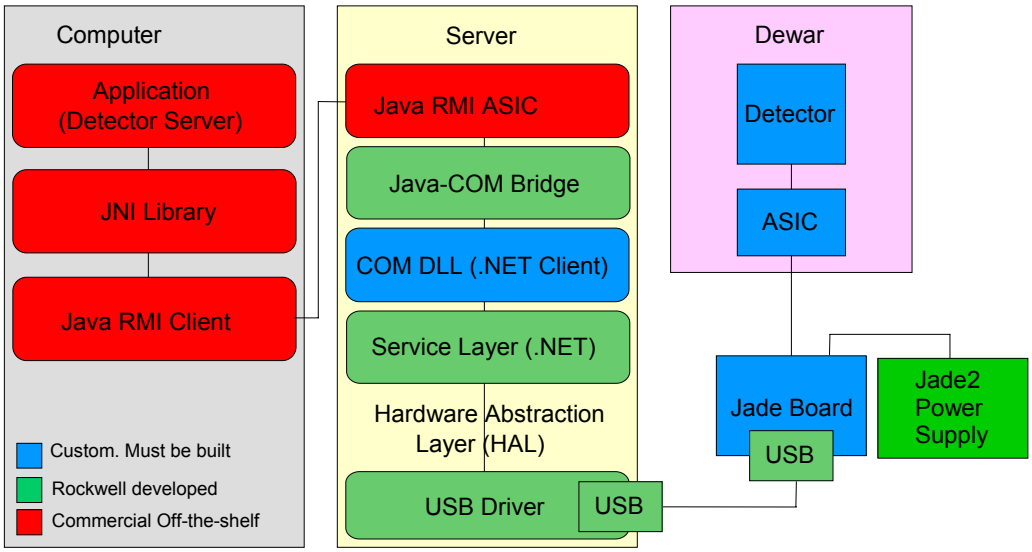

Figure 5.25: GPI Detector System Control Diagram

The Teledyne SIDECAR ASIC uses a proprietary interface to a module called the “Jade2”, also supplied by Teledyne. The Jade2 provides power conditioning for the H2-RG, the ASIC and a USB 2.0 compliant

interface to the detector target computer. All of the detector control communications and data are transferred over the USB 2.0 interface.

Teledyne uses a third party USB driver (Bitwise Systems QuickUSB) and their own hardware abstraction layer (HAL), which translates application commands into driver specific commands, hiding USB-specific driver detail from a higher-level application layer. The HAL in turn uses a second Teledyne-supplied software component called the "COM DLL" to communicate with the HAL using the Microsoft .NET web service. The COM DLL application allows third party software to interface to the HAL and in turn to the ASIC via USB and the Jade2.

A computer running Windows XP is required to run the USB driver, HAL software and COM DLL. This computer, which is equipped with a flash drive and rack-mounted in one of the IFS electronics cabinets, will function as the detector control computer. This computer will be located on a private network within the instrument and it will not be accessible via network communications except through the IFS host computer. The system will not require the use of less secure applications such as web browsers, reducing the need to implement frequent security updates.

5.4.2 Pupil Viewing Camera

The pupil viewing camera will be a commercial InGaAs camera identical to the one planned for use in the calibration unit. The model is SU320kTx-1.7RT from Goodrich Sensors Unlimited. The camera has 320x240 pixels with a 40 micron pitch. It is sensitive out to 1.7 microns, and we'll use it with an H-band filter to limit its bandpass to 1.5 to 1.7 microns. See Appendix 5.03 for its spec sheet.

Figure 5.25 The SU320kTx-1.7RT camera. It mounts to the dewar with a standard C-mount.

5.4.3 Motor Control

Motion control is provided by a Galil DMC-2183 controller and 2 Galil SDM-20242 which are 4-axis full/half-step driver cards that install directly to the DMC-2183. These are identical to the Galil controller cards used throughout GPI and used previously by HIA. See appendix 5.04 for details. This set of 3 boards can set fast and will occupy less than 2U of rack height, a minimal space in the rack.

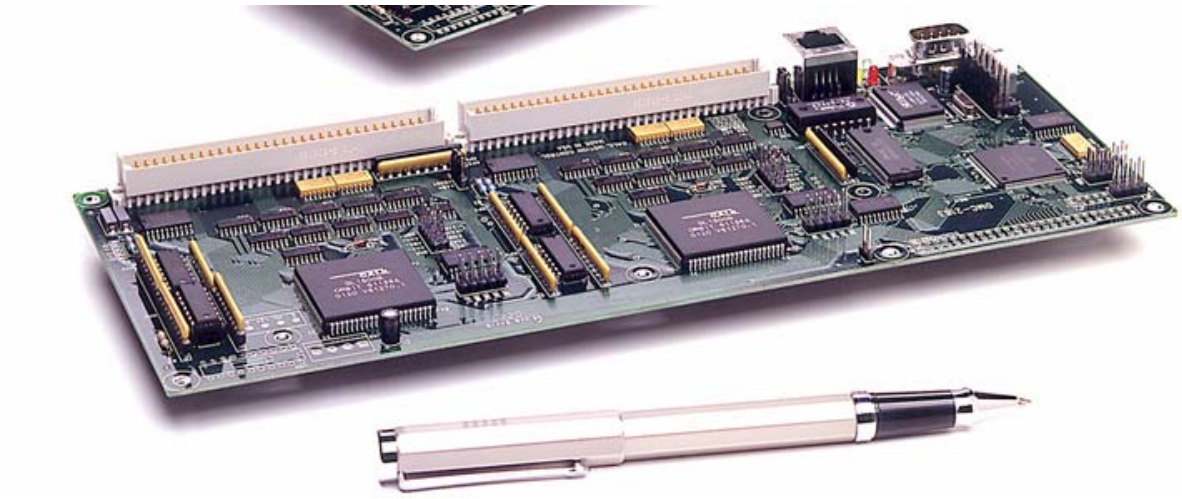

Figure 5.26 Galil DMV-2183 Controller.

5.4.4 Environmental Controls

5.4.4.1 Temperature Monitoring and Control

The IFS will use a Lake Shore model 340 temperature controller (Figure 5.27) to control detector head temperature and to provide monitoring of temperatures at various points inside the dewar. As well as providing two temperature control loops, the model 340 controller can house a plug-in card which allows it to monitor an additional 8 temperature sensors. Using this card in the 340 allows us to condense all the temperature monitoring and control functions into one unit, saving valuable rack space.

5.4.4.1.1 Detector Head Temperature Control

The detector head will incorporate two temperature sensors. Both will be cabled all the way to the 340 controller, with one acting as the primary sensor and the other serving as a backup. They will be connected to the A and B inputs on the back of the controller. If any problem arises with the internal detector wiring that puts the primary sensor out of action, the backup sensor can be brought into use by selecting it in software, avoiding the need to warm up the dewar immediately.

Figure 5.27 The Lakeshore 340 will be packaged in the electronics rack.

The Lake Shore 340 has two control loops. We will use the primary loop which has a heater drive capable of sourcing up to 100W into the heater on the controlled component (though our heater will draw only a few Watts). The controller can maintain the temperature of the load to typically 10mK. An additional feature of the 340 is a ramp rate setting, limiting the temperature slew when changing setpoints. This is useful for protecting delicate detector arrays from thermal shock when an instrument is cooling down.

5.4.4.1.2 Dewar Temperature Monitoring

The 340 with the addition of the model 3468 plug-in card can read an additional 8 temperature sensors. These sensors will be distributed throughout the dewar at appropriate points, such as the cold head finger, the main optical bench, and the cold shield. These can be read back via software as sensors C1-C4 and D1-D4.

5.4.4.1.3 Sensor Choice

The Lake Shore sensors we typically use are the DT-470-CU silicon diodes. The –CU designation refers to the physical packaging of the diodes. They are mounted on a small copper puck with a through hole for a mounting screw. Previous experience with other form factors has led us to standardizing on these sensors. The connecting wires are rather delicate, and this style of packaging lends itself to mounting the sensor with minimal risk of breaking them off.

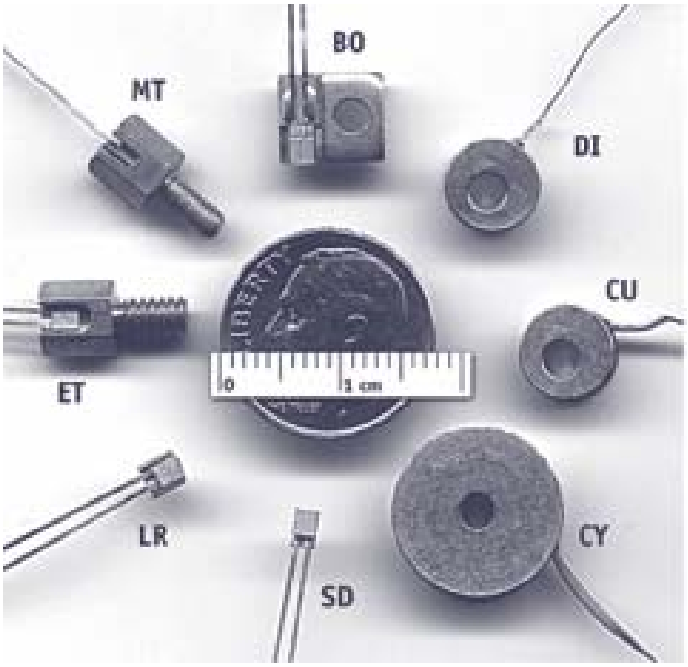

Figure 5.28 The various sensor packages available. The CU form we'll use is on the right.

5.4.4.2 Pressure Monitoring

The vacuum pressure in the IFS dewar will be monitored by a Varian Multi-gauge Controller. This controller is a modular system with plug-in cards for reading various types of vacuum gauge sensors, displaying the pressure, and interfacing to the computer. The system will have one low-vac gauge (Varian Convectorr) and two high-vac gauges (Varian IMG series). The Multi-gauge Controller has an RS232 interface, which will be connected to the terminal server in the electronics rack.

5.4.4.3 CCR Head Power

Gemini supplies compressed helium to instruments within the Cassegrain ports, but they do not provide electrical power for the head itself. Like previous cryogenic instruments, we will provide a power supply within the 19-inch rack for the head.

5.4.5 Cabling

Because the IFS is constructed in a cryostat, each cable consists of several sections often with bulkheads at each interface. The bulkhead connectors at the electronics rack and dewar vessel both must be hermetic, but with slightly easier requirements on the rack end. Internally, the connectors must withstand many thermal cycles and maintain excellent connections at temperatures below 77K. Internal cables must also have low thermal conduction while maintaining reasonable electrical conduction, and we will often use constantine wiring. A final consideration is outgassing from cable materials, solder and trapped volumes in connectors. We have assembled an extensive library of material properties and

will make final material selections during critical design with these constraints in mind. This section describes some of our choices for connectors.

5.4.5.1 Connector selections

All the connectors feeding through the dewar wall will be true hermetic MIL-C38999 series III circular connectors. Each connector is denoted by a number of the form nn-mm, where the first number denotes the shell size of the connector, and the second the feedthrough arrangement. This latter number is usually, *but not always*, the number of pins. For instance nn-5 connectors have 5 pins, but nn-35 connectors have 37 pins. The size (gauge) listed for the pins denotes the size range of the wire that can be soldered or crimped to them – a size 20 for instance can take no larger than a 20 gauge wire but as small as a 26 gauge.

The different style of connector is the one carrying the signals between the Jade2 board outside the dewar and the SIDECAR ASIC board inside, next to the Hawaii2-RG detector. This connector is a micro-D style. It is actually a feedthrough structure consisting of a male and a female connector mounted back to back in a hermetic sub-plate; ribbon cables mate to it from either side.

Connector	Description	Connector selection	Pin count & size (gauge)
0000-00	Motor drive to dewar internal mechanisms	19-32	32, 20
0000-00	Status switches from dewar internal mechanisms	15-35	37, 22D
0000-00	Dewar internal temperature sensors	15-18	18, 22D
0000-00	Detector head and dewar heater temperature sensors	11-5	5, 20
0000-00	Detector head heater and dewar heater power	15-5	5, 16
0000-00	Jade2 board to ASIC board	MDM-37	37

Table 5.9 Description of the 6 primary cables between the electronics rack and the IFS.

Choosing the connectors first by the minimum required pin count and wire gauge, we have arrived at a set where every one is unique. We have located a vendor (Alvatek Electronics) which has all of the designated Mil 38999 series III connectors and accessories available. Table 5.10 is the appropriate list of connectors and accessories.

Connector	Description	Price Ea USD	Lead Time
4154-39-21Y-19-32PN	Box Mount Receptacle (True) Hermetic	$647.65	8-10 Weeks
4154-39-20F-19-32PN	Panel Mount Receptacle Environmental	$116.42	1 Week
41-54-39-26F-19-32SN	Cable Plug	$139.03	1 Week
4154-85-38-19N	Cable Plug Backshell	$33.47	1 Week
4154-39-32W19N	Cable Plug Cover	$84.71	1 Week
4154-39-33W19R	Hermetic Receptacle Cover	$68.82	1 Week
4154-39-21Y-15-35PN	Box Mount Receptacle (True) Hermetic	$587.65	6-8 Weeks
4154-39-20F-15-35PN	Panel Mount Receptacle Environmental	$117.11	1 Week
4154-39-26F-15-35PN	Cable Plug	$130.98	1 Week
4154-85-38-15N	Cable Plug Backshell	$42.33	1 Week

4154-39-32W15N	Cable Plug Cover	$82.93	1 Week
4154-39-33W15R	Hermetic Receptacle Cover	$68.47	1 Week
4154-39-21Y-15-18PN	Box Mount Receptacle (True) Hermetic	$551.87	6-8 Weeks
4154-39-20F-15-18PN	Panel Mount Receptacle Environmental	$127.32	1 Week
4154-39-26F-15-18PN	Cable Plug	$124.29	1 Week
4154-85-38-18N	Cable Plug Backshell	$42.33	1 Week
4154-39-32W15N	Cable Plug Cover	$82.93	1 Week
4154-39-33W15R	Hermetic Receptacle Cover	$68.47	1 Week
4154-39-21Y-15-5PN	Box Mount Receptacle (True) Hermetic	$545.98	6-8 Weeks
4154-39-20F-15-5PN	Panel Mount Receptacle Environmental	$120.19	1 Week
4154-39-26F-15-5PN	Cable Plug	$122.47	1 Week
4154-85-38-15N	Cable Plug Backshell	$42.33	1 Week
4154-39-32W15N	Cable Plug Cover	$82.93	1 Week
4154-39-33W15R	Hermetic Receptacle Cover	$68.47	1 Week
4154-39-21Y-11-5PN	Box Mount Receptacle (True) Hermetic	$549.88	6-8 Weeks
4154-39-20F-11-5PN	Panel Mount Receptacle Environmental	$128.99	1 Week
4154-39-26F-11-5PN	Cable Plug	$123.98	1 Week
4154-85-38-11N	Cable Plug Backshell	$41.88	1 Week
4154-39-32W11N	Cable Plug Cover	$83.55	1 Week
4154-39-33W11R	Hermetic Receptacle Cover	$70.33	1 Week

Table 5.10 A complete list of connectors and components including costs and current availability for all of the mil cables between the electronics rack and the dewar.

Detector Cabling

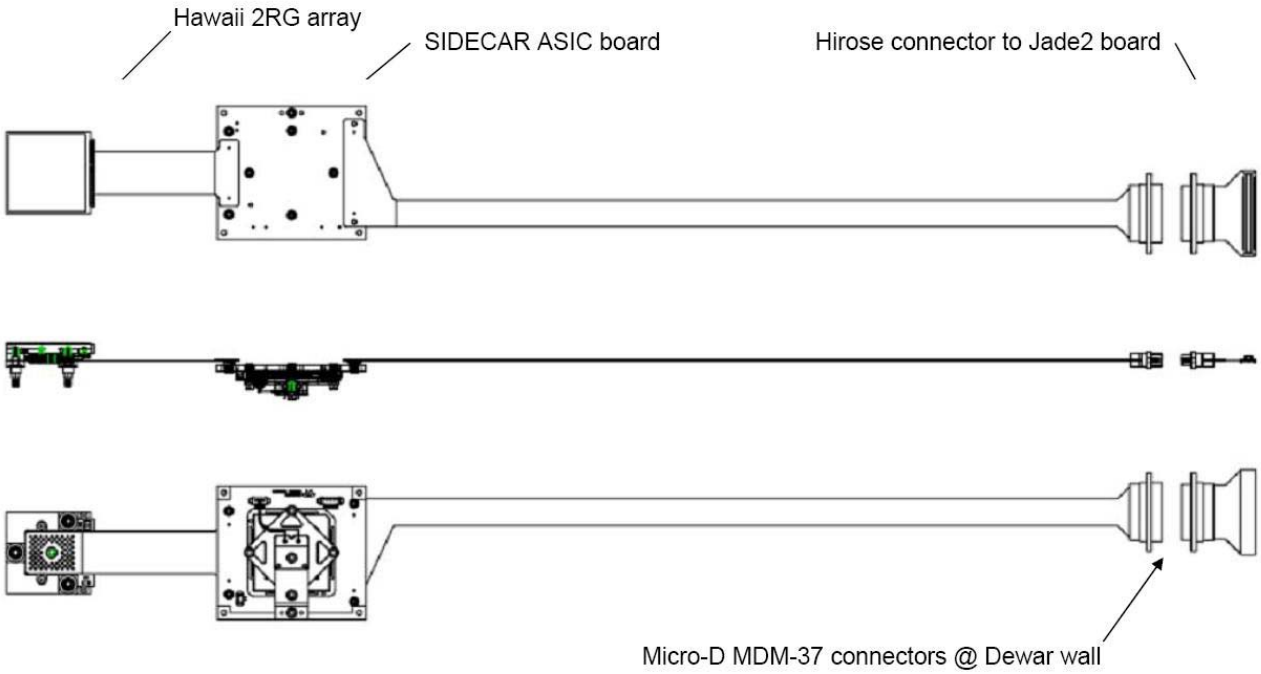

Figure 5.29 Three views of the cabling to the detector including the ribbon cables, ASIC board and bulkhead connectors. All are manufactured by Teledyne and will be procured as part of the detector contract.

5.5 IFS sensitivity and simulations

5.5.1 Throughputs

The lenses will be coated with standard A/R coatings, with less than 1.5% reflectivity for a waveband between 1.00 and 2.40μm. Figures 5.30 through 5.32 give example curves from existing instruments.

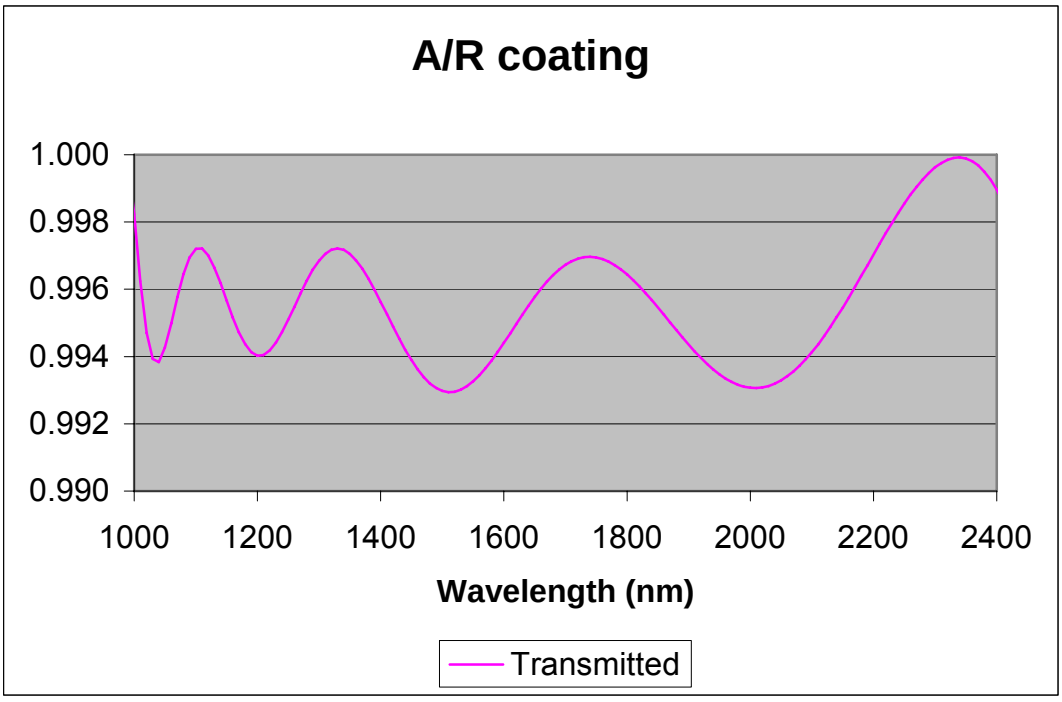

Figure 5.30 Coating best performances INO-3 (INO-Si/SiO2 coating – WIRCAM camera/CFHT).

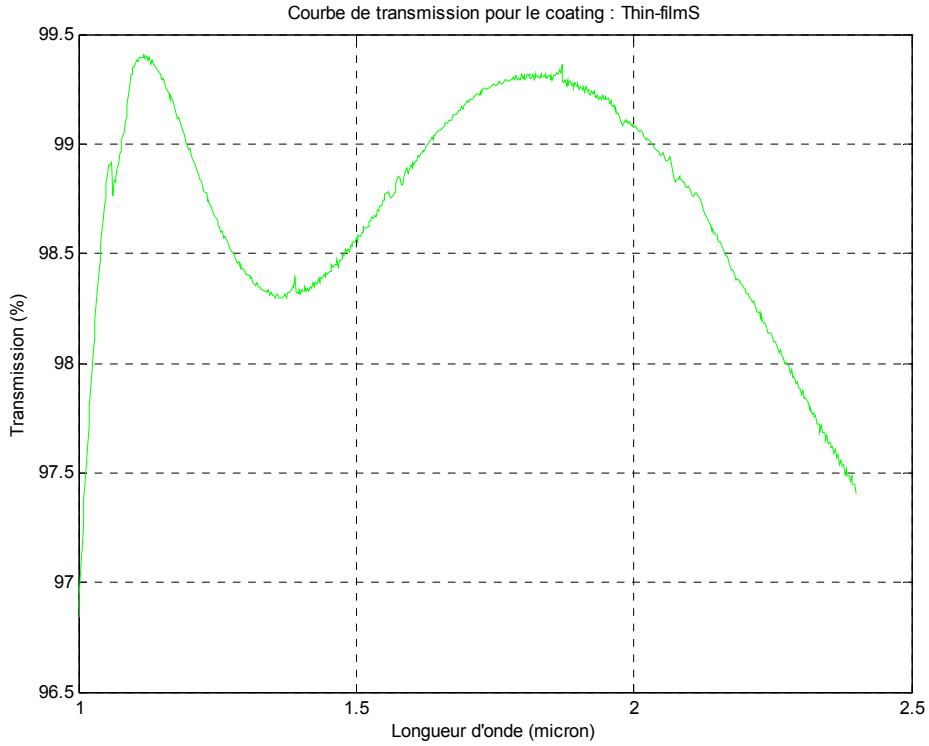

Figure 5.31 Coating transmission of TF1000 (Thim Film Lab coating).

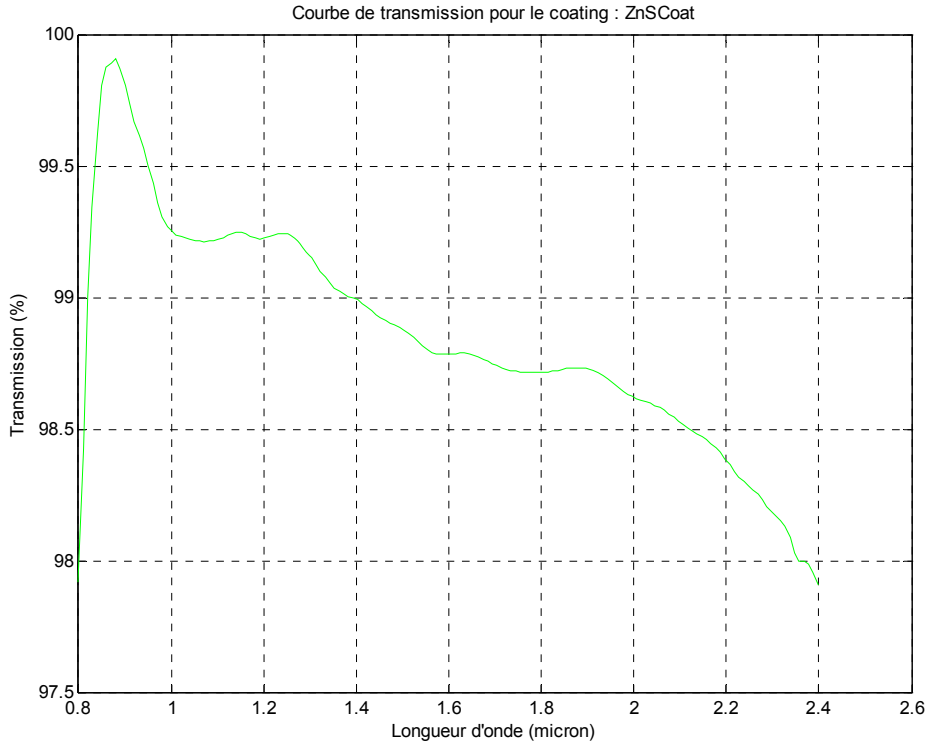

Figure 5.32 Coating transmission of Cleartran lenses.

Considering the coatings, the number of surfaces and the absorption of materials used, but not considering the filter, lenslet array and window we will have a mean transmission of 75% using the proposed coating choice. The transmission curve in Figure 5.33 shows reasonable estimates of transmission values based on past project experiences.

Table 5.11 gives the throughputs for the standard operating mode (dispersed, but no polarization). These throughputs do not include apodizing of the primary mirror with the apodizer (~63%) Lyot stops, calibration beamsplitter (80% science transmission) or the remainder of the GPI optical system. For reference, total throughput from the entrance of GPI to the IFS window is 37%. For the lenslet array it does include an estimate for the fill factor based on 2 micron gaps and a 110 micron pitch. Filter throughputs are based on the OSIRIS as-built curves.

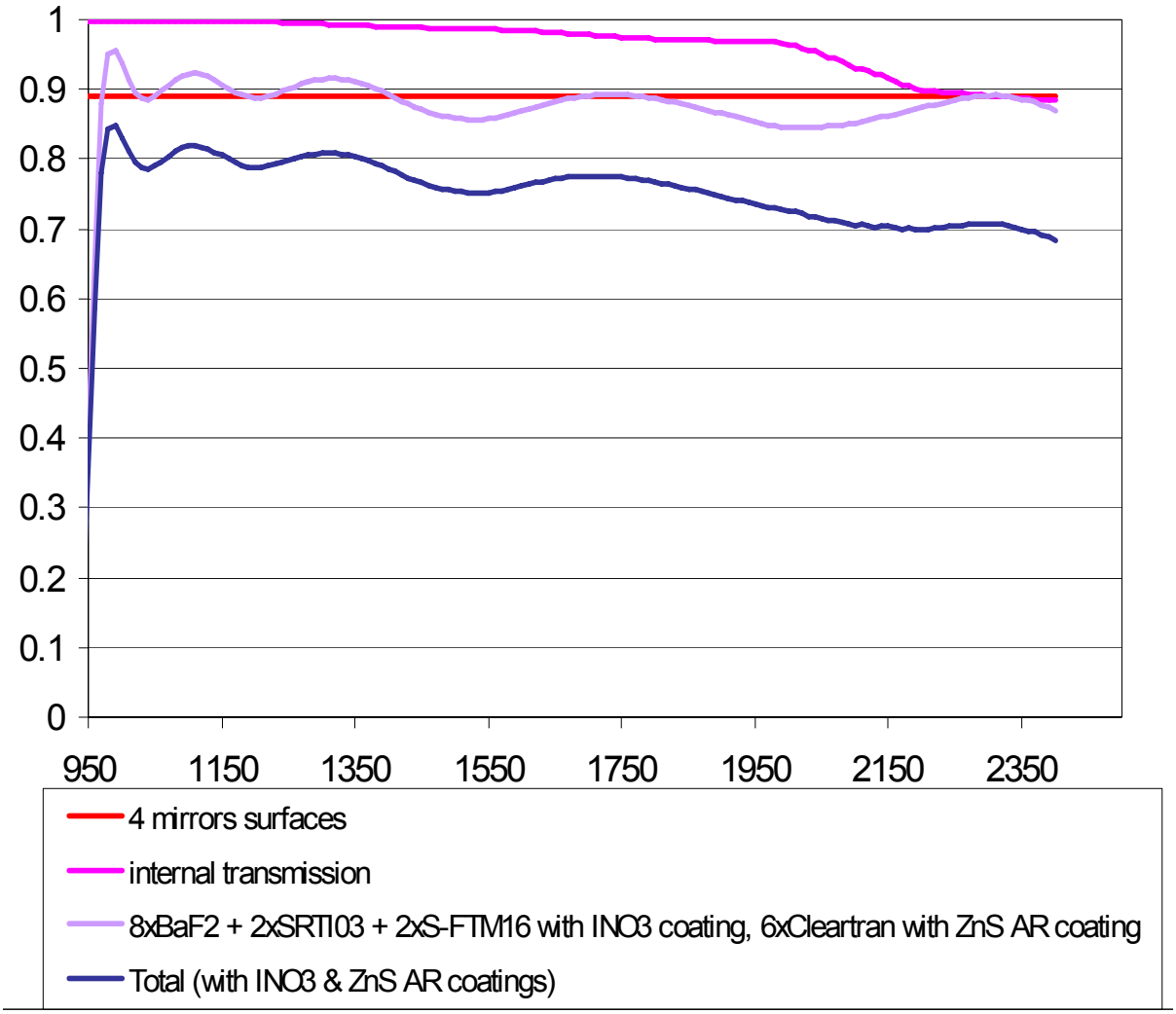

Figure 5.33 Transmission function for the baseline design with available AR coating (including re-imaging mirrors, excludes: lenslet array, filters, polarizer, cryostat window). INO3, TF1000 refer respectively to INO and Thim Film Labs AR coating available.

Element	Y-Band	J-Band	H-Band	K-Band
Window	0.98	0.98	0.98	0.98
Lenslet Array	0.94	0.94	0.94	0.94
Filter	0.85	0.80	0.9	0.85
Spectrograph	0.69	0.69	0.69	0.69
Detector	0.8	0.8	0.8	0.8
Total	**0.43**	**0.41**	**0.46**	**0.43**

Table 5.11 Total IFS throughputs combining figure 5.33 for the spectrograph with estimates for the window, lenslet array and detector. The filters assume the existing OSIRIS filter transmissions.

5.5.2 Sensitivities

The total estimated throughput for all of GPI in the H-band (primary discovery band) is 15% (section 2.6). For a zero magnitude star this implies $2.1x10^{10}$ photons per second at the science focal plane (assuming no coronagraphic masks are in place). With a plate scale of 0.014 arcsec per pixel which is roughly 3 times smaller than the diffraction limit at H, we estimate that the peak lenslet will receive about 10% of this flux or $2.1x10^{9}$ photons per second. With a spectral resolution element corresponding to 1.65μm divided by the resolution of 45, $2.4x10^{8}$ detected electrons per second per spectral resolution element in the brightest lenslet element.

The dominant background in the H-band is OH night sky lines. At R~45 these are completely blended together, so a rough noise level can be found from the average sky background. We assume a conservative sky brightness of 14.2 mag/sq arcsec in H (23.5 mag per 0.014 mas lenslet) which corresponds to 8 electrons per second per lenslet. In each spectral resolution element this results in When dispersed at R~45 this results in 1.0 electrons per second per spectral resolution element.

The detector read noise has been demonstrated with multiple reads at 5 electrons per exposure. Dark current even in the engineering-grade detector for the MOSFIRE instrument is only 0.001 electrons per second making dark noise essentially irrelevant. Since roughly three pixels are needed to enclose a single spectral channel and 2 channels to make a resolution element, we take 13 electrons as the detector noise per spectral resolution. So to be background limited (background noise ~ detector noise), individual exposure times must be approximately 160 seconds long. If we round to 180 second exposures, then the total noise per resolution element including sky and detector is 18 electrons. So in an hour, the noise per resolution element is 80 electrons in every lenslet spectrum. In order to produce a spectrum with 5 sigma significance in every spectral channel in the brightest lenslet, a source must then produce 400 electrons in the brightest lenslet for each resolution element or 0.11 electrons per second per lenslet per resolution element. Based on the first paragraph where a zero mag star produces $2.4x10^{8}$ electrons per second per lenslet per resolution element, this 5-sigma limit corresponds to a 23.3 mag star in the peak-flux spatial element. In a 7-lenslet photometric aperture the 5-sigma per resolution element limit in an hour is 24.1 mag. If all spectral resolution elements (~9) are further combined, then the resulting 5-sigma broad-band equivalent limit in one hour would correspond to approximately 25.6 mag. All of these calculations ignore noise from the halo of the central star. Final sensitivity will of course be much more strongly limited by scattered starlight, as discussed in Chapter 2, and more modeling using AO simulated PSFs will occur in the critical design phase.

5.5.3 Saturation Levels

Many users will be interested in looking at quite bright stars, potentially without the coronagraphic masks. Assuming a well depth of 100,000 electrons for the science detector, and that the central pixel at a given spectral slice has ½ of the light of that wavelength range, and that the shortest exposure is 1 second (conservative and assumes slower digitization channel of the ASIC), we find that saturation would occur for stars brighter than 200,000 electrons per second per spectral channel. From section 5.5.2 above, this would correspond to a star of magnitude 6.7 at H-band. All brighter stars will need either a fast readout mode (perhaps subarray), or neutral density filters in the beam.

5.6 IFS References

[1] Brown, Epps & Fabricant, 2004, PASP, 116:833-841

[2] Lord, S.D. 1992

6 Calibration Module

6.1 Overview

6.1.1 System Description

Non-common path wave front errors, it not sensed and corrected, will set the limit for achievable contrast for a ground based AO system. These errors are particularly vexing due to their temporal evolution. If they were perfectly static, they could be measured once and then subsequently removed in post processing. If they were perfectly random, they would average out to a smooth floor over long integrations. Non-common path errors that limit contrast tend to evolve over times scales of a few minutes to 10's of minutes and therefore must be sensed and corrected during a science observation. The main goal of the calibration system for GPI is to sense these wave front errors and provide a measurement to the AO system so that they may be corrected. The most crucial wave front errors are those at spatial frequencies corresponding to the "dark hole" region of the PSF and outside the coronagraph's inner working distance – 4-22 cycles per pupil. The calibration subsystem that will measure these mid-spatial frequency errors is called the high-order wave front sensor, HOWFS.

Many coronagraphs, including the apodized pupil Lyot coronagraph (APLC) employed by GPI, are very sensitive to the location of the star on the focal plane mask – mis-centrations of as much as 3 miliarcseconds can begin to degrade contrast. As a separate task the calibration system will employ a low-order wave front sensor to establish the boresite of the instrument and ensure the centering is sufficient for achieving and maintaining high-contrast. This boresite will also be sufficiently accurate and stable for precision astrometry. This calibration subsystem is known as the low-order wave front sensor, or LOWFS, and will also measure the low-spatial-frequency wave front errors (e.g. focus) that the HOWFS is blind to.

A sufficient walk through of the calibration subsystem is most easily accomplished by following the path of the starlight path followings when encountering it. The system level drawing (Figure 6-1) on the next page will aide in this discussion. The light after leaving the apodized pupil converges to the focal plane to form an image at the focal plane mask. The light falling within the hard-edged focal plane mask will compose the reference arm, the light reflected will form the science arm, and the light that goes down both arms will meet again at the re-combination beamsplitter and be sensed at the HOWFS. The discussion will then be in the same order: reference arm, science arm and HOWFS arm.

6.1.1.1 Reference arm:

The starting point for the reference arm is the focal plane mask, or more specifically, the hole in the center of the focal plane mask. Several different focal plane masks are available in the focal plane mask occultor mechanism. The masks will be provided by our collaborators at AMNH while the mechanism itself is the primary responsibility of HIA.

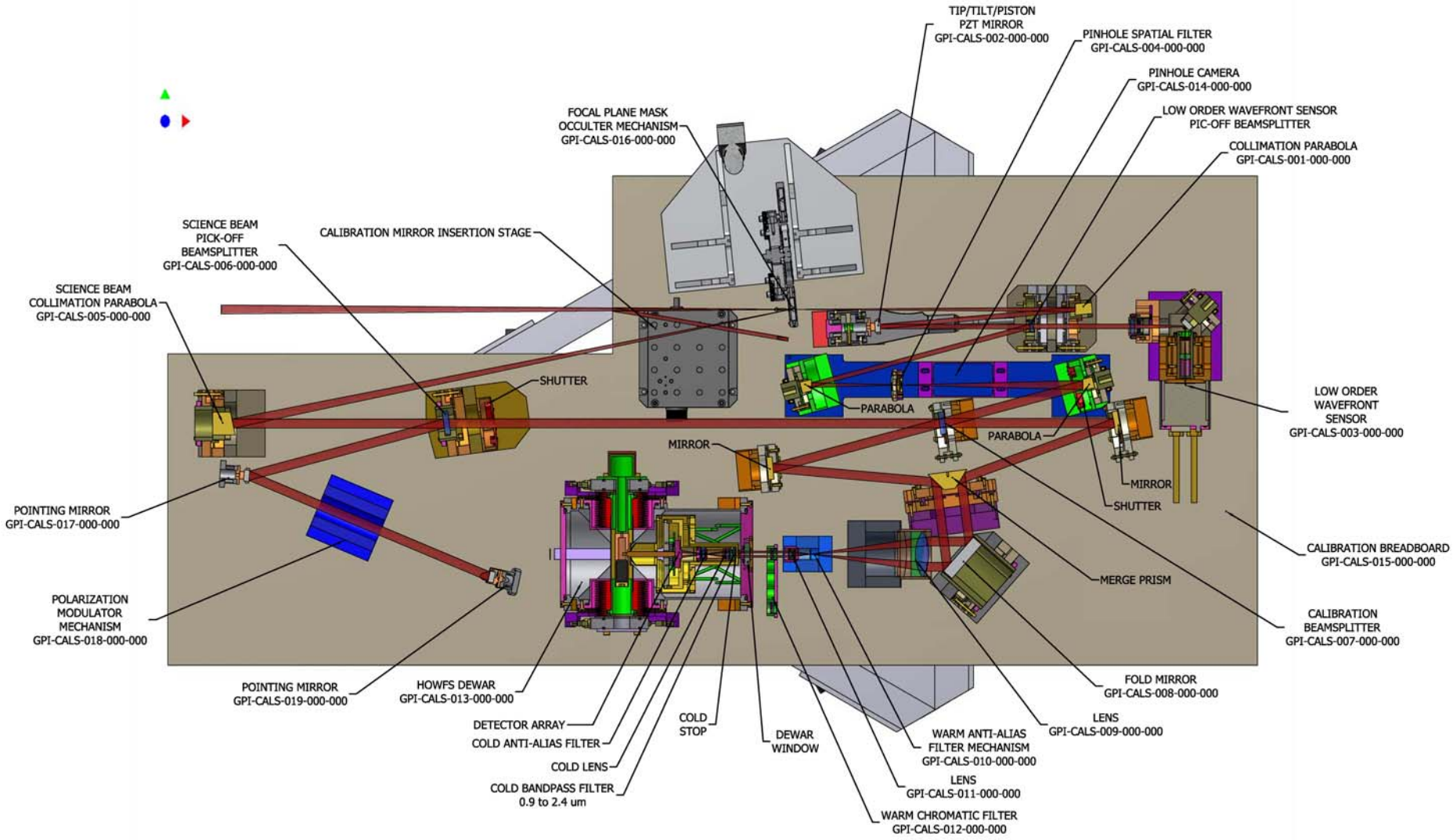

Figure 6-1 FOpto-mechanical layout of the GPI Calibration Wavefront Sensor.

The calibration system will host this mechanism and has accommodated the interface requirements. In one path, the on-axis starlight falls through the center of this mask and passes into the calibration system to serve as a reference wave front. The subsequent optic is the reference arm recollimation OAP. This will provide a five millimeter diameter beam such that the phase shifting is done in a collimated beam and all points in the pupil are shifted in phase equally. Upon reflection from this optic, the beam strikes the Tip/Tilt/Piston PZT mirror. This mirror plays several roles: 1) phase shifting for the high-order wave front sensor and 2) pointing correction for the pinhole spatial filter.

After the phase shifting mirror, the beam is divided between the LOWFS and the pinhole spatial filter. The light that passes through the LOWFS pick-off beamsplitter will form a pupil shortly afterwards. A real, compressed image of this pupil on the lenslet array is created by a pair of real lens and a fold mirror. The spots from these lenslets are then formed directly on the final detector image plane. A mechanical housing also allows rotation alignment of the lenslet to detector array. The LOWFS detector is sensitive out to 1.7 μm and therefore does not cover the full science band. For observing scenarios where the science band is not observable by the LOWFS camera (> 1.7 μm) we will have a combination of measurements and models to determine the optimum correction from the LOWFS to science band. When the Atmospheric Dispersion Corrector (ADC) of the GPI system (Appendix 2.7) is in use it collapses the wavelengths over the whole 1-2.5 μm range and the open-loop corrections should be small; even without the ADC, the correction between 1.7 μm and the primary science wavelength is straightforward to calculate and small enough that the LOWFS will continue to receive light . Subsequent to the LOWFS pick-off beamsplitter is the spatial filter assembly. This is the assembly that serves to remove residual wave front errors on the beam such that the phase and amplitude of the reference beam electric field at recombination is largely uniform. The first OAP of the assembly forms a focus at the pinhole (currently sized to 1.4 λ/D, diameter, at 1.635 μm). The spatially filtered light passing through this pinhole is re-collimated by the second OAP in the assembly to roughly ten millimeters in diameter. Centering of the light on the pinhole is crucial to consistent, repeatable performance for the HOWFS. However, sensing where this beam is when it is only slightly off-center on the pinhole is a challenge; when well-centered, almost all of the light disappears into the pinhole. (This sentiment is captured by the title of a classic country and western song: “When the phone don’t ring, I’ll know its not you”.) To expedite the acquisition we have implemented what we call the pinhole camera which allows us to directly measure the starlight relative to the pinhole and to expedite the co-alignment. In the baseline design, this will be used for initial alignment (perhaps on each target) and possibly for closed-loop tracking of the pinhole. Finally, we have a shutter in the reference arm that allows us to block the light. This option is necessary for allowing us to measure the transmission function of the input pupil apodizer and establishing detector darks without affecting the operation of the rest of the instrument. The beam is now ready to meet itself at the recombination beamsplitter, having passed through the science arm.

6.1.1.2 Science arm:

For the science beam, the starlight suppression has just occurred at the focal plane mask, and the science re-collimation OAP creates a beam that is ten millimeters in diameter and parallel to the beam incoming to the focal plane mask (offset by 128 millimeters). Most of the light continues to the science IFS, but a small portion of this light (currently 20%) will pass through a spectrally-neutral, broadband beam

splitter. This light will then pass through the science arm shutter (if it is open) and on to the recombination beamsplitter. The light that gets reflected from the science pick-off beam splitter heads to the pointing-and-centering mirror pair that feed the Integral Field Spectrograph (IFS). This mirror pair ensures proper image-plane and pupil-plane alignment between the calibration sub-system and the IFS. While not responsible for these optics and mechanics, we are hosting them on our breadboard. In a similar fashion, the calibration system is home to the polarization modulator optic and mechanism. We are in close contact with our colleagues at HIA to guarantee that we have provided enough room for these elements.

6.1.1.3 HOWFS Arm:

After recombination between the reference and science/measurement beams at the beamsplitter, 50% of the combined beams are reflected and 50% transmitted. Either way, the next element it strikes will be a fold mirror that will then redirect the beam to a merge prism. This merge prism assembly allows us to ultimately image the beams from both the front and back of the recombination beamsplitter side-by-side on the HOWFS detector. It happens that the pupil image is reformed at the face of the merge prism. After this merge prism, the beams are parallel to each other. The main function of the remaining optics in the beam train is to relay the pupil pair at the prism vertex to the HOWFS detector. These pupil relay optics occur in several stages: 1) The pupil is imaged to infinity with the first, large HOWFS lens 2) a de-magnified real image of the pupil is created by the first, small HOWFS lens and 3) a 1:1 relay lens puts the final pupil image on the detector array. At the focus of the first large HOWFS lens is an anti-aliasing filter that will remove scattered light from the HOWFS detector. In the collimated beam after the first small HOWFS lens are the warm chromatic filters, the window to the dewar and the cold short-wave-pass filter ($\lambda < 2.4$ μm). In the intermediate focus between the 1:1 relay lens and the final image, we place a slightly oversized cold field stop. The HOWFS dewar has been designed to have no internal moving mechanisms. The bandpass filters, focus and registration degrees-of-freedom are all warm. This greatly reduces the complexity, cost and maintenance of these devices. It also makes the dewar opto-mechanics very simple, minimizes the thermal load and cool down time of the camera. Since the primary filters are warm, there will be a thermal background signal onto the detector, but given its update rate and fine sampling (the light from the ~3x3 arcsecond cold field stop is spread over ~1800 HOWFS pixels) this background is negligible compared to the readout noise.

6.1.2 Calibration Modes and Algorithms

For the calibration system to operate successfully, it needs to have established a state where a series of conditions have already been met. Some of these states can be done infrequently, some nightly, and some at a rate that we can't yet determine (depending on system stability and flexure.). These modes can be divided into a few major groups: 1) alignment through the focal plane mask and pinhole 2) LOWFS operation 3) registration of the HOWFS 4) phasing of the HOWFS and 5) amplitude and phase calibration of the HOWFS. This order is generally the sequence in which these tasks will be run or established as being complete. They will be described is this order:

6.1.2.1 Calibration Alignment:

Centering of the star on the focal plane mask is a requisite first step. Once the AO system has established closed-loop, stable operation on either a star or internal source, the image will be near the center of the focal plane mask. If it is through the mask, it will light up both the LOWFS and the pinhole camera. In the intial alignment and operation of the calibration system with the AO system, it may be the case that the light doesn't make its way through the occultor. If this is the case, the IFS can be used as a wide-field(!) guider to bring it within the occultor, but on typical nights, open-loop flexure lookup tables will ensure that some starlight falls through the occultor hole. To center the light in the occultor, the easiest method is to use the pinhole camera. A tilt on PZT stage will remove the spatial filter pinhole from the field-of-view of the occulter. Centering the PSF within the boundary defined by the occultor is straightforward. After this is accomplished the PZT can be tilted to center the spatial filter pinhole on the already-centered occultor/PSF. The PSF is both centered on the focal plane mask and the spatial filter pinhole. If necessary, auxiliary centering can be done using the science camera or pupil-viewing images.

6.1.2.2 LOWFS operation:

At this point the LOWFS can be used in closed loop. It will provide part of the wave front error signal to the AO system. In particular, the tip/tilt portion of the error signal will be used to keep the light centered on the focal plane mask. At this point, both the science and reference beams should be interfering at the recombination beam splitter and interfering on the HOWFS array.

6.1.2.3 HOWFS Registration:

Mapping of the AO tweeter DM elements to the HOWFS pixels is one-to-one. This minimizes the noise penalty of reading out several pixels per DM element. The registration is done by shuttering the reference arm and poking up a fixed pattern on the tweeter DM. The phase perturbations will cause the corresponding elements post-coronagraph to brighten up on the HOWFS camera. By centroiding on these bright pixels, it will be possible to determine the misregistration (x and y offset) with the HOWFS array. These elements can be re-aligned using a combination of the HOWFS fold mirror and the large HOWFS lens. The sensitivities of these opto-mechanical alignments will be given in detail later in Section 6.4.4 .

6.1.2.4 HOWFS phasing:

With the same tweeter DM actuators poked up, they will provide a strong interferometer signal. The first step however is to phase the signal. Opening up the reference shutter will provide this interference. Using a broadband (or pseudo broadband) source, the white light fringe can be acquired by slowly scanning the coarse phasing stage and looking for the signal modulation in the bright pixels. After a long scan, the phasing stage is reset to the point where the modulation was greatest. Calibration of the PZT stroke is accomplished by a coordinated piston-only stroke of the three-axis PZT stage. At the inflection points of the interference pattern, a parabola is fit to precisely determine the correspondence between average wavelength and PZT voltage. After this PZT stroke calibration, the PZT can be left in dither mode for the next steps.

6.1.2.5 HOWFS amplitude and phase calibration (calibration of the calibrator):

Pupil dependent system transmission is necessary in order to correctly renormalize the HOWFS phase and amplitude estimate. The normalization is for the input flux, and the electric field transmissivity of both the reference and science arm. An estimate of the total flux is provided by part of the reference arm that doesn't interfere with the science arm because of the secondary obscuration. The normalized transmission of science and reference arms is determined by shuttering each arm separately, measuring the flux, normalizing and then square root. These pupil-dependent transmissivities along with the flux estimate are used to properly scale the HOWFS measurement. The pupil dependent transmissions can be measured (as a function of wavelength) and then stored as a reference for HOWFS measurements.

We also need to quantify the phase and amplitude errors internal to the calibration system that will systematically bias the estimate of the wave front if left un-calibrated. In order to do this calibration of the cal system, we present to the focal plane mask a known high quality wave front injected by a pair of carefully aligned spherical mirrors. This optical assembly will be fed with a single mode optical fiber that is a fundamentally perfect wave front. The configuration of the spherical mirrors will relay this wave front to the focal plane mask with extremely high quality (< λ/100 peak-to-valley wave front error). A measurement of the calibration system with this wave front will give the residual phase and amplitude errors internal to the cal system. These errors are taken into account in the processing of the calibration data.

6.1.2.6 Calibration Algorithms:

In this section we derive the algorithm that allows us to estimate the phase and amplitude errors pre-coronagraph. Figure 6-2 below will serve as a useful cartoon for describing the fundamentals of the system. Our approach is to describe the pupil dependent electric field in both the science arm and reference arm of the interferometer. We will then combine these beams and measure the resultant intensity with a detector located at the re-imaged pupil plane. Modulation of this signal will allow us to extract the amplitude and phase errors before the coronagraph. We start with a pupil that has been well corrected by the AO system. In this condition, we can take the small angle approximation to express this field in terms of the residual phase and amplitude errors.

$$E = Ae^{i\varphi} \approx A(1+\varepsilon)(1+i\varphi) \approx A + A(\varepsilon + i\varphi) \qquad \text{Equation 6.1.1}$$

After passing through the APLC, the electric field picks up a pupil-dependent transmission:

$$\left(A + A(\varepsilon + i\varphi)\right) t_{APLC}(x,y) \qquad \text{Equation 6.1.2}$$

The effect of the focal plane mask (coronagraph) is to send the DC component of this light to the reference arm and the higher-order terms are sent to the science arm. At the re-imaged pupils in the science and reference arms, the electric fields in the pupils are given by:

$$E_{ref} = A\, t_{APLC}(x,y)$$
$$E_{sci} = A\left(\varepsilon + i\varphi\right) t_{APLC}(x,y) \qquad \text{Equation 6.1.3}$$

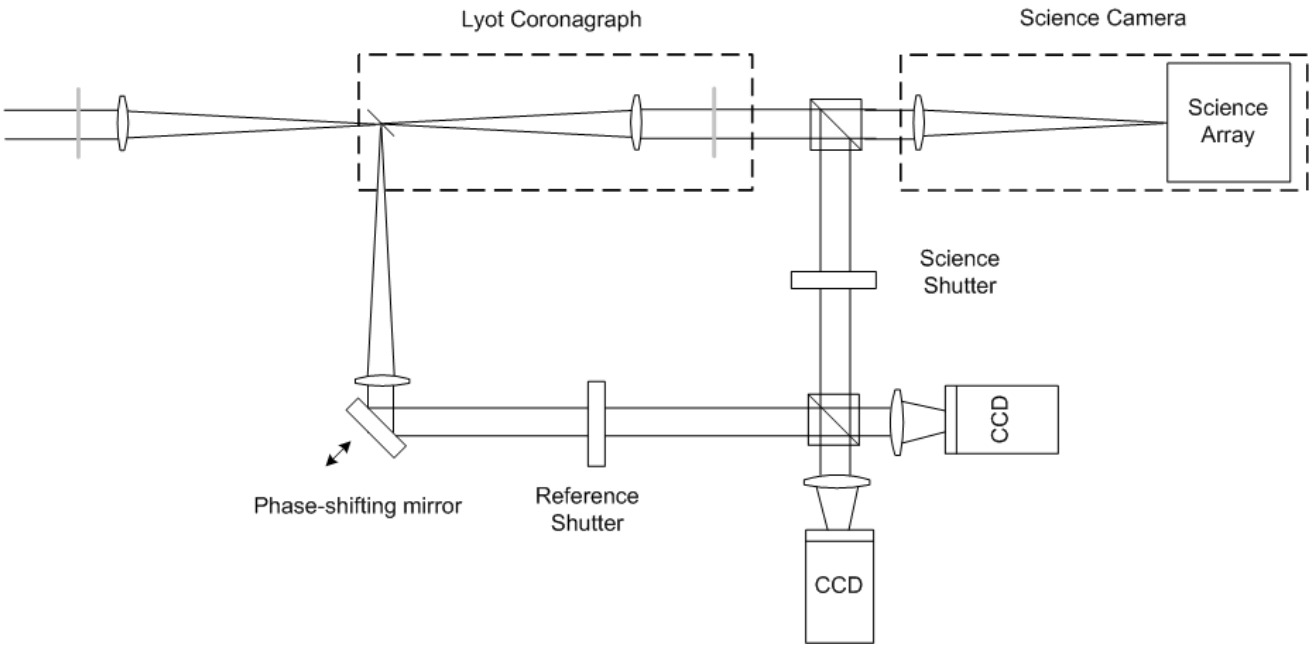

Figure 6-2 Conceptual calibration wave front sensor. Light enters the system on the left where it passes through an apodized pupil to the focal plane. The reference arm is in the bottom left of the diagram, and the science beam is picked off with the cube beamsplitter.

Before the beams are recombined, they are modified by a few other elements. The reference beam passes a phase-shifting mirror and then through a spatial filter. The spatial filter has the effect of passing the average amplitude of the phase-shifted beam and also producing a pupil-dependent amplitude transmission function of its own. The science beam is picked off by a spectrally neutral beamsplitter and then recombined at the calibration beamsplitter. Putting all of these terms together leads to the following expression for the electric fields:

$$E_{ref} = A \left\langle t_{APLC} \right\rangle e^{i\theta} t_{pinhole}(x,y) \frac{1}{\sqrt{2}}$$

$$E_{sci} = A(\varepsilon + i\varphi)\, t_{APLC}(x,y)\, r_{sciBS}(x,y) \frac{1}{\sqrt{2}}$$

Equation 6.1.4

We next make the simplifying assumption that the transmissions and reflections affect only the amplitude of the electric fields and not the phases (r and t are real numbers only) then we can represent them as the square-root of the intensity reflection/transmission (R and T).

$$E_{ref} = A \sqrt{\left\langle T_{APLC} \right\rangle} e^{i\theta} \sqrt{T_{pinhole}(x,y)} \frac{1}{\sqrt{2}}$$

$$E_{sci} = A(\varepsilon + i\varphi) \sqrt{T_{APLC}(x,y)}\, \sqrt{R_{sciBS}}\, \frac{1}{\sqrt{2}}$$

Equation 6.1.5

The intensity is then the absolute value of the sum of the electric fields.

$$E_{final} = E_{ref} + E_{sci}$$
$$I_{final} = E_{final} E^{*}_{final}$$

Equation 6.1.6

$$I_{final} = \frac{1}{2} A^2 \left(\begin{array}{l} \langle T_{APLC} \rangle T_{pinhole}(x,y) + T_{APLC}(x,y)\ R_{sciBS}\left(\varepsilon^2 + \varphi^2\right) + \\ 2\sqrt{\langle T_{APLC} \rangle}\sqrt{T_{pinhole}(x,y)}\sqrt{T_{APLC}(x,y)}\ \sqrt{R_{sciBS}}\ \varepsilon\ Cos(\theta) + \\ 2\sqrt{\langle T_{APLC} \rangle}\sqrt{T_{pinhole}(x,y)}\sqrt{T_{APLC}(x,y)}\ \sqrt{R_{sciBS}}\ \varphi\ Sin(\theta) \end{array} \right)$$

We now take four different phase-shifted images with phase values of θ = 0, π/2, π, 3π/2. If we call the corresponding pupil images I_1, I_2, I_3 and I_4, then it is possible to determine the pupil-dependent residual phase and amplitude errors.

$$\varepsilon(x,y) = \frac{I_1 - I_3}{2I_0\sqrt{\langle T_{APLC} \rangle}\sqrt{T_{pinhole}(x,y)}\sqrt{T_{APLC}(x,y)}\ \sqrt{R_{sciBS}}}$$
$$\varphi(x,y) = \frac{I_2 - I_4}{2I_0\sqrt{\langle T_{APLC} \rangle}\sqrt{T_{pinhole}(x,y)}\sqrt{T_{APLC}(x,y)}\ \sqrt{R_{sciBS}}}$$

Equation 6.1.7

6.1.3 Operating Modes

6.1.3.1 Daytime Calibrations:

In order for the calibration system to work properly, a set of pre-determined instrumental parameters must be measured. These are: the normalized transmission functions for the calibration and reference arms, the PZT displacement calibration, registration of the HOWFS to the tweeter DM, and the measurement of the internal amplitude and phase offsets (calibration of the calibrator). These calibrations have been described previously in section 6.1.2. The daytime calibration operation provides an opportunity to measure and store these values so that they may be used immediately during the nighttime operation.

6.1.3.2 Nightime operation:

When on target, the calibration system will quickly run through a sequence of operations in its process of determining the low- and mid-spatial frequency errors. The centering of the starlight on the focal plane mask and the spatial filter pinhole will use the pinhole camera. At this point, there will be light on the LOWFS and HOWFS. Once the LOWFS has closed its loop and stabilized its feedback, the HOWFS will begin operation. The parameters determined during daytime calibration (reference and science arm transmission, PZT stroke, HOWFS registration and calibration offsets) will be used to provide correct feedback to the AO system.

6.2 Modelling, Simulation, and Performance

The performance of the GPI calibrator is quantified via our simulation. This section provides an overview of the simulator and representative results from the software. A comparison of the simulation results with analytic expressions for tip/tilt performance provides a sanity check.

6.2.1 Simulation Overview

Figure 6-3 shows the APLC and Calibrator from the simulator's point of view. The calibrator has two wave front sensors. The Low-Order Wavefront Sensor (LOWFS) sees the light from low spatial frequency errors (<3 cycles/pupil) that go through the focal-plane mask (FPM), and the High-Order Wavefront Sensor (HOWFS) measures the mid-spatial frequency wave front errors (4-22 cycles/pupil) from light reflected by the FPM. The quantity of interest is the electric field at the apodizer (element 5 in Figure 6-3), which is at a pupil. Since this field is imaged at the focal plane and separated cleanly by the FPM, it is advantageous to estimate the field at the focal plane by each sensor, and in that plane "stitch together" the low spatial frequency aberrations estimated by the LOWFS with the mid-spatial frequency errors estimated by the HOWFS.

The simulator, which is written in MATLAB, evaluates the field at phase screens corresponding to each numbered element in Figure 6-3 . The model is an integrated wave-optics simulation, utilizing Fast Fourier Transforms (FFT's) to provide Fraunhofer propagation. No near-field (Fresnel) propagation is performed in the current version of the simulation. This section focuses on the simulation of the two primary sensors in the integrated model: the LOWFS and the HOWFS. After a brief description of each of these, the performance results obtained so far are presented.

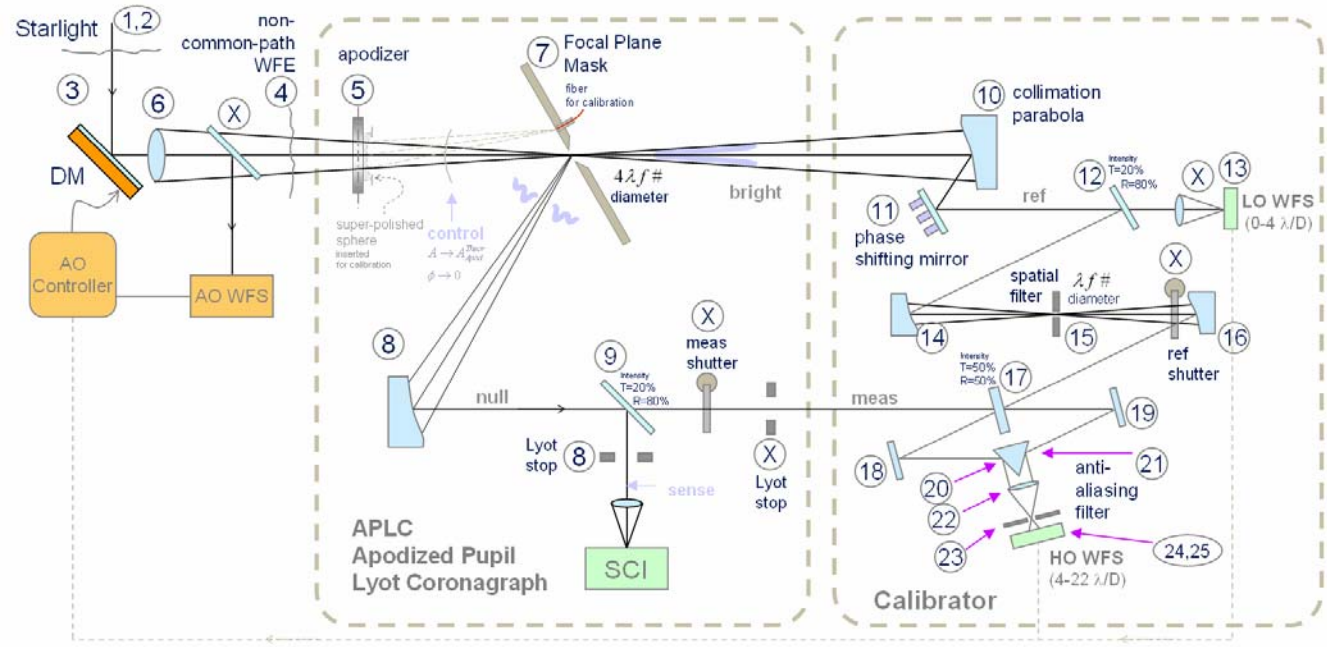

Figure 6-3 The elements included in the GPI Calibration simulator. The numbered elements are described in the text. These elements correspond one-to-one with the elements in the optical layout of the calibration system.

6.2.2 LOWFS Simulation Description

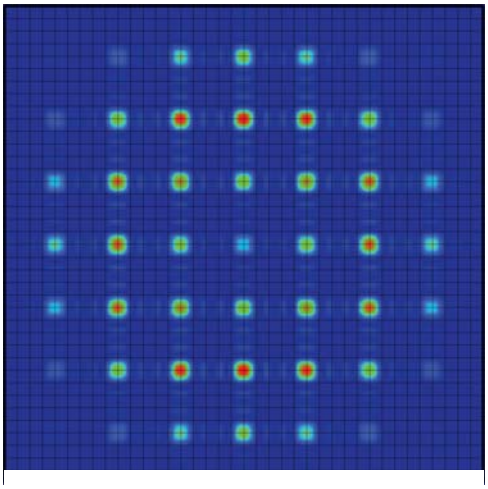

Figure 6-4 The Shack Hartmann spot pattern in the LOWFS.

The LOWFS is a Shack-Hartmann sensor with a 7x7 array of square lenslets; its spot pattern is shown in Figure 6-4. The model of LOWFS used in the simulation uses individual FFT's to produce the image spots. The focal plane is modeled as an array of quad cells, each centered on a lenslet, with 50e- of read noise per pixel. In each read cycle the signals (in electrons) from each quadrant (labeled A though D) from each spot are measured. These signals are converted into X and Y differences and an intensity measurement Q from each subaperture.

Note that we do not compute the x centroid (X/Q) or y centroid (Y/Q). Using differences rather than the centroid has a S/N advantage, as will be seen in 6.2.4.2.

$$X = (B+D) - (A+C)$$
$$Y = (A+B) - (C+D)$$
$$Q = A+B+C+D$$

Equation 6.2.1

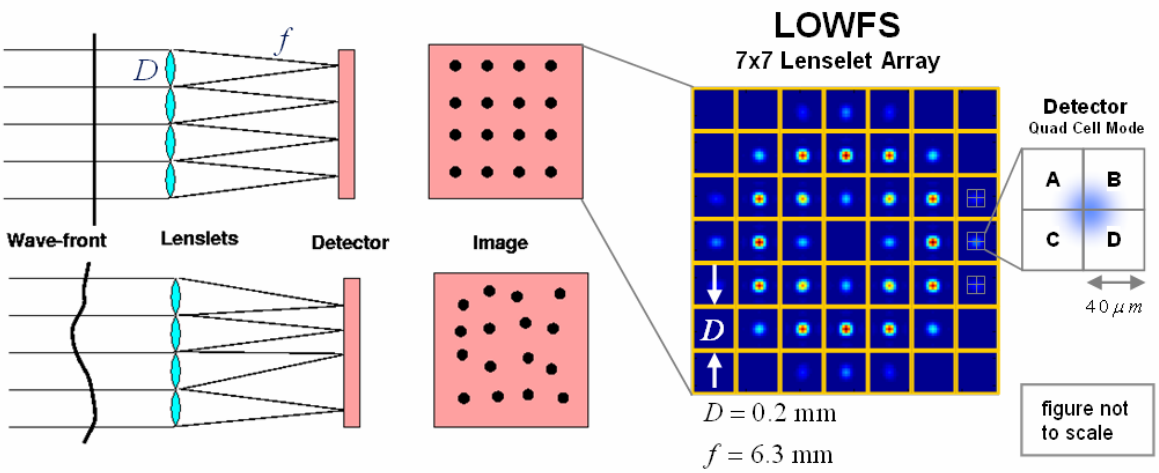

Figure 6-5: A 7x7 Shack-Hartmann lenslet array, the LOWFS, measures the average tip and tilt and the total intensity over each subaperture. The detector plane is designed to provide a quad cell for each lenslet. The apodization profile is clearly visible in the spot pattern.

The LOWFS is also used to estimate the electric field at the FPM hole for the purpose of reconstructing the full electric field at the apodizer. The LOWFS estimate of the field is obtained via a pseudo inverse solution which provides the real and imaginary deviations from the nominal field expected at the hole. The nominal field is assumed to have zero phase and have amplitude that is the product of the apodizer and pupil transmission functions. Because of the pupil geometry and the apodization, the amount of light received by the lenslets varies greatly. Of the 49 lenslets, 36 receive greater than 10% of the maximum light level (see Figure 6-4). The LOWFS data is used to estimate the complex field in the image plane at 37 points in FPM plane within a 7x7 grid which envelops the FPM hole (see Figure 6-6). The number of measurements is given by the number of useful lenslets (36) times 3 (corresponding to the measurements X, Y, Q). The number of unknowns is the number of field points (37) times 2 (for real and imaginary parts) minus 1 (a Shack-Hartmann is not sensitive to overall piston).

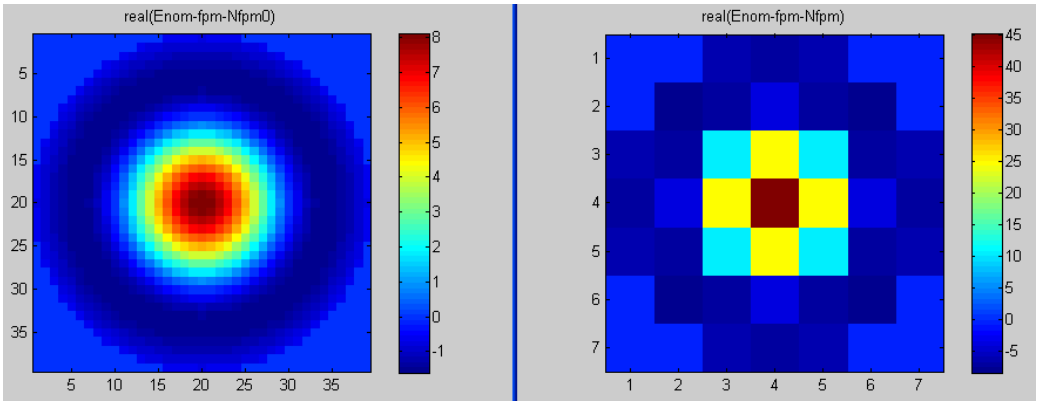

Figure 6-6: The real part of the nominal electric field at the FPM hole, with fine (left) and coarse (right) sampling. In the coarse-sampled case, 37 pixels are within the hole.

6.2.3 HOWFS Simulation Description

The Calibration System High Order Wavefront Sensor (HOWFS) is a spatially filtered interferometric pupil-plane wave front sensor. Its main responsibility is to detect and correct for slowly time-varying non-common path errors. Phase and amplitude offsets are measured and (after combination with the complementary LOWFS measurements) the total phase offset is then applied to the GPI deformable mirror (DM); each HOWFS subaperture corresponds directly to a single element of the DM.

The HOWFS is tightly integrated into the wave-optics simulation of the Cal system. After the complex wave fronts are split by the Focal Plane Mask and recombined at the final Cal beamsplitter, the HOWFS spatial filter is simulated using a hard-edged stop in Fourier space. The filtered images are then brought back into pupil space and imaged on the HOWFS detector. The simulated detector includes the effects of photon noise, read noise (20 e- per read), and detector losses. Intensity is "lost" at the detector both from (1) a detector quantum efficiency (assumed at 0.75) and (2) the finite time required to reset and read the focal plane array array – approximately 5-10 msec per read/reset and 10 msec per reset, but quantified below. An example of a set of HOWFS ABCD measurements is shown in Figure 6-7 .

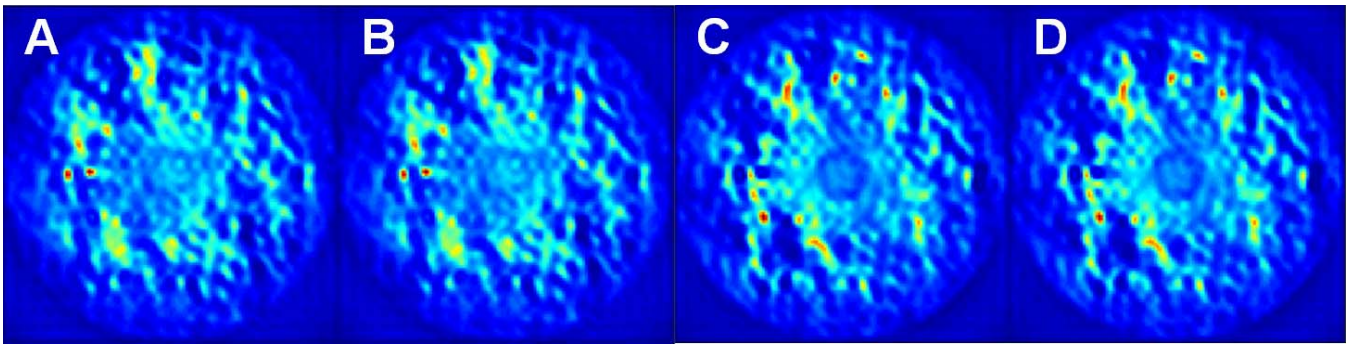

Figure 6-7 Sample HOWFS ABCD measurements for a typical AO-corrected atmospheric phase screen.

6.2.4 Performance of Cal sensor

The performance of the Cal system's two primary sensors are evaluated separately here. In the future, the combined performance resulting from the stitching of the electric field at the focal plane will be investigated. This section first covers the LOWFS and then the HOWFS performance.

6.2.4.1 LOWFS Performance, by Simulation

The response of the LOWFS to a pure tilt applied at the apodizer is shown in Figure 6-8. A pure tilt is applied in the x direction and the X signal, defined in Equation 6.2.1, is plotted for both the ideal, noise-free case and the case with noise. The units of the signals are electrons.

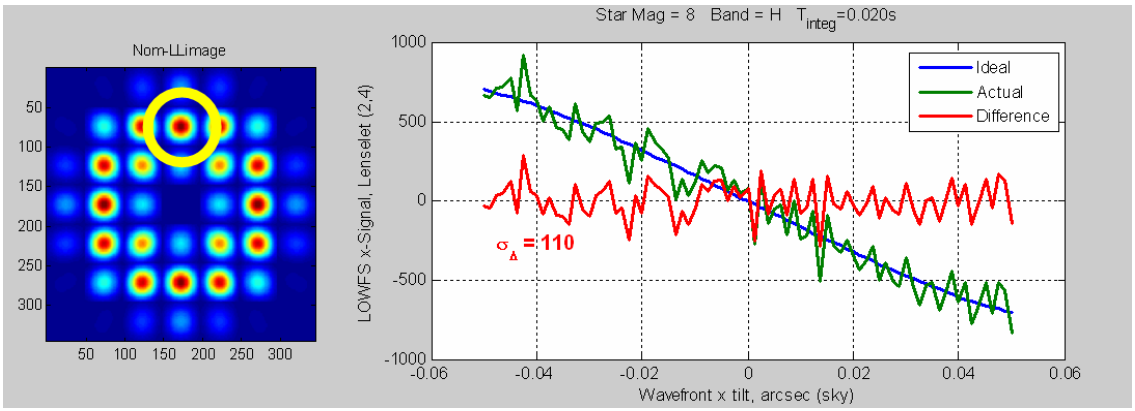

Figure 6-8 LOWFS lenslet at location (2,4) is highlighted on the left. The X signal (electrons) is plotted on the right against tilt applied at the apodizer. Ideal means no noise, and Actual assumes an 8th magnitude star and H-band filter.

A basic performance metric is the tip/tilt estimation noise from the LOWFS when the tilt at the apodizer pupil is constant and zero. Figure 6-9 shows a histogram of a simple Monte Carlo run to estimate the noise in the estimated tilt for an 8th magnitude star in H band with an integration time corresponding to the LOWFS readout rate of 1/60 seconds. The single-frame noise is estimated to be 2.4 mas, in good agreement with an analytical calculation.

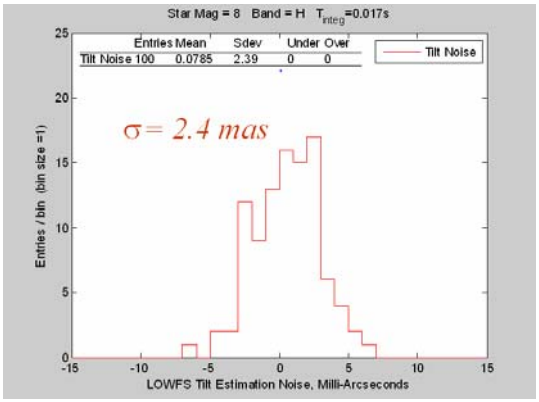

Figure 6-9: LOWFS Tilt estimation noise, in milli-arcseonds on the sky, for an 8th magnitude star in H band with 1/60 second of integration.

The performance of the LOWFS for higher spatial frequencies (up to the maximum frequency passed by the FPM hole) is evaluated by applying a phase error corresponding to non-common path errors, propagating it through the system, and using the LOWFS to measure the portion that goes through the FPM hole. For evaluation purposes the LOWFS-estimated electric field at the FPM hole is propagated to the pupil just before the LOWFS to compare with the actual field at the same location. Since the apodizer makes the pupil amplitude profile very non-uniform, the usual metric of rms residual wave front error is not optimal in this case. Instead, the metric chosen is the rms phasor error over the illuminated portion of the pupil. This error is given by

$$\varepsilon_{LOWFS} = rms\left\{\left(\frac{\left|\vec{E}_{Est} - \vec{E}_{True}\right|}{\max\left(\left|\vec{E}_{True}\right|\right)}\right)_{\text{pixel } i}\right\}_{\text{entire pupil}} \qquad \text{Equation 6.2.2}$$

The results from a random initial phase error are shown in Figure 6-10. The typical phasor estimation error (rms phasor error), computed per above equation, is less than 2%.

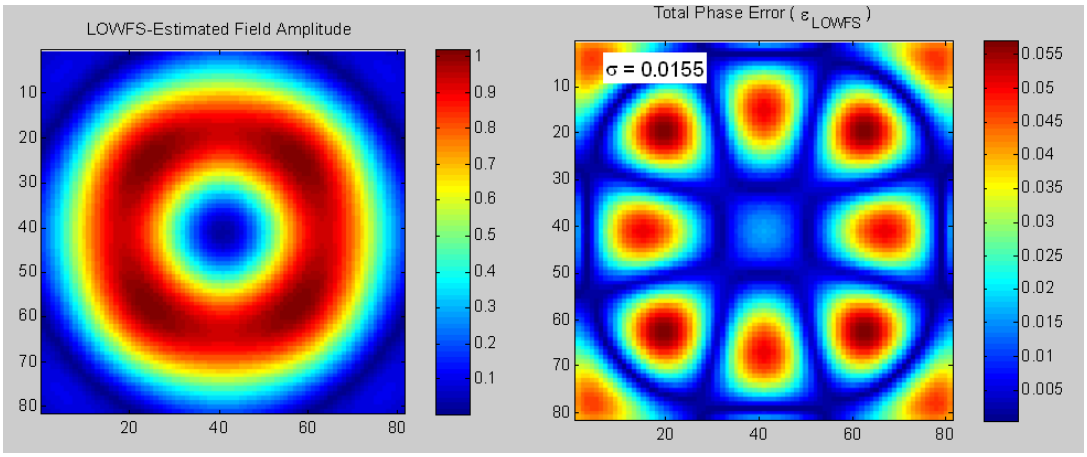

Figure 6-10: The magnitude of the electric field at the pupil in front of the LOWFS (left) and the rms phasor error metric (right), which is 1.6% in this case (note the scale difference).

The purely-phase part of the estimated field can also be compared, though the large variation of the field amplitude due to the apodization makes this a less indicative metric than the phasor error. This comparison is shown in Figure 6-11, which indicates that the standard deviation of the phase estimation error is 6% of the standard deviation of the actual error.

It should be emphasized that these results are for one particular method of inverting the Shack-Hartmann data to estimate complex electric field. It may be that some of the estimation errors are artifacts of the coarse gridding shown in Figure 6-6, as suggested by the symmetry of residuals seen in Figure 6-10. The best way to invert the LOWFS data to estimate a complex field is still the subject of discussion.

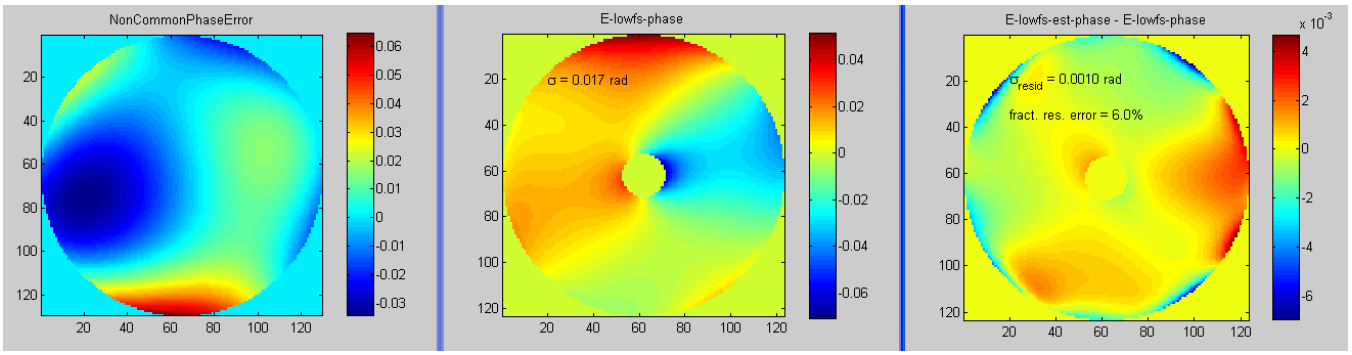

Figure 6-11: A random low-order phase error (left) applied at the apodizer is propagated to the pupil in front of the LOWFS (middle). The rms estimated residual LOWFS phase error is 6% (right) relative to the original error (note the scale difference).

6.2.4.2 Analytical LOWFS Performance

We can also derive analytic expressions for the LOWFS performance. This is particularly easy to do for tip or tilt, where neither the apodizer nor the occulter invalidate simple geometric considerations. For

this case only, the Shack-Hartmann spots all move together. Considering x-tilt only, the relation between normalized x centroid value and angle on the sky in radians, for every subaperature, is given by:

$$c = \frac{2d}{\lambda}\theta$$ Equation 6.2-3

Here d is the edge size of the square subapertures on the primary, 8000/7 mm in our case. This relation is easily derived from standard expressions for the far-field diffraction pattern of a square aperture.

Let us call the x moments each subaperture x_i and the intensity sums s_i, with the units of electrons per subaperture per frame. These correspond to X and Q in Equation 6.1-1.

Let us add together the tilts measured by each subaperture with weight w_i to get a composite measure of angle on the sky. The sum of the weights is kept equal to 1. Let us also write down an expression for the variance in this angle, calling the read noise per quadrant n. In our case n is 50 electrons rms, per frame, at the fixed frame rate of 60 Hz.

$$\theta = \frac{\lambda}{2d}\sum \frac{x_i}{s_i} w_i$$
$$\sigma_\theta^2 = \left(\frac{\lambda}{2d}\right)^2 4n^2 \sum \frac{w_i^2}{s_i^2}$$ Equation 6.2-4

A couple of further definitions and some simple relations fall out. Call S the total signal in electrons per frame in the whole pupil (the sum of all the s_i) and call the normalized spot intensities f_i. These f_i can be measured, as the long-term average of s_i / S, or can be calculated. Normalized spot intensities were calculated for the LOWFS using Zemax diffraction propagation, and entered into the CAL photometry spreadsheet "GPI Photon Flux", in Appendix 6.2.

$$\theta = \frac{\lambda}{2dS}\sum \frac{x_i w_i}{f_i}$$
$$\sigma_\theta^2 = \left(\frac{\lambda n}{dS}\right)^2 \sum \frac{w_i^2}{f_i^2}$$ Equation 6.2-5

Two kinds of weighting will be considered here. The first is equal weighting of the brightest M spots, the second is a noise-optimal weighting. The first weighting was considered in Section 6.2.4.1, the simulation analysis, with M=37. Notice that neither of these is classical centroiding, with division by the per-subaperture intensity; both are a variation on the denominator-free theme, with division only by the total intensity in the pupil.

In the case of equal weighting of M brightest, we have the following. The summations are only over the included subapertures.

$$\theta = \frac{\lambda}{2dSM}\sum\frac{x_i}{f_i}$$
$$\sigma_\theta^2 = \left(\frac{\lambda n}{dSM}\right)^2\sum\frac{1}{f_i^2}$$

Equation 6.2-6

An expression for noise optimal weighting can be derived by taking the partial derivative of the variance in Equation 6.2-6 with respect to any weight, and setting it to zero. The resulting noise optimal weights, the angle on the sky and the variance in the angle are given by Equations 6.2-7.

The noise optimal weighting is derived in Appendix 6.2, with the following results:

$$w_i = \frac{f_i^2}{\sum f_i^2}$$
$$\theta = \frac{\lambda}{2dS}\frac{\sum x_i f_i}{\sum f_i^2}$$
$$\sigma_\theta^2 = \left(\frac{\lambda n}{dS}\right)^2\frac{1}{\sum f_i^2}$$

Equation 6.2-7

Notice that equal-weighted variance has a sum of reciprocals, and the noise-optimal variance has the reciprocal of a sum. It is apparent from these that the equal weighted case suffers a noise increase when faint spots are included, while the noise-weighted version counts faint spots weakly, and spots with no light do not count at all.

The increase in variance of pointing angle for equal-weighting over optimal-weighting is 1.8x for 12-brightest, 1.63x for 37-brightest and 473x for all 49 spots, where the very faint corner spots contribute a great deal of noise.

These equations are evaluated in the CAL photometry spreadsheet "GPI Photon Flux", in Appendix 6.2. The spreadsheet includes a full tabulation of optical losses by element, and reports results both by wavelength band and summed over wavelength. The analytical estimate of rms tilt error, for H-band only, 37-brightest, is 2.0 milliarcsec rms per frame at 8th magnitude, in substantial agreement with the simulation results in Section 6.2.4.1.

Broadband Noise-optimal	Broadband 37-brightest	H-band only Noise-optimal	H-band only 37-brightest	
1.62E-03	2.08E-03	1.06E-02	1.35E-02	Noise-equivalent x centroid, per frame
1.17E-09	1.499E-09	7.635E-09	9.76442E-09	RMS tilt error, per frame (radians on sky)
0.000242	0.0003091	0.0015749	0.002014056	RMS tilt error, per frame (arcsec on sky)
3.12E-05	3.991E-05	0.0002033	0.000260014	RMS tilt error in one second (arcsec on sky)

Table 6-1 Summary of LOWFS Tip/tilt Performance. The rms tilt error, per frame at 60 Hz, is 1.6 mas on the sky for noise-optimal and 2.0 for 37-brightest LOWFS algorithms, for H-band only. With no filter (broadband case), the rms tilt error is 0.24 and 0.31 mas.

6.2.4.3 Analytical HOWFS Performance

The HOWFS is responsible for measuring the mid-spatial frequency errors to within 1 nm on an H=5 star (and to 5 nm for H=8) in a one-hour exposure. Along with the brightness-dependent error term already implicit in its performance requirements, the HOWFS is subject to myriad other quasi-static effects such as induced wave front error from beam walk on the Calibrator optics, changing registration of the HOWFS detector to the DM (and of the Calibrator beams to the HOWFS detector), demodulation of the phase-shifting mirror, broadband and chromatic errors, and other errors.

In order to properly consider all possible effects, the ability of the Cal system to meet its requirements is therefore evaluated primarily by use of the Cal Error Budget (described elsewhere in this document). The error budget terms have been derived from analytic performance estimates; in turn, the Cal simulation is used to validate these analytic estimates.

The intensity at a HOWFS subaperture is given analytically above in Section 158 and in simplified form here:

$$I_{HOWFS} = Q\frac{A^2}{2}\left[T_{ref} + T_{sci}\left(\varepsilon^2 + \phi^2\right) + 2\sqrt{T_{ref}}\sqrt{T_{sci}}\left(\varepsilon\cos\theta + \phi\sin\theta\right)\right], \qquad \text{Equation 6.2.8}$$

where A is the amplitude of the electric field incident on the apodizer, θ is the phase step of the phase shifting mirror (0, $\pi/2$, π, or $3\pi/2$), ε and φ are the amplitude and wave front errors to be measured, T_{ref} and T_{sci} are the effective transmissivities through the reference and science arms, respectively, and Q is the detector efficiency. The detector efficiency Q depends both on the quantum efficiency of the detector array used and on the effective integration losses due to finite read/reset times.

The framerate of the HOWFS Picnic detector is tunable; the valid framerates and corresponding effective integration times are given by

$$f = \frac{500kHz}{(50+4)(50+1)(n+3)}, \quad t = 2\mu s(50+4)(50+1)(n+1), \quad (n = 0,1,2,...255). \qquad \text{Equation 6.2.9}$$

Deparameterizing this relationship provides the dependence of the effective efficiency of the detector on the frame rate, *f*, measured in Hz:

$$Q_{timing} = 1 - 0.01164 f. \qquad \text{Equation 6.2.10}$$

As the phase shifting mirror moves through its phase steps four intensity measurements are made, from which the phase and amplitude errors in each subaperture can be calculated using the following two relations:

$$\phi = \frac{I_1 - I_3}{2QA^2\sqrt{T_{ref}}\sqrt{T_{sci}}}, \quad \varepsilon = \frac{I_2 - I_4}{2QA^2\sqrt{T_{ref}}\sqrt{T_{sci}}}. \qquad \text{Equation 6.2.11}$$

While the detector read noise is constant, the photon noise depends on the brightness of the observed star. In the case of low-magnitude errors, the reference arm dominates the HOWFS intensity profile and the photon noise is simply

$$\sigma^2_{photon} \approx I^{perfect}_{HOWFS} = Q\frac{A^2}{2}T_{ref}. \qquad \text{Equation 6.2.12}$$

After taking into account the fact that two images are needed for each measurement, the effective measurement error due to photon and read noise is given by

$$\sigma_\phi = \frac{\sqrt{2}\left(\sigma^2_{photon} + \sigma^2_{read}\right)^{1/2}}{2QA^2\sqrt{T_{ref}}\sqrt{T_{sci}}}. \qquad \text{Equation 6.2.13}$$

A plot of this detector-induced error as a function of HOWFS integration time is shown in Figure 6-12. The individual and combined effects of read noise, photon noise, and detector timing losses are all plotted.

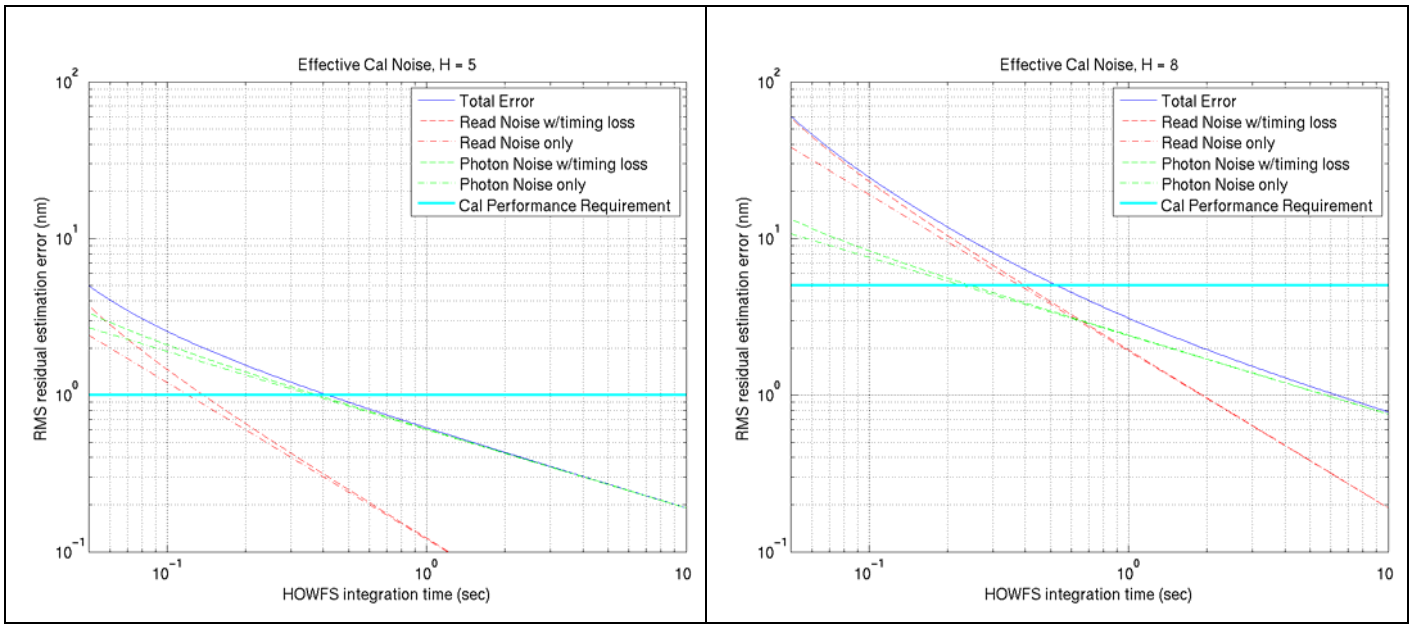

Figure 6-12: Measurement errors due to photon and read noise as a function of HOWFS integration time for an H=5 star (left) and an H=8 star (right) plotted against the HOWFS performance requirement for those stars. Measurements of both stars meet their requirement levels at exposure times of approximately 0.5 seconds, corresponding to a one Cal wave front estimate per second.

6.2.4.4 HOWFS Performance, by Simulation

The result of a simulation validating the analytical expression described above is shown in Figure 6-13. The full numerical simulation confirms that for an H=5 star at a wave front estimation rate of 1 Hz (consisting of two readouts per second) the error from read and photon noise is approximately a 1 nm RMS effect.

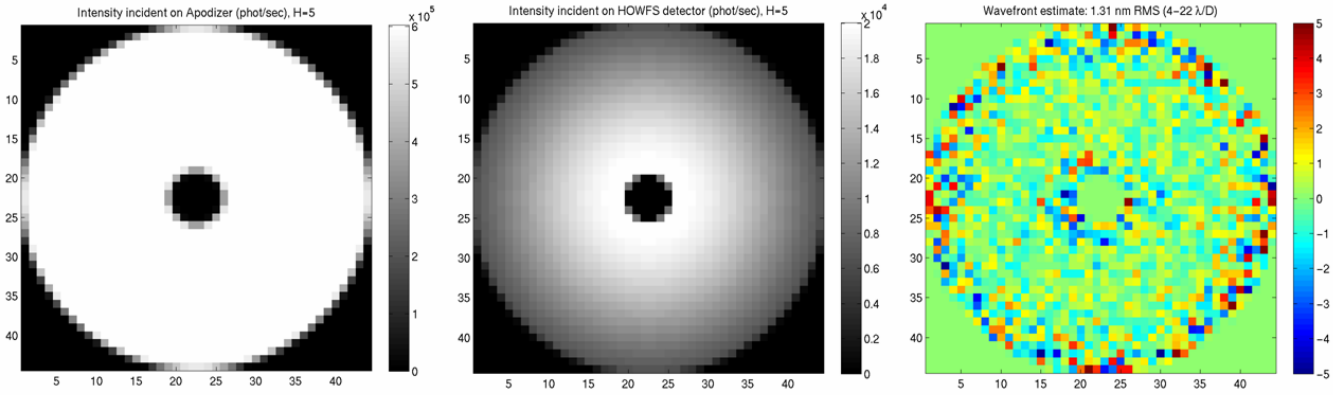

Figure 6-13: Measurement error on an H=5 star (right) when the HOWFS is integrating for 0.5 sec per exposure. The intensity incident on the Cal system (left) is reduced by a factor of ~30 by the time light reaches the HOWFS detector (center). The total residual error due to photon and detector noise is 1.3 nm RMS.

An example of a HOWFS measurement of a static atmospheric phase screen in the absence of measurement noise is shown in Figure 6-14. In the absence of measurement noise the HOWFS

simulation accurately captures essentially all the mid-spatial frequency wave front errors: the residual consists of low spatial frequencies which will be detected separately by the LOWFS.

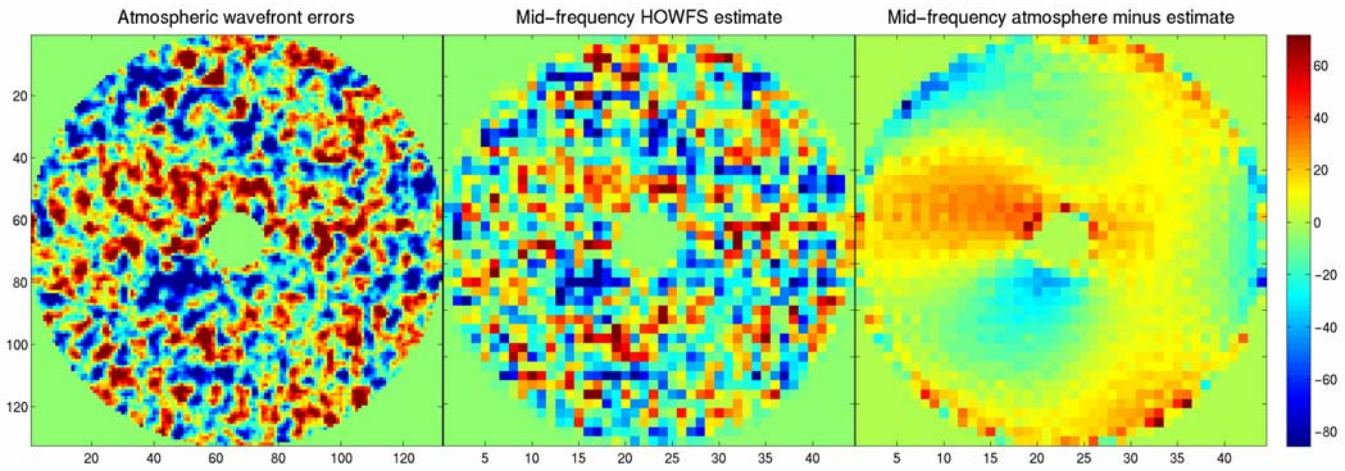

Figure 6-14 HOWFS estimation of atmospheric mid-spatial frequencies without measurement errors. A static atmospheric phase screen (left) is run through the Cal simulation to form the wave front estimate (center). The residual errors (right) are outside of the HOWFS' detectable bandpass.

6.3 Optical Design

The calibration subsystem consists of three primary sub-elements: the high-order wave front sensor (HOWFS), the low order wave front sensor (LOWFS) and the pinhole camera. This section will offer a description of the relevant parts of each sub-element, a description of the driving optical concerns and a ray trace of the sub-element. We have a throughput and photometry budget for the whole calibration system that tracks the reflectivity/transmission of each optical element as a function of wavelength and also estimates the number of photons per second at each of the sub-elements. We use this photometry budget to estimate the performance of the HOWFS and LOWFS. Finally, we discuss the tolerances and alignment sensitivities of each of the optical sub-elements and compare it with the preliminary gravity-induced flexure analysis.

6.3.1 Top-level optical layout

First, we begin with a top level overview of the calibration system optics. In the optical layout shown below, we trace the rays from the location of the apodized pupil plane through to the final focal plane array of the HOWFS. In the science arm, the input pupil is re-imaged by the science re-collimation parabola to a location near the vertex of the merge prism. The HOWFS optical train will be described and detailed starting from this location to the final focal plane pupil image. On the reference arm side, the input pupil is re-imaged to a location roughly 75 mm behind the front surface of the LOWFS beamsplitter: a very convenient location. The pinhole camera images light that is reflected from the back side of the spatial filter pinhole with a simple finite-conjugate relay to give the appropriate magnification.

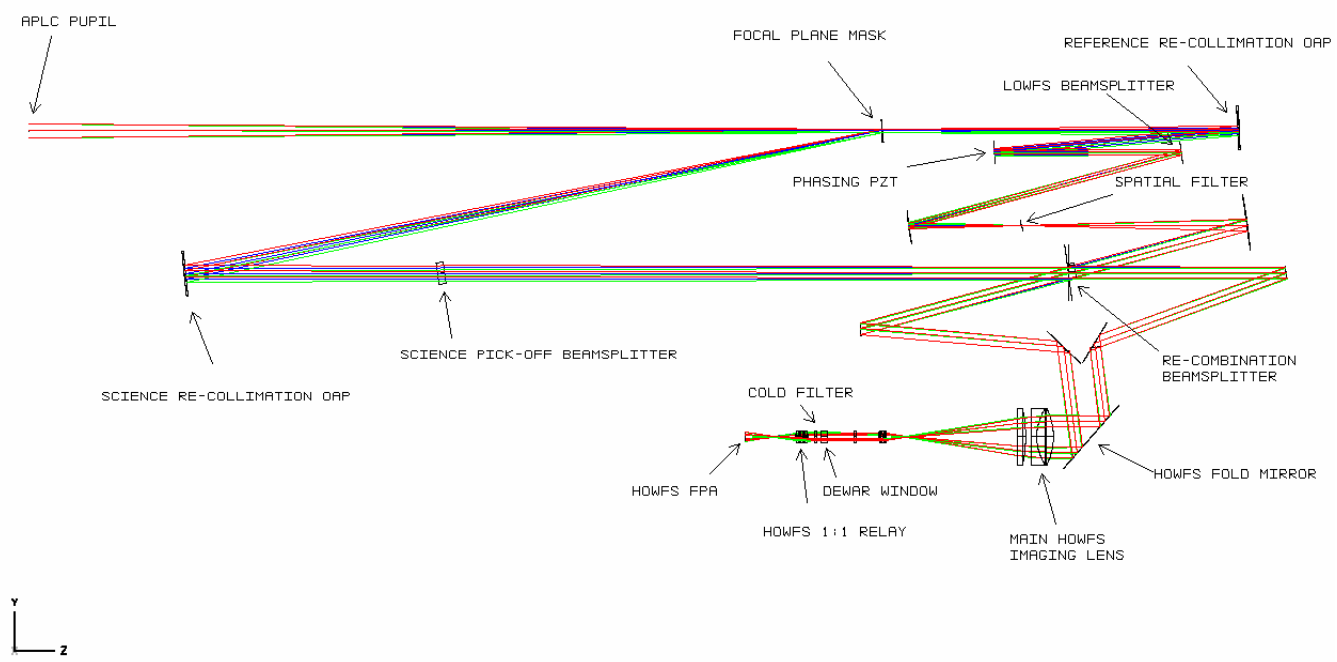

Figure 6-15 Calibration wavfront sensor ray trace.

6.3.2 HOWFS Optical Layout

As mentioned previously, the optical layout of the HOWFS sub-element will begin at the location of the re-imaged pupil which occurs after the beams have been re-combined. This pupil is formed very near to vertex of the merge prism. Now, there are some optical matters that need to be addressed before the re-combination beamsplitter, and this is because the calibration HOWFS is a broad-band, white-light, phase-shifting interferometer. For the interferometer to perform properly, its internal optical paths, as a function of wavelength, from the point of separation at the focal-plane mask to the point of recombination must match to within a small fraction of a micron. This puts a constraint on the allowable dispersion (differential glass thickness) and DC phasing between the two arms of the interferometer. An interferometer is also sensitive to internal optical pathlength disturbances. In our case, these pathlength vibrations are only problematic when they are near the demodulation frequency. If they are at a higher frequency, they will average out during the integration time of a single measurement, while if they are slower, they will be frozen out. We have designed the optical beam height (and mechanical mounts) from the mounting surface to be small so as to increase any mount-related resonant frequency.

Since we're working on a broadband astronomical instrument, atmospheric refraction is of necessity a concern. Left uncorrected, the residual atmospheric refraction will produce a chromatic smearing in the image plane and chromatic shear in the pupil plane. Both of these would have detrimental effects on the performance of both the LOWFS and HOWFS. The ADC has been added to mitigate against these effects. All of these optical aspects have been addressed before the HOWFS relay.

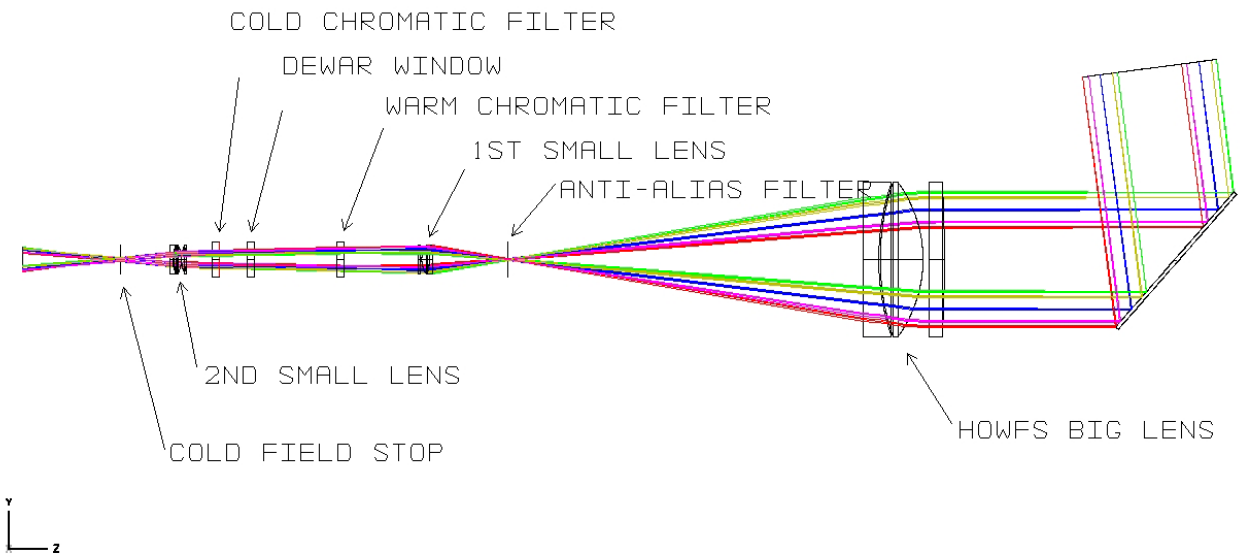

Figure 6-16 An optical layout of the HOWFS relay. The light enters from the upper right where the input pupils are located. These pupils are ultimate re-imaged to the focal plane array on the far left. All of the tranmssivie optics are designed to work broadband from 0.9 μm to 2.4 μm..

The layout of the HOWFS optical relay is shown above in Figure 6-16. The pupil is traced from the upper left. The pupil size is ten millimeters in diameter and the separation is designed such that upon demagnification, the two pupil images are on separate readout quadrants of the PICNIC array. The HOWFS fold mirror redirects the light to the HOWFS pupil lens. This lens is designed such that the input pupil is located at the back focal length so it is imaged to infinity. At the front focus of this lens is located the anti-aliasing spatial filter. The HOWFS pupil lens is a triplet designed to give good, broadband imaging from 0.9 μm – 2.4 μm. The lens materials are common for the visible/near-infrared and the lens surface shapes are plano-spherical.

The next optical element is the pupil re-imaging lens. It is also a triplet based upon the design of the HOWFS pupil lens. In the space before this lens, the pupil is at infinity, so after this lens it is re-imaged to the back focal length and de-magnified to the size and separation that will occur on the final image plane. This pupil image is formed near the location of the warm chromatic filters, this is advantageous as it makes the final image location of the focal plane array insensitive to the wedges in the warm chromatic filters. These filters contain the exact spectral filters as defined by the IFS plus a few neutral density filters for doing some calibrations without the focal plane mask. After the warm chromatic filters are the dewar window and the cold chromatic filter. The cold chromatic filter suppresses light longward of 2.4 μm to mitigate the noise from the emissivity of warm filters.

The final lens in the HOWFS relay is the 1:1 imaging lens that relays the real, de-magnified imaged to the final focal plane. This lens is also a triplet, it's a symmetric design with only two common glasses and three unique radii of curvature so we don't anticipate that it will be difficult to manufacture. Between this lens and the focal plane is a cold field stop that is oversized from the anti-aliasing filter,

but small enough to still significantly limit the solid angle seen by each pixel. This cold stop will be thermally tied to the cold finger of the cryo-cooler to give a temperature close to 80K.

6.3.3 LOWFS Optical Layout

In the reference arm of the calibration system, a real pupil image is formed approximately 75 millimeters after the LOWFS pick-off beamsplitter. The optical layout for the LOWFS, a traditional Shack-Hartman, is shown in the image below:

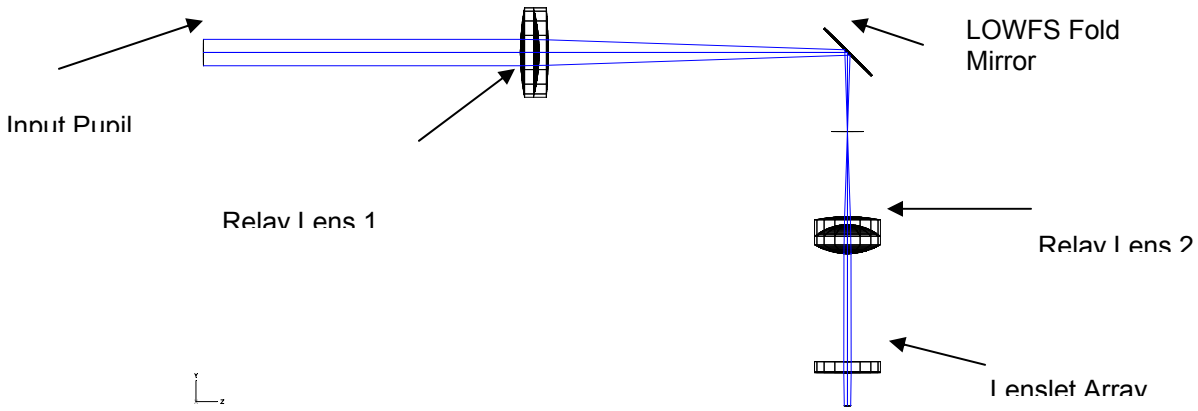

Figure 6-17 Optical layout of the LOWFS sub-element. The input pupil in the upper left is formed immediately after the LOWFS pick-off beamsplitter. The two relay lenses compress form s demagnified image of the pupil at the lenslet array. The lenslet array is the final element before the focal plane.

The two lenses are off-the-shelf and serve to compress the beam to the appropriate size for the lenslet array. The lenslet is also off-the-shelf and samples the pupil with an array of 7x7 subapertuers. These spots are then imaged directly onto the final Shack-Hartmann sensor. A geometrical optics analysis of this wave front sensor is only useful to get pupil locations and sizes correct. The sensor works by measuring tilts in diffraction PSF's and has been modelled extensively and this work is described in the performance simulation section. A qualitative image of the final focal plane spots is given in Figure 6-5 so that one can appreciate the effect of the apodized pupil on the relative illumination of the sub-apertures.

6.3.4 Pinhole camera optical layout

The pinhole camera re-images the plane that contains the spatial filter in the reference arm of the calibration sub-system. This camera allows us to directly measure the centration of the star with respect to the pinhole. An optical layout of the pinhole camera system is given below:

The light enters the system from the first OAP in the spatial filter assembly and reflects off the back side of the pinhole. This pinhole is tilted out of plane by 8 degrees to that the light reflected back comes out of plane to avoid the incoming light. A subsequent fold mirror reflects the light to an achromatic relay designed to operate from 0.9 μm – 1.7 μm. Another fold mirror then feeds this beam to the final pinhole camera focal plane.

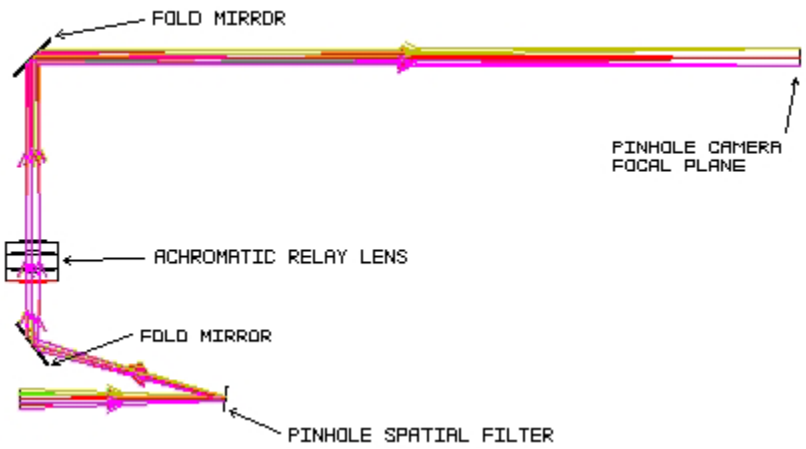

Figure 6-18 Optical layout for the pinhole-camera optics. The light converges to the pinhole in the reference arm from an OAP (not shown) on the left hand side of the image. The focus/pinhole image is magnified by about a factor of 3 by the achromatic relay lens.

6.3.5 Spherical mirror for calibration

The calibration system will have residual phase and amplitude errors in the optical system due to fabrication and alignment errors. If left un-corrected, these errors would give a systematic offset to the true phase and amplitude errors in the wave front before the coronagraph. Therefore, we plan on calibrating the cal system with an input wave front that is of known high-quality. The optical layout of this system is shown below in Figure 6-19.

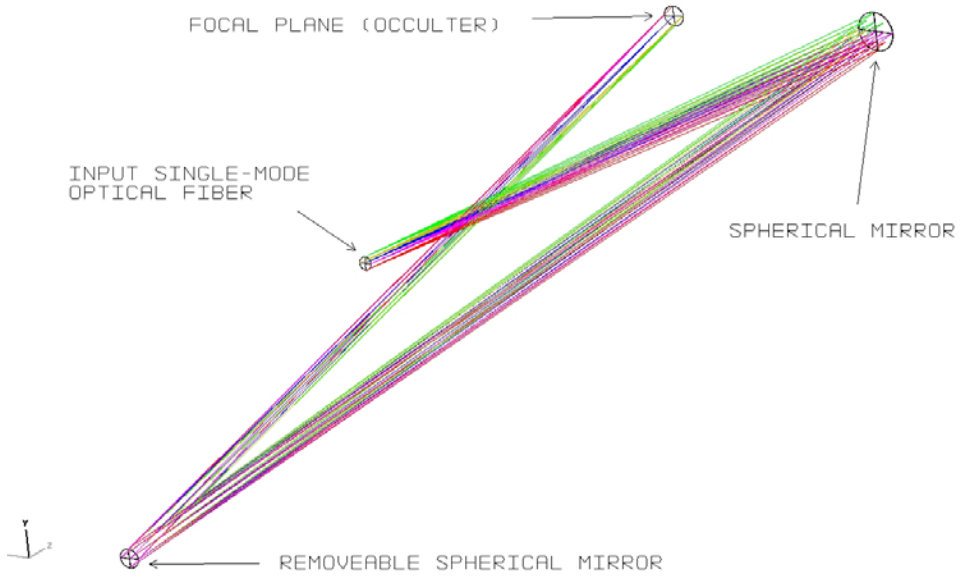

Figure 6-19: Ray trace for the optical train that calibrates the calibration subsystem. This layout is intrinsically non-planar due to the folds in two orthogonal axes on the spherical mirrors.

It consists of an input, single-mode optical fiber. This fiber provides a perfect spherical phase front with a well known ampliutude. This wave front is then presented with two super-polished spherical mirrors. These mirror have the same angle of incidence, but in two orthogonal directions. After these two reflections, the resulting, converging wave front at the focal plane is of very high quality (< λ/100 peak-to-valley for a 2 mm diameter motion of the fiber from nominal). In this way, offsets to the calibration system can be measured directly.

6.3.6 Throughput

6.3.6.1 Throughput

Throughput calculations for the calibration system are done in several steps. First, the throughput through the Telescope and AO system up to just before the pupil of the APLC is determined. This first stage includes the optics of the telescope and all the optics (windows, ADC, mirrors, DMs and dichroic) of the AO system. The throughput (transmission or reflectivity) of a given surface is tracked as a function of wavelength band for all of the specified science bands as well as some standard astronomical bands in the visible. We have an understanding of the transmission of the telescope optics from published papers. For the reflective optics in the AO system, we assumed a bare gold reflectivity. For the transmssive optics (instrument window, ADC and pick-off dichroic) we made reasonable assumptions about coatings and intrinsic absorption losses in the substrate materials.

At the focal plane mask, the throughput for the reference and science arms is tracked separately. The basis for most of the throughput calculations is again a thin-films model of the reflectivity of the coating material. Specifically, we assume a bare gold coating for all of the reflective optics internal to the calibration system. There are a couple of significant exceptions to this approach. The first is the focal plane mask where the transmission/reflection is field dependent. The second is the transmission of the pinhole spatial filter where an accurate accounting must be done with Fraunhoffer diffraction both at the pinhole and the subsequent re-collimation optic.

Once the science beam and reference beam are re-combined at the beamsplitter, the throughput to the final focal plane is straightforward and can be done with consideration for the reflection/transmission properties alone (no need for diffraction calculations). This throughput is in the form of an excel spreadsheet.

6.3.6.2 Photometry

The determination of the number of photons per unit solid angle per unit time per unit bandwidth is straightforward. We use standard constants for the power per square meter of collecting area per astronomical spectral bandpass (in nm) for a zero magnitude star. We have vetted this spreadsheet internally here at JPL, and have also shared it with GPI member institutions HIA and LLNL and we believe it captures the instrument with high fidelity. We use the data from the photometry spreadsheet as inputs into our numerical simulations for the pupil flux (in integrated photons per second) at the APLC pupil plane for both the HOWFS and LOWFS performance simulations. In the same spreadsheet, we

have an estimate of the performance of the LOWFS for a given stellar magnitude and sample rate, and read noise at various levels.

6.3.7 Fabrication and Alignment tolerances

6.3.7.1 Fabrication Tolerances

The fabrication tolerances are largely driven by the allowable calibration offset (currently 20 nm) split between four optics: science re-collimation OAP, science pick-off beamsplitter, calibration re-combination beamsplitter, and reference arm spatial filter re-collimation OAP. The optics before the spatial filter in the reference arm can be loosely specified owing to the effect of the spatial filter to remove all but very low spatial frequency errors. Therefore, only the four optics mentioned previously have a moderately high specification on the fabrication errors. And since two of these four are planar optics, and therefore easier to meet surface figure specifications, we feel these are not challenging fabrication needs.

6.3.7.2 Alignment Tolerances

Alignment tolerances for the LOWFS and HOWFS sub-system are driven primarily by the requirement to 1) minimized unsensed pointing error in the LOWFS and 2) minimize unsensed pupil shear in the HOWFS. The small tilts and de-centers responsible for this mis-alignment have negligible effects on the alignment wave front quality. The error budget for these misalignments is detailed at the end of the mechanical section.

6.4 Mechanical Design

The calibration unit consists of optical elements, supports, and mechanisms mounted to a 101.6 mm thick optical breadboard. The breadboard is designed to act as stiff mounting platform to structurally support all calibration unit components. The breadboard will be of sufficient stiffness such that all components move as a rigid body with respect to each other when subjected to changing gravity vector orientations. The breadboard is mounted to the GPI Instrument Opto-Mechanical SubSystem (OMSS) by three bipods. Each bipod is designed to restrain only two degrees of freedom so that the breadboard mounting is statically determinate. The statically determinate mounting of the breadboard ensures that deformations in the OMSS do not result in additional deformations and structural stresses in the Calibration Subsystem structure. A general preliminary mechanical layout of the Calibration subsystem is shown in Figure 6-20

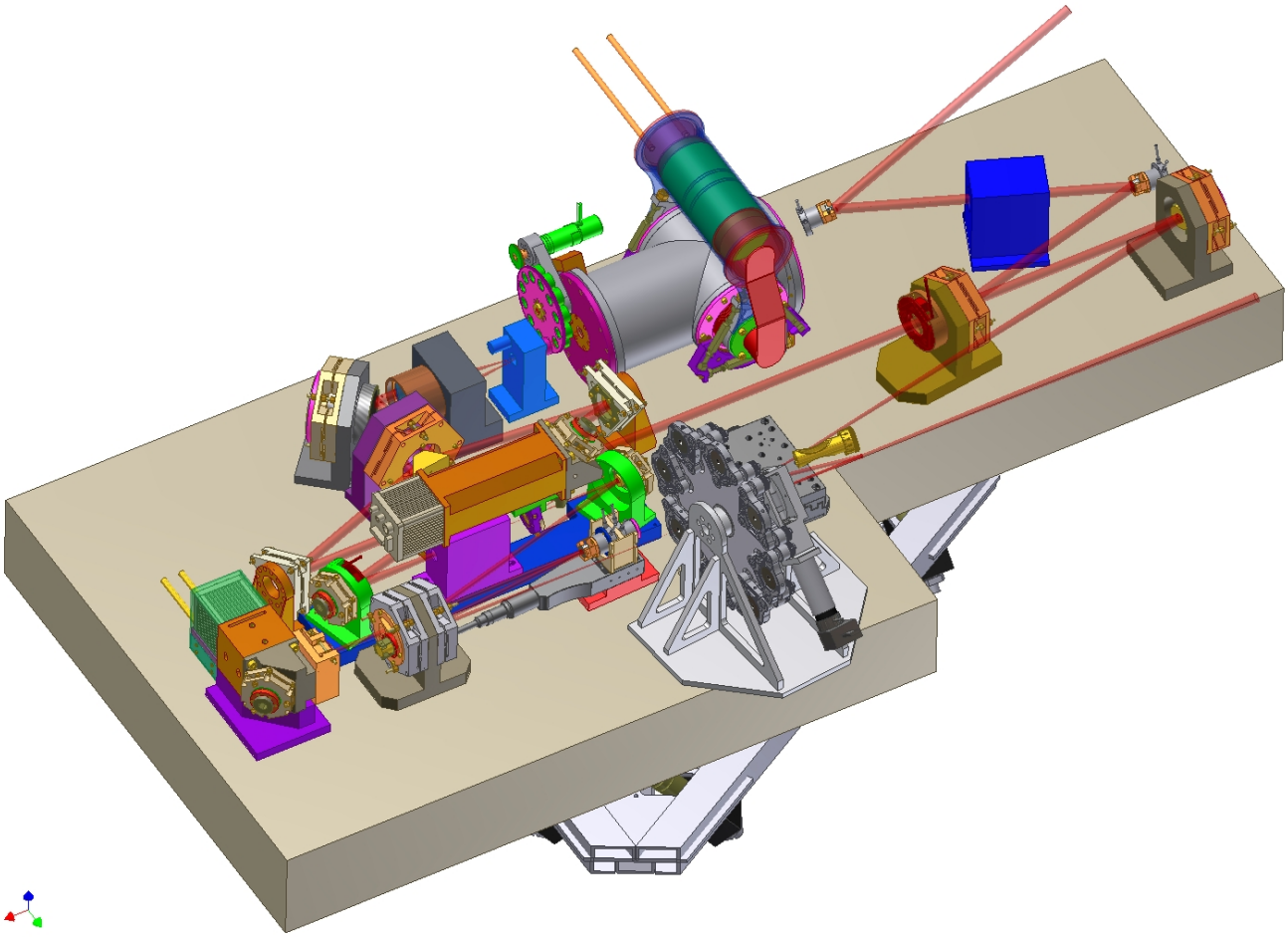

Figure 6-20: Calibration System opto-mechanical layout

6.4.1 Mechanisms

The calibration unit has thirteen mechanisms with 28 degrees of freedom to configure the calibration system and compensate for dimensional changes due to structural flexure, mechanical disturbances, and thermal changes. In addition to these there are four mechanisms associated with thermal control. The location of these mechanisms and main sub-assemblies are shown in Figure 6-21.

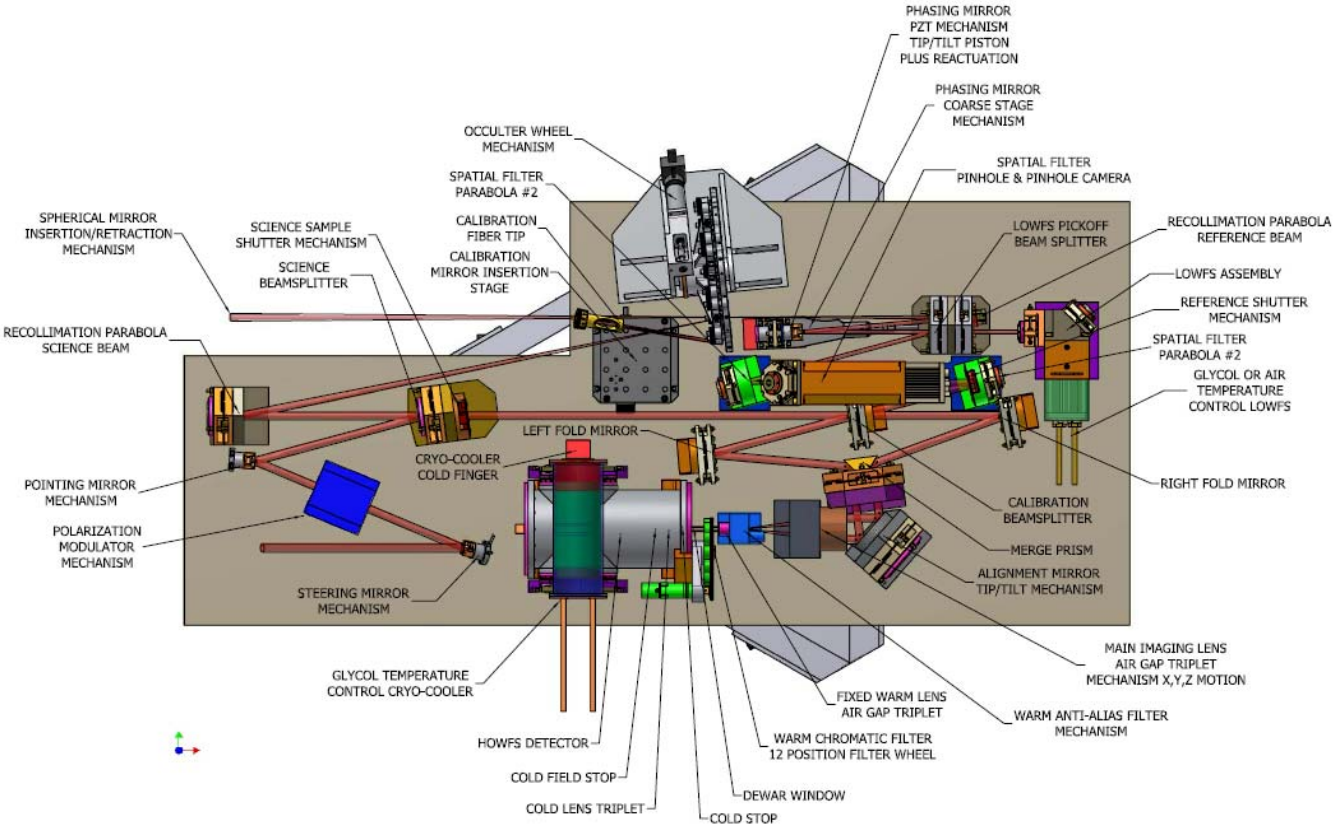

Figure 6-21: Calibration System mechanisms and components.

6.4.1.1 Occulter Wheel:

The occulter wheel mechanism provides a means of configuring the GPI instrument by selecting one optic from the eight wheel positions. This mechanism is a single degree of freedom rotation mechanism. This mechanism shall be fabricated by HIA and delivered to JPL for integration.

6.4.1.2 Coarse Phasing Stage:

The coarse phasing mirror stage is part of the phasing and alignment subassembly. The purpose of the coarse phasing stage is to match the optical path lengths of the two arms of the calibration system interferometer from the occulter optic to the calibration beamsplitter. One arm of the interferometer is the reference arm and the other arm is a sample from the science beam. The control system for the Calibration System uses the coarse phasing stage to maintain the piston motion of PZT path length compensation mechanism in the center of its travel range. The coarse phasing stage is a single degree of freedom mechanism. The mechanism has +/- 5 mm of travel which can compensate for up to +/- 6.6mm of Optical Path Difference (OPD). This range of motion will result in +/- 435 microns of beam shear at the LOWFS pick-off beam splitter. Additional information on coarse phasing can be found in Appendix 6.4.

6.4.1.3 PZT Tip/Tilt and Piston Stage:

The PZT phasing and alignment mirror stage is part of the phasing and alignment subassembly. The PZT mechanism provides high bandwidth dynamic control of the GPI calibration system interferometer optical path difference and reference arm spatial filter focus location. The PZT Tip/Tilt/Piston mechanism is a six degree of freedom mechanism. Three degrees of freedom are tip, tilt, and piston and three additional degrees of freedom to momentum compensate for the tip, tilt and piston degrees of freedom.The PZT mechanism can provide 6 microns of piston with no Tip/Tilt compensation or +/- 300 micro-radians of tip-tilt with no piston. In order to maximize the available tip-tilt range the Calibration System control system uses the coarse phasing stage to maintain the piston motion of PZT path length compensation mechanism in the center of its travel range. One micron of PZT travel is allocated to OPD compensation and the remaining PZT range is allocated to provide +/- 250 micro-radians mechanical (+/- 500 micro-radians optical) of tip/tilt compensation. The PZT mechanism can provide 0.5 nm of piston control resolution and +/- 0.1 micro-radians of tip/tilt control resolution. Additional information on the PZT mechanism can be found in Appendix 6.4.

6.4.1.4 Reference Shutter Mechanism and Science Beam Sample Shutter Mechanism:

Both the reference beam shutter mechanism and the science beam shutter mechanism permit the Calibration System to choose either beam within the High Order Wave Front Sensor. The baseline shutter is a Vincent Associates Uniblitz BDS25S1T0. The Uniblitz BDS25S1T0 is an un-housed shutter that is power off stable in either the normally open or normally closed position. The Uniblitz shutter has two degrees of freedom from a controls point of view. One degree of freedom is to open the shutter and one degree of freedom is to close the shutter. There is a separate solenoid coil for open and close. Additional information on the shutter mechanism can be found in Appendix 6.4.

6.4.1.5 Alignment Mirror Tip/Tilt/Piston mechanism:

The alignment mirror mechanism is located after the Calibration System beamsplitter, relay mirrors, and merge prism. The purpose of the alignment mirror is to control the tip/tilt of the optical beam in order to obtain instrument pupil images in the proper locations on the HOWFS detector array surface. This mechanism requires a minimum of 2 degrees of freedom, tip and tilt. However, the mechanism is being planed for 3 degrees of freedom tip, tilt, and piston because the 3rd degree of freedom will allow the mirror to have tip and tilt without beam shear. The mirror mechanism will need to actuate a 63.5 mm diameter mirror in order to accommodate two 10 mm diameter sub-apertures separated by 28.444 mm. at a 41.25 degree angle of incidence. Detailed mechanism requirements based on optical requirements have not been specified at this time. It is desirable to use a PZT based mechanism with flexure guidance because this kind of mechanism provides a high bandwidth, has high resolution, and is reliable. A flexure/ PZT mechanism may not be appropriate if the range of motion is too large. It will probably be possible to use a PZT mechanism if the range of active angular motion control is less than approximately +/- 0.25 degrees. The angular resolution would be on the order of 1 part in 50000 or 0.2 micro-radians for a +/- 0.25 degree tip/tilt angular range of motion.

6.4.1.6 Main Imaging Lens Mechanism:

The main imaging lens mechanism moves the main lens assembly in the X and Y directions perpendicular to the light beam propagation direction. Lens assembly motion in the X and Y directions is required to position the focal point in the center of the Anti-Alias filter. This mechanism has three degrees of freedom, X, Y, and Z motion, that requires closed loop control from the Calibration System computer. The main imaging lens mechanism also moves the lens assembly in the Z direction along the direction of light beam propagation. Z direction motion permits the GPI instrument pupil to be focused on the surface of the HOWFS detector array. Detailed mechanism requirements based on optical requirements have not been specified at this time. It is desirable to use a PZT based mechanism with flexure guidance because this kind of mechanism provides a high bandwidth, has high resolution, and is reliable. A flexure/ PZT mechanism may not be appropriate if the range of motion is too large. It will probably be possible to use a PZT mechanism if the range of linear motion under active control is less than approximately 300 microns. The linear resolution would be on the order of 1 part in 50000 or 6 nanometers for a 300 micron linear travel range.

6.4.1.7 Warm Anti-Alias Filter:

The warm anti-alias filter will be a square aperture special filter located at the focus of the main imaging lens assembly. The purpose of the anti-alias filter is to remove the side lobes from the pupil image using a square aperture. The required size of the square aperture is dependent upon the wavelength of light being processed. The mechanism will be a single degree of freedom mechanism that will configure the size of the square aperture from approximately 0.5 mm to 2.5 mm. The precise size range and size tolerances for the square aperture have not been specified at this time. The mechanism is envisioned to be two blades mounted on linear motion flexures. Each blade has an overlapping square aperture in it. The blades move the same magnitude in opposite directions along the direction of one of the diagonals of the square apertures to change the aperture size. The movement of the blades will be initiated by means of a dc gear motor with appropriate linkages to produce the desired range and precision of motion. Due to space limitations in the area of the anti-alias filter the mechanism and gear motor will need to be small. A candidate brushless gear motor and drive electronics is provided in Appendix 6.4.

6.4.1.8 Warm Chromatic Filter Wheel:

The Gemini Planet Finder Calibration System has warm chromatic filter wheel in front of the Calibration System High Order Wave Front Sensor Dewar. The filter wheel shall be able to select among twelve 12.7 mm diameter warm chromatic filters. In order to maintain a compact design the filter wheel shall be a 3.5 inch pitch diameter gear with 336 teeth mounted to a duplex bearing pair mounted back to back. The gear will have 0.535-40 taped holes to accept Thorlabs half inch diameter lens tubes that are 0.3 inch long. These lens tubes can accept 12.7 mm diameter filters. The gear will be driven by an anti-backlash pinion that has a 1.0 pitch diameter and 96 teeth. The anti-backlash gear is mounted to a HD systems RH-5A-5502-E050A0 DC motor gear actuator. This actuator has an 80:1 harmonic gear box driven by a DC motor with a 500 pulse per revolution encoder. One encoder pulse corresponds to approximately 2 microns of movement at the chromatic filter centerline. There will be a Hall Effect home switch sensor to index the filter wheel so that the control computer knows where to start counting encoder pulses in order to position the filter wheel at the desired filter. The warm chromatic filter wheel

mechanism has 1 degree of freedom (rotation). Additional information on the filter wheel mechanism can be found in Appendix 6.4.

6.4.1.9 Pointing Mirror Mechanism:

The pointing mirror mechanism provides a means of aligning the calibration system exit beam centerline to the IFS input aperture centerline. This mechanism is a three degree of freedom mechanism, tip/tilt and piston. This mechanism requires a minimum of 2 degrees of freedom, tip and tilt. However, the mechanism may be planed for 3 degrees of freedom tip, tilt, and piston because the 3rd degree of freedom will allow the mirror to have tip and tilt without beam shear. This mechanism shall be fabricated by HIA and delivered to JPL for integration.

6.4.1.10 Polarization Modulator Mechanism:

The polarization modulator mechanism rotates the polarization state of the science light about the optical axis to permit the characterization of the science light stokes parameters. The polarization modulator is a single degree of freedom mechanism. This mechanism shall be fabricated by HIA and delivered to JPL for integration.

6.4.1.11 Steering Mirror Mechanism:

The steering mirror mechanism provides a means of aligning the calibration system exit beam propagation direction to the IFS input aperture centerline. This mechanism is a three degree of freedom mechanism, tip/tilt and piston. This mechanism requires a minimum of 2 degrees of freedom, tip and tilt. However, the mechanism may be planed for 3 degrees of freedom tip, tilt, and piston because the 3rd degree of freedom will allow the mirror to have tip and tilt without beam shear. This mechanism shall be fabricated by HIA and delivered to JPL for integration.

6.4.1.12 Linear Stirling Cryogenic Cooler:

The HOWFS dewar will have a cryogenic cooler that will maintain the temperature of the internal detector array and optics at a temperature below 80 Kelvin. Vibrations induced by the cryogenic cooler are a big concern since they have the potential of causing dynamic changes in the calibrations system interferometer optical path difference. A preliminary analysis shows that approximately one watt of cooling power is required in steady state to maintain the detector and optical temperature below 80 K. A pulse tube cryogenic cooler is generally accepted to be the type of cooler that produces the least amount of vibration. However, the pulse tube cryogenic cooler does not work in all gravity orientations. A linear Stirling flexure cooler that is momentum compensated with flexure mounted pistons moving in opposite directions has been base-lined for the HOWFS dewar. This type of cooler is believed to be the best available choice for a cryogenic cooler that can provide several watts of cooling power while being subjected to changing gravity vector orientations. This type of cooler is designed to produce minimal vibrations that are estimated to be 1.7 N RMS axial and 0.35 N RMS radial. The cryogenic cooler will be mounted on vibration isolators to reduce the vibrations induced into the calibration system. Analysis has not been done at this time to estimate the effect that these vibration levels have on the calibration

system interferometer. The compressor of the cryogenic cooler will be encased in a glycol cooled cold plate / jacket to remove the heat generated by the compressor. The cold finger base may also need to have a glycol jacket attached to keep its temperature within the required 2 degrees Celsius of ambient. Additional cryogenic cooler information is provided in Appendix 6.4.

6.4.1.13 Compressor & Cold finger Temperature glycol flow control valve:

The temperature of the compressor skin and the cold finger head skin are required to be within 2 degrees Celsius of the ambient instrument temperature. The compressor and cold finger skins will be attached to cold plates with shields that are glycol cooled. The peak rate of heat removal required by the glycol is expected to be 100 watts. Under steady state operation the rate of heat removal by the glycol is expected to be on the order of 55 watts. In order to keep the cold plates and shields within 2 degrees of ambient the temperature of the cold plates and shields will be temperature controlled by means of closed loop glycol flow control. The glycol flow rate will be controlled by a DC motor driven needle valve. Allowing a 5 degree Celsius temperature rise of pure glycol requires approximately 2 liters per minute glycol flow rate to remove 100 watts. Control feedback will include motor encoder counts, valve position, travel limit switches, cold plate temperature, and glycol flow rate.

6.4.1.14 Spherical mirror insertion mechanism

The general concept of this mechanism would be to place the spherical mirror on a linear stage that will insert and remove the optic into the proper location in a repeatable manner.The spherical mirror insertion mechanism is designed to insert and retract a spherical mirror into the entrance beam path to the Calibration System. The spherical mirror will reflect a diverging cone of light from a fiber tip such that it becomes a converging cone of light with a focus at the center of the occulter optic. The beam of light from the fiber tip will provide a “perfect” wave front that will be used to calibrate the systematic errors present in the Calibration System. The detailed optical design, optical tolerances, stability, and repeatability of the calibration system reference optics have not been established at this time.

6.4.1.15 LOWFS and Pinhole Camera Temperature Control - Air Circulation Fans:

The LOWFS and Pinhole cameras will each generate approximately 1.3 watts within the instrument. In Order to maintain component skin temperatures within 2 degrees Celsius as required this power needs to be dissipated. One choice would be to glycol cool these cameras with closed loop temperature controllers similar to that required for the cryo-cooler compressor. This is technically very complicated and produces an additional risk of glycol leaks for just 2.6 watts of power. The base line approach for removing the heat from each camera will be to enclose the camera housing in a thermal shield and circulate air between the thermal shield and the camera housing using a small DC motor fan. The fans will be operated at a fraction of their design speed and be mounted on vibration isolation mounts so that vibrations will not be introduced into the instrument. The inlet and exhaust air will enter and exit through diffusers away from optical elements so that air currents do not adversely affect instrument performance.

6.4.2 Mechanical Analyses

6.4.2.1 Flexure analysis:

A preliminary flexure analysis was performed on the GPI Calibration System optical bench. The flexure analysis was performed to estimate the changes in optic element positions when the Calibration Source optical bench is subjected to changing gravity vector orientations that will occur when the GPI instrument is mounted on the telescope pointed at different locations on the sky. The output of this analysis is subsequently used as an input into ZMAX optical models to predict expected changes in calibration system and GPI instrument optical performance to satisfy the following project requirements:

- (Mech 2) OMSS, CAL, IFU – Preliminary flexure analysis of the structure, using lump masses for the mechanisms showing adequate levels of performance and safety margin.
- (Mech 9) CAL – Preliminary tolerance to flexures/pointing errors.

The flexure analysis was performed using Finite Element Analysis (FEA). The structural model for the FEA of the calibration system was based upon the preliminary calibration system optical layout and solid model. The honeycomb core breadboard providing the structural support and stiffness for the GPI Calibration System was modeled with finite elements. The masses of the objects mounted to the breadboard were distributed on the FEA breadboard and tied to the FEA breadboard nodes at locations consistent with the three dimensional solid model. Monitoring locations tied to the breadboard model were established in the FEA model at the optic positions so that the FEA could output the optic position movements in response to an input gravity vector.

The FEA analysis was performed for a set of 74 gravity vector orientations provided by Darren Erickson of HIA. The set of 74 gravity vectors was used by all GPI institutions so that the flexure analysis results of each institutions subsystem can be used to determine the overall instrument performance for each of the 74 gravity vector orientations. A detailed description of the finite element analysis and associated results can be found in Appendix 6.4.

6.4.2.2 Thermal analysis:

A preliminary thermal analysis was performed on the cryogenic dewar for the Gemini Planet Imager High Order Wave Front Sensor. The dewar is required to maintain the HOWFS detector array at a temperature of 80 degrees Kelvin or less. The objectives of the analysis were as follows:

- Preliminary steady–state thermal analysis showing the temperature distribution at the end of a cool down cycle.
- Preliminary cool down analysis incorporating the cooler capacity as a function of temperature. The model should be adequately detailed to give the cool down time with a maximum error of 50%

A lumped parameter thermal model was used to perform the thermal analysis of the HOWFS dewar. The technical details of the thermal model are provided in Appendix 6.4. The differential equations of the thermal model were solved numerically using MATLAB to produce a cool down simulation of the HOWFS dewar. The steady state performance of the dewar was obtained by looking at the final values of the cool down simulation after the dewar components had reached their steady state temperature.

The HOWFS dewar cool down simulation assumed that 1.75 watts of cooling power was available. The thermal analyses assumed that the detector was off and not dissipating heat until the detector reached its final operating temperature below 80 degrees Kelvin. The HOWFS dewar simulation model took approximately 11 hours to reach a steady state temperature below 80 degrees Kelvin. The HOWFS dewar radiation shields reached their steady state temperature after approximately 40 hours.

Once the 80 degree Kelvin detector temperature was achieved, it took the dewar simulation model approximately 1 watt of cooling power to maintain the HOWFS dewar component temperatures at their steady state values in a 293 degree Kelvin ambient environment assuming a maximum detector heat load of 0.25 watts.

6.4.2.3 Mass analysis:

A preliminary mass analysis was performed on the GPI Calibration System optical bench and electronic rack components. The mass analysis was performed to satisfy the following GPI project requirement:

Preliminary instrument weight estimate, going down to each mechanism and structure, including the electronics cabinets. Indicate weight and location of ballast needed to meet the weight and CG requirements.

The mass model for the main optical bench was constructed by making solid models of each of the Calibration system subsystem in Autocad Inventor. Appropriate mass properties were applied to each solid model such that the modeling software was able to compute the mass properties of each Calibration System subassembly. The mass properties of the main honeycomb bench were estimated using the FEA model. The masses and estimated center of mass locations for each calibration system optical bench subassembly was tabulated. The overall mass of the Calibration Subsystem optical bench without the OMSS truss pyramid attached was subsequently estimated to be 120 Kg with a center of mass location (Xcg= 163.3 mm, Ycg = -24.78 mm, Zcg = 26.76 mm) in local Calibration Subsystem coordinates. The mass of the Calibration System rack mounted electronics was estimated by tabulating the masses of each electronic component based upon manufacturer data sheets. The electronics subrack volume is 482.6 mm wide by 311.15 mm high by 500.0 mm deep. The center of mass of the electronics subsystem was assumed to be at the center of the calibration system subrack due to the small size of the subrack. The total mass of the JPL electronics equipment was estimated to be 53.25 Kg. A tabulation of the Calibration System mass components and locations is provided in Appendix 6.4.

6.4.2.4 Assembly Drawings:

Assembly drawings were produced to satisfy the following project requirement:

- Preliminary assembly drawings of all mechanisms, and preliminary analysis to show they meet the opto–mechanical tolerances.

The top level drawing is shown in Figure 6-1, which shows the functional layout. The rest of the assembly drawings are provided in Appendix 6.4:

6.4.3 Integration and Test:

For the purposes of integration and test the Calibration System shall be mounted to a integration and test frame mounted on casters so that it can be rolled around the laboratory. This cart shall be capable of orienting the calibration system properly such that it can be rolled over to the OMSS and positioned in its proper final position in relationship to the OMSS for installation. Once the Calibration unit is positioned properly with respect to the OMSS it will be fastened to the OMSS. Once the calibration unit has been safely attached to the OMSS during I&T, it will be detached from the integration cart. The integration cart will also be designed to permit the calibration unit to be oriented in various direction do that it can demonstrate in specification operation when subjected to various gravity vector orientations.

6.4.4 Optical Sensitivity analyses

6.4.4.1 LOWFS Alignment Sensitivity

The LOWFS has a requirement to maintain the pointing centration of the PSF on the focal plane mask to with 1 mas, rms over the observation period. This error is composed of two major parts: the random error (associated with how well we can sense this tilt) and the systematic error associated with how the optics/mechanics change in position and thereby introduce a false tilt into the LOWFS detector. The random errors of the measurement have been characterized and described in the section of performance simulation for the LOWFS. The results in the table below are the results of analytical calculation to determine impact of element variation on the residual tip/tilt on the sky. The derivation of these results is given in the appendix.

Element			Value	Equivalent value on sky
Focal Plane Mask	Displacement	x	0.25 um	0.102 mas
		y	0.25 um	0.102 mas
Re-collimation OAP	Tilt	α	0.06 arc sec	0.075 mas
		β	0.06 arc sec	0.075 mas
	Displacement	x	0.20 um	0.081 mas
		y	0.20 um	0.081 mas
Phasing Mirror	Tilt	α	0.06 arc sec	0.075 mas
		β	0.06 arc sec	0.075 mas
LOWFS Lens 1	Displacement	x	0.05 um	0.087 mas
		y	0.05 um	0.087 mas
LOWFS Fold Mirror	Tilt	α	0.5 arc sec	0.083 mas
		β	0.5 arc sec	0.083 mas
LOWFS Lens 2	Displacement	x	0.05 um	0.087 mas
		y	0.05 um	0.087 mas
LOWFS Lenslet	Displacement	x	0.01 um	0.057 mas
		y	0.01 um	0.057 mas
LOWFS Detector	Displacement	x	0.01 um	0.057 mas
		y	0.01 um	0.057 mas
			Sum X tilt	0.705 mas
			Sum Y tilt	0.705 mas
			Qsum	1.00 mas
			Qsum (all)	0.337 mas

The above analysis assumes that the errors for each element are random and uncorrelated so that the net effect can be estimated by taking a quadrature sum of the individual elements. This is not the case in a real opto-mechanical system where elements that are collocated tend to have a common proper motion. In this case, its possible for the individual elements to have errors much larger than in the table above, but the differential motion with neighboring elements is still small so the correlated motions tend to cancel each other.

We have performed a finite element analysis of calibration optical system under varying gravity vectors and modeled the induced displacements and tilts to determine the systematic effect of misalignments on the LOWFS tilt measurement. We did this analysis assuming that the calibration system was stiffly mounted to the AO system at three hard points defined by the back of the calibration mounting structure. We modeled the compliance of this flexure interface. We also modeled the mechanical properties of the breadboard with input to the details of the model provided by HIA. Gravity vector and instrument orientation cases were defined by HIA and run here at JPL to match completely. Specifically, Port 1 (side-looking) and port 3 (up-looking), Zenith angles at 20, 40 and 60 degrees and Cass Ring Rotations of 0, 30, 60, 90, 120, 150, 180, 210, 240, 270, 300 and 330 degrees. There was a nominal case for Port 1 and 3 at Zenith angle of 0 for each. This resulted in a total of 74 cases, 37 for each Port position.

Element			Range Port 1	Range Port 3
Focal Plane Mask	Displacement	x	-2.24 – +1.38 um	-0.29 – +1.96 um
		y	-0.804 – +0.937 um	-0.781 – +0.96 um
Re-collimation OAP	Tilt	α	-0.06 – +2.50 arc sec	-2.9 – +3.34 arc sec
		β	-0.20 – +1.42 arc sec	-0.04 – +0.187 arc sec
	Displacement	x	-1.549 – +1.051 um	-0.17 – +1.34 um
		y	-0.33 – +3.970 um	-3.9 – +4.68 um
Phasing Mirror	Tilt	α	+0.08 – +1.24 arc sec	-1.92 – +1.97 arc sec
		β	-0.208 – +0.162 arc sec	-0.033 – +0.193 arc sec
LOWFS Lens 1	Displacement	x	-1.44 – +1.19 um	-0.05 – +1.127 um
		y	-0.38 – +4.97 um	-5.04 – +5.93 um
LOWFS Fold Mirror	Tilt	α	+0.062 – +2.34 arc sec	-3.102 – +3.48 arc sec
		β	-0.18 – +0.171 arc sec	-0.010 – +0.155 arc sec
LOWFS Lens 2	Displacement	x	+0.07 – +1.88 um	-2.525 – +2.885 um
		y	-0.34 – +5.63 um	-5.961 – +6.819 um
LOWFS Lenslet	Displacement	x	+0.07 – +1.86 um	-2.538 – +2.882 um
		y	-0.34 – +5.62 um	-6.044 – +6.796 um
LOWFS Detector	Displacement	x	+0.08 – +1.86 um	-2.544 – +2.876 um
		y	-0.33 – +5.62 um	-6.071 – +6.799 um

The table above list the ranges of the values assumed by the different elements over the range of the gravity cases for the two ports. At first blush, it would appear that these motions are significant given that the range of these modeled misalignments is larger than the values in the un-correlated case by as much as a factor of 100. On closer inspection however, its evident that the motion of some optics are

indeed highly correlated (i.e., the LOWFS lenslet and LOWFS Detector). A linear sum of the individual errors gives the magnitude of the final pointing error in two axes. It's difficult to quantify this in a simple graph, so below we show magnitude of the resulting pointing error due from flexure induced optical misalignments for the two different ports. To be clear, on the x-axis, FEA Cases 1 – 12 correspond to a Zenith of 20 degrees, Cases 13 – 24 to a Zenith of 40 degrees, and 25 – 36 to Zenith of 60 degrees; so to consider tracking a single target, we should compare e.g. the reference case (zenith) to case 1 (20 degrees) to Case 13 (40 degrees.) We have goal of maintaining a pointing stability of 1 mas on the focal plane mask over a 1 hour observation. This translets into <1.3 mas in change over the 20 degree Zenith angle shifts shown here. It can be seen that the displacements from the reference to 20 degrees (Case 1-12) are of this order but slightly exceed the requirement; from 20-40 degrees the displacements are more significant. Open-loop correction or re-calibration half-way-through a science exposure may be necessary, but overall the motions are encouragingly close to the goals. It can also be seen that some rotator orientations are more stable than others, another aspect that will be studied in CDR to develop preferred observing orientations.

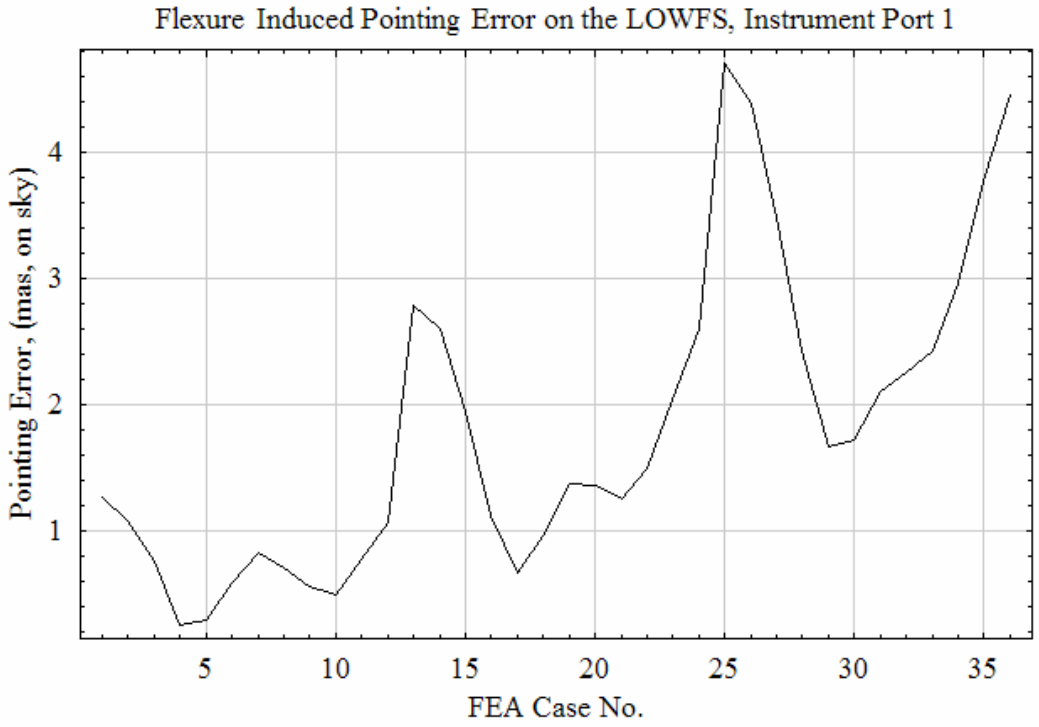

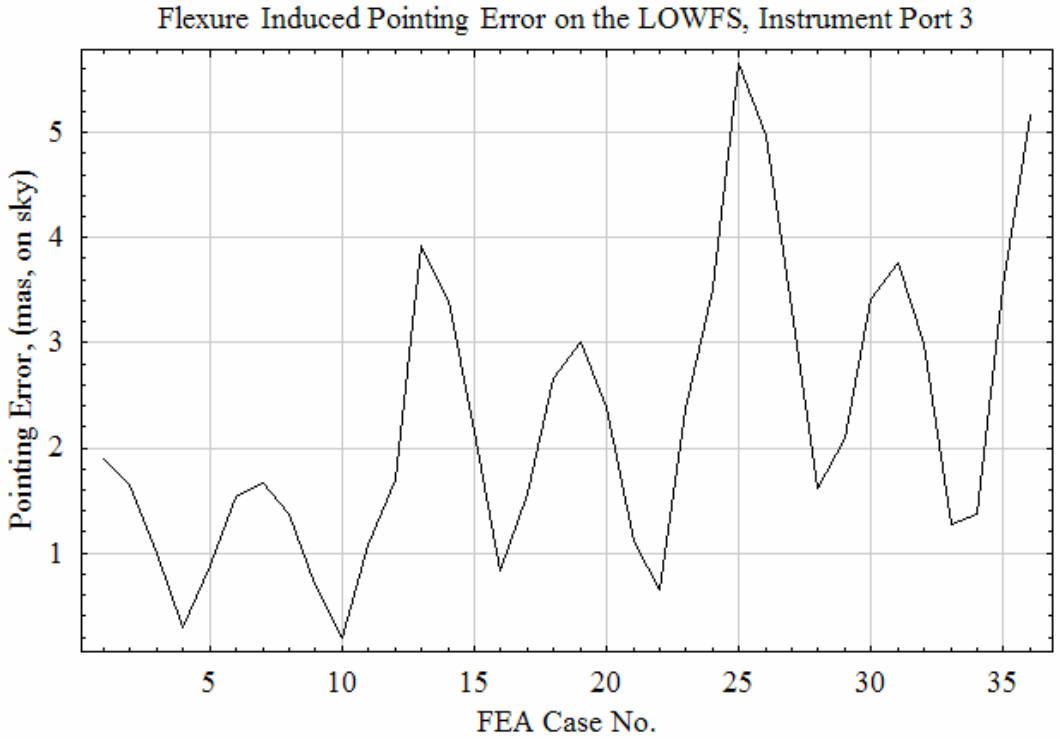

Figure 6-22 Magnitude of flexure induced pointing error on the LOWFS. FEA Cases 1 – 12 are for a Zenith of 20 degrees, Cases 13 – 24 are for Zenith of 40 degrees, and Cases 25 – 36 are for Zenith of 60 degrees. Our goal is to maintain a 1 mas pointing accuracy on the focal plane mask during an observation. This will not be possible over all Zenith angles without intermittent re-calibration.

6.4.4.2 HOWFS Alignment Sensitivity

The HOWFS alignment is driven primarily by the need to maintain the one-to-one registration of the HOWFS focal plane array pixels with the tweeter elements. A single HOWFS pixel is 40 microns, and its reasonable to expect a registration error to within 10% of a single pixel (4 microns) is a reasonable goal. In a similar fashion to the LOWFS sensitivity analysis, the contribution of each element to misalignment is given in the table below:

Element			Value	Equivalent Pupil Shear, HOWFS FPA
Focal Plane Mask	Tilt	α	1.5 arc sec	0.829 um
		β	1.5 arc sec	0.829 um
Science OAP	Tilt	α	0.8 arc sec	0.976 um
		β	0.8 arc sec	0. 976 um
	Displacement	x	2 um	0.794 um
		y	2 um	0.794 um
HOWFS Re-combination Beamsplitter	Tilt	α	3 arc sec	0.98 um
		β	3 arc sec	0.98 um

Merge Fold Mirror	Tilt	α	6 arc sec	0.954 um
		β	6 arc sec	0.954 um
HOWFS Fold Mirror	Tilt	α	0.5 arc sec	0.882 um
		β	0.5 arc sec	0.882 um
HOWFS Pupil Lens	Displacement	x	5 um	0.9 um
		y	5 um	0.9 um
HOWFS Small Lens	Displacement	x	0.9 um	0.9 um
		y	0.9 um	0.9 um
HOWFS 1:1 Relay Lens	Displacement	x	0.9 um	0.9 um
		y	0.9 um	0.9 um
HOWFS Detector	Displacement	x	0.9 um	0.9 um
		y	0.9 um	0.9 um
			Sum X tilt	9 um
			Sum Y tilt	9 um
			Qsum	12.75 um
			Qsum (all)	4.04 um

Element			Range Port 1	Range Port 3
Focal Plane Mask	Tilt	α	-0.186 – +1.48 arc sec	-1.718 – +1.101 arc sec
		β	-0.163 – +0.177 arc sec	-0.010 – +0.149 arc sec
Science OAP	Tilt	α	-1.95 – +2.21 arc sec	-1.852 – +2.32 arc sec
		β	-0.255 – +0.330 arc sec	-0.058 – +0.311 arc sec
	Displacement	x	-3.83 – +3.66 um	-0.52 – +3.76 um
		y	-3.925 – +3.975 um	-4.176 – +3.724 um
HOWFS Re-combination Beamsplitter	Tilt	α	+0.08 – +1.79 arc sec	-2.51 – +2.81 arc sec
		β	-0.180 – +0.172 arc sec	-0.019 – +0.169 arc sec
Merge Fold Mirror	Tilt	α	-0.173 – +1.33 arc sec	-0.914 – +1.52 arc sec
		β	-0.152 – +0.178 arc sec	-0.029 – +0.169 arc sec
HOWFS Fold Mirror	Tilt	α	-0.173 – +1.33 arc sec	-0.914 – +1.52 arc sec
		β	-0.152 – +0.178 arc sec	-0.029 – +0.169 arc sec
HOWFS Pupil Lens	Displacement	x	-1.03 – +1.7 um	-0.16 – +1.432 um
		y	-0.28 – +1.371 um	-1.35 – +1.247 um
HOWFS Small Lens	Displacement	x	-1.74 – +2.00 um	-0.02 – +1.47 um
		y	-1.54 – +2.01 um	-2.05 – +1.11 um
HOWFS 1:1 Relay Lens	Displacement	x	-2.25 – +2.24 um	-0.15 – +2.014 um
		y	-2.14 – +2.56 um	-2.72 – +1.33 um
HOWFS Detector	Displacement	x	-2.30 – +2.31 um	-0.17 – +2.08 um
		y	-2.50 – +2.85 um	-3.08 – +1.45 um

Like the LOWFS sensitivity analysis, these excursions appear large but are largely correlated. The sum of the contributing elements are linearly summed for a given instrument orientation, and the resultant vector pupil shear displacement can be determined. In the plots below, we plot the magnitude of this shear for two different instrument Ports and for the different Zenith and Cass angles. Although pupil

shear is at worst ~5% of a subaperture in the extreme case, and it is well below that for the vast majority of cases. This suggests that HOWFS FPA and tweeter co-registration need occur only infrequently.

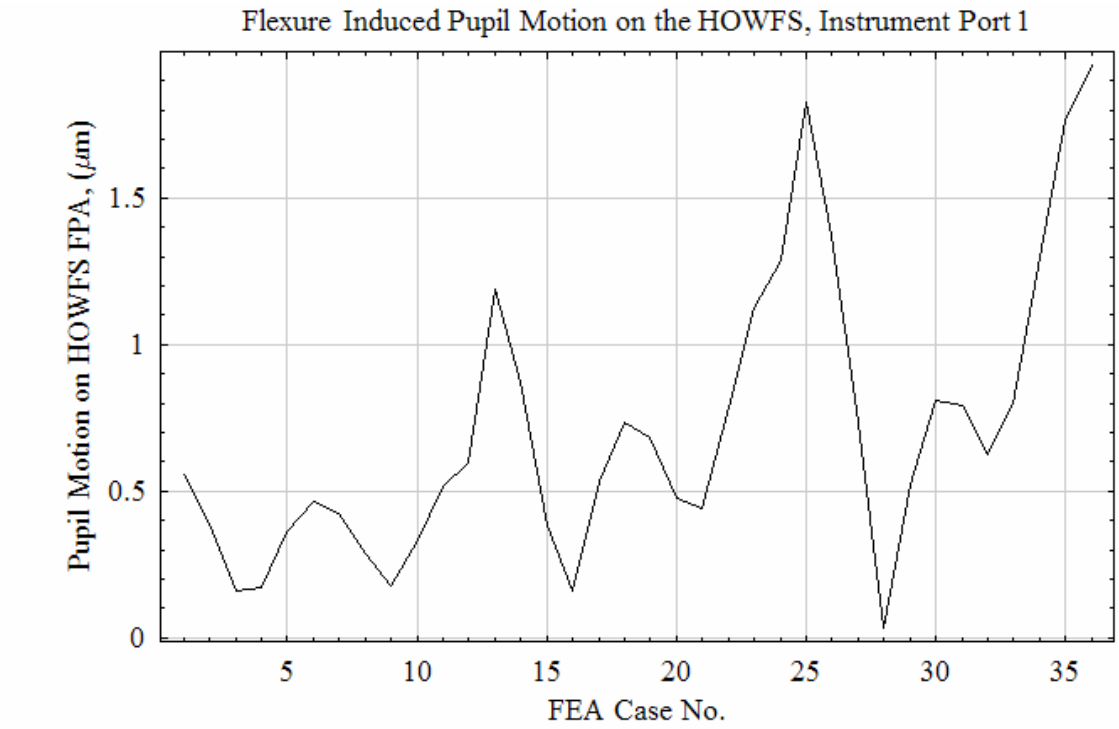

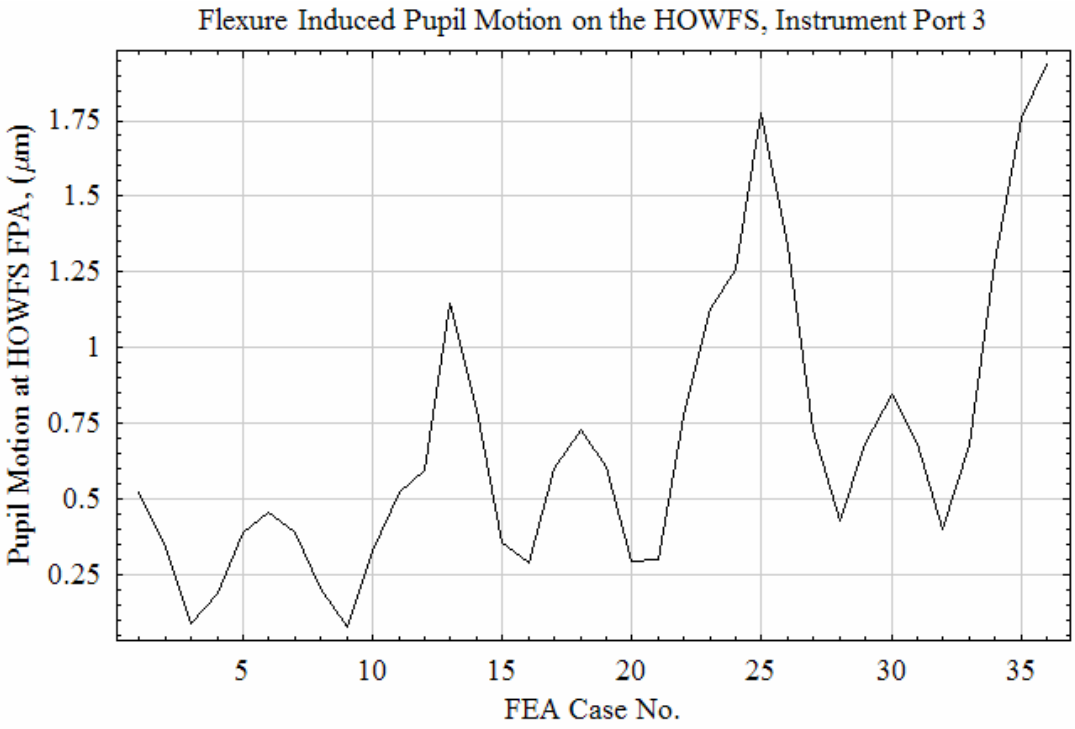

Figure 6-23 Magnitude of flexure induced pupil shear on the HOWFS FPA. FEA Cases 1 – 12 are for a Zenith of 20 degrees, Cases 13 – 24 are for Zenith of 40 degrees, and Cases 25 – 36 are for Zenith of 60 degrees. Our goal is to maintain registration to within 10% of a HOWFS pixel (4 um) accuracy during an observation. Analysis shows that this can be achieved to within 5% over the whole range of simulation orientations.

6.5 Instrumentation (Components)

6.5.1.1 HOWFS Camera

The wavelength range, noise, and frame rate requirements for a CAL HOWFS array reduce the choices to HgCdTe (MCT) devices from Teledyne (former Rockwell) and Raytheon (former SBRC). Arrays made of InSb would work but require much colder operating temperatures, and the 2.6 um version of InGaAs has more noise and dark current than desirable. Of the MCT arrays available currently, the ALADDIN chip from Raytheon would work but at 1024x1024 is much larger than is needed. The PICNIC device from Teledyne, at 256x256 with four readout ports, is a reasonable match to the HOWFS task. To support high QE at the shortest science wavelength of 1.05 μm, a backside illuminated version may be selected.

By imaging the two pupil images onto matching corners of two quadrants, each pupil is read out of a port. At 500 KHz per port on a 50 x 50 image, a reset or read operation takes 5.51 msec. The allowable frame rates and exposure times in a reset-read-read pattern are given by:

$$f = \frac{500KHz}{(50+4)(50+1)(3+n)} \quad , \qquad \text{Equation 6.5.1}$$

$$t = (2\mu\text{sec})(50+4)(50+1)(1+n)$$

where n = 0 to 255. Notice that the fastest frame rate, 60.52 Hz, has a 5.51 msec effective integration time, only 1/3 of the frame time. This very large timing overhead shrinks quickly as the frame rate becomes slower, plus more advanced readout schemes such as Fowler sampling become possible. All this must be considered in optimizing the frame rate of the camera.

6.5.1.2 HOWFS Update Rate.

The update rate of the complete HOWFS, that is, the rate at which a new measure of wave front error is available, is equal to the frame rate if only phase errors are measured (an "AC" measurement sequence), and one half the frame rate if both phase and amplitude errors are measured (an "ABCD" sequence).

6.5.1.3 HOWFS Interface.

The interface to the HOWFS camera is the Matrox O 10G 5M DBCLE, a combined framegrabber and vision processor in the Odyssey line. Figure 6-24 shows the internal organization of the board.

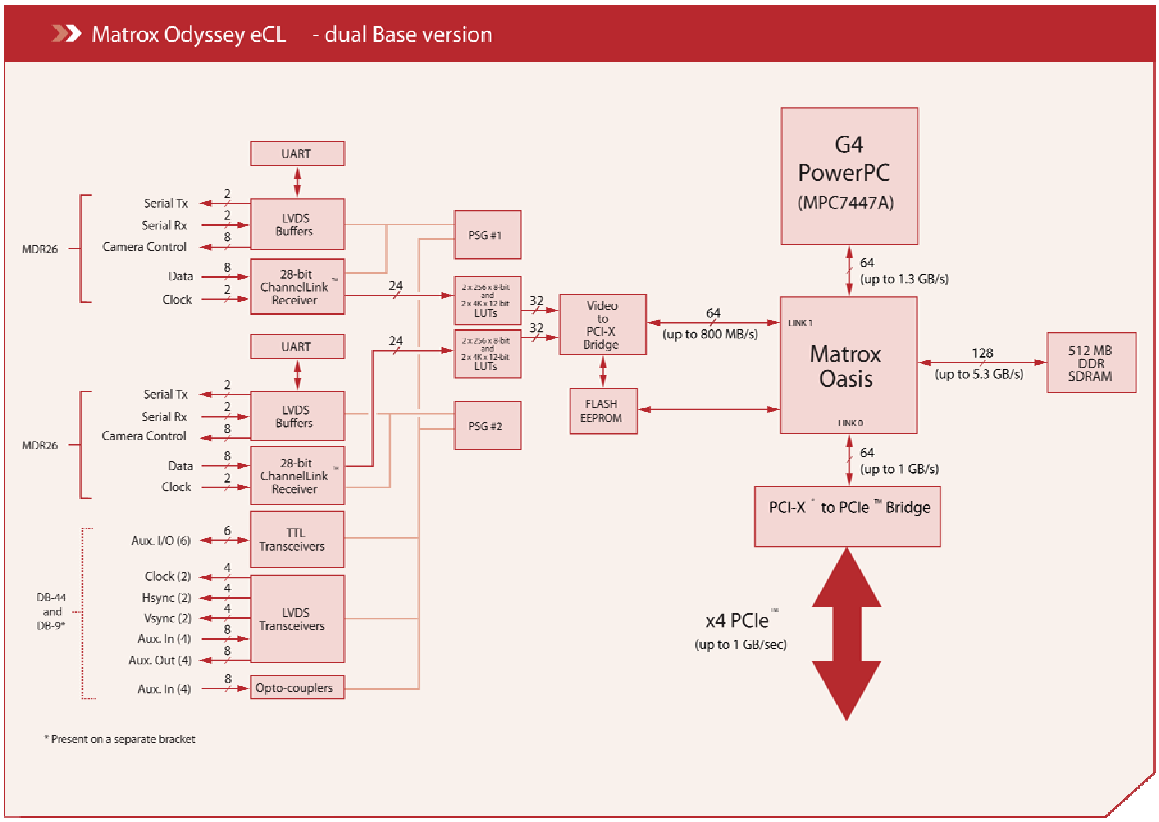

Figure 6-24 HOWFS Interface and RT Processor - Block Diagram

We propose to perform all CAL real-time processing on this board plus the corresponding LOWFS interface board. Section 6.5.2.2.1 will discuss frame synchronization with the PZT-driven scanning mirror, and section 6.6.4 will discuss the HOWFS and LOWFS processing algorithms and data flow.

6.5.1.4 LOWFS Camera

The requirements on the LOWFS camera are considerably less severe than for the HOWFS camera, and accordingly the camera can be much simpler. The LOWFS camera receives directly the bright central beam through the occulting mask, and divides that light up into fewer subapertures. Also, because the atmospheric dispersion corrector for the instrument is a broad-band design, the LOWFS works with broad-band light, i.e., without a filter wheel.

The number of subapertures in the LOWFS flows down from its function of measuring those wave front errors that make it through the occulting hole, 0 to 4 cycles per pupil or so. This requirement and its connection to science requirements have been the subject of some discussion in the larger GPI group, leading to an agreement to start with the plausible configuration of a 7-across Shack-Hartmann WFS and then to analyze its performance (Section 6.2.4). The LOWFS optics (Section 6.3.3) is designed to change dimensionality with relative ease, should this be indicated.

The camera proposed for the LOWFS is the Goodrich/Sensors Unlimited SU320KTX-1.7RT InGaAs camera. The following are important camera properties; a full description is in Appendix 6.5.

- 320 x 240 pixels, 40 um pitch
- QE > 60%, 0.9 to 1.7 um
- 50 electrons noise
- 60 Hz frame rate
- Exposure time 127 usec to 16.27 msec.
- Uncooled operation
- Complete camera is 270 gm, 1.8 W
- Standard Camera-Link interface

Figure 6-4 shows how the Shack-Hartmann spots overlay the pixels of the LOWFS camera. The lenslet array, with 200 um pitch, directly images onto the focal plane, with 40 um pitch, with no intermediate optics. Both the focal plane array and the lenslet array are considerably oversized. If a different order LOWFS is desired, only the simple relay optics before the lenslet need to be modified to change the pupil diameter at the lenslet array.

The computer interface for both the LOWFS camera and the Pinhole camera (see next section) is the Matrox HEL 2M DBCL E board, in the Helios eCL line. This is a dual Camera-Link interface with some on-board processing. This frame grabber board will extract the 40x40 region of interest shown in Figure 6-4, perform background subtraction and flat fielding, and compute spot intensities and x- and y-differences. It then performs any needed frame averaging, and forwards these reduced data to the HOWFS board for further processing and the merger of HOWFS and LOWFS data. The transfer size is 3x45 floats, or 540 bytes. The transfer may occur via DMA, or via auxiliary digital I/O. Raw images and other intermediate data are available on request from the host.

6.5.1.5 Pinhole Camera

The camera proposed for the pinhole camera is the same as for the LOWFS -- the Goodrich/Sensors Unlimited SU320KTX-1.7RT InGaAs camera. A single frame-grabber board, described above, supports both cameras, which need not be synchronized. For the Pinhole camera, the frame grabber performs background subtraction and flat-fielding only, then passes the full image to the host. The host then performs any feature extraction and control algorithms, and commands actuators to keep the image centered on the pinhole, on a relatively slow time scale.

6.5.2 Calibration Cameras

6.5.2.1 System overview of the instrument from the electronics perspective.

Figure 6-25 shows the organization of the CAL electronics. Three cameras, two shutters and several motors and piezo-electric translators reside on the optical bench. The two framegrabber boards for the three cameras reside inside the rack-mounted CAL computer. Much of the remaining electronics, namely the PZT Driver Board, the Shutter Driver, the Motor Controller and all power supplies, reside in a 3U chassis which can be pulled out of the electronics rack for servicing. The cryocooler drive electronic are too large for this chassis, and will be mounted separately in the back of the rack. They are in a closed canister, with no switches or indicators, and are commanded by serial connection.

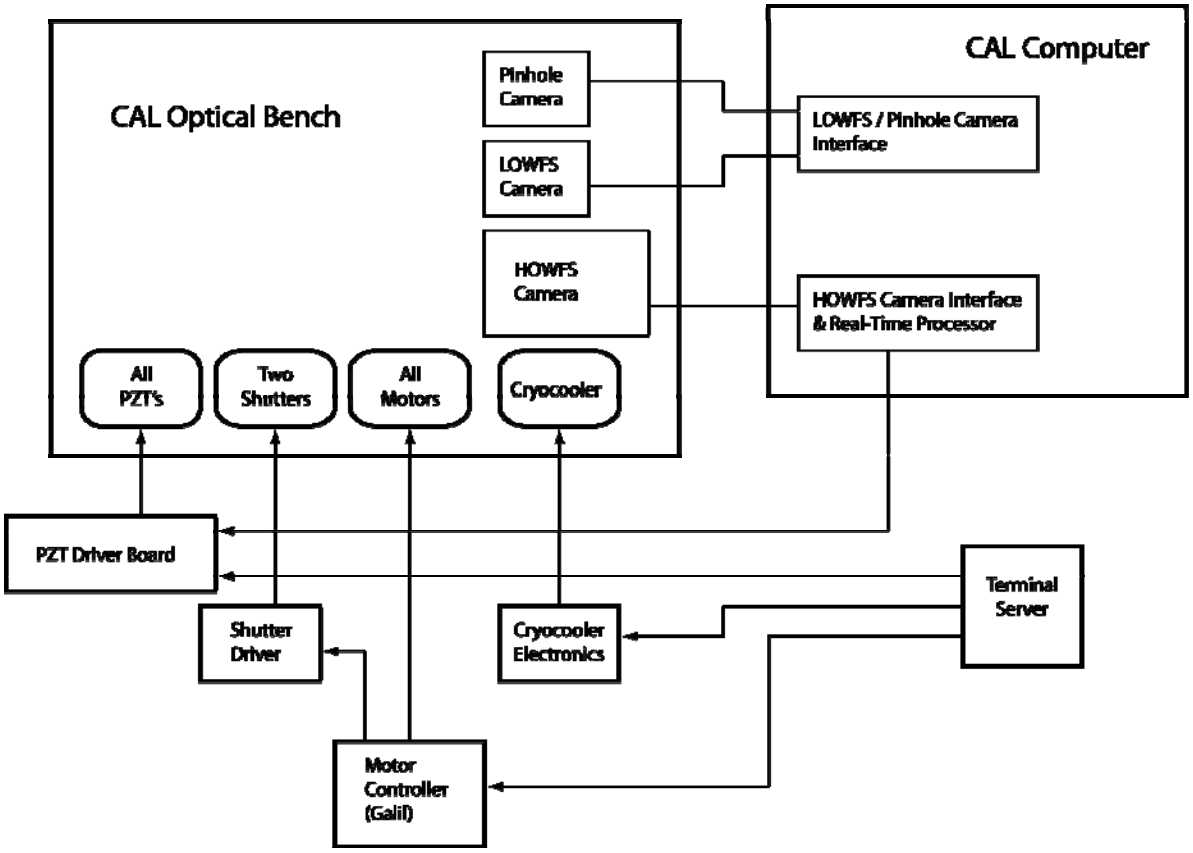

Figure 6-25 CAL Instrument Control Physical Overview

6.5.2.2 CAL Mechanisms and Electronic Subsystems

An exhaustive list of all mechanisms, electronics and cables for the CAL system can be found in Appendix 6.5, as "Enumerated GPI CAL Electronics List". Figure 6-26 shows the CAL cabling and electronics in graphical form. A summary of the kinds of mechanisms and electronics follows:

The CAL computer is a commercial rack-mounted unit, as similar as possible to the other computers in GPI. The only special requirements are: two full-length PCIe slots, at least x4, for the framegrabber boards. The piezoelectric translators (PZTs) are all commercial units, from Physik Instrumente. The LOWFS and Pinhole cameras are commercial SU320KTX-1.7RT units from Goodrich/Sensors Unlimited. Motors, shutters and motor drive electronics are all commercial. The motor drive electronics are the Galil models selected as the GPI standard. Cables and connectors are common with the rest of GPI.

The HOWFS camera is a mixture of commercial and custom pieces. The focal plane is a standard Teledyne product, and its control electronics are slightly modified version of their Microcam product. The modifications consist of firmware changes to support the dual 50x50 readout, and hardware changes to support 500KHz pixel rate. The cooler and cooler controller for the camera are commercial products. The dewar is a custom fabrication.

The PZT Driver Board is a custom design. It is described in the next section.

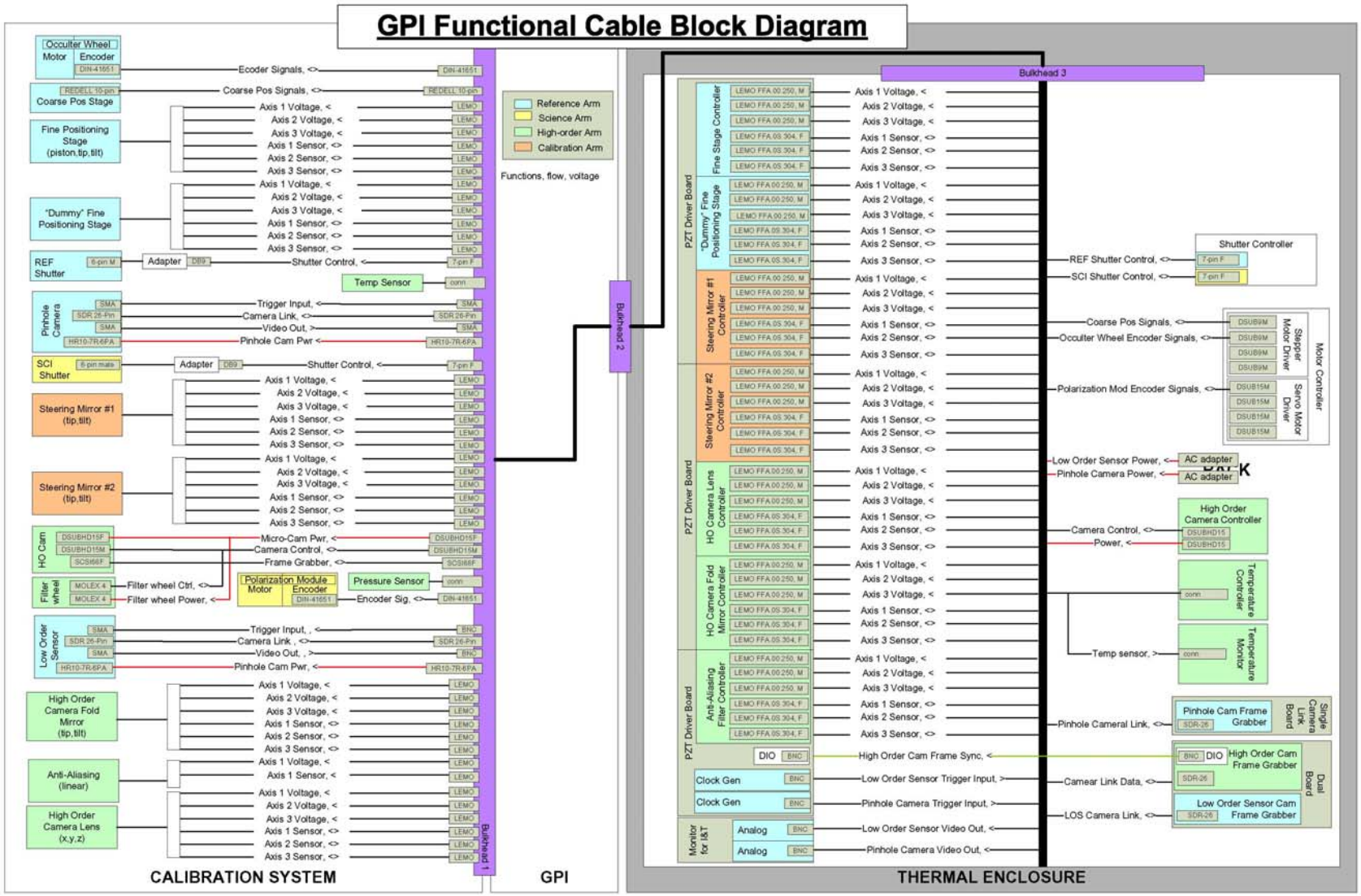

Figure 6-26 Cabling and Electronics Summary

6.5.2.2.1 PZT Driver Board

The only custom electronics proposed for the CAL system is a multi-channel PZT Driver Board. The justification is the large number of PZT translators being driven and the requirement to support PZT scanning synchronized with the HOWFS camera exposures. As many as twelve channels of PZT are needed for the Cal subsystem, six of which are "Scanning PZTs". Most channels will require strain gauge feedback. A sixteen channel board is proposed, to provide spares and expansion space.

The block diagram of the PZT Driver Board is shown in Figure 6-27.

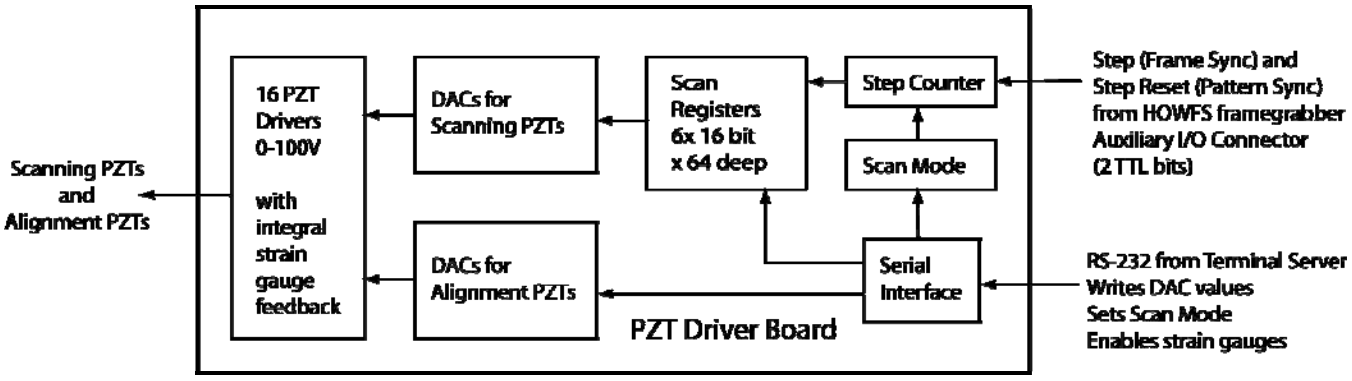

Figure 6-27 PZT Drive Board Block Diagram

"Scanning PZTs" are the six PZTs that are the fine positioners for the interferometer mirror. When "scan mode" is enabled, a set of preset positions are stepped through in synchronism with exposures of the HOWFS camera. This is to support "ABCD", or time-slice, frame accumulation, and the subsequent (A-C) and (B-D) subtraction to obtain wave front data. Up to 64 preset positions are stored in Scan Registers, which are written to from a serial interface.

Synchronization with the HOWFS is provided by connecting two digital-out bits on the Auxiliary I/O header on the HOWFS interface board with Step and Step Reset inputs on the PZT driver board, via shielded cable. A transition on the Step input moves all the scanned outputs to the next preset. If Step Reset is high, the outputs move asynchronously to the starting preset. The HOWFS real-time software, embedded on the HOWFS interface board, is responsible for generating these sync signals in coordination with acquiring and processing frames from the HOWFS.

"Scan Mode" is a register which is written to from the serial interface. It is a byte, where bit 7 enables or disables scanning, and bits 0-5 encode which preset of 64 is active if scanning is disabled. The power up default is 0x0, which is "scanning disabled, preset zero".

Not shown is a 16 bit register to enable and disable strain gauge feedback by channel. This is both for configuration and to aid in remote diagnostics.

Besides the Scanning PZTs, there are 10 channels of Alignment PZTs which are driven statically. The DACs for these channels are written to directly from the serial interface.

The serial interface is to be connected to the GPI/CAL terminal server.

All logic for the board including the serial interface will reside in a small CPLD. To support the use of this board in applications where the scanning feature is not needed, scanning functions will be disabled and all channels will act as Alignment PZTs if the sync cable is not connected.

6.6 Instrument Control

6.6.1 CAL Instrument Control Physical and Logical Overview

6.6.1.1 Physical Overview

Figure 6-25 summarizes CAL instrument control from a physical perspective. There is the CAL computer itself, containing the two camera interfaces cards described in 6.5.1.1, and a terminal server providing a remote serial interfaces to a motor controller, the cryocooler electronics, and the PZT driver board. Shutters are controlled indirectly, via auxiliary digital outputs on the motor controller wired to the shutter driver. Synchronization of HOWFS camera exposures with PZT drive is provided by auxiliary digital outputs on the HOWFS camera interface. CAL real-time control will be described in detail in 6.6.4.

6.6.1.2 Logical Overview.

The CAL software system is constrained on three boundaries: One, the electro-mechanical hardware that must be signaled and read in order to collect all of the necessary data. Two, functional and communication requirements being imposed upon the CAL system from the TLC and AOC. Three, the architectural requirements being imposed upon the GPI instruments from the Gemini system. Within this chapter we will attempt to cover the influence of these three boundaries upon the architecture and design of the CAL system starting with one in Section 6.6.1 and then a combination of two and three in the remaining sections.

In order to keep a very detailed architecture and design discussion of the CAL software brief, I will be using the patterns listed in “Design Patterns: Elements of Reusable Object-Oriented Software” to convey the concise meaning of complex ideas. Also, it will be helpful if the reader knows UML syntax for a Finite State Machine (FSM). For a complete understanding of the architecture and design of the CAL software system, please refer to SRS, SDD, and ICD in Chapter 3.

6.6.1.3 Software Requirements

All direct requirements for the CAL system software have been mapped to requirements from Gemini, GPI instrument, and TLC requirements. A detailed table of this mapping is in Appendix 6.6.

6.6.1.4 CAL System Software Architecture – Overview and Ground Rules

In the architecture given, (below) each of the bubbles will be developed independently allowing for a surrogate to replace any (or all) of the actual implementations satisfying the testing and integration

requirements. This also means that there is no actual implementation delivery dependence, but there is a dependence between the TLC and CAL that defines the RPC interface and between the CAL and GMB that defines the shared memory interface. Both of those units could then supply stub surrogates for the CAL to develop against and possibly functional surrogates until full-up integration. Here are the rules for the CAL system architecture:

1. Model, View, Controller pattern (MVC) is to be used to separate the CAL system into manageable parts. In the bubble picture, the TLC, RPC Handler, and RPC/XML translator are the controller. The State Monitor, Telemetry Monitor, and GMB are the view. Lastly, the Cal Control is the model. Advantage of the MVC pattern is that it is well known in the industry and shown to work extremely well for keeping a system decoupled.
2. Use and label design patterns in all class diagrams to improve maintainability and readability.
3. Dependencies must be unidirectional to improve maintainability. Circular dependencies are extremely hazardous to the well-being of a software design as they add severe brittleness.
4. Threading synchronization regions (overlap or rendezvous) must be minimized to improve maintainability and performance.
5. Use Façade and Strategy patterns liberally to improve plugability and extensibility. (see Refernce to the book, 'Design Patterns')
6. XML is used for communication among the model, view, and controller internal to the CAL system. Advantages of XML are that it is human readable.
7. Communications among the model, view, and controller should implement an observer pattern. Advantages of an observer pattern are: adding a debug observer is trivial, and since the data being broadcast is XML, the human can already read it.

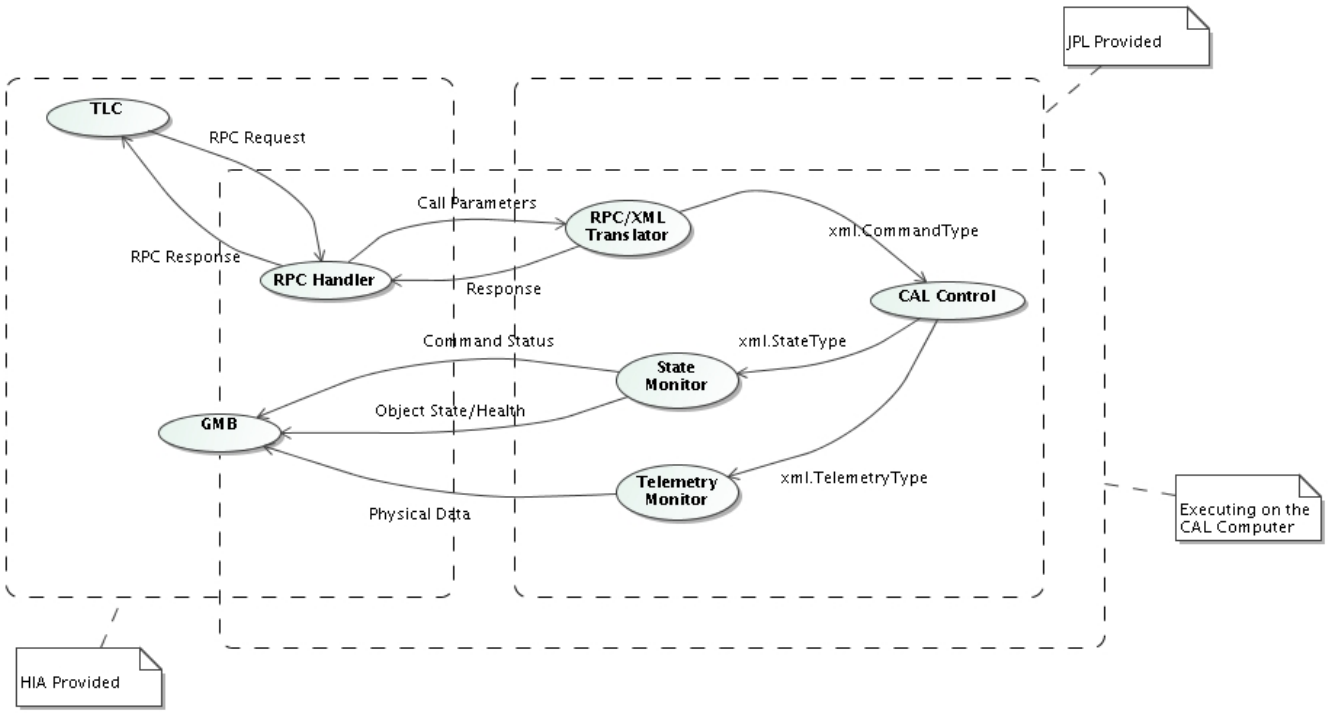

Figure 6-28

6.6.2 CAL Software Sequencing, Data formats and Dictionary

(SW 3) CAL – Information should be included on items to be controlled, sequencing issues, and FITS data formats the instrument will write. The initial dictionary of status items and configuration items should be produced.

6.6.2.1 Items To Be Controlled

From Figure 6-1, the devices of concern for the software (require software drivers):

- 6 PZTs at the phasing mirror (GPI-CALS-002-000-000)
- 3 PZTs at Fold Mirror (GPI-CALS-008-000-000)
- 2 PZTs at Anti-Alias Filter (GPI-CALS-010-000-000)
- LOWFS and HOWFS via RTC (GPI-CALS-003-000-000 and ??)
- Pinhole camera (GPI-CALS-014-000-000)
- Movable lens before LOWFS for pupil alignment
- Slow[2] devices that require communications with the TLC in order to actuate.
- 3 motors HOWFS Lens (GPI-CALS-009-000-000)
- 1 motor phasing mirror (GPI-CALS-002-000-000)
- 2 shutters
- chromatic filter wheel (GPI-CALS-012-000-000)

As can be seen from the list of devices that there are three classes of drivers that will be needed: 1. PZT driver, 2. camera driver, and 3. TLC track mode driver. A strategy pattern wraps the drivers and the complexity of the coordinated moves is delegated to a Component (see Section 6.6.3 for details) within the CAL system. The short list of items also enumerates the commands needed for the lowest level of control that needs to be exposed to external systems.

6.6.2.2 Initial Dictionary

An initial dictionary has been produced, and is in section 7.2 of the GPI_TLC_CAL_ICD. The complete dictionary is far too large to include here. Here is the HOWFS subset as a sample. A similar set exists for each of the movable components in the CAL system: Phasing mirror, LOWFS, pinhole camera, HOWFS fold, anti-aliasing filter, and the environment.

2 The definition of slow is defined in the GPI_SDD_Overall section 6.5 (version of 23 APR 07)

Status Name	Type	Range	Description
cal.howfs			High Order Wave Front Sensor
registration	integer[2]	0 <= i <= 3	[pixels] Maps sysAmp(0, 0) to amp(m, n) where m and n are indices 0 and 1 resprectively.
dark	unsigned short[50][50]	0 <= x < 2^14	The dark image to be used for background subtraction
flat	unsigned short[5][50]	0 <= x < 2^14	The flat field image to be sued for scaling
gains	float[50][50]		Calibrated gains for the amplitude and phase maps
sysAmp	float[47][47]	float range	[?] Measured amplitude error that has been merged with LOWFS data
sysPhase	float[47][47]	float range	[radians] Measured phase error that has been merged with LOWFS data
amp	float[50][50]	float range	[?] The last measured amplitude error
phase	float [50][50]	float range	[radians] The last measured phase error
avgCount	unsigned byte	0 <= i <= 255	Number of images to average over
ampAvg	float[50][50]	float range	[?] avgCount of amplitude error images averaged together
phaseAvg	float[50[50]	float range	[radians] avgCount of phase error images averaged together
stepCount	unsigned byte	0 <= i <= 255	Number of phasing meter steps used between one wavelength to compute the amplitude and phase error images
steps	unsigned short[64][50][50]	0 <= i < 2^14	A stack of raw images that used were used for computing amp and phase
science	float[50][50]	0.0 <= x <= 2.0^14	An averaged image that is the transmission map of the science arm
reference	float[50][50]	0.0 <= x <= 2.0^14	An averaged image that is the transmission map of the reference arm
ratio	float	float range	LOWFS Flux divided by the HOWFS Flux

Internal CAL sequencing uses Finite State Machine (FSM) technology (see section 6.1.1 for details on substate machines). The substate machines are independent and can be executed in any order, however, the required conditions for each of the substate machines (see GPI_ICD_TLC_CAL in the Volume 3) states the ordering that will produce meaningful results.

6.6.3 CAL Software Flow Diagram

The software design should be described to the level of detail required to explain how the system will operate under typical required situations using a uniform methodology such as UML, data flow diagrams, or other graphical representations.

Most of the system being documented here already exists from previous efforts at JPL such as the High Contrast Imaging Test Bed (HCIT) and several segmented telescip technology efforts. They are being reused to reduce cost and schedule impact. I have tried to highlight the new parts but may have bits here and there. Unless specifically mention as new, then it assumed already implemented, tested, and being used on some other project at JPL.

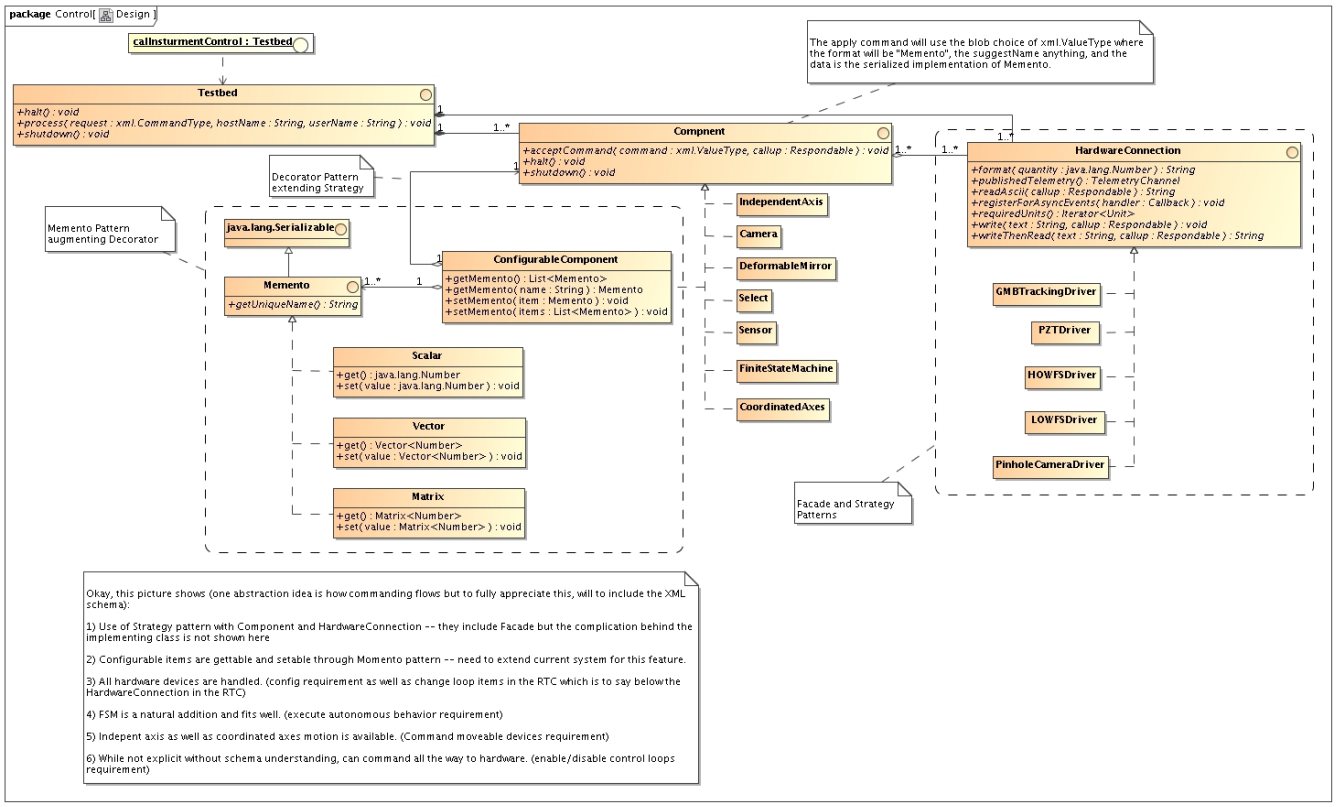

Figure 6-29

Figure 6-29 is design for the Model meeting Gemini architectural rules, configuration, and other requirements. The interfaces are actually facade patterns as well as strategy patterns that allow the system to be extended without system rewrites or refactoring. The memento pattern was used to add the run-time configuration requirement. Two new implementations of the Component have been added to meet the autonomous behavior requirement and coordinated motion. New drivers will be required for the camera and are immediately usable because the HardwareConnection uses the strategy pattern.

Figure 6-29 is designed for the Controller meeting commanding requirements. All of this design and implementation is new. While I currently support C/C++, python, and bash interfaces to the existing system, the use of RPC will be new. However, since the RPC calls will be in C/C++ I do not foresee any potential problems. The design basically uses an abstract method (pure virtual in C/C++ lingo) and then inheritance to define what that abstract method means in each new class. Polymorphism will then do the work calling the correct concrete implementation of the abstract method. This is plain and simple extension through inheritance.

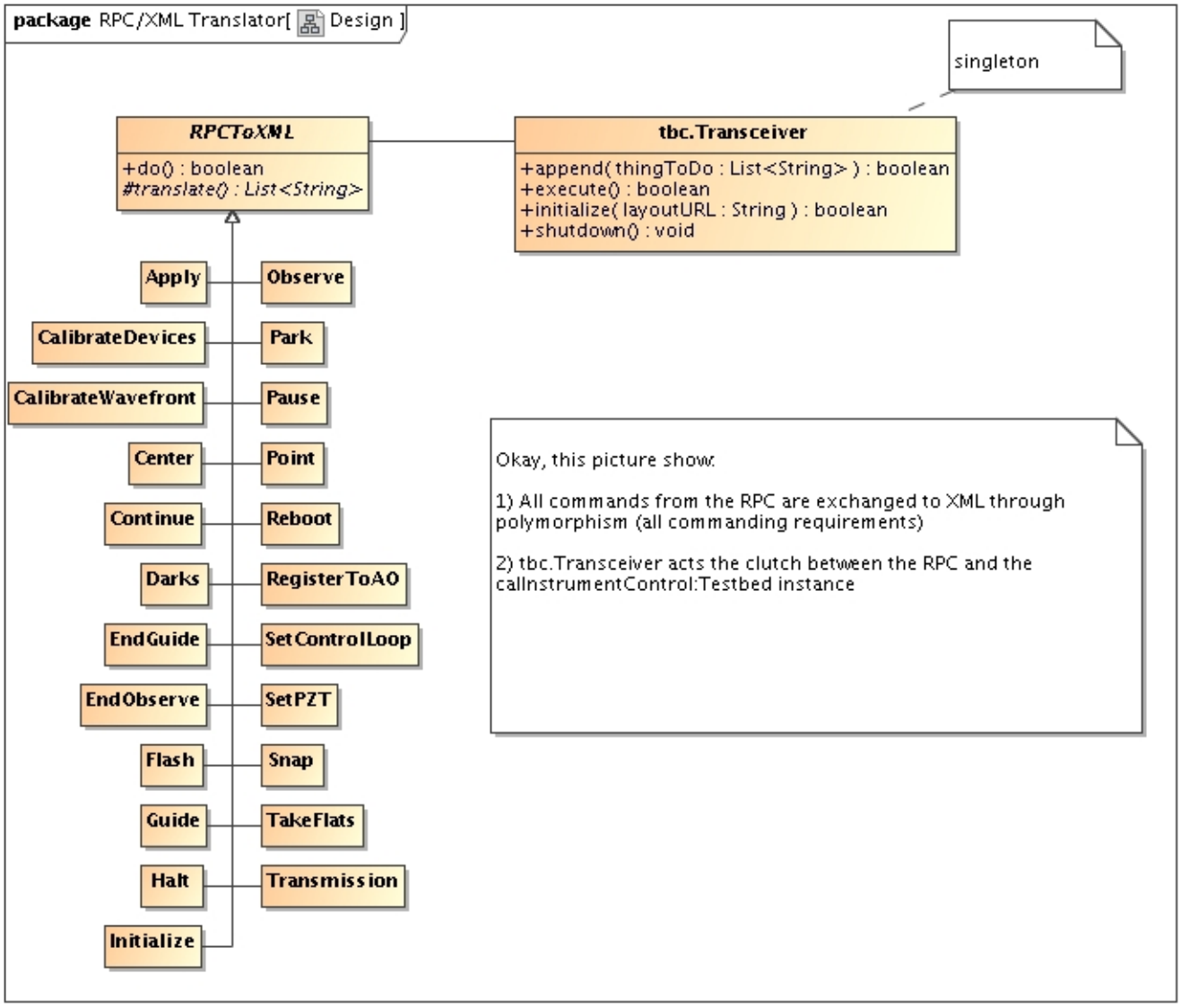

Figure 6-30

is designed for the Controller meeting commanding requirements. All of this design and implementation is new. While I currently support C/C++, python, and bash interfaces to the existing system, the use of RPC will be new. However, since the RPC calls will be in C/C++ I do not foresee any potential problems. The design basically uses an abstract method (pure virtual in C/C++ lingo) and then inheritance to define what that abstract method means in each new class. Polymorphism will then do the work calling the correct concrete implementation of the abstract method. This is plain and simple extension through inheritance.

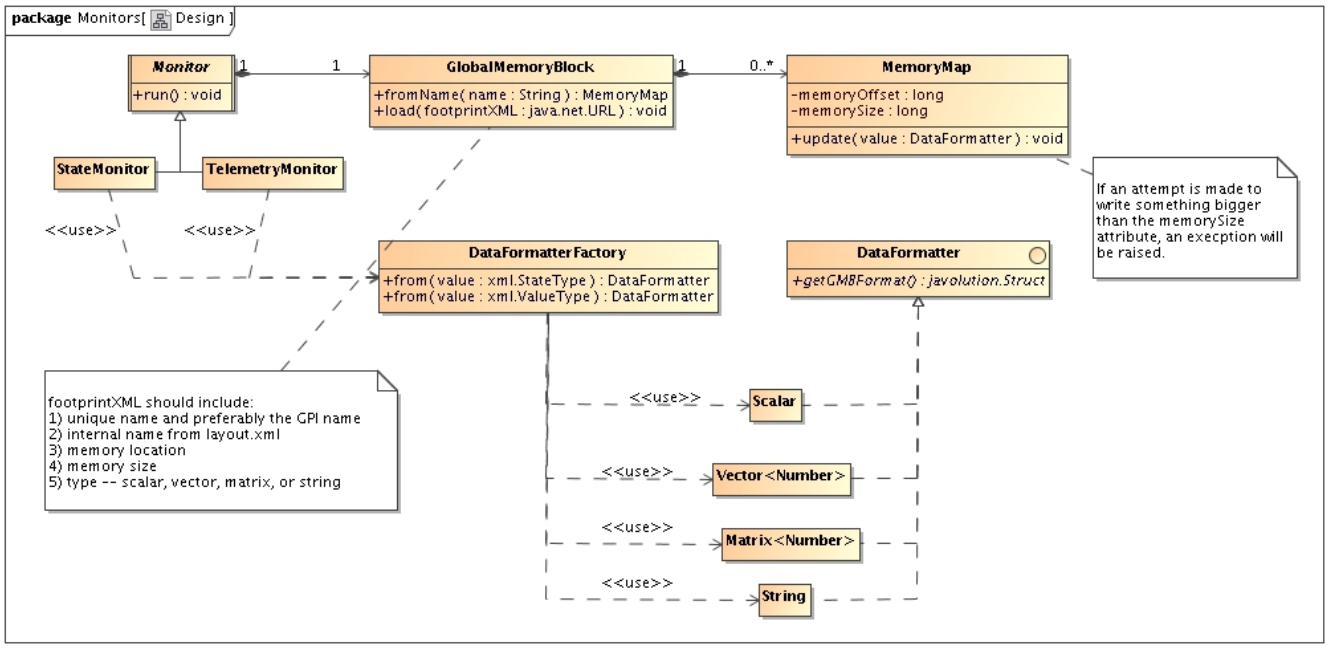

Figure 6-31

Figure 6-31 is designed for the View meeting telemetry and health/status requirements, and, while I have lots of different monitors currently, none of them do this translation. We have a couple of key items in this diagram to cover that turned out to be more difficult than expected. Somewhere in the bowels of the CAL system a HardwareConnection or Component decides it has a status or telemetry item it needs to report. The HardwareConnection or Component takes that piece of information and wraps it up in either a TelemetryType or StatusType and sends it out to the broadcaster in the observer pattern – see section 6.6.7 for the gory details of how this works. It is then one of the two monitors that receive the new data and the diagram below becomes important. Unfortunately, the Java and XML structures that are being passed around at this point are not compatible with communicating with other systems through the GMB. So, the monitor uses the DataFormatterFactory – most likely it will end up implementing the abstract factory pattern – to convert from the XML types to C/C++ types. It does this through a strategy pattern and using a third party tool Javolution (http://www.javolution.org). The strategy pattern is extended to the types that will be sent where status is always a string and telemetry is dependent on hardware. The list of extensions are not fully inclusive, but give a very good idea how it is to be done. Now that the data has been mapped to C/C++ types, the MemoryMap is updated. The observe pattern will maintain the order of the data sent with respect to the GMB update order. While not shown, the StateMonitor and TelemetryMonitor implement the observer pattern making sure that SRS requirements cf-014, cf-015, and cf-016 are met

6.6.4 CAL Real-time Control and Interfacing

Figure 6-32 shows the organization of the CAL real-time control and interfacing. The functions of the CAL Real-Time Control are to:

Synchronously command moves of the interferometer mirror, via the PZT Driver Board, and exposures of the HOWFS camera.

Asynchronously (at a different frame rate) command exposures of the LOWFS camera.

Process HOWFS and LOWFS pixel data into wave front maps and merges the maps to a single data structure.

Evaluate S/N or other figure of merit and merges this into data structure

Transfer completed data structure to host memory

Command exposures of the pinhole camera and transfers images to host. The host then evaluates pinhole centration error and implements alignment control, as a non-real-time task.

Transfer raw images and other intermediate data products on request to local host or to storage

The HOWFS, LOWFS and pinhole cameras, and their interface hardware, have been described in Section 6.5.2, and the PZT Driver Board in Section 6.5.2.2.1

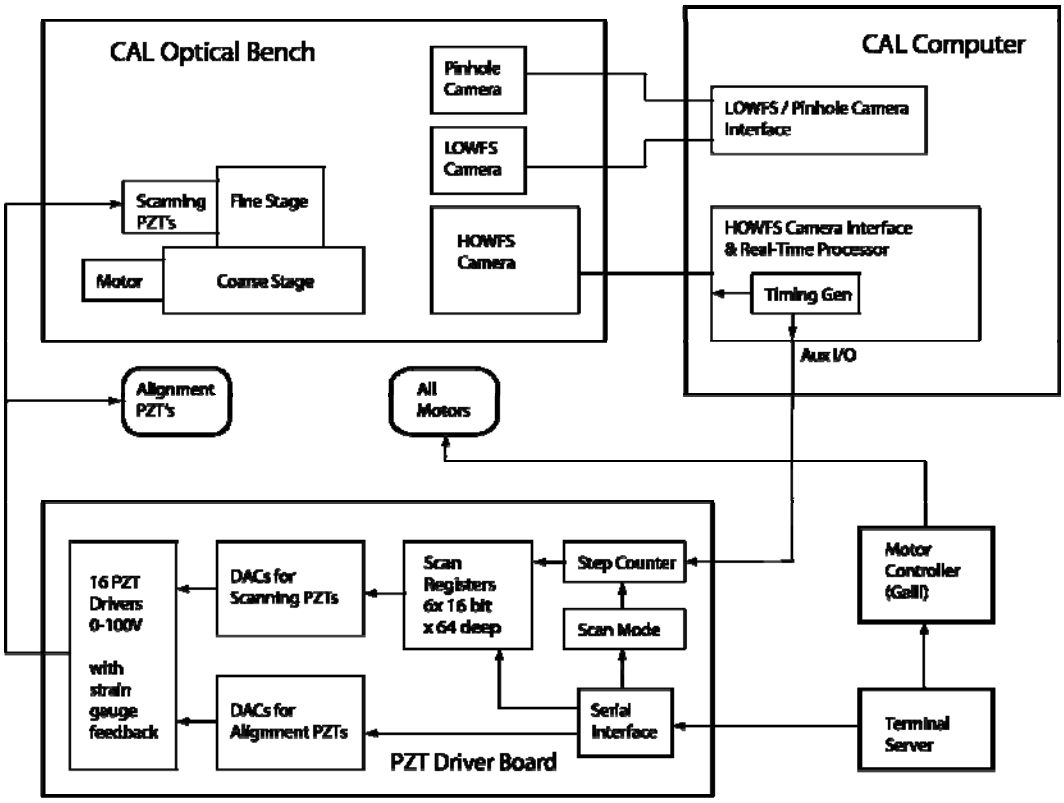

Figure 6-32 CAL Real-Time Data Flow Block Diagram

6.6.4.1 RTC Data Flow Overview

Figure 6-33 is a block diagram of the real-time processing. HOWFS processing consists of raw pixel to logical array conversion, time-slice (ABCD) accumulation, and intensity normalization. This gives a map of the complex E-field in pupil (post-apodizer) space. While this is the natural output format of the CAL wave front processing, the merger of HOWFS and LOWFS data is most logically performed in the occulter focal plane. Accordingly the HOWFS pupil map is fourier-transformed to the occulter focal plane. The original map is also made available as an intermediate data product on request.

LOWFS processing starts with of extraction of quad cells from raw pixels and computation of x-differences, y-differences and intensities (X,Y,I) of the 7x7 array of Shack-Hartmann spots. For the remaining LOWFS processing, the goal of which is a phase and amplitude map in the occulter focal plane, there are at least two algorithms under consideration. One of these is a conventional matrix multiply to give phase and amplitude in LOWFS pupil space, followed by an FFT to occulter space. A second algorithm being considered is a direct matrix multiply from the XYI arrays to the occulter focal plane. In either case, the transformation is to a common grid with the HOWFS focal plane data.

HOWFS and LOWFS data are then merged in occulter space, with relative weights assigned as a function of radius from the optic axis. Locations inside the occulter hole are taken from LOWFS data, and those outside from HOWFS data, with a smooth transition. The result is transformed via FFT to form a composite E-field map in post-apodizer pupil space. Tip, tilt and focus are projected out of the phase portion of the pupil space E-field map, and kept in a separate array (3 floats). Phase, amplitude, tip, tilt, focus and header information are formed into a final structure and transferred to host.

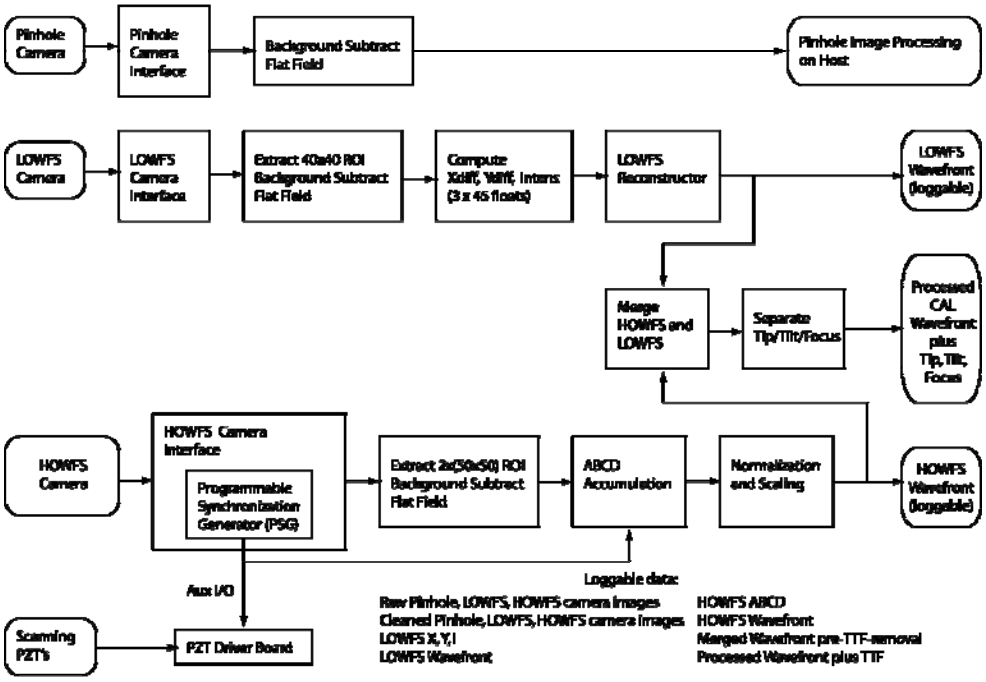

Figure 6-33 CAL Real-Time Data Flow Block Diagram

6.6.5 CAL Software Operations Example

Section 7.1.4 of the CAL SDD covers data flow from the origins of a command to the conclusion of health, status, and telemetry (data). All data that is to be reported external to the CAL system (see TLC/CAL ICD sections 7.1 and 7.2) use an Observer Pattern -- in (an over) simplified statement, a post on change design technique -- to ensure that any value changes are always reflected in the GMB. All commands are received from the TLC via RPC and translated into XML when the CAL system consumes them. The XML is required to reuse a large amount of software, covered in the CAL SDD, in order to mitigate schedule and cost risks.

6.6.6 CAL Software Integration and Test

A detailed roadmap has been prepared for developing, testing, and integrating the CAL software system. Here is an outline of the plan, which is included in fully-expanded form in Appendix 6.6 as "CAL Software Integration and Test Plan".

Steps for getting the four subsections for each of the independent layers to a deliverable level
Plan for TLC/CAL Communications Layer
Plan for GMB/CAL Communications Layer
Plan for Autonomous Behavior
Plan for Hardware Drivers

6.7 Operations Analyses

6.7.1 Optics Alignment Plan

6.7.1.1 Alignment plan for Initial Build

The alignment for the calibration system can be done in sub-assemblies first that can then be integrated into a whole. Specifically, the LOWFS camera, HOWFS camera and spatial-filter/Pinhole Camera system can be done individually. The re-maining powered optics in the system, the Reference and Science arm re-collimation OAP's must be aligned on the breadboard with a phase-shifting interferometer. Once these two optics are in place, the remaining sub-assemblies can be wrapped around to complete the system.

6.7.1.1.1 LOWFS Alignment

The LOWFS assembly is done with the aid of a well know input beam, ideally a laser beam collimated with an achromatic lens. Since the input beam diameter is only 5 mm, a reasonable off-the-shelf 1" optical element will provide very high quality over such a small sub-aperture. The beam-compressor optics can be aligned first using a shear plate. The alignment of a Shack-Hartmann has been previously

done here by building up a simple suite of frame acquisition hardware and reconstruction software such that the wave front can be quantitatively generated. The ability to record frames and reconstruct wave fronts is consistent with our hardware and software development schedule and is not seen as particularly challenging.

6.7.1.1.2 HOWFS Alignment

There is only one powered optic inside the HOWFS dewar. This lens is a 1:1 relay lens that will relay the compressed pupil images to the final focal plane array. This alignment must be done such that when the system is cold, the focus will be at the final, desired location. The procedure is do this is as follows. First, the 1:1 relay lens will be delivered as a final assembly in cylindrical invar housing. This lens assembly will be spaced inside a threaded tube and preloaded with spring flexures against a threaded retaining ring. Thermal simulations will be done in Zemax to determine the focal shift between room temperature and the final steady state temperature. The alignment will begin at room temperature. A focus will be formed at the location of the dual pupils before the dewar window (roughly at the location of the warm filters). This spot will then be relayed to the front of the focal plane array by the 1:1 relay lens. This focus spot will auto-collimate off the front of the array. Using a shear plate, it will be possible to adjust the point of auto-collimation to within a quarter of a fringe in the visible, at room temperature. Using the values from the Zemax thermal model, it will be possible to introduce the requisite offset to the retaining ring with great precision. At temperature, the imaging quality can be checked with a single mode fiber at the wavelength of interest (the 1:1 imaging properties of the relay lens is largely achromatic). This process can be iterated as necessary, but with the aid of the small lens at the output to help refocus, its likely that the iterations can be kept to a minimum.

6.7.1.1.3 Spatial-filter assembly/Pinhole camera

The spatial filter assembly lends itself to alignment with a phase-shifting interferometer. The input beams are parallel and collimated, so defining the retro-condition with a flat mirror is a starting point. The input OAP can be bonded into place with the correct rotation to bring the reflected, focused beam into the plane of the optics, near the spatial-filter pinhole. With the pinhole out, the second OAP is aligned in rotation to give a return beam on the Zygo. The remaining degrees of freedom (either out-of-plane displacement or element rotation along with mount rotation) are iterated with each measurement of the Zygo to minimize the residual wave front errors. (The magnitude and angle of the residual astigmatism can be used as clues as to which degree of freedom needs adjustment.) Once this process converges (and it does), then the spatial filter pinhole can be re-installed. The pinhole camera can then be powered on and the location of the image of the pinhole centered on the array by adjusting the pinhole periscope fold mirror just before the camera.

6.7.1.1.4 Reference/Science Arm OAP alignment

These optics are best aligned again with a phase-shifting interferometer. Start with a long flat mirror that can span the space between the focal plane mask and the re-collimated science beam. With a converging element in the Zygo, auto-collimate off the front surface of the long mirror. This will define the beam input angle and position. (We use a long mirror that has a clear polish on the back side and effectively

no wedge, in this way the optic can be flipped about its vertical axis and when properly aligned with the input beam, give no angular deviation. This insures that the input beam is horizontal to the optical table.)

Replace the converging reference on the Zygo with a flat reference, and adjust this reference to produce a flat fringe on the flat mirror. This flat mirror can now be translated sideways to define the auto-collimation for the science OAP. Re-install the converging reference optic in the Zygo and also install the focal plane mask wheel such that it is at the focal plane spot. With a beam reflected off the focal plane mask, install and adjust only the science re-collimation OAP to establish the auto-collimation condition on the Zygo. (Don't touch the long mirror in the process.) Using the magnitude and orientation of the astigmatism, adjust the OAP alignment to minimize this residual mis-alignment aberration. This mirror can now be rotated using a precision stage to the reflection angle of the reference arm OAP. By moving to the clear position in the focal plane mask wheel, the reference arm OAP can be aligned in a similar manor.

6.7.1.1.5 Installation of planar optics and pre-aligned sub-assemblies

At this point, the planar optics can be placed in the beam train with the aid of portable coordinate measuring device. This will permit placement to within a few microns of the planned location. These optics include the phase-shifting mirror, the science pick-off beam splitter, the re-combination beamsplitter, HOWFS merge mirrors, HOWFS merge prism, and HOWFS fold mirror, pointing and centering pair and polarization modulator. Once these optics are installed, then the pre-aligned sub-assemblies can also be installed using the co-ordinate measuring device: 1) the spatial-filter assembly/pinhole camera, LOWFS and HOWFS. The final assembly to be installed is the HOWFS relay that relays the dual beams to the HOWFS FPA. These can be done as a separate assembly first, or done with the coordinate measuring machine in place.

6.7.1.2 Alignment plan for diagnostic checking

For diagnostic checking, we plan on using our own internal calibration source. This is a single mode fiber which generates a perfect optical wave front. This is relayed to the focal plane mask with the aid of two spherical mirrors tilted in two orthogonal directions. Since the input to the focal plane mask is quite

Slow (f/64) it's possible to perform this optical relay while also maintaining very high wave front quality. The beam is injected into the system by translating the second optic into the beam place before the focal plane mask. This single axis insertion is followed by a minor adjustment of the fiber tip to center the PSF on the focal plane mask. The single mode fiber will have a single-mode cut-off wavelength somewhere short of 0.9 um and will transmit, with some loss due to coupling efficiency and intrinsic material absorption to near 2.0 um and will therefore be suitable for a host of different sources both narrow- and broad-band.

6.7.1.3 Alignment plan for removal and replacement of individual components

Most optics are hard to easily extract from their mounts due to our efforts to create a mechanically stable system. Therefore, removal and replacement of individual components necessarily means extraction of the associated mount. Insuring that this can be done repeatedly and accurately means referencing the

location of a mount with mechanical precision. Once the mount itself has been mechanically reference on the breadboard and removed, equal care must be made in establishing the optical reference with respect to the mount. This can be done in several ways, but depends largely on the type of optic under consideration. Planar optics can be reference with a Zygo interferometer and planar reference, while powered optics can be more complicated to reference with a converging reference on a Zygo and reference flat or by using the optic at its radius-of-curvature. If care is taken in both the mechanical and optical referencing, the optic can be removed and replaced with great accuracy requiring only a modest level of re-alignment, if any.

6.7.2 CAL Reliability, availability and maintainability

The availability of the Gemini Planet Imager instrument will be improved by selecting high reliability mechanisms and components. Most equipment suppliers express reliability of a component or system in terms of Mean Time To Failure (MTTF). Industry generally uses the L_{10} life, the time after which 10 % of the sample fails, as the time the supplier uses for the MTTF. The MTTF is very consistent across manufacturers for a given type of mechanism. The MTTF for various mechanism types is as follows:

- Mechanisms with roller bearings (e.g. ball screw, ball bearings, etc.)
  - MTTF = 20000 Hours. = 2.28 years 100% duty cycle
  - Number of revolutions of bearing rolling element or ball nut: 10^6 to 10^9
  - Life dependent on the level of contamination.
  - Life dependent on the condition of the lubrication.
- Mechanism with lubricated sliding surfaces (e.g. ACME screw/nut)
  - MTTF = 5000 Hours. = 0.57 years 100% duty cycle
  - Life dependent on the level of contamination.
  - Life dependent on the condition of the lubrication.
- Mechanism with PZT:
  - Life dependent on average applied voltage (best if V<100)
  - Life dependent on humidity (best if humidity < 50%)
  - PZTs crack under tensile stresses
  - Preload PZT to keep ceramic in compression under dynamic loads
  - Reduce high accelerations as practical to improve live. (Step inputs can cause damage with large inertial loads)
  - Lifetimes on the order of 10^9 cycles and 20 years should be possible if properly designed and operated.

In order to provide the highest availability the Calibration System has tried to use flexure motion constraints designed for infinite fatigue life on mechanism where possible since these do not require maintenance and provide the highest reliability.

The calibration has tried to use items with roller bearing contacts over sliding surfaces where possible to improve reliability. A mechanism with a MTTF of 5000 hours (lubricated sliding surfaces) should last 10 years as long as a mechanism is used less 5 % of the time and has its sliding surfaces cleaned and lubricated at regular intervals. The roller element and sliding surface mechanisms such as the filter wheel, coarse phasing stage, anti-alias filter mechanism, and shutters are operated a very small amount

of time and therefore will likely last the life of the instrument as long as the bearing surfaces are cleaned and re-lubricated once per year. The service life of mechanisms with roller bearing or sliding surfaces will be improved if the mechanism operated through the full range of motion to allow lubricant to be re-distributed. Mechanisms that operate at a single set point will tend to have lubricant starvation at the contact point. Therefore, service life will be improved if the mechanism is operated through the full range of motion to allow lubricant to be re-distributed at regular intervals. Additional reliability information is provided in Appendix 6.7.

PZT mechanisms such as the Calibration fine / high bandwidth phasing mechanism will operate with the highest duty cycle. This mechanism will operate 100% of the time during instrument operation. These mechanisms should be turned off when the instrument is not in use to extend their lifetime. The PZT mechanisms will extend their useful life if they are maintained in an environment with a relative humidity less than 50%. PZT actuators will survive longer the lower the average applied voltage. Hence it is best that PZT mechanisms be coarse aligned to a level that they can operate with a low average voltage. It is very important not to subject the PZT elements to high dynamic forces that will crack the PZT. High dynamic forces are generated by subjecting a PZT mechanism with a large inertial load to high frequency large amplitude commands such as step inputs. Subjecting a PZT mechanism to high dynamic forces that may crack the PZT is the largest risk to PZT mechanism reliability.

The most critical mechanism within the Calibration System from a reliability standpoint is the Cryogenic Cooler for the HOWFS. Since the HOWFS dewar is estimated to take approximately 11 hours to cool down the cryogenic cooler must operate 24 hours a day during periods where the instrument is operated every night. It is only practical to turn the cryogenic cooler off in order to extend its useful life when the instrument will not be used for a week or more. The highest MTTF stated by a manufacturer for a cryogenic cooler is 20000 hours or 2.28 years at a 100% duty cycle. Hence it is likely that the cryogenic cooler will need to be serviced or replaced during the lifetime of the GPI instrument. The base line cryogenic cooler compressor uses flexure bearing and non contact voice coil type actuators to operate in order to provide the highest level of reliability.

6.8 Summary

6.8.1 Technology Development, Risk Items, Manufacturing risks

6.8.2 Optical Manufacturing Risks and Long lead items

The table below summarizes the optical manufacturing risks. There are only four optical elements that require special attention. This is because in the reference arm, a spatial filter will mitigate the effect of the fabrication and alignment errors for mid-spatial frequencies. Therefore the only optics of concern in the reference arm are due to the re-collimation OAP after the pinhole and the recombination beamsplitter. In the science arm, the optical surfaces of concern are the science re-collimation OAP and the science pick-off beamsplitter. Errors in these four optics will introduce a phase error in the calibration phase estimate. This effect can be calibrated out; specifically, the calibration system can take a measurement of a known, perfect wave front and the resulting error in the measurement is the offset of

the cal system in normal operation. However, our goal is to minimize the magnitude of this systematic phase correction. The smaller this systematic error is, the smaller the change during observation. We have set ourselves a goal of a total of 20 nm, rms un-calibrated wave front error in these optics. Given that two of the four optics are planar, and can be manufactured to very high quality with only modest additional expense, we believe this tolerance is neither unreachable nor costly.

Optical Subsystem	Element	Manufacturing Risk	Comment
Science Arm			
	Science Arm	Medium Risk	Custom, good surface
	Re-collimation OAP		
	Science Pick-off Beamsplitter	Medium Risk	Custom, good surface
Reference Arm:			
	Reference Arm	Low Risk	Custom, not challenging
	Re-collimation OAP		
	Phase Shifting Mirror	Low Risk	Off-the-shelf
	LOWFS Pick-off Beamsplitter	Low Risk	Custom, not challenging
	Pinhole OAP #1	Low Risk	Custom, not challenging
	Pinhole OAP #2	Medium Risk	Custom, good surface
LOWFS:			
	Relay Lens	Low Risk	Off-the-shelf
	Fold Mirror	Low Risk	Off-the-shelf
	Lenslet Array	Low Risk	Off-the-shelf
Pinhole Camera:			
	Fold Mirror	Low Risk	Off-the-shelf
	Relay Lens	Low Risk	Custom, not challenging
	Fold Mirror	Low Risk	Off-the-shelf
HOWFS:			
	Recombination Beamsplitter	Medium Risk	Custom, good surface
	Merge Folds	Low Risk	Off-the-shelf
	Merge Prism		Custom, not challenging
	HOWFS Fold Mirror	Low Risk	Off-the-shelf
	Large HOWFS lens		Custom, not challenging
	Small HOWFS lens		Custom, not challenging
	Bandpass filters (warm)		Custom, not challenging
	Short-pass filter (cold)		
	Dewar Relay Lens		Custom, not challenging

7 Opto-Mechanical Superstructure

7.1 Overview

The Opto-Mechanical Superstructure (OMSS) comprises two independent sub-systems: the External Frame Structure (EFS) and the Flexure Sensitive Structure (FSS). The external frame structure supports the electronics cabinets, provides proper routing of wiring and services, provides external lifting and handling features, and incorporates light-tight panels to enclose the optics (Figure 7-1). The EFS truss framework attaches to a mounting plate that is located at the interface to the Gemini Instrument Support Structure. This framework is completely independent from the components of the flexure sensitive structure (except at the shared mounting plate) so that the weight and possible vibration sources within the electronics cabinets have a minimal impact on the sensitive optical components of the FSS. In essence, the EFS and FSS form two nested structures, with minimal physical connections between them.

The flexure sensitive structure contains the major optical sub-systems: the AO module, coronagraph, Calibration module (CAL), Integral Field Spectrograph (IFS), as well as a mechanical framework that locates and supports each optical system (Figure 1-4 and Figure 7-3). The support framework is attached to the shared mounting plate in a similar fashion to the EFS. This framework, in turn, supports each optical sub-system through the use of semi-kinematic bipod flexures. The primary role of the framework is to provide a lightweight and stiff structure to locate each of the optical sub-systems. These sub-systems house the optical elements, mounts and mechanisms needed to achieve the optical requirements of the system.

This chapter will first present the OMSS optical prescription. This includes the AO relays, AO wave front sensor, coronagraph (all but the Lyot stop), and the transfer optics that feed the IFS. The prescriptions that deal with the internal design of the CAL module and IFS will be presented in their respective chapters. Next, the chapter will present the design and analysis of the external frame structure. Following this, the flexure sensitive structure will be presented, along with a description of all the optical mounts and mechanisms on the AO optical table. Finally, some specialized procedures and equipment required for instrument handling are shown.

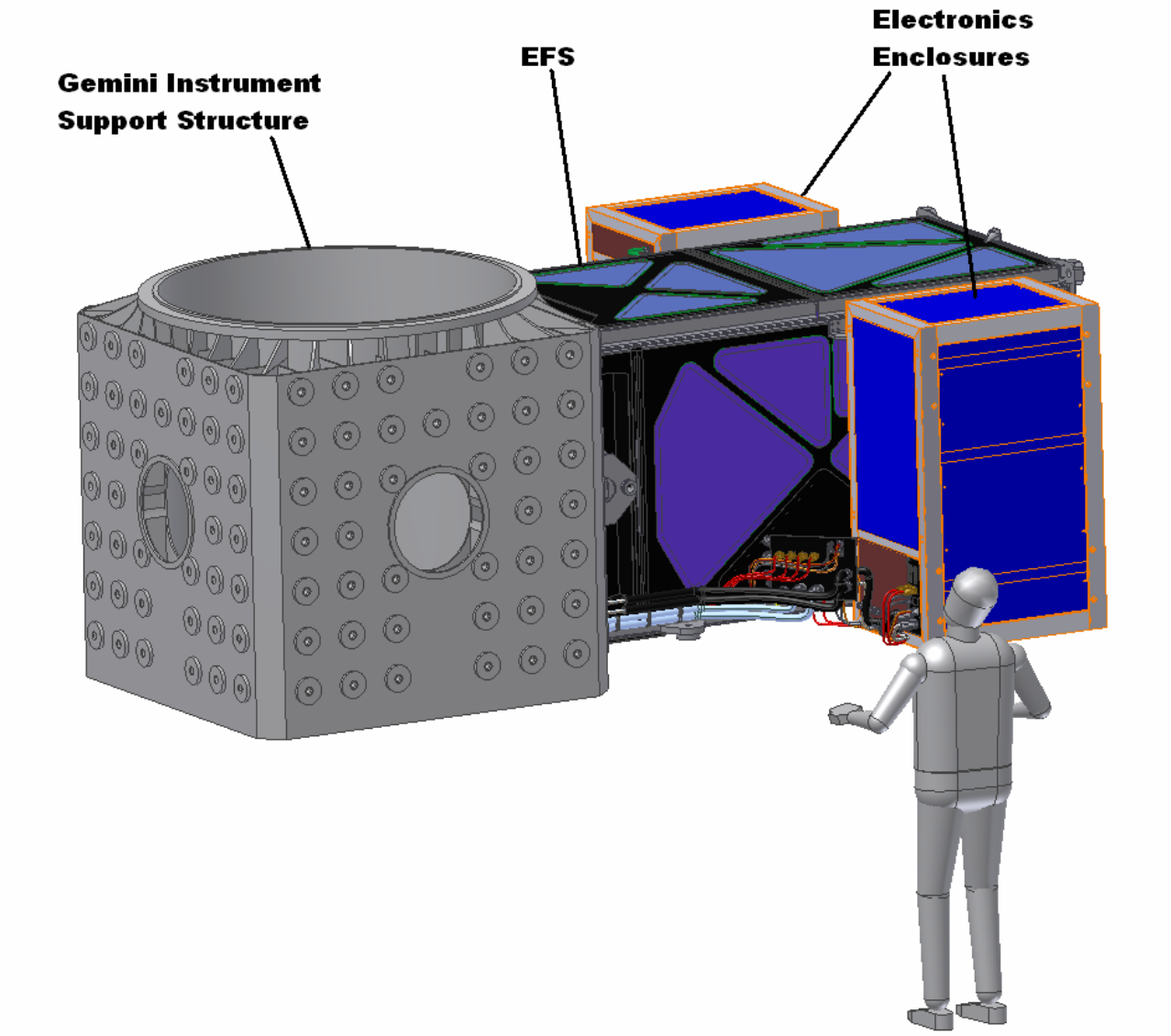

Figure 7-1 EFS mounted on Gemini ISS.

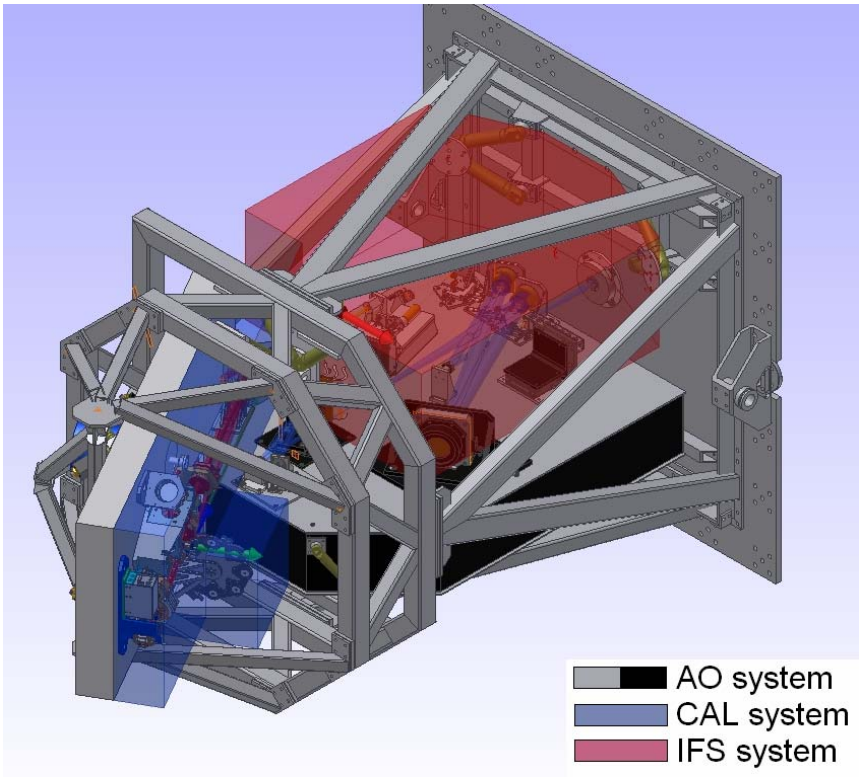

Figure 7-2: Flexure Sensitive Structure (iso view).

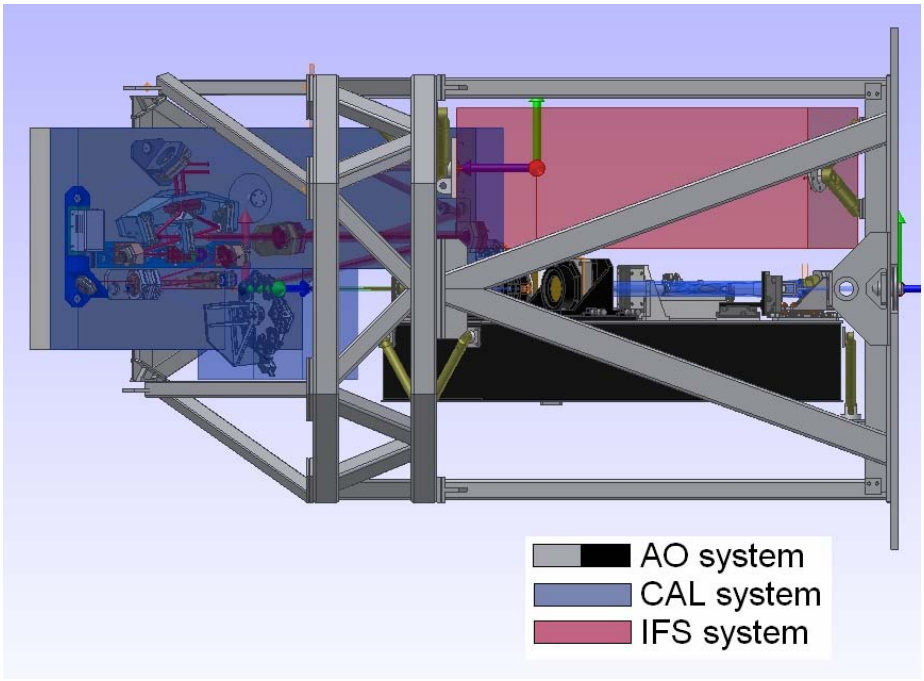

Figure 7-3: Flexure Sensitive Structure (side view).

7.2 Optical Design

7.2.1 AO Module

7.1.1.1 AO Module Optical Requirements

The optical requirements for the AO module are given in Table 7-1 below.

Category	Description	Requirement
General optical requirements	Wavelengths	0.7-0.9 μm WFS band 0.95-2.4 μm aggregate science band (about 20% bandwidth at any one time); allow refocus after changing filter [REQ-OCD-0040]
	Field size	2.8 x 2.8 arcsec square (full dimensions, not half-dimensions) [REQ-OCD-0160]
AO relay requirements	First-order specifications	Input: f/16, aperture stop at secondary Output (leading into coronagraph): f/64, 12 mm transmissive exit pupil
	Pupil wander/distortion	< 1 % of the pupil
	Tip-tilt range	± 2.5 arcsec on sky [error budget: atmosphere]
	tweeter	44 actuator pitches across beam diameter = 17.6 mm for 400 μm pitch MEMS [error budget atmosphere, WFS error]
	woofer	40 mm diameter beam at woofer
	Wavefront error	see text
WFS requirements	Number of subapertures	44 subapertures illuminated across pupil diameter [error budget: atmosphere, WFS error]
	Plate scale	1.4 arcsec / pixel [error budget: WFS measurement]

Table 7-1 Optical requirements

7.1.1.2 AO Module Layout

7.1.1.3

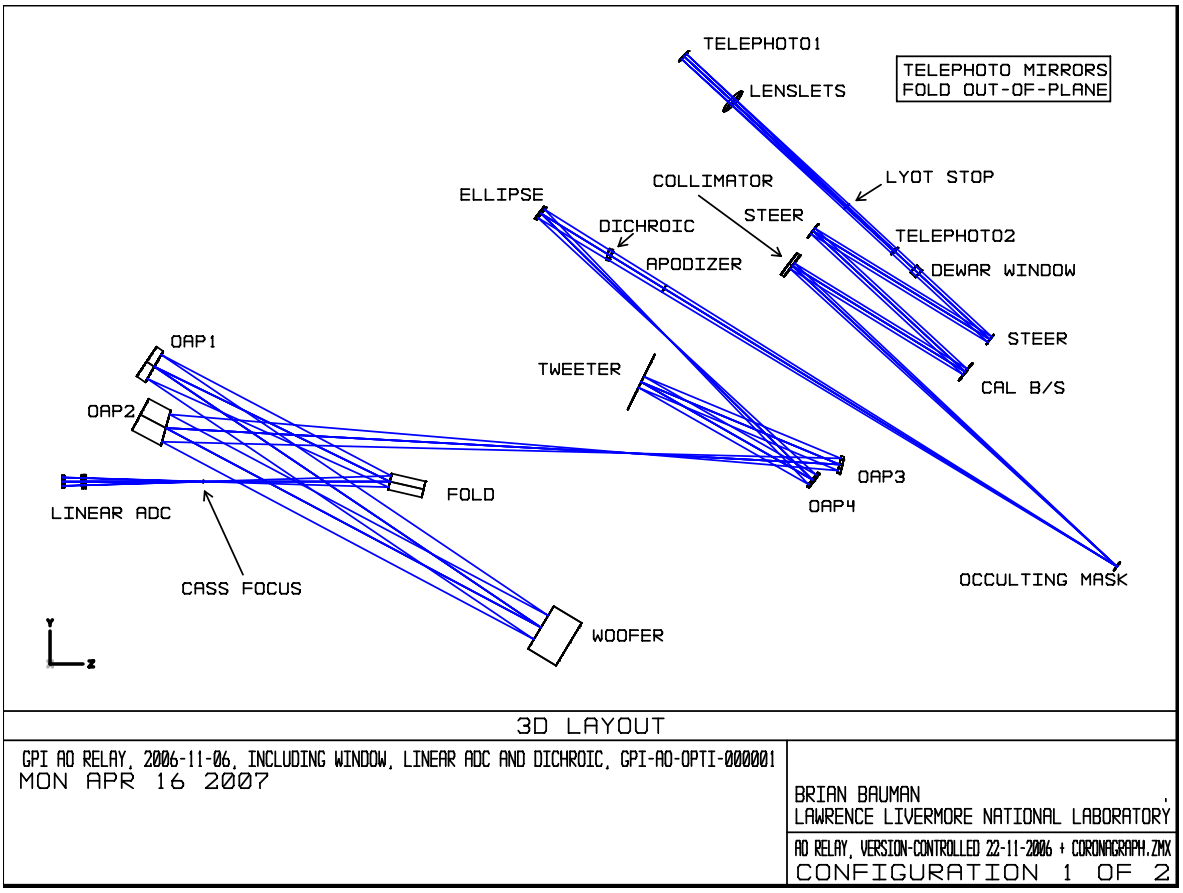

Figure 7-4 AO module, excluding WFS path. The distance between OAP2 and OAP3 is approximately 1 m.

7.1.1.4 Design Description

The AO module consists of the optics from the telescope ISS interface to the f/64 input of the coronagraph (Figure 7-4). The design can be broken into four parts: the window/ADC; the woofer section; the tweeter section; and the apodizer/coronagraph section. Each section is designed to be relatively modular for ease of integration and testing, as well as for greater flexibility in handling design changes. This has allowed us to decouple design decisions when needed.

We start with a deployable two-glass linear atmospheric dispersion corrector (ADC) in front of the Cassegrain focus; the ADC design is detailed in Appendix 7.2. Upstream of the ADC, there may also be an instrument window (to provide environmental control) at the front of the instrument at the ISS face. Alternatively, the first ADC element may also be used as the instrument window; that decision will be made early in the critical design phase. The woofer section consists of an off-axis parabola (OAP) that collimates the f/16 beam from the telescope, creating a 40-mm pupil at which the first DM is placed (the woofer mirror with tip-tilt stage). A second OAP focuses the beam back to f/16. The tweeter section

follows, consisting of a third OAP that collimates the light again, creating a 17.6-mm pupil, where the tweeter DM is placed. The next mirror is another OAP that focuses the beam back to f/16. The apodizer/coronagraph section follows, and more details are in Chapter 4. There is an elliptical mirror that takes the f/16 light and relays it to a 12-mm pupil for the apodizer and an f/64 image for the focal plane mask (FPM, or occulter). Some light leaks through the center of the FPM into the calibration unit. The light that reflects off the FPM is collimated by an OAP and then strikes the calibration beam splitter. The transmitted part of the light enters the calibration system where it interferes with the light that leaked through the FPM; details are in Chapter 6. The light that reflects off the calibration system is science light, which subsequently hits two steering flats that direct it tinto the IFS. Internal to the IFS there is the Lyot stop in collimated space followed by a two-element reflective telephoto (using super polished spherical mirrors) that focuses the beam to f/200. The IFS lenslets are located at the f/200 focus.

During the preliminary design phase, we considered changing the relay to a three-element system, but we eventually selected this five-mirror design for flexibility reasons. The trade study is detailed in Appendix 2.1. Other significant changes since CoDR include changing the woofer size from 17.6 mm to 40 mm, changing the apodizer size from 15 mm to 12 mm, adding an ADC, and imposing requirements on the beam wave front error at each point in the optical train, not just at the FPM.

The various angles at which the OAPs are used and the use of the ellipse are driven by the requirements for image quality, absence of pupil and image plane tilt at the apodizer and FPM respectively, and a desire to reduce the number of packaging folds. The CoDR design minimized the number of surfaces by eliminating fold mirrors, but at the cost of a more "stressed design[3]" with tighter tolerances. The benefit of reducing optic count was relatively small, and we eventually needed to have folding flats for packaging reasons, so for the preliminary design phase, we adopted a more "relaxed" design that performs better and has eased tolerances.

The performance of the nominal AO relay design is indicated in the rms wavefront error versus field angle plots in Figure 7-5. The four plots are for field points along the four directions extending from the center of the field, up to a maximum of 1.4 arcsec off-axis; full scale on the vertical axis is 10 nm rms. The plots show that the rms wavefront error is generally less than 1 nm rms. Figure 7-6 shows wave fans that illustrate that the aberrations are dominated by low-order aberrations such as astigmatism and coma.

When deployed, the ADC produces approximately 80 nm rms of astigmatism that is roughly independent of the amount of dispersion corrected. We have analyzed the wave optics effects of this optic and have determined that the impact is acceptable after correction by the woofer; see Appendix 7.2.

We plan that the ADC will be deployable and that the position of the Cassegrain image will be according to an "ADC-out" configuration. When the ADC is deployed, the Cassegrain focus will shift

[3] A stressed design is one that has large aberrations created by one optic that are corrected by a subsequent optic, as opposed to one which distributes the aberrations evenly between elements.

because of the thickness of glass introduced. We will adjust the focus of the telescope accordingly to keep the focus in the same position in space relative to the ISS.

Object position	On-axis	4 λ/D (side/corner) (req)	22 λ/D (side/corner) (req)	2.8" square (side/corner) (req)
Design rms wavefront error	0.8 nm	1.0 nm/1.1 nm (20 nm)	1.9 nm/2.4 nm (60 nm = 95% SR)	3.0 nm/4.0 nm (120 nm = 80% SR)
Worst WFE at intermediate location	0.8 nm	3.1 nm/4.3 nm (20 nm)	16.6 nm/24.0 nm (200 nm = 55% SR)	31.8 nm/ 46.1 nm (N/A)

Table 7-2 Required and actual wave front error of AO relay for various points in the field.

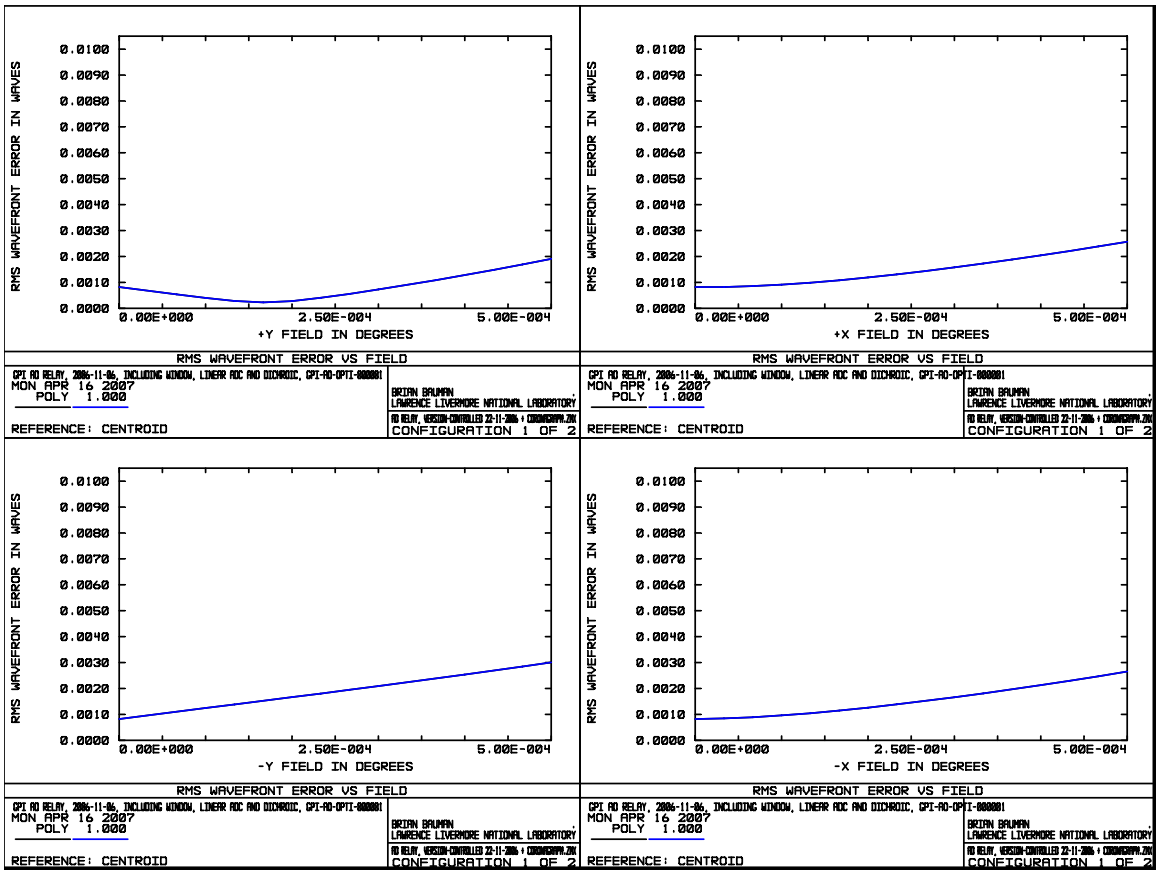

Figure 7-5 RMS wave front error in microns in four directions extending from the center of the field, up to a maximum of 1.4 arcsec off-axis. The full scale on the vertical axis is 10 nm rms. These results show that the rms wavefront error is generally less than 1 nm rms.

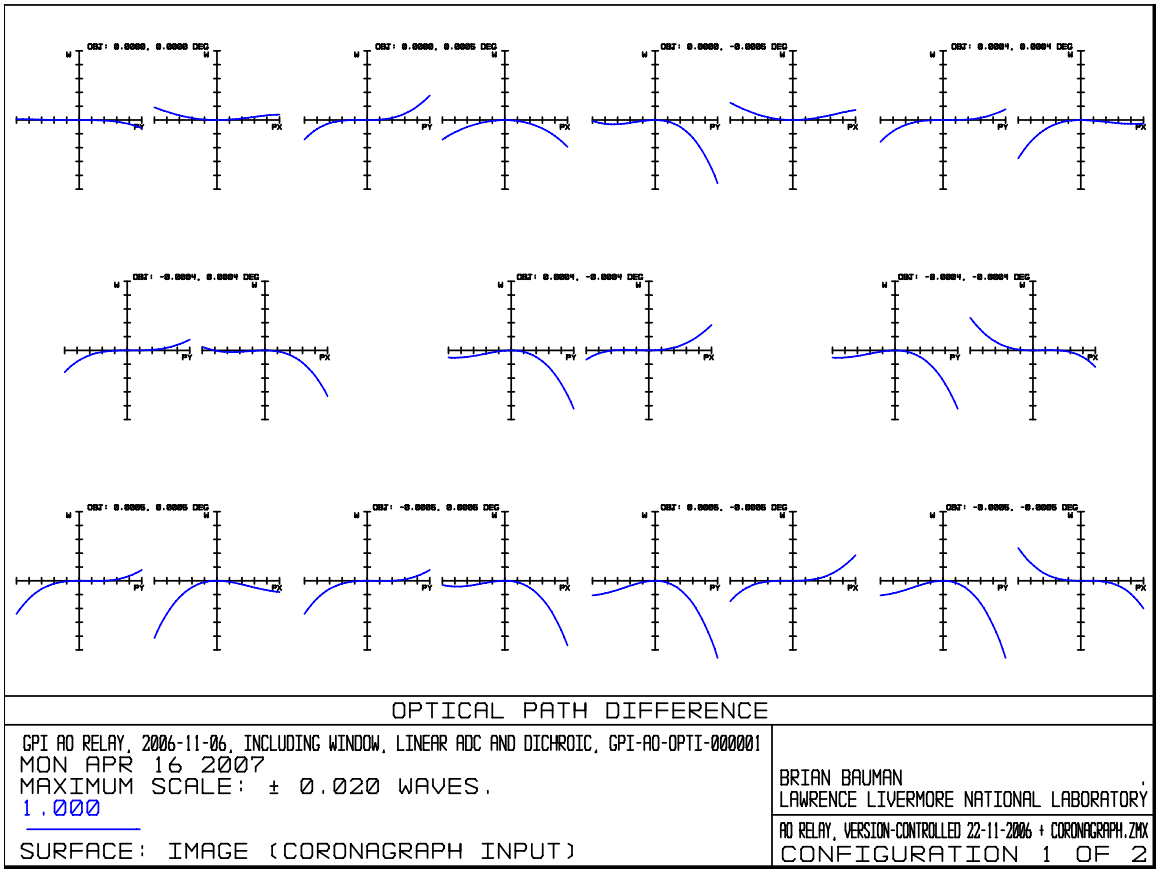

Figure 7-6 OPD fans of AO relay nominal design for several field points within the 2.8 x 2.8 arcsec field of view, showing mostly small amounts of focus, coma, and astigmatism.

7.1.1.5 Tip/Tilt Mirror

For CoDR, we had identified several possible approaches to implementing tip/tilt correction:

Use a DM located on a tip/tilt platform;

Use a woofer DM that has enough stroke and speed to accommodate the tip/tilt requirements (~50 μm mechanical stroke);

Use a separate tip/tilt mirror at a pupil;

Use a separate tip/tilt mirror away from a pupil, but not so distant so as to cause excessive pupil wander as the tip/tilt mirror moves.

As detailed in section 7.3.2.1.6, we were able to place the woofer on a tip/tilt platform and thereby eliminate a number of optical surfaces.

7.1.1.6 AO Wave Front Sensor

The light for the AO wave front sensor (AOWFS) is split from the science light at a dichroic just before the input to the coronagraph. Besides the dichroic, the AOWFS consists of two steering flats, a spatial filter located at the f/64 image plane, a collimating OAP, and a Shack-Hartmann (SH) wavefront sensor. The two steering flats form a pair to steer the image ("pointing") and to steer the pupil ("centering") onto the calibrated positions in the SH WFS. The SH WFS includes a lenslet array located at a pupil plane and a two element 1:1 relay (the "dot relay") to image the SH dots onto the WFS detector. Due to the very short focal length (<1 mm) of the lenslets, it is necessary to relay the Shack-Hartmann "dots" created by the lenslet array. The dot relay is a simple refractive "4f" style system using achromats. An unfolded layout of the WFS leg from the 12-mm pupil to the WFS CCD is given in Figure 7-7 below. Selected characteristics of the WFS are listed in Table 7-3 below.

Figure 7-8 shows the map of the telescope aperture, DM actuators, and WFS subapertures; the actuator pitch and subaperture pitch are 18.1 cm in the optical space of the telescope primary mirror. A layout of the "dot relay" is shown in Figure 7-9. Details of the designs are provided in Appendix 7.2.

As of PDR, the WFS detector selection has not been made. However, using the characteristics of the candidate detectors, it was possible to establish the space required for the WFS leg, independent of the eventual choice. Preliminary designs of the WFS for the likely cases have been completed, and the designs are similar—the only difference is the magnification of the relay that matches the size of the lenslet array and the detector. The beam following the dichroic, steering mirrors, spatial filter, collimating OAP, and the lenslet array pitch have been selected, and these are independent of detector selection.

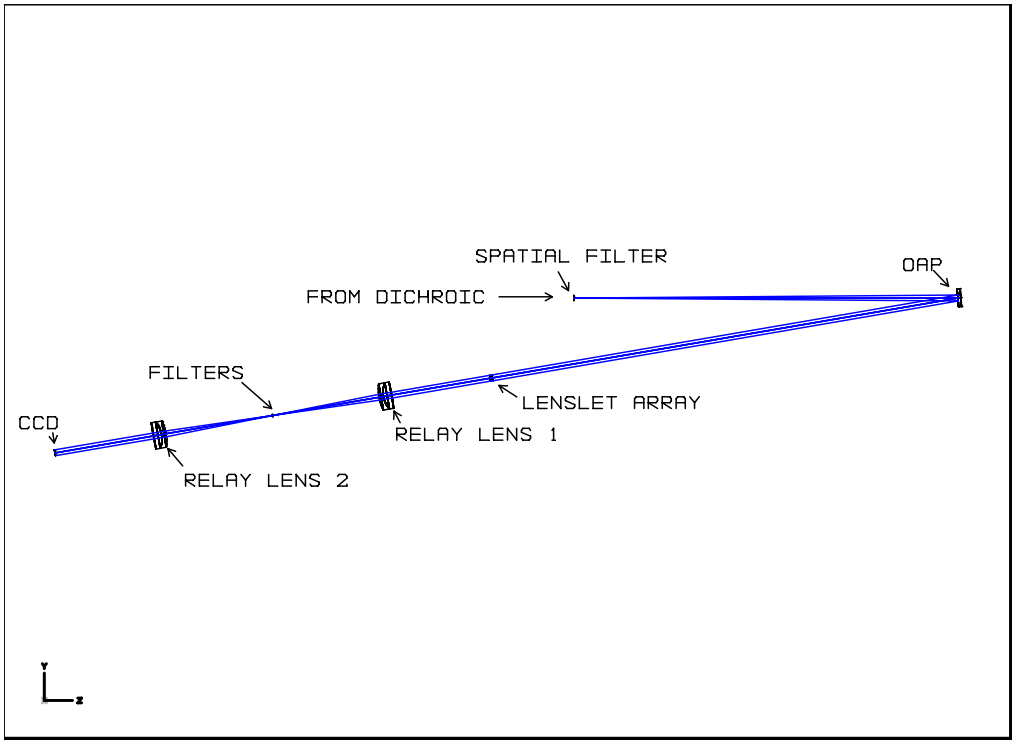

Figure 7-7 An unfolded layout of the WFS leg from the 12-mm pupil to the WFS CCD .

Input focal ratio	f/64
Collimating OAP focal length	135 mm
Number of subapertures	44 x 44 subapertures mapped onto 17.6 mm MEMS, 44 subapertures illuminated across the diameter of the pupil (18.2 cm square subapertures when mapped onto the telescope primary mirror)
Pupil size at lenslet array	2.109 mm
Lenslet pitch	48 μm
Lenslet focal length	depends on detector selection
Plate scale	1.4 arcsec/pixel
Number of pixels per subaperture	3 x 3 pixels or 4 x 4 pixels, depending on number of pixels on detector
Field	On-axis only; guide star will be pointed and centered onto calibrated position in WFS
Field steering mechanism	two fold mirrors

Table 7-3 Characteristics of WFS

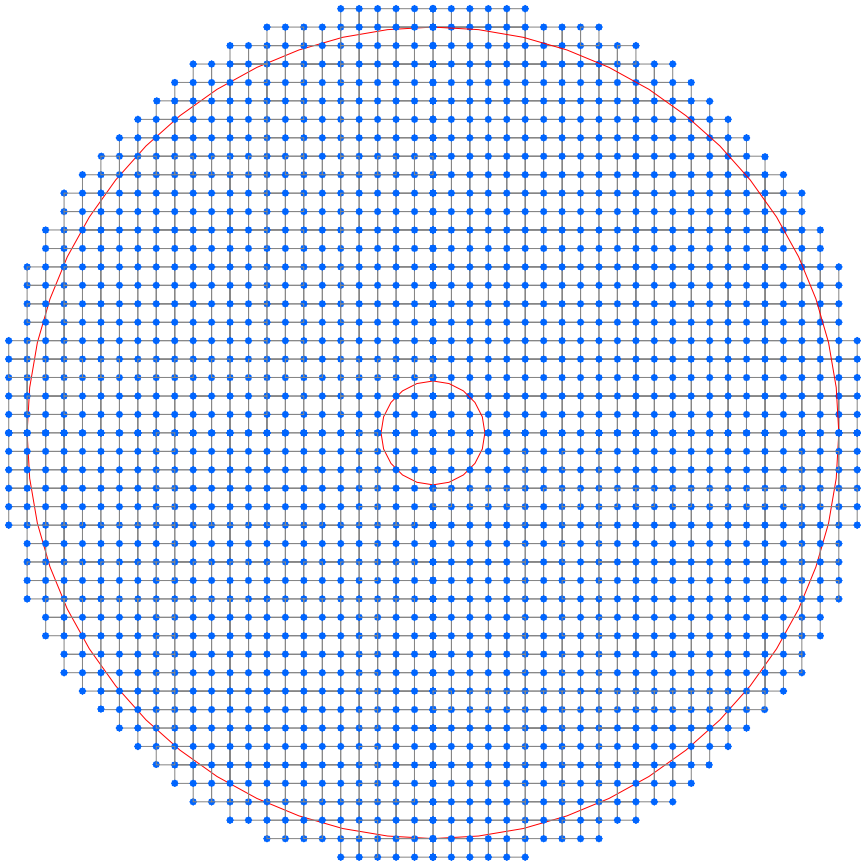

Figure 7-8 Map of telescope aperture (red), tweeter actuators (blue), and subapertures (gray).

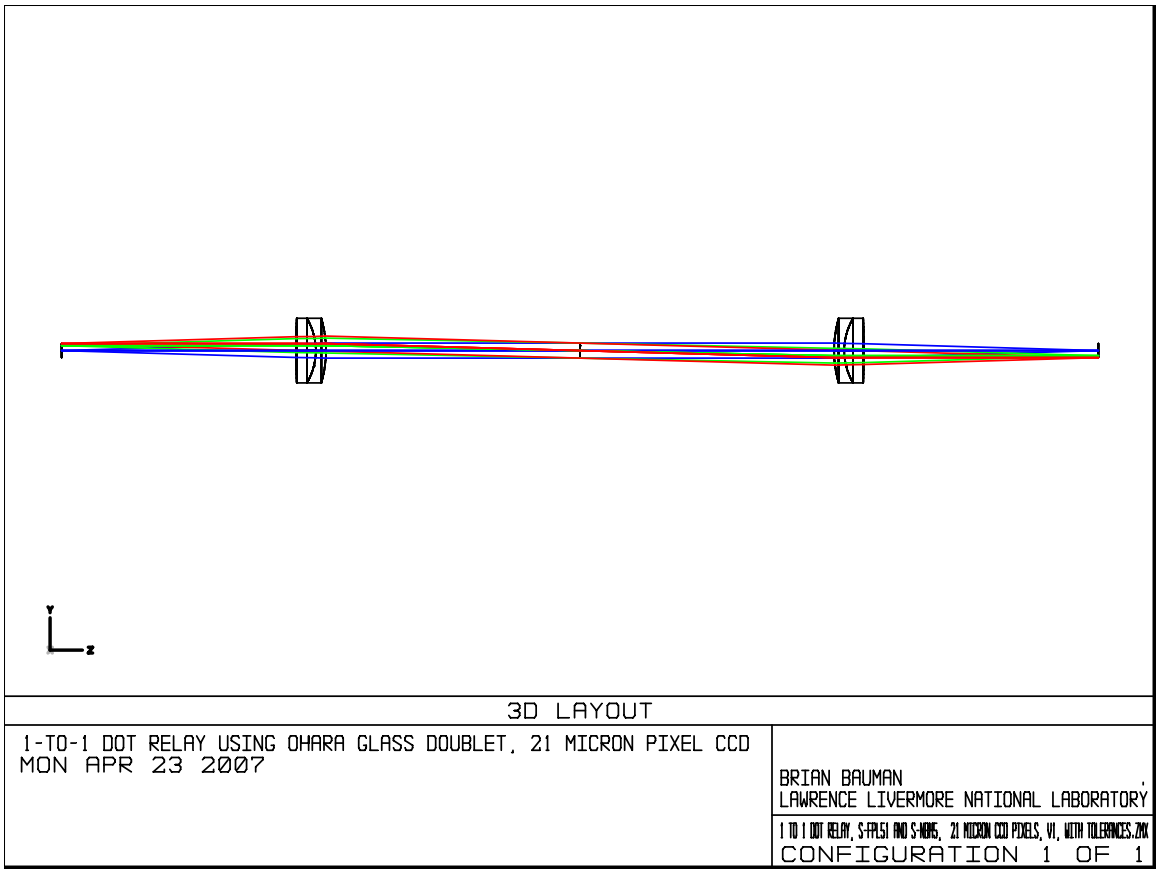

Figure 7-9 Dot relay between the SH dots and the WFS detector for the 21 μm pixel, unit magnification case.

7.2.2 Pupil distortions

Pupil distortions play into the performance of the AO system and of the coronagraph. The performance of the AO control loop can be impacted if the pupil distortion between the DM plane and the lenslet array on the WFS is too great to calibrate well, or if the distortions change too much between calibrations. The efficacy of the coronagraph can be affected as well since the coronagraph expects a specific apodization function and pupil distortion can impose additional, unrequired apodization.

Typically, the notion of pupil aberrations is not a driving issue in current-generation adaptive optics systems. However, as an AO system reduces DM size (e.g., MEMS), increases field, and increases the number of actuators, pupil aberrations become increasingly important. Pupil aberrations are discussed at some length in Bauman, 2004 [1] . The main effects of pupil aberrations are to produce field-dependent pupil wander, which leads to a type of anisoplanatism, and to produce field-dependent pupil distortions with respect to the on-axis pupil mapping between DM and WFS. In the case of GPI, these effects are small (~ 0.2%) because of the very small field over which the WFS needs to operate: The nominal pupil distortion in the system is on the order of 0.1% (1 part in 1000), as compared to a specification of 1%. In the AO system design, and in its tolerancing, we have tracked pupil distortions as a requirement.

7.2.3 Telescope (M1, M2 & M3)

Appendix 7.2 includes the telescope prescription that was assumed.

While phase errors on M1 and M2 can be negated by the DMs, reflectivity variations (amplitude errors) across the pupil cannot. We evaluated the effect of measured M1 reflectivity non-uniformity, as indicated in measurements from Gemini where the reflectivity at many places on the mirror was taken at 0.47 μm, 0.65 μm, and 2.2 μm. The rms variation was about 1% at 0.65 μm and 0.36% at 2.2 μm. If the data are taken at face value, a 0.01 (1%) rms in intensity means 0.005 rms in amplitude, which is equivalent (in broad strokes) to 0.005 radians rms in uncorrected phase, which is equivalent to 0.8 nm rms at 1 micron. In general, reflectivity increases with wavelength, therefore at 2.2 μm, the effect of these errors should be reduced. We also expect that the actual non-uniformity is much less than this because the visible and infrared reflectivity data were not strongly correlated, and so much of the apparent variability across the pupil is in fact just due to measurement noise.

The presence or absence of M3 represents a notable effect on the performance of the system because M3 is the only non-pupil optic that is not part of GPI. M1 and M2 are both near the pupil/ground (optically conjugate to within about 100 meters) and so any wave front error remains as a phase error and does not have enough propagation distance to turn into a significant amplitude error. In contrast, M3 is conjugate to 17.6 km below ground, which is significant compared to the Talbot length of 65 km in object space for the highest spatial frequency of our system and $\lambda = 1$ μm. These effects are discussed in detail in Appendix 2.25.

7.2.4 Reflective Optics

The small error budget for mid-spatial frequency errors places a premium on obtaining high quality optics. Certainly not every optics vendor is experienced with mid-spatial frequency errors or capable of ~ 1 nm rms wavefront error optics. Fortunately, other projects such as Extreme Ultraviolet Lithography and TPF have paved the way for our requirements. We have begun consultations with vendors to establish ROM costs and to establish the feasibility of our requirements. Our draft list of optics and specifications is given in the Table 7-4 below:

	Diameter (+0 – 0.2 mm)	Radius of curvature (± 0.1%)	Conic constant (± 0.1%)	Off-axis distance
OAP1	50 mm	1292.17 mm (CC)	-1	90.4 mm
OAP2	50 mm	1292.17 mm (CC)	-1	285.2 mm
OAP3	25 mm	579.16 mm (CC)	-1	99.5 mm
OAP4	25 mm	579.16 mm (CC)	-1	75.0 mm
ellipse	25 mm	398.76 mm	-0.3511644	76.4 mm

		(CC)		
OAP collimator	25 mm	1257.7 mm (CC)	-1	127.0 mm
telephoto 1	25 mm	1000.00 mm (CC)	0	--
telephoto 2	25 mm	219.94 mm (CX)	0	--

Table 7-4 List of optics and specifications

The tolerance that drives the cost of the optics is the wave front error requirement. Our draft wave front error requirements are as follows: After removal of piston, tip, tilt, and focus, the wavefront aberrations (i.e., reflected wave front errors, not surface errors) shall be:

- < 10 nm rms for spatial frequencies less than 4 cycles across the nominal beam size;
- < 1 nm rms integrated for spatial frequencies between 4 and 22 cycles across the nominal beam size;
- < 10 nm for spatial frequencies greater than 22 cycles across the nominal beam size;
- Surface roughness: <2 Å.

We have discussed these requirements with two vendors: SSG Tinsley Laboratories and Precision Asphere (PA). Tinsley is very well qualified for this work, as they have made Extreme Ultraviolet Lithography mirrors with mid-spatial frequency tolerances considerably tighter than ours (1 nm rms for mid-spatial frequencies). Based on this list of requirements, Tinsley has estimated a cost of $95k for each off-axis parabola, and $140k for the off-axis ellipse; each figure includes a non-recurring engineering cost. Precision Asphere may be significantly less expensive (perhaps one-third of the cost), but are also much more of an unknown quantity. Since PA makes off-axis sections from a parent optic, they could produce multiple mirrors from the same parent for nearly the price of one off-axis component. However, we found that this was of marginal benefit.

The spherical telephoto mirrors in the coronagraph and the flats can be fabricated economically by super polishing vendors such as General Optics of Moorpark, CA and Research Electro-Optics of Boulder, CO.

7.2.5 Refractive Optics

7.1.1.7 Surface Quality

The specifications for the refractive optics are roughly similar to those for the reflective optics, and their derivation is discussed in Appendix 2.25. We have purchased super polished glass optics and we have found that “off-the-shelf” super polished parts meet our requirements and do so very inexpensively. According to the vendors, we can achieve the same surface figure for any of the glasses that we are contemplating in GPI.

7.1.1.8 Inhomogeneity and Birefringence

The GPI system will have a number of transmissive elements, and for those elements we need to control inhomogeneity and birefringence. Inhomogeneity can be treated in the same way as surface figure on reflective optics, i.e., we have error budget terms for the spatial low-frequency, mid-frequency, and high-frequency content of the optics. Glass is typically specified with a maximum inhomogeneity, e.g., $\Delta n \approx 1.0 \times 10^{-6}$ (for a high-quality homogeneity class) but spatial frequency content is not implied by this measure, nor is it typically gathered. Our glass thicknesses will be on the order of 5 mm, which would yield optical path differences (OPDs) due to inhomogeneity of 5 nm peak-to-valley (P-V), or very roughly about 1.3 nm rms. This is similar to the specifications used for the reflective optics over just the mid-spatial frequencies, so we would expect that the inhomogeneities would be acceptable.

We also must consider stress birefringence in our transmissive parts. If we use unpolarized light for science, then birefringence represents a wavefront error that cannot be recovered fully because it cannot be corrected for all polarizations simultaneously. Similar to inhomogeneity, glass is typically specified with a maximum birefringence, e.g., < 4 nm per cm of glass thickness for a precision annealing. For 5 mm glass thickness, this represents approximately 1 nm P-V, or 0.2 nm rms of uncorrectable error—distributed over all spatial frequencies.

To minimize our risk, we are in the process of obtaining quotes for samples of the glasses that we expect to use, with the dimensional, inhomogeneity and birefringence specifications that we expect to use in the fielded optic. In addition to receiving the manufacturer's data, we would also measure the inhomogeneity and birefringence of the samples and characterize the index variations in terms of spatial frequencies. The samples are anticipated to be inexpensive (a few hundred dollars per sample), but should be adequate to retire the risk. We can also use these samples to verify that our opto-mechanical mounting mechanisms are not introducing birefringence.

7.1.1.9 Ghost Analysis/Baffling

A preliminary analysis of ghost images has been performed in order to identify and mitigate potential problems. With a contrast requirement of order 10^{-6}, it is vital to keep ghosts under control. In the AO system, there are five refractive optical elements, and each one requires its own approach and analysis. The five optics are: the GPI instrument window (located at the front of the ISS, where the light first enters the instrument); the atmospheric dispersion correctors (ADCs); the MEMS window; the dichroic (which splits the light between WFS and science legs); and the apodizer. The considerations in ghost analysis are as follows:

- how the refractive optic affects the direct (unghosted) beam, in terms of aberrations, pointing and centering;
- how the refractive optic affects dispersion of the direct beam (e.g., if the ghost is eliminated by wedging an optic, then the direct beam is dispersed);
- where the ghost is directed in pointing/centering, and how it is aberrated.

While anti-reflective coatings are necessary and appropriate for ghost control, they are not sufficient to eliminate ghosts on their own. For a ghost to reach the focal plane mask, the light would need to reflect off of two refractive surfaces. The reflection would need to be 10^{-3} (0.1%) in order to attenuate the

ghost to 10^{-6} of the direct beam. This is an unrealistic level across GPI's very broad wavelength band. Therefore, we need to control ghosts by directing them in ways that will not impact the instrument performance, typically by kicking them sufficiently outside the field and then stopping them with baffles near the image planes. We have completed a preliminary ghost analysis and we have been able to design the transmissive optics so as to mitigate ghosts. The details of the ghost analysis are given in Appendix 7.7.

Optic	Ghost mitigation
Instrument window	tilt window + wedge window
ADC's	tilt one ADC with respect to the other
MEMS window	plane parallel plate, tilted with respect to MEMS surface
Dichroic	wedge
Apodizer	wedge

Table 7-5 Transmissive optics and measures taken to mitigate ghosts. All optics also used anti-reflective coatings with <1% reflectivity.

Besides ghost reflections, stray light can also reach critical planes by a secondary path, which is eliminated by baffling. Other than baffling near focal planes for ghost reflection, baffling is appropriately a critical design phase task since the actual mechanics of the system play a part in considering secondary paths.

7.1.1.10 Coatings

We have obtained theoretical reflectivity plots for anti-reflective coatings for the transmissive optics and have found that we can expect to achieve reflectivities mostly in the 0.50-0.75% range at a level of difficulty that would be characterized by the vendor as "developmental, but probably achievable". See Figure 7-10. While the actual coating design will vary according to the glass used for the substrate, the performance will be approximately the same for any of the glasses that we are considering. We expect that the cost will be on the order of $10,000 per run, which is reasonable on this project.

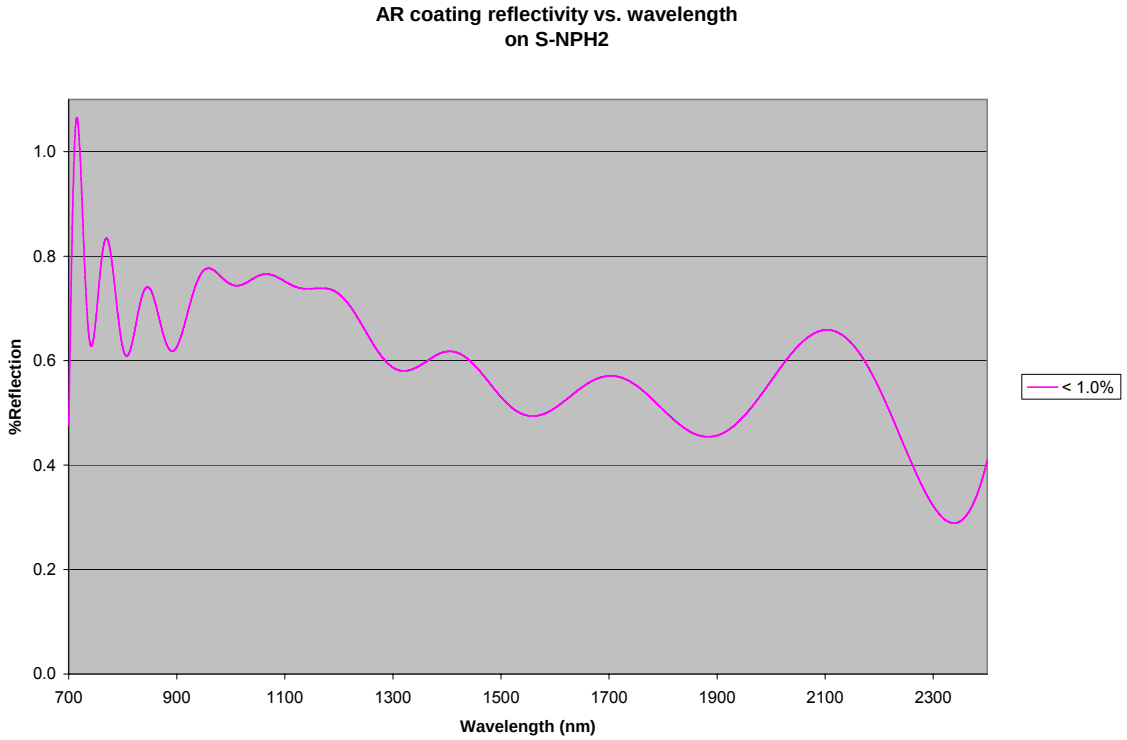

Figure 7-10 Plot of design reflectivity versus wavelength for broadband antireflective coating on Ohara S-NPH2. Performance of antireflective coating on other glasses is expected to be similar.

7.3 Mechanical

7.3.1 External Frame Structure (EFS)

7.1.1.11 Truss Framework

The EFS truss framework is a rectangular box-like structure, made from assemblies of welded tubing. During the assembly process, the walls of the box are bolted to the ISS Mounting Plate (as shown in Figure 7-11) and each other to completely surround all the interior components. The top wall is split into two sections, one a permanent feature and one removable (as shown in Figure 7-11) for IFS installation/removal clearance. The end wall is removable for CAL system installation/removal (also shown in Figure 7-11). Both the end wall and the removable top wall are bolted in place.

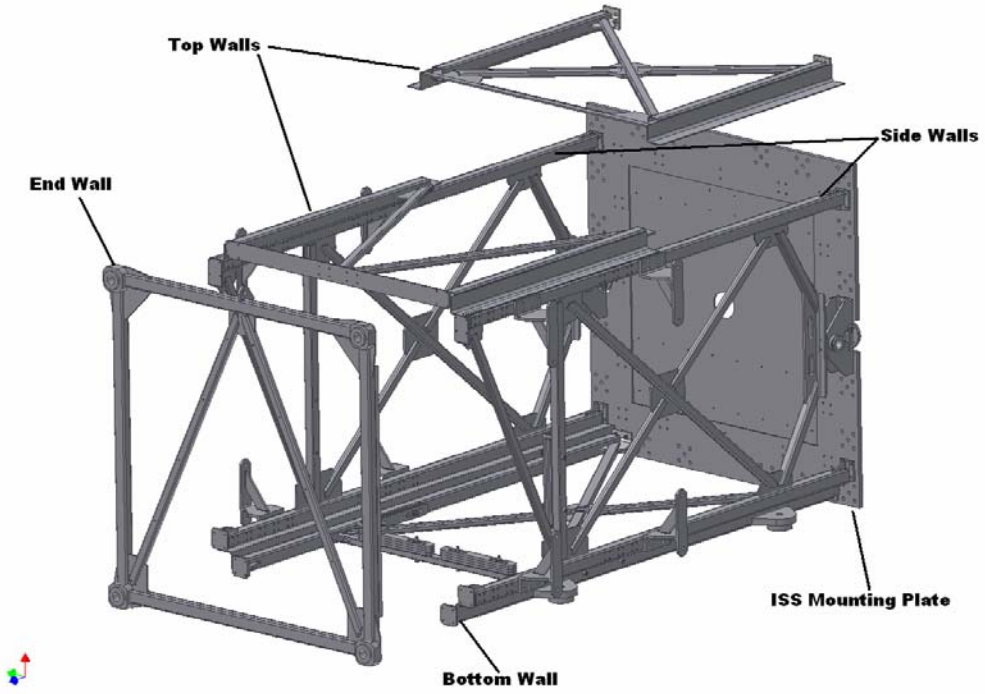

Figure 7-11: EFS assembly

The EFS truss framework has been designed to provide access to the components inside at all times. The interior components must be accessible with the full frame intact while the instrument is mounted on the telescope or handling cart (as discussed in Section 7.3.3.1.3) or sitting in a side-looking orientation on the floor.

The sidewalls each have features that support the electronics enclosures and ballast mass as shown in Figure 7-12. All walls include features for mounting the ballast mass, cables and wiring, system

services and cover panels. In general, the electronics enclosures, cables, services and all non-optical components will be mounted to the EFS frame members.

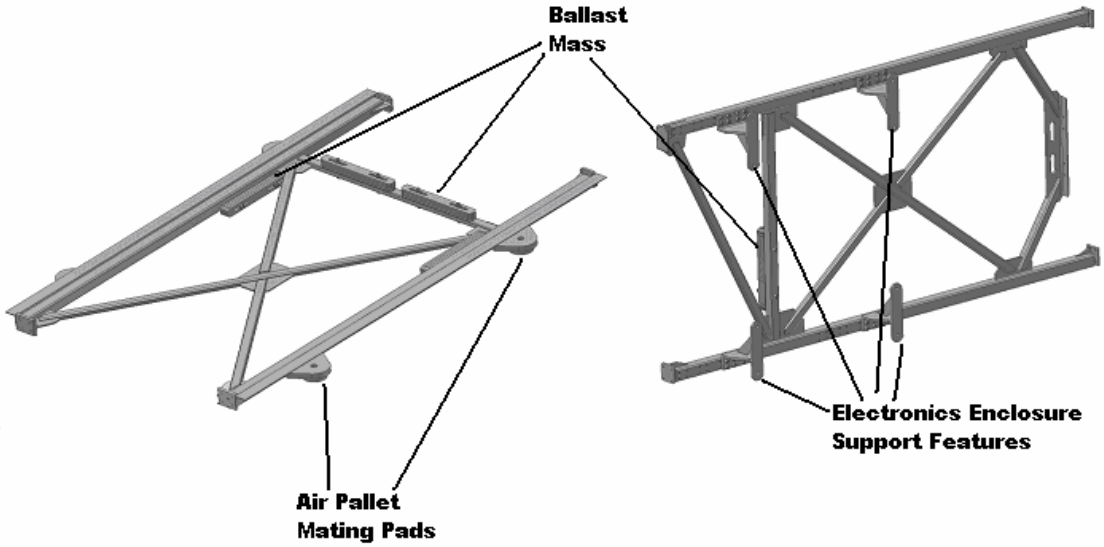

Figure 7-12 Bottom wall and sidewall.

The bottom and end walls have four mounting pads that interface with the Gemini air pallet (as per Gemini ICD 1.9/2.7 see Appendix 2.22) for safe and convenient handling of the instrument at the Gemini facility in both the side-looking and upward-looking orientations. Further information regarding the design of the EFS frame is available in Appendix 7.37.

7.1.1.12 Electronics Enclosures

Two electronics enclosures are based on the Gemini standard enclosures as described in Gemini ICD 1.9/3.7 (see Appendix 2.17) with customizations for the GPI instrument. The enclosures will be mounted to the EFS using the mounting features as shown in Figure 7-12.

The overall height of the enclosures is 1300 mm, which meets the Gemini height requirement for instruments. The width of the enclosures is 600 mm, leaving room for standard 19-inch mounting racks and space for an air plenum for cooling. The depth of the enclosures is 800 mm, with 500 mm reserved for the depth of the electronics in the standard 19-inch racks, 100 mm reserved in the front, 150 mm in the back for cooling air flow and cable routing and the remainder reserved for insulation and panel thickness.

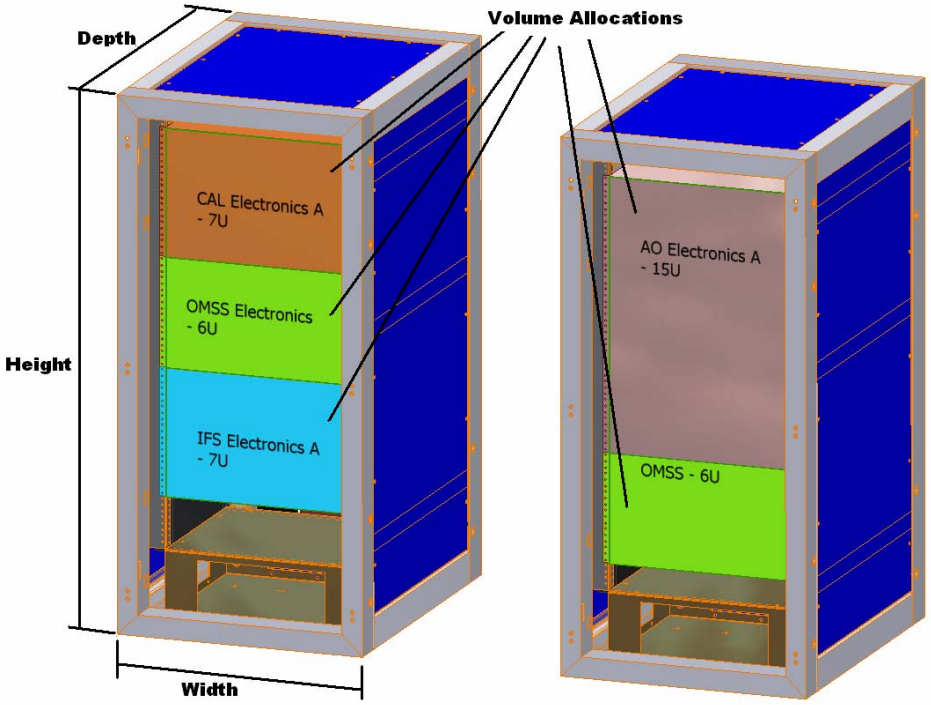

Figure 7-13 Electronics enclosures. The overall height is 1.30 m, the width is 0.60 m, leaving room for standard 19-inch racks and space for cooling. The depth is 0.8 m, with 0.50 m reserved for electronics in the standard racks.

Each box has 21U of standard rack space for a total of 42U. The 42U of rack space has been divided between each of the subsystems as shown in Figure 7-13. The position of components is still under consideration and may change before the instrument is delivered.

Wiring bulkheads on the electronics enclosures will be provided with quick disconnects and connectors similar to the standard issue cabinets. There is a possibility that there will be an additional bulkhead mounted on the upper portion of one or both enclosures, to allow a more direct cable routing between the components in that enclosure to the EFS. All subsystems are allocated distinct bulkhead space as outlined in subsystem ICDs (refer to Appendices 2.11, 2.13 and 2.14). Cable and services routing inside the electronics enclosures are not shown in the figure and will be discussed in Section 7.1.1.14.

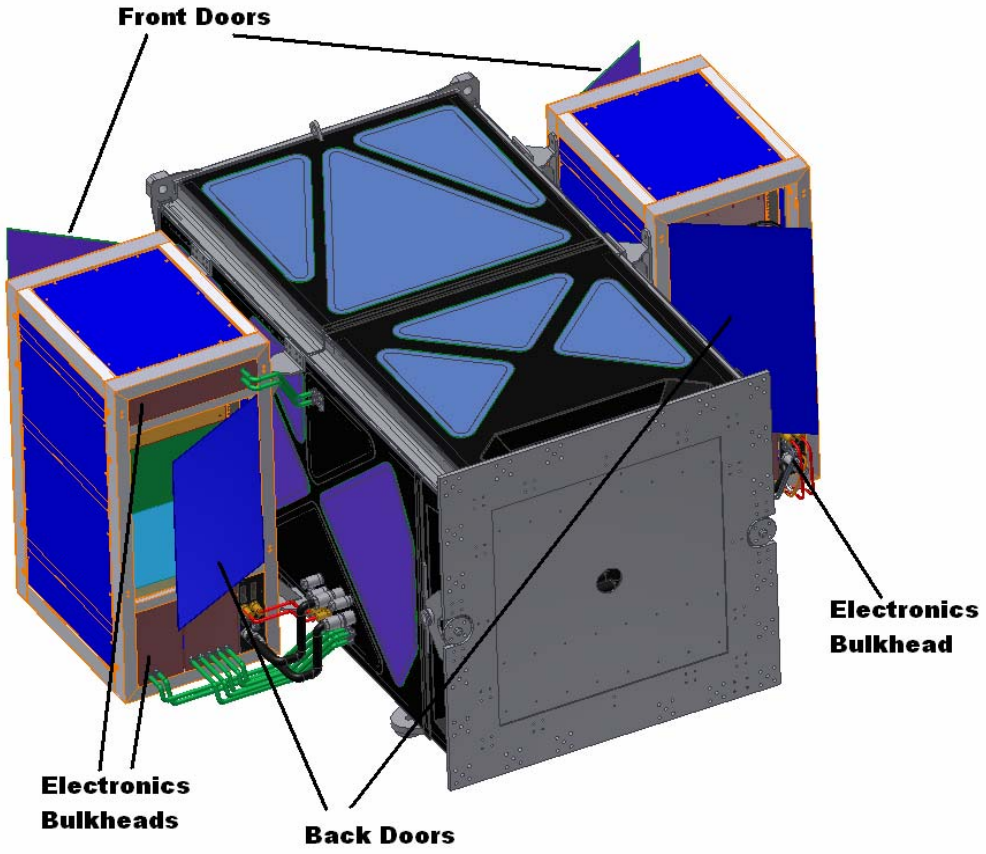

Figure 7-14 Electronics enclosure doors and bulkheads

The doors to the electronics enclosures will be nominally mounted so that they open as shown in Figure 7-14 and will provide ample access for maintenance and replacement of components. Details of the hinges and fasteners are not yet specified but the chosen hardware will be convenient and durable.

The electronics enclosures will be thermally insulated and cooled by a fan, with the heat being removed through a heat exchanger that is in turn supplied with chilled glycol from Gemini facility supply. The fans will be specified to have low vibration and will be mounted on vibration isolators. The front of the cabinets forms the cold-air plenum. Cooling air flows through the front of electronics, exhausting out the sides and rear and down the back to the heat exchangers.

The mass allocated to each electronics enclosure is 200 kg, with 90 kg allocated for the mass of the enclosure without electronics components added. It should be noted that the center of gravity location for the electronics enclosures will be continuously refined, once all electronics components have been specified.

Further work continues as more information becomes available regarding the actual components to be mounted in the enclosures. It should be noted that the AO and CAL computers are currently specified to be 26.5 inches (673.1 mm) in depth, encroaching on the air space allowed for cooling in the cabinet and

interfering physically with the doors. Situating these computers at the top of their enclosures, spacing them towards the front, and providing additional volume in the doors will accommodate this.

A third, smaller enclosure is being considered to house the controller for the tweeter DM to alleviate cabling concerns for its electronics and provide additional rack space. A preliminary analysis indicates that there is space available on the EFS frame under the AO optical table to support such an enclosure. This will be resolved early in the CDR phase.

7.1.1.13 Light-Tight Panels

The cover panels on the EFS structure are required to seal the instrument from light and dust. Each wall of the EFS truss structure has a thin aluminum alloy cover panel frame attached to it, with openings cut into them as shown in Figure 7-15. It may be possible to incorporate the cover panel frame directly into the EFS truss assembly to save mass, and this continues to be explored. Cover panels (coloured blue in the figure) fit into depressions in the cover panel frames. Light and air seals will be maintained by appropriate location of fasteners and the use of gaskets along all seams and cracks. Details of this assembly are available in Appendix 7.37.

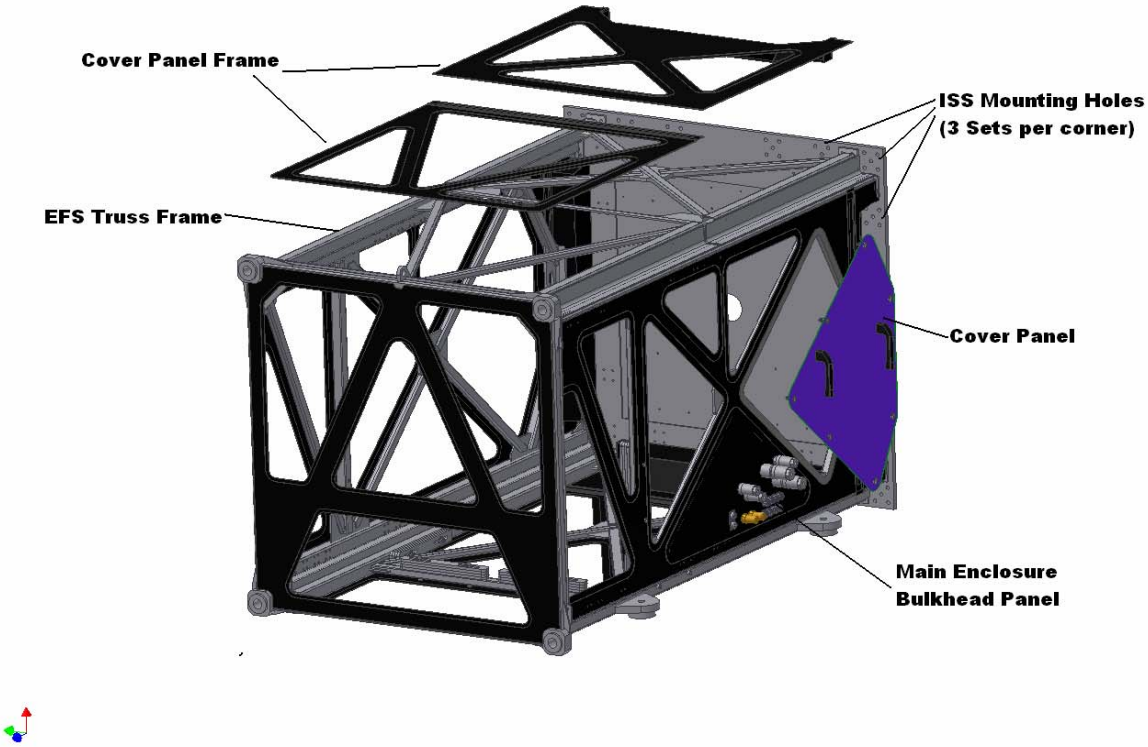

Figure 7-15 EFS cover panel frame.

The panels will employ easy-to-use fasteners selected in collaboration with Gemini operations personnel, as well as handles to provide easy handling. The instrument main optical enclosure will have bulkhead panels for cables and services routing at different locations on the instrument.

7.1.1.14 Cable/Services Routing

All cables, wires and services will be clearly labeled at both ends and due to the varying operational gravity vectors, all cable/service routing will be securely fastened throughout the instrument. The tweeter DM cable has special considerations due to its fragile nature that will be discussed in Section 7.3.2.1.7.

The main instrument patch panel (Figure 7-16) will be provided in the location described in Gemini ICD 1.9/3.6 (Appendix 2.16), which has been recently updated by Gemini. All systems services provided by Gemini will be patched into this panel using quick disconnects, using connectors specified in ICD 1.9/3.6. Mounting and support for the patch panel have yet to be designed into the system but is not expected to present any difficulties.

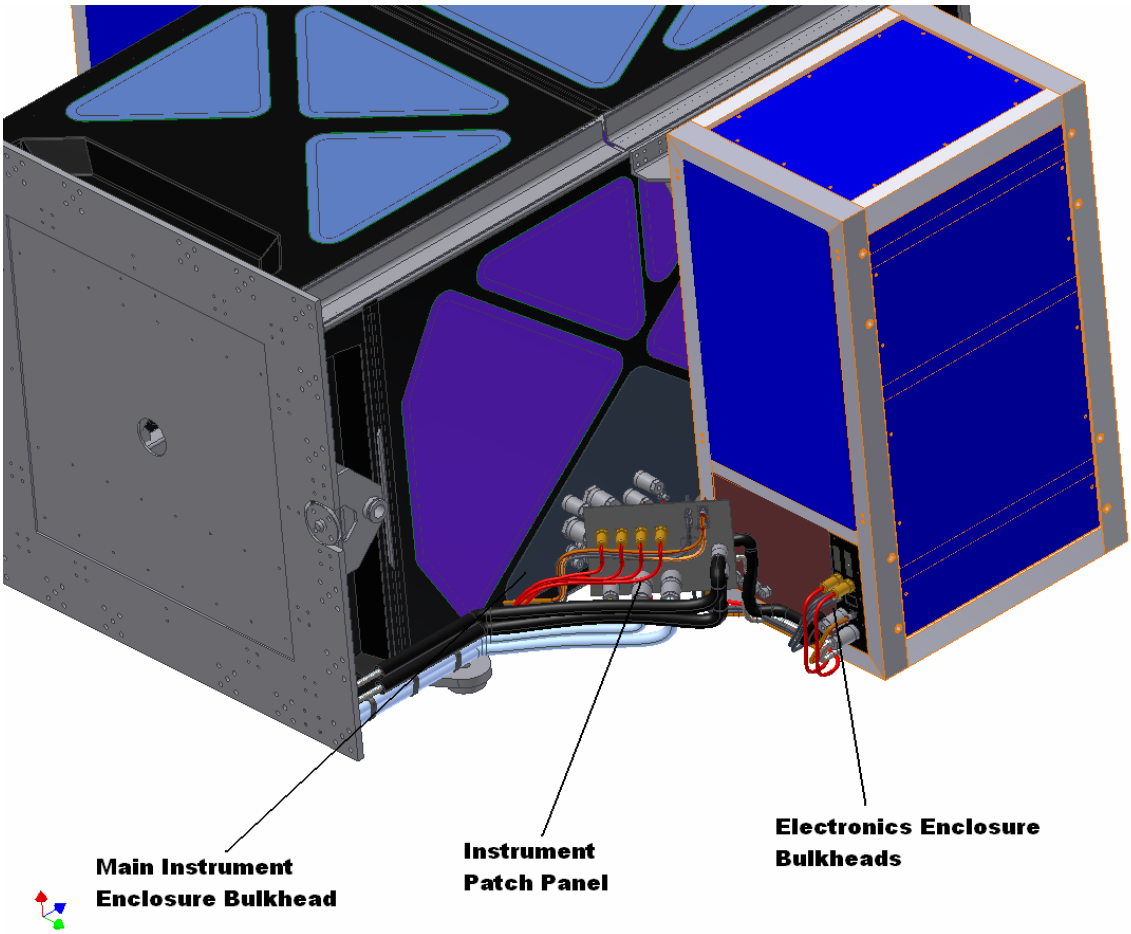

Figure 7-16 Instrument patch panel. All systems services provided by Gemini will be patched into this panel using quick disconnects.

Each electronics enclosure has at least one bulkhead using Gemini recommended connectors as discussed in Section 7.1.1.12. The optics enclosure will also have bulkhead panels (see Figure 7-16 and Figure 7-17) with quick disconnects and connectors that allow cables and services to be attached and removed without interfering with the enclosure structure or protective cover panels. These bulkhead

panels will be very similar to the light-tight cover panels (discussed in Section 7.1.1.13) in that they will be cut from aluminum alloy sheets and include gaskets to provide seals against light and dust. However, the bulkhead panels will not be removable in the same manner as the cover panels.

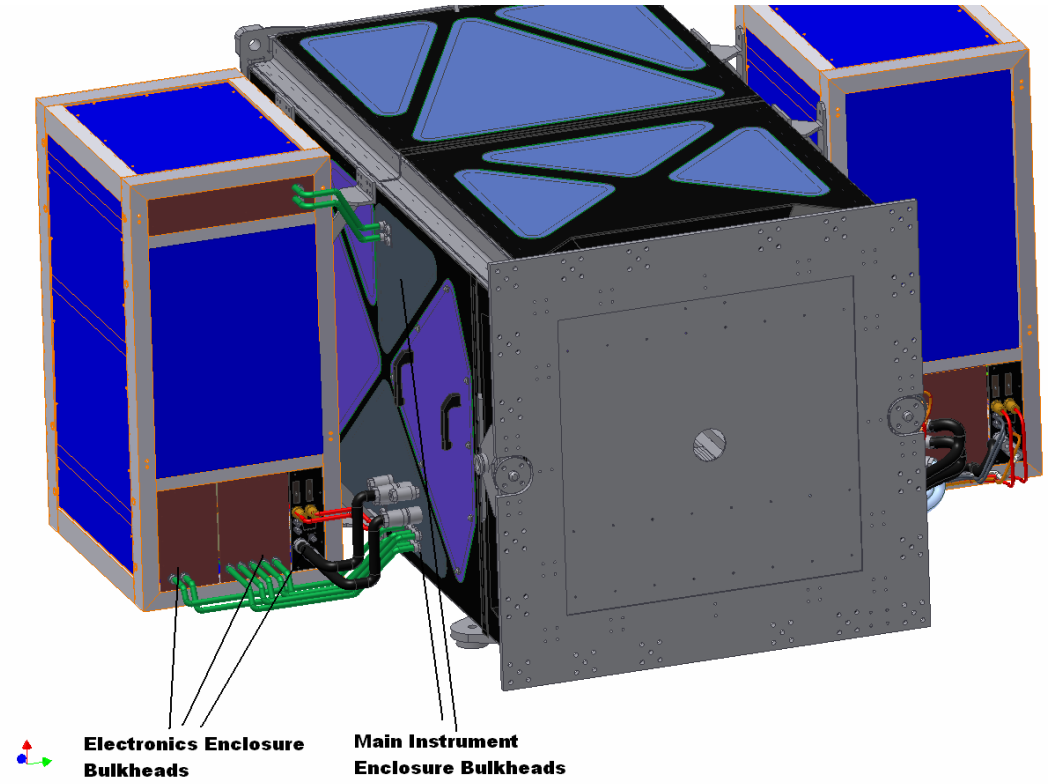

Figure 7-17 Instrument enclosure bulkheads. The enclosures will have bulkhead panels with quick disconnects and connectors that allow cables and services to be attached and removed without interfering with the enclosure structure or protective cover panels.

From the patch panel, services will be routed based on where they are used in the instrument. Some will be routed directly into the two electronics enclosures and others routed into the main instrument enclosure. Some services, such as the glycol, will be split and fed several different subsystems simultaneously.

In general, the cables inside the electronics cabinets will be routed from their location on the standard 19" racks, down the sides of the enclosure to the bulkhead. This is shown in general in Figure 7-18.

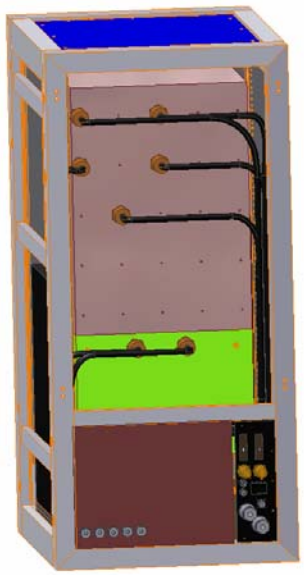

Figure 7-18 EE cable routing. In general, the cables inside the electronics cabinets will be routed from their location on the standard 19" racks, down the sides of the enclosure to the bulkhead.

All of the glycol lines will be insulated along their entire length to improve the efficiency of the heat removal throughout the system and to avoid condensation inside the optics enclosure. The helium lines will likely require vibration damping wherever they are fastened to the instrument and will be routed as directly as possible from the instrument patch panel to the IFS subsystem. An air supply has been provided for although air filtration has not yet been designed into the system. The addition of air filtration is not expected to cause any difficulties. A discussion of cable and services routing is available in Appendix 7.3. Planning of the layout is ongoing as more details about system and subsystem requirements are identified.

7.1.1.15 EFS System Analysis

7.3.1.1.1 Mass / Centre of Mass Analysis

The mass of the EFS is currently calculated to be 947 kg with the centre of mass located at (x,y,z) = (6, -89, -1329) mm. This will continue to be updated as the design becomes more mature. Work to reduce the overall mass of this assembly is ongoing, in conjunction with the FEA analysis of this structure (see Section 7.3.1.1.2). The centre of mass of the instrument will be adjusted using ballast mass. At the current state of the design, two sets of additional ballast masses are being planned: round disks bolted to the ISS face and long solid bars that are located mid-way down the instrument as shown in Figure 7-19.

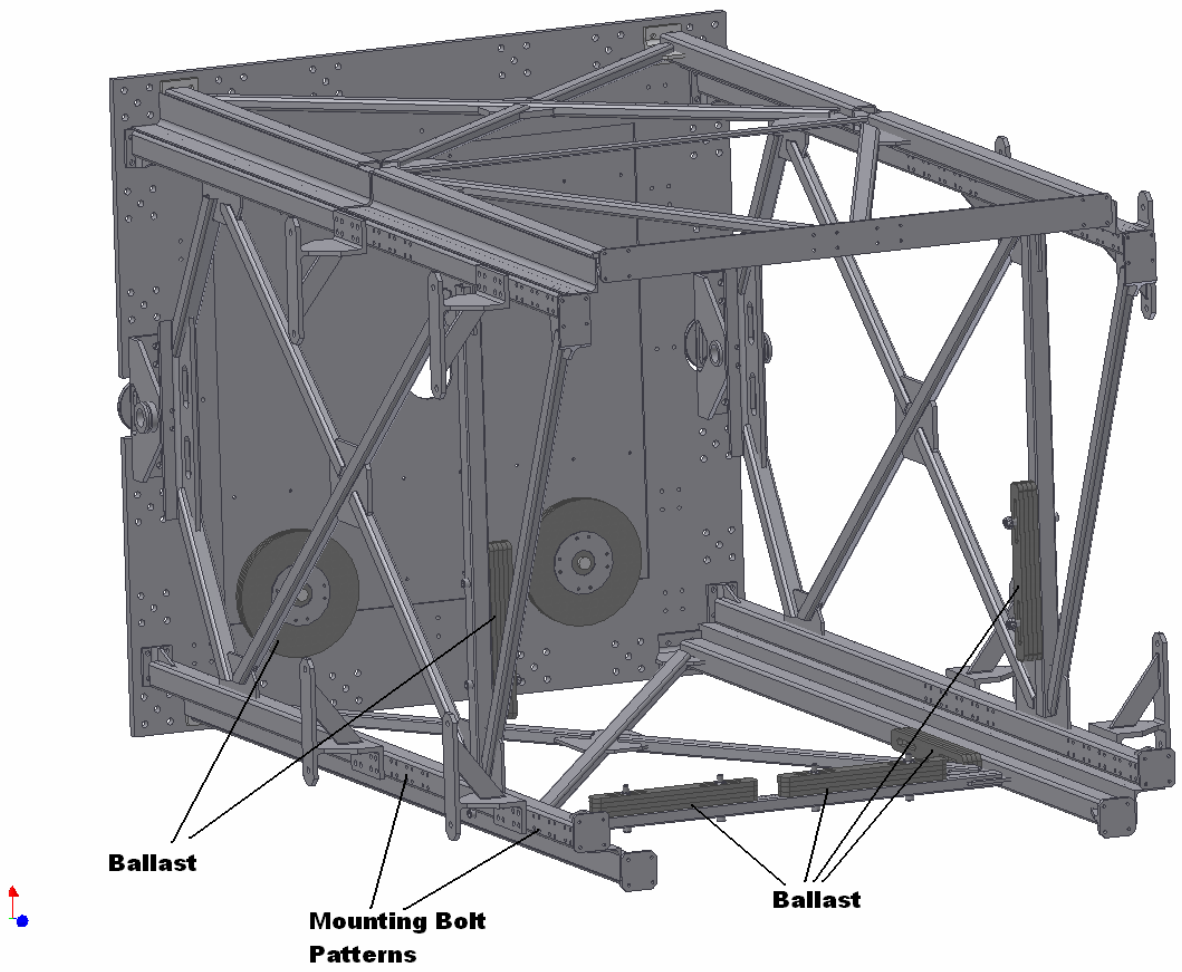

Figure 7-19 Ballast mass and extra mounting bolt patterns.

In addition to the ballast masses, the locations of the electronics enclosures are adjustable in the Z-direction by the provision of extra mounting points along the lengths of the EFS sidewalls at 100 mm increments. The position of the ballast mass in the instrument will be finalized as the design of all systems and subsystems matures.

7.3.1.1.2 FEA Flexure Analysis

The EFS Truss Framework is required to be strong and stiff under all expected loads and in all expected orientations. The load cases can be divided logically into two categories: Operational (while installed on the Gemini ISS) and Handling (while in storage, during assembly and integration, while being maneuvered about the Gemini Observatory). Details of all of the load cases are discussed in Appendix 7.38. During operational conditions, the EFS Truss Framework must support its own mass and the electronics enclosures in almost all gravity orientations. During handling conditions, the EFS Truss Framework must support its own mass, the mass of the electronics enclosures, the ISS Mounting Plate and the entire FSS truss and attached components. Also during handling, there is a smaller selection of gravity orientations to consider but there are load cases that involve additional mounting and handling

features on the EFS truss structure (e.g., the air pallet mounting pads, Figure 7-12 and the lifting pintles and eye,Figure 7-79).

During handling conditions, the EFS is required to support all required loads. This is also true during operations, with the additional requirement that the structure must not deflect enough to make contact with the components of the enclosed FSS system or to create light and air gaps in the cover panel assemblies (see Section 7.1.1.13)

The EFS truss framework was analyzed with a specific goal in mind: to determine the flexure and stresses in the framework under all conceivable load conditions. In order to perform an efficient analysis using ANSYS FEA software, the structure was created as a set of points, lines and areas. Details of assumptions and the analysis method are in Appendix 7.39. These geometries were used to create a series of ANSYS elements that represent the GPI instrument (see Figure 7-20).

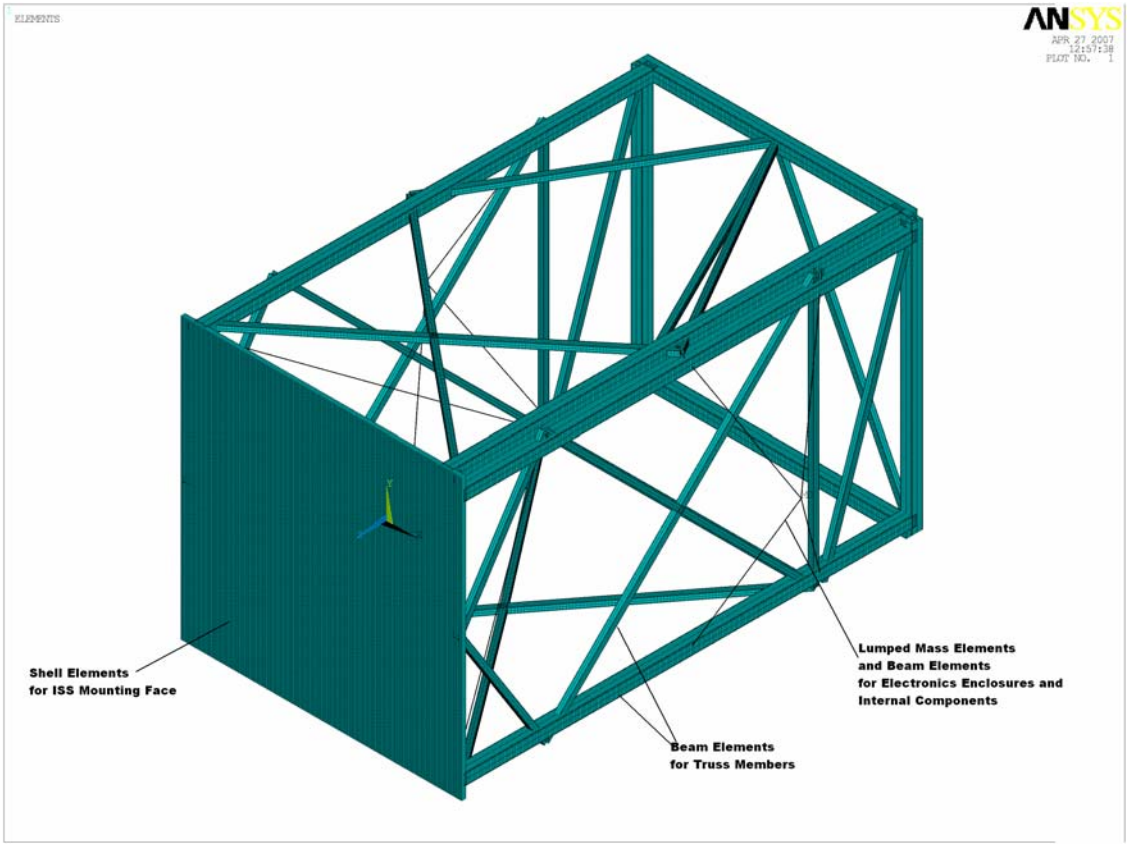

Figure 7-20 EFS FEA elements.

The electronics enclosures were modeled as lumped masses that imparted no additional structural rigidity to the EFS truss members. It is assumed that in reality, any rigidity will help support the electronics enclosures but this assumption has not yet been verified. Beam elements were used to join the lumped mass elements to the truss structure at coordinates that represent the mounting points of the electronics enclosures to the truss structure.

It was assumed that the ISS Mounting Plate was made of mild steel and contributed to the strength of the structure in certain load cases. Since the ISS mounting plate characteristics are not fully modeled at this time, it will be prudent to check this assumption later in the project schedule.

It should be noted that the FEA analysis performed did not take into account buckling of members and this analysis is being done separately. Forces in the members of a selection of representative cases will be taken from the FEA results and used to analyze the members for possibility of buckling. Further analysis will continue through CDR.

The worst case of stress and deflection during operational conditions was found when the instrument was in a horizontal orientation (mounted on a side-looking port with the telescope at zenith). The maximum stress found in the structure was 50.5 MPa (Figure 7-21). Some of the stresses appear very close to nodes and will be looked at more thoroughly as the design for connections and joints progresses. The maximum deflection was 0.3 mm over the total instrument (Figure 7-22). These stress and deflection results are well within the design requirements.

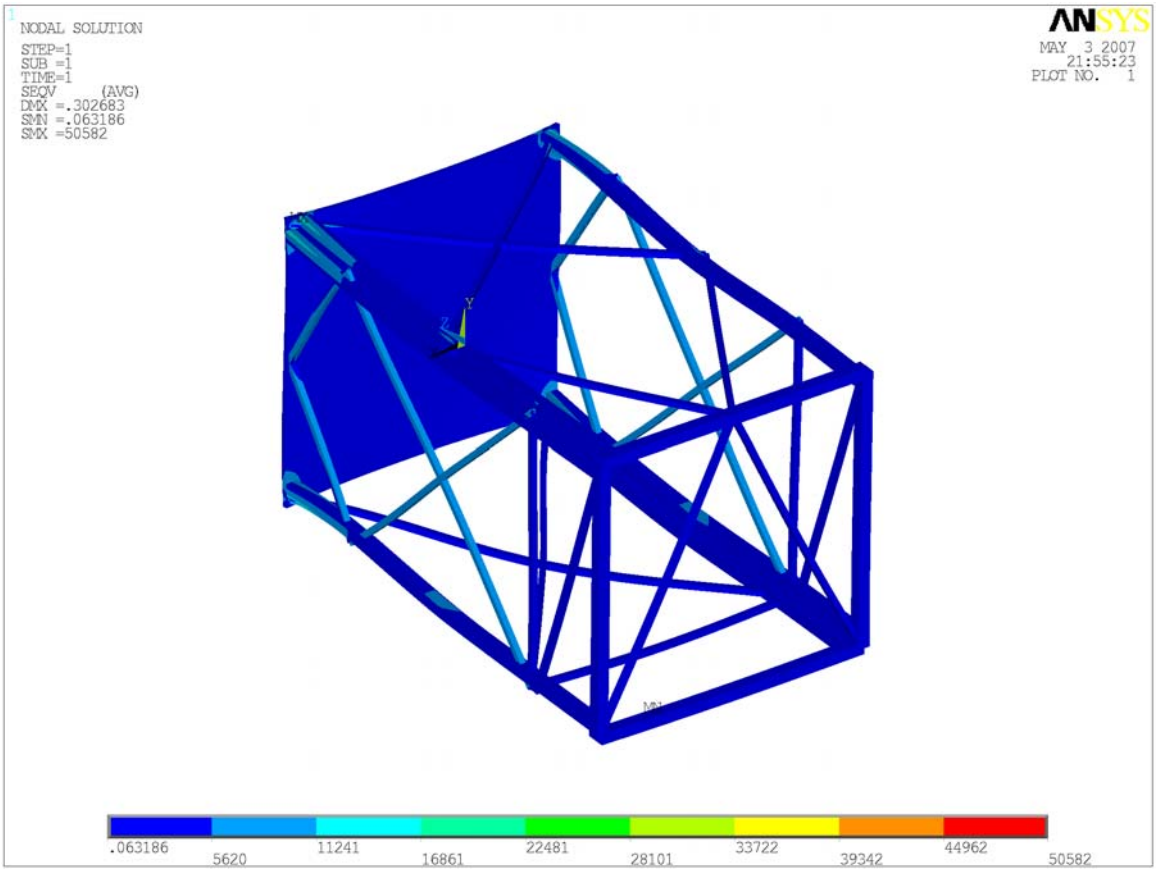

Figure 7-21 EFS stress for load case 1 (mounted on a side-looking port with the telescope at zenith). The maximum stress is 50.5 MPa.

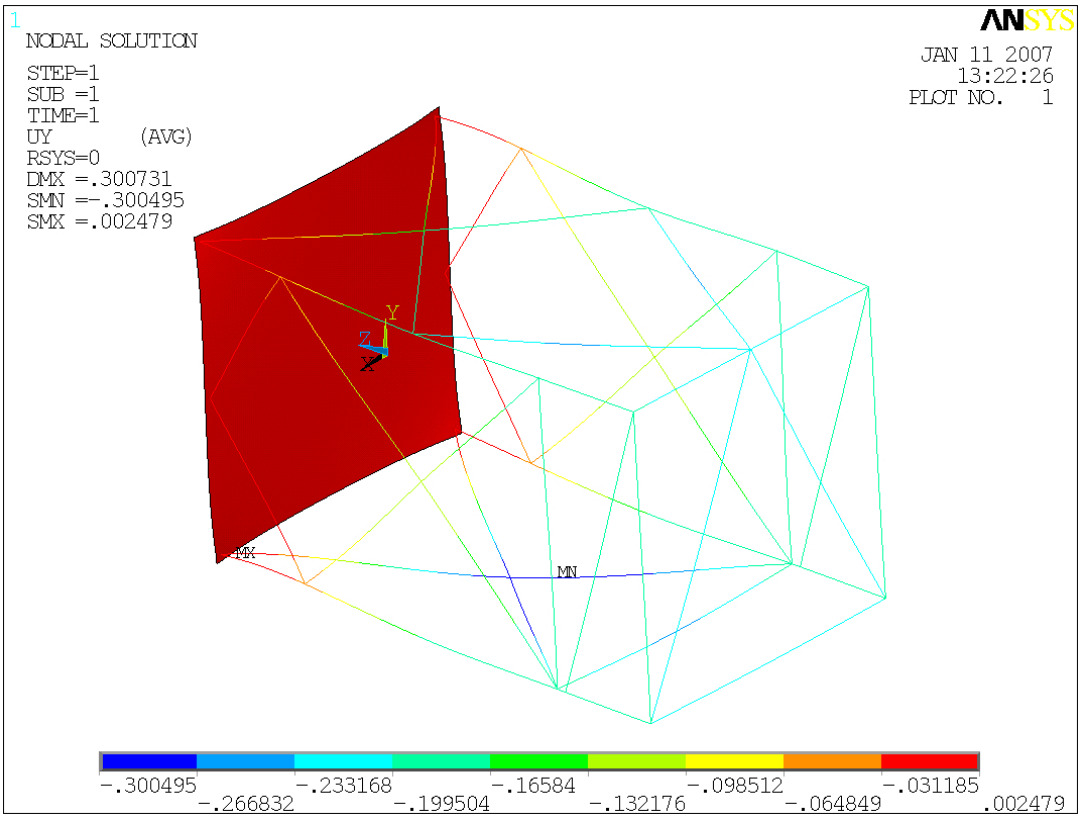

Figure 7-22 EFS deflection for load case 1 (mounted on a side-looking port with the telescope at zenith). The maximum deflection is was 0.3 mm.

During handling, a special case (load case 7 of Appendix 7.38) was analyzed. The instrument in this case would be fully assembled, sitting on the floor on its four side-looking mounting pads and the top removable panel and end panel would be removed as shown in Figure 7-23. This was a severe load case for stress and deflection; however the calculated values were reasonable. This gives confidence to the design for the truss structure.

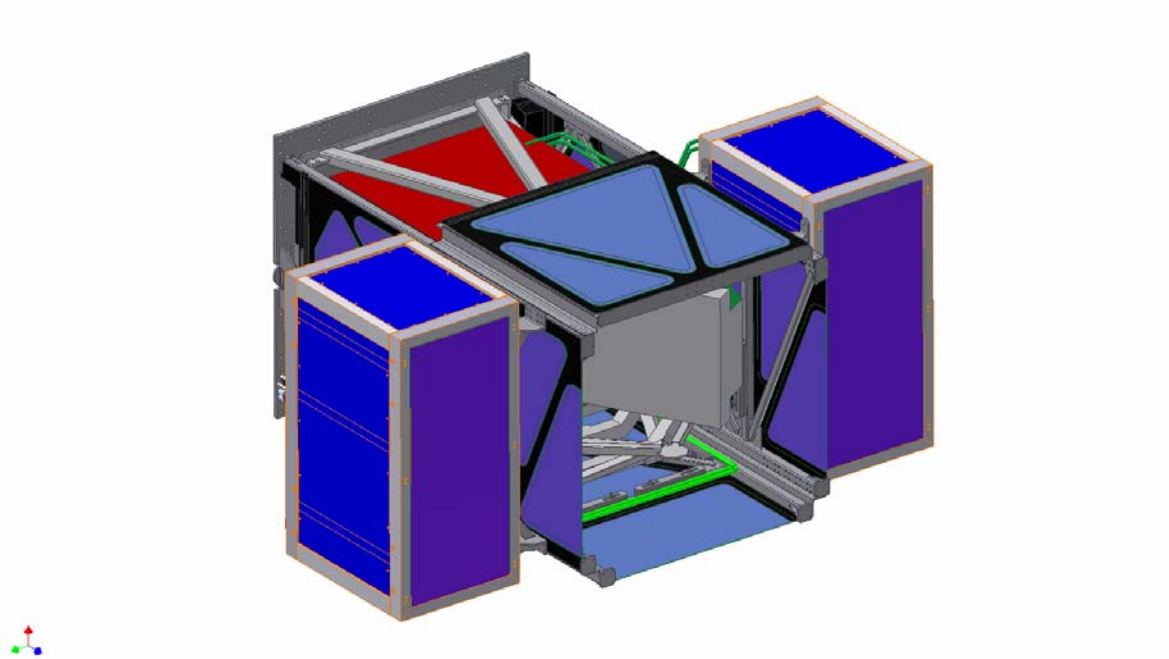

Figure 7-23 EFS load case 7 (handling). The instrument is fully assembled, sitting on the floor on its four side-looking mounting pads and the top removable panel and end panel removed.

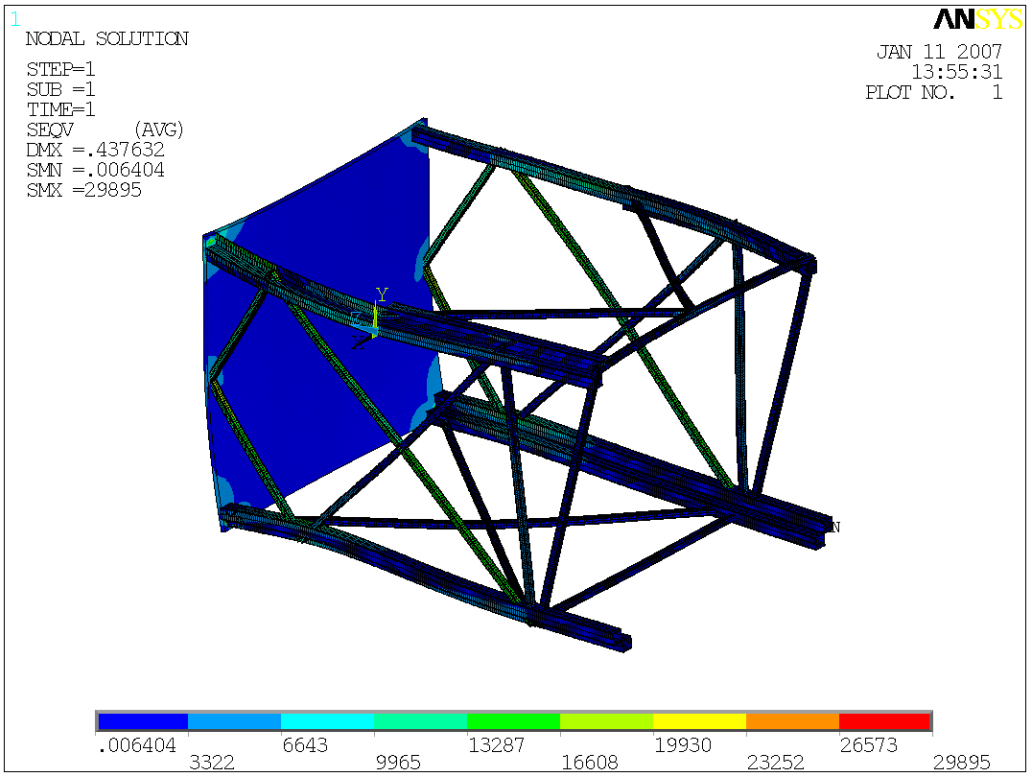

Figure 7-24 EFS stress results for load case 7 (handling).

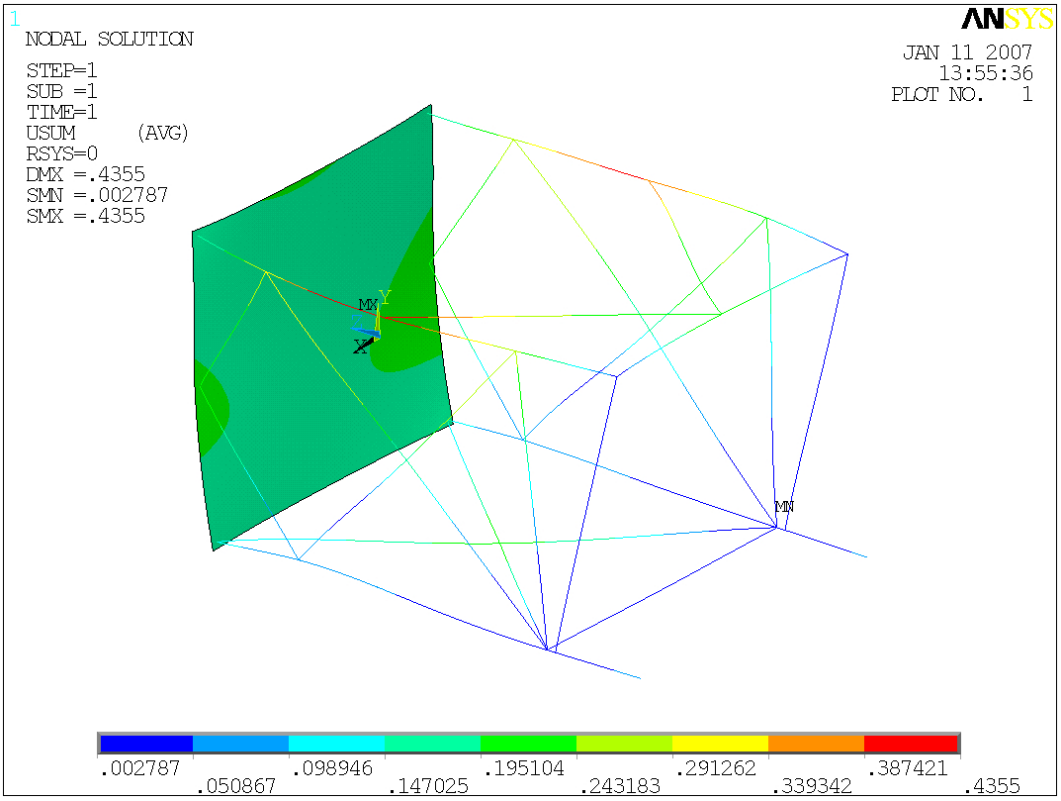

Figure 7-25 EFS deflection results for load case 7 (handling).

It is expected that light-weighting will be possible by identifying members that are not supporting significant loads in any configuration and possibly replacing them with gussets. Adding members that are more efficient in the sense that they provide support in more than one orientation will likely be a fruitful avenue to pursue. More detailed analysis of connections and joints will be ongoing through the next phase of the project. An analysis verifying that the ISS mounting plate supports the structure will be performed as well.

7.3.2 Flexure Sensitive Structure (FSS)

7.1.1.16 Mounting Plate Assembly

The Mounting Plate assembly forms the mechanical interface between GPI and the Gemini Instrument Support Structure (Figure 7-26). The plate includes an array of boltholes to attach the instrument to the telescope. The plate also serves as the mechanical link between the Flexure Sensitive Structure and the External Frame Structure. When the instrument is mounted on the telescope, the FSS and EFS are supported independently from this plate. However, when the instrument is sitting on the air pallet or handling cart, the weight of the FSS is transferred through the mount plate, into the EFS and subsequently into the handling fixture. For this reason, the mount plate needs to strong enough to react the forces and moments of the cantilevered FSS. To provide the required strength, and to match the coefficient of thermal expansion of the Gemini ISS cube, the Mount Plate is made from 18 mm of mild steel, with a central section that is thinner to reduce weight.

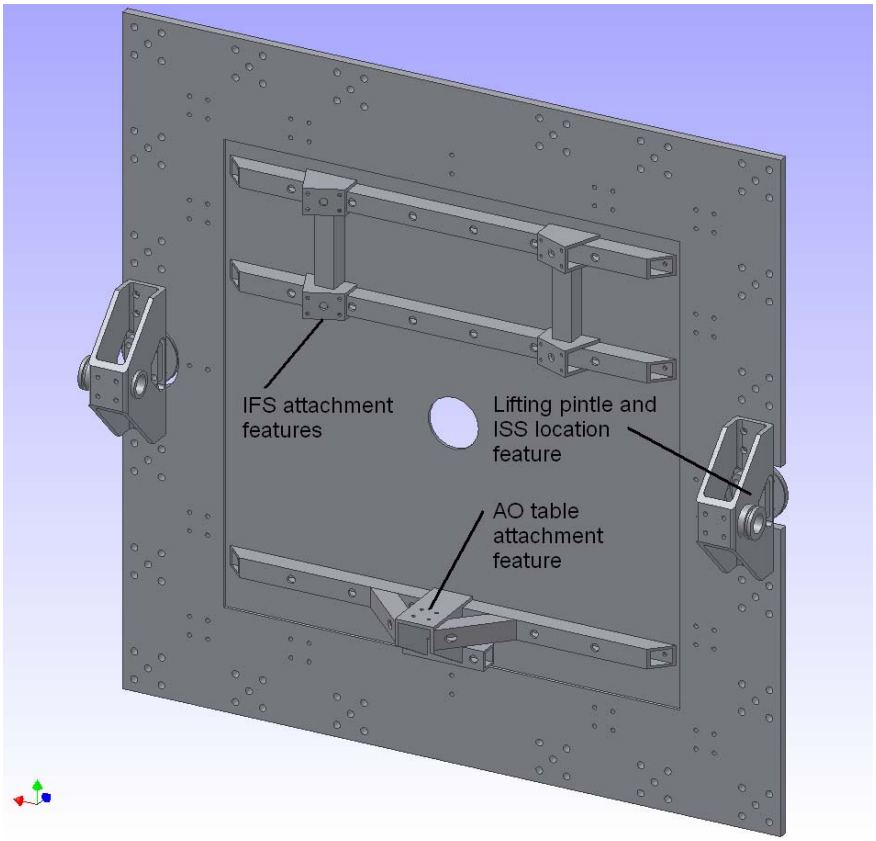

Figure 7-26 FSS mounting plate assembly.

The Mount Plate serves other functions as well, such as providing a semi-kinematic mounting interface between GPI and the telescope. This is accomplished through the use of two posts that are initially attached to the Gemini ISS (Figure 7-27). Once these posts are attached, GPI is mounted and the posts are located in two features shaped like a "V" and "flat" (Figure 7-28). These features uniquely locate

the instrument in the X and Y directions, and constrain rotations about the Z-axis. To provide final adjustment of the overall instrument location, each feature will include a mechanism for fine adjustment of its position. This adjustment procedure requires that the weight of GPI be removed from the locating posts. Once the adjustments are made, the location features will also provide a tensioning device (such as a jacking screw) to ensure that each location post is fully engaged with its associated mating feature. This jacking screw will assist in accurately locating the instrument when mounted on port 1 of the ISS, where gravity does not assist in seating the location features.

Finally, near each location feature is a pintle for attaching lifting slings to the instrument. These pintles are used both for lifting and assist in the rotation of the instrument to the upward-looking orientation (see Section 7.3.3.1.2) below.

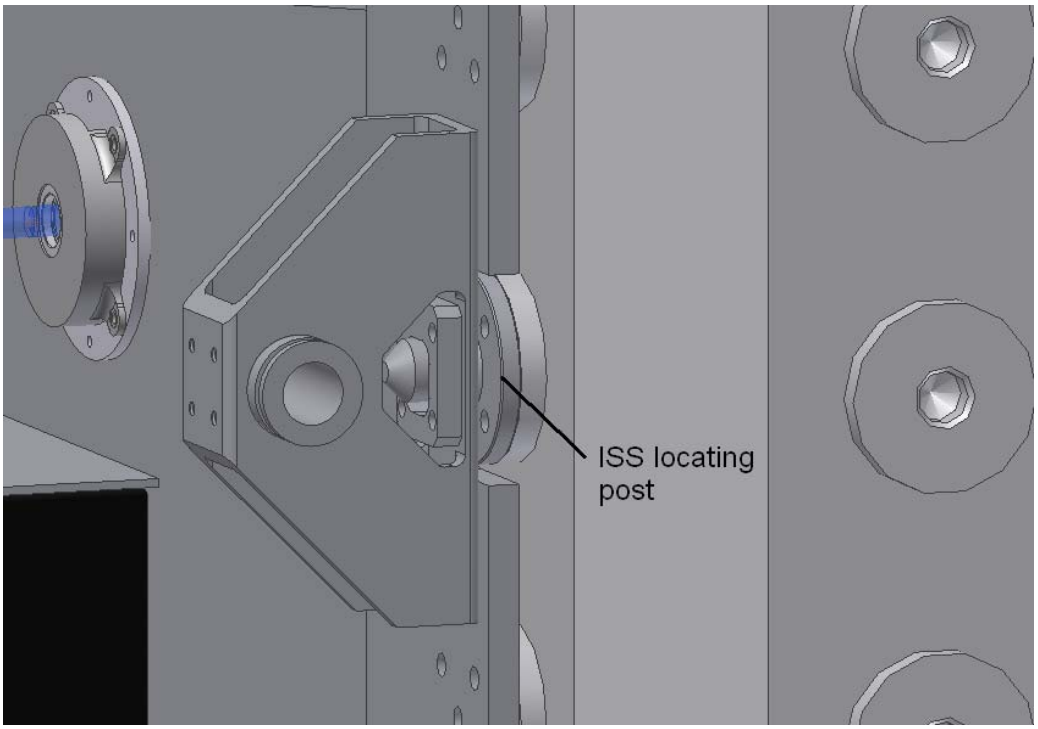

Figure 7-27 Mounting interface details.

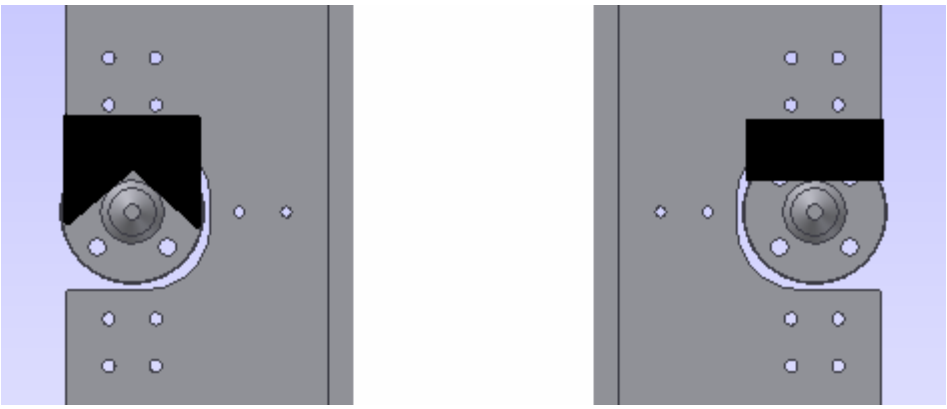

Figure 7-28 Semi-kinematic "V" and "flat" locating features (schematic view).

7.1.1.17 Truss Framework

The FSS Truss Framework is composed of several independent welded assemblies that are bolted together (Figure 7-29). The main truss members form a box-like structure with triangular walls that is reminiscent of the common Serrurier truss found in many telescope systems. The purpose of this structure is to support an octagonal truss called the Interface Ring. This ring is designed to be extremely stiff, since it supports all three optical sub-systems (AO module, CAL module, and IFS). On the aft end of the truss system are two more truss assemblies that support the CAL optical table. All trusses are made from welded mild steel tubing to provide high strength, stiffness and to maintain a consistent coefficient of thermal expansion throughout the structure.

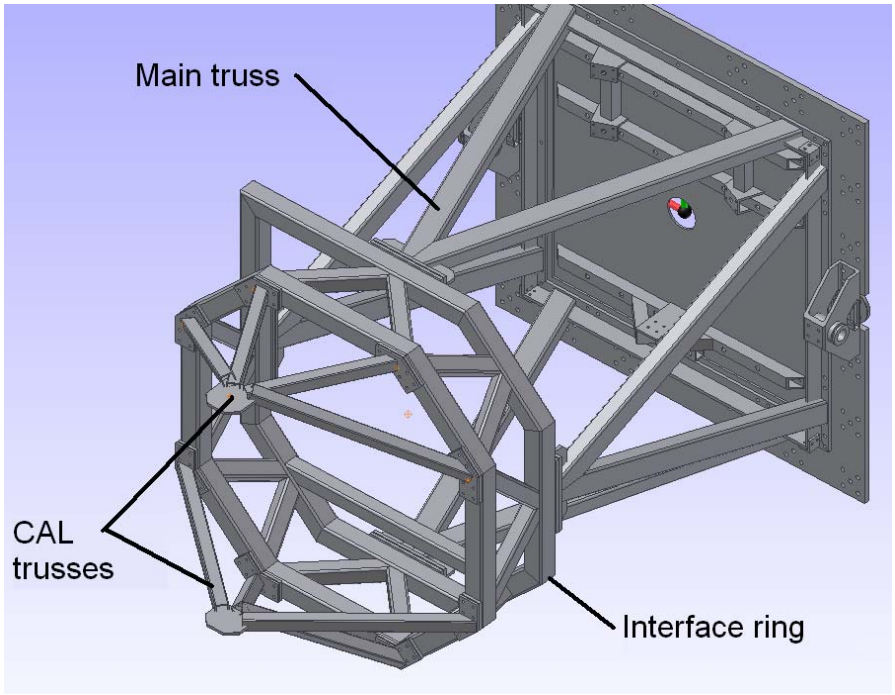

Figure 7-29 FSS truss framework.

7.1.1.18 AO Optical Table

The AO optical table (Figure 7-30) is located within the main truss, between the Mounting Plate and the Interface Ring. The incoming light from the telescope forms the Cassegrain focus 80 mm above the surface of the table, and approximately 150 mm inside the leading edge. All opto-mechanical assemblies that are part of the AO module are mounted to this table, except the entrance window and shutter which are attached to the Mounting Plate.

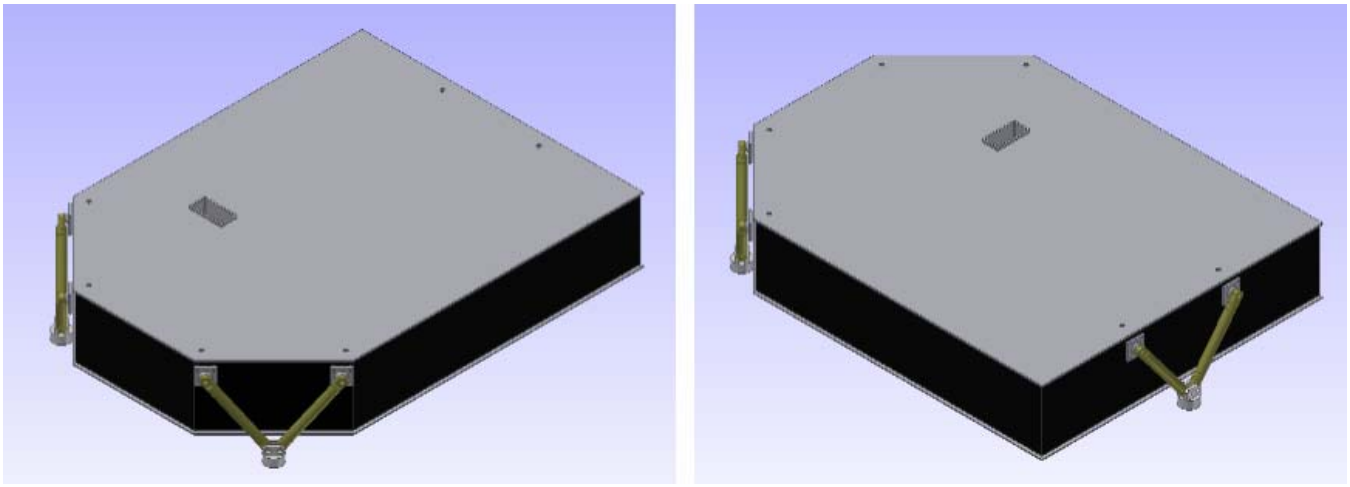

Figure 7-30 AO optical table.

The table is located by three identical flexure bipods attached to the outer edge (Figure 7-31). These bipods uniquely constrain the six degrees of freedom of the table, and thus provide theoretically distortion-free location. The bipods themselves are made from ∅25 mm bars of titanium 6Al-4V, which is renowned for its high micro-yield strength but moderate stiffness; both desirable qualities for flexures. The length and materials of the flexures have also been chosen to offset the thermal contraction of the aluminum optic mounts and mechanisms, providing a nearly athermal optical system in the direction normal to the table surface.

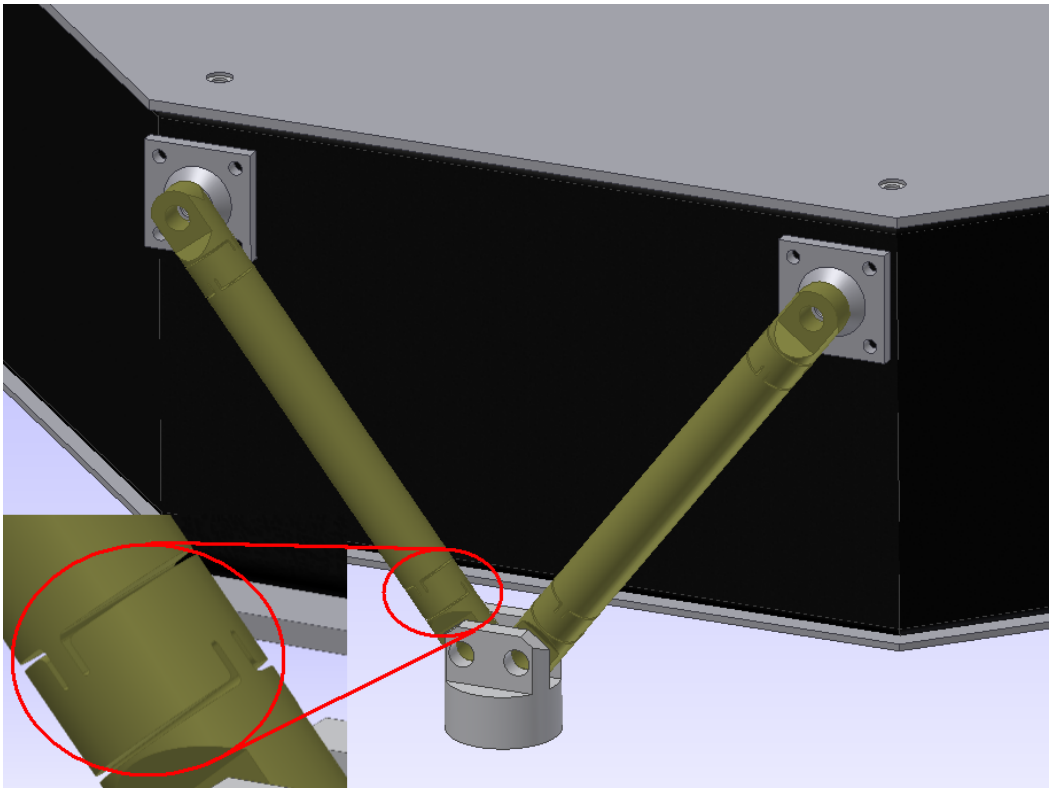

Figure 7-31 Detail of the AO table flexure bipod. The bipods are made from ∅25 mm bars of titanium 6Al-4V.

The table mimics the typical construction of commercial optical tables, with an upper and lower face sheet separated by an 8" (203.2 mm) thick mild-steel honeycomb core. The upper face sheet contains a grid of M6 x 1.0 threaded holes on 25 mm spacing. To accommodate the special needs of GPI (with its variable temperature and gravity vector orientation) the table has several customizations. First, two of the corners include 45° chamfers which provide mounting locations for two of the flexure bipods. Second, the side wall construction will be modified to provide additional shear stiffness between the upper and lower face sheets, as well as stiffness at the bipod attachment points. Through-thickness stiffeners will be added to increase the tension loading capacity between the upper and lower face sheets. Finally, there is a rectangular port cut through the thickness of the table for the tweeter DM cabling. Due to the fragility of this cabling, and the difficulty of routing it on the surface of the optical table, these cables will be passed through the table directly behind the DM.

7.1.1.19 CAL Module

The Calibration module (CAL) accepts the AO corrected light after it leaves the AO optical table (Figure 7-32). The CAL is also built upon an optical breadboard, which is adjacent to but not touching the AO optical table. The CAL breadboard, which is 4" (101.6 mm) thick, is supported by a truss framework that is attached to the interface ring. Between the truss framework and the breadboard are three bipod flexures, arranged at 120° angles around the approximate centre of mass (Figure 7-33). These bipods are similar to the ones used on the AO table, except that each leg includes a fine adjustment screw for changing the length of the leg. This fine adjustment permits alignment of the CAL module to the AO module with control over six degrees of freedom.

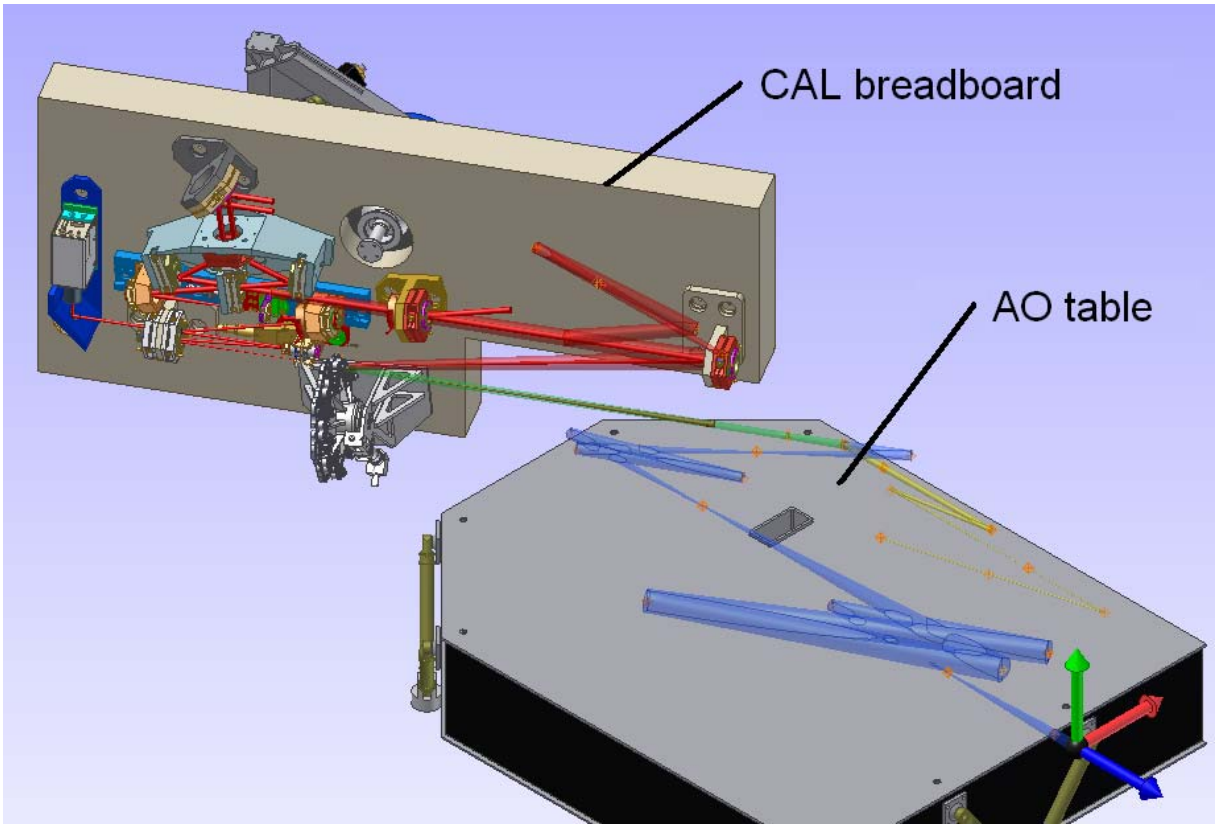

Figure 7-32 CAL system breadboard.

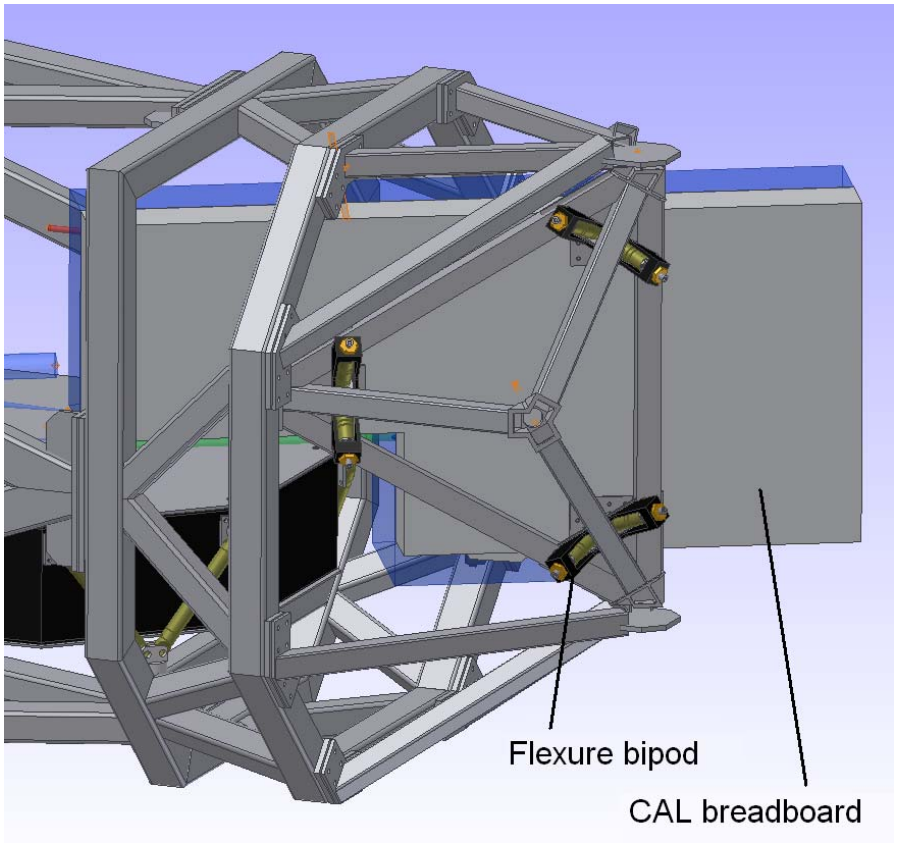

Figure 7-33 CAL system bipods and support truss.

7.1.1.20 IFS

The IFS is a large and heavy (~ 300 kg) sub-system within the FSS. To meet the centre of mass specifications of the instrument, the IFS was positioned as close to the Mounting Plate as possible, in a location above the AO optical table (Figure 7-34). The science light that leaves the CAL system reflects off a pair of steering mirrors that direct the beam into the IFS. This steering pair will be used to compensate for the inevitable flexure that results from mounting this heavy sub-system.

The IFS is attached to the Mounting Plate and the Interface Ring with flexures (similar to the AO table and CAL breadboard). Due to the weight and configuration of the flexures, an additional seventh flexure was required to improve the constraint. Near the entrance window of the cryostat there is a flexure tripod that attaches the IFS to the Interface Ring (Figure 7-34). This constrains all three linear degrees of freedom at this location. At the opposite end, there are two flexure bipods to constrain the remaining rotational degrees of freedom (Figure 7-35). Although seven flexures result in an over-constrained system, the bipods have been oriented so that their compliant direction intersects the fixed point created by the tripod. This means that when the aluminum cryostat and steel truss contract differentially in the cold, the flexures permit relative motion in the required direction while maintaining the location of the entrance window and minimizing stresses in the supports.

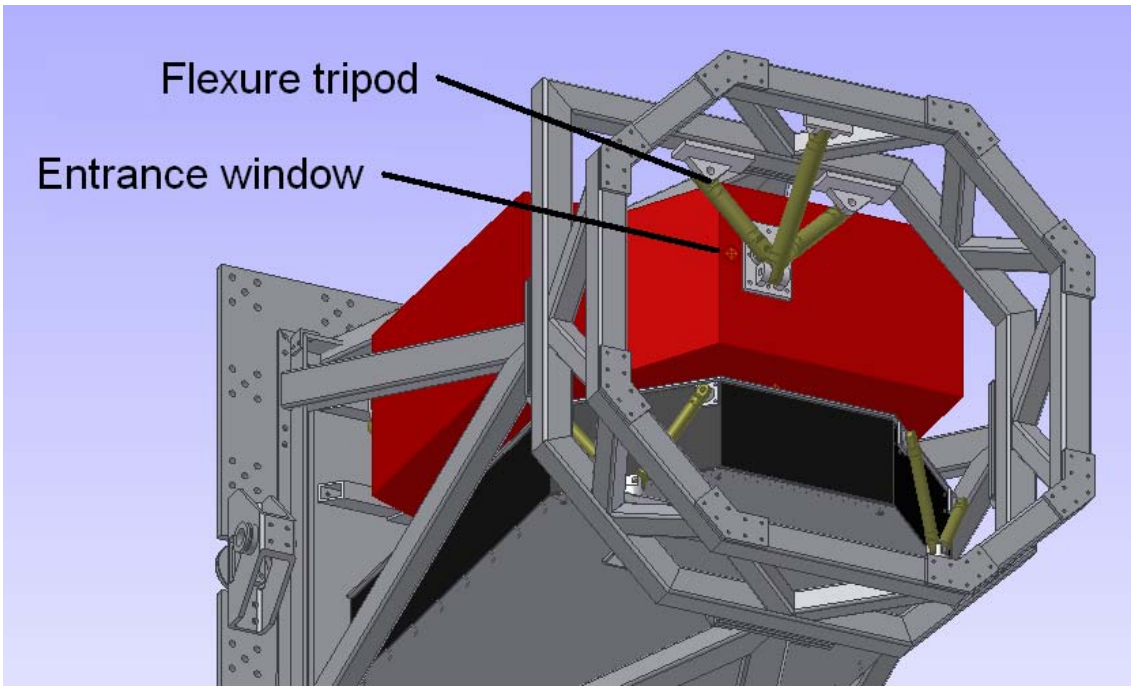

Figure 7-34 IFS volume and tripod flexure.

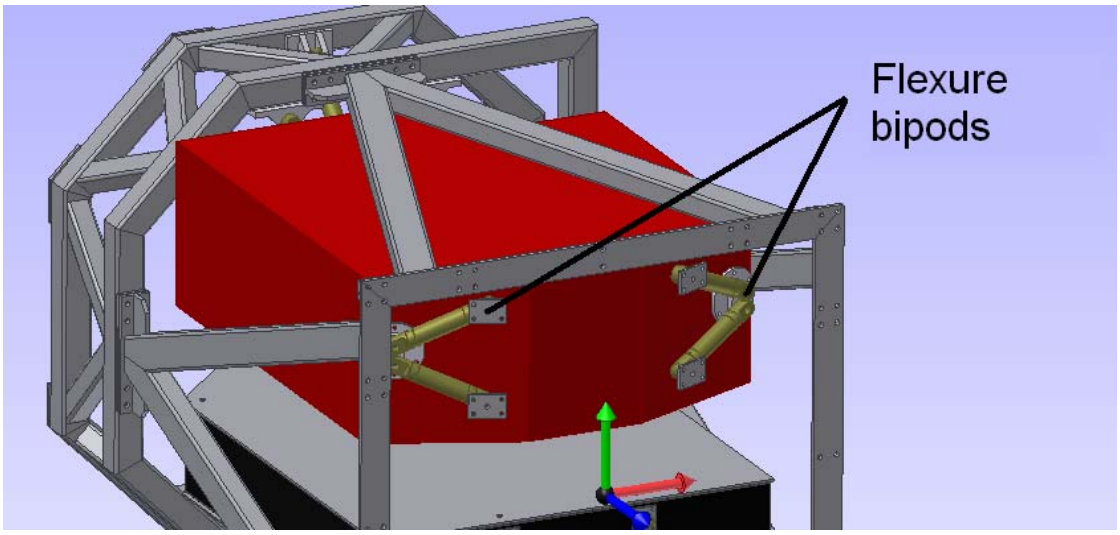

Figure 7-35 IFS bipod flexures.

7.1.1.21 Layout of Optics Path

The optical prescription has been presented thoroughly in Section 7.2.1 above. Recall that the prescription can be broken down into four primary components: the AO module; Coronagraph; Calibration module; and the Integral Field Spectrograph. The physical layout of the AO module plus the first two elements of the Coronagraph are shown in Figure 7-36 below. The "back-end" path that forms

part of the CAL module and supplies light to the IFS is shown in Figure 7-37. Additional views including the optical mounts and mechanisms are shown in Figure 7-38 through Figure 7-40.

Within the AO module, the AO wave front sensor can be thought of as an additional sub-system. The visible light entering the AOWFS is sent to a P/C pair of mirrors that are used to steer the guide star simultaneously onto the spatial filter as well as the lenslet array (Figure 7-39). The WFS camera is a single assembly made up of: the lenslet array; a pair of re-imaging doublets; a filter wheel; and the detector. The design of this assembly permits alignment as a unit in the laboratory before final integration into the instrument.

Within the CAL module, the light enters the interferometer along two paths (Figure 7-37). The first is the on-axis light, which falls through the central hole in the occulter focal plane masks. The reflected light from the off-axis field is then collimated by an OAP and sent to an approximately 80/20 intensity beam splitter. The transmitted light forms the second input to the interferometer, while the reflected light is sent to the IFS. Before entering the IFS, the light is reflected by another P/C pair of mirrors that provide some beam-steering capability to compensate for mechanical flexure and thermal distortions in the system (Figure 7-40). This collimated beam of light forms a pupil within the IFS at the Lyot stop (the final piece of the coronagraph).

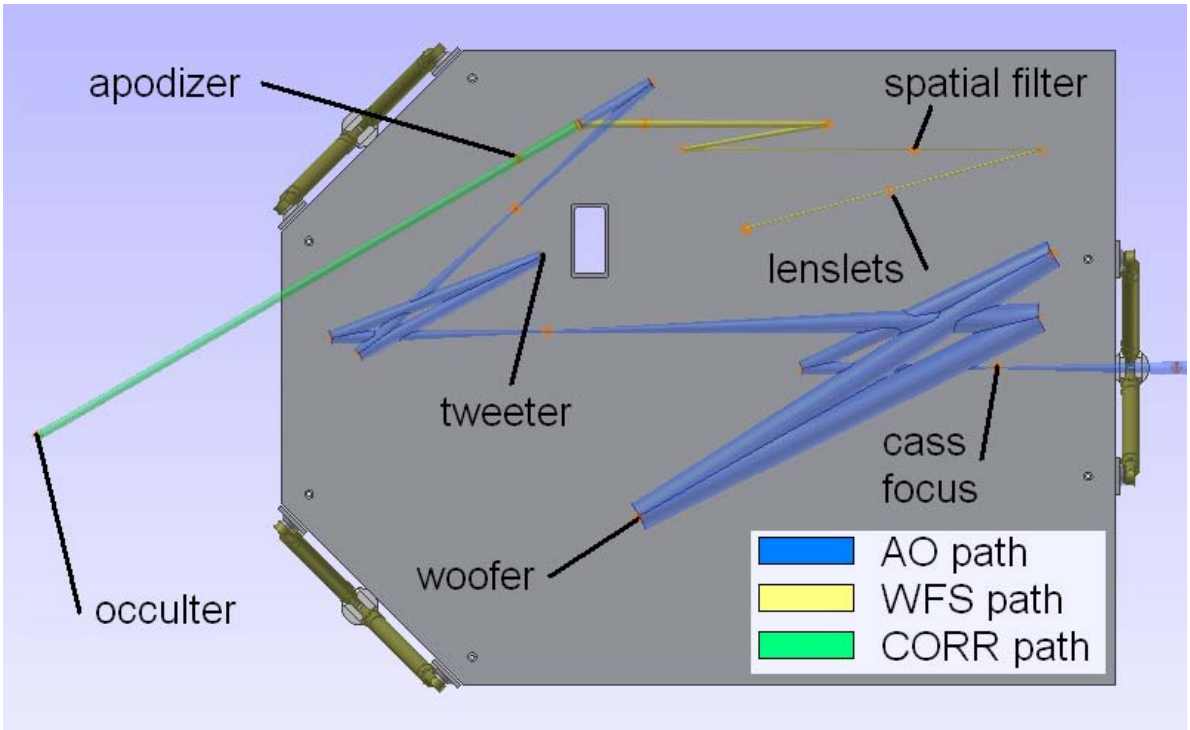

Figure 7-36 AO optics path (top view).

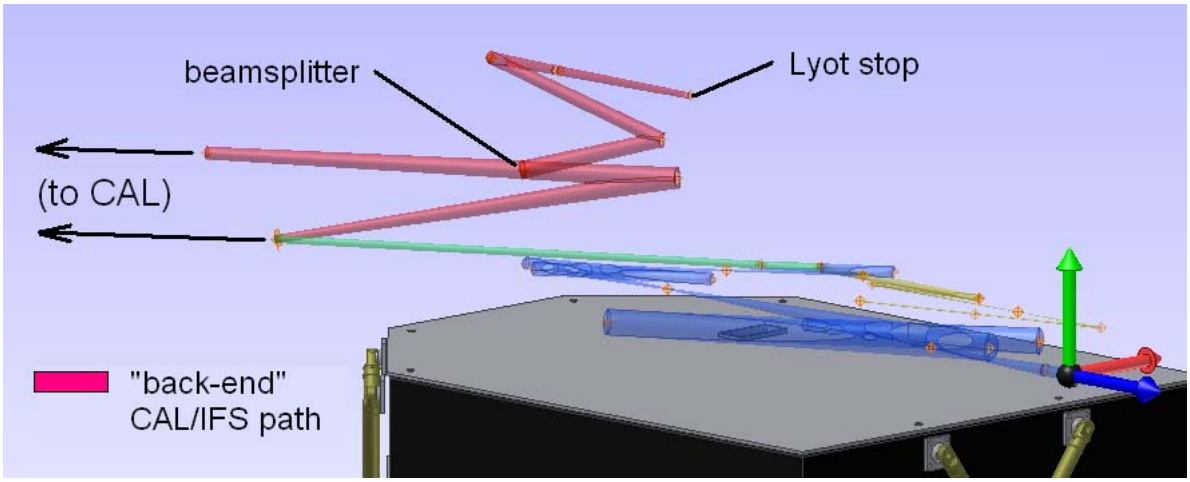

Figure 7-37 CAL and IFS optics paths.

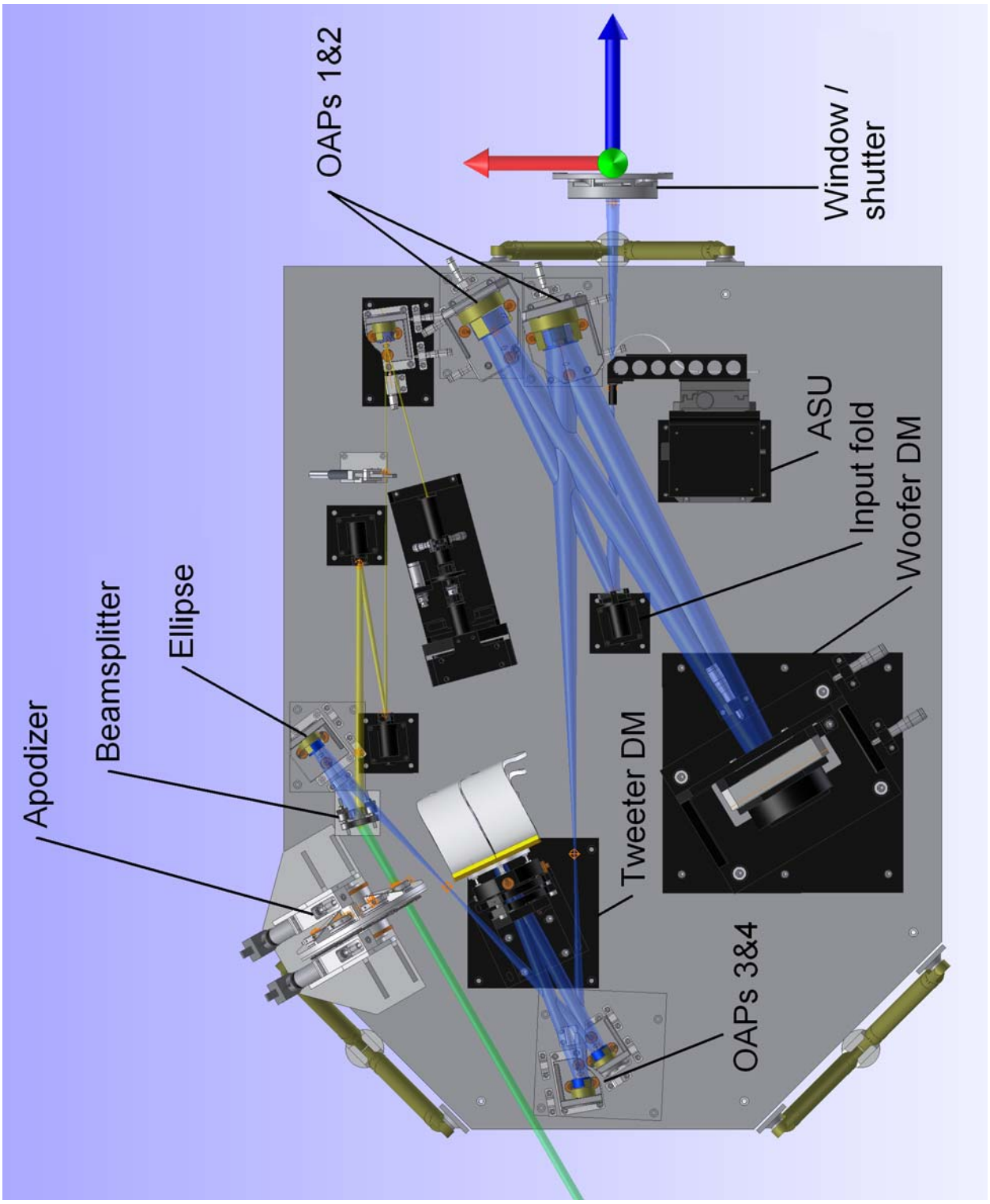

Figure 7-38 AO path with mounts and mechanisms.

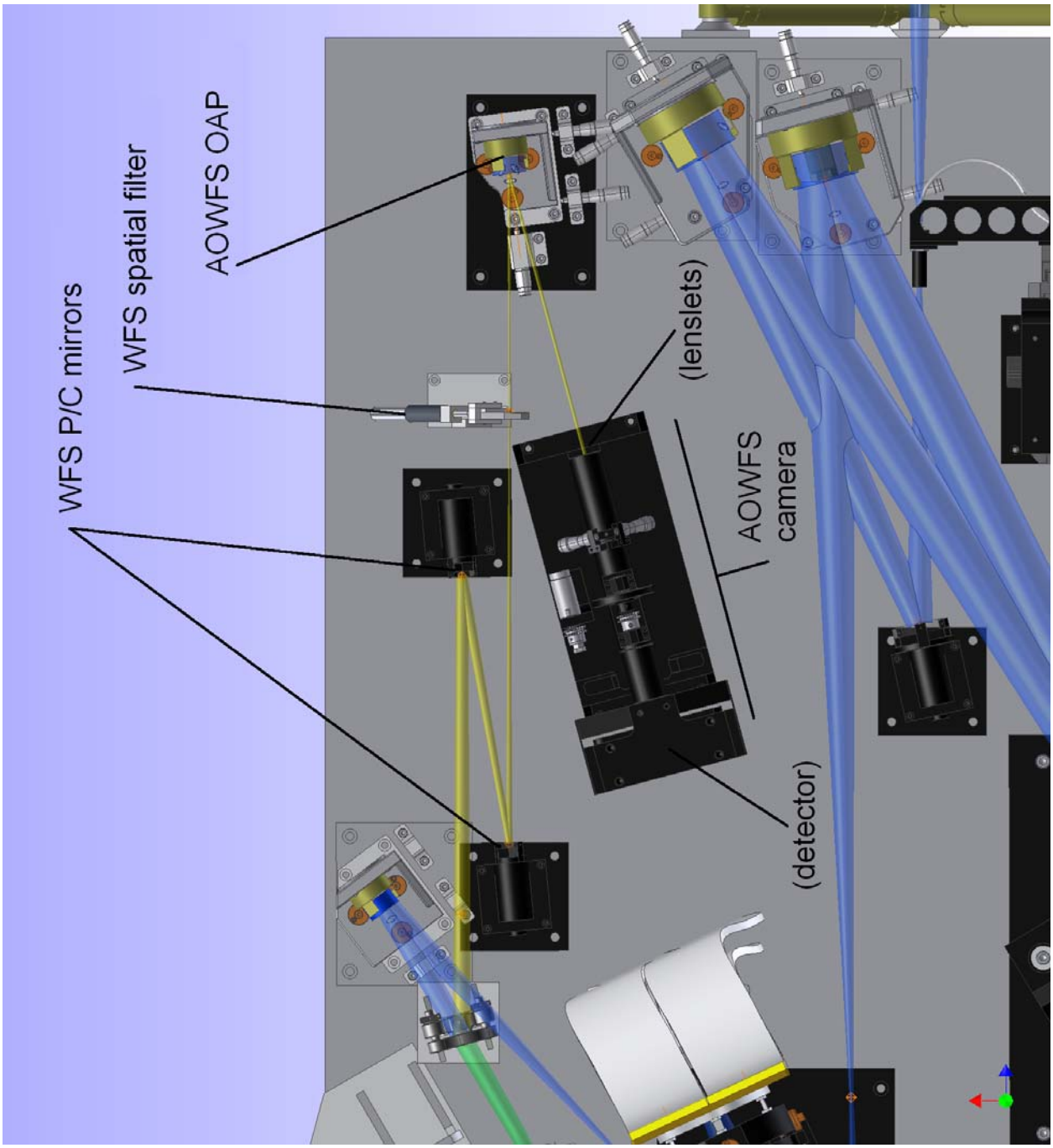

Figure 7-39 Details of AOWFS path.

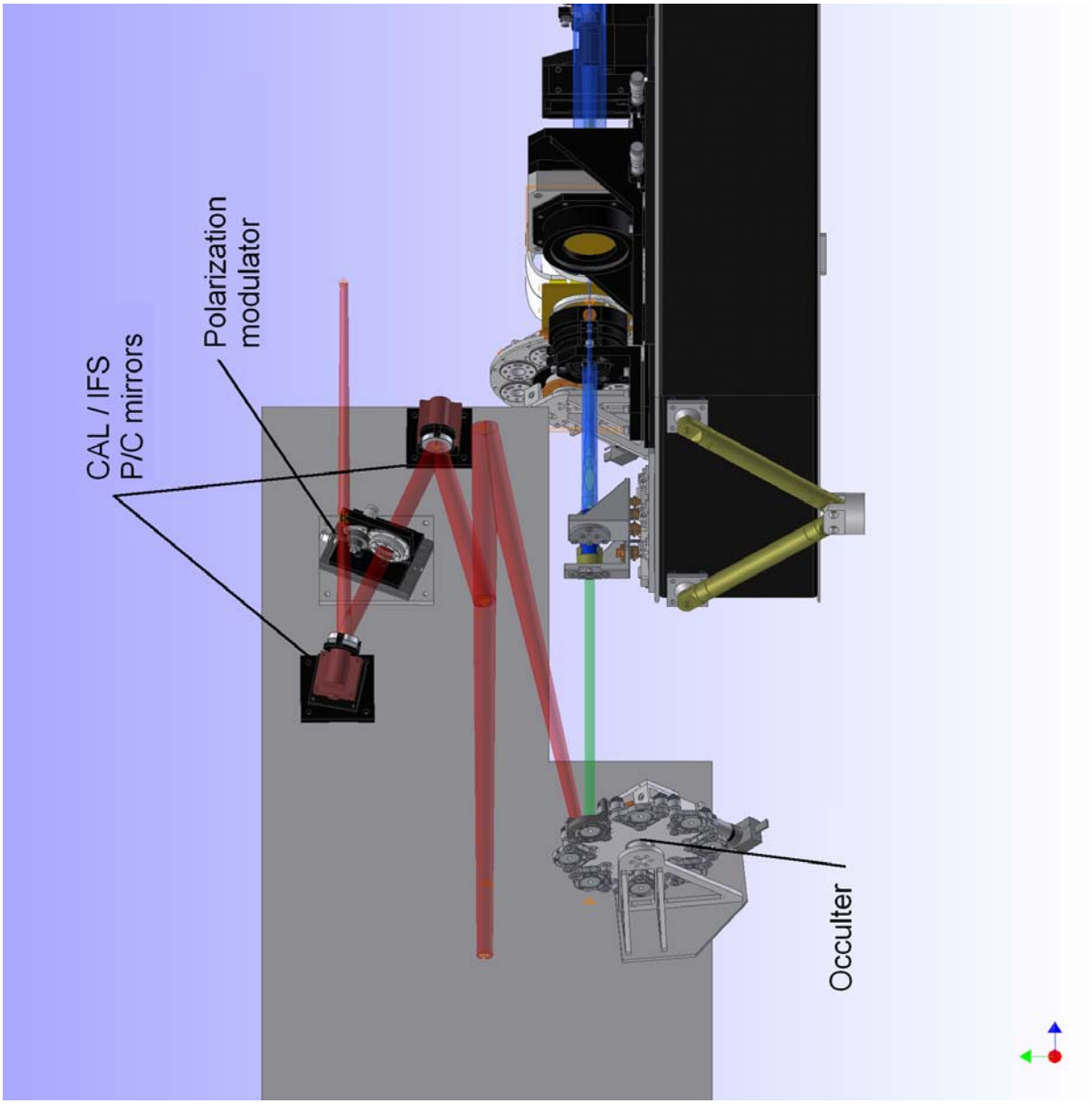

Figure 7-40 Details of the "back-end" CAL/IFS path.

7.1.1.22 Optics Mounts and Mechanisms

7.3.2.1.1 Entrance Window/Shutter

The entrance window and shutter are combined into a single assembly that is attached to the Mounting Plate (detailed in Appendix 7.10). This mechanism consists of a shutter, an entrance window and several mounting components (see Figure 7-41). The shutter is an NS45, Uniblitz II from Vincent Associates modified for bi-stable operation (the shutter can be either opened or closed and then powered off). This shutter can be manually actuated in the event of an electronics malfunction.

The approximate beam diameter at the location of the entrance window is 25 mm. The window clear aperture is chosen to be 28 mm to minimize the positioning accuracy required. The entrance window will be a standard 30 mm diameter Infrasil optic positioned at an angle of 3.75 degrees relative to the incoming beam (this angle is used to eliminate the effects of optical ghosting, see Appendix 7.7 for further discussion). Further information for the entrance window and shutter can be found in Appendix 7.10.

Figure 7-41 Entrance window and shutter (L: assembled, R: exploded showing shutter).

7.3.2.1.2 Linear ADC

The Atmospheric Dispersion Corrector (ADC) is a deployable mechanism located directly behind the entrance window and shutter. This mechanism includes a pair of prisms, which are used to correct the atmospheric dispersion that results from observing off-zenith. One prism is fixed in its position along the optical axis, while the other translates. The separation distance between the pair is adjustable from 5 to 70 mm. In addition to translation, the prisms must also rotate 360° in unison, about the optical axis. Finally, the entire mechanism must be deployable so that it can be completely removed from the beam for some observing programs. The combination of deployment, translation along the optic axis and coordinated rotation about the axis make this a challenging opto-mechanical mechanism.

The optical design of the ADC was a matter of great discussion during the preliminary design phase, with the final decisions not being made until late in the phase. For this reason, the mechanical design of the ADC is immature at this time. One possible concept is shown in limited detail in Figure 7-42. The prisms are mounted inside a barrel assembly with two rotational degrees of freedom. If one motor is used to rotate the barrel, the movable prism translates along the optical axis due to an internal screw pitch. If both motors are used, the entire barrel rotates, with no translational motion. This type of mechanism is analogous to the common zoom-lens assembly found in photographic cameras. A third motor and linear stage will be employed to deploy or extract the entire optical assembly. Due to its present state, the ADC will undergo a significant amount of design effort during the next project phase. Additional details are found in Appendix 7.11.

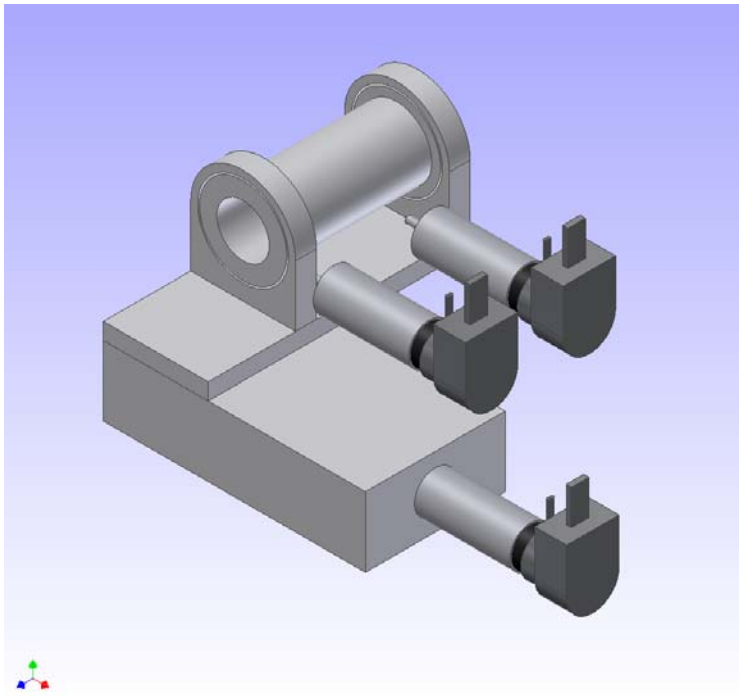

Figure 7-42 ADC concept.

7.3.2.1.3 Artificial Source Unit

The Artificial Source Unit (ASU) is a calibration tool that must be deployed at the Cassegrain focus and allow the source to patrol the entire field (detailed in Appendix 7.12). The ASU has two degrees of freedom allowing the insertion/retraction and positioning of one of three possible optical sources anywhere within the nominal beam. As shown in Figure 7-43, one linear stage provides the lateral motion required to insert and retract the source and a second linear stage provides the vertical motion required to patrol the entire field. Both linear stages are Newport VP-25X precision stages.

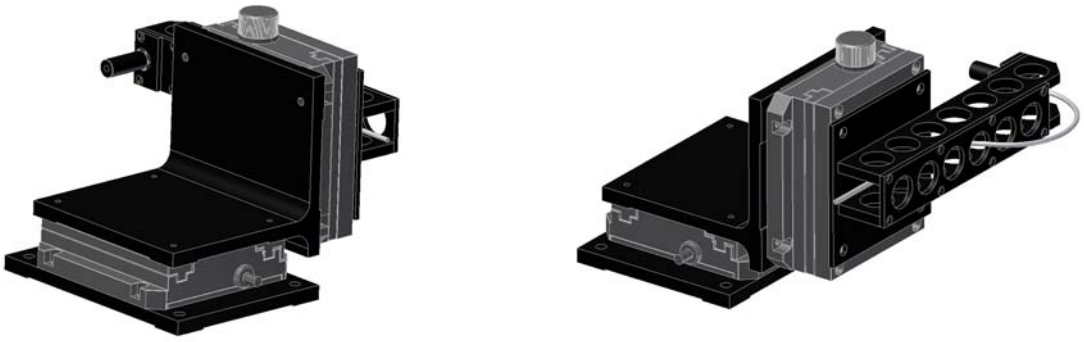

Figure 7-43 Artificial Source Unit.

The three sources are provided via a single "trifurcated" optical fibre. The "trifurcated" optical fibre combines three completely independent fibres, with separate jackets and connectors at one end, into a

single assembly at the ASU probe end. The three fibres are not spliced together but, instead, remain continuous separate fibres bundled together into a single jacket and connector. At the ASU probe, the three fibres are positioned adjacent such that they are arranged in a trianglar pattern with the center-to-center distances equal to their cladding diameters (see Figure 7-44). Although the nominal fibre diameter is 50 μm, the image size of each source at the focus will be defined by three 4 μm pinholes positioned at the end of the trifurcated fibre (see Appendix 7.1 for details regarding the required image size). Finally, stray light into the rest of the instrument will be minimized by a baffle located on the end of the fibre defining an f/8 beam.

The trifurcated fibre facilitates the use of three independent light sources mounted in the EE cabinet and each tailored to a specific wavelength range and light intensity. The three sources required are: a white light source, an IR laser and a visible-light laser.

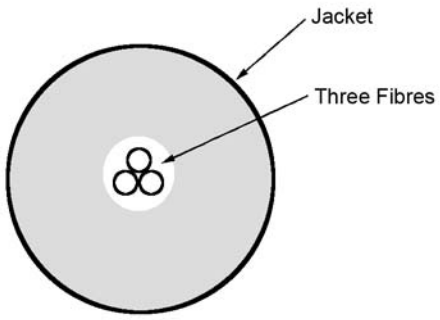

Figure 7-44 Cross-sectional view of a "trifurcated" fibre.

7.3.2.1.4 Input Fold Mirror

The Input Fold Mirror (IFM) is located after the Cassegrain focus (see Figure 7-38), and reflects the incoming beam into the AO optical system. The minimum requirements for the IFM include a clear aperture of 25 mm and an angular tip/tilt range of ±0.03 mrad. The IFM consists of a 37.5 mm diameter flat mirror positioned by a piezo tip/tilt platform (see Figure 7-45). The baseline device is the Nano-MTA2X tip/tilt actuator from Mad City Labs.

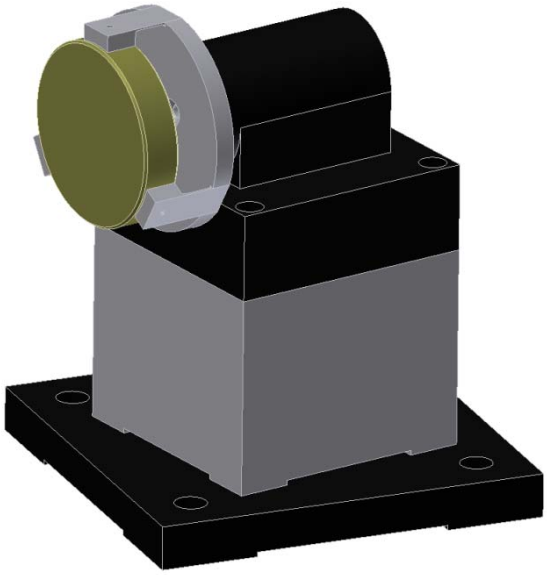

Figure 7-45 Input fold mirror assembly.

7.3.2.1.5 6dof Mirror Mounts

It was desirable to create a design for a 6dof static mirror mount that can be easily modified and scaled for optics in the AO path. Some different types of mounts were briefly compared for suitability: a commercial Newport mount; a typical mount commonly used by JPL; and an HIA custom mount. A trade table for this is shown in Appendix 7.9. The HIA custom design was chosen, mainly because neither the JPL-style mount nor the Newport mount provided all of the adjustments required in the space allowed without developing a custom mount anyway. It should be noted that some elements of the JPL-style mount were incorporated into the basic 6dof mount, most notably the flexure piece.

7.1.1.22.1.1 6dof General Design

The 6dof mount is supported by an interface plate with standard hole pattern to match the grid of holes on the optical table (as discussed in section 7.1.1.18). Ball-end micrometers (from Newport, see Appendix 7.43 for specifications) provide three accurately known positions for adjusting 3dof in the plane of the optical bench (Figure 7-46). The main support stage is secured to the interface plate using screws in oversized clearance holes. When loosened, the main support stage is free to move in the plane of the optical bench.

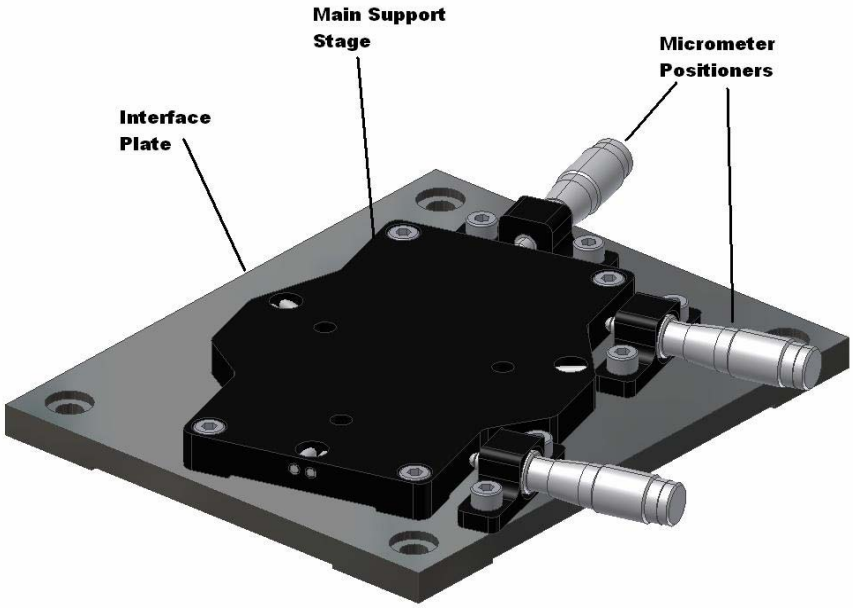

Figure 7-46 6dof interface plate and main support stage.

A spring-loaded 3dof stage is mounted to the main support stage and provides alignment in clocking and tip as well as linear translation perpendicular to the optical bench (as shown in Figure 7-47). Three fine-thread locking Newport actuators (see Appendix 7.43 for specifications) push the L-bracket and Main Support Stage apart while strong tension springs hold them together. The Newport actuators have ball ends which rest on three V-grooves to ensure kinematic alignment is maintained in all orientations.

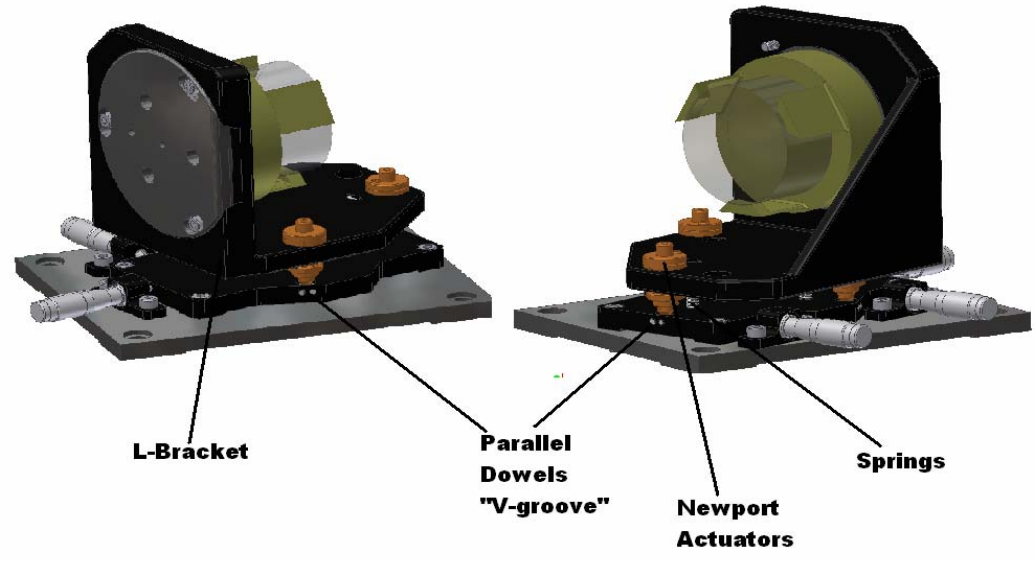

Figure 7-47 6dof spring-loaded stage.

A third flexure stage is comprised of the optic, a flexure piece made of a thermally matched material and an interface disk (as shown in Figure 7-48). The flexure blades will be bonded to the optic and the flexure mount will be secured to the interface disk with screws and is pinned for repeatability. The flexure mount will reduce stress in the optic due to differential thermal contraction effects. Loosening three cap screws and allowing them to rotate in slots provides a rough clocking adjustment.

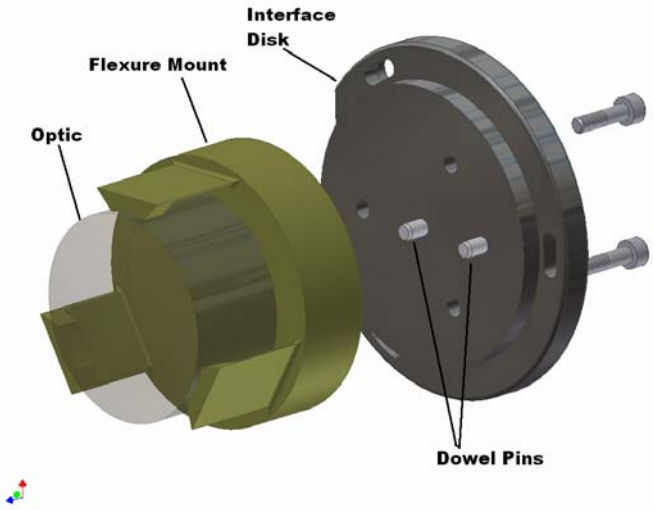

Figure 7-48 6dof flexure stage.

Testing of a generic mount of this type has been ongoing at HIA. A generic mount of the same construction has been manufactured and a report showing current progress and results is in Appendix 7.8. The main purpose of these tests is to evaluate the stability and strength of the spring-loaded stage. Chief results of these tests so far are that the mount is performing within expectations. Future plans are outlined in Appendix 7.45, including cold temperature stability tests. Further refinements to the design will likely be incorporated into the finished design of the mount.

The general design was selected and modified to suit the following AO optical elements: four OAP mirrors, the off-axis ellipse and the WFS (collimating) OAP. The majority of modifications were either to avoid interference with adjacent beam paths or to scale the mount for different sized optics. Detailed discussions of the both the 6dof mount general design and modifications to the 6dof mount for each of these optics is discussed in Appendix 7.14. For discussions of these optical elements, see Section 7.2.1. Protecting the optic during assembly/alignment, storage and shipping will be explored further. Design of features to allow the entire mount to be removable for shipping and handling without realignment will also progress.

7.3.2.1.6 Woofer DM

The woofer Deformable Mirror will be located on the optical bench, as shown in Figure 7-38 and the woofer's function in the AO system is described in Section 7.2.1. The woofer and integral tip/tilt platform will be a vendor supplied module shown in Figure 7-49. The baseline design is a Cilas 9x9

piezo-stack mirror, mounted using a custom interface in a commercial piezo tip/tilt stage. The baseline tip-tilt stage is a commercially available stage, manufactured by Physik Instrumente (specifications in Appendix 7.42). The vendor specifications are being developed, such as a definition of the mounting interface to the woofer DM Mount.

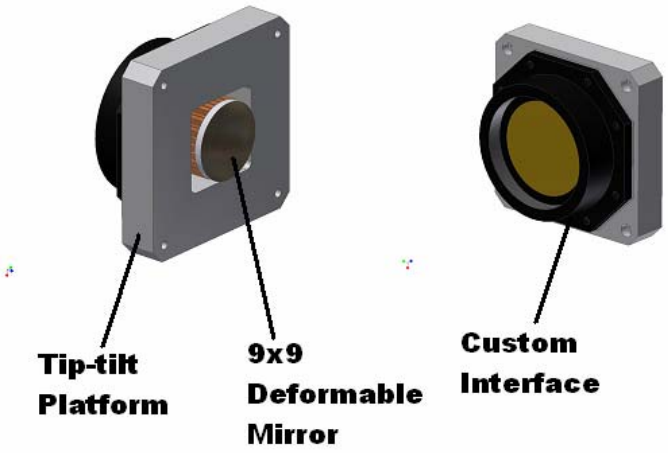

Figure 7-49 Woofer DM and tip/tilt platform.

The woofer DM mount is discussed in detail in Appendix 7.15. Volume limitations are not stringent on the woofer assembly, with the exception of the height of the assembly, which is restricted by the IFS overhead. Alignment requirements are driven by the necessity of aligning the mirror with the Wavefront Sensor and tweeter DM and to ensure the mirror is located on the pupil plane.

During the alignment (as outlined in Appendix 7.5), the AO system will be aligned first with a flat mirror in place of the woofer DM. As a result, the woofer DM Mount consists of three main subassemblies: the woofer Base Assembly, the woofer DM Assembly and the woofer Flat Mirror Assembly. The woofer Base Assembly, shown in Figure 7-50, is designed to accept the woofer DM Assembly and the woofer Flat Mirror Assembly interchangeably.

Figure 7-50 Woofer DM base assembly.

The surfaces of the flat mirror and the surface of the nominally flattened woofer DM will both be located at the pupil plane and identical mounting features will help assure that this is the case. The woofer DM Assembly is not designed to provide adjustment independent of the woofer Base Assembly, other than a small amount of clocking, for stability reasons.

The woofer Base Assembly provides for alignment in the plane of the optical bench using Newport ball-end micrometers (see Appendix 7.43 for specifications). Adjustment perpendicular to the bench is provided only through the use of shims.

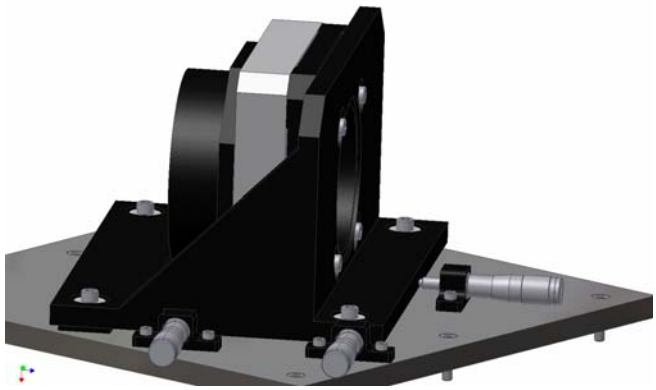

Figure 7-51 Woofer base assembly with woofer DM assembly.

The Flat Mirror Assembly houses the 50-mm diameter flat mirror in a commercial Newport tip-tilt mount (see Appendix 7.45 for specs), with an interface plate between the woofer Base Assembly and the Newport tip-tilt mount. The Newport tip-tilt mount is mechanically actuated and required to be stable

for a series of gravity and thermal tests. The mount is being tested for stability and suitabilty at HIA. Results of some ongoing tests are in Appendix 7.46 and plans for future testing are in Appendix 7.47.

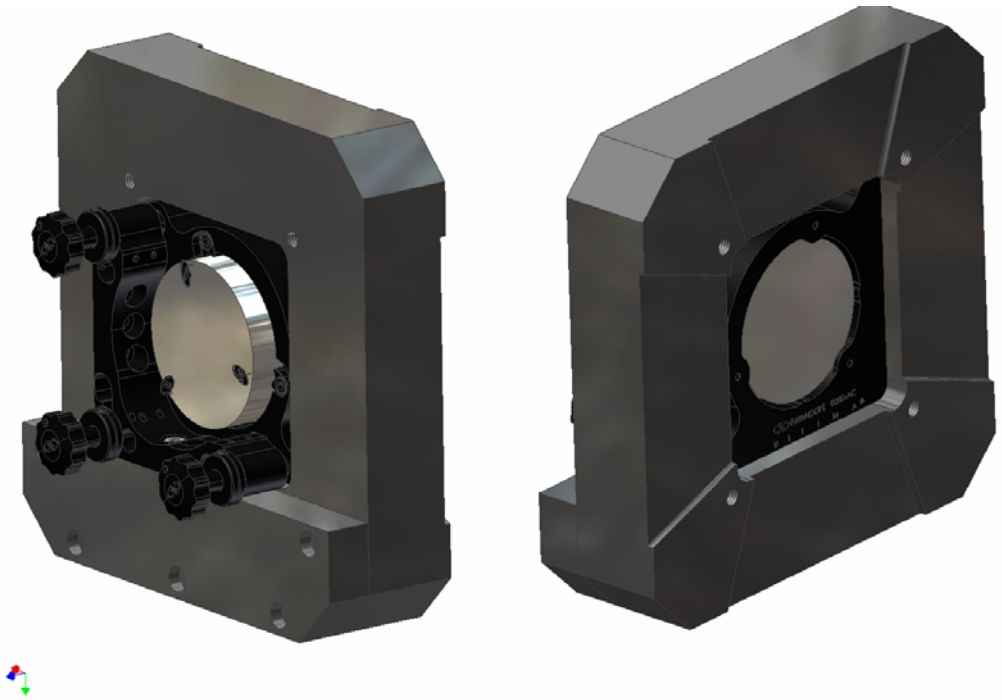

Figure 7-52 woofer flat mirror assembly.

Analysis will be done on the vibration characteristics of this mount due to the fast tip-tilt speed and if necessary, specifications will be given to vendors to limit the induced vibration. Also, interface details with the vendor will be finalized. Protecting the optic during assembly, storage and shipping will be explored further. Design of features to allow the entire mount to be removable for shipping and handling without the requirement for realignment once the assembly has been reassembled will also progress.

7.3.2.1.7 Tweeter DM

Discussion of the tweeter's function in the AO system is described in Section 7.2.1. The tweeter DM is being developed in collaboration with Boston Micromachines Corporation (BMM). The deformable mirror has a 64x64 array of actuators, of which on the "best" 44x44 patch of actuators will be used to provide the wave front correction required. The tweeter DM will be supplied on an alumina chip carrier with eight connectors (in two rows of four) wire-bonded to the non-mirror side (as shown in Figure 7-53). BMC will be providing the chip carrier with thermally matched material (such as Kovar) brazed onto the front of the carrier for mechanical attachment. Figure 7-53 shows the thermally matched material in the shape of a ring, however BMC is planning to test various geometries to see their effect on the mirror.

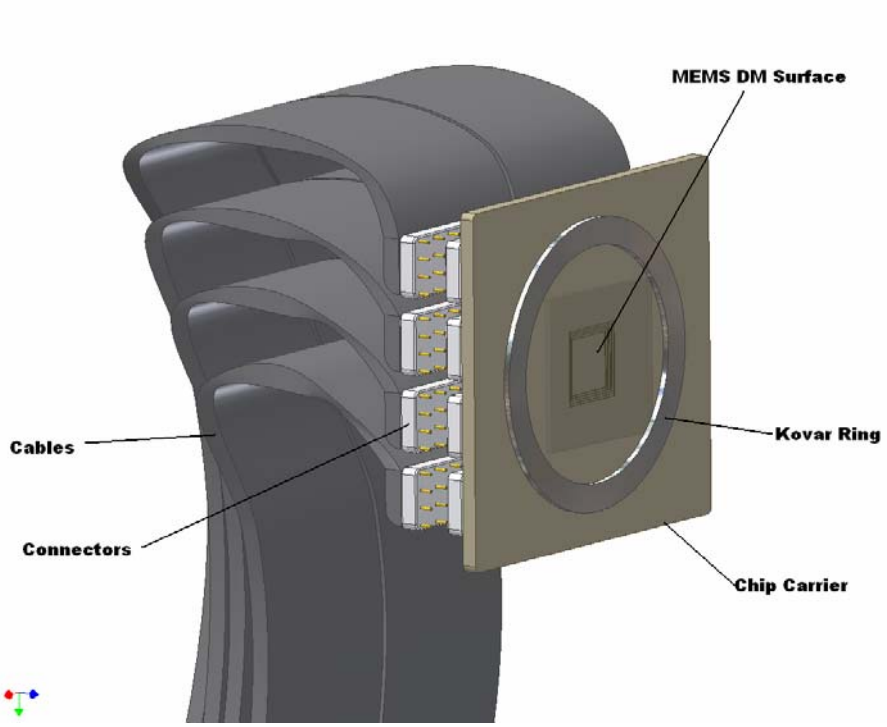

Figure 7-53 Tweeter DM to be delivered by Boston Micromachines Corporation.

The tweeter DM mount is required to fit within very tight space restrictions as the DM is bounded on two sides by the optical beam. The second challenging requirement is a small resolution but large range for translation in X and Y. These are driven by the requirement to closely align the wave front sensor detector with the tweeter DM actuator arrays and the requirement to use the "best" 44x44 patch of actuators respectively.

During alignment (as outlined in Appendix 7.5), the AO system will first be aligned with a conventional flat mirror installed in place of the tweeter DM. This mirror will simulate the tweeter DM in a nominal flat position located on the 17.6-mm pupil plane. The tweeter DM mount design consists of three main subassemblies: the tweeter Base Assembly, the tweeter DM Assembly and the tweeter Flat Mirror Assembly. The tweeter Base Assembly (Figure 7-54) is designed to accept both the tweeter DM Assembly and tweeter Flat Mirror Assembly interchangeably with identical mounting features. The surfaces of the flat mirror and the surface of the nominally flattened tweeter DM will both be located at the pupil plane.

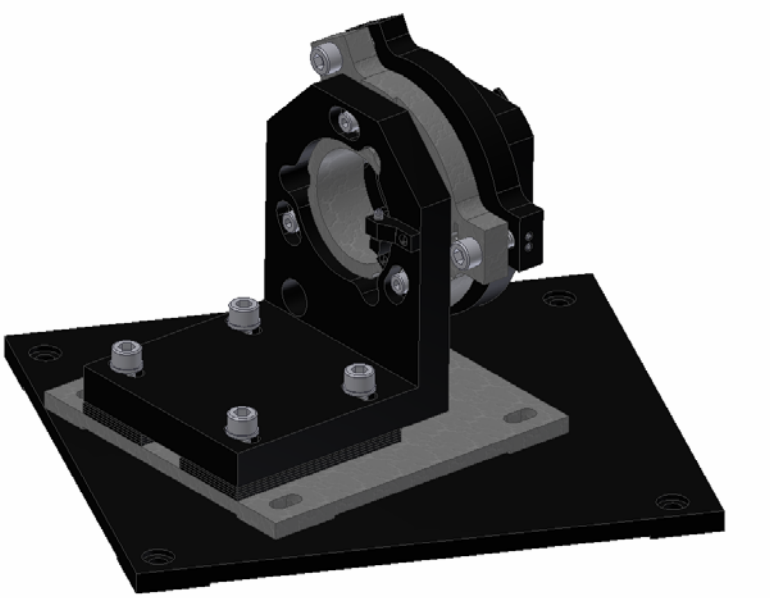

Figure 7-54 Tweeter base assembly.

The tweeter Base Assembly has three basic stages; a Tip-Tilt stage, a Clocking stage and a coarse X-Y-Z stage. All stages are described in greater detail in Appendix 7.16. Fine adjustment in linear X and Y are important for the tweeter DM only and are provided separately on the tweeter DM Assembly and not the Flat Mirror Assembly.

The tweeter DM Assembly includes the MEMS DM, connectors and cabling to be delivered by BMM as well as a set of flexures fastened to the brazed-on surface of the alumina carrier and also a ring of aluminum alloy to interface to the tweeter Base Assembly as shown in Figure 7-55.

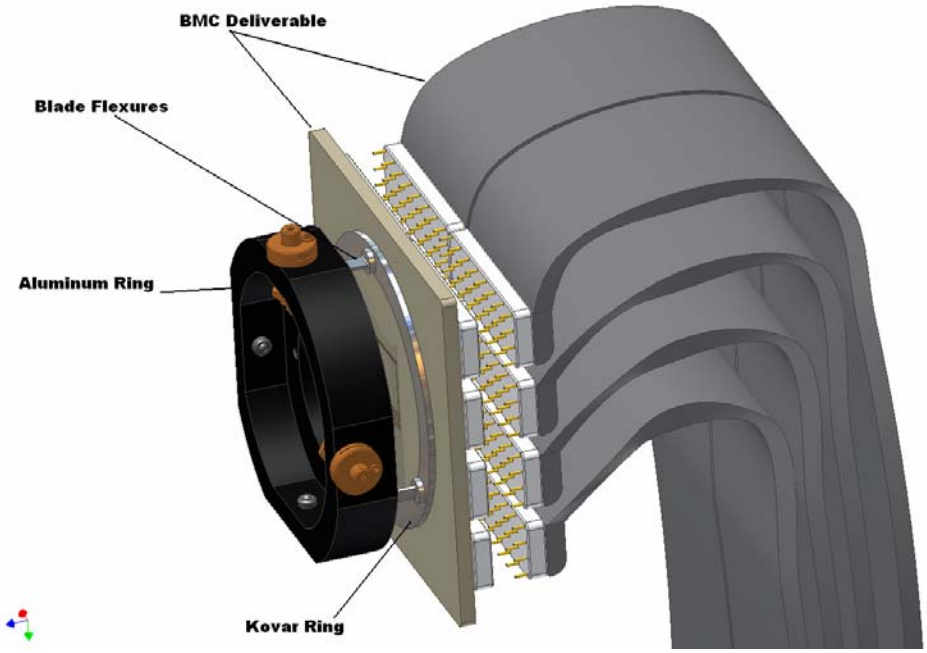

Figure 7-55 Tweeter DM assembly.

The flexures are still being developed and their design will be driven in part by the results of testing at BMM. Fine X-Y translation is provided by fine thread locking actuators purchased from Newport Company (see Appendix 7.43 for specifications).

The tweeter Flat Mirror Assembly will interface to the same features as the tweeter DM Assembly on the Base Assembly. The tweeter Flat Mirror Assembly is in development but is not expected to present any difficulties.

Tweeter cable lengths are being procured by BMM. The length has been limited to a maximum of 2.25 m based on the distance from the optical bench to the electronics enclosure. Due to the expensive and delicate nature of the cables and connectors and their bulky size in a congested area, the tweeter cables will be fed through the AO optical table via a hole cut for that purpose. It will be important to provide strain relief for these cables as they can be damaged or can impart forces on the mirror very easily.

Work is continuing in collaboration with BMM. Protecting the optic during assembly, storage and shipping will be addressed as well. Design of features to allow the entire mount to be removable for shipping and handling without realignment will also progress.

7.3.2.1.8 WFS Dichroic Beamsplitter

The AOWFS Dichroic Beamsplitter is a simple optical assembly consisting of the beamsplitter optic, a commercial 1" Newport tip/tilt mirror mount and a custom pedestal (Figure 7-56). The beam diameter at this location is approximately 15 mm, so a standard 25 mm optic diameter is assumed. The primary requirements for adjustment are tip and tilt, which are provided by the mirror mount. Positioning on the

AO optical table will be aided with commercial nudgers. Additional information can be found in Appendix 7.17.

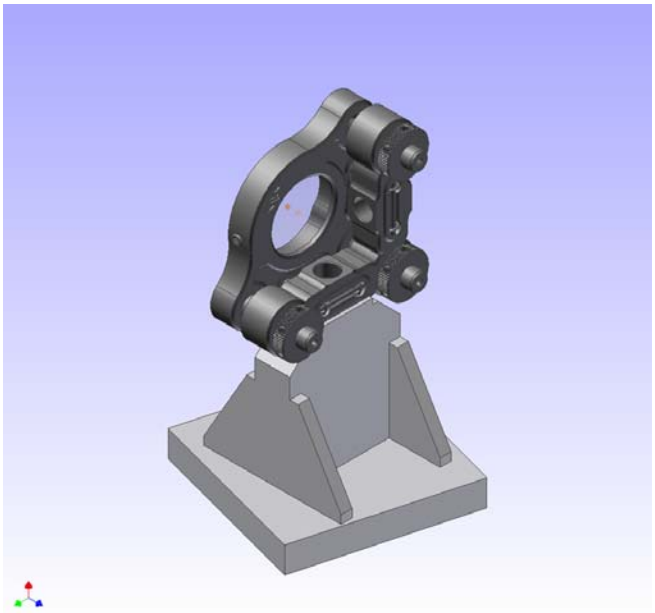

Figure 7-56 AOWFS dichroic beamsplitter.

7.3.2.1.9 Apodizer Wheel

The Apodizer Wheel contains 8 apodization masks that can be independently selected (Figure 7-57). The masks are placed in the beam at a ∅12-mm pupil. Currently there is a provision to rotate each mask about the central axis of the beam. To accomplish these motions, each mask is held within a rotating cell and all 8 cells are fixed to a wheel. To select a particular mask, the wheel is rotated into position using a DC servo motor and worm gear drive train. To rotate the cell, a second DC servo motor is used to rotate a planetary gear system. More details can be found in Appendix 7.18.

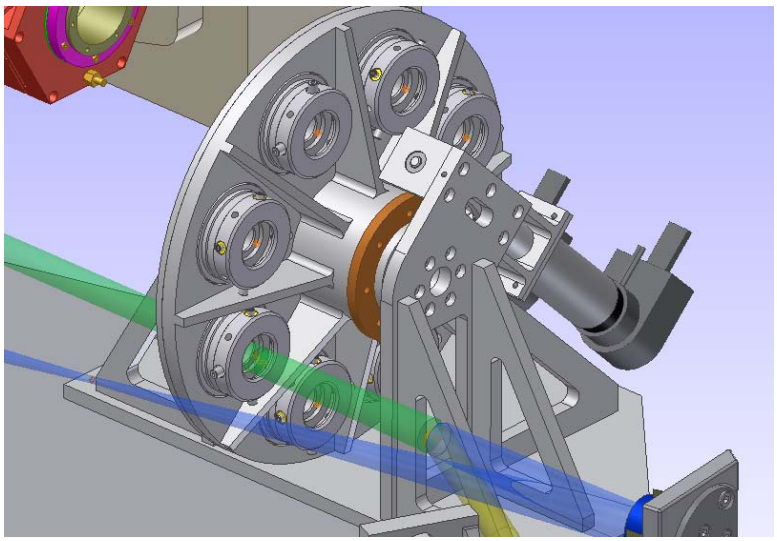

Figure 7-57 Apodizer wheel mechanism.

7.3.2.1.10 Occulter Wheel

The Occulter Wheel contains eight focal plane masks and is located at the f/64 focus (Figure 7-58). Each mask, which is a mirror with a central hole, is mounted in a commercial kinematic mirror mount. This mount provides tip/tilt control for alignment purposes. The individual masks are selected by rotating the wheel into position, using a single DC servo motor and worm gear drive. More details can be found in Appendix 7.19.

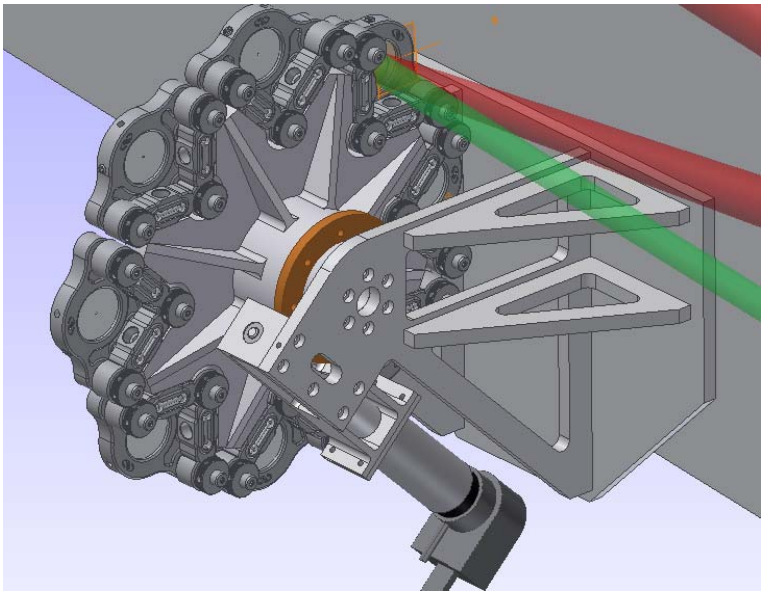

Figure 7-58 Occulter wheel mechanism.

7.3.2.1.11 CAL/IFS P/C pair

The two CAL/IFS Pointing and Centering (P/C) mirrors are mounted on the CAL module breadboard: the P/C 1 mirror is positioned between the CAL Science Beamsplitter and the Polarization Modulator, and the P/C 2 mirror is positioned after the Polarization Modulator, directing the beam to the IFS. These two P/C mirror assemblies, shown in Figure 7-59, are designed around the Nano-MTA2X tip/tilt actuator from Mad City Labs. The design is very similar to the Input Fold Mirror described above in Section 7.3.2.1.4 except that the required T/T range of ±0.85 mrad is larger than that specified for the Input SM (still within the capabilities of the selected actuator). The clear apertures required for P/C 1 and 2 are 30 mm and 23 mm, respectively. Thus, both of these P/C mirrors are 37.5 mm diameter flats, as with the Input SM. The P/C 2 assembly has an additional complication since the beam must be steered out-of-plane to the CAL module breadboard. To accommodate this, the mount for the Nano-MTA2X T/T actuator has an additional angle out-of-plane from the breadboard of 15.3 degrees. Additional details are provided in Appendix 7.20.

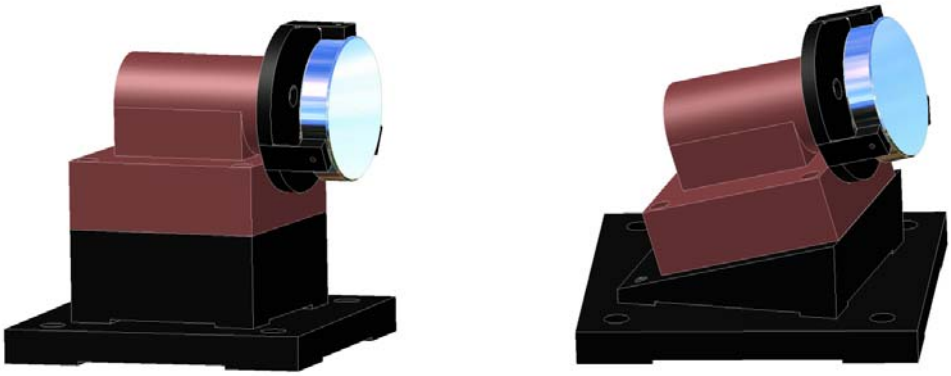

Figure 7-59: CAL/IFS P/C Pair: P/C 1 (left) and P/C 2 (right).

7.3.2.1.12 Polarization Modulator

The Polarization Modulator (PM) is a mechanism that allows for the insertion/retraction of a wave plate and, while inserted in the beam, the wave plate can be continuously rotated to any orientation. The PM is located between the two P/C mirrors on the CAL module breadboard and has a minimum clear aperture of 22.0 mm (a 24.0 mm clear aperture is used in the design). The PM design consists of a custom rotational stage mounted on a commercially available linear stage. The custom rotational stage consists of the polarization optic cell supported by a bearing and driven by a 1500-series MicroMo zero-backlash motor/gear-head combined with an anti-backlash spur gear. The linear stage combines a Newport UMR8.51 precision linear stage with a LTA-HS motorized linear actuator with 50 mm of available travel. Further details provided in Appendix 7-21.

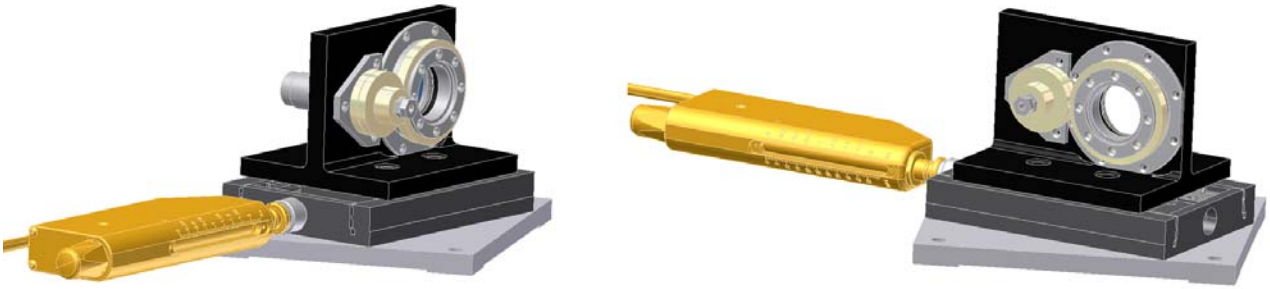

Figure 7-60 Isometric views of the polarization modulator (wave plate).

7.3.2.1.13 WFS P/C Pair

Similar to the CAL/IFS P/C 1 mirror described in Section 7.3.2.1.11, above, the two WFS P/C mirrors combine a Nano-MTA2X T/T actuator with a 15.0 mm diameter fold mirror to achieve the ±2 mrad required motion. Both of the WFS P/C mirror assemblies (shown in Figure 7-61) are mounted to the AO optical table and are positioned immediately after the WFS beamsplitter in the WFS optical path

(see Figure 7-39). The second P/C mirror assembly also has a Newport M-426A linear stage incorporated into its base to provide the ±1 mm required focus adjustment. Further details are provided in Appendix 7.22.

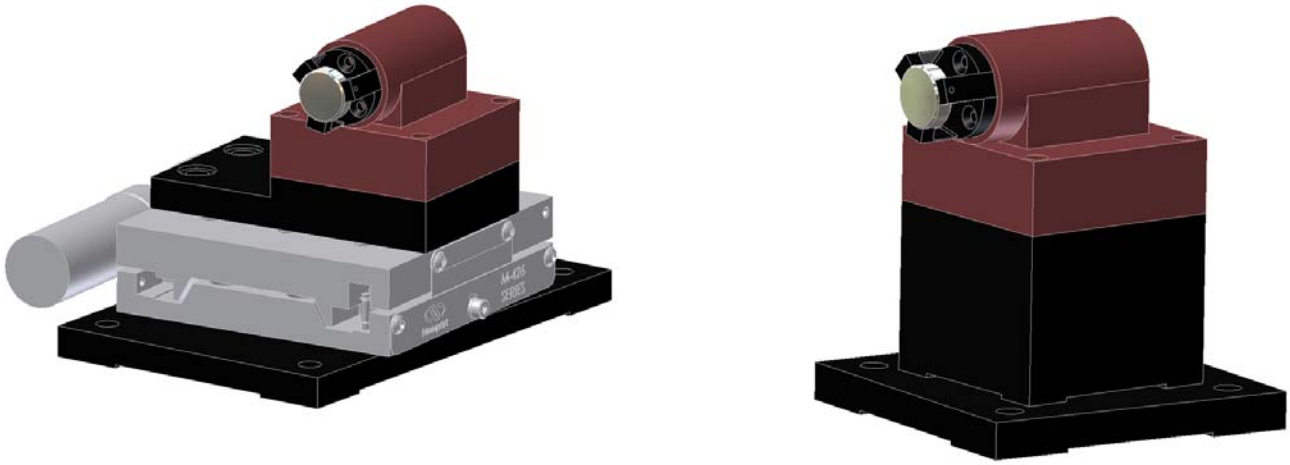

Figure 7-61 Isometric views of WFS P/C mirror 1 (right) and 2 (left).

7.3.2.1.14 WFS Spatial Filter

The Spatial Filter (SF) is one of the components in the WFS path and is located between the WFS OAP and the WFS P/C pair (see Figure 7-36). The design of the SF, based on the original design by Chris Lockwood at UCSC, consists of two opposing blades that are actuated relative to one another by a Thor Labs linear actuator. The action of the actuator controls the size of the square aperture providing an adjustable spatial filter. The size of the square aperture must vary between 1.970 mm and 6.720 mm, in maximum increments of 47 μm. Further details are provided in Appendix 7.23.

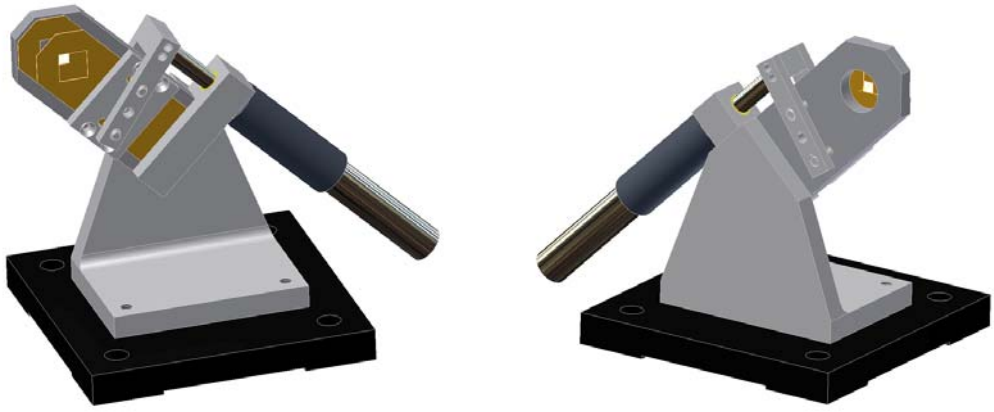

Figure 7-62 Isometric views of the adjustable spatial filter.

7.3.2.1.15 WFS Camera Assembly

The WFS Camera Assembly is the final assembly in the WFS optical path and is located after the WFS OAP. The WFS camera assembly consists of the lenslet array, the first reimaging doublet, the filter changer, the second reimaging doublet and the AO WFS detector (see Figure 7-63). The design of this assembly provides for the initial internal alignment followed by precise alignment of the entire assembly with respect to the remaining WFS path. The initial internal alignment is accomplished through the use of an optical barrel arrangement rigidly supporting the optics to minimize relative flexure during operation. Rotational alignment of the lenslet array with the AO WFS detector is achieved with a pair of micrometers configured to adjust the orientation of the lenslet array with respect to the larger assembly (see Figure 7-64).

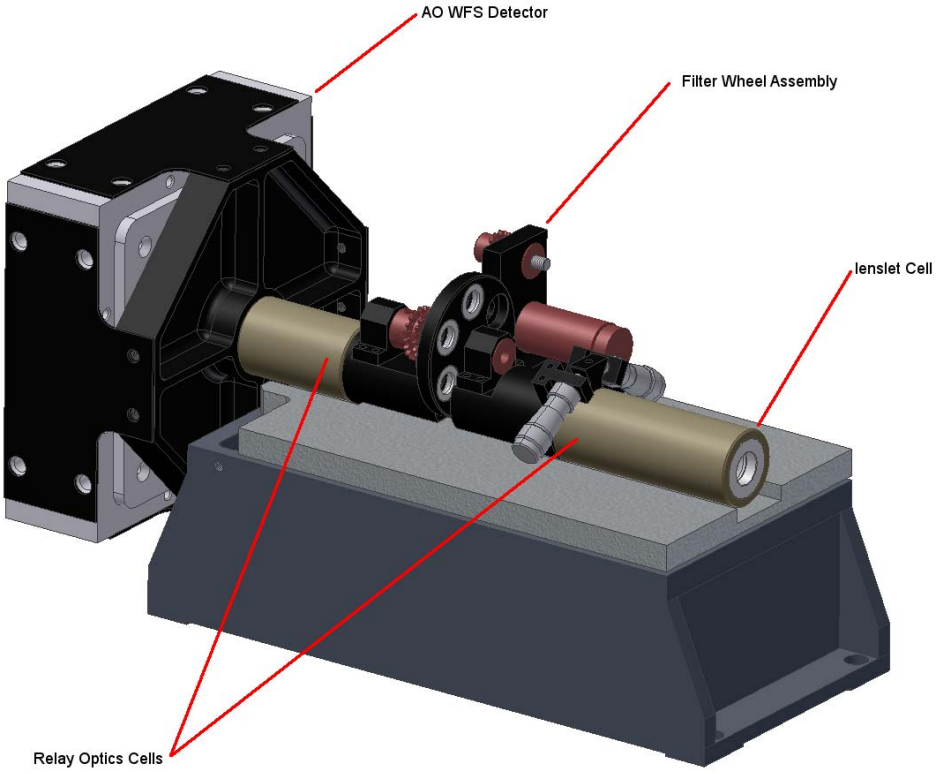

Figure 7-63 Isometric view of the WFS camera assembly

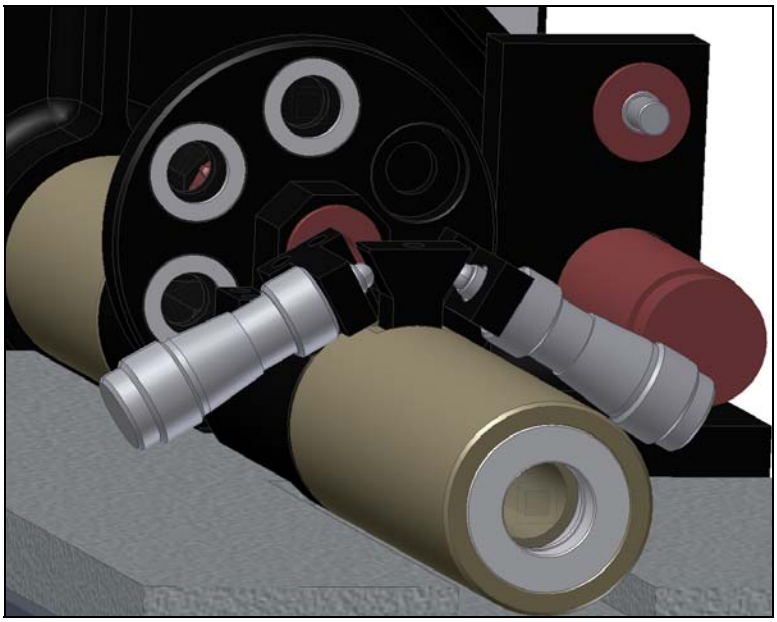

Figure 7-64 Detail view of angular adjustment for the lenslet array

The WFS optical barrel assembly is kinematically mounted to the base structure through three ball contacts (see Figure 7-65). The entire assembly can be tilted in the vertical plane about an axis aligned with the lenlet array.

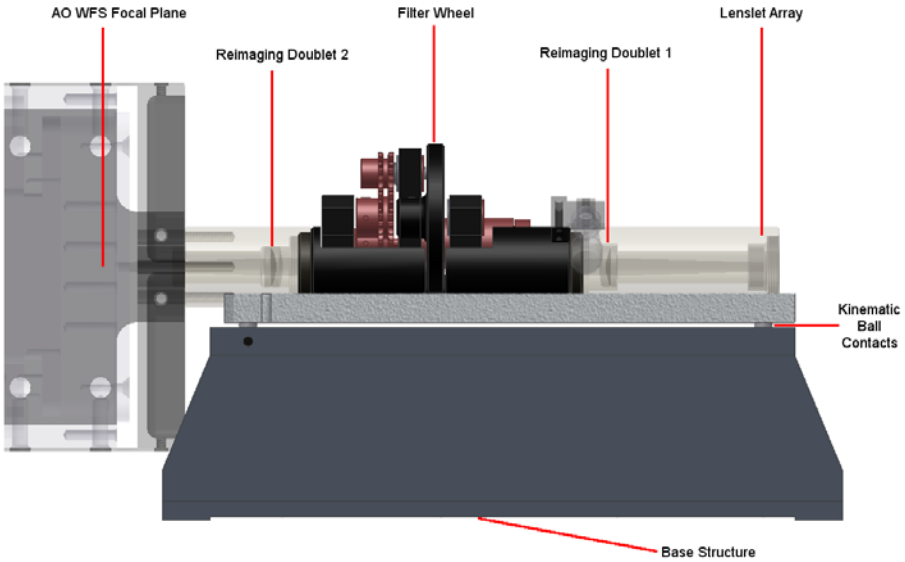

Figure 7-65 Optical layout within the WFS Camera Assembly.

The filter changer, shown in Figure 7-66, is a compact wheel design with six selectable filters. The filter wheel is driven by a 1500-series MicroMo zero-backlash motor/gear-head combination connected to the filter wheel through a preloaded Posi-Drive belt. Further details for the filter changer and the WFS camera assembly are provided in Appendix 7.24.

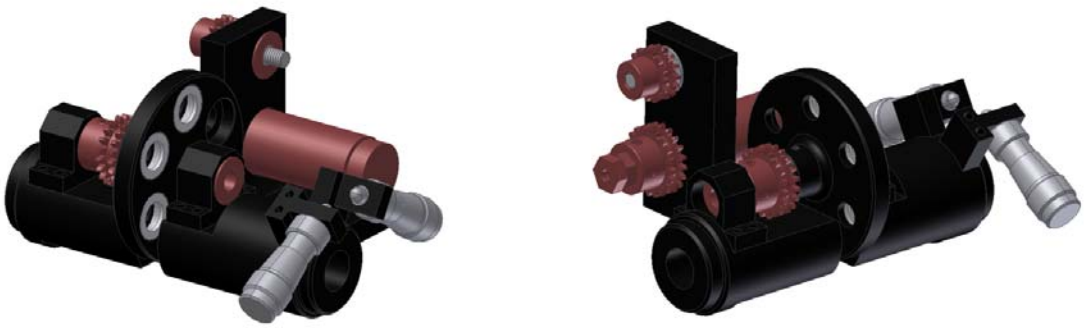

Figure 7-66 Isometric views of the Filter Changer.

7.1.1.23 FSS System Analysis

7.3.2.1.16 Mass / Centre of Mass Analysis

The weight of GPI is required to be 2000 kg, with the centre of mass located at (x,y,z) = (0, 0, -1000) mm in the Gemini instrument coordinate system (as defined in Gemini ICD-G0014). The following summary shows that the mass specification is being met, through the use of a small amount of ballast. The centre of mass specification is also being met (to within the +/- 20 mm tolerance) by adjustment of the locations of the ballast mass. A more detailed analysis is presented in Chapter 2. The ballast mass makes up less than 10% of the total mass of the instrument; which is a concern at this stage of the project. This issue will continue to be monitored closely, and every measure will be taken to reduce mass where feasible.

FSS	Mount plate & truss	465	kg
	AO system	148	kg
	CAL system	120	kg
	IFS system	300	kg
	Wiring/services	20	kg
EFS	Truss and panels	350	kg
	Electronics cabinets	365	kg
	Wiring/services	50	kg
	Ballast	182	kg
	Total:	2000	kg

Table 7-6 GPI mass summary

Centre of mass position: (x,y,z) = (0.4, -0.4, -999.7) mm.

7.3.2.1.17 FEA Assumptions and Philosophies

Finite Element Analysis generally requires that certain assumptions be made regarding the physical properties, construction, and response of the structure being analyzed. These assumptions are often based on accepted test data, such as linear elastic material properties. Sometimes, however, the FEA model must incorporate idealizations that are based on the modeler's judgment and experience. Some ofthe major assumptions made during this analysis are listed below.

- Material properties are based on widely available and commonly accepted test data, a detailed list of which can be found in Appendix 7.25. These material properties follow the assumption of linear elasticity.
- Optical tables built using a honeycomb core can be adequately modeled using solid volume elements with appropriate orthotropic material properties. A detailed study of this modeling technique can be found in Appendix 7.26.
- Truss members can be assumed to join at nodes of infinitesimal size. The finite size of welded truss joints can be neglected since these joints are believed to be very stiff, and therefore exhibit little internal deformation.
- Flexures can be adequately modeled using ANSYS LINK8 elements, which have no rotational stillness at the ends. This assumption implies that the flexure is infinitely flexible in its compliant directions, and only possesses axial stiffness. This assumption is believed to be conservative, and a more detailed study is found in Appendix 7.27 and Appendix 7.28.
- To account for the reduced axial stiffness in each flexure due to the pivot cut-outs on each end, the diameter of each flexure has been reduced to model the effective stiffness.
- The optics mounts and mechanisms on the optical tables are assumed to be infinitely stiff. The deflection of each optic is only a function of the rigid body motion of the table plus the local deformation of the table surface at the location of the mount.
- Each optic mount has an associated mass, centre of mass location and optic surface location. The two locations need not be coincident. A detailed explanation of how the mass and optics elements are coupled to the optical table is given in Appendix 7.29.

More details regarding each point can be found in the associated appendix. In addition to these assumptions, a number of verification tests have been performed to ensure that the FEA model is generating appropriate and physically meaningful results. A further explanation of these verification exercises can be found in Appendix 7.30.

Although the current FEA model is believed to be representative of the designed system, some further verifications are possible. In the next project phase, some detailed studies will be made to test certain assumptions or modeling techniques. A few of these tests are described below.

- Model a truss connection point in detail to verify the assumption that finite size beams can be modeled as connecting at a single infinitesimal point, not a more complex joint of finite size.
- Model a flexure bipod in more detail and with more complex elements to test that simple links are physically realistic.
- Model the actual connection between the flexure bipods and the AO table or IFS to ensure that there is no significant local deformations which the current model is not accounting for.
- Model the Mounting Plate and its associated bolted connections in more detail to determine more

accurately the induced stresses in this plate. Verify that these stresses are within acceptable factors of safety for all modes of handling and operation.

7.3.2.1.18 Flexure Analysis

Flexure analysis has been performed using ANSYS Finite Element Analysis software. It was determined that the analysis should cover a multitude of load cases, spanning: two instrument locations (port 1 and port 3), zenith angles from 0° to 60° in increments of 20°, Cassegrain rotator angles from 0° to 330° in increments of 30°, and temperature changes from +20°C to -5°C. A calculation of the gravity vector orientation for each combination of instrument port, zenith angle and Cassegrain rotator angle is found in Appendix 7.31.

Below are plots of total deflection (vector sum) of the entire instrument for two orientations: on the side port (port 3) while the telescope is pointed at zenith (Figure 7-67), and on the bottom port (port 1) when the telescope is pointed at zenith (Figure 7-68). The deflections shown in the plots below are small; 0.247 mm and 0.151 mm for the port 3 and port 1 cases, respectively. These results are very encouraging, considering that the FSS weighs more than 1000 kg, and is a cantilevered structure. A more thorough investigation of the flexure results is found in Appendix 7.32.

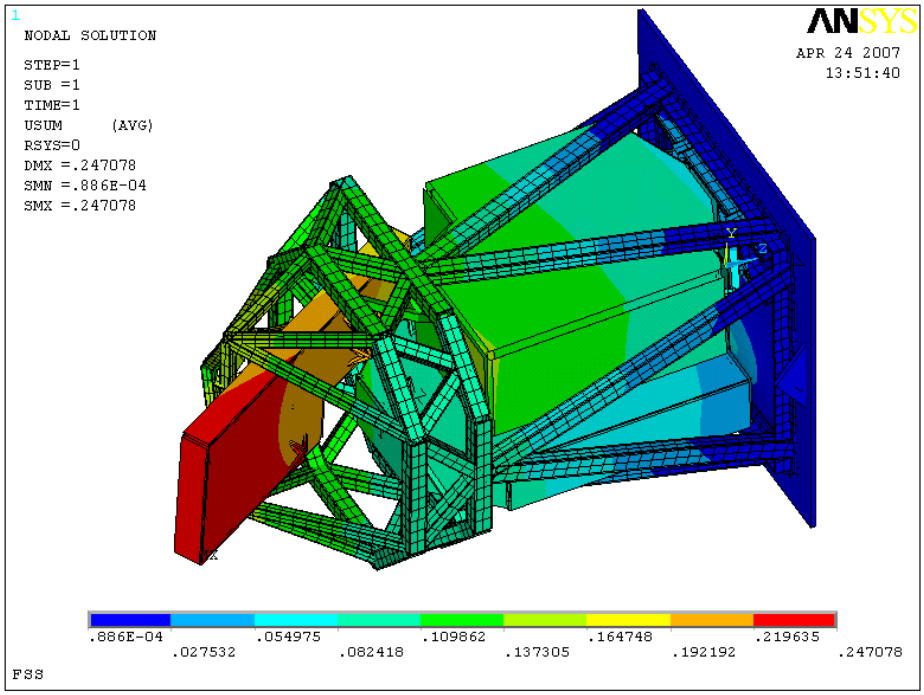

Figure 7-67 Flexure (port 3, zenith pointing, T = 20° C).

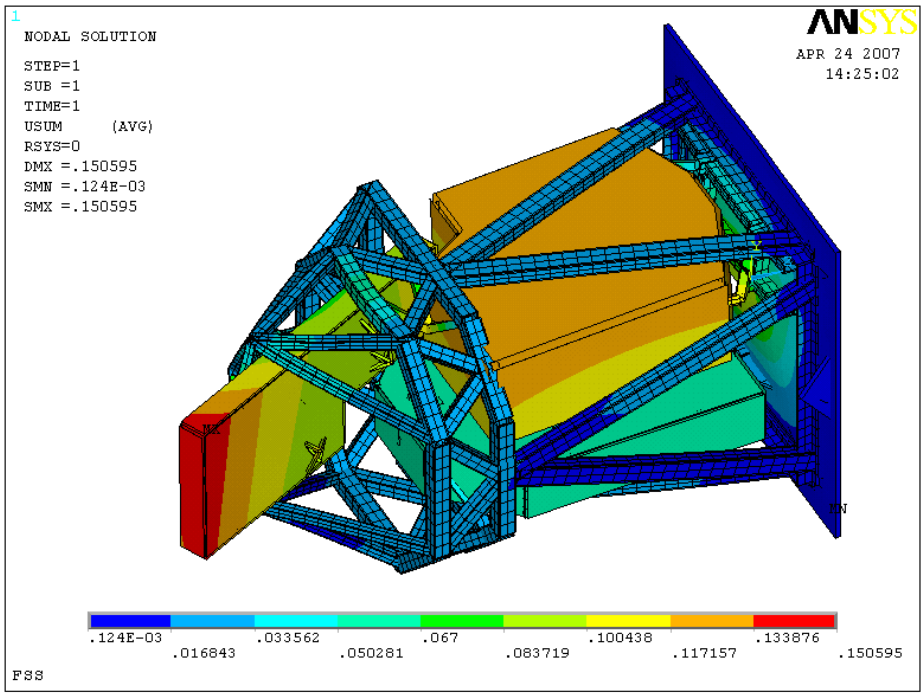

Figure 7-68 Flexure (port 1, zenith pointing, T = 20°C).

The largest amounts of flexure were observed as rigid-body motions of the CAL module and IFS. A detailed investigation indicates that much of this flexure is due to two factors: the flexure bipods should be stiffened (either through the use of larger diameter material, or by changing the angles between the legs of the bipod), and in both cases the bipod positions should be adjusted to better align with the centre of mass of each sub-system. These changes will be implemented in the next phase, as more information on the mass of each sub-system becomes known.

In addition to flexure, this analysis also calculated the induced stresses in the structure. It was found that the stresses were minimal everywhere except at the Mounting Plate. This is reasonable considering that the plate supports the entire cantilevered mass of the instrument. Plots of the von Mises stress condition are shown for two instrument orientations in Figure 7-69 and Figure 7-70 below. The maximum calculated stress was approximately 19 MPa using these two load cases. For comparison, the 0.2% yield stress for annealed AISI 1020 mild steel is 295 MPa. It is certain that additional load cases should be verified, and a more detailed study of stress concentrations should be performed, but based on this data there is good indication that material stress will not be a factor in the design of the instrument.

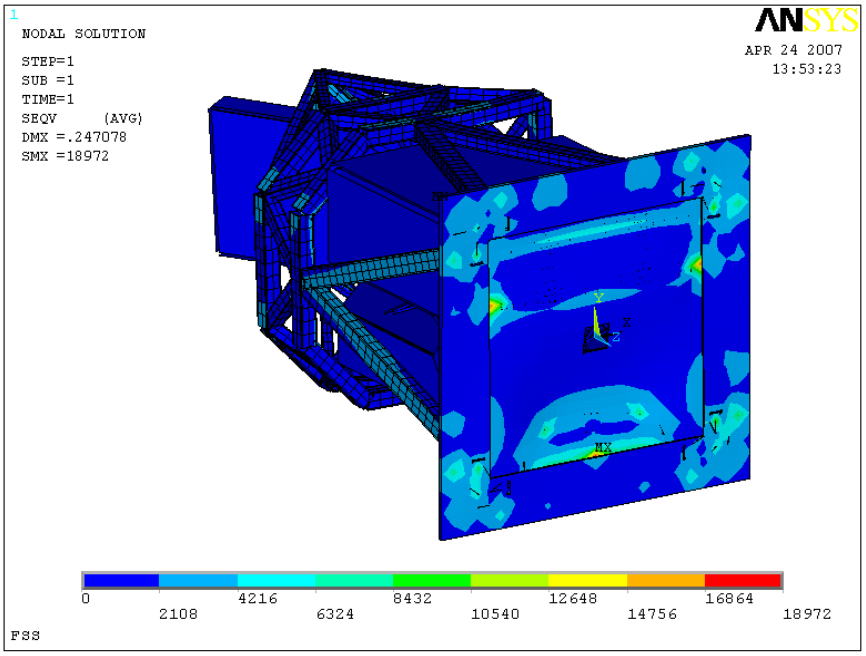

Figure 7-69 Von Mises Stress (port 3, zenith pointing, T = 20°C).

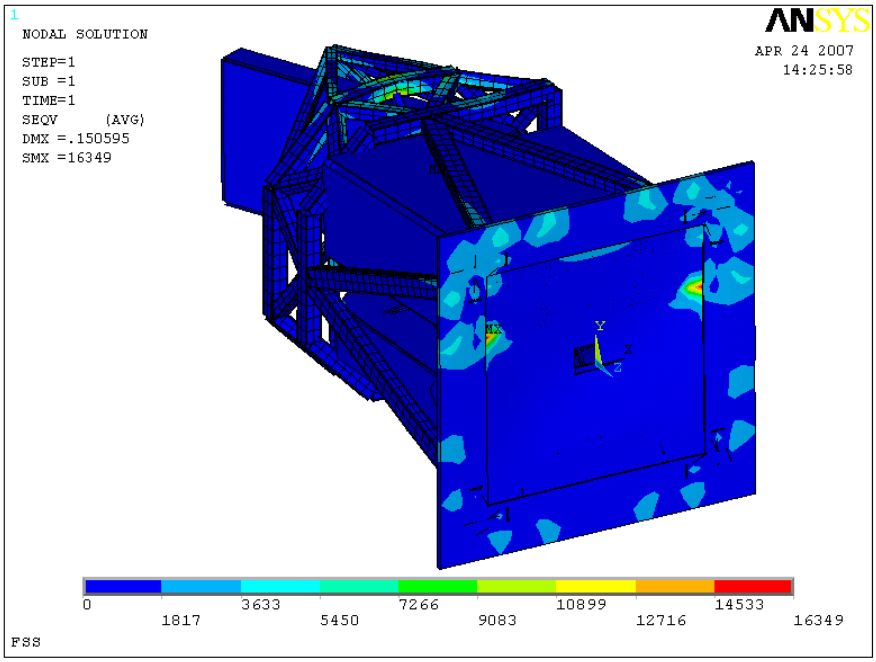

Figure 7-70 Von Mises Stress (port 1, zenith pointing, T = 20°C)

A more detailed data reduction was also performed on the motion of the critical optical elements. The deflections of each optic were calculated using the method described in Appendix 7.29. Load case 38 at a temperature of 20°C corresponds to the conditions in which GPI will be built and aligned in the lab. It is assumed that perfect alignment will be achieved. Therefore, this is considered to be the reference case, and all flexure/thermal alignment results were subtracted from this reference to determine the deviation from the perfectly aligned case.

The deflection of a critical optical element (the tweeter DM) is shown for load case 1 in Figure 7-71 below. This plot shows that the bulk motion of the tweeter is well contained within a sphere of radius 0.17 mm, which is 1% of the pupil diameter at this location. This result was achieved without compensating the pupil motion using M2 and the Input Steering Mirror. Once this compensation is included, even better results will be realized. Additional results for other elements of interest can be found in Appendix 7.32.

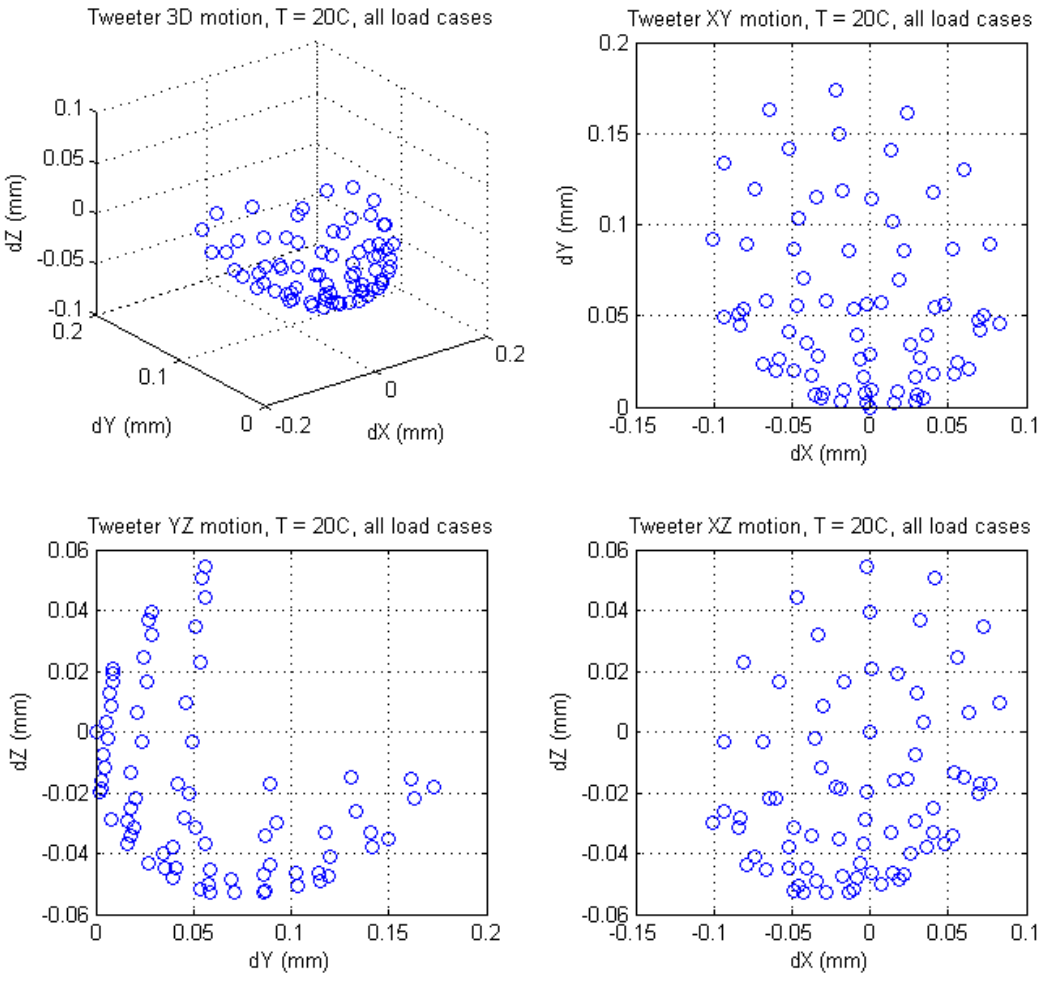

Figure 7-71 Flexure of tweeter DM (T = 20°C).

7.3.2.1.19 Thermal Distortion

In addition to gravity-induced flexure, the effects of variable temperature were also investigated. For this study, two orientations were chosen (port 1 and port 3 with the telescope at zenith). In each of these orientations, the temperature was varied between -5°C and +20°C in increments of 1°C. The results at 0°C and +10°C for port 1 are shown below. The maximum deflections in each case were found to be 0.499 mm and 0.240 mm respectively. Additional analysis is found in Appendix 7.34.

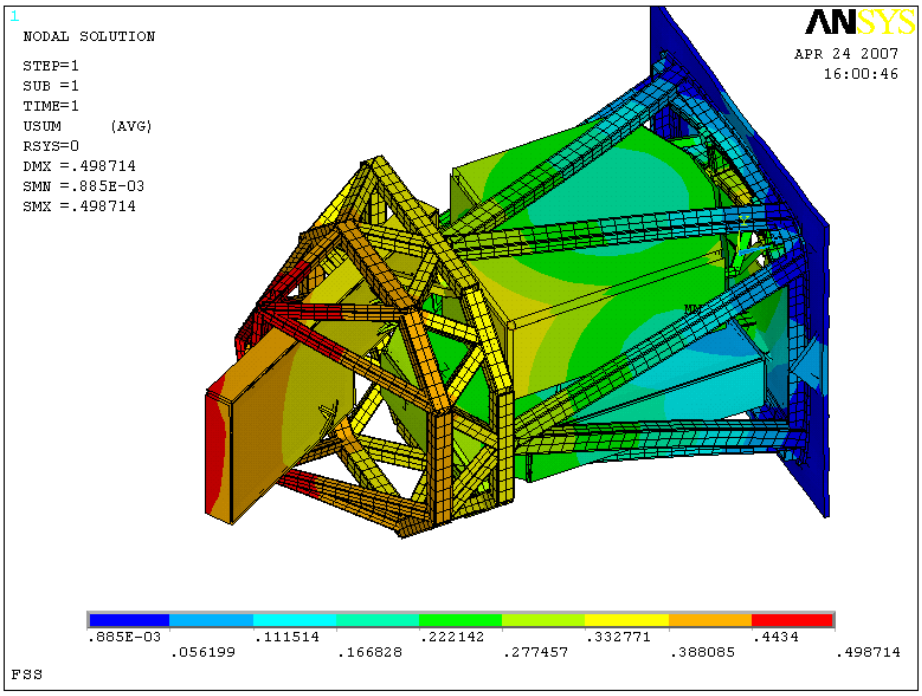

Figure 7-72 Thermal distortion (port 1, zenith pointing, T = 0°C).

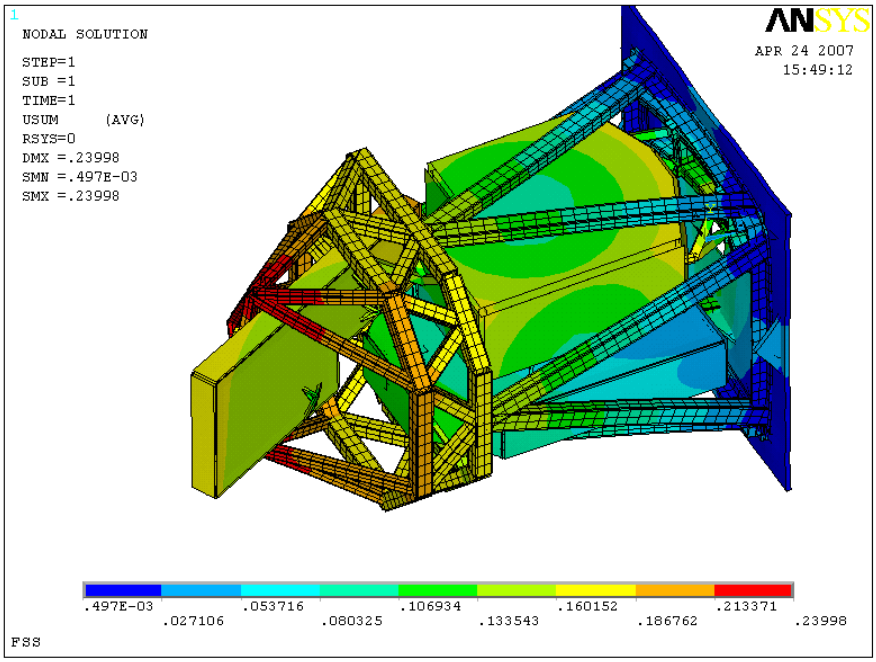

Figure 7-73 Thermal distortion (port 1, zenith pointing, T=10°C).

A more detailed post-processing of the thermal data was performed for selected optical elements. The motion of the tweeter DM was plotted against temperature as shown in Figure 7-74 below. As expected, the greatest deflection was observed at -5°C, and the deflections returned to zero at 20°C (the reference temperature). Motions at intermediate temperatures follow a linear response.

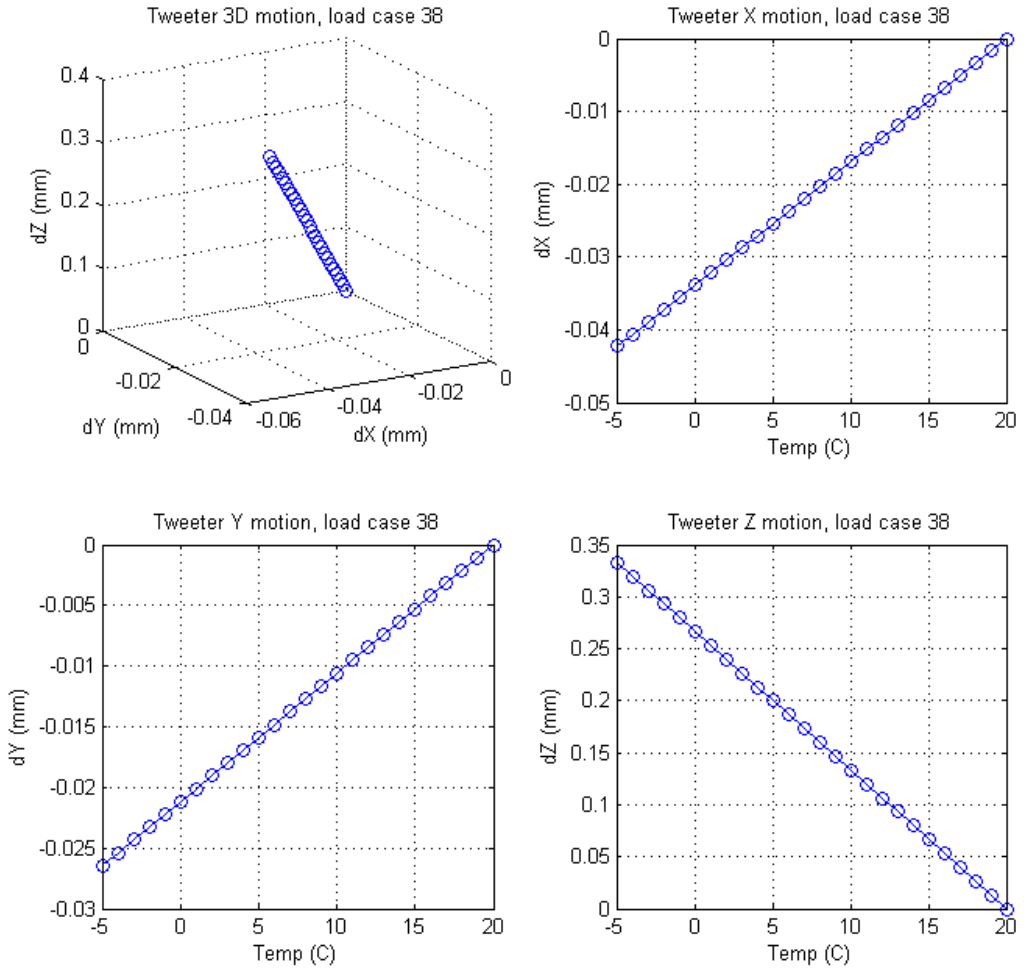

Figure 7-74 Temperature induced motion of tweeter DM (load case 38).

Flexure results from the various gravity vector load cases and temperatures can also be combined in a single plot. Figure 7-75 below shows the motion of the tweeter DM for all gravity load cases and temperatures of 0°C, 10°C and 20°C. From these graphs, it is evident that the largest displacements due to gravity flexure are similar in magnitude to a temperature change of 10-15°C. Put another way, during a typical night, the overall flexure of the tweeter DM is expected to be made up of equal parts gravity flexure and thermal distortion.

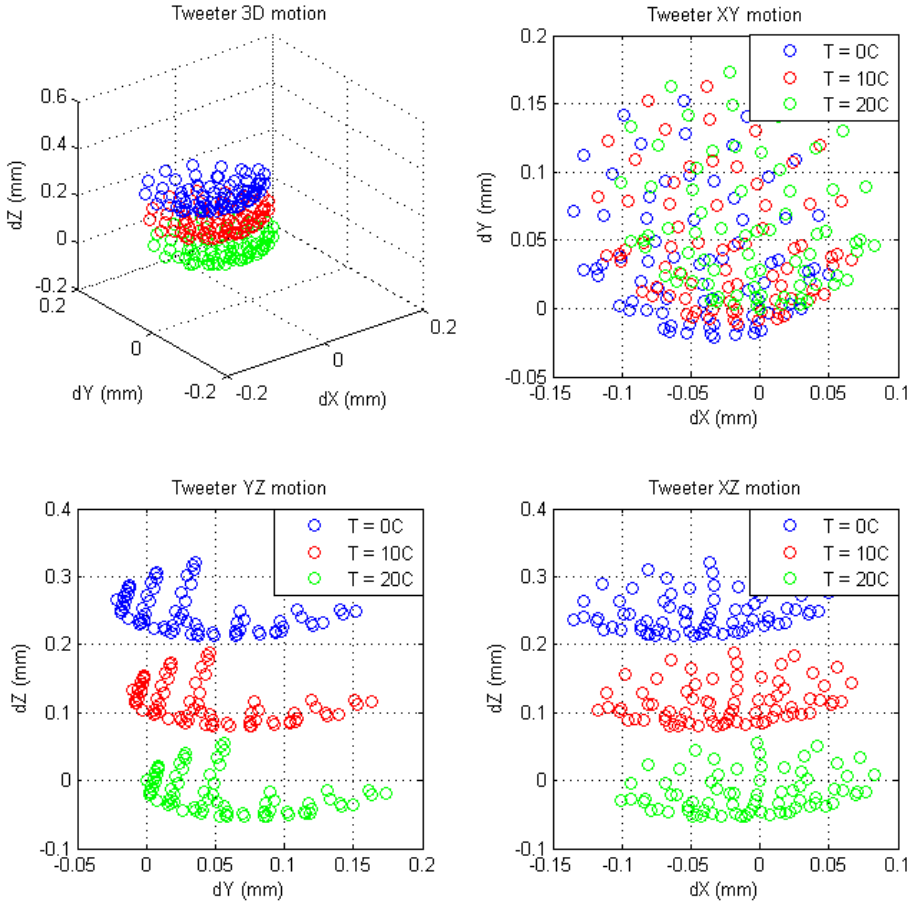

Figure 7-75 Combined motion of tweeter (all load cases, T=0°, 10°, & 20°C).

7.3.2.1.20 Modal Analysis

Modal analysis is used to determine the undamped natural frequency of a structure, and can be used to illustrate areas that may require stiffening. The first ten vibration modes, and their associated mode shapes were calculated using FEA analysis. A plot of the first mode shape and a summary of the frequencies and modes are shown in Figure 7-76 and Table 7-7 below. Additional plots of higher order mode shapes are shown in Appendix 7.33.

Mode	Freq (Hz)	Mode description
1	39.1	rigid-body CAL motion
2	42.3	rigid-body CAL motion
3	47.9	rigid-body CAL motion
4	48.1	rigid-body CAL motion
5	55.5	mount plate membrane deflection

6	60.1	mount plate membrane deflection
7	62.6	mount plate membrane and AO support bending
8	69.9	torsion of the IFS due to bipod bending
9	71	multiple, coupled motions
10	74.4	torsion of the IFS due to bipod bending

Table 7-7 Modal frequencies and shapes.

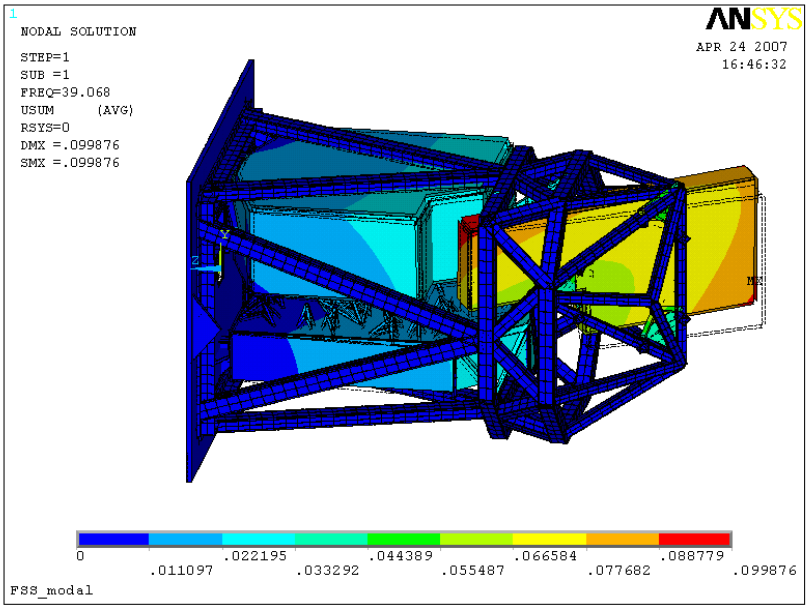

Figure 7-76 Vibration mode 1 (rigid-body motion of the CAL).

From the mode shapes and frequencies shown above and in Appendix 7.33, it is evident that rigid-body motion of the CAL and IFS sub-systems are the primary modes of vibration. Based on these observations, the following actions will be taken during the next project phase: 1) the CAL bipod flexures will be stiffened, 2) the IFS bipod flexures will be stiffened, 3) the mounting plate will be reinforced near the IFS bipod attachment points to prevent membrane deflection.

7.3.2.1.21 Heat Sources

Localized heat (or cold) sources are a problem for optical instruments because the heat can generate a cell of convective turbulence. This turbulent cell can degrade the image quality if it passes through the beam. Evidence of this has been seen with sources emitting as little as 2 W. Particular attention must be paid to sources that are emitting during regular observations. While most mechanisms are quasi-static during observations, the expected primary heat sources are the woofer tip/tilt platform (6 W) and the AO WFS camera detector (10 W). A more detailed analysis of sources is found in Appendix 7.35.

There are numerous ways of mitigating the effects of localized heating. It may be possible to extract the extra heat at the source by circulating chilled glycol or air through a closed-loop system. Both services are available from the telescope. Cold glycol would be much more efficient at extracting heat, compared to air, but there is an added risk of component damage in the event of a leak. It may also be feasible to slowly circulate the ambient air to speed thermal mixing and break up local turbulent cells. These options will be studied in detail during the next project phase.

7.3.2.1.22 Integrated Opto-Mechanical Analysis

The Finite Element Analysis presented above has been used to show the physical displacement of optical elements (such as the tweeter DM) from their nominal position. Although the gravity and thermally induced flexure analysis is useful for studying the response of the structure, it does not fully answer the fundamental question. Namely, does the instrument maintain a sufficient level of optical alignment to achieve its scientific goals?

To help answer this question, an integrated opto-mechanical analysis has been initiated. This analysis uses the deflection results that are calculated for each optic via FEA, and feeds those perturbations back into Zemax, the optical modeling software (Appendix 7.36). From within Zemax, ray-tracing is then used to determine the effects that perturbed elements have on the optical performance of the system. The co-alignment of the various pupils in the system is of particular interest; as are the motions of the image planes.

A pipeline is being developed to automatically process the multitude of load cases that were created using FEA. This work is ongoing to date. In an attempt to preview the results, one particularly severe load case (#33 at T=0°C) was determined based on the vector sum of the X-Y-Z displacements of each element (see Figure 7-77 below). Load case 33 represents not only a large total displacement for each pupil plane optic, but also a large relative displacement between the woofer DM, tweeter DM and apodizer mask. This load case occurs when the telescope is pointed 60° from zenith, with a Cassegrain rotator angle of 210°. (GPI is nearly “upside-down”).

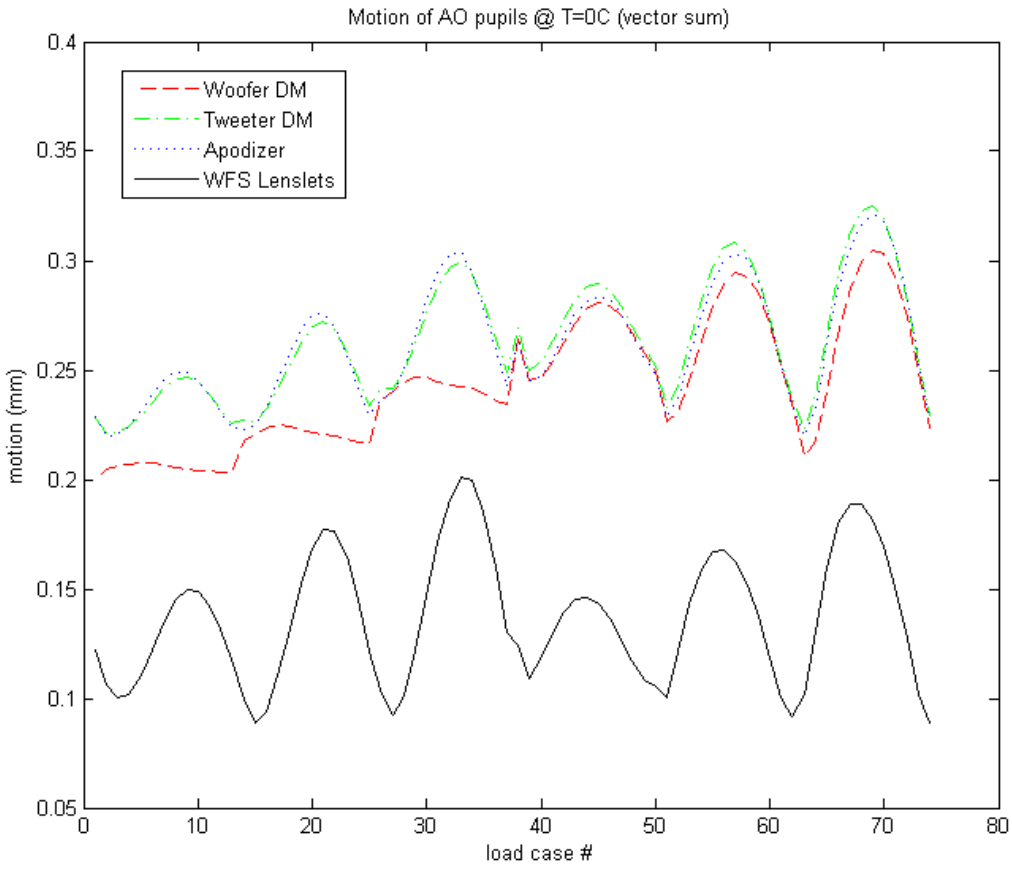

Figure 7-77 Pupil displacements (vector sum).

The ray-tracing results were generated in two distinct ways. First, the new beam footprint was calculated on each optic without using any optical compensators to adjust the system, (ie, no mirrors were adjusted). Next, the telescope secondary, the input fold mirror and the woofer tip/tilt platform were adjusted to re-centre the beam on the tweeter DM and re-point the image on the occulter mirror. The calculated offsets between the beam gut-ray and the centre of each optic are summarized for each case in Table 7-8 and Table 7-9 below.

Element	Beam Motion x (mm)	y (mm)	Vector sum (mm)
Woofer DM	0.074	0.071	0.103
Tweeter DM	-0.030	-0.061	0.068
Apodizer	-0.014	-0.011	0.018
Occulter	-0.787	-0.225	0.818

Table 7-8 Motion of selected beam footprints (no P/C compensation).

Element	Beam Motion x (mm)	y (mm)	Vector sum (mm)
Woofer DM	0.006	-0.067	0.067
Tweeter DM	0.000	0.000	0.000
Apodizer	-0.034	-0.052	0.063
Occulter	0.000	0.000	0.000

Table 7-9 Motion of selected beam footprints (after P/C compensation).

From these results, it is evident that the beam is well aligned at the tweeter DM and occulter mirror. The displacement of the compensated beam footprint on the apodizer mask is 0.063 mm, calculated using the vector sum of the X and Y components. It is interesting to note that this displacement is greater in the case using optical compensation than without. In any event, this displacement is small compared to the pupil size (0.5%). Therefore, to prevent light from "leaking" through the coronagraph, the aperture stop at this location should be undersized by 1%, according to this analysis. A plot of the beam footprints on the apodizer is shown in Figure 7-78 below. Green symbols indicate the uncompensated positions of the rays while red symbols indicate ray positions after beam pointing and centering. The aperture stop has been reduced by 1% in this case, and both beams were found to completely over-fill the aperture. A similar analysis was performed for the woofer DM, and a 1% aperture reduction was found to be sufficient as well.

A complete discussion of optical alignment tolerances, optical compensation and closed-loop control of the system is presented in *Chapter 2, System Engineering*.

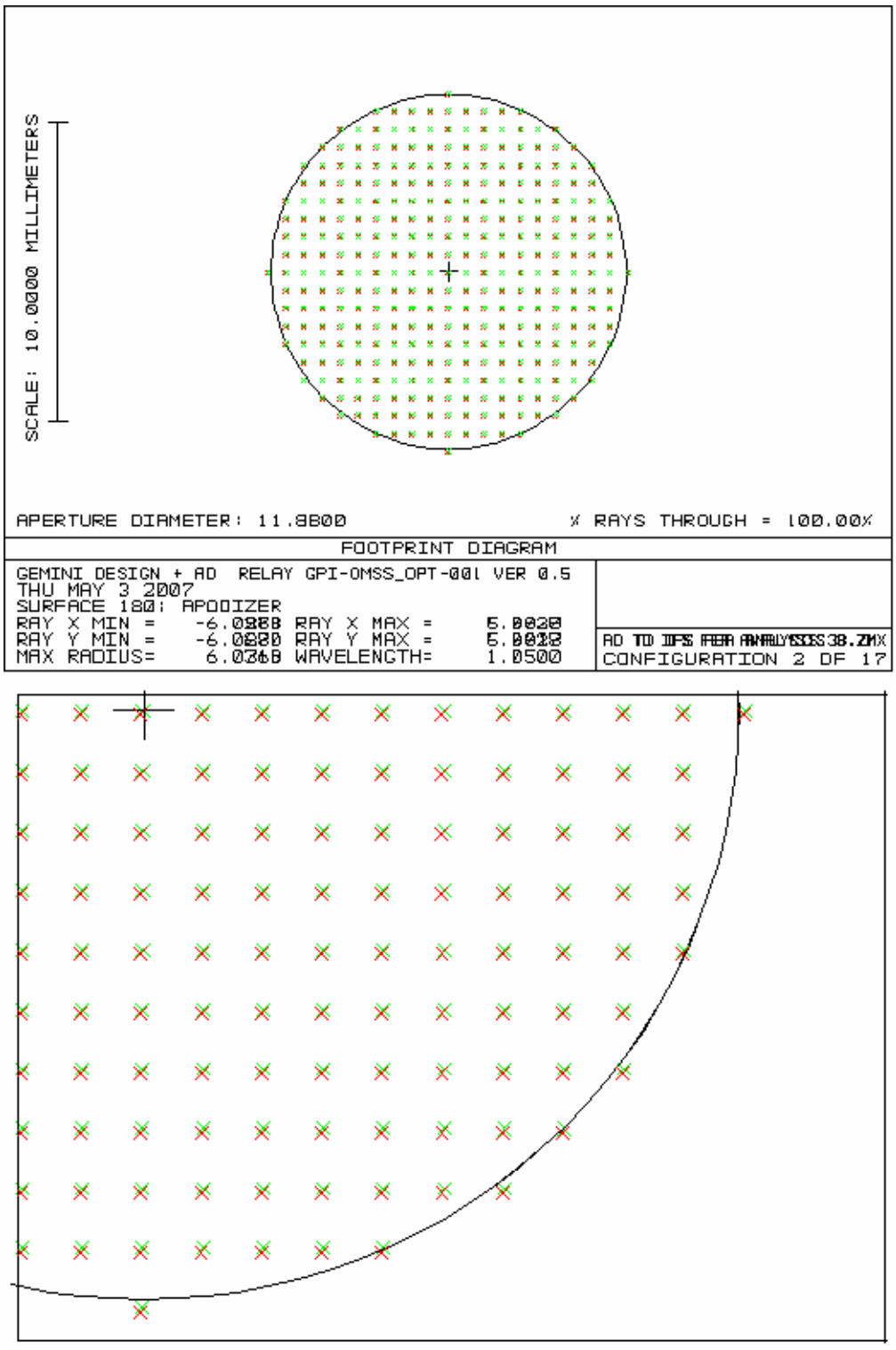

Figure 7-78 Beam footprints on apodizer (green = no compensation, red = beam re-steered).

7.3.3 Handling

7.1.1.24 Handling Features on the OMSS

The bottom and end walls of the EFS each have four mounting points that mate in the side or upward looking orientations (respectively) to the handling equipment at Gemini Observatory (see Gemini ICD1.9/2.7, Appendix 2.22). Also, the pintles and a lifting eye are provided which can be used to lift the instrument with a crane.

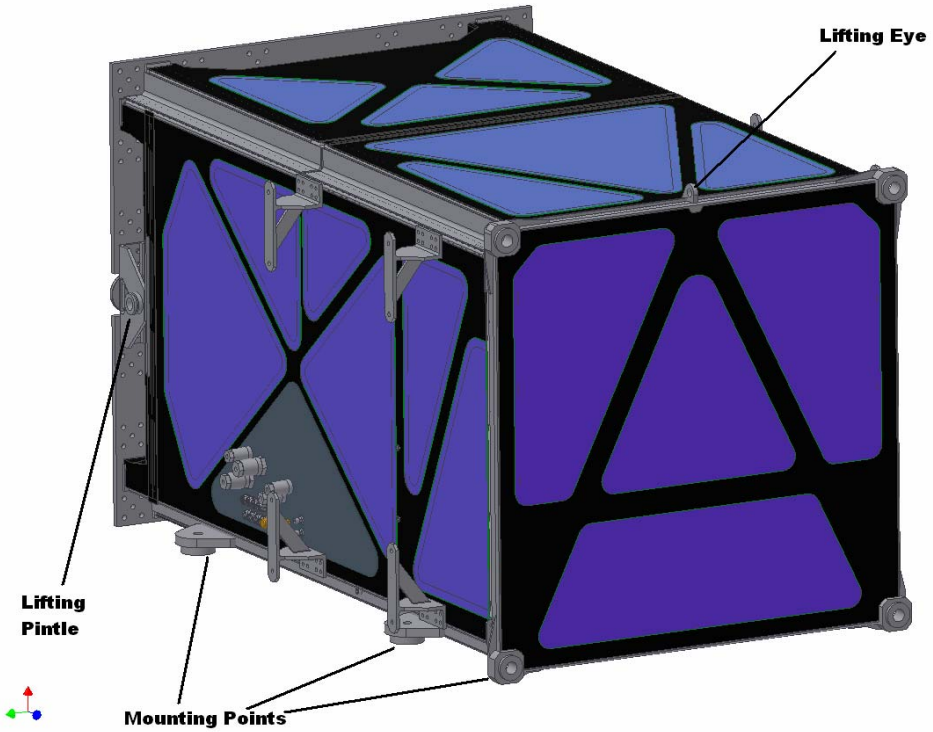

Figure 7-79 Lifting eye and pintles.

7.1.1.25 Handling Equipment used during I&T

There are three ways to move GPI during I&T, specifically:

- Overhead lift in horizontal ("side-looking") orientation;
- Overhead lift in vertical ("up-looking") orientation;
- Transport on handling dolly.

In order to move GPI, two pieces of handling equipment have been designed: a lifting ‘T’, shown in Figure 7-80, and a handling dolly show in Figure 7-81. The lifting ‘T’ is a two-piece assembly, which is used in the assembled state to lift GPI in the horizontal orientation, while the cross member alone is used when lifting GPI in the vertical orientation.

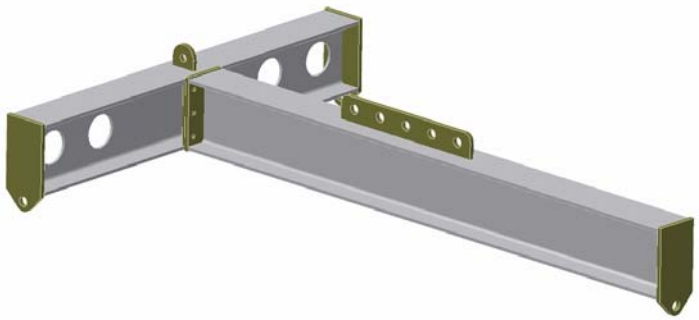

Figure 7-80 GPI lifting "T" (assembled).

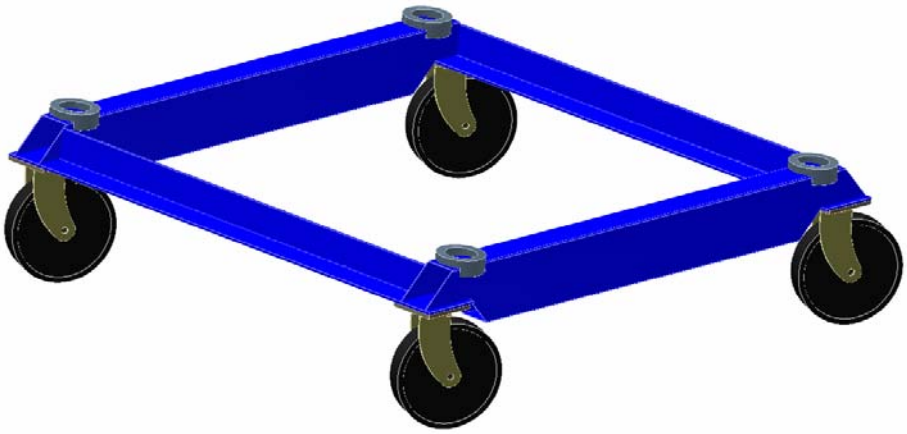

Figure 7-81 GPI Handling Dolly.

7.3.3.1.1 Lift in Horizontal (Side-Looking) Orientation

Lifting GPI in the horizontal orientation requires use of the assembled lifting ‘T’. Three lifting slings are attached at the three dedicated lifting points on GPI (two pintles and one tail lug) as shown in Figure 7-82, at which point the lift proceeds.

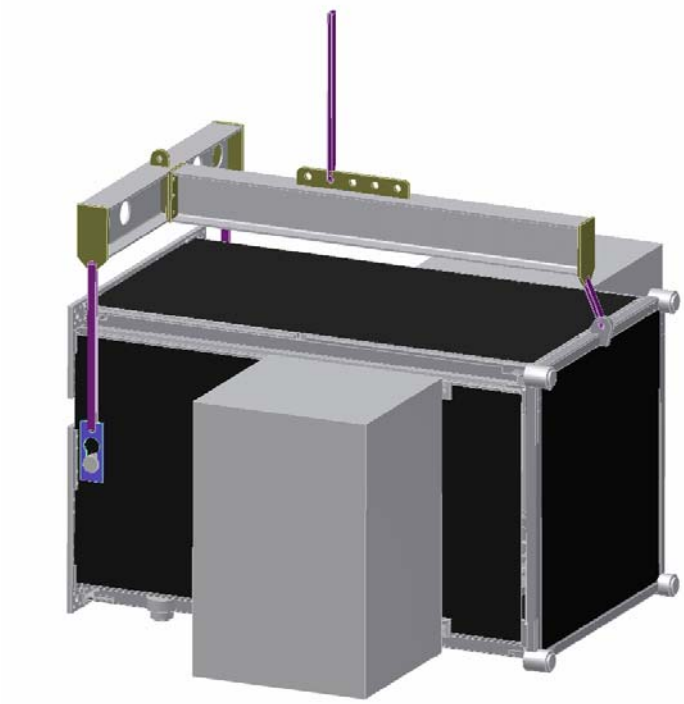

Figure 7-82 Lifting GPI in horizontal orientation.

7.3.3.1.2 Rotation to Vertical (Up-looking) Orientation and Lift

Rotating GPI to the vertical orientation requires only the top of the 'T' (Figure 7-83).

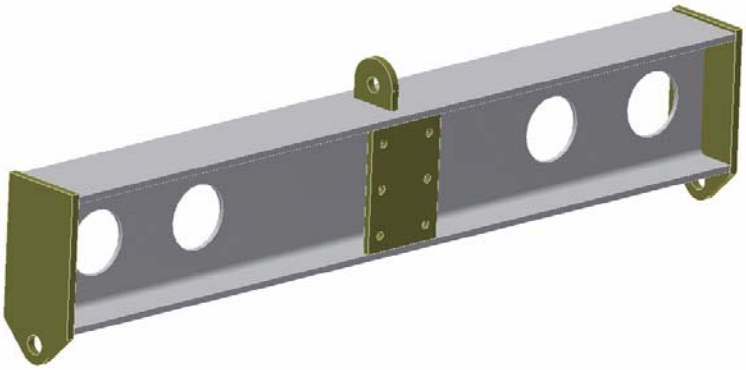

Figure 7-83 GPI lifting "T" (top of "T" only).

In this case a beam clamp is attached to the lateral translating beam of the overhead crane to which a chain winch (manual or powered) is attached. The lifting 'T' is attached to the pintles at the front of GPI and the chain winch is attached to GPIs tail lug. The instrument is then lifted from the floor, using both

the overhead crane and the chain winch in a coordinated manner in order to keep it level until sufficient ground clearance is attained (Figure 7-84).

Figure 7-84 Lifting GPI for rotation to vertical.

At this point the chain winch is reversed to allow the rear of GPI to slowly rotate down until it is in the vertical ("up-looking") orientation (Figure 7-85).

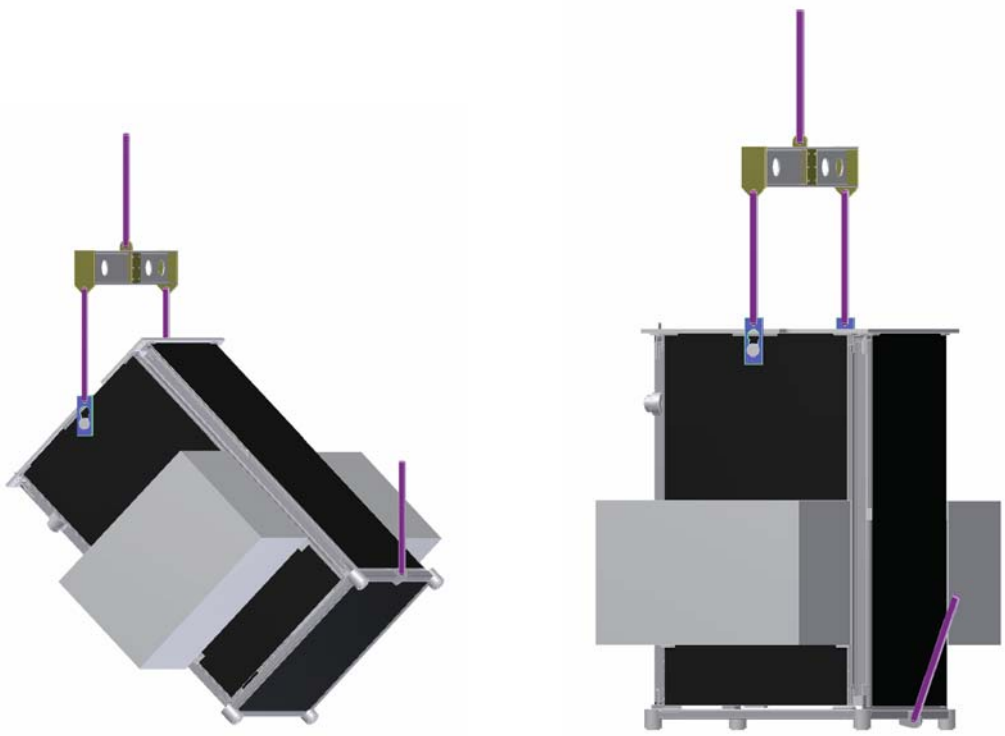

Figure 7-85 Rotating GPI to vertical.

GPI can then either be placed on the ground or on the handling dolly. In order to rotate GPI from vertical orientation to horizontal, the procedure is simply reversed.

7.3.3.1.3 Transport on Handling Dolly

The handling dolly is a simple square tubular aluminum frame with four caster-type wheels. The frame has mating discs spaced to match the standard instrument interface spacing. As GPI has two sets of interface "pucks" one on the bottom and one on the back face, the handling dolly can be used to transport GPI in either the horizontal or vertical orientation (Figure 7-86). Once mounted on the handling dolly, two people can roll GPI to the desired location.

Figure 7-86 GPI on handling dolly.

7.3.3.1.4 Handling of Electronics Enclosures

A pair of smaller handling carts dedicated to GPIs electronics enclosures is also provided. In cases where the electronics enclosures are removed from GPI, when placed on these carts, the enclosures can be easily moved around a work area, or moved out of the way for temporary storage.

7.3.3.1.5 L –Frame

The GPI L-frame is designed to support GPI in the same manner as would be expected on Gemini's Instrument Support Structure in the horizontal or "side-looking" configuration. The L-frame is a tubular steel structure, and incorporates a mounting face drilled to the same bolt pattern as the ISS mounting faces. Figure 7-87 shows the L-Frame, while Figure 7-88 shows GPI mounted on the L-Frame. GPI will be both assembled and initially tested on the L-frame, and the L-frame will be shipped to the Gemini summit facility, for assembly and testing prior to mounting on the telescope. The L-frame is equipped with six wheels to allow movement around an I&T facility, and includes six leveling feet in order to both level the instrument and relieve the wheels of some load during testing periods.

Figure 7-87 L-frame design.

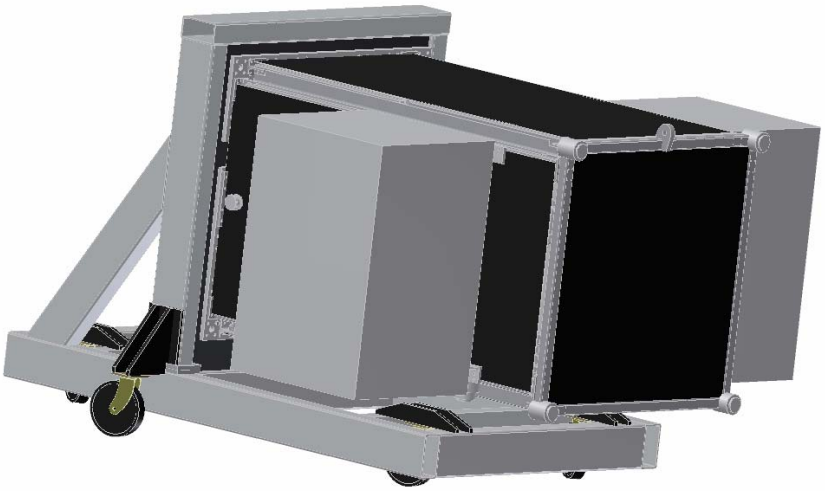

Figure 7-88 GPI on L-frame.

7.1.1.26 Handling Equipment Used at the Telescope Site

It is assumed that, as per the previous sections, GPI will be mounted on the L-frame for final testing at the telescope site, and transported about the telescope site by use of the handling dolly, along with the electronic enclosure carts as required. Lifting and re-orientation of the instrument will be performed using the lifting devices and procedures as previously outlined, with the exception that, at the telescope

site two overhead cranes will be used when rotating GPI to vertical as opposed to the use of one overhead crane combined with a chain winch at HIA.

7.1.1.27 Installation/Removal from ISS

7.3.3.1.6 General Installation and Removal

To install GPI on the ISS, it must first be oriented on the Gemini air pallet according to whether it is being installed on a side port or the bottom port. The two mounting posts are then attached to the ISS using the central dowel hole for alignment. GPI is then moved into a position where the mounting posts engage with the oversized holes near the "V" and "flat" location features. Cutouts have been made in the side of the pintle gusset so that the telescope technicians can view the insertion process, and adjust the air-pallet accordingly if needed. On the side ports, it may be possible to engage the mounting posts with the location features simply by lowering the air pallet, and using the weight of the instrument. On the bottom port, this is not feasible so jacking screws will be provided to tighten the instrument location features against the mounting posts.

Once properly located, bolts must be inserted and tightened around the periphery of the instrument Mount Plate. The cover panels on the EFS have been designed so that it is not necessary to remove any panels to complete this operation. This feature will speed and simplify the assembly process, and protect the optics from any dropped hardware.

7.3.3.1.7 Initial Installation and Alignment

The initial installation of the instrument is somewhat more complicated than the general case described above. This is because the optical axis of the ISS may not be in perfect alignment with the bosses on the ISS face that are used to attach the instrument location features. This means that once installed, the light from the telescope may not be in alignment with the GPI optical axis.

7.3.3.1.8 Recall that the optical beam can be steered within GPI using a combination of the Input Steering Mirror and the telescope secondary (M2). Therefore, it should be possible to determine the amount of initial misalignment by scanning these mirrors through their ranges of travel until an on-axis star is registered with the centre of the AO wavefront sensor. Using the mirror angles required to bring this star on-axis, the X-Y misalignment of GPI can be determined. Once known, the instrument is then lifted off the location features, and the X-Y positions of the "V" and "flat" are adjusted accordingly. Features, such as jacking screws or shims, will be provided for fine control of the adjustments. It is assumed that this mechanical adjustment will bring the instrument to within +/- 0.5 mm of the telescope optical axis. The final alignment will be accomplished by using the M2/steering mirror pair mentioned above to point and centre the beam to high precision.

7.1.1.28 Storage

When not on the telescope, GPI should be stored on either the handling cart or L-frame described above. Cleanliness is very important for this instrument, so the cover panels should be left on at all times, and they should only be removed while in a clean room. If not in service for extended periods, it is recommended that the mechanisms by cycled a few times per week, to maintain proper lubrication.

7.4 OMSS References

[1] Bauman, Brian J., "Anisoplanatism in adaptive optics systems due to pupil aberrations", Astronomical Adaptive Optics Systems and Applications II, edited by Tyson, Robert K.; Lloyd-Hart, Michael. Proceedings of the SPIE, Volume 5903, pp. 236-247 (2005).

8 OMSS and Top Level Electronics

Functionality of GPI is realized on different levels by control software. The goal of top level electronic design is to provide physical connections between the computers on which the software runs and the mechanisms and sensors in the Optomechanical Enclosure on one hand, and with the Observatory networks and systems on the other. The tasks in the design of the top level and OMSS electronics are as follows

- Deliver power to the GPI subsystems and components
- Assure physical integrity of connections in the computer networks
- Control OMSS mechanisms with the command signals originating in software
- Coordinate the control of the CAL and IFS mechanisms for compatibility with OMSS
- Assure the signals from sensors in the Optomechanical Enclosure are free of interference
- Provide the interface between the GPI and the Gemini Interlock System GIS
- Monitor temperatures and humidity inside the Electronics Enclosures and the Optomechanical Enclosure

8.1 System overview

The main electronic components of GPI are 4 Linux computers (TLC, AOC, CAL and IFS). These computers communicate with the networks and systems of Gemini observatory and on the internal GPI LAN with 5 Galil multi-axis motion controllers. The topology and protocols of these connections and the network equipment involved are illustrated by diagrams and described in detail in Chapter 9. These computers also connect to various peripherals through a variety of interfaces – also described in Chapter 9 and in chapters specific to AOC, IFS and CAL (Chapters 3, 5 and 6). The control software running on these computers realize various tasks in the chain of events leading to acquiring and observing astronomical targets as described in detail in Chapter 9. During these tasks the sensor data is collected from the Optomechanical Enclosure and digital commands are outputted to specific electronic control systems which in turn generate and amplify control voltages to the levels required by their respective actuators in the OE.

The electronic control systems employed by the OMSS are described in detail in the next sections of this chapter. The similar control systems of CAL and IFS are also touched upon in these sections while further expanded upon in Chapters 5 and 6.

The AO subsystem employs separate electronic control systems to drive the woofer/T/T assembly and the tweeter. These systems are described in detail in Chapter 3 and are only mentioned here as the receivers of the AC power.

The computers, their peripherals and control electronics all generate heat and must be housed in thermally insulated cabinets from which the heat is removed by liquid coolant as described in detail in Chapter 7. The Electronics Enclosures (EEs) have a limited space available and the components of GPI subsystems have been carefully distributed between the two cabinets to make the best use of that space as described below in 8.1.3.1. Because of hermetic thermal enclosures the connections between GPI

computers and control electronics must be done through bulkhead panels in the EEs 1 and 2 and Optical Enclosure (OE) as described in 8.1.4.

Heat generation by the GPI electronics is a major issue in the system operation. A failure in the glycol coolant circulation could lead to catastrophic overheating of electronic components in the insulated cabinets. Therefore temperatures will be monitored of the incoming and outgoing glycol and of air in several locations in both thermal cabinets. The air temperatures and temperatures of all motors inside the OE will also be monitored to detect the possibility of heat plumes in the optical path of GPI. The relative humidity in both Gemini observatories is known at times to approach 100% and such high humidity could be damaging for the electronics. To detect such conditions the sensor chain in both EEs and the OE will also include humidity sensors. The 1-Wire sensor chain will be used as a simple and cost-effective solution to collect the temperature and humidity readings in multiple locations. The EEs also include thermal cut-outs to provide protection in the event of cooling failure that goes un-noticed.

8.1.1 Schematic conventions

8.1.1.1 CAD software

All electrical circuits of GPI are designed using the Altium Designer suite of programs. The entire cycle of circuit design from schematic capture through circuit simulation and connection integrity testing, to printed circuit layout and Bill of Material (BOM) generation is handled by various components of the suite. Finished diagrams of GPI electrical circuits will be kept both in Altium specific binary files (*.schdoc) and in PDF files that are easy to view and print without proprietary software.

8.1.1.2 Schematic file names

Similarly to other documents of GPI the files with electrical schematics are given names and sequential numbers by a web application Docstore running on one of the HIA servers. A database of Docstore keeps track of all the document names issued, together with author's name, date of creation and a short description of document content. The schematics specific to the OMSS and top level electronics are named *"GPI-omss_sch-xxx.*"* where xxx are sequential numbers starting at 001 and * is a filename extension such as 'sch' or 'pdf'. Similarly the schematics specific to CAL and IFS are named *"GPI-cal_sch-xxx.*"* and *"GPI-ifs_sch-xxx.*"*, the sequencing xxx of each also starting at 001. Schematic filenames are not case sensitive (MS Windows convention) and thus the "GPI-OMSS_SCH-001" and "GPI-omss_sch-001" refer to same diagram and can be used interchangeably.

8.1.1.3 Cable labeling and enumeration

GPI cables are named as: *CAxxxx* where *xxxx* is a unique 4 digit number. The first digit of the number is assigned as follows:

'1' – cables external to Electronic Enclosures 1, 2 and OE
'2' – cables inside EE1

‘3’ – cables inside EE2
‘4’ – cables inside OE

8.1.1.4 Connector naming and enumeration

Connectors and their mates at other cables and assemblies are named as:

Jxxxx – ‘Jack’, a connector with female contacts (sockets)
Pxxxx – ‘Plug’, a connector with male contacts (pins)

Two mating connectors share the same four digit number *xxxx*. In case of hermaphroditic connectors the J and P are assigned arbitrarily to form J-P pairs.

The first digit of a connector number is assigned as:

‘1’ – connectors at ISS services panel
‘2’ – connectors at EE1
‘3’ – connectors at EE2
‘4’ – connectors at OE

The rules of schematic file naming, cable labeling and connector enumeration are illustrated in Figure 8-1, a snippet of the top level block diagram *GPI-omss_sch-001.schdoc* (See the complete diagram in Appendix 8.1)

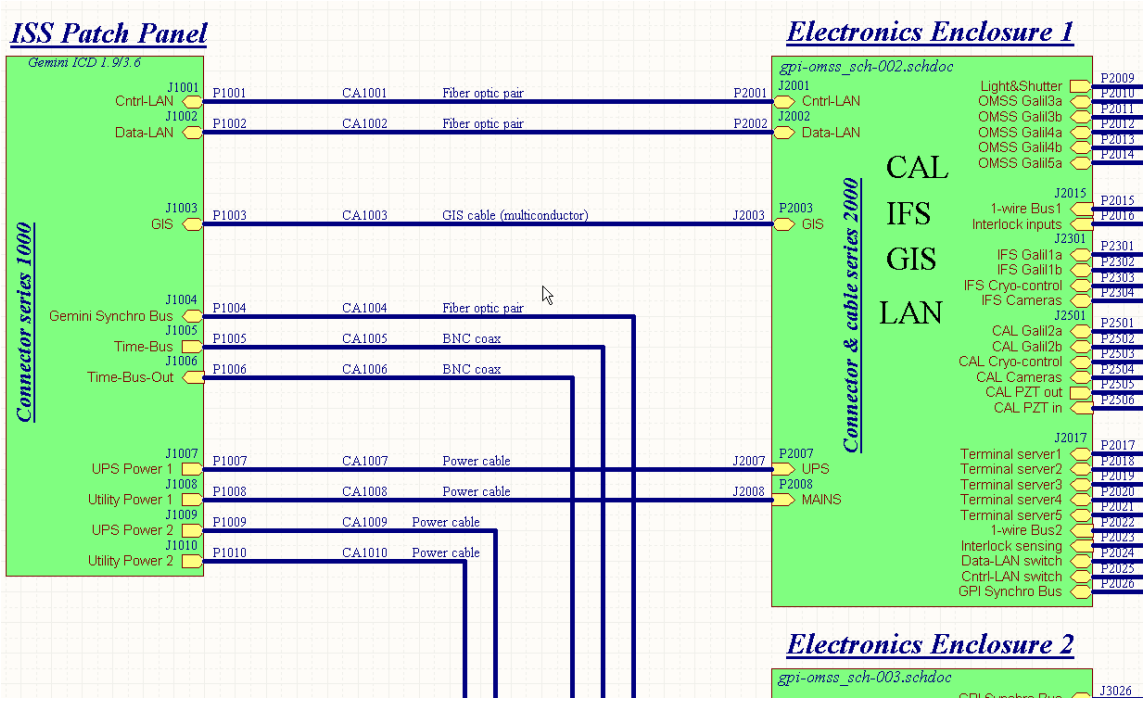

Figure 8-1 Cable and connector naming and schematic file reference example (part of the Top Level Block Diagram)

8.1.2 Interconnects overview

A top level view of interconnects between GPI sub-assemblies and components is captured in the top level diagram GPI-OMSS_SCH-001 and three sub-diagrams GPI-OMSS_SCH-002-4 (Appendices 8.1 – 8.4). The sub-sections below further describe the interconnections between the blocks and devices in these diagrams.

8.1.2.1 AC power interconnects

All GPI components draw their power from the AC 120V outlets of Gemini ISS (Gemini ICD 1.9/3.6). The Gemini South AC frequency is 50Hz while the Gemini North is 60Hz. Two separate power sources are provided by the Gemini facilities: MAINS and UPS. The MAINS is an ordinary wall outlet power of the observatory and the UPS is an uninterruptible power backed up by facility's battery banks and emergency generators. Both these powers are protected by 20A sized circuit breakers. In order to satisfy GPI power needs which exceed 20A at 120V its components must be distributed between these two power sources. It is a logical choice to have all the computers and network hardware plugged into the UPS power while having the remaining electronics powered by the potentially less reliable MAINS power.

The MAINS and UPS powers are brought into both electronics enclosures of GPI by the standard facility power cables with NEMA L5-30P connectors. Power is distributed to individual receivers inside the thermal cabinets via 4 power bars: PB1-PB4. Microprocessor controlled power bars Baytech RPC22 - 20NC (Appendix 8.9) have been selected to serve this purpose. These power bars are connected by an RS-232 serial line to the GPI terminal server and Ethernet which supports the telnet protocol for selective turning on and off their outlets by ASCII encoded commands. Each power bar provides 12 AC outlets. Physical shape of these power bars (1.95"x1.72"x56.25") is convenient for mounting along the sides of the thermal cabinet back rails, one on each side. Power bars PB1 and PB2 deliver the MAINS and UPS in the electronic enclosure EE1 while the enclosure EE 2 hosts PB3 and PB4 for the same purpose.

In order to retain the control over the power bars when all their outlets are turned off by software, the Network Switch and the Terminal Server are plugged directly into the UPS power, bypassing the Baytech bars. All the rest GPI component get their power via the Baytech bars.

When selecting commercial electronics for GPI a strong preference was given to 19" rack compatible enclosures powered directly by 120V AC. In keeping with this preference all the custom electronics are also housed in 19" rack enclosures that include their individual 120V AC power supplies. Table 8-1 summarizes all GPI components that draw the 120V AC power. Power loads in the table are the best guesses at the time of writing. Consult Chapter 2 for more up to date power estimates.

Component	Make and model	UPS load [W]	MAINS load [W]	Connected to	U-size
AOC computer	HP ProLiant DL580	1100		PB2 UPS	4
TLC computer	Augmentix 1950	244		PB2 UPS	2

CAL computer	HP ProLiant DL580	500		PB1 UPS	4
IFS computer	Augmentix 1950	244		PB1 UPS	2
Network switch	Cisco Catalyst 2960	30		PB1 UPS	1
Terminal server	Perle CS9000	25		PB1 UPS	1
Power Bar 1	Baytech RPC-22	5		UPS	
Power Bar 2	Baytech RPC-22		5	MAINS	
Power Bar 3	Baytech RPC-22	5		UPS	
Power Bar 4	Baytech RPC-22		5	MAINS	
OMSS Galil box	Custom HIA		150	PB1 MAINS	3
CAL Galil box	Custom JPL		40	PB1 MAINS	
IFS Galil box	Custom UCLA		40	PB1 MAINS	2
OMSS PZT controller	Mad City Labs		120	PB2 MAINS	6
CAL PZT controller			200	PB1 MAINS	3
CAL cryocooler			120	PB1 MAINS	2
IFS cryocooler control	Lakeshore		20	PB1 MAINS	3
AO T/T controller	PI E-710/3		60	PB2 MAINS	
woofer controller	Cilas		100	PB2 MAINS	3
WFS camera controller	SciMeasure		50	PB2 MAINS	4
MEMS DM controller	Cambridge Innovations		40	PB2 MAINS	3
Calibration source controller	Xantrex		40	PB1 MAINS	
Total		2153W	990W		

Table 8-1 List of GPI components plugged into the 120V AC power

8.1.2.2 Copper and fiber network interconnects

Optical fiber pairs connect the Gemini Control LAN and Data LAN to their respective virtual network switches within the Cisco 2960. The switches provide copper network connections to both LANS for the 4 GPI host computers: TLC, IFS, CAL and AO. Additionally the Control LAN also connects to the 5 Galil controllers, to the RS232 terminal server and the 1-Wire bus controller. All these connections are made using standard 10/100baseT patch cords.

A pair of optical fibers connects the AO computer to the Gemini Synchro Bus. A separate internal Reflective Memory bus within GPI uses single optical fibers between Reflective Memory cards in TLC, AOC, CAL and IFS hosts to form a closed loop circuit.

8.1.2.3 RS-232 interconnects

The Perle CS9000 (Appendix 8.7) terminal server is a node of the Gemini Ctrl LAN and it provides the RS232 serial connections to GPI components via TCP/IP protocols. The RS-232 connections of GPI serve several functions:

- console connections to the host computers
- consoles for the Galil controllers
- configure and control the Baytech power bars
- communicate command data to the CAL PZT controller
- control and monitor the cryocoolers of CAL and IFS
- control the brightness of the broadband calibration source

All serial peripherals connected to the terminal server are summarized in Table 8-1

Port no	Peripheral
1	TLC console port
2	AOC console port
3	CAL console port
4	IFS console port
5	Galil 2183 #1
6	Galil 2183 #2
7	Galil 2183 #3
8	Galil 2183 #4
9	Galil 2183 #5
10	Baytech PB1
11	Baytech PB2
12	Baytech PB3
13	Baytech PB4
14	CAL PZT controller
15	CAL cryocoolers
16	IFS cryocoolers
17	Xantrex light source controller

Table 8-2 List of RS-232 peripherals connected to the terminal server

8.1.2.4 Data connections to cameras

There are 5 cameras in GPI belonging to the AO, CAL and IFS subsystems. Cameras use high data rate cables to transfer images from the cameras to the AOC, CAL and IFS computers and the cables are specific to camera make and model. These cables will be procured with appropriate lengths to make the required connections and with quick disconnects allowing crossing the bulkheads as described in section (8.1.4) below.

8.1.2.5 Interconnects to mechanism actuators and position sensors

This is the largest group of interconnects within the electronics of GPI. All the mechanisms of GPI are summarized in the Mechanisms Table, Appendix 2.28. Actuators and associated position sensors fall into three distinct categories: servo-motors, stepper motors and PZT stages. These categories are described in detail in section 8.2 . To reduce the number of cables running between GPI enclosures the signals required for controlling several individual mechanisms will be combined into single multiple conductor cables, as described in section 8.1.4.

8.1.2.6 GIS interconnects

The Gemini Interlock System (GIS) interface of GPI connects to Gemini ISS service panel with a standard 4 twisted pairs shielded cable with MIL-spec bayonet-lock connectors as described in Gemini ICD 1.9/3.6 (Appendix 2.16). The GPI GIS inputs signals from the interlock switches safeguarding the doors of Electronic and Optomechanical Enclosures. These signals are brought to the GIS circuits by a multi-conductor cable. For details of GIS see section 8.6.1 below.

8.1.2.7 Environment monitoring network (1-Wire)

The 1-Wire bus (see section 8.7.1) is applied to collect the information from sensors placed in strategic locations in GPI enclosures. The temperature, humidity and voltage sensors are strung along a 3 conductor cable carrying the 1-Wire signal, the 5V power and the reference ground. Several branches of these cables are brought together into the 1-Wire Bus Master housed inside the OMSS Galil box. Along the branches of the 1-Wire network the individual sensors are plugged into the bus using 3-pin Molex MicroFit connectors (Appendix 8.8). See details on sensors in section 8.7 .

8.1.2.8 AO woofer and T/T interconnects

These are proprietary multi-conductor cables that will be procured at the right lengths from the vendor of the DM woofer and its T/T stage. The cable run between the controller box and the DM and T/T inside the OMSS must be ordered with disconnectors along the way allowing crossing the bulkheads as described in section 8.1.4 below.

8.1.2.9 MEMS tweeter interconnects

The tweeter DM is driven by 4096 signals varying between 0 and 300V. These signals are generated by the DM controller electronics manufactured by Cambridge Innovations. The baseline cabling is eight 528 conductor ribbons fabricated as 6 layer flexible printed circuits terminated with 528 contact MegArray connectors at both ends. The 16 additional wires in each cable are used as the ground return. The MegArray connectors couple with proper mates at the controller box and the BMM MEMS mirror. Due to the huge number of signals and risk associated with introducing unnecessary contacts along the signal path, the MEMS signal connection is exempted from the requirement of crossing the bulkheads with mated connectors. Instead, an appropriate pass-through and strain relief arrangement will be mechanically designed to allow bulkhead crossing. An alternative being investigated early in the CDR

phase is a third, dedicated thermal enclosure mounted directly to the EFS, minimizing the number of connectors and risk to the delicate cabling.

8.1.2.10 Calibration source fibers

Three multi-mode fibers will carry calibration light from the sources located in the Electronics Enclosure 1 into the OE. The fibers will cross the bulkheads using standard optical fiber couplings, nominally of the FC variety. At the OE bulkhead the three fibers will be combined into a custom 3-core fiber attached to 3 pinholes deployable into the Gemini primary focus. For details on calibration sources see section 8.5 .

8.1.3 Thermal Enclosures

All active electronics of GPI that generate measurable heat and can be located outside the Optical Enclosure are housed in 2 hermetical cabinets incorporating 19" instrumentation racks. Each cabinet can house a stack of standardized 19" cases of a total height of 21U (1U=1.75"). The purpose of these thermally insulated and liquid cooled enclosures is to prevent generation of heat plumes inside the Gemini dome by the electronics packages of GPI. These enclosures are described in detail in Chapter 7. Thermal enclosures incorporate manually reset-able, passive thermal power cut-offs for both the MAINS and UPS (Gemini ICD 1.9/3.7 – Appendix 2.17). These cut-offs are set to trip when the temperature inside the cabinets reaches 50deg C.

8.1.3.1 Panel space allocation

Based on the anticipated volumes and panel space usage (last column of Table 8-1) of electronics contributed by the AO, CAL, IFS and OMSS teams the front panel space in the racks has been allocated according to the diagram shown in Figure 8-2.

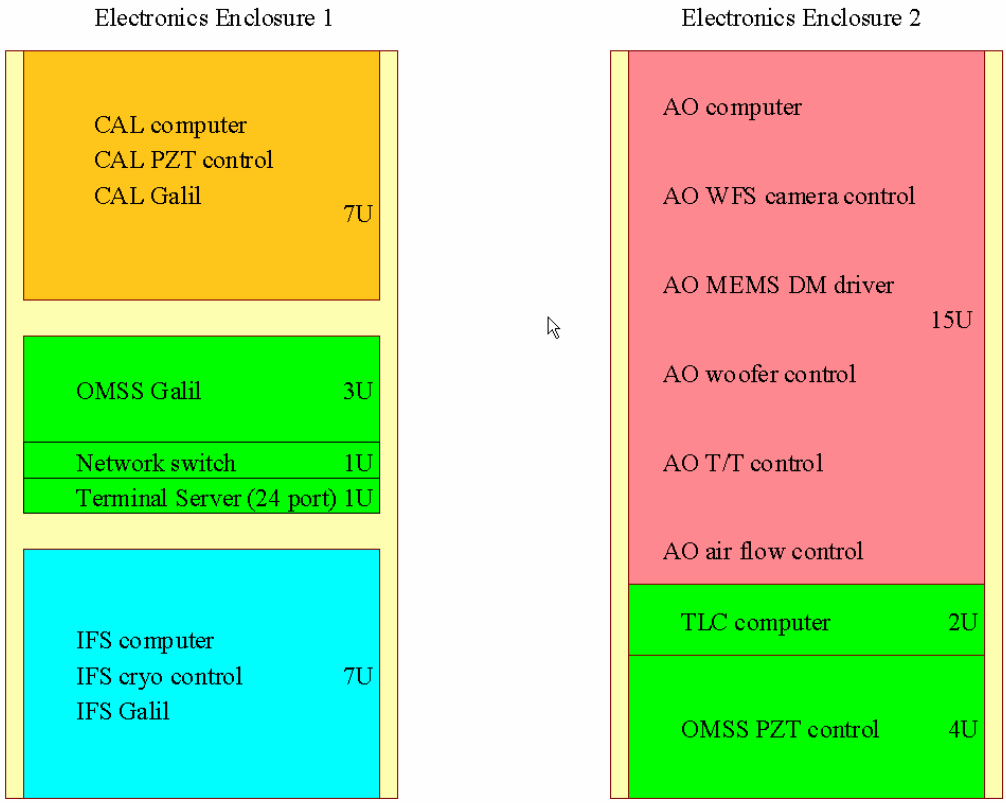

Figure 8-2 Thermal cabinets space allocation – orange, blue, red and green marked space given to CAL, IFS, AO and OMSS contributions with the U sizes as indicated

The details of space allocations are formally spelled out in the ICD documents on CAL, IFS and AO to OMSS interfaces, Appendices 2.10 to 2.14.

8.1.3.2 Bulkhead panel allocation

Bulkhead panels of both thermal enclosures and OMSS will be subdivided into smaller separate panels that will be supplied to the IFS and CAL teams for populating with connectors and feedthroughs. Used during sub-system integration and testing, these sub-panels will be the same ones used in the final integration of GPI. The exact sizing and layout of the sub-panels will be determined prior to CDR.

8.1.4 Cabling scheme

A typical cable connecting a control circuit inside the electronics enclosure with a sensor or actuator inside the optics enclosure must cross the bulkheads of the two enclosures. It is required that the bulkhead crossing for all the cables be done via mated connectors, one mounted in the bulkhead, the other at the end of the cable. Generally the connector that supplies electrical power should be of a female gender (sockets) and the connector for power receiver should be male (pins). A typical cable run is shown in Figure 8-3. The figure is also exemplifying cable and connector numbering conventions

from 8.1.1.3. Alternatively a bulkhead pass-though adapter can be mounted in the panel, allowing coupling the male and female ends of the cables to its two sides.

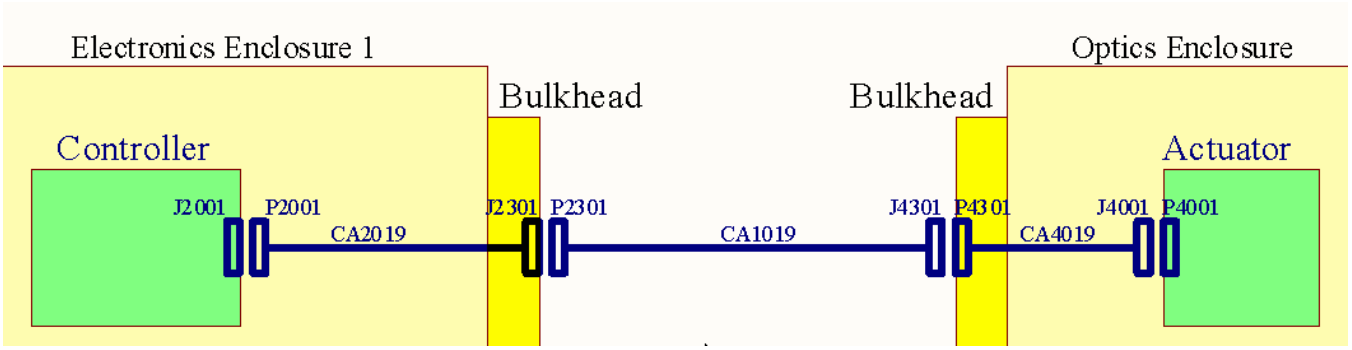

Figure 8-3 A typical cable run between the controller box inside EE1, and actuator inside the OE. Note the female-male (J-P) connector couplings through bulkheads and at signal source and load.

Since connector reliability and ruggedness is of utmost importance, the MIL connectors will be used to make the majority of interconnects between the EE1, EE2 and OE.

Wherever possible the signals destined to separate sensors or actuators in the OE will be combined in multi-conductor cables with multi-pin connectors and thus reduce the number of cables between the EE1, EE2 and OE bulkheads.

8.2 Computers and networks

GPI relies for its computing needs on general purpose Intel architecture based computers running linux. GPI computers have been tentatively selected based on the following criteria:

- computational power (type of CPU and number of CPU cores, amount of RAM)
- expandability (number and type of expansion slots: PCI, PCI-X, PCI-E of various widths)
- form factor – must be 19" rack compatible
- ruggedness and altitude/temperature hardening
- Commonality; as few different models as possible.

8.2.1 TLC and IFS

The IFS and TLC computers have very similar hardware requirements. The Augmentix A+ 1950 is a ruggedized industrial computer based on the standard production Dell model 1950 and has a form factor of a 2U case compatible with 19" rack. (Appendix 8.20) Its operating altitude and temperature meet the requirements of both Gemini South and North. The A+1950 features 2 PCI-X slots that will host the Reflective Memory and Time Bus cards. A low power model with a single dual core 3.73 GHz Xenon draws an average power of 244 W.

8.2.2 AOC and CAL

The AOC requires as much computational power as available in a 4U seized package, it must also have at a minimum 8 expansion slots. A ruggedized computer of this class has not been identified therefore a high end server from one of the major suppliers is a baseline. (HP ProLiant DL580 – see Appendix 8.21). The 26.7" front-to-back size of this server exceeds the depth of thermal enclosures reserved for electronics packages and as such restricts the airflow inside the cabinets. A special arrangement will be required to accommodate this depth with the server box mounted at the top end of the rack to minimize the effect of airflow obstruction. For detailed requirements of the AOC and CAL computers see Chapters 3 and 6.

8.2.3 Network equipment

One managed network switch, a Cisco Catalyst 2960 (Appendix 8.22), connect the network nodes of GPI to the Gemini Data and Control LANs and an internal, GPI LAN. The terminal server, a Perle CS 9000 (Appendix 8.7) with 24 serial ports, connects all electronic devices requiring RS-232 link with the TLC and optionally with the outside world via Gemini gateways.

8.3 CAL, IFS and AO subsystems

The details that go beyond the Top Level Block Diagram overview of 8.1.2 are described in the respective chapters of the CAL module (Chapter 6), the IFS (Chapter 5) and the AO system (Chapter 3).

8.4 OMSS mechanisms

All mechanisms of the OMSS, CAL and IFS are summarized in the mechanisms table in (Appendix 2.28) These mechanisms comprise several different types of actuators. The subsections below present electronic control circuits that drive these actuators.

8.4.1 Galil controllers

The Galil DMS-2183 8-channel motion controller (Appendix 8.8) have been proposed in CoDR [2] as suitable for controlling servo and stepper motor mechanisms of GPI. Following the CoDR two examples of DMS-2183 have been acquired and underwent extensive testing in the HIA electronics lab. The tests validated fully the choice and subsequently a suite of support software has already been developed for use in GPI (see Chapter 9)

8.4.1.1 Servo-motors

The OMSS mechanisms will utilize 15 servo-motors equipped with position encoders and will be controlled by 3 Galil controllers. The Maxon A-max 22, a 3.5W motor (Appendix 8.12) has been chosen to power all 15 OMSS servo axes. Since each motor requires a maximum continuous power of 3.5W the 4 channel linear amplifier module Galil AMP-20341 (Appendix 8.11), which is capable of delivering

20W power per channel, is adequate to run all GPI servo-motor axes. The OMSS will utilize 5 of these modules to control 15 axes with 5 amplifier outputs designated as spares. The baseline for the CAL subassembly will be to use the same arrangement.

8.4.1.2 Stepper motors

The IFS subassembly will use 5 stepper motors specially prepared for vacuum operation at cryo-temperatures. Motion control will be performed by a single Galil 2183 equipped with 2 stepper motor output modules, Galil SDM-20240 (Appendix 8.11). See IFS documentation for details (Chapter 5).

8.4.1.3 Extended IO

The optional mezzanine card Galil DB-28040 (Appendix 8.11) provides 8 analog inputs and 40 programmable digital IO. The 40 bits are functionally divided into 8-bit banks that are programmed as whole either for input or output function. A version -5V of this card has open collector outputs instead of standard TTL and in this version only the first 3 banks can be configured as outputs and the remaining banks can only function as inputs. In the OMSS Galil box a DB-28040-5V will be installed on one of the Galils primarily for communication with the GIS interface circuits but also to trigger the bi-stable shutter and to turn on and off the calibration sources.

8.4.2 PZT stages and controllers

Both OMSS and CAL subsystems incorporate piezoelectric actuators based on led zirconate titanate ceramics (*Plumbum* Zirconate Titanate – PZT). These actuators require drive signals of 0-150V and present themselves to driver amplifier as capacitive loads, usually 1-20μF, depending on the actuator size. The PZT actuators are subject to hysteresis and displacement drift with time and for accurate and repeatable positioning must be driven by a servo circuit with a position feedback. Typically the feedback signal is generated by resistive strain gauges affixed to the actuators. Capacitive sensors may also be used to generate the position feedback signal.

The OMSS incorporates 5 PZT tip/tilt mounts for GPI optical components. Based on the required displacements the selection was made to use the mounts produced by Mad City Labs (MDL). MDL uses a proprietary strain gauge feedback system combining the gauge resistor bridge with a solid state preamplifier on a single chip mechanically fixed to the PZT actuator. Because of this unique feedback system the MDL mounts must be used with MDL's own servo-controllers.

The PZT stages of the CAL subsystem utilize conventional strain gauge position sensors and will by driven by the JPL custom servo-controllers. There is a goal during CDR to utilize these same controllers for the OMSS stages. See CAL documentation for details (Chapter 6).

8.4.3 Bi-stable shutters

The OMSS subsystem incorporates one shutter – a bi-stable version of a Uniblitz NS45. A bi-stable shutter has an advantage of not requiring power to hold in either the open or closed state – thus not

producing any heat plumes inside the OE. Typically the shutter state is flipped to the opposite by a short pulse of a few tens of volts. A ready made controller by Uniblitz is big, bulky and unnecessarily complicated for GPI which doesn't require the microsecond precision of shutter timing. Therefore a custom built shutter trigger circuit will be incorporated in the OMSS custom electronics enclosure.

The CAL subsystem also comprises a pair bi-stable shutters and it is expected that a common approach to controlling the shutters will emerge in cooperation with JPL during the CDR phase.

8.5 Calibration light sources

GPI optical systems require 3 calibration light sources: a broadband white-light, and visible and IR lasers. These sources will illuminate 5um pinholes through optical fibers and will be deployable in the Gemini focal plane.

8.5.1 Broadband tungsten halogen source

This source, in R band, shall produce a variable flux rate equivalent to a range of 5^{th} to 10^{th} magnitude The same source must also produce flux from 0.7 to 2.3 microns. The flux variation at the science wavelengths isn't stringent. These requirements will be met with an incandescent light source driven by a variable voltage power supply. By decreasing the supply voltage an arbitrary attenuation of the light will be accomplished (Appendix 8.13). A tungsten halogen light source, Ocean Optics HL-2000 has been selected as adequately bright at the maximum. A programmable power supply with an RS-232 serial interface will be used to vary the filament temperature and the resulting photon flux by a computer command as required. The source HL-2000 produces significant amount of heat (6W) and will be housed in the thermal cabinet EE1 while the light will be brought to the optical bench of OMSS by a multi-mode fiber using FC fiber connectors to cross the EE1 and OMSS bulkheads.

8.5.2 VIS laser

The VIS source will be a red laser with a wavelength of 670nm, bright enough to visually trace the beam through the optical path in GPI. A panel mounted 1mW 670nm laser diode, Edmund Optics M56-943 (Appendix 8.18), with a fiber receptacle will serve that purpose. The diode will be mounted in the back panel of the OMSS Galil box and the broadband fiber will bring the light through the bulkheads into the optical bench. The diode will be driven by a small driver board (Edmund Optics 56-805) mounted inside the OMSS Galil box and supplied from the 5V power supply.

8.5.3 IR laser

The IR source has been tentatively selected as the Edmund Optics M56-116, a 1mW 1550 nm laser diode. This source is within the requirement of 1.58 +/- 0.3 microns. The IR laser diode will also be mounted in the OMSS Galil box and driven by a second driver board (Edmund Optics 56-805). We will look during CDR for a source that meets the goal of 1.58 +/- 0.1 microns.

8.5.4 Laser safety

The VIS laser at 1mW is a class II device, “Emits in the visible region. It is presumed that the human blink reflex will be sufficient to prevent damaging exposure”.

The IR source is also a 1mW laser but doesn’t have the benefit of safety by the blink reflex; therefore it is a class IIIA device [4] . It may be necessary to include the supply of power to IR source in the GIS interlock system that will prevent the operation IR source when any of the GPI doors are open. The safety issue will be fully developed during the CDR phase.

8.6 OMSS custom electronics

It was decided from the start that as many components as possible would be procured as off-the-shelf commercial components, compatible with the 19” instrumentation racks, utilizing industry standard interconnect cables and communication interfaces and powered by the 120V AC outlet power.

There are two components of GPI to be fully custom designed and fabricated from individual electronic parts: the GIS interface and the shutter trigger circuit. The commercial sub-assemblies that are customized for GPI are also described in this section. These sub-assemblies will be purchased as fully assembled circuit boards and will be installed in a custom enclosure, supplied with appropriate DC voltages. The design details for interconnects and custom cables are presented in the following sections.

Because of the space limitations in the thermal cabinets it has been decided that all custom electronics of OMSS will be housed in a single 3U case jointly referred to as the OMSS Galil Box, and be powered from a common power supply included in the enclosure. Combining these electronics in a single component package has a side benefit of reducing the number of interconnects between the components. For instance the GIS electronics board will use the Galil board for its digital IO and the interconnect cables will be contained within the 3U case. See Appendix 8.5 for the overall block diagram of the OMSS Galil Box.

8.6.1 GIS interface

The purpose of Gemini Interlock System and the requirements for the instrument side GIS are detailed in the Gemini ICD 1.1.13/1.9 [6]

GPI implementation of the instrument side GIS interface described here is based on two similar interfaces previously developed at HIA and incorporated in the GMOS and ALTAIR.

These earlier systems were designed to communicate directly with a parallel port within the VME chassis. For consistencies sake, the decision was made to utilize instead the extended digital I/O capabilities of the Galil DMC-2183 provided by the DB-28040 mezzanine card (8.4.1.3).

8.6.1.1 Signals and logic

The observatory side GIS connects to the instrument GIS with a GIS cable: 4 twisted pairs #22AWG shielded cable (Belden 8304) terminated with MS3120-F12-10P/F connectors (10 contacts). The pins are assigned GIS signals according to Table 8-4 which repeats pin naming conventions of ICD 1.9/3.6 (Appendix 2.16).

Pin (* twisted Pairs)	GIS signal	GPI GIS node
A	Cable Shield	GND
B *	+5 VDC	PLUS5
C *	Event TTL1 (high)	ilcke
* D	+5 VDC GND	PLUS5RET
* E	Event TTL2 (low)	/ilcke
F *	+5 VDC	PLUS5
G *	Demand TTL1 (high)	ilckd
* H	+5 VDC	PLUS5
* J	Demand TTL2 (low)	/ilckd
K	NC	

Table 8-3 GIS signal assignment to MS3120-F12-10P pins and GPI schematic node names

There are 2 signals carried over the GIS cable: the Event signal originates in the instrument GIS and is received by the observatory side GIS, and the Demand originates in the observatory side and is received by the instrument. Both these signals are carried as complementary pairs of signals at high and low TTL logic levels. Both the Demand and Event have voltages referenced to the observatory side GIS circuits and are relayed to the instrument side GIS circuits by opto-isolators. The GIS cable provides the observatory side 5V power and ground to supply the instrument side opto-isolator sender. The loss of complementarity of both Demand and Event (the TTL1 and TTL2 simultaneously high or low) will generate an error and set the motor shutdown.

The instrument side GIS circuits monitor the condition of interlock switches placed at all enclosure doors. The GIS Event signal is generated when any of the switches are flipped to the ‘open’ side. In addition to door switches the system will also include manually operated switch (shutdown paddle) for quickly shutting down motors when the instrument operator or service person decides the immediate shutdown of GPI mechanisms and Gemini motors is necessary. In addition to interlock switches and manually operated shutdown paddle the GPI GIS circuit will also monitor the health of the control computer software and hardware which will be based on a 1Hz watchdog timer pulse (‘wdpulse’) outputted by the control software running on TLC. The disappearance of ‘wdpulse’ will trigger GPI motor shutdown and generate the GIS Demand.

The reliability of GIS circuits is of utmost importance, and to assure robustness it will be based on simple discrete logic rather than a microprocessor circuit. This choice eliminates the possibility of a software hang-up of the GPI GIS. Following the GMOS and ALTAIR design the discrete logic of GIS will be based on Programmable Logic Devices (PLD). The interlock switches will be of a ‘double throw’ variety: each switch outputting two signals. With this arrangement opening a door flips one

signal from high to low, the other from low to high. Having both these signals at the same level indicates an error. The use of complementary pair signals from door switches precludes the possibility of a disconnected or shorted switch being interpreted as normal condition.

8.6.1.2 GPI GIS schematic

The complete GPI GIS interface schematic is attached in Appendix 8.6. The interface employs two PLD devices to perform the logic operations that otherwise would have to be performed by 10-20 TTL chips. Functional blocks cut out of the overall schematic are discussed in this section.

First such a block processes the complementary signals from switches. The logic is implemented in the first PLD: the Atmel AT22LV10-20PC in a 24pin DIP housing (Figure 8-4). The complementary signals from the switches are driven by the 10k pull-up resistors (Bourn 10pin SIP) which are selectively shorted to ground by the double-throw interlock switches. The complementary nodes in the diagram are labeled as 'ditlk_' and '/ditlk_' with the slash '/' preceding the label to denote the 'NOT' logical operation.

All in all 7 door switch inputs are provided: 2 for EE1, 2 for EE2 and remaining 3 for doors and hatches of the OE.

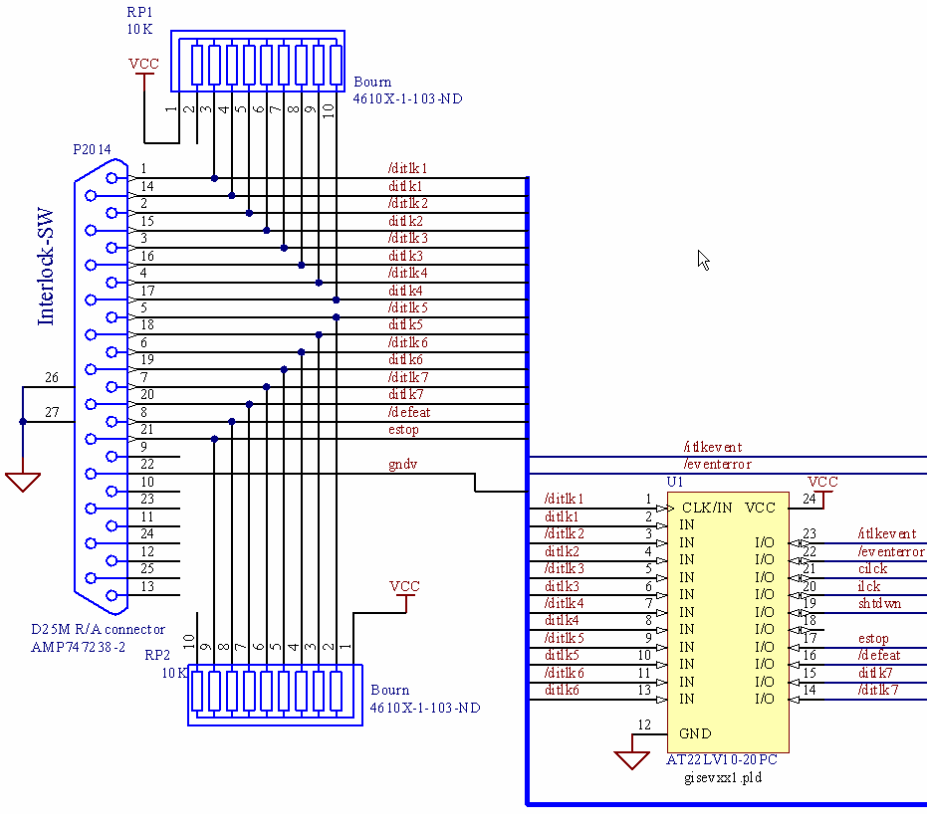

Figure 8-4 GIS interlock switch input circuits

Five output signals are generated in response to the state of the door interlock switches 'ditlk_' and the manual switch 'estop': '/itlkevent', '/eventerror', 'click', '/click', 'shtdwn'. The complementary pair 'click'-'/click' is passed on to the opto-isolator and is outputted to the observatory side GIS as a Demand signal. The '/itlkevent', '/eventerror' outputs drive the indicator LEDs to show the occurrence of events and errors. These signals are also passed along to the second PLD circuit shown in Figure 8-5.

The second PLD device labeled in the schematic as U4 is Atmel ATF16LV8C in a 20 pin DIP housing. The circuit block shown in Figure 8-5 performs 3 separate functions. First it executes motor shutdown based on the condition of the GIS demand lines and the outputs from the door switch PLD. The shutdown signal is generated according to the formula given in Figure 8-5. Second function is to de-bounce the interlock switches – essentially to ignore short lasting transients in the logic circuits. This function is performed by a gate with hysteresis U3B and a low pass RC circuit with a time constant 10us formed by the R6 and C11. Third function programmed into the PLD is driving the shutdown and demand error LEDs with inverted signals 'shutdown' and 'demanderror'. The 'shutdown' signal is connected to the 'abort' input of all Galil controllers. The 3 OMSS Galils have their 'abort' inputs wired directly to the interlock board with short jumper wires and the CAL and IFS Galils receive the 'shutdown' through 4-pin MIL connectors in their individual enclosures.

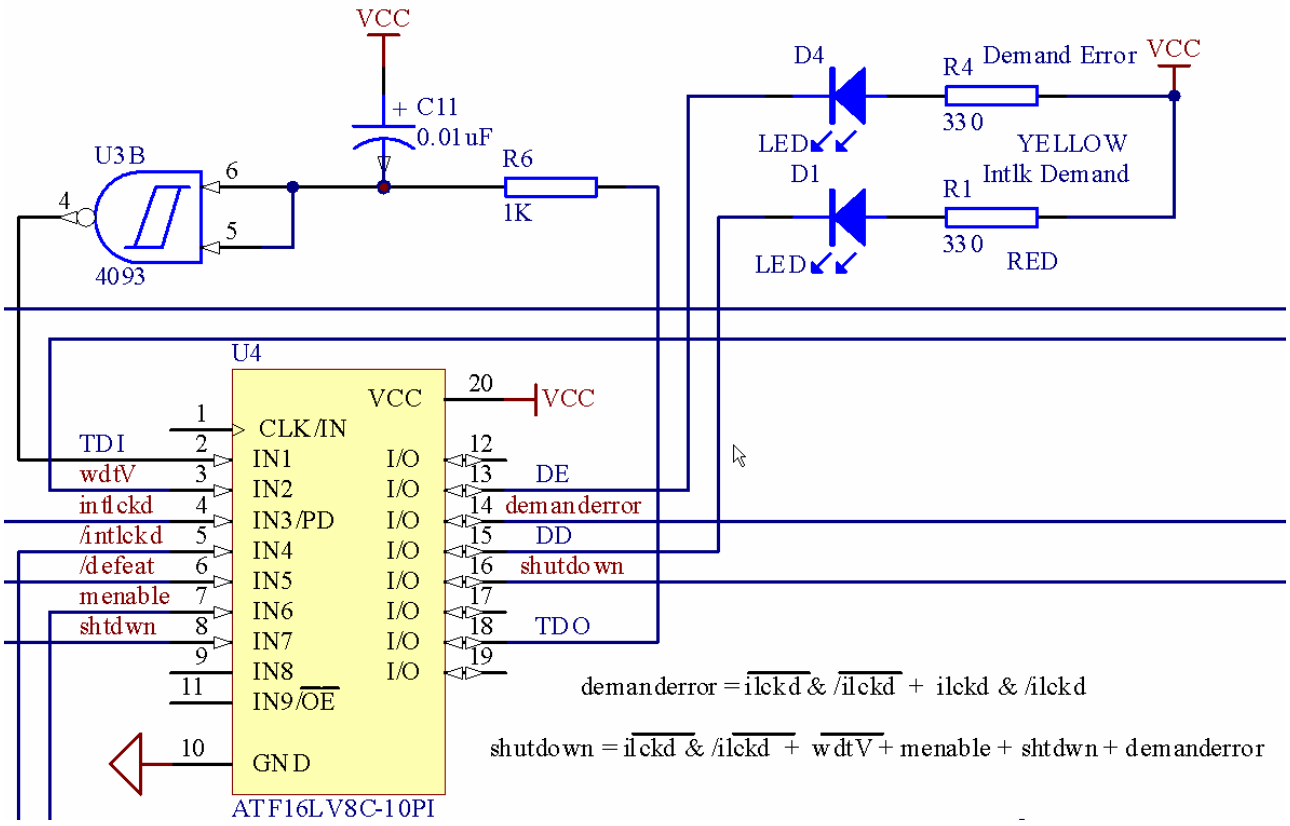

Figure 8-5 GIS output and switch debounce logic

The interface of GIS to the Galil extended IO is shown in Figure 8-6. The input banks 5 and 6 monitor the status of interlock switches 1-7, the manual shutdown paddle signal 'estop' and several signals generated by the GIS, as labeled in the figure.

Bank 2 is configured as output and drives to GIS signals: the ‘wdpulse’ is the watchdog timer signal; a 1 Hz square wave generated by the control software of the TLC, and the ‘menable’ is the enable signal from the TLC that must be ‘high’ to allow motors to run.

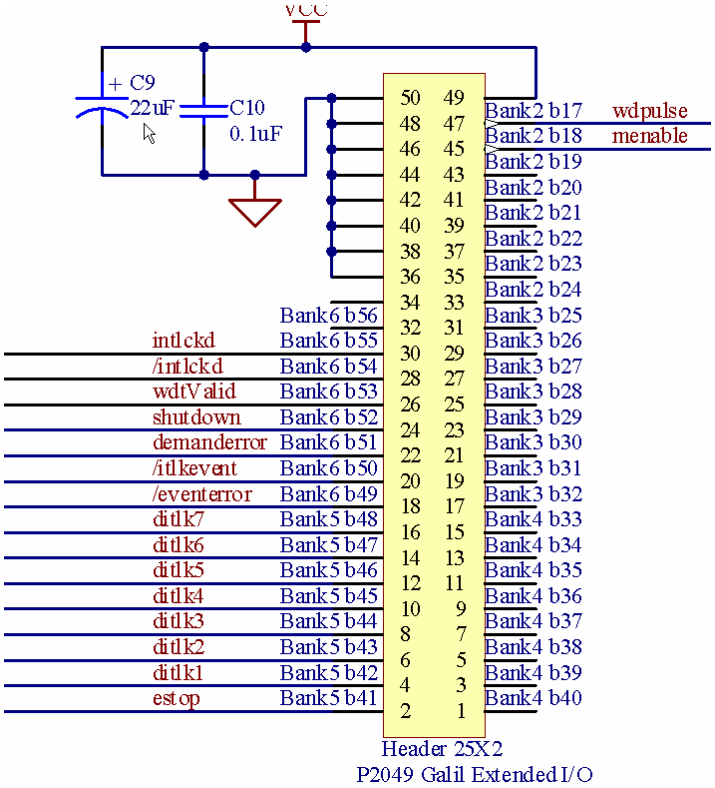

Figure 8-6 GIS interface to the Galil extended IO.

The circuit for monitoring the presence of watchdog timer 1Hz square wave ‘wdtpulse’ is shown in Figure 8-7. The gate U3A buffers and normalizes the signal to GIS TTL levels. The square wave is rectified into DC by a circuit made of C8, CR1 and CR2 and charges up the capacitor C7. At the same time the capacitor is discharged by the 3.3M R7 resistor and the input of a CMOS D flip-flop U2A. Since the CMOS load is small comparable with R7 the time constant for the discharge is on the order of 3s. When driven with the 1Hz ‘wdtpulse’ the output of the flip-flop ‘wdtValid’ is high. This output goes low when the watchdog pulse disappears for longer than 2 cycles which in turn generates the GIS Event and causes GPI motor shutdown. The green LED is on when the watchdog pulse is present, and goes off when the pulse stops.

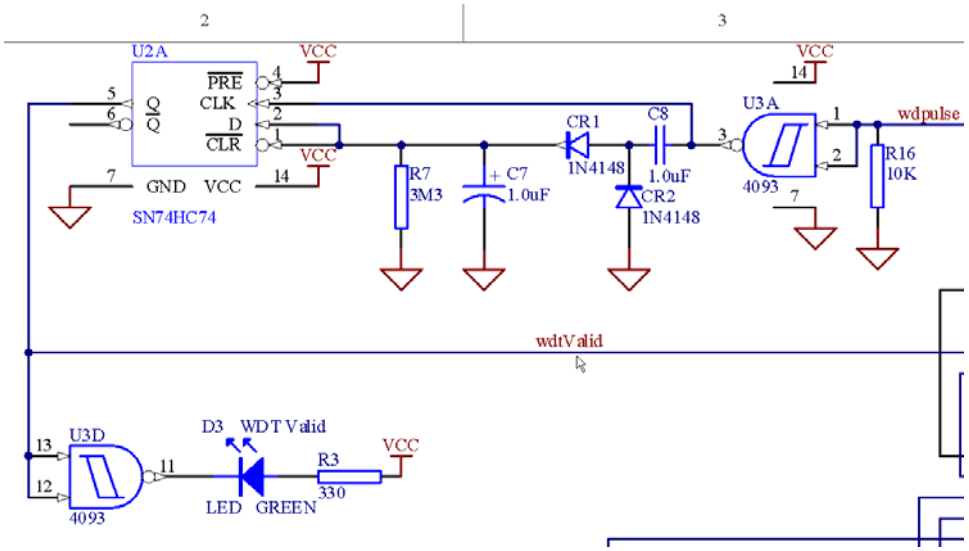

Figure 8-7 GIS diagram – the watchdog timer circuit

The opto-isolator part of the diagram serves the purpose of interfacing the observatory GIS circuits with the OMSS GIS circuits without introducing ground loops and interference as required by the GIS ICD. Two dual opto-isolators are employed U5 and U6. The U5 which handles the demand signal 'ilckd' is supplied with 5V power of GPI and is referenced to GPI ground GND. The U6 transmits the OMSS signal 'ilcke' and is supplied with power and ground by the observatory GIS circuits.

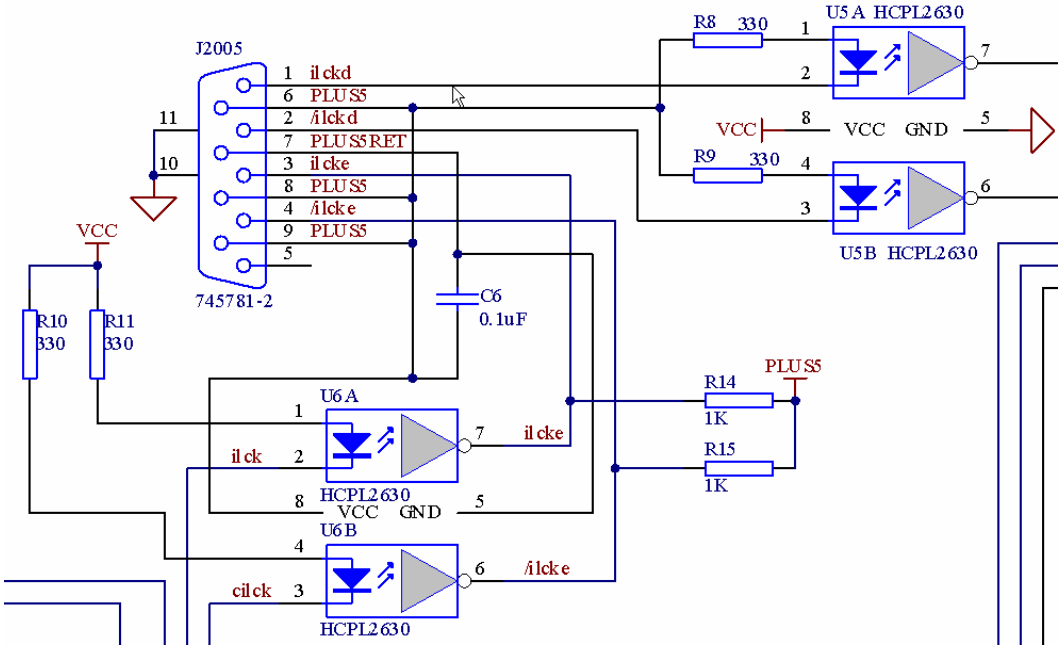

Figure 8-8 GIS interface opto-isolators

8.6.1.3 GPI GIS printed circuit board

The GIS printed circuit board has been laid out to fit in the available space in the OMSS Galil box (Figure 8-14). The design uses a 2 sided printed circuit without internal layers which is easy to fabricate and inexpensive to order prototypes. The board will be mounted on stand-offs behind the front panel with the GIS status indicator LEDs protruding through holes in the front panel as shown in Figure 8-14.

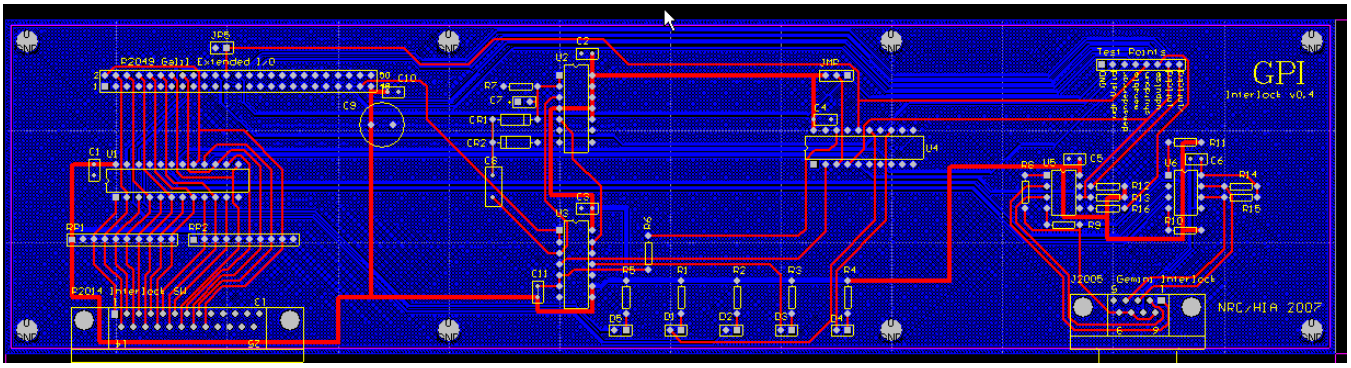

Figure 8-9 GPI GIS printed circuit board

8.6.2 Servo-motor cable design

The OMSS mechanisms include 15 DC servo-motors with encoder feedback. Each mechanism employing a servo-motor is also equipped with a home switch, the forward and reverse soft limit switches that communicate the end of allowable travel to the Galil controller, and the forward and reverse hard limit switches that prevent further motion even if motor power continues to be supplied by the controller. Temperature of the motor is continually monitored with a 1-Wire temperature sensor affixed to motor's body. All the components are wired together as shown in Figure 8-10.

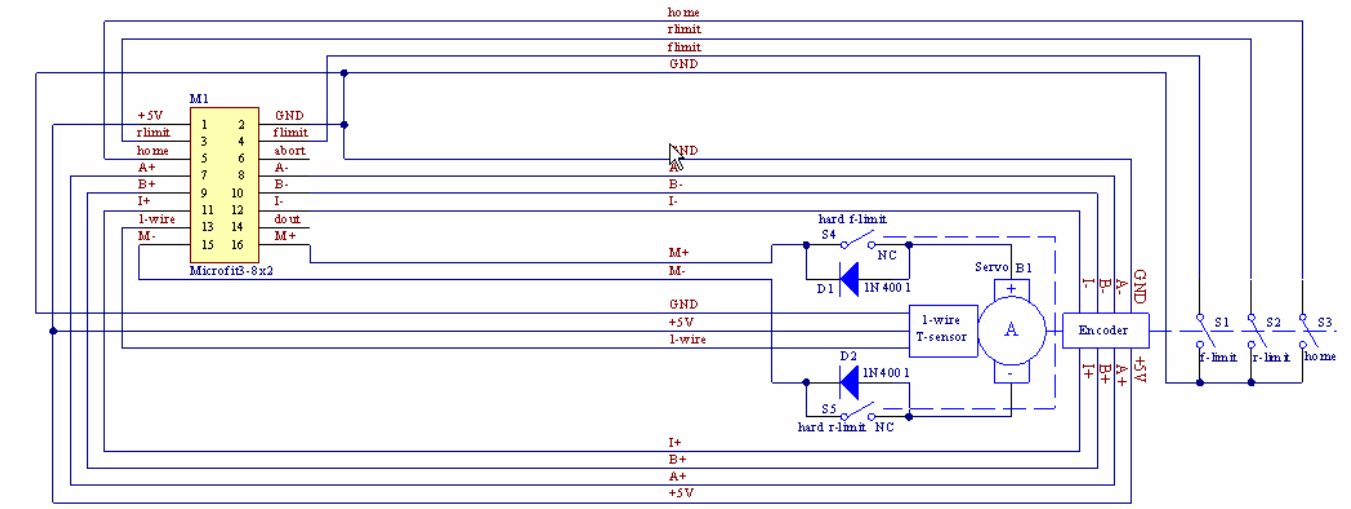

Figure 8-10 Schematic of wiring of the OMSS servo-motor stage

The hard limit switches S4 and S4 have by-pass diodes that allow reverse motion after the forward motion has been disabled by the switch.

The encoder is mechanically coupled to the motor shaft and is supplied with the 5V power to generate 3 signals, A, B and I. The A and B signals are square waves in quadrature, generated at 500 cycles per turn and the index I is a single square pulse per turn. These signals are outputted as pre-amplified balanced line signals A+ A-, B+ B-, I+ I- and are compatible with the Galil controller encoder inputs. To minimize the cross-talk and interference the balanced signals will be carried by shielded twisted pair wires. The 1-Wire temperature sensor Dallas DS-1820 (described closer in 8.7.2.1) is a TO-92 device that requires 3 signals, GND, +5V and 1-Wire. The GND and +5V are common with the encoder. All 14 wires connecting the servo-motor, encoder and switches are combined in a 16 position connector, Molex MicroFit3-8x2. Two contacts of this connector not used by the stage devices are wired to the general purpose IO port of the Galil. The 'dout' is a single TTL level output line, and the 'abort' is a TTL input line of the Galil that is internally configured to trigger a selective abort for the particular axis.

The MicroFit connector will either be mechanically fixed to the stage frame or will be on a short pigtail. Pin assignments of the servo-stage MicroFit connector are summarized in Table 8-1.

1	+5V	9	B+
2	GND	10	B-
3	rlimit	11	I+
4	flimit	12	I-
5	home	13	1-Wire
6	abort	14	dout
7	A+	15	M-
8	A-	16	M+

Table 8-4 List of signals connected to the OMSS servo-stage

8.6.2.1 Combining servo-axes into multi-conductor cables

In the Galil controller the channels are organized into 2 banks of 4 outputs, each bank served by a single amplifier having a common supply voltage and reference ground. It emerges as a natural choice to combine the unique axis signals with the signals common to 4 axes in one multi-conductor cable. In Table 8-4 there are 3 signals that can be made common for the 4 axes: +5V, GND and 1-Wire. The remaining 13 signals are unique; therefore a 55 conductor cable is needed to make a connection to 4 axes. A proper multi-conductor cable should include twisted pair wires in individual shields to ensure no cross-talk between the encoder lines of different axes.

A snippet of block diagram (Appendix 8.14) in Figure 8-1 shows combining Galil servo-channels in groups of 4 into multi-conductor cables according to the scheme outlined above.

The Belden 8773 is a 27 shielded pair 22AWG cable that is suitable for carrying GPI servo-motor signals. For the quick disconnects of the 55 conductor cable (27 pairs + shield) there is a choice of two MIL-spec connector families: either the Amphenol MIL-DTL-38999/22-55 or Amphenol MIL-C-

2648222-55, which both share the same pin insert layout and both are available for printed circuit mounting (Appendix 8.16). The 38999 series has been selected tentatively as the baseline for PDR. Since the MIL connector families 38999 and 26482 have similar characteristics the final selection of the connector family will be made based on the availability of mounting accessories in both families when the detailed design of bulkheads is finalized in the CDR phase.

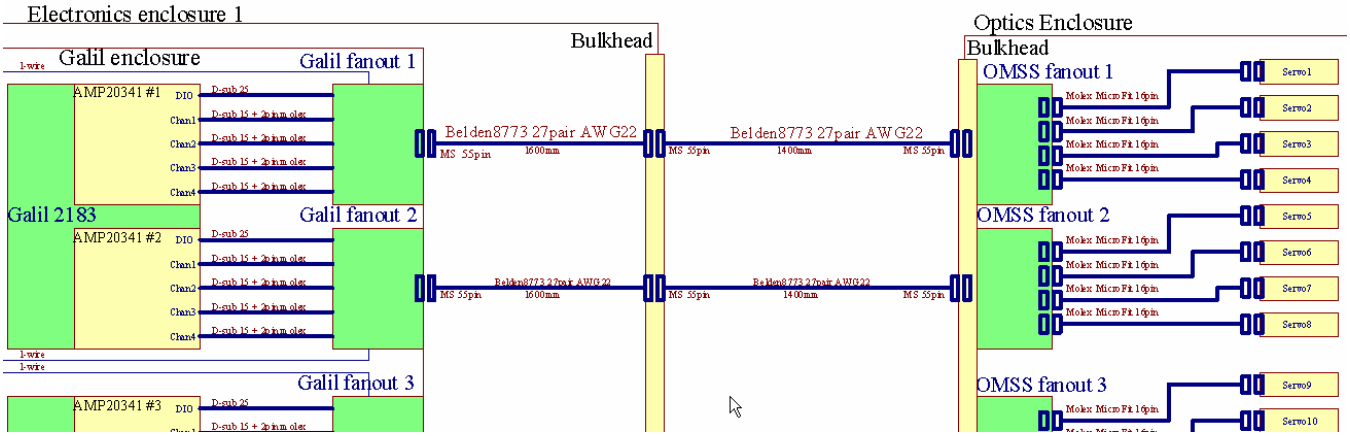

Figure 8-11 Block diagram of OMSS servo-motor cabling (fragment)

Note: having the 1-Wire temperature sensors attached to motors has a secondary diagnostic purpose of supplying a digital ID of the motor to which it is fixed. Since the 1-wire signal is carried along the servo signals in the same cable the presence of a given temperature sensor on the 1-Wire bus also indicates that the whole chain of connectors from the Galil box to the servo stage is connected through.

8.6.2.2 Fanout boards

The number of Galil outputs that must be wired into the 55pin MIL connectors to realize the scheme outlined above (20 axes wired into 5 55pin connectors - 275 wires altogether) justifies the design and fabrication of dedicated printed circuit boards as an alternative to manually wiring each pin.

The fanout board for the Galil box (Figure 8-12) has been designed to use 14-pin header connectors to connect to the encoder inputs of Galil AMP-20341 amplifiers. Separate 2-pin Molex connectors connect the M+/- motor power. The short jumper cables from the amplifiers to fanout boards will be fabricated with minimum effort using 14-wire ribbon cable and crimp-on connectors at both ends. The fanout board also connects with a 2-pin header to the 1-Wire bus master.

The board has been designed using 2 sides for connections and no internal layers so that it can be fabricated inexpensively. An effort has been made in the pin assignment of MIL-38999-55 to use adjacent pins to carry complementary bipolar signals and to run the traces carrying these signals close to each other – to minimize the cross-talk.

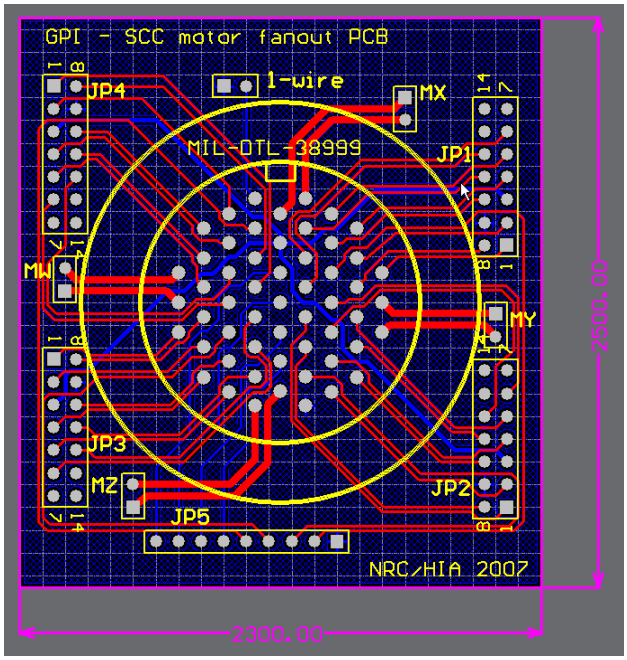

Figure 8-12 Galil controller fanout printed circuit board

The fanout board for the OE bulkhead has been designed similarly, except the 16-pin MicroFit connectors have been used for the servo-stage connection with the pinout given in Figure 8-10. The fanout board combines the motor drive power with the encoder signals and the 1-Wire bus in a single MicroFit connector. The board also includes an electrolytic capacitor for decoupling the 5V supply of the encoders and provides a 3-pin 1-Wire bus connector for additional temperature and humidity sensors.

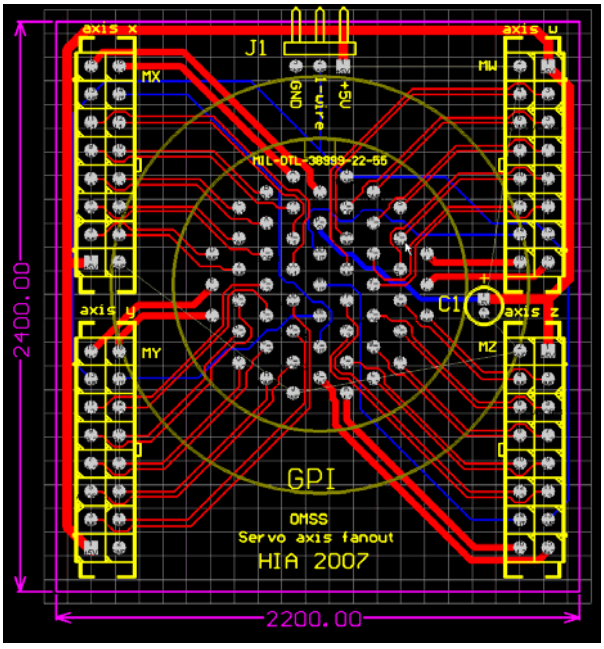

Figure 8-13 Optical Enclosure servo-motor fanout board

8.6.3 OMSS Galil box

The OMSS Galil box provides the housing for 3 Galil DMC-2183 motion controllers and their mezzanine amplifiers and extended IO boards, the Ethernet 1-Wire bus master, the GIS interface circuits, the VIS and IR calibration lasers and their support circuits, the shutter control circuits and the power supply to supply all circuits with multiple DC voltages. Having to put several independent electronics subsystems into a single enclosure was dictated by the space shortage in the thermal cabinets EE1 and EE2 but it also simplifies the connection of Galil extended IO signals to their destination in the GIS interface, the laser suppliers and the shutter control. See the overall block diagram of the Galil box in Appendix 8.5.

8.6.3.1 Power supply

The Galil DMC-2183 motion controller requires 3 voltages as summarized in Table 8-5.

+5V	1.1A
+12V	40mA
-12V	40mA

Table 8-5 Power supply requirements of a Galil DMC-2183

The Galil AMP-20341 linear amplifiers require separate bipolar power source of +/-12-30V DC depending on the required voltage of the motors it drives. The 3.5W Maxon A-max 22 DC motors (Appendix 8.12) selected for the OMSS stages require 0-12V therefore the linear amplifiers can be driven from the same bipolar +/-12V source that drives the controller.

The combined power draw as given in Table 8-5 for 3 Galil controllers is 20W. Total output power required to run 15 servo-stages each at the rated power 3.5W: 52W. Assuming a 50% efficiency of the AMP-20341 amplifiers the required capacity of a power supply is 120W. Starting out with these requirements and applying safety margins a selection was made to use the ASTEC LPQ250, a 250 Watt switcher power supply (Appendix 8.15).

8.6.3.2 OMSS Galil box layout

A 3U height rack enclosure, Schroff 10828-054, has been mechanically designed to hold the 3 Galil controllers of the OMSS, the GIS interface card, 5 fanout boards and a power distribution board which will also contain circuitry required by the bi-stable shutter. Figure 8-14 shows the placement of components inside the Schroff enclosure and the front and back panels with all the connectors. The drawing omits the ribbon cables that will carry signals between the components inside the enclosure.

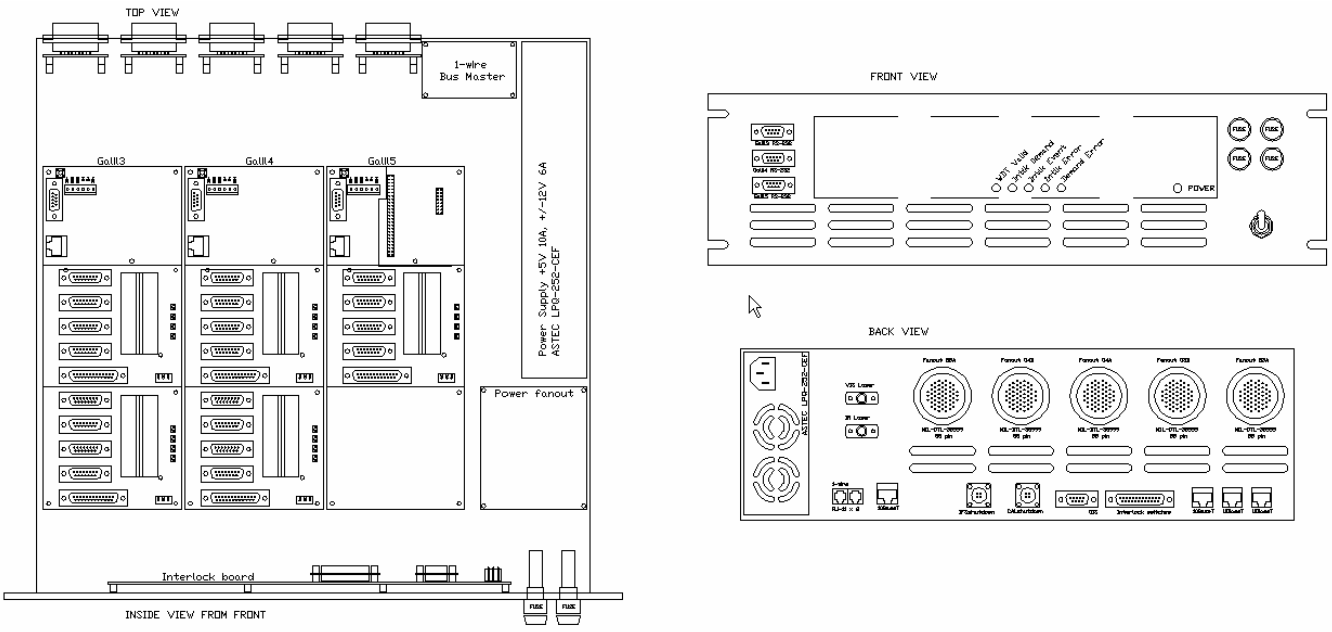

Figure 8-14 OMSS Galil Box component layout. The slots for air circulation in the front and back panels are nominal. The actual size and number of the slots will be determined through mechanical analysis of the air flow in thermal cabinets.

8.6.3.3 1-Wire bus master

The 1-Wire bus master provides an interface between the sensors attached to the bus and the outside world. A USB based bus master has been experimentally evaluated with samples of sensors intended for use in GPI. It has been found that the USB interface is somewhat difficult to handle under linux because of a scarcity of linux drivers and compatibility issues arising with different linux distributions and kernel releases. To avoid these problems an Ethernet based bus master has been selected to handle the sensors of GPI.

The Embedded Data Systems HA7Net (Appendix 8.17) is accessed as a network node and supports a variety of communications protocols including HTTP, HTTPS, Telnet, Multicast, DHCP and SNTP. In a most straight forward setup the HA7Net is seen in the LAN as a web server with the data from 1-Wire sensors presented in web pages. The HA7Net bus master (Figure 8-15) will be installed inside the OMSS Galil box with appropriate cut-outs in the back panel to allow access to 10BaseT LAN interface and two 1-Wire RJ-11 outlets. The HA7Ne will draw 12VDC power from the ASTEC power supply.

Figure 8-15 Ethernet 1-Wire bus master

8.6.3.4 GIS interface

The printed circuit board described in 8.6.1.3 will be mounted behind the front panel of the Galil box as shown in Figure 8-14 with the GIS status LEDs visible through appropriate openings in the panel. It will connect with ribbon jumper cables to the Galil extended IO card and with a multi-wire cable to the door switch connector in the back panel.

8.6.3.5 Bi-stable shutter control

A small printed circuit board with the shutter control circuit will be designed in the CDR phase. It will fit in the available space in the OMSS Galil box and will be supplied with DC power from the 12V supply of the ASTEC power supply.

8.6.3.6 Laser diode control

Two laser diode driver boards, from Edmund Optics, each approximately a 60mm square (Appendix 8.19) will be mounted in the available space in the OMSS Galil box. Both boards will be supplied from the 12V DC output of the ASTEC power supply.

8.7 Environment monitoring

The purpose of 1-Wire sensor network in GPI is to have monitoring available for temperature and relative humidity in various parts of the electronics cabinets and optics enclosure. The reading from environment sensors can also be logged by the TLC. In addition for keeping sensor reading records for the off-line performance analysis and troubleshooting of GPI operation, the TLC will issue warnings if certain high temperature threshold is approached inside a thermal cabinet and will shut down the power to all components if a danger threshold is crossed.

8.7.1 1-Wire bus

The 1-Wire bus (Appendix 8.23) is a minimalist networking system designed by Dallas Semiconductor for connecting instrumentation into a low cost, slow data rate network. This network, often referred to as MicroLAN consists of a bus master and a number of slave nodes connected with a single signal line and

a signal return ground. Because of low data speeds the wave propagation effects don't show at connections that span distances of a few hundred meters, the sensors can be connected in every possible way that preserves the electrical continuity of the signal wire and its return. Examples of typical topologies are shown in Figure 8-16.

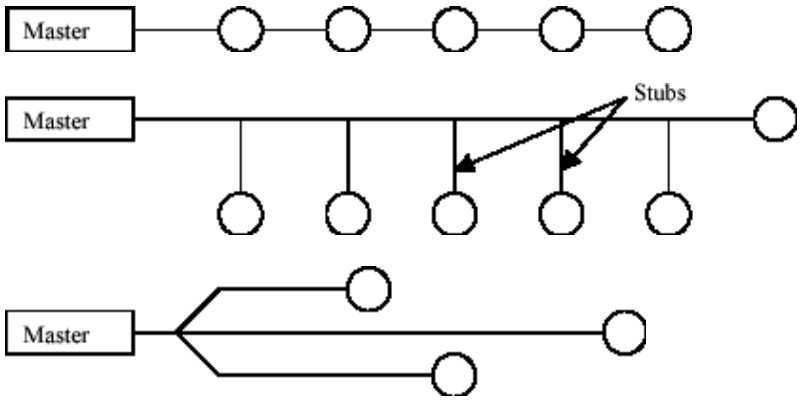

Figure 8-16 Examples of 1-Wire network topologies

All communication in MicroLAN is initiated by the Master and the slave nodes only respond to specific queries of the Master. This scheme of communication is only possible because of all 1-Wire devices having unique 64 bit ID numbers encoded in them in the semiconductor production line. On the power-up the Master performs the enumeration of nodes during which all 1-Wire devices connected to the MicroLAN are detected and their ID numbers are identified and stored in Master's registers.

In the practical use of a 1-Wire sensor network the low level details of data communication to slave devices are hidden from the user or the client program which communicates with the 1-Wire Master through either parallel port, RS-232 or USB. Each of these connections requires specific drivers to run on the client computer to reduce the data acquisition and control of 1-Wire devices to simple ASCII commands and ASCII encoded data streams. Alternatively the 1-Wire master can be based on a microcontroller that is set up as a Web server connected to a TCP/IP LAN. This type of 1-Wire Master has been selected for GPI, as described in 8.6.3.3.

An important parameter for the 1-Wire bus is the combined length of the bus. The bus length consists of the physical length of all the MicroLAN branches and the equivalent length of sensors attached to it. The sensors on average contribute 0.5m length per sensor. The combined length of the bus according to manufacturer's recommendations should never be more than 750m.

8.7.2 Sensors

8.7.2.1 Temperature

The Dallas DS1820 1-Wire temperature sensor (Appendix 8.24) measures temperatures from –55C to +125C with a +/-0.5C accuracy. The sensor is available in a TO-92 transistor-like housing. Several samples of DS1820 have been evaluated experimentally at HIA and have proven to produce accurate temperature readings without glitches or measurement errors. The DS1820 can be connected either as a

2 terminal device that runs on parasitic power drawn from the 1-Wire data line or a 3 terminal device with the 3rd pin connected to a 5V power line. The parasitic mode of operation limits the number of temperature sensors that can be simultaneously on the bus and it will not be used in GPI. Instead the +5V power will be brought together with ground and 1-Wire signal to all sensor locations. The DS-1820 sensors will be placed in several locations in EE1 EE2 and in OE for air temperature monitoring. The DS-1820 sensors will be also used to monitor the temperature of glycol lines, one incoming and one outgoing in both EE1 and EE2 and for that will be clamped to the glycol pipes. Additionally the DS-1820 sensors will be used to provide a digital ID and to monitor the temperature of all servo-motors, as described in 8.6.2.

8.7.2.2 Humidity

The Honeywell HIS-4000 humidity sensor is a 3 pin device that converts relative air humidity into voltage. 3 samples of HIS-4000 have been experimentally evaluated in HIA electronics lab with a 1-Wire 4channel A/D chip Dallas DS2450. The tests were successful and the same combination of HIS-4000 and DS2450 will also be used to monitor relative humidity inside the EE1, EE2 and OE.

8.7.2.3 Voltage

The Dallas DS2450 (Appendix 8.25) is a quad A/D converter in a small 8-pin SOIC housing. It requires +5V power supply in addition to 1-Wire line (cannot run parasitically). It has a user programmable voltage range of either 2.56V or 5.12V and a resolution from 8 to 16 bits. A DS2450 mounted on a printed circuit board and connected with appropriate voltage dividers will be used to monitor the power supply voltages +5V and +/-12V in the OMSS Galil box (8.6.3.1).

8.7.2.4 Sensors table

There will be at least 20 1-Wire sensors in GPI as listed in Table 8-6. The combined equivalent network length of these sensors is 10m which is insignificant in comparison to 750 m MicroLAN limit. Additional sensors may considered in the CDR phase for monitoring the temperature of other components potentially contributing heat to OE, such as cameras or warm ends of cryocooler heads.

location	parameter	sensor	number
EE1	Air temperatures	DS1820	4
EE1	Glycol in/out temperature	DS1820	2
EE2	Air temperatures	DS1820	4
EE2	Glycol in/out temperature	DS1820	2
OE	Air temperature	DS1820	4
EE1	Humidity	DS2450 + HIS-4000	1
EE2	Humidity	DS2450 + HIS-4000	1

OE	Humidity	DS2450 + HIS-4000	1
Galil box	Voltages	DS2450	1

Table 8-6 GPI 1-Wire sensors

8.8 Electrical/Electronics Risk Mitigation

8.8.1 Observatory environment

The electronic components of GPI will be exposed to harsh environment of the observatory as described in Gemini ICD-0013 [5] . These conditions will be taken into account in the procurement of GPI parts. Diminished cooling efficiency by air circulation in the rarefied atmosphere at the 4500m attitude will be factored in by selecting higher power rating of components than required at the sea level. In the custom electronics MIL versions of components will be used to allow for below 0deg C temperatures. The ruggedized (altitude and temperature hardened) components will be sought from the manufacturers of the off-the-shelf components. The air temperature and humidity will be monitored by the sensors network and GPI operation will be shut down after crossing thresholds for the critical temperatures and humidity. The relevant thresholds will be determined during the CDR phase.

8.8.2 Equipment grounding and preventing cross-talk

Grounding within the instrument consists of two main areas, shielding of signals and eliminating ground loops. The shielding of signals requires that all signals that may radiate noise into other circuits or circuits sensitive to such noise be contained within a Faraday cage. This is accomplished by enclosing the circuit inside a metal box or, in the case of signal cables, ensuring that all of the conductors within a cable are covered by a grounded shield. It is important to ensure that the shielding of a cable is continuous along the entire length of the cable as well as continuing through the connector.

Ground loops can cause currents to flow in unanticipated paths through circuits. The usual way to minimize or alleviate these currents is to make certain that all grounds are referenced from the same point. This is most readily accomplished by consistently tying all grounds to one point within a chassis.

The grounding methods and principles outlined in the Gemini Electronic Design Specification [3] will be followed in the detailed electrical design of the CDR phase and in the subsequent phases of implementation and integration of all systems.

8.8.3 Early acquisition and testing of component samples

The commercial components that nominally satisfy the GPI requirements, such as the ASTEC power supply or the HE7Net 1-Wire bus master will be procured and experimentally evaluated for stability of operation and electrical interference with other components, prior to the CDR. Alternative components will be sought if the performance is not satisfactory.

8.9 Top Level Electronics References

[2] "ExAOC Conceptual Design Review Document"

[3] Garry Sedun "Electronic Design Specification" Gemini SPE-ASA-G0008 (23.02.1994)

[4] U.S. Department of Labor Occupational Safety & Health Administration – "OSHA Technical Manual" *http://www.osha.gov/dts/osta/otm/otm_iii/otm_iii_6.html#4*

[5] ICD-G0013 Gemini Environmental Requirements.pdf

[6] ICD-1.1.13/1.9 Interlock System to Science Instruments ICD, Gemini Observatory

9 Control Software

9.1 Control Software Summary

The control software will realize the functionality of GPI. GPI's relationship to other Gemini systems can be seen in Figure 9-1. GPI will receive all commands from the Observatory Control System (OCS) and provide status back via the Gemini Instrument API (GIAPI).

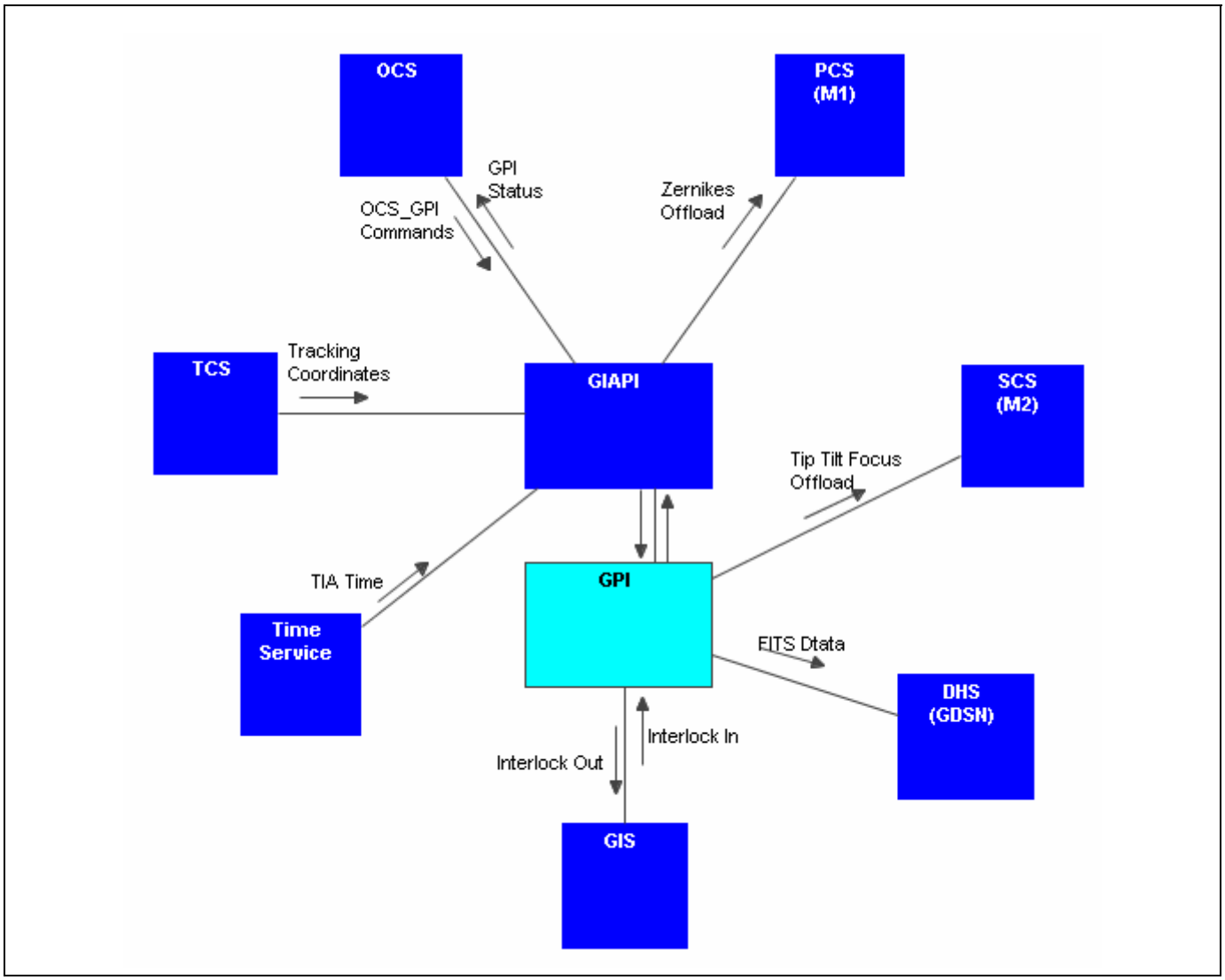

Figure 9-1 - GPI Interactions

The Telescope Control System (TCS) will provide tracking coordinates as well as a World Coordinate Service that enables GPI to fulfill the requirements for making World Coordinate System data available for headers.

The Gemini Interlock System (GIS) will provide an interlock demand as a way of locking out GPI systems and the GPI will provide an interlock event to the GIS.

GPI will offload Zernikes to the Primary Control System (PCS).

GPI will also offload tip, tilt and focus demands to the Secondary Control System (SCS) via the Syncro Bus.

GPI writes datasets to a mounted file system and then notifies the Gemini Data Storage Network (GDSN).

Time is available though the Time Service.

The top level of GPI software decomposition is based on GPI's major instrument subsystems. The GPI control software has four separate controlling subsystems. The software for each of those four subsystems is being developed at different sites.

1. TLC – Top Level Computer and the Acceptance Test and Engineering User Interface or ATEUI (developed at HIA)
2. CAL – Calibration Computer (developed at JPL)
3. AOC – Adaptive Optics Computer (developed at LLNL)
4. IFS – Integral Field Spectrograph (developed at UCLA)

Note that the GIAPI will be provided by Gemini but will physically exist on the GPI computers. The Gemini side of the GIAPI interface - known as the Gemini Master Process (GMP) - will be on the TLC. The GPI side of the GIAPI (a smaller Glue API) is required for each computer that communicates with the GMP. The TLC will handle all but the SynchroBus access service which will be done by the AOC.

9.1.1.1 Physical Interfaces

Physical interfaces will be utilized for the following purposes:

GPI Internal interfaces:

- Dedicated virtual LAN – to issue inter-subsystem commands (using RPC calls) and to communicate with motion control hardware and other Ethernet-enabled devices
- Reflective memory – to publish global inter-subsystem data
- Dedicated device electronics – to communicate between subsystems (including the TLC) and non-Ethernet devices

External interfaces:

- Gemini Control LAN – for command and status transfer between the OCS and the TLC
- Gemini Data LAN – for data transfer between the subsystems and the DHS

- Gemini Synchro Bus – for communication between the AOC and the TCS, for secondary mirror control
- Gemini Timebus – to get the current time to the TLC (if performance is adequate, a software NTP system will be used)
- Gemini Interlock System (GIS) – to send and receive interlock demands

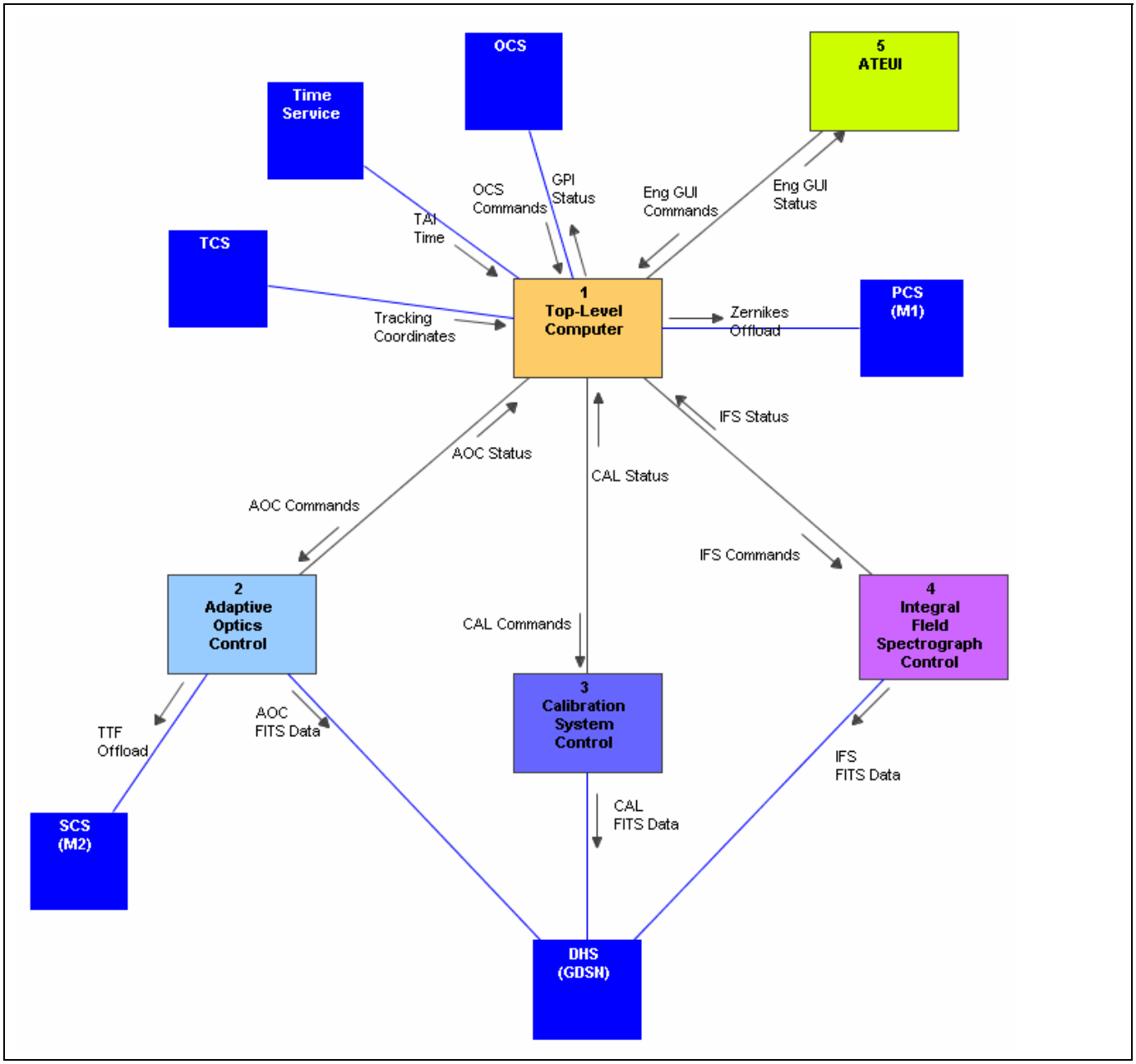

Figure 9-2 - GPI Main Context Diagram

Figure 9-2 shows the main context diagram for GPI. Each of the major subsystems use separate computers, which provides several benefits:

- The software on each subsystem can be developed, run and tested independently.
- Interactions between subsystems are controlled by the definition of explicit inter-computer interfaces. Resource contention between systems is reduced since each system has its own resources such as CPU, memory, and disks.
- The software for each subsystem is developed at a single partner institute that is generally where the mechanical parts will be developed. This means that as the mechanisms are being developed and assembled parts of the system can be tested.

9.1.1.2 Device Control

The decision was made early that there should common software to control the devices in GPI. That list of devices can be found in Table 9-1, which gives a description of the device, and sub-axis, the source of the targets and number of axis it affects. The motion control is handled by a single software bundle that is part of the TLC, but the source of the targets can be from another subsystem.

The devices not controlled by the common software are the mechanisms that have more strict real-time performance requirements, such as:

- The deformable mirrors and tip/tilt stage (controlled by AOC)
- All CCDs (each is controlled by individual subsystems, AOC/CAL/IFS)
- The fine/fast Phase Shifting stage (controlled by CAL)
- Cryostat controllers (each is controlled by individual subsystems, IFS/CAL)

HIA will provide a working Motion Control layer for the AOC/CAL/IFS, including:

- Linux Motion Control Daemon (MCD) which uses Galil's Linux DMC library
- Configuration file examples
- MCD user manual
- Fully functional generic 8-channel GUI

Description	Sub-axis	Source of Targets	# axis
OMSS			
Input Shutter	Shutter	TLC	1
ADC	Prism rotation	TCS/TLC	1
	Prism separation		1
	Deploy		1
Artificial source unit	X	TLC	1
	Y		1
	DM/pupil mask linear stage	TLC	1

Fold Mirror		AOC/TLC	2
Pupil plane mask (apodizer)	select wheel	TLC	1
	cell rotation		1
CAL calibration source	X (& deploy)	CAL/TLC	1
	Y		1
Focal plane mask (occulter)	select wheel	TLC	1
Polarization modulator	deploy	TLC	1
	modulation angle wheel		1
CAL-IFS P&C	P&C M1	TLC	2
	P&C M2		2
WFS	P&C M1	AOC/TLC	2
	P&C M2		2
	P&C Focus		1
	Spatial filter	TLC	1
	Filter selector	TLC	1
IFS			
Pupil viewer/polarizer	deploy	TLC	1
Filter mechanism	select wheel	TLC	1
Undisperser/ polarizer	linear	TLC	1
Lyot mask	select wheel	TLC	1
CAL			
Shutters	reference arm	TLC	1
	science arm	TLC	1
filter selector	Select wheel	TLC	1
spatial filter	Adjustable size square hole	TLC	1
coarse stage	Coarse phase shifting linear stage	CAL/TLC	1
Illumination Sources			
Artifical Star Unit	broadband	TLC	
	IR Laser		
	VIS Laser		
CAL	Cal calibrator	CAL/TLC	
TBD			
CAL	Lens translate	CAL/TLC	2
	SF select stage	TLC	1
	SF T/T mirror	CAL/TLC	2
OMSS	ADC If prisms on separate rotational stages		1
	If prisms on separate deploy stages		1

Table 9-1 - List of Devices that are Controlled Through the MCDs

9.1.2 System Design

The command structure for GPI is hierarchical. This means that a command coming into GPI is received by the TLC and that single command can translate into one or many commands within GPI. The top level commands are detailed in the TLC and Gemini ICD [3] .

Due to the distributed nature of the GPI development team as well as a desire to keep subsystems as autonomous as possible to simplify design and maintenance, all subsystems (including the TLC) should need to 'know' as little as possible about the other subsystems. For example, subsystems will use knowledge of their hardware to process their raw data into shareable data in agreed upon units. Subsystems will not process data to accommodate another subsystem's hardware; the second subsystem wi.. do that.

The role of each of the autonomous systems is show in Figure 9-3. As shown in the diagram, one connection between them all is the Global Memory Block (GMB), which is where a subsystem publishes data required by other subsystems.

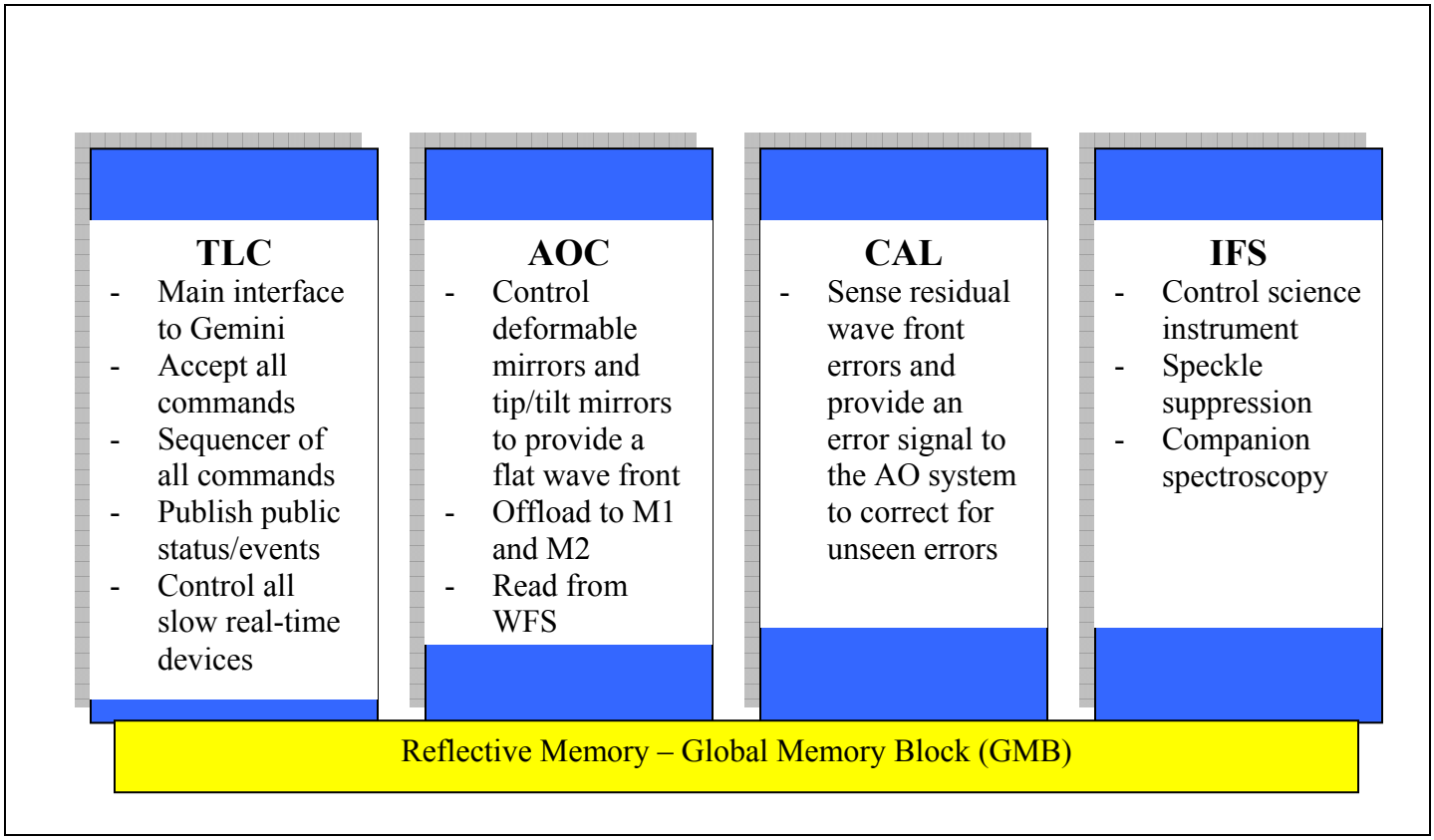

Figure 9-3 - Role of Computers

9.1.2.1 TLC Layout

The design of TLC is broken up into six primary entities (see Figure 9-4),

- the Instrument Sequencer (IS) – sequencer of GPI
- Components Controller (CC) – management of all slow real-time devices,
- Status Server (SS) – to allow subscription to status within GPI
- Subsystem SubServers (SUB) – handle the passing on and interface to subsystems (AOC/IFS/CAL)
- Acceptance Test and Engineering User Interface (ATEUI) – engineering GUI
- Command Event Handler (CEH) – interface to the GIAPI. Passes commands on to the Instrument Sequencer and report status back.

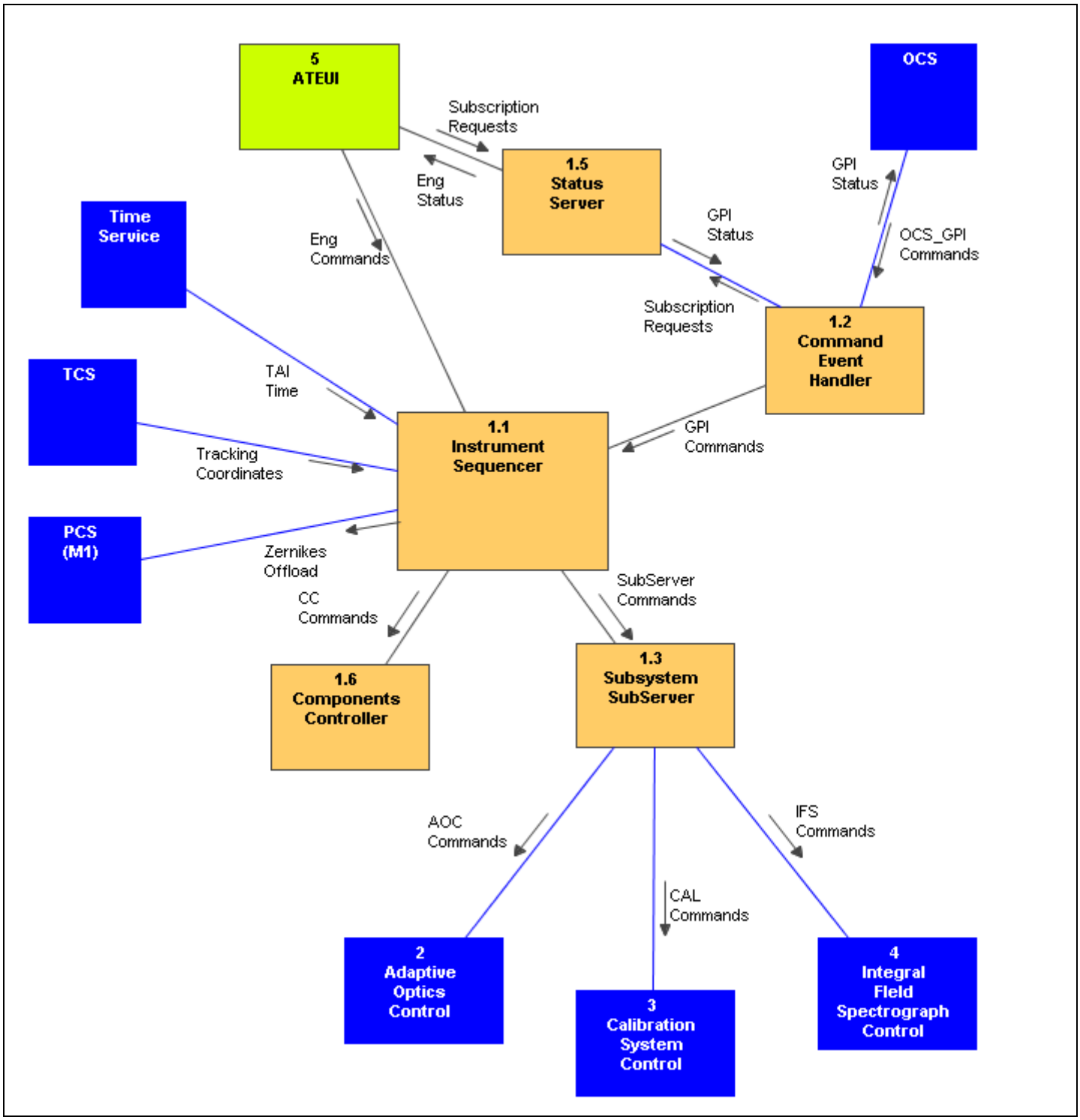

Figure 9-4 - GPI TLC Context Diagram

9.1.2.2 GPI Software Responsibilities

The major responsibilities of the GPI software are listed in Table 9-2

Responsibility	Component to handle the responsibility
Accept and respond to commands from GIAPI	The Command Event Handler will accept commands from the GIAPI, and then pass them on to the Instrument Sequencer.
Perform any sequencing required including passing on commands to other subsystems within GPI	The Instrument Sequencer is responsible for determining if the command can reasonably be started and will sequence the parts required to complete the command
Assume a commanded configuration within a reasonable amount of time	The Instrument Sequencer will direct this functionality.
Respond to sequence commands in a way that is appropriate for GPI	The Instrument Sequencer will take the sequence command and distribute to all subsystems. Each subsystem will handle the sequence commands that are relevant to GPI.
Provide up-to-date status of GPI.	The Status Server will provide up-to-date status to anyone who subscribes to the system. The Command Event Handler will report that status to Gemini via the GIAPI
Provide the software to move all slow real-time requirement motors	The Components Controller will provide those functions at both an assembly and device layer interface.
Provide the basis for the engineering GUI	The Acceptance Test and Engineering User Interface will be used.
Provide access to GPI commands without using the GIAPI	The Instrument Sequencer command set will be a superset of those provided as part of the GIAPI interface. All commands from the GIAPI are passed directly to the Instrument Sequencer

Handle alarm status	The Status Server will check and indicate alarm status.
Handle health status	Each individual subsystem will have its own health designation along with its own heartbeat. The Status Server will combine those health values into a single overall GPI health

Table 9-2 - GPI Major Responsibilities

Accepting of the GPI commands in broad strokes is shown in Figure 9-5.

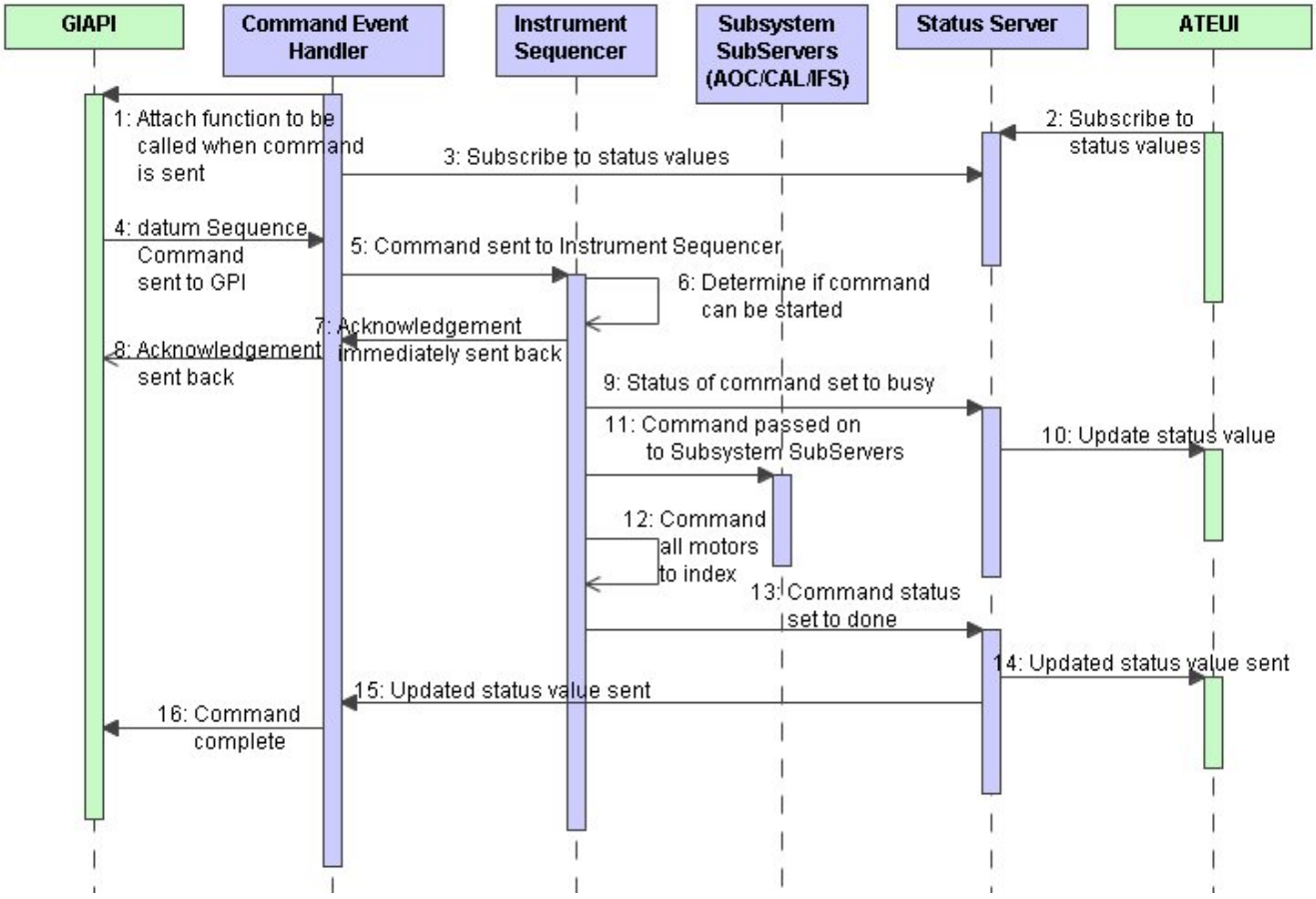

Figure 9-5 - GPI Accepting Commands

The Command Event Handler upon startup will use GIAPI methods to attach functions to be called when a command is received and it will subscribe to status from the Status Server that must be reported to Gemini. The Gemini OCS will issue a command to GPI via the GIAPI. In this example it is a "datum" sequence command. The command is passed on to the Instrument Sequencer to determine if

the command can start, and then an acknowledgement is sent back to the GIAPI that the command has started. The Instrument Sequencer will send a command to all Assemblies to index their motors, and it will also tell the Subsystem SubServers that they should do what is appropriate for the index. When everything is done, the status for that sequence command will be updated on the Status Server. Since the Command Event Handler subscribed to the data sequence command status item, it will be informed when that status changes, whether that be to indicate it is IDLE again or reached an ERROR. At that point the command completion is returned to Gemini via the GIAPI.

9.1.2.3 Design Considerations

Software reuse is a powerful method of reducing overall software costs and increasing software quality. In order to increase the potential for software it is important to design the system with reuse in mind. One example of code reuse in GPI is in the use of RPC (Remote Procedure Call) functions. GPI will be composed of a number of independent software programs that interact with each other using RPC mechanisms. This approach was successfully used in Altair.

Remote procedure calls can be sent to an RPC server on either the same computer as the calling program or a different computer. This allows the same mechanism and basic code to be used for all inter-process commands.

GPI software will be developed at several different locations. It is important to design for this distributed development team to function efficiently. This will require distributed source code control.

There are a number of standards, practices, and functions that can be common for all subsystems. Agreeing to those early on provides clear benefits by:

- reducing duplication of effort
- providing a support system to developers using the same environment
- reducing the integration effort
- delivering a unified system

In order to facilitate system integration and system maintenance, a common computing environment will be chosen and used by each of the development teams.

GPI will work independently, and have common software used throughout. The individual subsystems will need to be tested independently.

The experience to utilize a traditional EPICS based system is in-house at HIA, but the new Gemini Instrument API has many benefits to the distributed GPI team, the vast majority of which have no EPICS experience.

Each subsystem will do their software development at their site, and will be expected to provide software releases at regular intervals. This falls in line with the Gemini philosophy where agile development asserts that the software should be first built as a simple working system, with features added at each release.

9.1.2.4 Architectural Strategies

The GPI control system will use four Linux x86 based computers. The use of Linux on the commodity x86 architecture allows for lower cost hardware and software and follows the recommendations of the Aspen guidelines. In order to enable more efficient use of the computer systems and to avoid memory limitations the GPI computers will use 64-bit Linux rather than 32-bit Linux.

The GPI software system is composed of many separate processes rather than one large monolithic executable per computer. This modularity allows for easier integration of parts at partner sites and for simplified final integration, testing and debugging. The use of multiple processes also allows efficient use of today's multiple core machines.

All slow devices are controlled through the TLC using common code.

Design decisions:

- A global status server to deal with communication with the GUIs and GIAPI.
- Commands are transferred via RPC protocol.
- Reuse of some of Altair's software and design.
- Using C++ for the bulk of the (non-library) work, and Java for ATEUI graphical interface. Exceptions are the AOC, which will be using C for speed issues, and CAL system will be using JAVA.
- Using C for common library routines.
- Everyone will use the same reporting, debug, and simulation levels.

9.1.2.5 Instrument Interface

External communication between GPI and other systems can only occur via one of the following methods:

1. Gemini systems communicate with GPI using the Gemini Instrument API (GIAPI).

2. GPI sends Zernike values to the Primary Control System via the GIAPI. GPI sends Tip/Tilt/Focus values to the Secondary Control System by writing to the Synchrobus.

3. For testing purposes, a workstation can run the ATEUI (Acceptance Test and Engineering User Interface) client that uses RPC calls to send commands to GPI. The ATEUI client can also subscribe to status items so that the GPI can send a stream of values to the client.

One of the outputs from GPI is the science dataset. The data will be collected, unscrambled, and written by the IFS software to a FITS file format. The header will contain information on the current configuration of the instrument, such as filters used, state of polarization, etc. Completion of the gathering of data is indicated by a change in status in the GMB. This will trigger the TLC to send an event to Gemini via the GIAPI.

GPI's status is communicated to Gemini via the GIAPI. A list of that status is described in [3] .

It is necessary that Gemini deliver the GIAPI during the critical design phase of GPI. This will ensure that the design proposed for the Command Event Handler (CEH) will meet the interface proposed. It is critical that the GIAPI be delivered on time. Our reliance on software external to our system makes it a risk area for us. This risk will be mitigated by having a single command interface (the CEH) with the GIAPI. Also, the Instrument Sequencer will be designed to accept the same commands directly - while the GIAPI/CEH interface is not fully functional or for test purposes.

In order to make sure that GPI has a smooth integration at the telescope, all interfaces to GPI must be available as simulators well in advance. GPI has plans to have an agile development cycle where we are delivering features to Gemini as they because available. A proposed schedule of these features is given in Section 9.1.10.

9.1.2.6 Inter-instrument communications

All communication between GPI processes will occur via one of the following methods:

1. Remote procedure calls allow a process to execute calling functions on another (or the same) computer.

2. The GPI Global Memory Block contains data that is available to all GPI computers. Each data item within the GMB is written by only one of the computers but can be read by any of the computers.

3. If two processes on the same computer need to exchange data then Unix Shared Memory can be used. UNIX shared memory is faster than the reflective memory used in the GMB since shared memory is accessed as regular RAM. The use of Unix shared memory also restricts access to the memory to only those processes on the computer containing the shared memory. The UNIX shared memory on the TLC computer is referred to as the TLC Shared Memory.

9.1.2.7 Common Library Functions

In order to reduce the amount of duplicate effort expended on common programming tasks, a library of commonly used functions will be developed. The use of this library will reduce development and maintenance costs, and increase the quality of the delivered GPI software. A short list of some of the software that will be included in the library is as follows:

- Common RPC client and server code

- Routines to allocate/release and connect/disconnect to the Global Memory Block

- Routines to manipulate UNIX shared memory: allocate/release, connect/disconnect, lock/unlock.

- System debugging (logging) functions.

- FITS library (CFITSIO)

9.1.3 System Decomposition

As previously stated, the TLC is broken up into six primary entities (see Figure 9-4). Each of the primary entities is, in turn, composed of a hierarchical structure of sub-entities. The following will give more detail on the functionality of the components.

The Instrument Sequencer (IS) provides a high level entry into GPI that will perform the general sequencing of commands. Every command that is available external to GPI is available at this interface along with additional commands for testing and debugging purposes.

The Command Event Handler (CEH) is the handler for commands and status outside GPI. This will be the main interface with the GIAPI. There is no processing done at this level it simply passes the command along to the IS.

The Components Controller (CC) is composed of Assembly SubServers which are logical groupings of motion controllers, sensors, or commands. The Assembly SubServers have knowledge about how the logical grouping of motion controllers and sensors work together. Control of the motion controllers and sensors is through the Motion Control Daemons (MCDs). The Assembly SubServers will communicate with the appropriate MCDs, which control the slow real-time devices in GPI and deal with lower level information about the mechanisms (for example, number of steps per unit). Assembly SubServers and MCDs are all part of the TLC work package. The Assembly SubServers accept commands from the IS and the ATEUI.

The Subsystem SubServers (SUB) receive commands from the IS and pass them on to the various subsystems (AOC, CAL, IFS). Details on the interface between the SUB and subsystems are detailed in their respective ICDs (see Table 9-5). The subsystems software is used to control the fast real-time components and complex processing functionality of the AOC, IFS, and CAL subsystems; the functionality of the subsystems is detailed in their respective chapters. The SUBs provide the communication and interface for command receipt and then pass the commands on to the subsystems.

Both the Assemblies and SUBs use the SubServer general library. This allows the common functions like the communication interface to be written once and used multiple times.

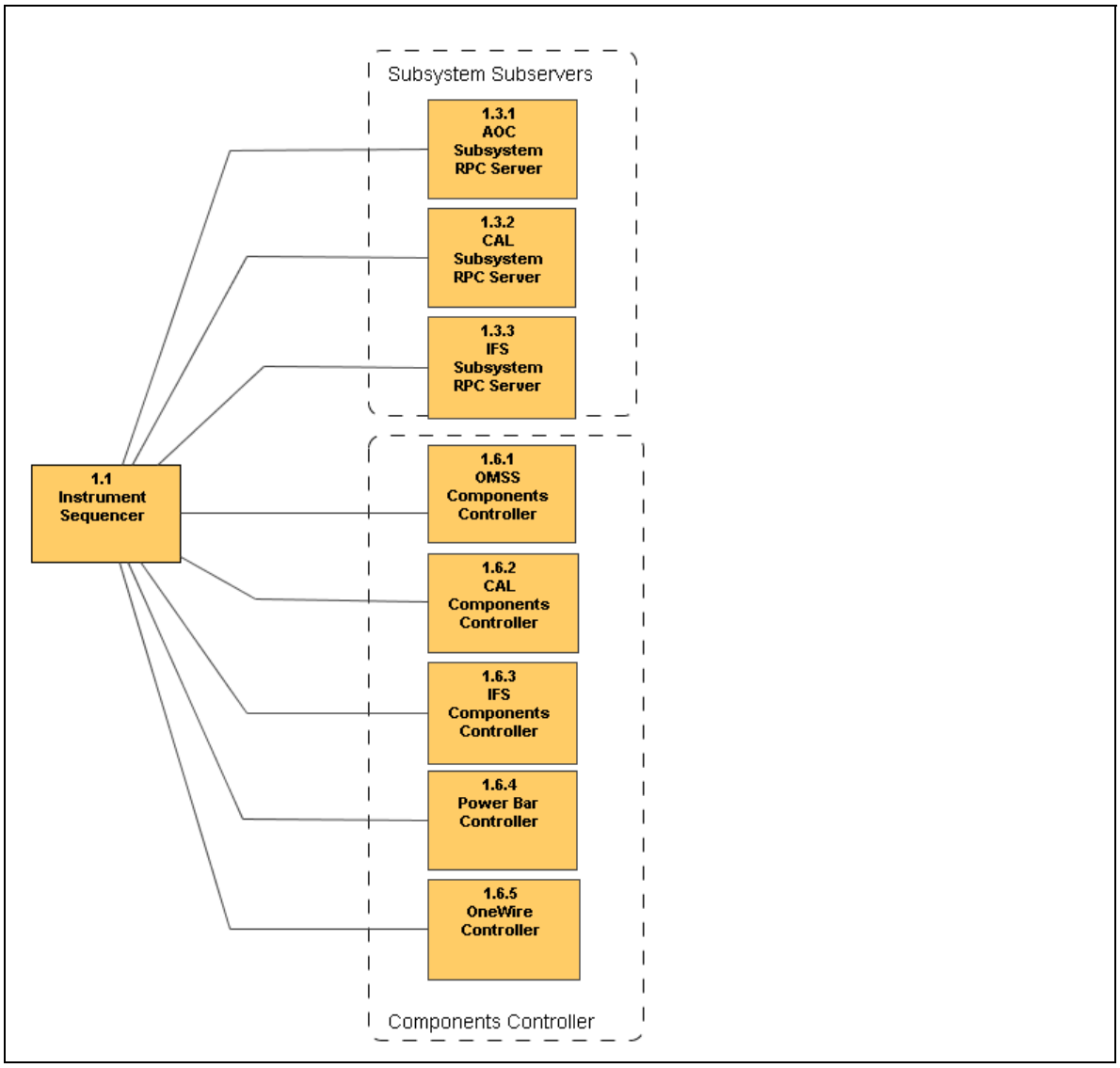

Figure 9-6 - IS Subservers

The Acceptance Test and Engineering User Interface (ATEUI) is the engineering interface for GPI. Common library functions will be provided for this functionality. This will be written in Java.

The Status Server (SS) provides the status to external clients. Internally, GPI maintains status in either the Global Memory Block (which is reflective memory across all subsystems) or locally using the TLC Unix Shared Memory (USM). The SS will use the updating of that memory to report to client subscriptions. At this time, those clients are the ATEUI and the Command Event Handler, which provides status updates for the GIAPI. Alarm handling will be handled within the Status Server.

Almost all systems are either updating or reading status from the Global Memory Block (GMB), which allows for quick updates and exchange of information. The TLC, AOC, CAL and IFS all have read access to the entire GMB and write access to only the sections that they are responsible for updating. This will be implemented using reflective memory between the various systems.

Unix Shared Memory (USM) will also be used. USM is on each local machine and is not shareable between machines but is accessible to all processes on a given machine. This technology is available via Posix style shared memory within each system.

The command structure for GPI is hierarchical which means that one command received by GPI translates into one or many commands internally. This means that each command coming into GPI is received by the TLC and that single command translates into one or many commands within GPI.

9.1.3.1 GPI Commands

The top level commands are detailed in the TLC and Gemini ICD [3] .

The following table lists the commands and their descriptions. The commands are divided into three sections: sequence commands, configuration commands, and one-of commands. The sequence commands are commands that are common for every instrument within Gemini. The configuration commands are settings for GPI that can generally be set at anytime and multiple commands can be selected at once, there is no need for any order. The one-of commands are commands that need to be executed individually. These are processes that must not be interrupted while executing, for example, trying to take an exposure while changing a light source would not be a good idea. Both the one-of and configuration commands are executed using the "apply" sequence command.

Command	Description
Sequence Commands - Common commands for all Gemini instrument	
abort	Terminate the current data acquisition prematurely and discard the data.
apply	Apply the action to the entire system configuration.
continue	Restart data acquisition that has been paused.
datum	Move mechanisms to their datum (homed or indexed) positions.
debug	Place GPI into a specified level of debugging mode.
endGuide	End the guiding operation. GPI accepts and acknowledges this command but does not perform any further actions.
endObserve	This command indicates to all principal systems that the instrument has completed the configured observation.
endVerify	System verification has finished.

guide	Begin the guiding operation. GPI accepts and acknowledges this command but does not perform any further actions.
init	Perform a complete initialisation.
observe	Carry out an exposure and initiate data transfer to the DHS
park	Adopt an internal configuration in which GPI computers can be shutdown and the instrument safely switched off.
pause	Temporarily halt the data acquisition
reboot	Perform a computer system reboot.
stop	Stop data acquisition.
test	Perform a self-test of software and hardware systems.
verify	Get into a state suitable to allow the configuration to be verified.
Configuration Commands	
configAdc	Configure the Linear Doublet ADC.
configArtificialSource	Select which light source is on or off, set intensity, deploy or extract DM pupil mask
configPolarizer	Configure the polarizer (waveplate modulator, pupil viewer/polarizer and undisperser/polarizer).
configPolarizationModulator	Configure the polarizer waveplate modulation assembly.
configShutters	Control the three GPI shutters.
configSteeringMirrors	Control the operating modes of the three pointing and centering mirror pairs (M2-GPI, WFS & CAL-IFS).
selectCoronagraphMode	Select coronagraphic mode.
selectFocalPlaneMask	Specify the Focal Plane Mask (occulter).
selectLyotMask	Specify the Lyot mask.
selectMagnitude	Specify the star magnitude.

selectNDFilter	Select the neutral density filters in the WFS Filter Wheel, Lyot Wheel and/or IFS Filter Wheel to act as a shutter.
selectPupilPlaneMask	Specify the pupil plane mask (apodizer).
selectWavelength	Select wavelength.
One-Of Commands	
calcMatrix	Determine lenslet influence matrix.
collectStats	Start/stop collecting statistics.
correct	Enable/disable the selected (AO or CAL) control loop.
flattenPath	Flatten the selected (SCI, WFS or DM) path.
measureWave	Measure the selected (AOWFS, LOWFS or HOWFS) control wave front.
optomizeWave	Determine science camera wave front optimization.
preparePath	Centre the selected (AO or CAL) path.
startAstrometry	Perform astrometry.
takeExposure	Take an exposure using the selected wave front sensor
takeFlats	Determine all necessary flats

Table 9-3 - GPI and GIAPI interface commands.

9.1.4 Hardware Layout

The following table (Table 9-4) presents a base specification of the hardware required to provide control and communication for the TLC in GPI. Specifications for the AOC/CAL/IFS are shown in their own sections.

Quantity	Description

2	**Augmentix A+1950 :** A Dell PowerEdge 1950 computer ruggedized and repackaged into a shorter chassis. The TLC and IFS computers.
2	**HP ProLiant DL580 G4:** The AOC and CAL computers. The A+1950 cannot be used due to the greater PCI card requirements of the AOC and CAL computers.
1	**Symmetricon bc635PCI-U :** PCI TimeBus card to interface with the Gemini TimeBus. This is only required if the use of the Gemini proposed software only solution of using the NTP time server is not viable.
4	**GE-Fanuc PCI-5565 :** 128 MB reflective memory card providing a high speed fiber connection between the GPI computers. Each card contains a copy of the GPI Global Memory Block.
1	**Embedded Data Systems HA7Net :** Ethernet interface to the 1-Wire bus used to interface with temperature and humidity sensors.
1	**Cisco Catalyst 2960G-24TC-L :** 24 port ethernet switch with fiber and copper connections. GPI will use 15 ports (copper) for the internal connections and 2 fiber ports for external Gemini connections. *This is supplied by Gemini.*
1	**Perle 24-port :** A terminal server is required to provide access to RS-232 devices. *This is supplied by Gemini.*
4	**Baytech Zero U RPC series :** Remote power bars
5	**Galil DMC-2183 :** Ethernet based servo and stepper motor controller. The OMSS will require 3 Galil controllers. The CAL system and IFS will each require a Galil controller. The TLC will control all of the Galil controllers.
2	**TBD :** Piezo controllers.
1	**Interlock Hardware :** Custom built at HIA. The GPI interlock hardware interfaces to the Gemini Interlock System.

Table 9-4 – TLC Hardware Specifications

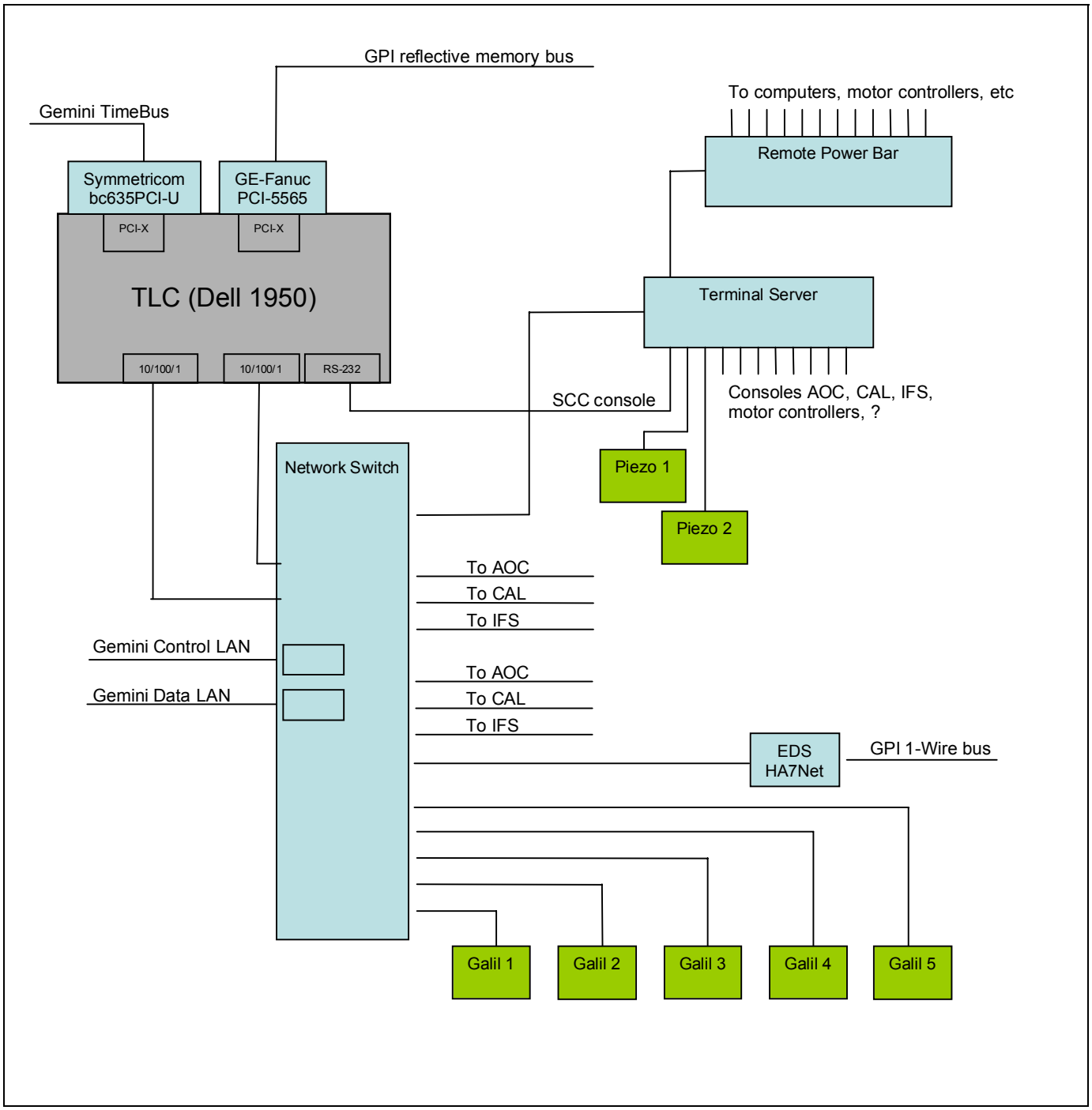

Figure 9-7 – TLC Hardware Layout

Figure 9-7 shows the hardware layout for the TLC.

9.1.5 Development Process

In this section we discuss the software development process rather than the software design.

Gemini is encouraging a more interactive relationship between the GPI software developers and the Gemini staff. In order to achieve this, we propose regular releases during the build phase. These will be a release of features in the software. Regularly bringing the code up to shippable quality means fewer surprises at the final integration. At this time we will make a guess on what features will be included in a given release based on what is perceived as important at the time. An option is to be firm on the features to be delivered, which will mean more flexibility on the delivery date otherwise quality may be sacrificed (or padding the estimates so that the schedule can be met). The alternative is that we leave the features more flexible and definitely hit the scheduled release dates.

Initially the releases will be directed at the GPI partners as the client. There are software modules that are provided by one partner for all partners. For example, the control of the slow real-time mechanisms and input/output control, as well as the ATEUI and subsystem interface. This software will be part of a release schedule during the critical design phase, whereas the release schedule during the build phase will consider Gemini as the client.

When releasing a new feature, each partner will have written and performed tests that exercise the new feature.

In order to streamline the documentation process, the GPI team will adopt the use of the doxygen documentation tool. This tool allows specially constructed comments in the source code to be extracted by the computer to form HTML web pages that contains the documentation for the software. This avoids the synchronization problems associated with creating the documentation as a Microsoft Word document.

In order to track changes to the software, a revision control system will be used at each local site to manage their source code. Possible candidates are: RCS, CVS and Subversion. As releases are made, Gemini will host the central source code repository for all parties.

The use of a central source code repository allows each development group to use the latest released versions of the software along with the current unreleased version of the software they are developing. This will allow early detection of problems caused by interface mismatch or a revised API.

9.1.6 Subsystem Interfaces

9.1.6.1 Slow Real-time Motion Control

All mechanisms that have no fast real-time requirements are controlled via the Motion Control Daemons (MCDs). These software entities are being developed at one location and being used at all locations to control the slow real-time devices. There will be one MCD for each motion control card. At this juncture there are only Galil motor controllers (which also handle some digital input/output control), but this will change as piezo motion controllers are selected.

It is important to not have multiple incantations of the same functionality. This will reduce debugging and maintenance time.

9.1.6.2 Interface Control Documents

The ICDs in the following table (Table 9-5) describe the external GPI-Gemini interfaces and the internal interfaces between GPI subsystems.

ICD	Description
GIAPI-GPI [3]	This ICD describes the majority of the interface between Gemini and GPI.
Timebus[7]	Time access will be part of the GIAPI and will access time either from the TimeBus (IRIG-B) or from a dedicated NTP server.
Synchrobus [8]	GPI will write TTF values directly to the synchrobus. The TTF values are read by the SCS (M2).
TLC-AOC[10]	This ICD describes the internal interface between the GPI top level computer and the GPI Adaptive Optics Computer.
TLC-CAL[12]	This ICD describes the internal interface between the GPI top level computer and the GPI Calibration Computer.
TLC-IFS[11]	This ICD describes the internal interface between the GPI top level computer and the GPI Science Computer.
GMB[13]	This ICD describes the GPI Global Memory Block (shared memory interface between the four GPI computers).

Table 9-5 - TLC Interfaces

9.1.7 Additional Software Details

To get a better comprehension of how the GPI software is envisioned to run, a simple example of how the GPI health status is communicated back to Gemini is given below. Health status is hierarchical. Each of the subsystems will have their own health status (including the CC) and heartbeats.

The heartbeat is to indicate that the system is alive and working. The TLC would be monitoring subsystem heartbeat status and would be responsible for assessing whether that subsystem is alive or dead but that health would be part of the particular subsystem health status (for example, the TLC determines that the AOC is dead and that will make GPI's health BAD). The Command Event Handler will communicate back to GIAPI the change in health. This is show in Figure 9-8.

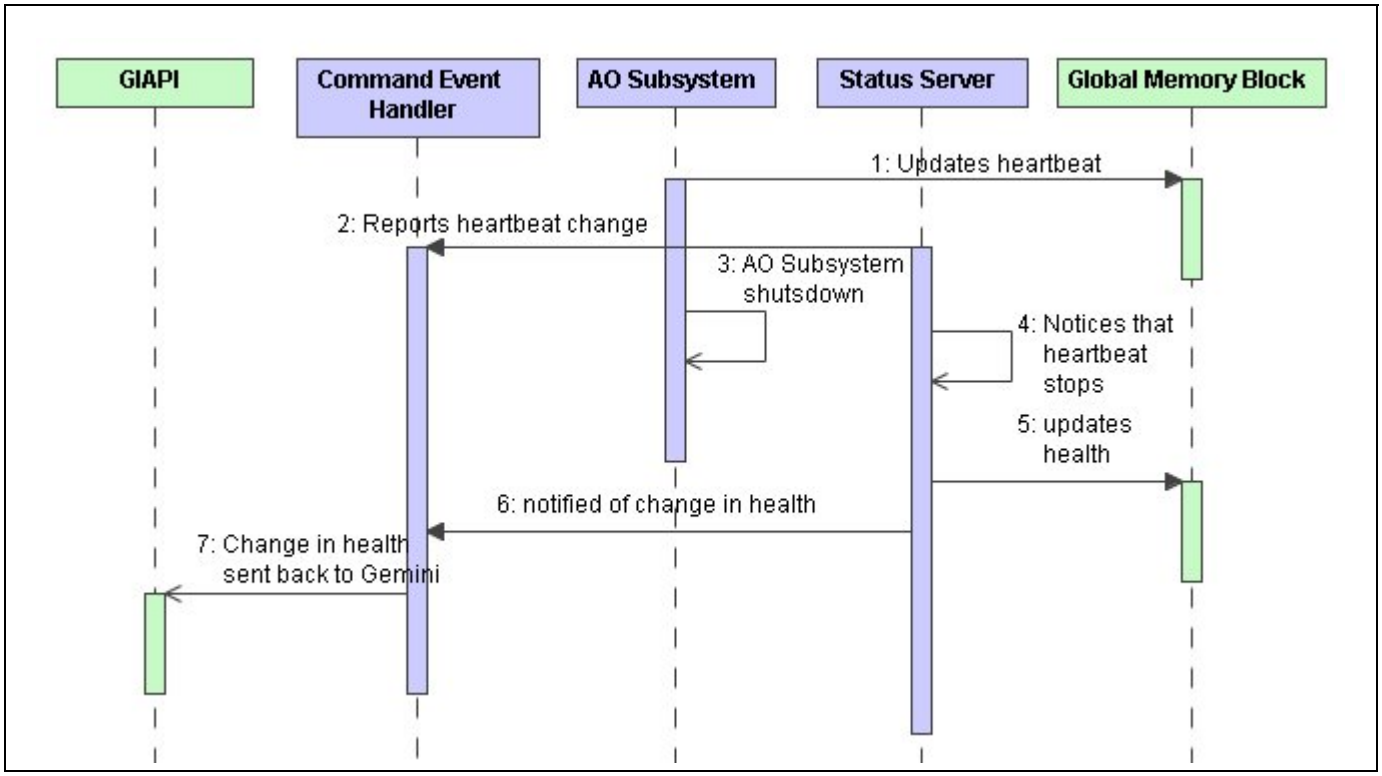

Figure 9-8 - Change in Health

9.1.8 Software Risks

9.1.8.1 GIAPI Dependencies

GPI is dependent on using the GIAPI to interface with the rest of Gemini. This means that GPI is relying on GIAPI being delivered from Gemini in a timely manner. In a perfect world, that would come bug-free, but this is not a perfect world. This means that debugging software will be more challenging because there is another new piece of software that may have bugs in it. Hopefully software bugs will be reported and quickly fixed. This will be mitigated to some degree by having the ability to execute the same set of commands using the same software, just a different communication interface. The GIAPI commands and status requests will come into the Command Event Handler that will pass the command on to the Instrument Sequencer and the status request to the Status Server. That means that all commands are available through the Instrument Sequencer and can be thoroughly tested there before testing with the GIAPI interface.

9.1.8.2 Provide Motion Control for Partners

HIA is providing motion control for the entire project, which means the functions need to be done early. The piezo controller interface is unknown at this time. This risk may be mitigated somewhat if the software interface used for the Galil controllers can be adapted for use with the TBD piezo controllers.

9.1.8.3 Global Memory Block

Currently the reflective memory card driver is not available for 64-bit Linux, which is our baseline for GPI. A 64-bit Linux driver is expected to be available late summer of 2007, which should allow enough time to make other arrangements if it is not delivered.

The current baseline card requires a computer with a PCI or PCI-X slot. The card is not available in PCI-e format which is quickly becoming the industry bus standard. The company that provides the reflective memory card has been asked when a PCI-e version is planned.

HIA has run tests on the reflective memory card using the 32-bit Linux driver. This Linux driver causes "out of memory" errors on machines with large amounts of RAM. This should not be a problem with the 64-bit driver. Already a work-around has been found for up to 2 gigabytes of RAM that involves modifying the Linux boot parameters.

It will also be important to test the selected reflective memory card in a system which also contains a Gemini Synchro Bus card. This is to ensure that the required drivers for the two cards do not conflict with one another or have mutually exclusive requirements. This will be done during the critical design phase.

9.1.9 Required from Gemini

GIAPI is required in a timely manner. Thus far we have received a GIAPI Design and Use document and have received a detailed response to comments provided. There are issues that need to be addressed and that interaction needs to be supported by both Gemini and the GPI partners.

GPI needs to produce an instrument that can work on the Gemini telescope; therefore GPI needs the ability to test running the instrument through the GIAPI interface. This could be something as simple as a command line interface.

Previously Gemini has provided all Gemini simulators and that was proven successful when Altair was delivered, with a smooth integration at the telescope. All interfaces to GPI must be provided (in simulate mode) well before the instrument is integrated into a single instrument.

9.1.10 Release Schedule

The following table (Table 9-6) details the first estimate of the release schedule. It is based on features that will be released and starts as early as the critical design phase. During the critical design phase there are software deliverables to be provided by HIA required by the other GPI partners. During the build phase there will be staged releases of the subsystems and the following list attempts to capture this. This list is dynamic and is the first pass. It does not try to assign dates; instead it is a chronological list of the release of features that will be addressing during the development stages. Some of these features may be rolled into one release, this is TBD.

ID	Month	Subsystem(s)	Features
CDR			
C1	**6**	TLC (MCD)	• Commands: init, index, simulate, move, stop, preset, park, test, track • Read in some configuration, set simulation mode • Command Line interface, Galil motion control only • Unix Shared Memory, • TK/TCL basic interface (already available)
C2	**8**	TLC (MCD)	• Piezo control • I/O Control and reporting
		TLC (Common Library)	• Common Library functions to be used by all subsystems
C3	**10**	TLC (SubServers)	• SubServer Library functions
		TLC (Generic Assembly)	• Assembly Command: simulate and init, read in configuration file, command line interface
C4	**12**	TLC (SubServers)	• SubServer Library functions, Subsystem SubServer Command: simulate and init, read in configuration file, command line interface
Build			
B1	**2**	TLC (Status Server)	• Accept connections, read reflective memory, report changes in values on command line
		TLC (ATEUI)	• Simple status screen, should report value change as they change
		TLC (IS, all RPC Servers, CEH and Assemblies)	• Accept an init command, return a response in simulation mode
B2	**4**	TLC (IS, all RPC Servers, CEH, and Assemblies)	• Command: datum, park, shutdown (return responses in simulation mode)
		TLC (ATEUI)	• Initial screens for all Subsystem SubServers, being able to do the init, global, and shutdown commands
		CAL (CAL RPC Server)	• Commands: CAL commands corresponding to init, global, and shutdown (return responses in simulation mode)

ID	Month	Subsystem(s)	Features
B3	**6**	TLC (Status Server)	• Using TLC Shared Memory
		TLC (ATEUI)	• All CAL SubServers commands and AOC commands as in B5
		CAL (CAL RPC Server)	• Commands: CAL commands corresponding to reboot, takeExposure and setObservatonConfiguration (return responses in simulation mode)
B4	**8**	TLC (IS)	• Command: verify, guide, endVerify, endGuide
		TLC (IS, SubServers, CEH)	• Command: observe/endObserve (return responses in simulation mode)
		TLC (Assemblies)	• Power Bar Assembly, Apodizer/Occulter Assembly, CAL Assembly, CAL Spatial/Source Assembly, WFS Assembly, Source Assembly
B5	**10**	TLC (IS)	• Command: apply the various configurations that can be applied
		TLC (Assemblies)	• ADC Assembly, IFS Assembly, Fold Mirror/IFS_CAL Assembly
		AOC (AOC RPC Server)	• Command: AOC commands corresponding to global and shutdown (return responses in simulation mode)
B6	**12**	TLC (ATEUI)	• All AOC SubServers commands and CAL commands as below
		AOC (AOC RPC Server)	• Command: AOC commands corresponding to takeExposure and setObservationConfiguration (return responses in simulation mode)
		IFS (CAL RPC Server)	• Command: IFS commands corresponding to global and shutdown (return responses in simulation mode)
B7	**14**	TLC (ATEUI)	• All IFS SubServers commands
		IFS (IFS RPC Server)	• Command: IFS commands corresponding to takeExposure and setObservationConfiguration (return responses in simulation mode)
B8	**16**	all	• All features functional (using simulation mode, as necessary)
B9	**18**	all	• Final Build release
I&T			

ID	Month	Subsystem(s)	Features
Ix	**when needed**	all	• I&T fixes and refinements

Table 9-6 - GPI Feature Release Schedule

9.1.11 References

[3] ICD 3.1/1.9.x, "GPI Software Top-Level Computer (TLC) and Gemini ICD", J. Dunn, April, 2007, v0.8

[7] Guidelines for Designing Gemini Aspen Instrument Software, Kim Gillies, AspenSoft-03072004-6

[8] ICD 21, "The TCS Time System", C. Mayer, D. Terret, P. Wallace

[9] ICD-20, "Synchro Bus – Node specifications" , C. Boyer, 24 November 1999

[10] ICD 1.9.x.5.x, "GPI Top Level Computer (TLC) and Adaptive Optics Computer (AOC) ICD, 2007

[11] ICD 1.9.x.5.x, "GPI Top Level Computer (TLC) and Integral Field Spectrograph (IFS) ICD, 2007

[12] ICD 1.9.x.5.x, "GPI Top Level Computer (TLC) and Calibration (CAL) ICD, 2007

[13] ICD 1.9.x.5.x, "GPI Shared Memory ICD", 2007

10 Data Pipeline

10.1 Overview

The GPI data pipeline consists of two main modules: the on-line data pipeline (OLDP) and the final data pipeline (FDP). The former is a simple tool used in real time at the telescope by the resident astronomer to display the data and derive basic information from it. This information is used to check that the instrument is properly set up prior an observing sequence and to monitor its execution. The FDP will be used for reducing an ensemble of raw science images and calibration data into a final calibrated dataset ready for scientific analysis. This section describes both software modules in detail.

10.2 On-Line Data Pipeline

10.2.1 Top Level Requirements

In spectroscopy mode, raw GPI images will consist of ~40000 18-pixel long spectra interleaved on a 2048x2048 infrared detector (see Figure 10-1). Similarly, polarimetric data will consist of two low-resolution (R~15) spectra of orthogonal (*o* and *e*) polarization state. The main purpose of the OLDP is to convert these raw data into meaningful images (e.g. a broad band image resulting from a collapsed spectral data cube or Stokes *I*) that can be quickly displayed and used on-the-fly for analysis like Strehl measurement, aperture photometry, centroid calculation, contrast, etc. The OLDP receives and processes data; it does not send commands to the instrument. The OLDP and its quick look display are nothing but a user interface to display the instrument parameters and monitor the execution of an observing sequence. Once an image is received from the data handling system, the OLDP automatically reduces the incoming image and display it with the default display option. Various commands can then be issued from the OLDP interface to preprocess and visualize the set of images received so far.

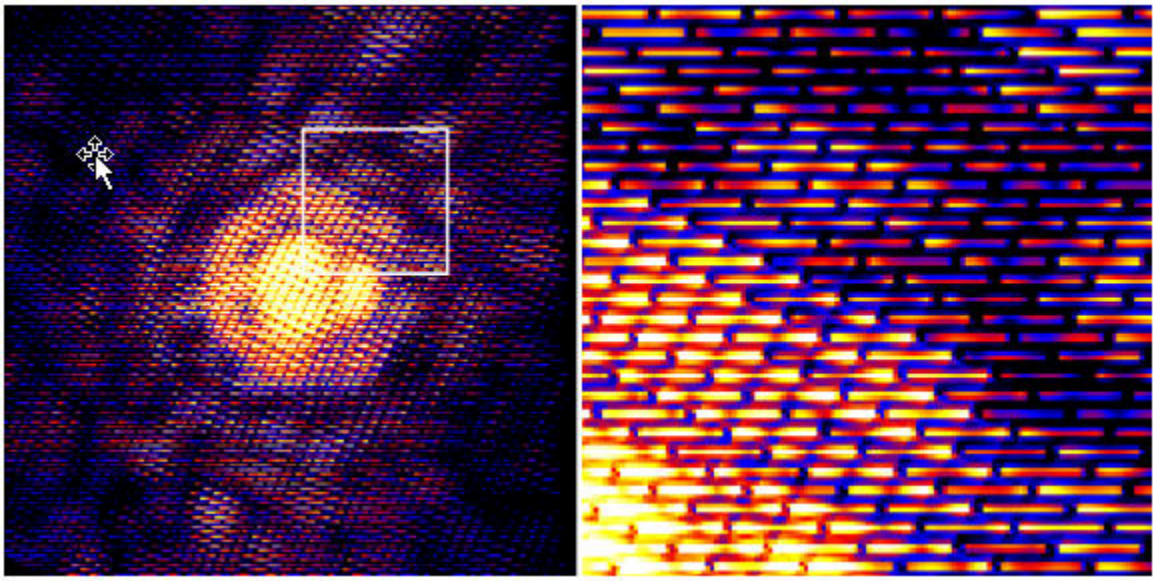

Figure 10-1 Right: simulated GPI image of the central 512x512 (~0.7"x0.7") sub-section of the 2048x2048 detector. The PSF is a very short (instantaneous) exposure in the *H* band sampled at R=45 with a spatial sampling of 14 mas per lenslet. Left: zoom region shown by the square on the left. The image was simulated without geometrical distortion with a nominal spectral spacing of 4.5 pixels perpendicular to the dispersion direction. Note how the signal from micro-pupil spectra is alternating from being perfectly centered or exactly in-between a detector line. This is an artifact of the simple assumptions used for generating the image. In practice, micro-pupils will fall on arbitrary non-integer pixel values due to geometrical distortion and slight rotational misalignment of the lenslet array wrt the detector.

10.2.2 OLDP Functions

The OLDP shall have the following functions, all described in more detail in Appendix 10.1

- Image display
- Status window
- Strehl Calculation
- Contrast Curve
- Image statistics
- PSF Fitting
- Aperture photometry
- Aperture spectroscopy

10.2.3 Proposed OLDP Implementation

The OLDP will consist of an image display interacting with a graphical user interface (GUI) featuring buttons and pull-down menus for selecting the various functions listed in 10.2.2. The GUI will also include a graphical window for displaying various plots (aperture spectrum, contrast curve, radial profile, etc). The proposed image display is DS9 (SAOIMAGE) and the GUI will be based on IDL.

10.3 Final Data Pipeline

10.3.1 Top Level Requirements

The final data pipeline will be used for reducing and combining an ensemble of observations and calibrations into a final dataset ready for scientific analysis. In spectroscopy mode, this corresponds to a co-added spectral data cube properly calibrated in photometry, astrometry and wavelength and optionally processed for speckle suppression. In polarimetry mode, the final dataset will be Stokes *I*, *Q* and *U* images processed for speckle suppression.

The FDP is designed to operate automatically without human intervention but it will feature a user interface for customizing data reduction sequences (e.g. to flag a bad image that FDP failed to identify), visualize and analyze individual images and the final result. The FDP user interface will include the same image display and analysis functions of the OLDP.

The FDP shall run on standard computer platforms (Windows, Macintosh & Unix) and shall be available free of charge to the general community.

10.3.2 Software Architecture

10.3.2.1 Data Format

GPI images are stored in standard FITS format with a filename that comply with the Gemini naming convention. It is assumed that this filename does not carry any particular information on the image content. All the information needed for data reduction is to be retrieved from the FITS header by the DRP. The FITS keywords of a given image provide a unique description of the instrument configuration and the type of observations acquired. This information is then used by the DRP to initiate various automatic data reduction sequences.

Table 10-1 gives a subset of FITS keywords specifically needed for the DRP. For example, the OBSTYPE keyword specifies the image type which can be “Object”, “Flat”, “Dark” or “Wavecal”. An “Object” is in turn classified as “Science”, “SpecSTD”, “AstromSTD”, “PolarSTD” corresponding respectively to a normal science observation, a telluric standard, an astrometric binary and a polarization standard.

10.3.2.2 Data Structure

GPI images are structured using the “dataset” concept already implemented in many Gemini instruments. A dataset is an ensemble of images sharing a common data reduction pipeline (ex: a sequence of science observations or a set of flatfield images). A dataset is identified through the FITS keywords OBSID and DATALAB. The former uniquely identifies a specific observation programmed into the PhaseII tool and DATALAB (“datata label) is the keyword OBSID concatenated with an incremental number identifying the image within the dataset.

Class	Name	Description
Telescope	RA	RA of Target
	DEC	Declination of Target
	EQUINOX	Equinox for Target coordinates
	DATE-OBS	Observation date (UT)
	TIME-OBS	Beginning of Observation (UT)
	CRPA	Current Cass Rotator Position Angle
	CRFOLLOW	Cass Rotator follow mode (yes|no)
Quality	RAWGEMQA	Gemini Quality Assessment
	AVGRNOT	Average R_0 during the exposure
	AVGWFERES	Average wave front error residual during exposure
	SKYTRANS	Average sky transparency during exposure (from WFS data)
Instrument	INSTRUME	Instrument used to acquire data
	INSTRMSUB	Instrument sub-system (IFS, CAL…)
Configuration	FILTER1	Filter name
	FILTER2	Wollaston (in/out)
	FILTER3	Half-wave plate position
	FILTER4	ADC (in/out)
	WAVELENG	Filter central wavelength
	OCCULTER	Occulter position
	LYOTMASK	Lyot mask position
	APODIZER	Apodizer position
Exposure	EXPTIME	Exposure time (s) for each frame
	COADDS	Number of coadds summed
Target	OBJECT	Object Name
	OBSTYPE	Observation type (Object, Dark, Flat, Wavecal)
	OBSCLASS	Observe class (Science, SpecSTD, PolarSTD, AstromSTD)
	OBSID	Observation ID
	DATALAB	Datalabel
	HMAG	H magnitude of the target if science observation
Coordinates	CTYPE1	the coordinate type for the first axis
	CRPIX1	x-coordinate of reference pixel
	CRVAL1	First axis value at ref pixel
	CTYPE2	the coordinate type for the second axis
	CRPIX2	y-coordinate of reference pixel
	CRVAL2	second axis value at ref pixel
	CD1_1	Partial of first axis coord w.r.t. x

CD1_2	Partial of second axis coord w.r.t. x
CD2_1	Partial of first axis coord w.r.t. y
CD2_2	Partial of second axis coord w.r.t. y

Table 10-1 FITS header Keywords needed for the Data Reduction Pipeline

10.4 Data Reduction Sequence & Algorithms

The DRP consists broadly in the following steps:

- **Data parsing**
- **Initial calibration**
- **Data Cube extraction**
- **Speckle suppression**
- **Final calibration**

10.4.1 Data parsing

The first step is to parse the data i.e. scan all FITS headers to identify all datasets and initiate their corresponding data reduction sequence.

10.4.2 Initial calibration

The initial calibration refers to all procedures needed to remove the instrumental signature from the data. These are:

- **Bad pixel mapping**. A map of insensitive and/or "hot" (high dark current) pixels is produced using raw flatfield and dark images.

- **Flatfield**. A set of images illuminated by a continuum lamp (e.g a Quartz lamp) are combined to extract all flatfield spectra (one per micro pupil) within a specified aperture (nominally 3 pixels perpendicular to the dispersion direction) taking into account bad pixels. The resulting spectrum is divided by a low-order polynomial to remove the black-body response of the lamp. The flatfield spectrum is normalized to unity per spectral pixel. In polarimetry mode, two flatfield images are produced, one per polarization (*o* or *e*) state.

- **Dark**. Median combine all dark images of the same exposure time.

- **Wavelength solution.** A set of images illuminated by arc lamps or (TBD) narrow band images is used to determine the wavelength calibration solution of all micro-spectra. In polarimetry mode, a wavelength solution is provided for both polarization states.

10.4.3 Data Cube Extraction

This procedure is to convert a raw detector image as shown in Figure 10-1 into a 3D spectral data cube. The procedure is very similar for polarimetry data except that two data cubes are produced, one per polarization state. The steps are:

- **Dark subtraction (**optional). This step is avoided if the data is acquired in angular differential mode (ADI) (see below).
- **Flatfield.** Extract and flatfield all micro-spectra with the same extraction aperture used for reducing the flatfield.
- **Wavelength extraction.** Use the wavelength calibration solution to extract, through interpolation, all micro-spectra at a common set of wavelengths.

10.4.4 Speckle suppression

Atmospheric and quasi-static speckle noise will be suppressed using a number of speckle suppression techniques. Some of them are already proven to work effectively and others have yet to be explored. Obviously, the FDP will incorporate only those algorithms that are effective at reducing the speckle noise. The final selection of the algorithm will be made when test data is available and, most and foremost, with real on-sky data during commissioning. Appendix 2.25 shows the efficacy of these effects on simulated GPI data including quasi-static aberrations.

10.4.4.1 Multi-Wavelength Imaging (MWI)

The MWI technique consists of acquiring several narrow-band images simultaneously at adjacent wavelengths such as that provided by the IFS. Since optical aberrations at a pupil plane generate a speckle pattern that moves radially with wavelength, speckles can be suppressed by first re-scaling all wavelength images to a common scale and then subtract adjacent images close in wavelength. If the companion shows a strong spectral variation near these wavelengths (*e.g.* methane absorption at 1.6 μm), then the resulting subtraction will attenuate the speckle signal and leave the companion signal nearly intact in the residual image. The simplest MWI speckle suppression algorithm is the *single* difference defined as

$$SD = I_n - I_{n+1}$$

where I_n and I_{n+1} are the PSF intensities at adjacent wavelength λ_n and $\lambda_{n+1,}$ respectively. It can be shown [1] that a single difference attenuate the speckle noise by a factor $\sim\lambda/\Delta\lambda$ where $\Delta\lambda$ is the wavelength difference between and λ_1 and λ_2 with $\lambda\sim\lambda_1\sim\lambda_2$. Smaller residuals are obtained if a third wavelength is used in the subtraction; this constitutes a double difference (DD):

$$DD = I_n - I_{n-1}/2 - I_{n+1}/2$$

Theoretically, a *DD* can yield a speckle noise attenuation factor $\sim(\Delta\lambda/\lambda)^2$.

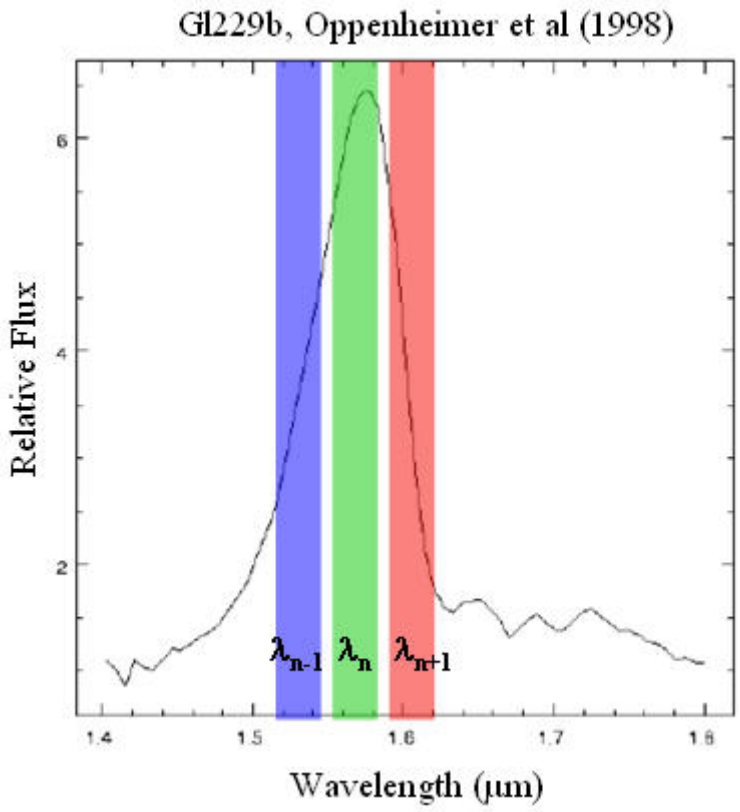

Figure 10-2 Spectrum of the cold brown dwarf Gl229b somewhat representative of cold giant exoplanets. The planet signal varies abruptly with wavelength due to methane absorption beyond ~1.6 μm. The spectrum of a normal star is featureless at these wavelengths. The hatched regions correspond to the narrow bandpass used to perform a double difference.

The double difference technique will work, albeit less effectively, even if the companion has a featureless continuum. In this case, the companion will be at a different separation in each of the re-scaled images: a companion is moved radially by $r\Delta\lambda/\lambda$ when two images are brought to a common scale, where r is the original separation of the companion, λ is the wavelength of one of the two images and $\Delta\lambda$ is the wavelength spacing between the two images. If the displacement of the companion between images is greater than ~2λ/D (diameter of first dark ring), then effectively at a given separation in the re-scaled image the companion is present in a single image and the above considerations apply, namely speckles can be subtracted and the signal of the companion will be preserved.

An alternative algorithm is to subtract a fitted spectrum from each "spectral pixel" of the re-scaled data cube rather than subtracting images [2] . In a re-scaled data cube, the intensity of a speckle intensity varies smoothly with wavelength and is easily fitted by a low order polynomial, which can be used effectively to subtract the PSF contribution to that pixel. A "robust" polynomial fitting algorithm i.e. one that excludes the most deviant data points in the spectrum has been shown to work very effectively (see Figure 10-3 and Figure 10-4). Polynomial fitting is the baseline algorithm for MWI speckle suppression but the DD will also be very useful for the OLDP since it is less computationally intensive. The optimal

weighting of the individual spectral channels depends in part on the chromaticity of the PSF – in regions of high chromaticity (e.g. where the chromaticity of the APLC coronagraph is significant), DD over a narrow wavelength range may be more capable than fitting the entire bandpass, particular in initial planet discovery mode.

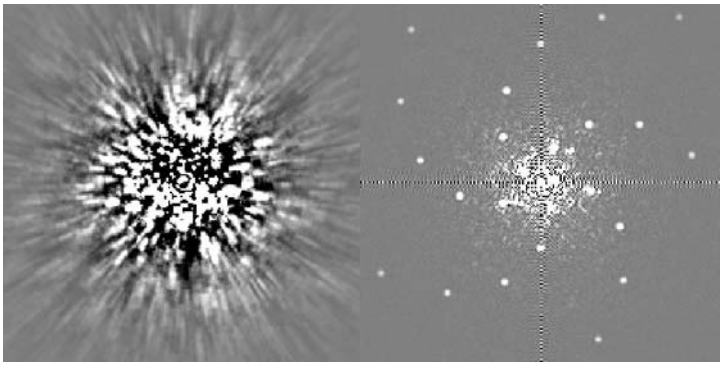

Figure 10-3 Left: simulated collapsed data cube including virtual planets with featureless spectra; an azimuthally averaged profile has been subtracted. Right: Residual collapsed data cube after subtraction with a "robust" polynomial fit of degree 1. Images are 3" on a side. Stretch of image on the left is 10 times that of the right one.

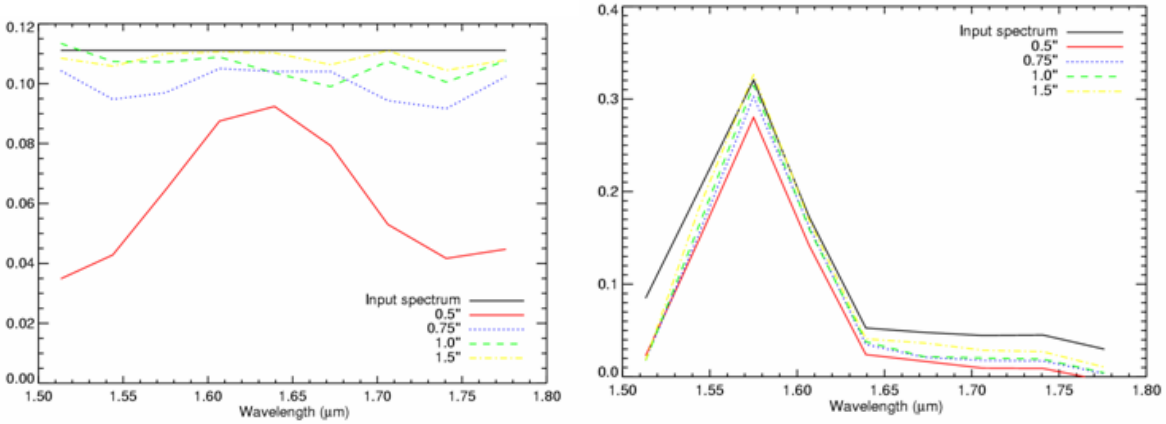

Figure 10-4 Recovered SED compared with input SED spectra for companions at various separations using a polynomial fit of degree 1 of (*left*) a flat spectrum and (*right*) a T8 spectrum. SED of input spectra with strong absorption features (right) are easily recovered at all separations whereas flat spectra can be revovered reliably beyond ~1".

10.4.4.2 Dual-Channel Polarimetry

For extended sources, such as debris disks, differential imaging between adjacent wavelengths cannot be used to discriminate between true sources and artefacts. As dust scatters the light of the parent star, to first order, the spectrum of star and the disk are the same. The primary difference between the starlight and the disk is caused by the fact that dust grains selectively scatter one polarization state selectively over the other. Small dust grains preferentially scatter light with the **E** vector oriented perpendicular to thescattering plane (the plane that contains the source, the scatter and the observer). To the extent that GPI does not introduce instrumental polarization, or that the instrumental polarization can be characterized, this intrinsic difference between the starlight and the disk light can be exploited to separate the two signals.

The dual-channel polarimeter of GPI provides simultaneous measurements at two orthogonal polarization states (*o* and *e* beam) with a modulator to change their polarization angle. The baseline retarder for GPI is a half-wave plate (π retardance). Rotating the half wave plate by 45 degrees changes the *o* and *e* beams with one another enabling a differential measurement of both Stokes *Q* and *U* through a double differencing technique illustrated in Figure 10-5. This technique eliminates unpolarized speckles, leaving the astrophysial polarized signal in the residual image.

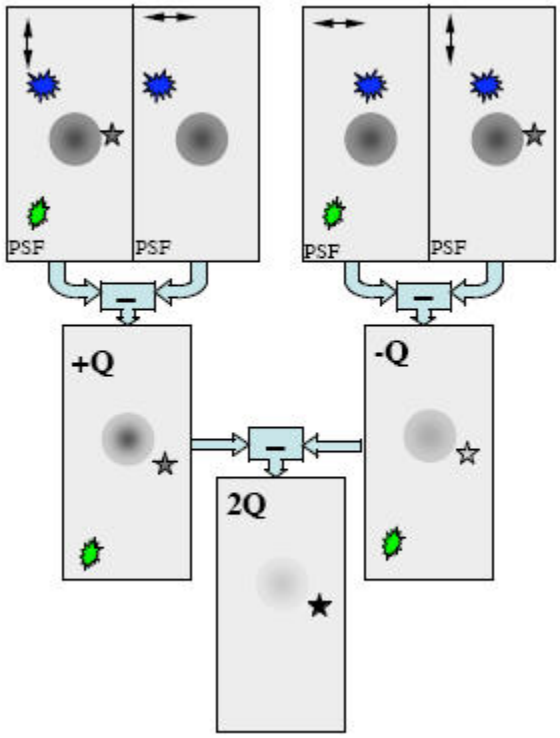

Figure 10-5 llustration of a double differencing with an dual-channel polarimeter with perfect π retardance. In this example, the modulator is a half-wave plate that is rotated exactly by π/4, which has the effect of swapping +*Q* and –*Q* (indicated by the horizontal and vertical double headed arrows) between the o- and e channels of the analyzer. The technique suppresses speckles due to common path wavefront errors (blue speckle) and non-common path errors (green speckle). In this example the uncorrected seeing halo is unpolarized, while the astrophysical signal (grey star) is polarized). Stokes U is obtained similarly by first rotating the half-wave plate by π/8 and then every π/4.

10.4.4.3 Angular Differential Imaging

The angular differential imaging (ADI) technique consists of acquiring a sequence of relatively short (~30-60s) exposure on an altitude/azimuth telescope with the instrument rotator off. This very stable configuration (telescope and instrument optics not moving with respect to each other) ensures a high correlation of all PSFs in the sequence and causes field rotation i.e. any off-axis source move angularly with time. For each target image in the sequence, it is possible to build an optimal reference image from other target images in which any companion would be sufficiently displaced due to FOV rotation. After subtraction of the reference image, the residual images are rotated to align their FOV and then co-added. Because of the rotation, the residual PSF speckle noise is averaged incoherently, yielding a detection

limit increasing nearly as the square root of the exposure time. ADI has been shown to be very effective on Gemini with Altair/NIRI; subtracting two successive images in an ADI sequence typically suppresses the quasi-static speckle noise by a factor of ~12 which increases to ~100 after 90 such independent differences are combined [4] [5] . ADI is anticipated to be the baseline observing mode for GPI and should be particularly effective at improving the contrast sensitivity beyond the control radius.

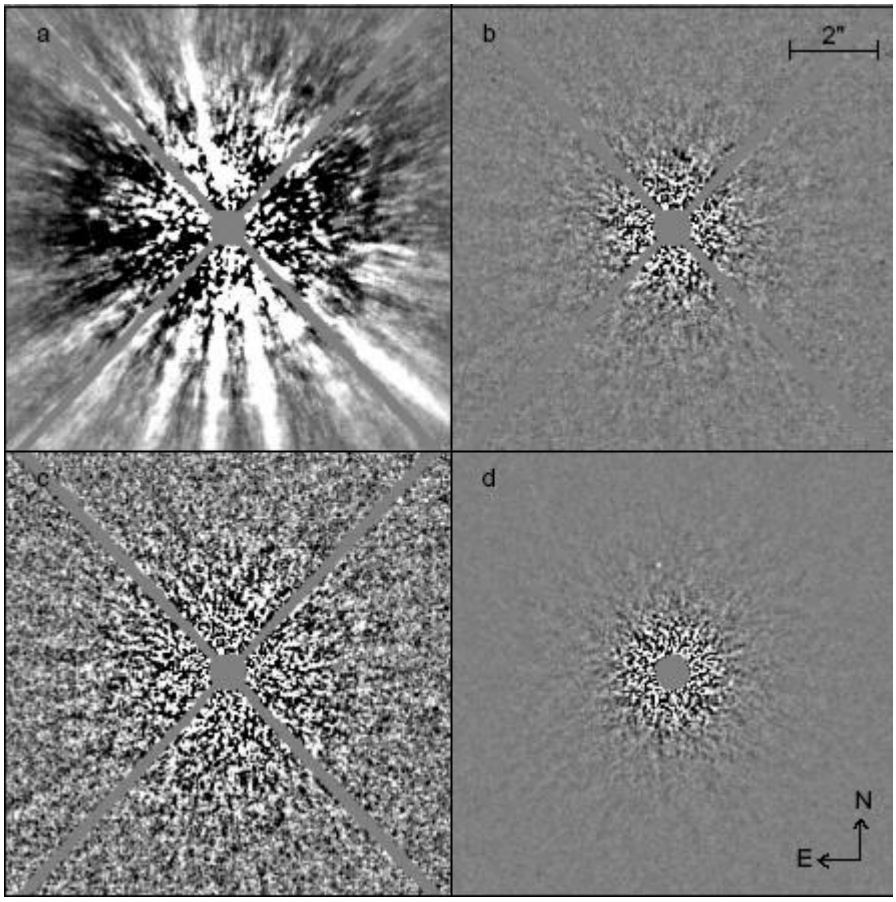

Figure 10-6 Illustration of the ADI noise attenuation process. Panel (a) shows an original 30-s image of the young star HD 691 after subtraction of an azimuthally symmetric median intensity profile, panels (b) and (c) both show, with a different intensity scale, the corresponding residual image after ADI subtraction, and panel (d) shows the median combination of 117 such residual images. Display intensity ranges are $\pm 5 \times 10^{-6}$ and $\pm 10^{-6}$ of stellar PSF peak for the top and bottom rows respectively. Each panel is 10″ on a side. The diffraction spikes from the secondary mirror support vanes and the central saturated region are masked. The faint point source ($\Delta m_H = 14.9$) visible in panel (d) at a separation of 2.43″ and P.A. of 7.3° could not have been detected without ADI processing. From Lafrenière et al 2007 (in preparation).

10.4.4.4 Other techniques

At very high Strehl, residual pure phase errors yield symmetric speckle pattern which can be attenuated by simply subtracting the PSF from itself after rotating it by 180. Pure amplitude errors yield a similar pattern, but mixed phase and amplitude errors produce both symmetric and anti-symmetric components. Thus, if both phase and amplitude errors have similar variance contribution, PSF symmetry cannot be

used for attenuating speckles. Appendix 2.25 studies these effects in detail. Finally, one could potentially use a reference PSF constructed from residual errors calculated by the calibration system.

10.4.5 Final calibration

The following calibrations will yield a data set ready for scientific analysis.

Telluric correction. This step is to correct for the telluric atmospheric transmission, obtained by observing a spectroscopic standard (known spectral energy distribution) from which an average atmospheric transmission spectrum is calculated. All science spectra are divided by the resulting spectrum.

Astrometric calibration. The purpose of this calibration is to accurately determine the plate scale and orientation of the detector. This could be done through observations of astrometric binaries.

Photometric calibration. This calibration is to convert data numbers into flux brightness (flux density of magnitude).

10.5 Software language

The top level software language to be used to develop both OLDP and FDP will be IDL, which stands for Interactive Data Language. This fourth generation language, which has been used for years in astronomical context, combines full GUI programming capability to powerful data handling, mathematical and astronomical libraries. For critical data processing operation, C interfacing is possible and will be considered.

The IDL language makes it possible to distribute a single compiled file fully compatible with all standard computer platforms (Windows, Macintosh & Unix). This is a no-cost method for IDL software developers to distribute compiled code applets, or entire applications without additional licensing requirements or fees. The source code of the OLDP and FDP will also be made available for experienced IDL users. The complete list of compatible computer platforms is presented in Table 10.2.

Platform	Vendor	Hardware	Operating System	Supported Version
Windows	Microsoft	Intel x86 32-bit	Windows	2000, XP
		Intel x86_64 64-bit	Windows	XP
Macintosh*	Apple	PowerMac	Mac OS X	10.3, 10.4
		G4, G5 32-bit	Mac OS X	10.3, 10.4
		Intel x86 32-bit	Mac OS X	10.3, 10.4
UNIX*	HP	PA-RISC 32-bit	HP-UX	11.0
		PA-RISC 64-bit	HP-UX	11.0
	IBM	RS/6000 32-bit	AIX	5.1
		RS/6000 64-bit	AIX	5.1
	SGI	Mips 32-bit	IRIX	6.5.1
		Mips 64-bit	IRIX	6.5.1

SUN	SPARC 32-bit	Solaris	Solaris 8,9,10
	SPARC 64-bit	Solaris	Solaris 8,9,10
various	Intel/AMD x86 32-bit	Linux**	Kernel version 2.4 Kernel version 2.6 glibc version 2.3
various	Intel/AMD x86_64 64-bit	Linux**	Kernel version 2.4 Kernel version 2.6 glibc version 2.3

Table 10.2 List of compatible computer platforms

10.6 Data Simulation Tool (DST)

A data simulation tool is under development for the purpose of simulating as accurately as possible spectroscopic and polarimetric raw images that can then be used as input to the OLDP and FDP for testing. Figure 10-1 is an example of such simulation produced by the DST. At this time, DST is only a simple tool for reformatting an input spectral data cube into a detector image. The current version includes the diffraction effect caused by the square lenslets. The next version will include instrumental signature (detector read noise, dark current, photon noise, bad pixel, intra-pixel response function, PSF), star and companion SED, sky emission and atmospheric transmission.

10.7 Data Pipeline References

[1] Marois, C., Doyon, R., Racine, R. & Nadeau, D. 2000, PASP, 112, 91.

[2] Oppenheimer, B. R.; Kulkarni, S. R.; Matthews, K.; van Kerkwijk, M. H. 1998, ApJ, 502, 932.

[3] Sparks, W.B. & Ford, H.C. 2002, ApJ, 578, 543.

[4] Marois, C., Lafrenière, D., Doyon, R., Macintosh, B., & Nadeau, D. 2006, ApJ, 641, 556.

[5] Lafrenière, D., Marois, C., Doyon, R., Nadeau, D., & Artigau, E. 2007, ApJ, in press, 660, 770.

[6] Perrin, M. D., Sivaramakrishnan, A., Makidon, R. B., Oppenheimer, B. R., Graham, J. R. 2003, Ap.J. 596, 702

10.8

11 Integration and Test

11.1 Description of phases

The major subsystems of GPI will be shipped to the University of California, Santa Cruz UCO/Lick Observatory where it will be assembled and tested before delivery to Gemini.

In order to reduce risk at this crucial stage of the project, it is important that the subsystems individually meet the defined interface and performance criteria before shipment to UCSC for integrated assembly and system testing. This will assure that I&T will progress on schedule through the phases outlined below. The I&T principal will be deeply involved in the process of setting requirements for subsystem acceptance, monitoring subsystem contractor's progress, and reviewing the subsystem acceptance test results.

11.1.1 Sub-system Acceptance

Subsystems are required to meet Subsystem Acceptance Test Plans (SSATPs) before they are shipped to the integration site (UCSC). The SSATPs will be drawn primarily from the subsystem's requirements, including software requirements, and the ICDs, as appropriate. These tests will demonstrate as full as possible full performance of the sub-system. If a subsystem doesn't pass its SSATP, whatever problems it has may have to be corrected before it is approved for shipment (e.g. an optical deficiency would delay shipping, a minor software issue might not).

Upon arrival at UCSC each subsystem will then be re-tested to check for survival of shipment and basic functionality. If the subsystem needs assembly, this will be done by the supplier on site. Space will be available in the Laboratory for Adaptive Optics for this purpose. Initial testing will be a series of simple power-up tests as proscribed by the subsystem supplier, followed by any testing necessary to ensure the sub-system still meets the performance demonstrated at the home Insititute. The following table lists testing per subsystem:

Subsystem	Supplier	Test	Process	I&T Equipment Requirements
CAL module	JPL	Basic Alignment	Send beam through system. Check for pupil & focus alignment & fringes.	Pencil beam alignment laser Flat wave front IR source
OMSS	HIA	Basic Alignment and functionality	Send beam through system. Check for pupil & focus alignment on DMs and WFS	Pencil beam alignment laser Flat wave front visible source Coordinate measuring machine

AOC	LLNL	Powerup	Boot computer and close AO loops	
IFS	UCLA	Basic Alignment	Check focus and vignetting	IR pencil beam alignment laser Flat wave front IR source

Table 11.1 Subsystem Post-Shipment Acceptance Tests

The initial testing will take place at the Laboratory for Adaptive Optics in Thimann Hall at the UCSC campus. When the OMSS arrives all the subsystems will be transferred to the UCO/Lick shops high-bay, where assembly, integration and testing will take place.

11.1.2 Integration

The UCO/Lick shops high-bay will be the location of system assembly and integrated testing, which will take place in the November 2009 through December 2010 time period. Assembly of the subsystems into the system will occur inside a cleanroom area. Assembly will proceed as follows:

- Install cleanroom in high-bay prior to OMSS arrival. The cleanroom is designed to minimize dust accumulation during assembly. It may or may not be combined with the cold room to be described later, depending on feasibility and efficiency in combining these. The level of the cleanroom specification is yet to be finalized but will most likely be class 100 [1].
- The OMSS is brought in on its handling cart (supplied by HIA) [2]. The handling cart holds the system in the horizontal orientation (equivalent to the Gemini ISS side port).
- The small optical bench with the telescope simulator and its sources is mounted on the back side of the handling cart's ISS interface port.
- Any optical cells that were removed from the OMSS for shipping are re-installed. Alignment is confirmed using the GPI Artificial Source Unit (ASU) and possibly the telescope simulator.
- The CAL module is mounted on the OMSS using the CAL module handling cart which has a vertical adjustment capability. The CAL module is initially aligned using the coordinate measuring machine and the CAL sub-system fiducials. Adjustment is initially through the use of machined shims on the mounting bipods, then with fine adjustment on the bipod arms. This will be adequate to propagate light through the system. The final optical alignment is accomplished using light propagated through the AO relay from the ASU. The CAL-IFS P&C pair will be initially aligned using a test camera jig at the IFS input plane.
- The Integral Field Spectrograph is mounted onto the OMSS using a mounting A-frame supplied by UCLA. It is aligned to mechanical reference positions using a coordinate measuring machine, and optically aligned to light coming from the calibration system, initiated at the ASU. Alignment is achieved with machined shims at the mounting fixtures, and with manual base adjustments of the CAL-IFS P&C pair.

11.2 Sub-system Acceptance Tests

Subsystem acceptance tests will be performed at the subsystem providers' home institutions. Upon assembly during I&T the systems will be adjusted to internal static alignment, to the diffraction limit, using the telescope simulator and fiber optical sources to serve as test stars. Final subsystem tests can then be performed by each subsystem provider to make sure it is operating to acceptable performance levels as assembled. This is not a complete repetition of the earlier acceptance tests but is instead intended to instill reasonable confidence that the subsystems are working according to the requirements and assumptions made for the overall system to meet performance goals. Details of the optical alignment procedures for the subsystems are given in the GPI Optical Alignment Plan [3].

11.3 Integration plan

Integration will proceed as follows

- Prior to integration, a power distribution panel is installed at the testing location (panel or specifications provided by HIA to UCSC).
- Electronics racks are populated with remaining electronics components from the IFS, CAL and AOC subsystems.
- Bulkheads and cabling from the electronics racks to the optics enclosoure (OE) are installed, following the layout plan furnished as part of the OMSS design.
- Power is provided to the electronics racks and computers are booted and tested for functionality.

11.4 System Tests

11.4.1 AO Control System

- Test adaptive optics system closed-loop performance using the ASU or telescope simulator at the input focal plane and an infrared camera at the output focal plane of the CAL module. This camera will be looking at a pickoff just before the beam enters the IFS.
- Test the calibration system's ability to offload corrections to AO system.
- Validate integrated performance of AO system real time software and system control software by running typical observing scenarios. For the dynamic AO and calibration system performance tests, an aberration simulator will be inserted into the test beam of the telescope simulator.
- Test integrated system performance in a simulated science observation sequence, including IFU spectrograph and data reduction pipeline.

11.4.2 Optical Throughput

Test system for optical throughput according to a process developed by the PI, SE and I&T manager. Tests are yet to be defined.

11.4.3 Contrast

Test system for contrast/planet detectability according to a process developed by the PI and I&T manager. Tests are yet to be defined.

11.4.4 Flexure

The GPI instrument under normal observing observation will undergo a changing gravity vector since it is mounted in a Cassegrain focus position on the telescope. In order to test the integrated system under a varying gravity load, the entire OMSS and mounted subsystems will be mounted to a welder's jig, which can rotate the instrument around in two axes. These tests will take place outside of the clean room thus the instrument will be closed up to mitigate dust accumulation during the tests.

The process will involve tests that verify performance of the system at various orientations using the permanently mounted sensors within the instrument, for example the wave front sensor, calibration camera, and IFS camera and with an IR source from the telescope simulator. The open-loop flexure compensation will be tested, and refined, during these tests. Operation of the closed-loop flexure compensation loops will be verified.

Mounting to the flexure jig will include:

- ISS mount plate attached to welder's jig. This can be one that is designed to be detached from the handling cart, or a separate one.
- The small table holding the telescope simulator is mounted on the jig behind the ISS mounting plate so that it feeds the beam appropriately.
- The OMSS is mounted to the ISS mounting plate.

Care must be taken to maintain balance and overall safety at all times during this procedure.

11.4.5 Cold Test

The environment in the telescope dome is generally at cold temperatures, approximately zero degrees Celsius. Testing of the entire GPI system at this temperature will check for unanticipated thermal structural variations and for cold operations of the electro-optics and electronics equipment.

The cold tests will take place inside of an insulated wall chamber. Mounting will most likely by on the handling cart, as opposed to the flexure jig, but this is yet to be finalized depending on layout and efficiency of operations in the high-bay. It is a goal to repeat the thermal testing at two orientations, equivalent to the side and upward looking ports with the Gemini telescope zenith pointing.

11.4.6 Shake Test

When mounted on the Gemini telescope, the GPI instrument will be subject to a level of vibrations present in the telescope structure. A shaker piston, accelerometer, and spectrum analyzer will be used in

these tests. The piston will push on the ISS mounting plate as this is where vibration will enter to the OMSS when it is mounted on the telescope. There are two basic shaker tests:

- Shake the instrument with a white noise spectrum and measure the spectral response. This will help determine the resonant modes of the system, which can then be compared to mechanical design predictions.
- The vibration spectrum as provided by Gemini will be programmed to move the piston and basic performance tests will be performed to analyze how the vibration affects system performance.

11.5 I&T References

[1] Stowers, I.F., "Optical Cleanliness Specifications and Cleanliness Verification," SPIE 3782, 1999.

[2] Erickson, D., "GPI Opto-mechanical Overview," Document 1543, presented at the GPI Mid-term PDR, March 20, 2007.

[3] Gavel, D., and Saddlemeyer, L., (eds.), "GPI Optical Alignment Plan," , document GPI-PROJ_SYS-013, April 12, 2007 (draft version).